UNIVERSITY OF CALGARY

RELATIVE-AMPLITUDE-PRESERVING PRESTACK TIME MIGRATION BY THE EQUIVALENT OFFSET METHOD

by

Hugh D. Geiger

A THESIS
SUBMITTED TO THE FACULTY OF GRADUATE STUDIES
IN PARTIAL FULFILLMENT OF THE REQUIREMENTS FOR THE
DEGREE OF
DOCTOR OF PHILOSOPHY

DEPARTMENT OF GEOLOGY AND GEOPHYSICS

CALGARY, ALBERTA
DECEMBER, 2001

January 22, 2002

ABSTRACT

The kinematics of prestack time migration by the equivalent offset method (EOM) are well established as a simple reformulation of the double-square-root equation of seismic imaging. EOM is implemented as a nonrecursive diffraction stack, where samples in the data space are weighted, filtered, and summed to produce samples in the image space. In this dissertation, I determine the exact optimum weighting function that produces an image as a stack of angle-dependent reflectivities, and suggest practical alternatives that are appropriate for imaging using prestack time migrations.

The imaging problem is treated as an inverse problem consisting of an estimation problem and an appraisal problem. As is typical in geophysical inverse problems, a quantitative solution is provided for the estimation problem, and the appraisal problem is replaced by a validation process. A framework for qualitative validation of prestack time migration is described in terms of accuracy of focusing, accuracy of relative positioning, and accuracy of absolute positioning. Quantitative validation is achieved by testing the weighting functions using synthetic seismic data.

The theoretical basis for acoustic wavefield extrapolation is developed from first principles. The Kirchhoff-Helmholtz integral representation, the fundamental equation of wavefield extrapolation and imaging, provides a mathematical description of Huygens' principle, yields simplified formulae for forward and inverse extrapolation from planar and non-planar interfaces, and gives reciprocity relations for Green's functions and acoustic pressure.

Two methods of depth imaging are developed, Kirchhoff-approximate migration and Kirchhoff-approximate migration/inversion. Both rely on the Kirchhoff approximation at the reflecting surface. The second method, determined from Born-approximate inversion, provides exact expressions for constant-wavespeed common-offset migration/inversion required for relative amplitude preserving prestack time migration. The common-shot and common-receiver migration/inversion formulae are shown to produce biased estimates for asymmetric acquisition configurations. Simplifications to the depth imaging formulae are proposed that greatly increase the efficiency of implementation without any significant loss of accuracy.

Relative-amplitude-preserving EOM prestack time migration is tested against conventional processing over a portion of LITHOPROBE SNORCLE line 1. EOM prestack time migration can provide a better image for interpretation because it enhances imaging of steeper dips, and improves relative positioning of reflectors with conflicting dips.

ACKNOWLEDGMENTS

For as long as I can remember, I have found waves fascinating and mountains enchanting. When I discovered that the present configurations of the mountains could be thought of as a snapshot of much slower waves of construction and destruction, and that this complex process could be deciphered and understood with the help of images created from seismic wavefields, I was hooked. My efforts to combine these two interests have taken me on a long and truly wonderful journey. There are many people I would like to thank, including:

Fred Cook, for teaching me to ask the simple question, because the simple questions are often the most interesting and challenging, and certainly the most fun; for encouraging my love of teaching, even when it interfered with my research; and for financial support during the early part of my studies and continued support in the many other essentials of research during the latter part.

John Bancroft, for freely sharing his many wonderful ideas on seismic migration and imaging, for his unfailing excitement during our many discussions at the whiteboard in his office, and for emphasizing the necessity of a geometric explanation as a tool for both communication and understanding.

Gary Margrave, for his calm competence, guidance, and support during my pursuit of a mathematical explanation; for showing me that it is both possible and useful to pursue and develop expertise over a wide range of topics relevant to exploration seismology; for showing me that teaching a course is a great way to learn advanced material; and then for providing me with opportunities to teach at a high level.

Marcelo Epstein, who, through his efforts as a teacher and mentor in continuum mechanics, helped to erase my self doubts and nurtured in me the first inklings that I might have the capacity to not only understand this subject but to make a contribution.

Michael Slawinski, Don Easley and Patrick Wu, who honoured and challenged me by seeking out my advice and assistance with their own research questions and who, in their own ways, set me on the path ‘across the street’ to Marcelo.

Sam Gray, for asking some tough questions, for guidance towards some of the essential concepts, and for assistance obtaining some of the essential literature.

Kris Vasudevan, Rolf Maier, Arie van der Velden, Elissa Lynn, and Kevin Hall, for helping to make the Lithoprobe Seismic Processing Facility a great place to do research, for letting me spread my stuff all over the lab, and for believing me when I said (on more than one occasion) that I was going to be finished in a couple of weeks. Thanks to Rolf in particular for careful and attentive editing.

Henry Bland, Darren Foltinek, Malcolm Bertrand, and Xinxiang Li for access to technical support, disk capacity, and processing speed that was otherwise not available, always asked for on short notice, and always provided with unfailing professionalism. Thanks to Xinxiang in particular for excellent insights and fine work on EOM at a time when my progress stalled.

The many CREWES and Lithoprobe students who shared their research problems with me, even when they were not planning to seek my advice. And the staff and faculty of the Department of Geology and Geophysics and the Gallagher library, who (to use an apt metaphor) let eat more than my share of donuts!

This thesis would not have been possible without the generous financial support from ‘the Grandmas’—Dot, Eileen, and Jill—who helped to keep our kids in clothes, toys, music, gym, and more; support from ‘the Grandpas’—Doug and Ernest—who helped keep us in a warm and expanding house as our family grew; and, most of all, support and love from my partner in life—Sheelagh—who worked harder and more consistently than I did on all things of real importance. Finally, thanks to Erin, Heather, and Ross, who seemed to understand why Daddy couldn’t always read them stories at bedtime or take them to the zoo, and who are all still saving for university! I am indeed fortunate to have had this opportunity to pursue my dream.

To Sheelagh, Erin, Heather, and Ross

TABLE OF CONTENTS

LIST OF TABLES

LIST OF FIGURES

CHAPTER 1: INTRODUCTION

1.1 MOTIVATION FOR THIS STUDY

Controlled-source reflection seismology is the most effective geophysical tool available for imaging the internal structure of the Earth's crust and upper mantle. Of the geophysical techniques, it provides the best resolved images at depth and can provide detailed information about subsurface rock properties. However, the processing of reflection-seismic data into an interpretable image requires a significant computational effort, often under expert supervision (e.g. Gray, 1998a). A reasonable goal, therefore, is to seek improvements to the efficiency, accuracy, and utility of existing imaging techniques.

One such technique is the equivalent offset method (EOM) of prestack time migration (Bancroft and Geiger, 1994; Bancroft et al., 1998). The kinematic or traveltime component of EOM prestack time migration is well established as an exact reformulation of the double-square-root (DSR) equation (Bancroft and Geiger, 1994; Fowler, 1997a[1]; Bancroft et al., 1998; Margrave et al., 1999; Li, 1999). The Fourier analogue of space-time EOM prestack time migration, known as the equivalent wavenumber method (EWM) of prestack time migration, is derived in Margrave et al. (1999). They propose a dynamic or amplitude component that, unfortunately, cannot be implemented easily in

---

[1] Fowler (1997a) describes a number of transformations from input acquisition variables to intermediate variables that in turn can be converted to fully migrated variables by a hyperbolic stack. EOM is one such transformation. Another well-known transformation is known as DMO-PSI (dip moveout prestack imaging, see Gardner et al., 1986; Forel and Gardner, 1988). Bancroft et al. (1998) compare EOM with DMO-PSI. EOM depends on a rough estimate of wavespeed (Li, 1999; Wang et al., 2000) while DMO-PSI is independent of wavespeed, although this independence is purchased at the cost of a radial DMO.

the space-time domain and does not produce a 'true-amplitude' stacked image, where peak amplitudes are proportional to an average of angle-dependent reflectivity. Cary (1998) suggests that the required amplitude component can be derived from the acoustic migration-inversion formula for the common-shot acquisition configuration, as given by Docherty (1991), and that the required weighting function for EOM prestack time migration will include Jacobians relating both the acquisition configuration and the output migrated image to the equivalent-offset domain (the intermediate domain of binned data created when using EOM prestack time migration). However, Cary does not establish that the common-shot migration-inversion formula is the correct starting point, nor how these Jacobians can be easily calculated. Fowler (1997b) also identifies the Jacobians as a key to the amplitude component, but does not determine how they might be calculated.

Thus, a comprehensive theoretical basis for true-amplitude EOM prestack time migration needs to be established. In this dissertation, a complete theoretical development is provided that yields expressions for 2-D, 2.5-D, and 3-D constant-wavespeed prestack modeling and migration. The migration expressions are then simplified to yield expressions suitable for practical application in Kirchhoff-type prestack time and prestack depth migrations (i.e. diffraction stack migrations—see Dellinger et al., 2000; Jaramillo et al., 2000). The simplifications are appropriate given seismic data from an inhomogeneous subsurface (i.e. with non-constant wavespeed) and given the averaging inherent in the output image, which is a sum of prestack migrated gathers. Additional expressions are provided that take advantage of coordinates in equivalent offset domain. Although amplitudes of the imaged reflectors are no longer 'true' as defined by Gray (1997), they remain consistent over a wide range of dips, depths and changes in acquisition configuration. The resulting imaging technique is best described as a 'relative-amplitude-preserving' EOM prestack time migration.

1.1.1 Economic and scientific value of reflection seismology

Reflection seismology has proven its economic and scientific value in the search for both petroleum and minerals, as well as in our quest to understand the structure and evolution of the Earth's crust and upper mantle. Worldwide expenditure for geophysical services is estimated to have exceeded US$4 billion in 2000, down from a peak of around US$7 billion in 1998[2]. The majority of these expenditures are for the acquisition, processing and library sales of reflection seismic data[3]. In fact, reflection seismic technology is the most significant technology influencing the oil and gas exploration and production business[4].

The reflection-seismic method spearheads the efforts of a number of national and international geoscience programs, including Canada's LITHOPROBE[5]. To date, more than 14,000 km of land and more than 3000 km of marine reflection seismic profiles have been processed and interpreted by LITHOPROBE geoscientists (Vasudevan et al., 2000). The patterns observed in these reflection seismic images allow geoscientists to project a detailed knowledge of surface geology into the subsurface, to compare images from different transects, and to constrain interpretations with numerical, physical and conceptual models of tectonic and depositional processes. Hence, an improved imaging

---

[2] First Break, November 1999, v. 17.11, p. 366.

[3] Non-exclusive seismic data sales are now estimated to account for the majority of new technology research, engineering and capital investment in seismic data acquisition (Elrod and Walker, 2000)

[4] As cited in surveys of projected worldwide E & P expenditures in 2000 for over 100 international oil and gas companies and more than 200 independents in Canada and the US (First Break, v. 18.2, p. 45).

[5] Other significant efforts include EUROPROBE, COCORP, BIRPS, DEKORP, ECORS, and INDEPTH.

technique could enhance existing interpretations and provide a better tool for future investigations.

1.1.2 Objective: efficient and accurate EOM prestack time migration

In this dissertation, I present a comprehensive physical and mathematical basis for EOM prestack time migration. An overview and careful critique of a variety of established imaging techniques leads to simplifications that are appropriate given the assumptions underlying the physics and mathematics, and given the limitations inherent in conventional reflection-seismic data sets. The practical goal of these simplifications is to reduce the computational effort and simplify the task of obtaining an image while retaining the accuracy of the basic theory. The expected result is an image that can be interpreted with more confidence than one produced by either conventional techniques or previous implementations of EOM prestack time migration (Bancroft et al., 1998; Margrave et al., 1999). In fact, on a test portion of LITHOPROBE SNORCLE[6] line 1, van der Velden et al. (2001) and van der Velden and Cook (2001), have already demonstrated that EOM produces better images of subsurface crustal structure than LITHOPROBE's conventional imaging approach of NMO, stack, and poststack phase-shift migration.

1.1.3 Apology to the reader for a long introduction

Some readers experienced in exploration seismology might consider the topics covered in this introduction as basic and perhaps unnecessary. However, I feel that the overall perspective on prestack time migration presented here is unique, and therefore valuable. The reader will also find important original contributions in the introduction. Although I

---

[6] Slave-NORthern Cordillera Lithospheric Evolution (SNORCLE) line 1 was acquired in 1996. Results from the original processing and interpretation can be found in Cook et al. (1999).

believe that the introduction should be read as a whole, the reader is welcome to skip to section 1.7 for a summary of original contributions presented in this dissertation, including those found in the introduction and appendices.

This introduction covers a significant amount of material, but the material and the order of presentation have been chosen with a specific intent in mind: to avoid pitfalls associated with conventional concepts and definitions used to describe seismic imaging in general, and prestack time migration in particular. Thus, I begin with basic principles of reflection seismology and work towards a clear definition of the main problem addressed in this dissertation.

Although I ask the reader to suspend their preconceptions, brevity demands that the reader be familiar with the basic theory, terminology and methods of reflection seismology and seismic imaging. Yilmaz (2001), Sheriff (1991), and Claerbout (1985) provide excellent descriptions, but occasionally resort to concepts and definitions that I prefer to avoid. Some alternatives are suggested in this chapter.

1.1.4 Towards an alternate approach to the kinematics and dynamics of prestack time migration

As an example of a concept that is in need of revision, consider the conventional derivation for prestack time migration, which typically begins by assuming a constant-wavespeed[7] subsurface. This assumption quickly leads to the conclusion that a non-recursive implementation of prestack time migration is strictly valid only for a constant-wavespeed subsurface, and perhaps justifiable for a subsurface with vertical variations in

[7] Here I follow Bleistein et al. (2001) and use the term wavespeed to refer to the material property that determines the speed of wave propagation, instead of the commonly used but imprecise term 'velocity'.

wavespeed. But practical experience shows that useful images can be obtained in areas with complex lateral and vertical variations (e.g. Gray, 1998a). These considerations suggest that the conventional derivations for prestack time migration are insufficient, or perhaps that the conventional criteria used to judge migration images are stated incorrectly. I argue that both could be revised, and propose an alternate approach. The following paragraphs expand on this discussion.

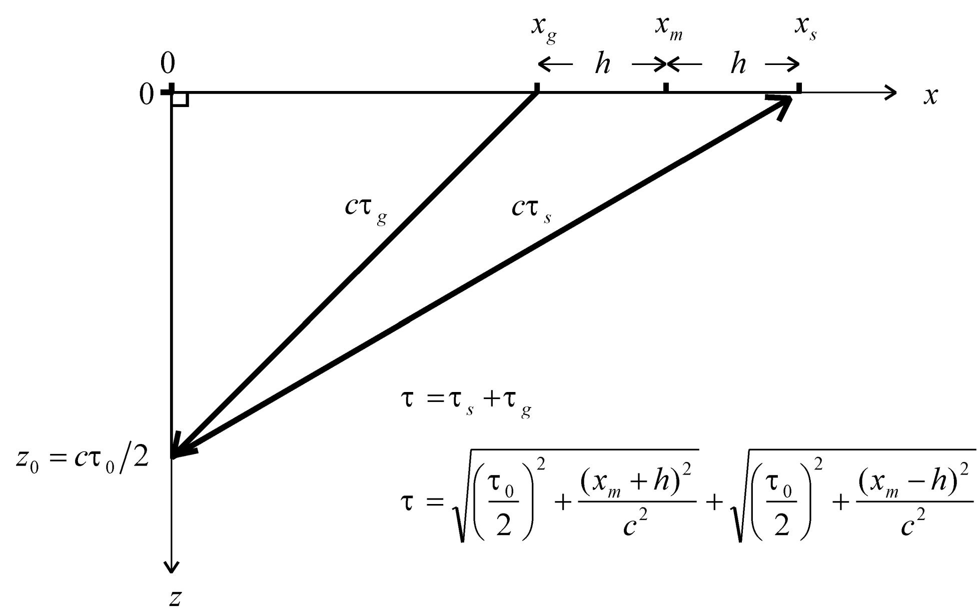

Figure 1.1. Equation (1.1) is derived by application of the Pythagorean theorem.

A basic derivation of the kinematics of prestack time migration can be found in Claerbout (1985 p. 163-165), who assumes a constant-wavespeed medium with wavespeed c and a 2-D acquisition configuration on a planar surface. The kinematics of prestack time migration can be derived by application of the Pythagorean theorem (Figure 1.1), yielding Claerbout's equation (3), which can be re-expressed as

$$\tau = \sqrt{\left(\frac{\tau_0}{2}\right)^2 + \frac{(x_m+h)^2}{c^2}} + \sqrt{\left(\frac{\tau_0}{2}\right)^2 + \frac{(x_m-h)^2}{c^2}}\,. \tag{1.1}$$

In equation (1.1), τ is the total traveltime from the source location to a subsurface point and back to the receiver location. The source-receiver midpoint is a distance x_m from the surface location directly above the subsurface point, while h is half the distance between the source and receiver. The two-way traveltime τ_0 is the total traveltime given a zero-offset source and receiver located directly above the subsurface point, i.e. when surface distances $x_m = 0$ and $h = 0$. The same equation applies in 3-D if both x_m and h are radial distances. A similar derivation can be found in Bancroft et al. (1998), who refer to equation (1.1) as the double-square-root (DSR) equation and use it as the basis for deriving the kinematics of EOM prestack time migration.

Claerbout also defines a different (but conceptually similar) DSR equation for double-downward continuation of the frequency-domain wavefield in either source-receiver or midpoint-offset wavenumber coordinates. The midpoint-offset DSR equation (Claerbout, 1985, equation 17, p. 181) can be re-expressed as

$$k_z = \frac{1}{2}\sqrt{\left(\frac{2\omega}{c}\right)^2 - \left(k_m + k_h\right)^2} + \frac{1}{2}\sqrt{\left(\frac{2\omega}{c}\right)^2 - \left(k_m - k_h\right)^2}\ , \qquad (1.2)$$

where ω is frequency and k is wavenumber. This DSR equation forms the basis for deriving the kinematics and dynamics of EWM (Margrave et al., 1999).

Claerbout makes the following statement about equation (1.2): “the double-square-root equation contains most nonstatistical aspects of seismic data processing for petroleum prospecting” (Claerbout, 1985, p. 181). The alternate viewpoint, as argued in this dissertation, is that the kinematic component of the DSR equation (expressed as equation 1.1) can be considered as a statistical migration operator, where we choose the best-fit ‘migration wavespeed’ c_{mig} for each output point in the image space. In section 1.5.2, I derive equation (1.1) for an inhomogeneous medium by a Taylor series expansion of squared-traveltime perturbations, and show that the migration wavespeed is a function of the curvature of the wavefield recorded on the surface, i.e. a best-fit parameter that is only indirectly related to subsurface wavespeed. The dynamic component suggested by equation (1.2) will be shown to be incorrect, because it is based on the concept of double-downward continuation of the prestack data. Hence, the derivation of the dynamic component also requires an alternate approach. The dynamic problem turns out to be much more difficult than the kinematic problem. Finding a practical solution is one of the main goals of this dissertation.

1.1.5 Overview of Chapter 1

In Section 1.2, reflection seismology is described as an echolocation technique, and migration as a transformation from a data space to an image space. In Section 1.3, I introduce some of the basic concepts and physical principles of reflection seismology. In Section 1.4, geophysical inverse theory is applied to the seismic imaging problem, and is shown to be the foundation for both the statistical kinematic approach and the theoretical dynamic approach. In Section 1.5, a new derivation of the DSR equation is presented. The DSR equation is shown to be a reasonable approximation for the kinematics of prestack time migration in a generalized inhomogeneous media. In Section 1.6, I return to the kinematics and dynamics of EOM prestack time migration. The kinematic solution has already been shown to be exact, and so do not need to be addressed further. However, previous approaches to the dynamics are shown to be in error. Thus, a dynamic solution is still required. The objectives and main contributions of the dissertation are summarized in Section 1.7.

1.2 BASIC PRINCIPLES OF REFLECTION SEISMOLOGY

In essence, reflection seismology is a remote-sensing technique based on the principles of echolocation[8]. An energy source at the surface of the Earth introduces sound waves that propagate through the various rock layers in the subsurface. Abrupt changes in the density and/or elastic moduli of the rock—which typically correspond to layer boundaries or structural discontinuities—impede the transmission of the sound waves. At each impedance contrast, or ‘reflector’, a small fraction of the propagating energy is reflected or diffracted and returns to the surface as a faint echo of the source. The magnitude of the fraction is commonly referred to as the reflection coefficient or the reflectivity. Receivers that measure either acoustic pressure or particle motion remotely sense the ‘reflection events’ that propagate back to the surface. The corresponding amplitudes are digitally recorded as time series known as ‘seismograms’, where the zero time on each seismogram is the initiation time of the source. To obtain repeated echoes from each reflector element in the subsurface, the basic bistatic experiment is repeated for numerous source and receiver locations distributed over the surface. The collection of seismograms can be thought of as forming a synthetic aperture. The overall objective is to process the seismograms to create an image or representation of the subsurface reflectors.

---

[8] *The New Penguin Dictionary of Science* defines echolocation as: A technique for finding the distance, and sometimes direction, of a remote object. A measurement is made of the time taken for a pulse of ... sound to reach the object and return from it after reflection”. *A Dictionary of Science* (Oxford University Press) and others restrict use of the word to the far more complex physiological process employed by animals such as bats. Using radar or sonar terminology, reflection seismology could also be described as a bistatic (i.e. source and receiver are separated) synthetic aperture approach to acoustic imaging.

Undesired signals are also recorded, including various direct and indirect arrivals from the source that do not represent primary reflections or diffractions, and signals from other natural and cultural sources. These undesired signals are considered as ‘noise’. The seismograms are processed to remove noise and to shape the desired reflections to represent a band-limited impulse corresponding to the arrival time of the reflected or diffracted source signal. Typically, additional corrections (such as time shifts or ‘statics’) are applied so that the seismograms correspond to a simpler physical model than the actual unknown true subsurface.

1.2.1 The data space

The collection of processed seismograms will be referred to here as the ‘data space’. The data space could be one-dimensional (i.e. a vector of all data elements), which will prove useful in Section 1.3 where the process of migration is described using matrices. More typically, the data space is multidimensional, with a ‘vertical’ dimension corresponding to traveltime on the seismograms, and a number of ‘horizontal’ dimensions corresponding to the coordinates chosen to define unique source and receiver locations for each seismogram[9]. Often, absolute and/or relative spatial coordinates for the source and receiver locations are transformed into more convenient coordinates, such as the midpoint location between the shot and receiver, the horizontal offset distance from shot to receiver, and an azimuth direction. Other possible horizontal coordinates include ordered numerals identifying unique sources, receivers, midpoints, and/or offset bins. The seismograms can then be sorted based on the chosen coordinates, which in turn determines the number of horizontal dimensions.

---

[9] Rice (1953) proposes a ’resolved-time’ hybrid data/image space with horizontal coordinates in time (see also Rice, 1955).

1.2.2 Migration: from data space to image space

The purpose of migration is to construct an image of the subsurface by transforming the information in the seismograms from the data space to an ‘image space’ (Figure 1.2). In essence, migration attempts to transform the reflection events into a ‘reflectivity map’ that represents the spatial distribution of impedance contrasts in the subsurface. Patterns in the reflectivity map can often be directly interpreted as representing layer boundaries or structural discontinuities. These geometries, in turn, can be interpreted to yield the depositional and tectonic history. At each subsurface location, it might also be possible to estimate the reflection coefficient (i.e. the fraction of energy reflected) at multiple angles of incidence. These amplitude variations with angle (AVA) can be interpreted to yield lithology, porosity, and fluid type (e.g. SEG course notes by Hilterman, 2001).

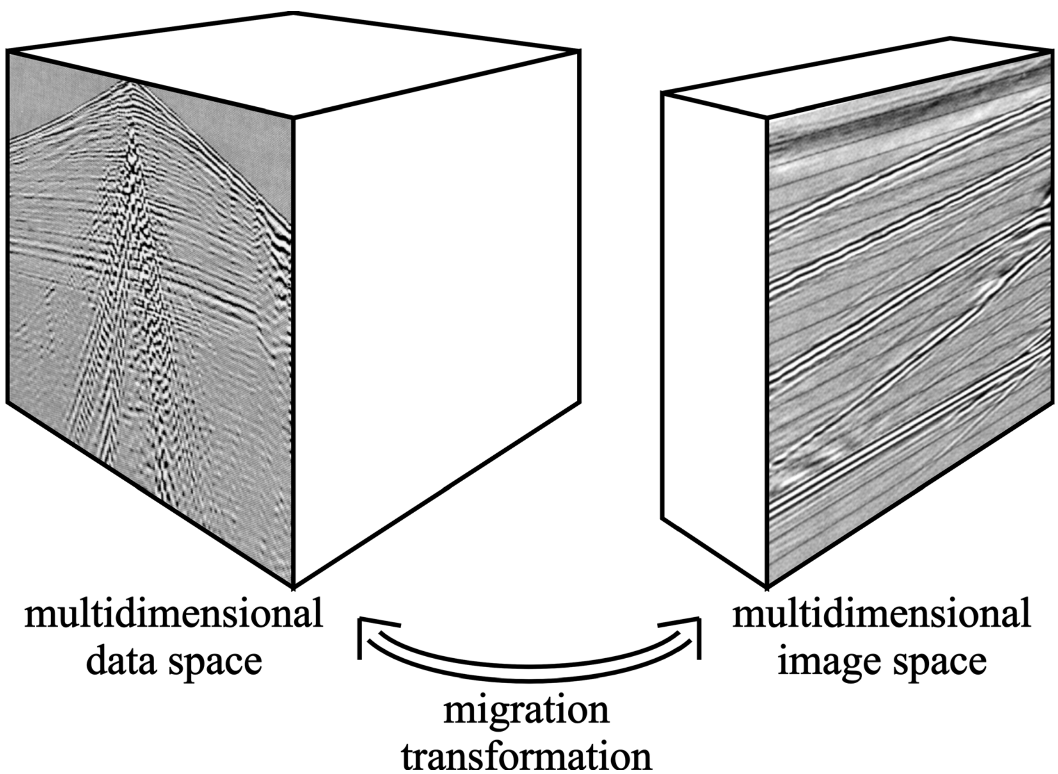

Figure 1.2. Seismic migration is a transformation from a data space to an image space.

In the above description of migration, I have avoided any reference to a particular choice of coordinates for the image space, or to a particular method of transformation. This is in contrast to commonly accepted definitions that imply spatial coordinates for the image space. Sheriff (1991) defines migration as "an inversion operation involving rearrangement of seismic information elements so that reflections and diffractions are plotted at their true locations", while Yilmaz (2001) states that "migration moves dipping reflections to their true subsurface positions and collapses diffractions, thus increasing spatial resolution and yielding a seismic image of the subsurface". The phrases "true locations" and "true subsurface positions" are somewhat ambiguous[10], but suggest that migration should produce an image with accurate absolute positioning, i.e. the coordinates of the image should be spatial coordinates and the positioning of reflectors within the image should correspond to their true subsurface location. These definitions are too restrictive, as they exclude a number of practical image spaces and their respective transformations. The image space of "true subsurface locations" is, however, a useful concept for developing a physical understanding of a hypothetical exact migration (see Section 1.3).

The more general description adopted here follows Claerbout (1992 p. 107), who defines migration as "any data-processing program that converts data into an image". Thus a seismic image can be any representation of the subsurface — just as a photograph is a

---

[10] What is "truth" in any practical implementation? As stated by Snieder and Trampert (1999 fn. p. 123) "It is not so difficult to formulate a vague definition such as 'the true model is the model that corresponds to reality and which is only known to the gods.' We are not aware of any definition that is operational in the sense that it provides us with a set of actions that could potentially tell us what the true model really is." An alternate approach follows first-order logic and yields a possibly infinite set of true models, where a true model is one that solves the inverse problem. However, this leads to a large and inefficient search space. The nature of truth in inverse theory is a topic of current research (e.g. Pfenning, 2001).

representation of objects in the real world — and the coordinates of the image can be any convenient coordinates. Depending on the coordinates, a criterion such as “accuracy of absolute positioning” may not have much meaning. Instead, we are probably more interested in accuracy of resolution (i.e. focusing) and accuracy of relative positioning (i.e. that the spatial relationship between two reflectors in the subsurface is preserved in the image space). These two criteria can be applied to any image space even when the concept of absolute positioning is meaningless. A good analogy is a photograph, which contains useful information despite distortions such as perspective and foreshortening.

1.2.3 The image space

In general, the method of transformation determines the dimensions and coordinates in the image space. Since the image space purports to be a representation of the subsurface, it typically contains two-dimensional image sections (i.e. vertical planes) or three-dimensional image volumes that represent their respective sections and volumes in the subsurface. However, the image space may contain additional horizontal dimensions such as angle, offset, or azimuth.

The concept of the image space as a representation implies that the coordinates of the image space do not need to be spatial coordinates. Typically, the vertical coordinate is either depth or traveltime and the horizontal coordinate(s) are absolute or relative distance (plus angle, offset, azimuth, etc. as required). Other possible horizontal coordinates include ordered numerals identifying unique sources, receivers, midpoints, and/or offset bins. Seismic images are often displayed with these non-intuitive horizontal coordinates, a practice that is partly historic, but can provide important information about acquisition parameters that might affect the interpretation.

Often, processes are applied that reduce the number of dimensions in the data space or image space to two or three, corresponding to the two or three dimensions of the desired image section or image volume representing the subsurface. These processes will be referred to here using the generic term ‘stacking’, although this term has a specific definition in seismic processing as the process of summation of data elements over offset after the application of normal moveout correction (NMO) or normal moveout correction followed by dip moveout correction (NMO-DMO). If stacking is applied to a data space, the result will be referred to as the stacked data space, or specifically as a stacked data section or stacked data volume if the number of dimensions is known. A transformation from a stacked data space to an image space with the same number of dimensions is defined here as a poststack migration. A transformation from an unstacked or partially stacked data space to any possible image space is defined here as a prestack migration.

The output image space for a prestack migration often includes an extra dimension of offset or angle. A stack after prestack migration can collapse this extra dimension, a process defined here as stacking prestack migrated gathers. The output image elements will be referred to here as ‘stacked reflectivity’. EOM prestack time migration is a transformation from an unstacked data space, through a stacked data space known as ‘equivalent offset gathers’, to image sections or image volumes of stacked reflectivity.

1.2.4 Towards a definition of time migration

The modifier ‘time’ in prestack time migration has not yet been defined. The alternative is usually considered to be some type of ‘depth’ migration[11]. Based on the discussion

[11] The terms ‘depth migration’ and ‘time migration’ should be treated simply as jargon that indicates whether or not an algorithm is capable of producing a correct image in the presence of strong lateral wavespeed gradients (Margrave, 2000). This suggests a spectrum of algorithms, with time migrations at

above, one might conclude that the output from a time migration is an image space with a vertical dimension of time. Yilmaz (2001 p. 464) supports this by stating “the migration process that produces a migrated time section is called a time migration”. For now, this is a reasonable working definition. A more precise definition is presented in Section 1.5.4.

1.3 BASIC PHYSICAL CONCEPTS OF WAVEFIELD PROPAGATION AND MIGRATION

In the previous section, I suggested that the processed seismograms contain reflection events, and then described migration as a transformation from the data space to an image space. In this section, I introduce some basic concepts of mathematics and physics required to understand a hypothetical exact true-amplitude migration, i.e. the transformation that maps a reflection event in the data space to a reflector in an image space of ‘true subsurface locations’, where the peak amplitude represents the angle-dependent reflectivity. At the end of this section, these concepts are expanded to a broader class of transformations and hence possible image spaces. The intent is to provide a background for the basic mathematics of geophysical inversion presented in Section 1.4 and for the more detailed mathematics of seismic wavefield propagation and seismic imaging presented in Chapters 2 and 3.

1.3.1 Geophysical inversion: driven by the seismic data

The purpose of geophysical inversion is to estimate earth properties from geophysical data. The basic idea is to infer a mathematical expression that explains how the physics of the experiment combines with the earth properties to create the recorded data. In this mathematical expression, the physics of the experiment and the recorded data are the

---

one end and depth migrations at the other end. Thus a time migration is strictly valid in $c(z)$ settings (perhaps only for constant wavespeed c), whereas a depth migration is valid for $c(x,y,z)$.

known quantities, while the earth properties are the unknown quantity. In principle, the expression can be solved or 'inverted' for the unknown quantity, thereby giving us the desired estimates of the earth properties.

Initially, we have only one known quantity — the geophysical data. For seismic reflection data, these are the seismograms recorded on the surface of the earth plus the source and receiver locations and characteristics. The other known quantity — the physics of the experiment – needs to be expressed in a mathematical form that could explain the data given the earth properties we wish to estimate. Determining synthetic data from the earth properties is called the forward problem. The inverse problem works in the other direction, since we need an expression that takes the data and 'backs out' some or all of the physics of the experiment, leaving the desired estimates. The resulting mathematical expression can be considered as a transformation from the data space to the image space, and therefore as a migration.

With both migration and geophysical inversion, we are free to base our forward and inverse mathematical expressions on any useful relation between the data space and the image space, no matter how approximate, suspect, or nonexistent the underlying physics. There are two reasons why this might be an acceptable approach. A useful image might be created using an empirical expression that cannot be explained by current physics and mathematics. Or, we might be willing to accept an image that, in some respects, is a distortion of the subsurface, especially if the image can be easily produced. Still, the most fruitful approach is to create expressions based on an understanding of the physics of the experiment. As stated previously, we start with one known quantity—the data. The information in the data places a fundamental constraint on the physics in the mathematical expressions and on the estimates we can obtain. Thus, it makes sense to start with the data and work backwards towards an understanding of the relevant physics.

1.3.2 Traveltime and amplitude information in the seismograms

The seismograms in the data space can be thought of as containing two main types of information: traveltime and amplitude. The traveltime for a particular reflection event in a single seismogram is the total time taken by the impulse of source energy as it propagates from the source location to the reflector element and back to the receiver location. Theory, supported by intuition and experiment, suggests that the traveltime for a nondispersive wave depends on the travelpath taken by the propagating energy as well as the wavespeed of the material along this travelpath. Fermat's principle of 'stationary time' tells us that knowledge of the wavespeed alone is sufficient to determine a travelpath[12]. Thus, for an exact migration that creates an image at true subsurface locations, the wavespeed is assumed to be known wherever a travelpath in the subsurface is possible.

The amplitude of the reflection event provides information about the strength of the impedance contrast. Assuming that the behavior of the source and receiver are well understood, the amplitude recorded at the receiver depends on a number of factors in addition to the impedance contrast at the reflector of interest. These factors include (but are not limited to): geometrical spreading of the propagating wavefield, transmission losses at discontinuities in the media, various mechanisms for anelastic attenuation, multiples, and noise.

Given the small displacements associated with wavefield propagation, and assuming that attenuation effects have been compensated for (or are negligible), earth materials can be approximated by a perfectly elastic continuum. Then, the behavior of a propagating

[12] Fermat's principle can only be formulated for convex slowness surfaces (M. Slawinski, pers. comm.)

wavefield is completely determined by the density of the material and elastic constants (stiffnesses) that relate stress and strain within the material. These material properties define wavespeeds for different modes of wave propagation. However, for the general case of an anisotropic and inhomogeneous earth, analytic solutions for determining travelpaths for a given mode are not available and numerical solutions are both approximate and costly.

The problem is greatly simplified by assuming that the subsurface is isotropic (but can still be inhomogeneous) and by neglecting transmission effects and mode conversions. If we are interested only in the compressional mode of wave propagation, the earth can be further approximated by acoustic materials. The acoustic earth model is the starting point for the theoretical development that begins in Chapter 2.

I now make two assumptions: that seismic reflection data can be considered as high frequency[13], i.e. that the kinematics of wavefield propagation can be accurately described by raypaths; and that wavefield propagation is linear, i.e. that the principle of superposition applies. Although these assumptions can be supported by theory, it is more important that they be supported by experimental evidence. Otherwise, a new theory would be required. Given that current practice does support these assumptions (e.g. Yilmaz, 2001), they can be considered as reasonable, independent of any theoretical justification.

1.3.3 Hagedoorn told us to use diffraction curves

For a given source and receiver location, the locus of all possible reflector locations that satisfy a constant traveltime is commonly referred to as an ‘isochron surface’. Thus, there

---

[13] They satisfy the WKBJ assumption (see Section 2.5).

is an isochron surface (possibly multivalued) for each reflection element in the data space. Applying the general principle of echolocation, and assuming a sufficient data space, the intersection of isochron surfaces determined from different seismograms identifies a unique location for the reflector element in the true subsurface. But the seismograms contain many reflection events from many different subsurface reflectors, so it may be next to impossible to choose the correct reflection event on each seismogram[14].

There are two approaches to this problem. The brute force approach is to determine the isochron surfaces for all elements in the data space, and then take the subset of these that intersect at one location in the true subsurface. This subset will identify specific traveltimes on particular seismograms. An alternate but equivalent approach is to take

---

[14] The identification of reflection events was a significant historical problem in the development of reflection seismology (see the collection of papers in Gardner, 1985). Imaging was limited to mapping subsurface reflectors where a reflection event could be clearly correlated from one seismogram to the next. Given a model of the subsurface wavespeed [typically $c(z)$], the location of the reflector could be estimated based on the change in traveltime of the reflection event over a small array of seismograms. Gaby (1945) was the first to propose that better relative positioning might be achieved in an image space with a vertical coordinate of time rather than depth. Hagedoorn (1955 p. 121) recognized the importance of isochron surfaces: "fundamentally, any (migration) method must be based on the determination of surfaces of equal reflection times", and the relationship between isochron curves and diffraction curves (see Hagedoorn's Fig. 6 on p. 93). However, Hagedoorn's diffraction curve lies, not in the data space, but in an intermediate space of "vertically plotted points" with a vertical coordinate of depth instead of time, a practical necessity in the days of chart migration before computers. His method produces an exact migration for common-offset sections if offset-dependent isochron and diffraction curves are used, but he proposes a practical method that is a simplification to zero-offset (see Hagedoorn's Fig. 25 on p. 122) and hence anticipates the conventional poststack migration of an NMO corrected stack with no DMO correction. This might explain why the necessity for DMO was not 'discovered' until the mid 1970's (Doherty, 1975; Sherwood et al., 1976; Judson et al., 1978; see also Yilmaz, 1980; Deregowski and Rocca, 1981).

one location in the subsurface and determine corresponding traveltimes in the data space. Obviously, these are the same traveltimes as found from the subset of isochrons. In the data space, the surface of these traveltimes is called a 'diffraction surface'[15]. Unfortunately, the diffraction surface tends to cross most reflection events, and, if tangent to a reflection event, has a tighter curvature. Thus, it is not immediately clear how the principle of echolocation can be applied.

An elegant solution was proposed by Hagedoorn (1955). Instead of reconstructing the reflector at a single output location, Hagedoorn suggested that the envelope of isochron surfaces from a (vertically plotted) reflection event would reconstruct the reflector surface. Bleistein (1999) presents a similar argument, but starts with a reflection event in a 2-D zero-offset data space (x,t) and assumes a 2-D medium (x,z) with constant wavespeed c (Figure 1.3a). Suppose the x-coordinate of the zero-offset source and receiver locations is denoted by $\bar{x}$, the reflection event is located in the data space at traveltime $t(\bar{x})$, and the apparent slowness is given by $\partial t(\bar{x})/\partial\bar{x}$. Then the family of isochron curves (circular arcs) can be described as

$$F\left(\mathbf{x}(\bar{x}),\bar{x}\right) = t(\bar{x}) - \frac{2}{c}\sqrt{(x-\bar{x})^2 + z^2} = 0\,, \tag{1.3}$$

where $\mathbf{r} = (x,z)$ is an arbitrary point on the isochron curve for a fixed $\bar{x}$ (Figure 1.3b). At different source-receiver locations $\bar{x}'$, the traveltime $t(\bar{x}')$ is different, and thus a new set of values $\mathbf{x}' = (x',z')$ is required to define another isochron curve in the family.

---

[15] To call it a surface, we have to assume smooth variations in traveltime with perturbations in the source and receiver locations. This is a reasonable assumption except in the vicinity of caustics. This smoothness assumption underlies the Taylor series expansion for the generalized hyperbolic traveltime relationships developed in Section 1.6.

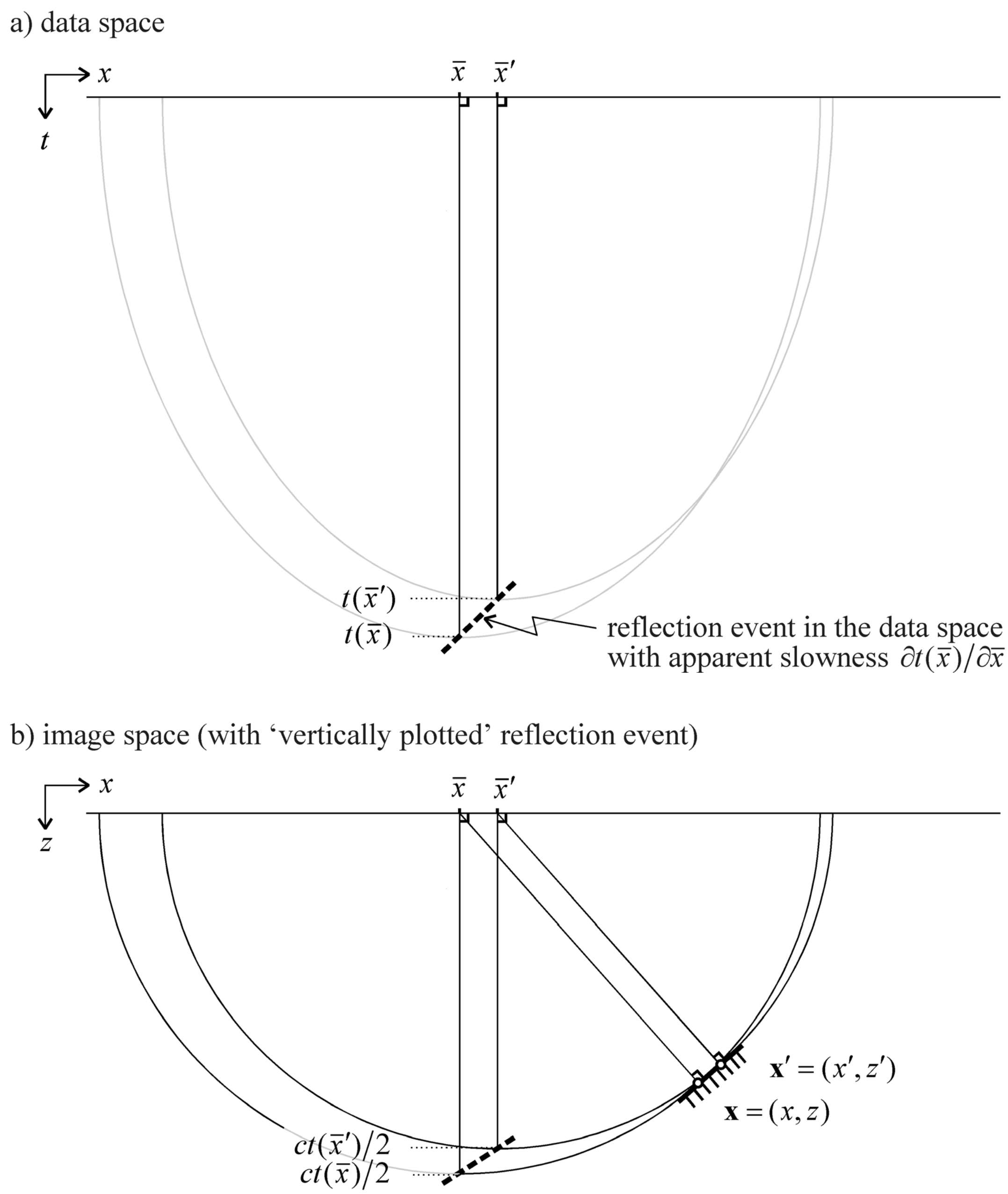

Figure 1.3. Given a zero-offset source-receiver location $(x, z) = (\bar{x}, 0)$, each reflection event at time $t(\bar{x})$ with apparent slowness $\partial t(\bar{x})/\partial\bar{x}$ in the data space (1.3a) defines an isochron curve $\mathbf{x} = (x, z)$ in the image space (1.3b). As $\bar{x}$ and $t(\bar{x})$ vary along a particular reflection event [e.g. to $\bar{x}'$ and $t(\bar{x}')$], a family of isochron curves $F\left(\mathbf{x}(\bar{x}), \bar{x}\right)$ is defined. In a medium with constant wavespeed c, each curve is a circular arc $t(\bar{x}) - \frac{2}{c}\sqrt{(x-\bar{x})^2 + z^2} = 0$. The envelope of isochron curves defines the reflector in the image space.

As Bleistein (1999) points out in an appendix, the envelope of the isochron surfaces satisfies two requirements: first, that each point of the envelope is also a point on some curve of the family for some value of $\bar{x}$, i.e. the envelope can be thought of as a parametric curve with $\bar{x}$ as the parameter; and second, right where the curve $F = 0$ is in contact with the envelope at $\mathbf{x} = \mathbf{x}(\bar{x})$, the tangents of the two curves must be collinear or anticollinear. Bleistein shows that, based on these two requirements, the partial derivative with respect to $\bar{x}$ is zero, i.e.

$$\frac{\partial F(\mathbf{x}(\bar{x}),\bar{x})}{\partial \bar{x}} = \frac{\partial t(\bar{x})}{\partial \bar{x}} - \frac{\partial}{\partial \bar{x}}\left(\frac{2}{c}\sqrt{(x-\bar{x})^2 + z^2}\right) = 0\,. \tag{1.4}$$

Given known values for $\bar{x}$, $t(\bar{x})$, and $\partial t(\bar{x})/\partial \bar{x}$, equations (1.3) and (1.4) can now be solved for the unknowns x and z, giving the desired location for the reflector in the subsurface. Although mathematically feasible, solving equations does not provide much insight into Hagedoorn's method.

Bleistein suggests a second method: 'to solve one of the equations for $\bar{x}$, usually the second, as a function of $\mathbf{x}$, and then substitute the result back into the other equation'. Expanding this statement leads to some valuable insight. First, consider that equation (1.3) can also be thought of as a family of diffraction curves (hyperbolas – see Figure 1.4a) at all possible values $t(\bar{x})$ for a fixed point on the reflector $\mathbf{x} = (x, z)$, i.e.

$$F(\mathbf{x}, \bar{x}(\mathbf{x})) = t(\bar{x}) - \frac{2}{c}\sqrt{(x-\bar{x})^2 + z^2} = 0\,. \tag{1.5}$$

Taking the partial derivative as before yields

$$\frac{\partial F(\mathbf{x},\bar{x}(\mathbf{x}))}{\partial \bar{x}} = \frac{\partial t(\bar{x})}{\partial \bar{x}} - \frac{\partial}{\partial \bar{x}}\left(\frac{2}{c}\sqrt{(x-\bar{x})^2 + z^2}\right) = 0\,, \tag{1.6}$$

which is identical to equation (1.4) but now expressed in terms of the diffraction curves. Equation (1.6) says that, in the data space, the apparent slowness of the reflection event

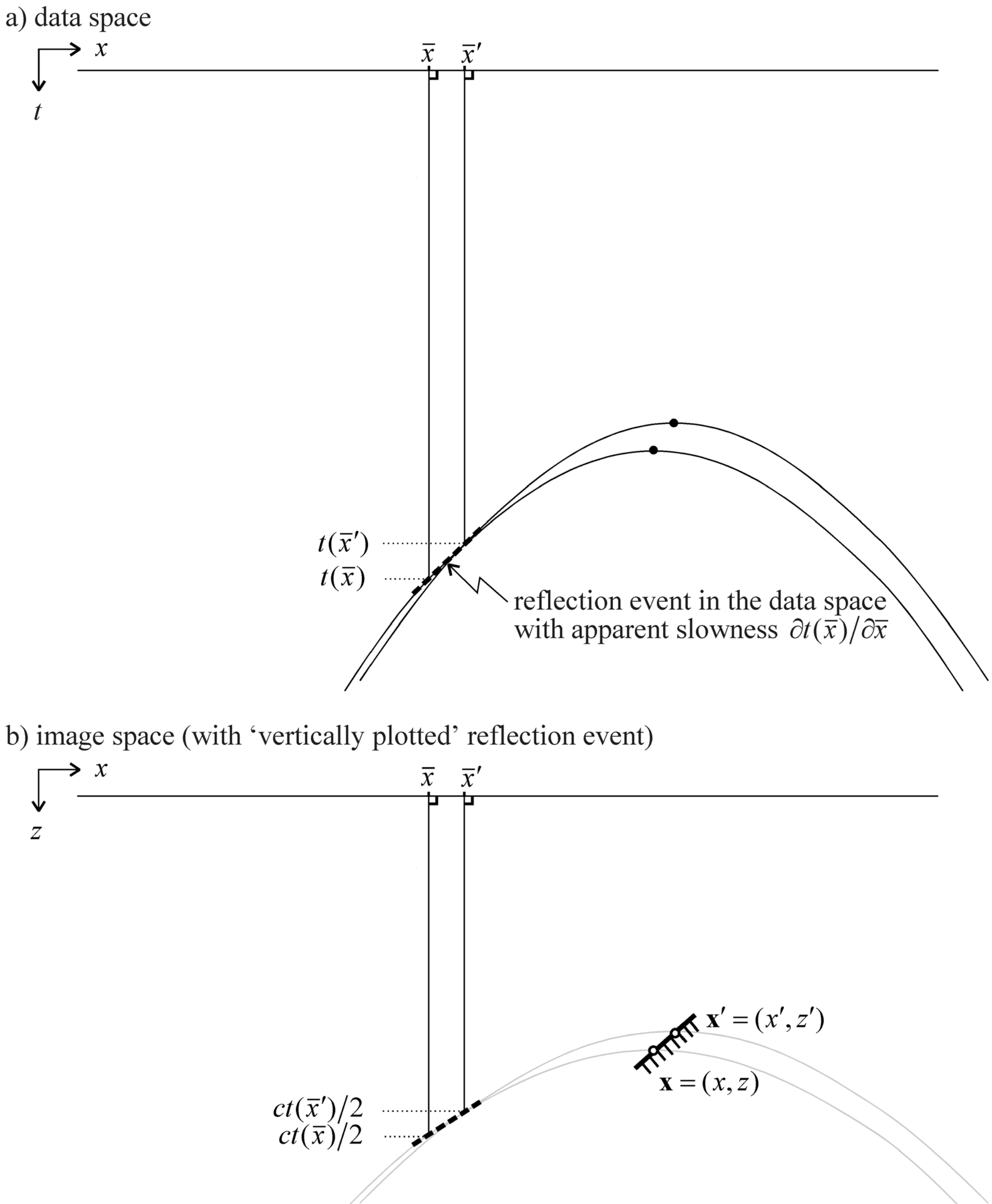

Figure 1.4. Each reflector location $\mathbf{x} = (x, z)$ in the image space (1.4b) defines a diffraction curve $\left(\bar{x}, t(\bar{x})\right)$ in the data space of zero-offset source-receiver locations (1.4a). As $\mathbf{x}$ varies along a particular reflector in the image [e.g. to $\mathbf{x}' = (x', z')$], a family of diffraction curves $F\left(\mathbf{x}, \bar{x}(\mathbf{x})\right)$ is defined. In a medium with constant wavespeed c, each curve is a hyperbola $t(\bar{x}) - \frac{2}{c}\sqrt{(x-\bar{x})^2 + z^2} = 0$. The envelope of the diffraction curves is the reflection event in the data space with apparent slowness $\partial t(\bar{x})/\partial \bar{x}$.

and the apparent slowness of the diffraction curve must be equal, i.e. that they are tangent. Thus the envelope curve for the diffraction curves is the reflection event in the data space.

Using diffraction curves, the practical method for finding the reflector is as follows: find the diffraction curve that is tangent to the apparent slowness of the reflection event in the data space and plot the position of the reflection curve at the apex $\mathbf{x} = (x, z)$ in the image space (Figure 1.4b). As Hagedoorn points out (p. 98 and his Figure 11, reproduced as Figure 1.5): "Obviously, from these considerations, the position of the migrated point P can be determined uniquely by use of the chart of curves of maximum convexity[16] alone, because the intersection P of the curve of maximum convexity with the curve of equal reflection times through Q must lie on the central axis of the chart of curves of maximum convexity." Note that Hagedoorn's statement is valid for a constant wavespeed subsurface or for a subsurface with vertical variations in wavespeed [i.e. $c(z)$ as illustrated in Figure 1.4a]. Lateral variations in wavespeed introduce additional complications that will not be discussed here (see Alcock, 1943; Black and Brzostowski, 1994). I return to the constant wavespeed case.

Equations (1.3) and (1.4) are now examined to see if there is a similar relationship for the isochron curves. Given that the isochron curves exist in the space of true subsurface locations, it is helpful to re-express both equations in dimensions of length by multiplying through by $c/2$, yielding

[16] A curve of maximum convexity is a diffraction curve converted to the space of vertically plotted points. The space of vertically plotted point is a data space where the vertical coordinate is the depth-converted zero-offset traveltimes, or depth converted NMO-corrected traveltimes for nonzero-offset.

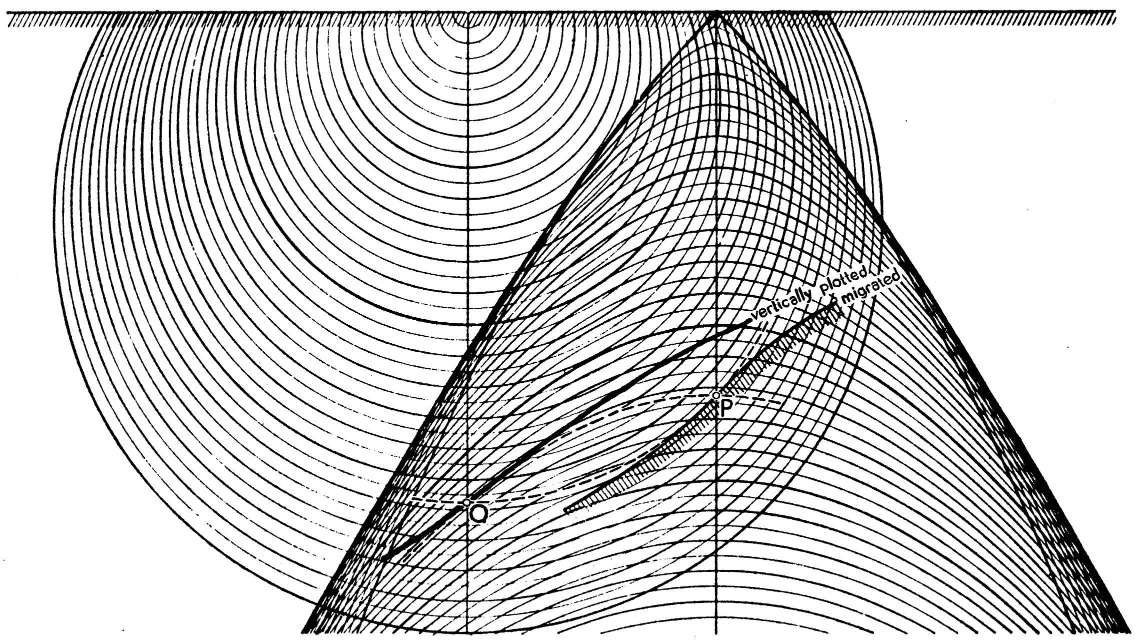

Figure 1.5. (Figure 11 of Hagedoorn, 1955). A reflection event at location Q in the space of vertically plotted points maps to a reflector at location P in the image space. The isochron curve and the diffraction curve that pass through Q and P are defined by the same equation [compare equations (1.3) and (1.5)]. The envelope of the isochron curves is the reflector, while the envelope of the diffraction curves is the reflection event.

$$\frac{c}{2}t(\bar{x}) = \sqrt{(x-\bar{x})^2 + z^2}\ , \tag{1.7}$$

and

$$\frac{c}{2}\frac{\partial t(\bar{x})}{\partial \bar{x}} = \frac{\partial\sqrt{(x-\bar{x})^2 + z^2}}{\partial \bar{x}}\ . \tag{1.8}$$

Equation (1.7) is the equation of the isochron curve (a circle). The RHS of equation (1.8) is the change in radius $\partial r = \partial\sqrt{(x-\bar{x})^2 + z^2}$ as the center of the isochron curve (the source-receiver location) is perturbed a distance $\partial \bar{x}$. Using basic triangle relationships as shown in Figure 1.6, the RHS equals $\sin\beta$, where β is the geologic dip. The LHS of equation (1.8) equals $\tan\alpha$, where α is the dip in the unmigrated section of vertically plotted points. Thus, equation (1.8) is the 'migrator's equation' $\tan\alpha = \sin\beta$ (e.g. Sheriff, 1991).

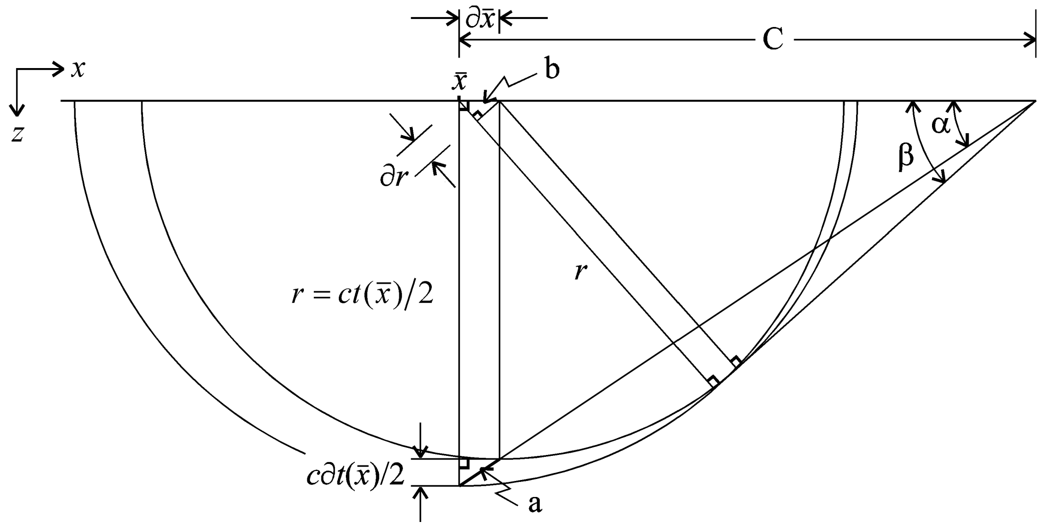

Figure 1.6. Graphical proof that equation (1.8) is the 'migrator's equation' $\tan\alpha = \sin\beta$. The small right-angle triangles a and b are similar to the large right-angle triangles with angles α and β, respectively. The large triangles share a common side C and their opposite sides are both equal to isochron radius $r = ct(\bar{x})/2$. Thus, $\tan\alpha = \sin\beta$.

Using isochron curves, the practical method for finding the envelope curve is as follows: find the isochron curve of radius $ct(\bar{x})/2$, measure and convert the apparent slowness to its depth equivalent $\tan\alpha$, use the migrator's equation to solve for the geologic dip β, determine the point on the isochron curve with dip β, and then plot this as the point $\mathbf{x} = (x, z)$ on the envelope curve. For a subsurface with vertical variations in wavespeed, the procedure is not so easily quantified, but can be simplified by using a chart of isochron curves identified by traveltime, with dip angles marked in physical units of apparent slowness. Then the traveltime and apparent slowness measured in the data space can be plotted directly as the reflector in depth. In fact, this was the accepted procedure (e.g. Musgrave, 1952; Dix, 1952) prior to Hagedoorn's novel method utilizing diffraction curves. So Hagedoorn did tell us how to do migration, but clearly argues that the reflector envelope can be found more easily using diffraction curves rather than isochron curves.

1.3.4 Hagedoorn's method as backprojection or backpropagation/imaging

Hagedoorn's method can be extended to a multidimensional data space, in which case the corresponding families of curves are multidimensional isochron surfaces and diffraction surfaces. The results from the previous section suggest that the most effective way to implement a migration is by summation over the portion of the diffraction surface that is tangent to the reflection event. The optimum portion of the diffraction surface corresponds to an aperture of seismograms in the data space, i.e. to an 'optimum migration aperture'. This is an active area of current research (Vanelle and Gajewski, 2001a; Sun, 2000). The synthetic tests presented in Chapter 4 utilize these concepts to minimize computation while ensuring accuracy.

As pointed out by Bleistein (1999), the process of finding an envelope of a family of curves is closely related to the method of stationary phase. The diffraction surface can be thought of as a function of phase. By summing the amplitudes of the seismograms as defined by this phase function, we might expect that the major contribution will occur where the amplitudes are stationary. Details of the method of stationary phase are not provided in this dissertation. Good discussions related to seismic imaging can be found in Bleistein et al. (2001) and Bleistein and Gray (2001).

Unfortunately, it is difficult to determine a priori which portion of the diffraction surface is tangent to a reflection event (i.e. the stationary point) and if there is more than one tangency. Thus, migration is typically implemented as a summation over the entire diffraction surface, i.e. as the brute force method mentioned earlier. Then, summation over a diffraction surface and superposition of isochrons are identical procedures (although practical considerations usually favor a diffraction summation). Since both concepts are valuable, they will be used interchangeably depending on the context.

Consider summation over an entire diffraction surface in the data space. Although it is clear from the previous section that the true subsurface location of the reflector can be identified, there is no assurance that the amplitude of the reconstruction will have any relevance to the desired reflectivity map of the subsurface. Typically, the subsurface is complicated and so there will be many reflection events in the data space. Hence, a given diffraction surface will cross many reflection events (as well as noise). The corresponding amplitudes on the seismograms will be part of the summation. It would appear that, unless we can assume that the summation of these undesired amplitudes will all fortuitously cancel, they will seriously affect the amplitude of the reconstructed reflector, and may distort reconstruction of the location.

The truly amazing thing is that, if the correct weighting function is chosen for the migration, these unwanted amplitudes in the summation do cancel (often even incorrect weighting functions result in reasonable cancellation). The details of how this might work are related to Huygens' principle as embodied in the Kirchhoff-Helmholtz theory of forward and inverse wavefield extrapolation (developed in Chapter 2 and Appendix B), or to backprojection of the data as embodied in the theory of generalized Radon transforms. The theory of generalized Radon transforms is not discussed in detail in this dissertation (see Beylkin, 1982, 1985; Miller et al., 1987; Jaramillo, 1999; Jaramillo and Bleistein, 1999), although the general results form a basis for the weighting functions developed in Chapters 3 and 4.

A weighted summation over an entire diffraction surface (or the equivalent, a weighted superposition of all possible isochrons) can be considered as a backprojection of the recorded data or as a backpropagation combined with an imaging condition (Esmersoy and Miller, 1989). Both can be implemented as a 'weighted diffraction stack'. The weighting function includes compensation for amplitude effects such as geometrical spreading and a Jacobian[17] that relates the surface sampling to an equi-angular distribution of isochrons at the image point. The resulting image of the subsurface can, in principle, provide accurate estimates of angle-dependent reflectivity. As mentioned previously, determining the correct weighting function is one of the primary objectives of this dissertation. The details are left to the main body of the dissertation.

Note that two purposes have now been given for the weighting function. The first purpose is to reconstruct the reflector location without contamination from other reflection events. This purpose can be expanded to include other sources of contamination such as insufficient data, other elastic wavefields in the data, operator aliasing, coherent noise, and a host of other possibilities. The second purpose is to reconstruct a peak amplitude that is an accurate estimate of the angle-dependent reflection coefficient, or an unbiased average of angle-dependent reflection coefficients. These two purposes may conflict, although it is a reasonable assumption that success of the second depends on the first. The discussion in this dissertation is limited to the second purpose.

Reconstructing accurate locations without regard to meaningful amplitudes is often called 'structural imaging'. Often, the term 'migration' is limited to transformations that yield structural images, and occasionally to transformations implemented as inverse wavefield extrapolation and imaging. Reconstructing accurate angle-dependent reflection coefficients is often called 'true-amplitude migration', or 'inversion'. Often, the term

---

[17] A Jacobian is the factor that arises with a change of variables in integration, for example the terms in forward modeling and migration formulas associated with equal-area sampling over a planar acquisition surface (the Earth's surface), as opposed to the mathematically simpler (but less practical) equal-area sampling over a spherical surface surrounding the spherically symmetric Green's functions.

'inversion' is limited to transformations implemented as a backprojection or as a least-squares solution to a matrix formulation (see section 1.4). I have chosen to use the term migration as a general descriptor for a transformation from the data space to an image space, in which case it is probably more realistic to consider 'relative-amplitude preserving' migrations.

In this and the previous section, the isochron surface was assumed to be a function of the spatial coordinates of the true subsurface locations, but the concept of an isochron surface can be generalized to any image space and its defining coordinates. As well, an isochron surface can be created for any point in the data space, not just reflection events. This suggests a more general definition for an isochron surface: the locus of all possible elements in the image space corresponding to a single point in the data space. An analogous concept relates a single point in the image space to a surface in the data space. This surface is referred to as a diffraction surface.

1.4 SEISMIC IMAGING AS GEOPHYSICAL INVERSE THEORY

Geophysical inverse theory provides a mathematical framework that allows us to make inferences about physical properties in the Earth's subsurface given data collected on the surface[18]. Seismic imaging methods, which go by various names including migration, migration/inversion and least-squares migration, are special cases of more general wavefield inversion procedures (Scales, 2001). Thus, the mathematics used to describe inversion provide an excellent platform for understanding imaging concepts as well as a foundation for the detailed mathematics and physics presented in this dissertation. The

---

[18] In general, the data do not need to be collected on the surface, but this restricted definition is appropriate for the seismic imaging problem addressed in this dissertation.

mathematics presented in this section follows previous work by Gray (1997). Here, I attempt to provide a slightly different perspective and, in particular, address issues related to time migration methods such as EOM.

1.4.1 Geophysical inversion and the validation process

The basic process of geophysical inversion can be separated into three steps (Figure 1.7). First, devise a mathematical expression, known as the forward problem, that describes the data in terms of the relevant physics and the desired subsurface properties. Second, use the forward problem to devise a mathematical expression that estimates the desired subsurface properties from the data. Finally, devise a mathematical expression that appraises how good these estimates are. Strictly speaking, the inverse problem is a combination of the latter two steps, which Snieder and Trampert (1999) call the estimation and appraisal problems[19].

The goal of geophysical inversion is to make inferences about physical properties in the Earth's subsurface. Thus we are free to choose any estimator, even if does not seem to be firmly based in relevant physics. This is a common situation in seismic processing and in many other areas of exploration geophysics where practicality, robustness, and successful application are more important criteria than the existence of a complete theoretical description. A good example is seismic deconvolution, which is based more on statistics than physics and yet satisfies all these criteria.

[19] In this dissertation, I follow the convention adopted in much of the seismic reflection literature and often use the term 'inverse' to describe the estimation problem by itself.

Even in the case of an arbitrary estimator, geophysical inverse theory can still be applied. The important problem becomes one of appraisal. However, devising a suitable expression for quantitative appraisal is seldom attempted. A more common approach is

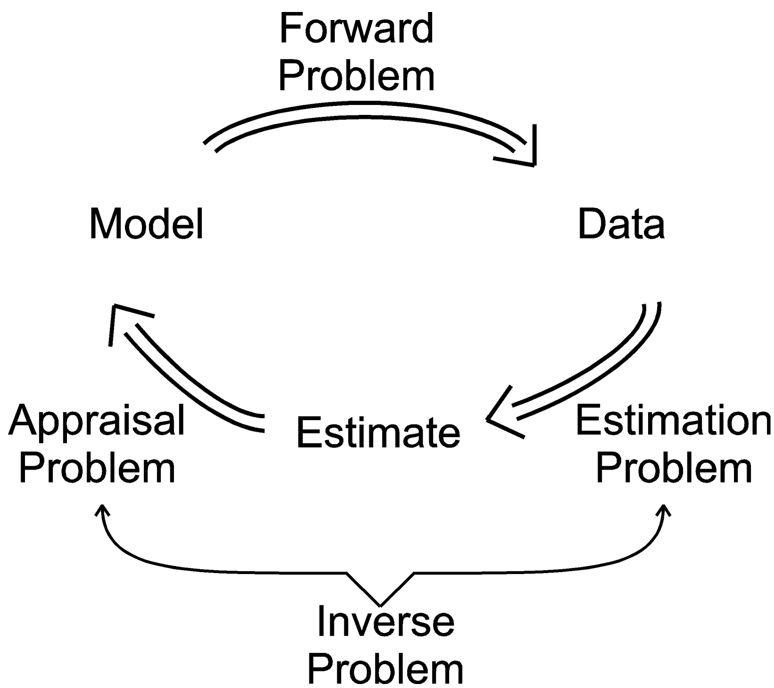

Figure 1.7. The inverse problem is a combination of the estimation and appraisal problems. In typical applications of seismic processing and imaging, only the estimation problem is addressed—and the estimation problem by itself is often referred to as the inverse problem. In this dissertation, the appraisal problem is replaced by a validation process, or assessed by qualitative (rather than quantitative) methods.

to replace the appraisal problem by a validation process. Common methods for validation include:

1. theoretical analysis using simple analytic forward problems;

2. quantitative or qualitative analysis comparing estimates from synthetic or physical model data against the known model parameters;

3. comparative analysis of estimates from field, synthetic, or physical model data against similar estimates from previously validated algorithms; and

4. comparative analysis of estimates from field data against well data or surface data projected into the seismic image (perhaps using geostatistics).

Another approach to the appraisal problem is to make a qualitative assessment of the origins and general characteristics of errors introduced by the estimation problem. Some of these characteristics may be acceptable, given the difficulty required to minimize them. For example, prestack time migration can often provide good focusing and accurate relative positioning of reflector elements with a loss of accurate absolute positioning. The concept of a qualitative appraisal categorized in terms of focusing, relative positioning and absolute positioning will be explored in more detail later in this introduction and appears as a recurring theme throughout the remainder of the dissertation. Note, however, that absolute positioning suggests a depth migration, which requires a detailed macro-model of the subsurface wavespeed. The estimation of the macro-model is an additional inverse problem with all the complications associated with estimation and appraisal (or validation). The imaging problem would be greatly simplified if this additional inverse problem could be ignored, or perhaps replaced by a simpler problem of determining estimators that are independent of the macro-model. In fact, this is exactly what prestack time migration offers. This alone is sufficient to justify prestack time migration as a valuable step in any processing sequence, even when the ultimate aim is an accurate depth migration. The following is a mathematical basis in support of this argument.

1.4.2 Towards a linear forward problem

The basic seismic experiment can be developed into a generalized mathematical expression that describes the forward problem:

$$d_i = f_i(m) + e_i, \tag{1.9}$$

where d_i is a discrete element of data (in an abstract n-dimensional space of measurements comprising the totality of samples, components, source and receiver characteristics and locations, etc.), f_i is a forward theory operator, m is the earth model, and e_i is a combination of measurement errors and misfit errors.

Although equation (1.9) represents the data space as discrete and possibly finite in number and extent, the data space could also be considered as continuous and infinite in number and extent, and therefore appropriate for the inverse wavefield propagation methods of Stolt (1978) and Schneider (1978) or the Fourier transform-like integral inversion methods of Cohen and Bleistein (1979), Cohen et al. (1986), and Bleistein et al. (1987)[20]. A continuous data space with infinite extent is assumed for much of the theory presented in this dissertation, partly because the forward theory operators are developed from principles of continuum mechanics, and partly because conventional approximations to the forward theory operators lead to linearized equations with known analytic inverses. However, data acquired in the real world are discrete and finite in number and extent. There is no approximation in the discrete representation if we assume a bandlimited experiment with adequate sampling.

Equation (1.9) is too general a representation for our intended purposes. The term $f_i(m)$ suggests a possibly nonlinear dependence of the forward theory operator on the model. A

---

[20] A complete description, with consistent notation, can be found in Bleistein et al. (2001).

linearized version will prove more useful for inversion and, since the discrete linear form can be expressed using matrix notation, is more useful for describing the approximations inherent in common migration schemes. The basic linearized form is given by Snieder (1999) as

$$d_i = \int_{\mathbf{x}} d\mathbf{x} f_i(\mathbf{x}) m(\mathbf{x}) + e_i \,, \tag{1.10}$$

where **x** is typically thought of as a vector of spatial coordinates, but could also be a generalized vector of model dependencies (e.g. frequency or angle of incidence).

Equation (1.10), although adequate, can be significantly improved by introducing a more explicit notation tailored to the seismic imaging problem. The basic intent of a more detailed notation is to provide additional physical insight. First, I explore the relationship between the earth model and the forward theory operator, and then discuss the significance of the error term.

1.4.3 Forward theory operator, earth model, misfit error, and data error

The earth model and the forward theory operator in equation (1.10) are linked, if only to maintain consistency in the physical units. One interpretation is that the earth model is a mathematical parameterization of specific physical properties (e.g. wavespeed and density) required to predict the data given the physics of the forward theory operator (Scales, 2001). An alternate interpretation is that the forward theory operator is an appropriate mathematical expression of specific physical phenomena (e.g. elastic wave propagation) required to predict the data given the parameterization of the earth model. Obviously then, there is a certain arbitrariness in choosing an appropriate combination of forward theory operator and model parameters, although an overly simple combination of model and forward theory operator could mean that much of the information in the data is described by the error term. As discussed previously, this may be acceptable depending on the tradeoff between the characteristics of error and the difficulties introduced by a more descriptive combination.

Typically, the appropriate combination of model and forward theory operator is often driven by the dictum "Ask only for what you deserve from the data"[21]. Properties such as wavespeed and density are well known to be 'blocky', i.e. they can be represented as piecewise continuous functions of the space coordinates with the jumps or steps located at the interfaces that give rise to reflections. Given the finite bandwidth of the seismic reflection data, it is not possible to obtain accurate estimates of full-bandwidth multi-step functions required to represent either wavespeed or density (see Figure 2.9 of Bleistein et al., 2001). A more appropriate goal is to invert for a physical property such as reflectivity, where each reflector can be represented by a singular function of a surface scaled by the angle-dependent reflectivity coefficient. With bandlimited data, then, the best estimate we could expect will correspond to a scaled bandlimited singular function whose peak value is the angle-dependent reflectivity coefficient.

The chosen earth model need only be a subset of the many possible physical parameters that might have an effect on the data. The forward theory operator could be functionally dependent on some of these other relevant physical parameters. For the seismic reflection problem, the classic separation places the rough portion of wavespeed and density (i.e. the angle-dependent reflectivity) into the model and the smooth portion of wavespeed (i.e. the macro-model) into the forward theory operator. Estimation of an accurate macro-model for the wavespeed can then be posed as a separate inverse problem, if required.

---

[21] Suggested by Bleistein et al. (2001) as a general guideline for solving ill-posed inverse problems such as the seismic inverse-scattering problem.

For time migration, an appropriate macro-model is chosen by simple statistical criteria such as a maximum coherency search and/or by qualitative criteria such as focusing and/or relative positioning in the image. That these two inversions can be treated as separate is related to the two main types of information—traveltime and amplitude—found in seismograms.

Note that, by choosing angle-dependent reflectivity, our earth model now depends on the forward theory operator. In other words, the earth model $m(\mathbf{x})$ is not a constant at any spatial location $\mathbf{x}$, but varies depending on the incident angle of the wavefield at the reflector. The incident angle is determined by the physics of the seismic experiment, as described by the forward theory operator. Thus, the set of physical experiments comprising the data for one inversion (an acquisition configuration) must support a single estimate of angle-dependent reflectivity. In practice, the data should include specular reflections from only one angle of incidence. Other angles of incidence and/or reflection should not produce specular reflections[22]. Otherwise, the estimate will be an average of angle-dependent reflectivities. Acquisition configurations that support these criteria include common-source gathers, common-receiver gathers, and common-offset gathers, as well as synthesized gathers that correspond to, for example, a plane-wave source. In general, a common-midpoint gather is not suitable, and an estimate derived from all the recorded data, as provided by Kirchhoff prestack time migration methods such as EOM, will estimate an average of angle-dependent reflectivities.

---

[22] As it turns out, an equally important criterion for an accurate and robust estimate is that these other angles of incidence and/or reflection must vary smoothly about the specular angle (Bleistein et al., 2001). Berkhout (1985) suggests a combined inversion that estimates reflectivity over a range of angles using all available data. The resulting estimate is a matrix of reflectivity values at each subsurface location. A concise summary can be found in Gray (1997).

With these considerations in mind, the linearized forward problem given by equation (1.10) can be re-expressed as

$$d_i = \int_{\mathbf{x}} dV f_i(\mathbf{x}, m_c) m_{R_\theta}(\mathbf{x}) + e(\int dV f_i m) + e(d_i), \tag{1.11}$$

where $\mathbf{x}$ now refers only to the spatial coordinate, $m_{R_\theta}(\mathbf{x})$ is the angle-dependent reflectivity, and $f_i(\mathbf{x}, m_c)$ the forward theory operator, now an explicit function of the subsurface location $\mathbf{x}$ and wavespeed macromodel m_c with all additional parameters (e.g. source and receiver characteristics and locations) denoted by the subscript (i). The error is explicitly represented as a combination of misfit error $e(\int dV f_i m)$ and measurement error $e(d_i)$. The notation chosen for angle-dependent reflectivity attempts to indicate an implicit dependence of the angle on the forward theory operator and hence on the acquisition configuration.

Equation (1.11) implies that there are no time-varying properties in the earth model $m = (m_c m_{R_\theta})$, a reasonable assumption even for time-lapse seismic studies where a set of experiments is repeated with intent of imaging 'snapshots' of an evolving model. The assumption of time invariance allows us to transform our forward theory operator from space-time to space-frequency, treat frequency as a constant, and hence reduce the dimensionality of the problem by one. This leads to simpler expressions for the forward theory operator (e.g. the Helmholtz equation instead of the wave equation), as well as all the usual benefits of computation in the frequency domain (e.g. multiplication instead of convolution, and that delta functions in time can be expressed as complex exponentials). Appendix A provides a brief review and establishes conventions as well as notation for delta functions, linear systems, and the Fourier transform.

Ideally, the forward theory operator $f_i(\mathbf{x}, m_c)$ should be a mathematical expression that explains all the physics relevant to the experiment. However, there is still a great deal of flexibility afforded by the error term, so it makes sense to choose a forward theory operator that simplifies the inversion problem with the expectation that it will not explain all of the data. Typically, we seek to express the forward theory operator in an analytic form that has a known analytic inverse or whose inverse can be determined numerically in a robust and efficient manner. Appropriate analytic theory operators for forward wavefield extrapolation and migration/inversion are developed in Chapters 2 and 3, respectively.

1.4.4 The estimation problem: resolution, misfit and measurement errors

Given that the forward problem is linear, the estimated model can by obtained as a linear combination of all the data elements:

$$\hat{m}_{R_\theta}(\mathbf{x}) = \sum_i f_i^{-g}(\mathbf{x},\hat{m}_c)d_i\,, \tag{1.12}$$

where $f_i^{-g}(\mathbf{x},\hat{m}_c)$ is the generalized inverse of the forward theory operator, now with dependence on an independently estimated wavespeed macro-model $\hat{m}_c$ and other factors implied by the subscript (i). For continuous data, the summation operator could be thought of as an integral over, say, acquisition configuration and time (or frequency). If so, some of the dependencies in the forward theory operator implied by the subscript (i) could then have to be stated more explicitly.

The relationship between the earth model $m_R(\mathbf{x})$ and the estimated model $\hat{m}_R(\mathbf{x})$ is found by substituting equation (1.11) into equation (1.12), yielding

$$\hat{m}_{R_\theta}(\mathbf{x}) = \underbrace{\int_{\mathbf{x}'} dV \sum_i f_i^{-g}(\mathbf{x},\hat{m}_c) f_i(\mathbf{x}',m_c) m_{R_\theta}(\mathbf{x}')}_{\text{finite resolution}} + \underbrace{\sum_i f_i^{-g}(\mathbf{x},\hat{m}_c) e\left(\int dV f_i m\right) + \sum_i f_i^{-g}(\mathbf{x},\hat{m}_c) e(d_i)}_{\text{error propagation}}, \tag{1.13}$$

The second term on the RHS of equation (1.13) describes the error propagation in the estimated model, i.e. the artifacts arising from application of the generalized inverse of the forward theory operator to the misfit and measurement errors. The first term on the RHS of equation (1.13) specifies the maximum resolution that can be obtained. This can be demonstrated by adding and subtracting the true earth model $m_R(\mathbf{x}) = \int_{\mathbf{x}'} dV\,\delta(\mathbf{x}-\mathbf{x}')m_R(\mathbf{x}')$:

$$\hat{m}_{R_\theta}(\mathbf{x}) = m_{R_\theta}(\mathbf{x}) + \int_{\mathbf{x}'} dV \left(\underbrace{\sum_i f_i^{-g}(\mathbf{x},\hat{m}_c) f_i(\mathbf{x}',m_c)}_{\text{resolution kernel}} - \delta(\mathbf{x}-\mathbf{x}') \right) m_{R_\theta}(\mathbf{x}')$$

$$+ \underbrace{\sum_i f_i^{-g}(\mathbf{x},\hat{m}_c) e\left(\int dV f_i m\right)}_{\substack{\text{misfit error} \\ \text{artifacts}}} + \underbrace{\sum_i f_i^{-g}(\mathbf{x},\hat{m}_c) e(d_i)}_{\substack{\text{measurement error} \\ \text{artifacts}}} . \quad (1.14)$$

If the resolution kernel $\sum_i f_i^{-g}(\mathbf{x},\hat{m}_c) f_i(\mathbf{x}',m_c)$ is equal to a delta function, the second term on the RHS of equation (1.14) disappears, and the estimated earth model is equal to the true earth model plus the error artifact terms.

The difference between the estimated earth model and (unknown) true earth model can be attributed to three basic factors: resolution error introduced by necessary approximations to the inversion operator combined with limitations inherent in the physical experiment, misfit error introduced by simplified physics of the forward model (simplified in both the forward theory operator and the chosen model), and measurement error arising from coherent and random noise recorded along with the ideal unknown true signal.

It would be a mistake to consider the resolution kernel to be a direct measure of spatial resolution, as wrongly suggested by Snieder and Trampert (1999). This will be true only if the error term in equation (1.11) contains no misfit error and the measurement errors are well behaved (i.e. uncorrelated with the forward theory operator). Consider an arbitrary forward theory operator with an exact inverse but a large misfit error. In this case, the application of the inversion operator to the error term, as shown in equations (1.13) and (1.14), could easily result in significant degradation of spatial resolution (e.g., a constant wavespeed forward modeling operator and inverse prestack time migration operator applied to data collected over a subsurface with complicated lateral and vertical wavespeed variations). On the other hand, the possible presence of a large misfit term does not necessarily indicate poor spatial resolution, although the artifacts might manifest themselves by poor absolute positioning.

1.4.5 Matrix notation: least squares and the conjugate transpose

Matrix notation simplifies presentation of the remaining concepts. Using matrix notation, where $\mathbf{m} = m_{R_\theta}(\mathbf{x})$ is the vector of earth model parameters (and so forth ,with bold capitals denoting matrices), equations (1.11) through (1.14) can be expressed as:

$$\mathbf{d} = \mathbf{Fm} + \mathbf{e}_{\mathbf{Fm}} + \mathbf{e}_{\mathbf{d}}, \tag{1.15}$$

$$\hat{\mathbf{m}} = \mathbf{F}^{-g}\mathbf{d}, \tag{1.16}$$

$$\hat{\mathbf{m}} = \mathbf{F}^{-g}\mathbf{Fm} + \mathbf{F}^{-g}\mathbf{e}_{\mathbf{Fm}} + \mathbf{F}^{-g}\mathbf{e}_{\mathbf{d}}, \tag{1.17}$$

and

$$\hat{\mathbf{m}} = \mathbf{m} + \left(\underbrace{\mathbf{F}^{-g}\mathbf{F}}_{\substack{\text{resolution}\\ \text{kernel}}} - \mathbf{I} \right)\mathbf{m} + \underbrace{\mathbf{F}^{-g}\mathbf{e}_{\mathbf{Fm}}}_{\substack{\text{misfit error}\\ \text{artifacts}}} + \underbrace{\mathbf{F}^{-g}\mathbf{e}_{\mathbf{d}}}_{\substack{\text{measurement error}\\ \text{artifacts}}} . \tag{1.18}$$

Equation (1.18) shows that, when the error terms are well behaved, perfect resolution is achieved if the resolution kernel is the identity matrix. However, the argument present in the previous paragraph (that the error artifacts could significantly affect spatial resolution) applies here as well.

As stated in the introductory paragraph to this section, all seismic imaging methods — including migration, migration/inversion and least squares migration — are special cases of wavefield inversion as described by geophysical inverse theory. Equation (1.16) is of particular interest. It states that the estimate we desire can be obtained by applying the generalized inverse of the forward theory operator to the data. Unfortunately, the generalized inverse is typically not available. In the following paragraphs, I provide a brief summary of some of the many ways that the generalized inverse can be approximated, and how these approximations relate to conventional seismic imaging techniques. This topic is well described in the literature (Pavis, 1989; Gray, 1997; Snieder and Trampert, 1999; Scales, 2001—and references cited therein).

There are three basic classes of inverse problems. If n is the number of parameters in the earth model and m is the number of data measurements, a problem is overdetermined if $m > n$ (i.e. data redundancy), underdetermined if $n > m$ (i.e. fundamental lack of data), and mixed if it contains characteristics of both. Most real seismological problems are mixed, in which case the pseudo-inverse solution is the unique one that simultaneously satisfies the least square criterion of overdetermined problems and the smallest model criterion for underdetermined problems.

For the unweighted least-squares problem[23], the pseudo-inverse solution can be found by minimizing the cost function

$$S = \|\mathbf{d} - \mathbf{Fm}\|^2 . \tag{1.19}$$

Standard least-squares procedures yield the following model estimate:

$$\hat{\mathbf{m}} = (\mathbf{F}^T\mathbf{F})^{-1}\mathbf{F}^T\mathbf{d} , \tag{1.20}$$

---

[23] See Scales (2001) for a discussion of the weighted least-squares problem.

where $(\mathbf{F}^T\mathbf{F})^{-1}\mathbf{F}^T$ is called the pseudo-inverse of the forward theory operator. Gray (1997) cites LeBras and Clayton (1988) in pointing out that $\mathbf{F}^T$ can be computed from its definition $\langle \mathbf{d}, \mathbf{Fm} \rangle = \left\langle \mathbf{F}^T\mathbf{d}, \mathbf{m} \right\rangle$, where the L_2 inner product $\langle \mathbf{x}, \mathbf{y} \rangle$ is the volume integral $\int_V dV \mathbf{x}^T\mathbf{y}$, and states that by writing out the integrals for both inner products, one can show that $\mathbf{F}^T$ is a poorly scaled kinematic migration operator that uses dynamic ray tracing to compute amplitudes and traveltimes. In other words,

$$\hat{\mathbf{m}} = \mathbf{F}^T\mathbf{d} \tag{1.21}$$

can be considered a reasonable estimate of the earth model. Thus, the transpose of the forward theory operator (or the conjugate transpose for a complex operator) provides a theoretical basis for a reasonable migration algorithm. As pointed out by Claerbout (1992), the transpose is a good approximation primarily because the phase of the transpose $\mathbf{F}^T$ is the same as the phase of the inverse $\mathbf{F}^{-1}$. Thus the additional term $(\mathbf{F}^T\mathbf{F})^{-1}$ in the least squares estimate (equation 1.20) is merely a weighting function that affects only the amplitude. Often, true-amplitude processing is not applied to the data prior to migration, so the extra effort required to estimate these weights is not warranted. A good discussion of the complete least-squares approach (equation 1.20), including considerations such as efficiency and practicality, can be found in Gray (1997) and so will not be discussed here.

When the forward theory operator $\mathbf{F}$ is dependent on phase, applying the transpose $\mathbf{F}^T$ is equivalent to convolution with the time-reversed forward theory operator, a process of cross-correlation sometimes referred to as ‘matched filtering’. Recall the care taken previously to place the wavespeed macro-model in the forward theory operator, while keeping the angle-dependent reflectivity in the earth model. Claerbout (1992, p. 108) argues that “It is a pitfall to imagine that carefully constructing the correct amplitude versus offset (i.e. AVO or angle-dependent reflectivity) in a diffraction operator will make the corresponding migration operator more effective.” The reason is because “effort expended to get the correct AVO in the modeling operator affects the migration operator (the conjugate) without necessarily making it closer to the inverse.”

1.4.6 The Delphi scheme: inverting a cascade of forward operators

In all the preceding discussions, it has been assumed that the forward problem describes the complete seismic experiment, from source initiation to wavefield recording. In order to make it tractable, the forward problem was linearized, but the forward theory operator was treated as a single entity. Consider instead the seismic experiment as a cascade of linear operators. Each of these component linear operators might have a simple analytic inverse, or be well approximated by a transpose. This is the approach adopted by Berkhout (1981), who introduced the ‘Delphi’ scheme (de Bruin, 1992, whose work forms the basis for the discussion presented here). The Delphi forward theory operator for a 2-D or 2.5-D common-shot seismic experiment[24] can be re-expressed as

$$\mathbf{d}(z_0) = \mathbf{G}_{up}(z_0, z_g)\mathbf{d}(z_g) = \left[\sum_{m=1}^{M} \mathbf{W}_{up}(z_0, z_m)\mathbf{R}(z_m)\mathbf{W}_{down}(z_m, z_0)\right]\mathbf{S}_{up}(z_0, z_s)\mathbf{s}(z_s), \qquad (1.22)$$

where the elements in the data vector $\mathbf{d}(z_g)$ are the monochromatic responses at the receiver locations (each could be an array of buried receivers at depth z_g) ‘regularized’ to a 1xN receiver vector $\mathbf{d}(z_0) = \mathbf{G}_{up}(z_0, z_g)\mathbf{d}(z_g)$ at the non-reflecting surface z_0, $\mathbf{s}(z_s)$ is a monochromatic source (possibly an array of buried sources at depth z_s) ‘regularized’ to a 1xN source vector $\mathbf{s}(z_0) = \mathbf{S}_{up}(z_0, z_s)\mathbf{s}(z_s)$, $\mathbf{G}_{up}(z_0, z_g)$ and $\mathbf{S}_{up}(z_0, z_s)$ are regularization matrices that might also include wavefield extrapolation between different depth levels, $\mathbf{W}_{down}(z_m, z_0)$ is the NxN forward wavefield extrapolation matrix that takes

---

[24] For 3-D notation, see Appendix A of de Bruin (1992).

the source wavefield from the surface at z_0 down to the reflector at depth z_m, $\mathbf{R}(z_m)$ is the NxN dip- and angle-dependent reflectivity matrix that relates the incident and reflected wavefields at depth z_m, and $\mathbf{W}_{up}(z_0, z_m)$ is the NxN forward wavefield extrapolation matrix that takes the reflected wavefield from depth z_m up to the surface at z_0 (Figure 1.8). For a 2-D point

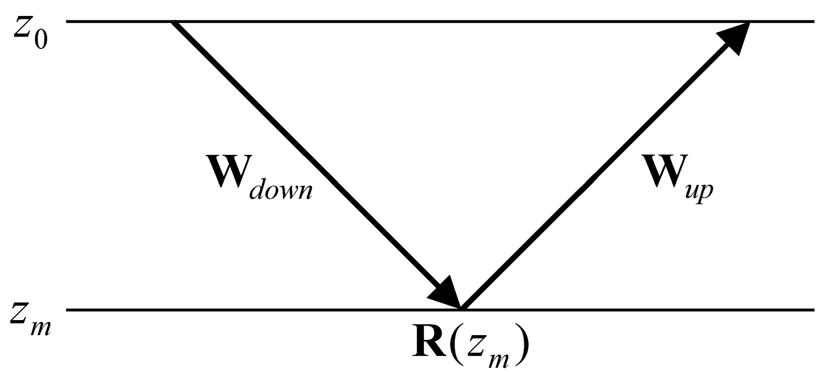

Figure 1.8. The Delphi scheme: The forward problem is separated into a cascade of forward wavefield propagators $\mathbf{W}_{down}$ and $\mathbf{W}_{up}$, and the angle-dependent reflectivity $\mathbf{R}(z_m)$. This simplifies the inverse problem because the exact inverse wavefield propagators $\mathbf{W}_{down}^{-1}$ and $\mathbf{W}_{up}^{-1}$ can be replaced by the conjugate transposes $\mathbf{W}_{down}^{*}$ and $\mathbf{W}_{up}^{*}$. The conjugate transposes are exact for the propagating modes and better behaved than the inverse wavefield propagators for evanescent modes. Angle-dependent reflectivity $\mathbf{R}(z_m)$ is the desired estimate, and so does not need to be inverted.

source at the surface, $\mathbf{s}(z_0)$ has only one non-zero element, but $\mathbf{s}(z_0)$ could represent any superposition of sources including a directed plane wave source or a focused plane wave source (Rietveld et al., 1992; Rietveld, 1994). The N regularized surface locations are each separated by a distance Δx, with the total length $N\Delta x$ extending beyond the receiver line-length to account for the migration aperture. Note that there is an implied dependency on frequency in equation (1.22) and subsequent equations.

Now compare the forward problem as described by equation (1.15) with the cascaded forward problem for a single shot gather as described by equation (1.22). With no loss of generality, the elements of the data vector $\mathbf{d}$ in equation (1.15) can also be considered as monochromatic responses from monochromatic sources. The vector of earth model parameters $\mathbf{m}$ contains all the coefficients of the *M* reflectivity matrices $\mathbf{R}(z_m)$. The forward theory operator $\mathbf{F}$ includes all the source, receiver, and wave propagation effects modeled by the cascade of forward theory operators described in the previous paragraph.

Thus, the wavefield extrapolation matrices $\mathbf{W}_{down}(z_m, z_0)$ and $\mathbf{W}_{up}(z_0, z_m)$ depend on the wavespeed macromodel, which is assumed to be known but in practice must be determined as a separate estimation problem. Note, however, that the misfit and measurement error terms found in equation (1.15) are not included in equation (1.22).

The conventional Delphi scheme expands the source vector $\mathbf{s}(z_0)$ into an *N*x*N* source matrix $\mathbf{S}(z_0)$ (i.e. one column for each 2-D point source, see Gray, 1997), which yields an *N*x*N* data matrix $\mathbf{D}(z_0)$ (i.e. one column for each common-shot record). Applying this expansion to equation (1.22) and simplifying the result gives

$$\mathbf{D}(z_0) = \sum_{m=1}^{M} \mathbf{W}_{up}(z_0, z_m)\mathbf{R}(z_m)\mathbf{W}_{down}(z_m, z_0)\mathbf{S}(z_0). \tag{1.23}$$

The goal of the Delphi scheme is to extract the reflectivity matrix at each depth in the subsurface. First, I examine the representation for a single common-shot gather. In regularized form, equation (1.22) can be simplified to

$$\mathbf{d}(z_0) = \sum_{m=1}^{M} \mathbf{W}_{up}(z_0, z_m)\mathbf{R}(z_m)\mathbf{s}(z_m), \tag{1.24}$$

where $\mathbf{s}(z_m) = \mathbf{W}_{down}(z_m, z_0)\mathbf{s}(z_0)$ represents the source wavefield forward propagated down to a reflector depth *m*.

Now apply the ideal inverse wavefield extrapolation operator $\mathbf{W}_{up}^{-1}(z_0, z_k)$ (for depth z_k) to both sides of equation (1.24):

$$\mathbf{d}(z_k) = \sum_{m=1}^{k-1} \mathbf{W}_{up}^{-1}(z_k, z_0)\mathbf{W}_{up}(z_0, z_m)\mathbf{R}(z_m)\mathbf{s}(z_m)$$

$$+\mathbf{W}_{up}^{-1}(z_k, z_0)\mathbf{W}_{up}(z_0, z_k)\mathbf{R}(z_k)\mathbf{s}(z_k)$$

$$+\sum_{m=k+1}^{M} \mathbf{W}_{up}^{-1}(z_k, z_0)\mathbf{W}_{up}(z_0, z_m)\mathbf{R}(z_m)\mathbf{s}(z_m), \tag{1.25}$$

where $\mathbf{d}(z_k) = \mathbf{W}_{up}^{-1}(z_k, z_0)\mathbf{d}(z_0)$ is the regularized data inverse extrapolated to depth z_k, i.e. the reflected wavefield at the depth of the reflector.

In any practical implementation, there could be 1000's of receivers and, to account for migration aperture, a much larger number of regularized surface locations. Finding the exact inverse $\mathbf{W}^{-1}$ of, say, a 10^5x10^5 matrix (and even larger for a 3-D survey) is not practical, especially if implemented as a cascade of recursive extrapolators where a separate inversion is required for each depth step *m*. In addition, the exact inverse exponentially gains noise in the evanescent modes. Fortunately, the conjugate transpose $\mathbf{W}^*$ handles propagating modes exactly as the inverse operator $\mathbf{W}^{-1}$ while exponentially damping the evanescent modes (see Gray, 1997 for a more detailed discussion). Using conjugate transpose operators in place of exact inverses, equation (1.25) can be re-expressed as

$$\mathbf{d}(z_k) = \sum_{m=1}^{k-1} \mathbf{W}_{up}^{*}(z_k, z_0)\mathbf{W}_{up}(z_0, z_m)\mathbf{R}(z_m)\mathbf{s}(z_m)$$

$$+\mathbf{W}_{up}^{*}(z_k, z_0)\mathbf{W}_{up}(z_0, z_k)\mathbf{R}(z_k)\mathbf{s}(z_k)$$

$$+\sum_{m=k+1}^{M} \mathbf{W}_{up}^{*}(z_k, z_0)\mathbf{W}_{up}(z_0, z_m)\mathbf{R}(z_m)\mathbf{s}(z_m), \tag{1.26}$$

where now $\mathbf{d}(z_k) = \mathbf{W}_{up}^{*}(z_0, z_k)\mathbf{d}(z_0)$.

If there is only one reflector in the subsurface at depth z_k, the first and third terms on the RHS of equation (1.26) are zero, and the second term simplifies with the assumption that $\mathbf{W}_{up}^*(z_k, z_0)\mathbf{W}_{up}(z_0, z_k) = \mathbf{I}$, yielding

$$\mathbf{d}(z_k) = \mathbf{R}(z_k)\mathbf{s}(z_k). \tag{1.27}$$

The diagonal of the monochromatic reflectivity matrix at depth z_k is estimated directly as an element-by-element deconvolution of the reflected wavefield by the forward propagated wavefield:

$$\mathbf{R}_{ii}(z_k) = \mathbf{d}_i(z_k)/\mathbf{s}_i(z_k). \tag{1.28}$$

The desired estimate of angle-dependent reflectivity is the output of the deconvolution at zero-time, which is achieved simply by averaging the reflectivities determined from each monochromatic experiment (dependence on frequency ω assumed)

$$\hat{\mathbf{R}}_{ii}(z_k) = \frac{\Delta\omega}{2\pi}\sum_{\omega}\mathbf{d}_i(z_k)/\mathbf{s}_i(z_k) \tag{1.29}$$

Equation (1.29) is commonly referred to as Claerbout's deconvolution imaging condition (Claerbout, 1971).

If there are many reflectors in the subsurface, the deconvolution imaging condition still produces a good estimate of reflectivity. To understand how this works, imagine equation (1.26) in the time-domain. The phase or traveltime of the inverse propagated data on the LHS will be the same as the traveltime of the forward propagated source, scaled by the reflectivity, found in the second term on the RHS. For the first term, the combination $\mathbf{W}_{up}^*(z_k, z_0)\mathbf{W}_{up}(z_0, z_m)$ with $k > m$ places the scaled sources at an earlier time, while for the third term, $\mathbf{W}_{up}^*(z_k, z_0)\mathbf{W}_{up}(z_0, z_m)$ with $k < m$ places the scaled sources at a later time. Each monochromatic estimate of angle-dependent reflectivity will not be a good estimate, but the average over frequency is equivalent to inverse Fourier transforming the reflectivity estimates and extracting the zero-time value. The deconvolution imaging condition forms the basis for common-shot and, invoking reciprocity, common-receiver methods of Kirchhoff imaging developed in Chapter 3. In Section 3.7, I propose a new zero-phase weighting function for the deconvolution imaging condition that extracts a chi-squared estimate of reflectivity at the zero-time value.

For the more complicated situation involving a data matrix $\mathbf{D}(z_0)$ and source matrix $\mathbf{S}(z_0)$, with reflectors at multiple depth levels *m*, the deconvolution given by equation (1.28) is replaced by

$$\mathbf{X}(z_k, z_k) = \mathbf{D}(z_k) / \mathbf{S}(z_k) \tag{1.30}$$

where $\mathbf{X}(z_k, z_k)$ the 'target impulse response' for depth z_k, $\mathbf{D}(z_k) = \mathbf{W}^*_{up}(z_k, z_0)\mathbf{D}(z_0)$, and $\mathbf{S}(z_k) = \mathbf{W}_{down}(z_k, z_0)\mathbf{S}(z_0)$. Hence, the RHS of equation (1.30) is a cascade of conjugate transpose and inverse theory operators applied to the data matrix $\mathbf{D}(z_0)$ given by

$$\mathbf{D}(z_k) / \mathbf{S}(z_k) = \mathbf{W}^*_{up}(z_k, z_0)\mathbf{D}(z_0)\mathbf{S}^{-1}(z_0)\mathbf{W}^*_{down}(z_0, z_k). \tag{1.31}$$

Using the cascade proposed by equation (1.31), we first right-multiply both sides of equation (1.23) with the inverse source matrix $\mathbf{S}^{-1}(z_0)$, which is assumed to exist and satisfy $\mathbf{S}(z_0)\mathbf{S}^{-1}(z_0) = \mathbf{I}$, yielding

$$\begin{aligned}\mathbf{X}(z_0, z_0) = &\sum_{m=1}^{k-1} \mathbf{W}_{up}(z_0, z_m)\mathbf{R}(z_m)\mathbf{W}_{down}(z_m, z_0) \\ &+ \mathbf{W}_{up}(z_0, z_k)\mathbf{R}(z_k)\mathbf{W}_{down}(z_k, z_0) \\ &+ \sum_{m=k+1}^{M} \mathbf{W}_{up}(z_0, z_m)\mathbf{R}(z_m)\mathbf{W}_{down}(z_m, z_0),\end{aligned} \tag{1.32}$$

where $\mathbf{X}(z_0, z_0) = \mathbf{D}(z_0)\mathbf{S}^{-1}(z_0)$ is the 'target impulse response' at the surface. Now left-multiply equation (1.24) by $\mathbf{W}^*_{up}(z_k, z_0)$, right-multiply by $\mathbf{W}^*_{down}(z_0, z_k)$, and evaluate the conjugate transposes in the second term on the RHS as exact inverses to give

$$\mathbf{W}_{up}^{*}(z_k, z_0)\mathbf{X}(z_0, z_0)\mathbf{W}^{*}(z_0, z_k) =$$

$$\sum_{m=1}^{k-1}\mathbf{W}_{up}^{*}(z_k, z_0)\mathbf{W}_{up}(z_0, z_m)\mathbf{R}(z_m)\mathbf{W}_{down}(z_m, z_0)\mathbf{W}_{down}^{*}(z_0, z_k)$$

$$+\mathbf{R}(z_k) + \sum_{m=k+1}^{M}\mathbf{W}_{up}^{*}(z_k, z_0)\mathbf{W}_{up}(z_0, z_m)\mathbf{R}(z_m)\mathbf{W}_{down}(z_m, z_0)\mathbf{W}_{down}^{*}(z_0, z_k). \quad (1.33)$$

Equation (1.33) indicates that all data are affected by the extrapolation operators appropriate for the desired depth level z_k, including data corresponding to shallower depths (first term on RHS) and data corresponding to deeper depths (third term on RHS). The second and third terms on the RHS of equation (1.33) are defined by de Bruin (1992) as the 'target impulse response' for depth z_k, i.e.

$$\mathbf{X}(z_k, z_k) = \mathbf{R}(z_k) + \sum_{m=k+1}^{M}\mathbf{W}_{up}^{*}(z_k, z_0)\mathbf{W}_{up}(z_0, z_m)\mathbf{R}(z_m)\mathbf{W}_{down}(z_m, z_0)\mathbf{W}_{down}^{*}(z_0, z_k), \quad (1.34)$$

and uses $\mathbf{X}(z_k, z_k)$ to estimate an average of angle-dependent reflectivity and angle-dependent reflectivity.

The average of angle-dependent reflectivity is just an average of the diagonal elements $\mathbf{X}_{ii}(z_k, z_k)$ over frequency (dependence on frequency ω assumed)

$$\hat{\mathbf{R}}_{ii}(z_k) = \frac{\Delta\omega}{2\pi}\sum_{\omega}\mathbf{X}_{ii}(z_k, z_k). \quad (1.35)$$

As in the single common-shot gather case presented above, equation (1.35) is equivalent to taking an inverse Fourier transform and extracting the zero-time value. Angle-dependent reflectivity is obtained by a spatial Fourier transform of each column of $\mathbf{X}(z_k, z_k)$ (i.e. from spatial coordinate x to wavenumber variable k_x) followed by a simple mapping of the wavenumber variable to the ray parameter p and a complex averaging over all frequency contributions (positive frequencies only). The angle-dependent estimation problem will not be discussed further here.

1.4.7 Problems with the Delphi approach

There are two subtle problems with de Bruins method for estimating the average of angle-dependent reflectivity, as given by equation (1.35). First, applying the cascade of conjugate transpose and inverse operators to the data matrix (equation 1.31) does not give the desired target impulse response $\mathbf{X}(z_k, z_k)$ (equation 1.34). Instead, the result is the RHS of equation (1.33), which is $\mathbf{X}(z_k, z_k)$ plus the sum of all data extrapolated to negative time. The negative-time data cannot easily be removed in the frequency domain. Allowing it to wrap around time zero to a large positive time is not a solution. One option is to Fourier transform the extrapolated data to the time domain, replace the negative-time data by zeros, and transform back to the frequency domain. However, Claerbout's deconvolution imaging condition (equation 1.35) works for the more general definition of $\mathbf{X}(z_k, z_k)$ as the complete RHS of equation (1.33).

The second problem is that average reflectivities based on the migration of common-shot gathers are, in general, biased estimates (Geiger, 2001). The bias depends on the dip and depth of the reflector but is negligible if the receiver spread is symmetric about each shot location. Bias increases with asymmetry in the receiver spreads and is a maximum for one-sided spreads common to marine acquisition. One possible solution is to synthesize symmetric spreads using the principle of reciprocity (Vermeer, 1990). A better solution should be possible. Finding a way to obtain robust unbiased estimates of average reflectivity appropriate for the implementation of EOM prestack time migration is the main objective of this dissertation.

1.4.8 Summary: geophysical inverse theory applied to seismic imaging

In this section, I presented three related but distinct approaches to applying geophysical inverse theory to the seismic imaging problem. For each approach, only the forward problem and the estimation problem were discussed. In seismic imaging, the appraisal problem—a necessary part of any complete inversion—is typically replaced by a validation process.

The first approach yielded equation (1.12) as a generalized formula for estimation, repeated here as

$$\hat{m}_{R_0}(\mathbf{x}) = \sum_i f_i^{-g}(\mathbf{x}, \hat{m}_c) d_i \,. \tag{1.36}$$

In essence, this is the migration/inversion method of Bleistein and co-workers, as well as Hubral and co-workers (see discussion and references in Gray, 1997). The unique aspect of this approach is that it can describe non-physical wavefields such as those found in a common-offset gather. In fact, I will show in Chapters 3 and 4 that this approach provides the basis for robust unbiased estimates of average reflectivity suitable for the implementation of EOM prestack time migration.

The second approach yielded equation (1.21) as a generalized formula for estimation, repeated here as

$$\hat{\mathbf{m}} = \mathbf{F}^T \mathbf{d} \tag{1.37}$$

This approach can be described as a matched-filter. The kinematic description of EOM prestack migration can be thought of as a conjugate transpose of a forward kinematic model[25]. As with all prestack time migrations, both the forward theory operator and the conjugate are approximations to a complete description of the underlying physics. The interesting aspect of this approach lies mainly in the description of the errors, given by

---

[25] It would be more correct to describe EOM in terms of continuous theory and employ the adjoint or Hermitian adjoint in place of the conjugate transpose. However, the concepts are essentially equivalent, but matrix notation has the advantage of being much more compact.

equation (1.18) but modified by replacing the generalized inverse $\mathbf{F}^{-g}$ with the transpose $\mathbf{F}^T$:

$$\hat{\mathbf{m}} = \mathbf{m} + \left(\underbrace{\mathbf{F}^T\mathbf{F}}_{\substack{\text{resolution}\\\text{kernel}}} - \mathbf{I} \right)\mathbf{m} + \underbrace{\mathbf{F}^T\mathbf{e}_{\mathbf{Fm}}}_{\substack{\text{misfit error}\\\text{artifacts}}} + \underbrace{\mathbf{F}^T\mathbf{e}_{\mathbf{d}}}_{\substack{\text{measurement error}\\\text{artifacts}}} . \tag{1.38}$$

Since the conjugate transpose of the kinematic operator is a good approximation to the generalized inverse, the resolution kernel is close to the identity matrix. Hence, there is the possibility of obtaining good focusing, even if the underlying forward theory operator is a poor approximation to the real physics. The trick is to base the kinematic component of the theory operator on a simple hyperbolic traveltime-moveout relationship known as the double-square-root (DSR) equation. A generalized derivation for the DSR equation based on a Taylor series expansion is presented in the next section. Applying the transpose of this simple forward theory operator as the estimator suggests that the majority of the error will be found in the misfit error artifacts, primarily as a loss of accuracy in absolute positioning. Accuracy in focusing and relative positioning may be preserved, depending on local smoothness of traveltime perturbations for specular reflected information in the data space.

The third approach is to view the linear forward theory operator as a cascade of linear operators, and to invert only those operators that are required to estimate the model. This is the approach initially proposed by Claerbout as the deconvolution imaging condition, expressed for a single shot-record as equation (1.21), repeated here as

$$\hat{\mathbf{R}}_{ii}(z_k) = \frac{\Delta\omega}{2\pi} \sum_{\omega} \mathbf{d}_i(z_k) / \mathbf{s}_i(z_k), \tag{1.39}$$

and expanded to multiple physical wavefields by the Delft group as equation (1.35), repeated here as

$$\hat{\mathbf{R}}_{ii}(z_k) = \frac{\Delta\omega}{2\pi} \sum_{\omega} \mathbf{X}_{ii}(z_k, z_k). \tag{1.40}$$

where the target reflection response $\mathbf{X}(z_k, z_k)$ is given by equation (1.34), repeated here as

$$\mathbf{X}(z_k, z_k) = \mathbf{R}(z_k) + \sum_{m=k+1}^{M} \mathbf{W}_{up}^{*}(z_k, z_0)\mathbf{W}_{up}(z_0, z_m)\mathbf{R}(z_m)\mathbf{W}_{down}(z_m, z_0)\mathbf{W}_{down}^{*}(z_0, z_k). \tag{1.41}$$

This approach can yield good results because the conjugate transposes of the forward wavefield extrapolation operators are excellent approximations to their inverses (and are more robust). As with the first method, a macro-model of the subsurface wavespeed is required for wavefield propagation.

The basic concept of constructing a forward theory operator as a cascade of linear operators is an intuitive approach adopted by all methods. In fact, all three methods will prove useful in the quest to establish both a kinematic and a dynamic solution to EOM prestack time migration. The kinematic solution has been known for some time as a simple re-expression of the DSR equation for a constant wavespeed medium (Bancroft and Geiger, 1994). However, the more general derivation presented in the next section explains the success of prestack time migration with data collected in areas where the subsurface wavespeed has both lateral and vertical variations.

1.5 KINEMATICS OF REFLECTION EVENTS AND DIFFRACTION TRAVELTIME CURVES

In the previous sections, I defined migration as a transformation from a data space to an image space. Using geophysical inverse theory, the migration problem was described as an estimation problem, where the desired reflectivity estimates are obtained by applying a generalized inverse theory operator to the recorded data. Ideally, the forward theory operator is based on the physics of wavefield propagation, which requires a reasonable macro-model of the subsurface wavespeed. It was shown, however, that a broader class of forward theory operators can be considered. Of particular interest are forward theory operators that are independent of a subsurface macro-model and have simple, robust inverses. These can provide good resolution as defined by the resolution kernel, but possibly at the expense of larger misfit-error artifacts. The task, then, is to determine a forward theory operator that describes the relevant information in the data (traveltimes and amplitudes) without recourse to a macro-model.

In this section, I review previous work that uses a Taylor series expansion to show that reflection traveltimes satisfy a generalized hyperbolic relationship independent of the subsurface wavespeed and reflectivity. The Taylor series expansion assumes local smoothness of traveltime perturbations in the vicinity of the source and receiver locations, but no other assumptions about the subsurface. I then show that diffraction traveltime surfaces can be defined by a similar hyperbolic operator. By expanding this diffraction operator about the surface location of the zero-offset image ray (and assuming an isotropic medium), the expression simplifies to the familiar double-square-root (DSR) equation. This defines the traveltime or kinematic portion of the desired macro-model-independent forward theory operator. Unfortunately, this approach does not provide the amplitude or dynamic portion. As stated previously, finding a suitable description for the dynamic portion turns out to be non-trivial exercise, and will be one of the primary objectives of this dissertation.

1.5.1 Kinematics of reflection events

Consider a generalized inhomogeneous isotropic medium and make only one additional assumption: that traveltime variations, as measured by perturbing the source and receiver locations, are locally smooth. Note that this assumption does not preclude discontinuous boundaries in wavespeed. Figure 1.9a illustrates the generalized configuration, where all

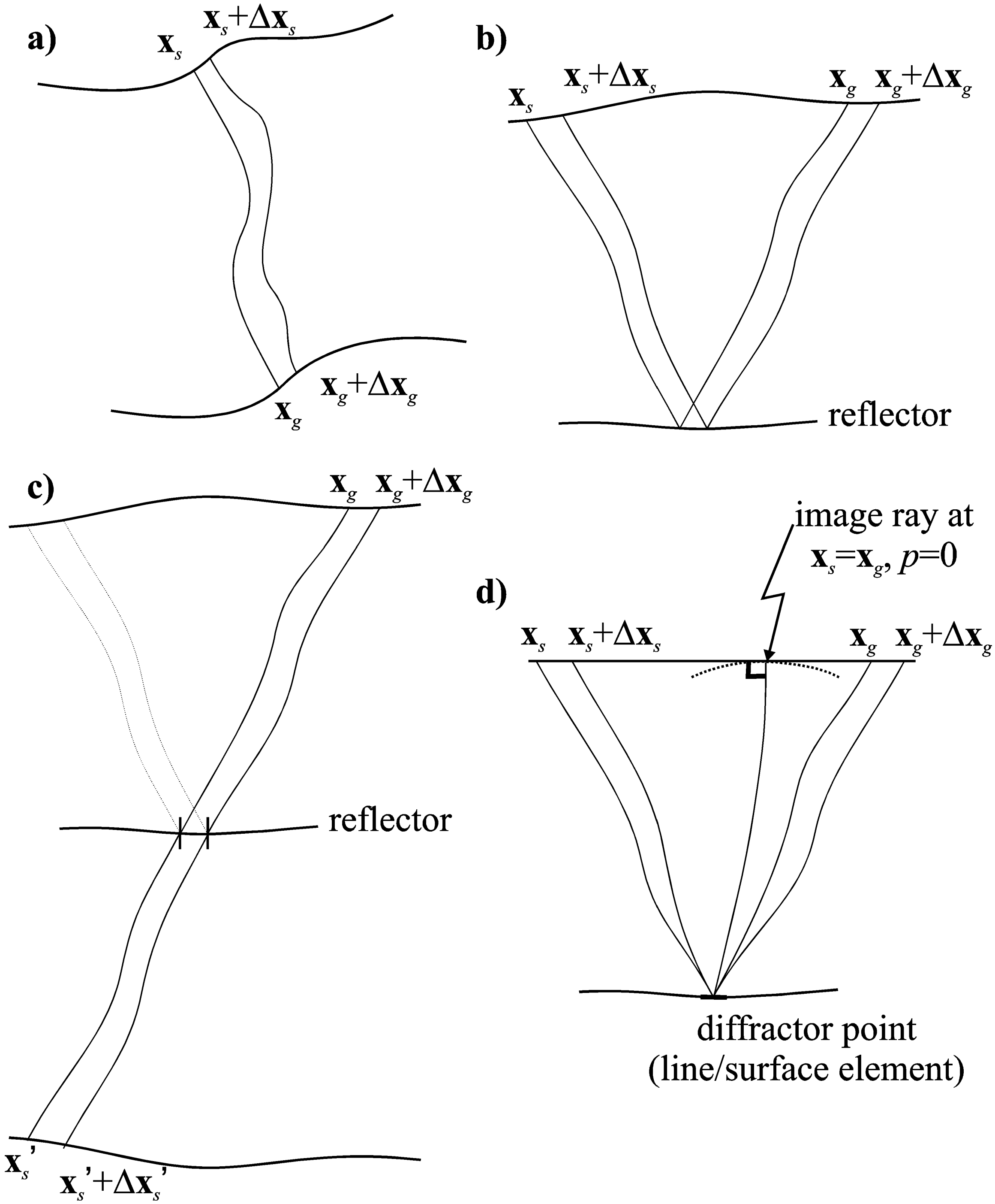

Figure 1.9. A generalized inhomogeneous isotropic medium with only one additional assumption: that traveltime variations, as measured by perturbing the source and receiver locations, are locally smooth. In the reflection configuration, where the generalized 'black box' (a) represents reflections (b) by image sources (c), perturbations at the source and receiver create a perturbation at the reflector. In the diffraction configuration (d), expansion on a flat surface about the image ray simplifies the generalized DSR equation to the standard DSR equation that can be derived for a constant wavespeed medium.

propagation effects in the medium, including reflections and refractions, are represented as a 'black box'. The only relevant information is the change in traveltime as the source and receiver positions are perturbed. In fact, this is a good description for the information content in seismic reflection data.

For each portion of a reflection event in the primary reflected wavefield, the black box subsurface can be thought of as containing a small portion of a single reflector where the wavefield propagating from the source is specularly reflected. As the source and/or receiver position are perturbed, the point of specular reflection changes. Figure 1.9b illustrates this from the surface, while Figure 1.9c illustrates the identical situation for an image source location. Invoking an image source is a powerful tool in the study of reflection seismic wavefields. It is based on the simple intuitive assumption that downward wavefield propagation from the source to the reflector is independent of the reflection, and that both of these are independent of the upward propagation from the reflector to the source. Combine this with an assumption of linearity — specifically that each reflector and each portion of wavefield propagation can be considered independently and summed to produce the desired result — and the subsurface can then be replaced by many subsurfaces, each individually tailored to the requirements of a particular reflection element. This tool will be used repeatedly throughout this dissertation.

Before proceeding with the Taylor series expansion, I establish some notation (adapted from Vanelle and Gajewski, 2001b). The perturbed source position vector $\mathbf{x}_s = (x_{s1}, x_{s2}, x_{s3})$ and receiver position vector $\mathbf{x}_g = (x_{g1}, x_{g2}, x_{g3})$ can be expressed in terms of variations $\Delta\mathbf{x}_s$ and $\Delta\mathbf{x}_g$ in the unperturbed source and receiver positions as $\mathbf{x}_s = \mathbf{x}_{s_0} + \Delta\mathbf{x}_s$ and $\mathbf{x}_g = \mathbf{x}_{g_0} + \Delta\mathbf{x}_g$. The slowness vectors $\mathbf{s}_0$ and $\mathbf{g}_0$ at the unperturbed source and the receiver positions $\mathbf{x}_{s_0}$ and $\mathbf{x}_{g_0}$ are defined as

$$s_{0i} = -\frac{\partial \tau}{\partial x_{s_0 i}} \quad \text{and} \quad g_{0i} = -\frac{\partial \tau}{\partial x_{g_0 i}} \tag{1.42}$$

while the second-order derivative matrices $\mathbf{S}_0$, $\mathbf{G}_0$, and $\mathbf{N}_0$ are defined as

$$S_{0ij} = -\frac{\partial^2 \tau}{\partial x_{s_0 i} \partial x_{s_0 j}} = S_{0ji}, \tag{1.43}$$

$$G_{0ij} = \frac{\partial^2 \tau}{\partial x_{g_0 i} \partial x_{g_0 j}} = G_{0ji}, \tag{1.44}$$

and

$$N_{0ij} = -\frac{\partial^2 \tau}{\partial x_{s_0 i} \partial x_{g_0 j}} \neq N_{0ji}. \tag{1.45}$$

The slownesses and the second-order derivatives are the inverses of the apparent wavespeed and the curvatures of the wavefield, respectively, at the unperturbed source and receiver locations.

Now expand the square of the traveltime as a Taylor series expansion about perturbations in the source and receiver location. In general, this will be valid everywhere except in the vicinity of caustics. The Taylor expansion $\tau^2(\mathbf{x}_{g_0} + \Delta\mathbf{x}_g, \mathbf{x}_{s_0} + \Delta\mathbf{x}_s)$ yields the hyperbolic traveltime expansion (Vanelle and Gajewski, 2001b),

$$\tau^2(\mathbf{x}_g, \mathbf{x}_s) = \left(\tau_{0gs} - \mathbf{s}_0 \Delta\mathbf{x}_s^T + \mathbf{g}_0 \Delta\mathbf{x}_g^T\right)^2$$
$$+ \tau_{0gs}\left(-2\Delta\mathbf{x}_s \mathbf{N}_0 \Delta\mathbf{x}_g^T - \Delta\mathbf{x}_s \mathbf{S}_0 \Delta\mathbf{x}_s^T + \Delta\mathbf{x}_g \mathbf{G}_0 \Delta\mathbf{x}_g^T\right) + O(3). \tag{1.46}$$

Equation (1.46) explains a significant characteristic observed in seismic reflection data: that all reflection information can be thought of as approximately hyperbolic in a generalized sense. A slightly different derivation, specialized to slowness vectors and second-derivative matrices defined on arbitrary curved surfaces, is provided by Schleicher et al. (1993). A Taylor series expansion in τ rather than in τ^2 (as above) suggests that reflection information can be thought of as approximately parabolic in a generalized sense. The hyperbolic approximation, however, is more accurate for simple subsurface media [e.g. $c(z)$] and exact for a constant-wavespeed medium.

1.5.2 Kinematics of diffraction traveltime curves: the DSR equation

A similar expansion can be developed for a fixed subsurface location, e.g. at a particular point on the reflector (Figure 1.7d). This point can be considered as an infinitesimally small oriented patch on the reflector surface, otherwise known as a diffractor (Deregowski and Brown, 1983). As we shall see in Sections 2.7 and 3.3, this definition of a diffractor as an oriented patch is more useful than the simpler and more common definition of a diffractor as a point. The orientation is necessary because the correct mathematical definition of Huygens' principle, as described by Fresnel and Kirchhoff, requires both dipole and monopole sources (see Section 2.7). The orientation of the dipole corresponds to the orientation of the reflector surface or to the orientation of any arbitrary surface used to reconstruct the wavefield.

The total traveltime from the source to the diffractor to the receiver is broken down into two components. The square of the traveltime from the source to a fixed diffractor location can be expressed as the hyperbolic traveltime expansion

$$\tau^2(\mathbf{x}_d, \mathbf{x}_s) = \left(\tau_{0ds} - \mathbf{s}_0 \Delta\mathbf{x}_s^T\right)^2 - \tau_{0ds} \Delta\mathbf{x}_s \mathbf{S}_0 \Delta\mathbf{x}_s^T + O(3), \tag{1.47}$$

while the square of the traveltime from the fixed diffractor location to the receiver can be expressed as the hyperbolic traveltime expansion

$$\tau^2(\mathbf{x}_g, \mathbf{x}_d) = \left(\tau_{0gd} + \mathbf{g}_0 \Delta\mathbf{x}_g^T\right)^2 + \tau_{0gd} \Delta\mathbf{x}_g \mathbf{G}_0 \Delta\mathbf{x}_g^T + O(3). \tag{1.48}$$

The sum of these component traveltimes yields the total diffractor traveltime

$$\tau(\mathbf{x}_g, \mathbf{x}_s) = \tau(\mathbf{x}_g, \mathbf{x}_d) + \tau(\mathbf{x}_d, \mathbf{x}_s), \tag{1.49}$$

which can be expressed as a generalized double-square-root (DSR) equation.

$$\tau(\mathbf{x}_g,\mathbf{x}_s)=\sqrt{\left(\tau_{0gd}+\mathbf{g}_0\Delta\mathbf{x}_g^T\right)^2+\tau_{0gd}\Delta\mathbf{x}_g\mathbf{G}_0\Delta\mathbf{x}_g^T}$$
$$+\sqrt{\left(\tau_{0ds}-\mathbf{s}_0\Delta\mathbf{x}_s^T\right)^2-\tau_{0ds}\Delta\mathbf{x}_s\mathbf{S}_0\Delta\mathbf{x}_s^T}+O(3). \qquad (1.50)$$

Consider a 2-D subsurface (constant in the x_2 direction) with the acquisition line on a planar surface in the x_1 direction. Thus, the coordinate system is oriented such that $\Delta x_{g1}=x_m+h$, $\Delta x_{s1}=x_m-h$, and $\Delta x_{g2}=\Delta x_{s2}=\Delta x_{g3}=\Delta x_{s3}=0$, where x_m is the distance of the source-receiver midpoint from an arbitrary origin $\mathbf{x}_{g_0}=\mathbf{x}_{s_0}=(0,0,0)$, and h is the source-receiver half-offset. The diffractor of interest lies in the plane $x_2=0$. The situation can be generalized to 3D, except that now distances to the source and receiver are measured as radials from the origin, and the midpoint distance x_m and half-offset h are half the sum and half the difference of these radial distances, respectively.

For the zero-offset ray from the diffractor emerging at the origin, $\mathbf{g}_0=-\mathbf{s}_0$ and $\mathbf{G}_0=-\mathbf{S}_0$. Hence, we can define zero-offset apparent slowness $\mathbf{p}_0\equiv\mathbf{g}_0=-\mathbf{s}_0$ with $p_{01}=p_{02}\equiv p$, zero-offset apparent curvature $\mathbf{P}_0\equiv\mathbf{G}_0=-\mathbf{S}_0$ with $P_{011}=P_{022}\equiv P$ and $P_{012}=P_{021}=0$ (Vanelle and Gajewski, 2001b), $\tau\equiv\tau(\mathbf{x}_g,\mathbf{x}_s)$, and $\tau_0/2\equiv\tau_{0gd}=\tau_{0ds}$. Inserting these into the generalized DSR equation (equation 1.50) yields

$$\tau=\sqrt{\left(\frac{\tau_0}{2}+p(x_m+h)\right)^2+\frac{\tau_0}{2}P(x_m+h)^2}+\sqrt{\left(\frac{\tau_0}{2}+p(x_m-h)\right)^2+\frac{\tau_0}{2}P(x_m-h)^2} \qquad (1.51)$$

or, equivalently

$$\tau=\sqrt{\left(\frac{\tau_0}{2}\right)^2+\left(\frac{\tau_0 p}{(x_m+h)}+\frac{\tau_0}{2}P+p^2\right)(x_m+h)^2}$$
$$+\sqrt{\left(\frac{\tau_0}{2}\right)^2+\left(\frac{\tau_0 p}{(x_m-h)}+\frac{\tau_0}{2}P+p^2\right)(x_m-h)^2}\ . \qquad (1.52)$$

Equations (1.51) and (1.52) have a much simpler and more familiar form if the expansion point is the emergence location on the surface of the 'image ray', i.e. the zero-offset ray from the diffractor that emerges vertically. In this case, the slowness $p = 0$ and either of these equations simplifies to

$$\tau = \sqrt{\left(\frac{\tau_0}{2}\right)^2 + \frac{(x_m + h)^2}{c_{mig}^2}} + \sqrt{\left(\frac{\tau_0}{2}\right)^2 + \frac{(x_m - h)^2}{c_{mig}^2}}\,, \tag{1.53}$$

with

$$c_{mig} = \sqrt{\frac{2}{\tau_0 P}} \tag{1.54}$$

as the wavefront-curvature fitting parameter commonly referred to as the 'migration velocity'. Equation (1.53) is the same DSR equation introduced as equation (1.1) in Section 1.1.4. Previously, it was derived for a constant wavespeed medium. Here it has been derived for an arbitrary inhomogenous isotropic medium and a planar acquisition surface.

1.5.3 The DSR equation as a Taylor series expansion: two perspectives

Equation (1.53) is a generalized diffraction traveltime expression for an arbitrary inhomogeneous isotropic subsurface. Although derived for 2-D, it can be applied in 3-D using radial distances as discussed above. The key is to expand the hyperbolic traveltime expression about the zero-offset image ray, which means that two-way traveltime τ_0 corresponds to this ray. As a forward-theory operator, equation (1.53) says that the traveltime or kinematic information in the data can be described by a single parameter that corresponds to the wavefront curvature at the image-ray location and traveltime τ_0. A reasonable question to ask, then, is how far away from this expansion point is the Taylor series still valid?

This question can be approached from two perspectives. Before I consider these, recall that the diffractor was defined as an oriented patch in the subsurface. Of all possible shot and receiver locations, only a fraction will correspond to a specular reflection. These will be the few seismograms that will make a significant contribution to the primary reflection events recorded in the data space. Hence, this is the important part of the data that the combination of forward theory operator and model must describe and, in turn, the key information that the estimator must address.

With this concept of 'specular reflections' in mind, consider the following two perspectives. The first looks at a diffraction point in the unknown earth model that generated the data space, with the Taylor series expansion about the emergent location of the zero-offset image-ray corresponding to this diffraction point. In combination with the two-way traveltime τ_0 along the image ray, this location defines the apex of the generalized hyperbolic traveltime surface in the data space, which Black and Brzostowski (1994) call the *true-diffraction curve*. Of course, the important information to fit is the specular reflection where we want the diffraction curve to be tangent to the reflection event. For a dipping reflector, this specular information may be some distance away from the image ray location. From this first perspective, then, it is unlikely that a good fit can be achieved unless the subsurface wavespeed varies slowly over this distance. In fact, it is well known (Dix, 1955) that an exact solution requires a constant wavespeed medium, and that a good approximate solution is possible in a layer cake medium near the image ray location (i.e. for shallow dips only) using the root-mean-square wavespeed c_{rms} as the migration velocity c_{mig}.

The second perspective is to look at each specular reflection event in the data space and find the best-fit hyperbolic curvature independent of any preconceived idea for the image-ray surface location and τ_0 that corresponds to a particular diffractor. Recall equations (1.46), (1.51), and (1.52), which show that reflection events and diffraction traveltime curves can be expanded about any source and receiver location. Hence we can expect that both the reflection events and diffraction traveltime curves are hyperbolic in a generalized sense, and that a DSR hyperbolic shape can be found that will fit. Thus, the apex of the generalized hyperbola will be defined wherever the best fit to the specular information is found. Black and Brzostowski (1994) call this best-fit generalized hyperbola the *time-migration curve* and point out that Hubral's (1977) assumption that the image ray connects time migration with depth migration is incorrect when the time-migration curve and true-diffraction curve do not coincide.

Typically, only one time migration curve is defined for each output point. Consider two adjacent diffractors with different dips in an inhomogeneous subsurface with lateral variations in the wavespeed. The traveltimes and locations in the data space for the specular reflection events corresponding to these two diffractors will depend on the travelpaths of the specular wavefield. In general, these specular reflection events will be separated in the data space. Thus it is likely that there will be two best-fit time-migration curves, each with a different apex location in the image space. If these time-migration curves are selected, the time migrated image will contain relative positioning errors. Alternately, a single best-fit time-migration curve could be applied in an attempt to place both diffractors at the same location in the image space. As pointed out by Bevc et al. (1995), the time migrated image will contain a focusing error. Absolute positioning, as discussed earlier, should not be considered an important objective for a time migration. However, a specific characteristic of absolute lateral positioning can be used to create a more explicit definition of time migration.

1.5.4 A more exact definition for time migration

For a flat reflection event, i.e. where the specular zero-offset data have no time dip, the apex of the time-migration curve will be tangent to the specular portion of the reflection event in the data space. Thus the output location in the image space will have the same lateral coordinates as a flat reflection event in the data space. Note that, in a medium with lateral variations in wavespeed, these reflection events may not correspond to flat reflectors in the subsurface. This observation suggests that the definitive characteristic of a time migration is that a reflection event in the data space at zero offset with zero time dip will have the same lateral coordinates in the image space (Margrave, 2000). This definition of time migration is more explicit than the simplified working definition proposed in Section 1.1 (that the output image space of a time migration has a vertical coordinate of time), but now encompasses a broader spectrum of possible migration operators, including some with an output vertical coordinate of depth and others that require a more detailed estimate of the wavespeed macro-model [e.g. Gazdag's (1978) phase-shift migration].

1.5.5 Extensions to the DSR equation

A logical extension to the DSR equation (equation 1.53) is to add an additional fitting parameter so that a larger class of hyperbolic shapes can be fit. One possibility is to shift the time origin that defines the DSR hyperbola. Following the work of de Bazelaire (1988) and Castle (1988), who applied shifted hyperbolas to common-midpoint (CMP) gathers, a shift τ_s can be applied to the DSR equation, yielding

$$\tau - \tau_s = \sqrt{\left(\frac{\tau_0 - \tau_s}{2}\right)^2 + \frac{(x_m + h)^2}{c_{mig}^2}} + \sqrt{\left(\frac{\tau_0 - \tau_s}{2}\right)^2 + \frac{(x_m - h)^2}{c_{mig}^2}} . \tag{1.55}$$

Shifted hyperbolae have been shown to be related to attributes used in macro-model-independent imaging by Hockt et al. (1999), and to Thompson's weak anisotropy parameter η in anelliptic prestack time migration by Suaudeau and Siliqi (2001). A tilted DSR equation has been proposed by Bancroft et al. (1999). Although promising, applications of shifted or tilted DSR equation will not be considered further in this dissertation.

1.6 KINEMATICS AND DYNAMICS OF EOM PRESTACK TIME MIGRATION

As discussed in Section 1.2, the basic concept of migration can be described in two ways: weighted spreading of each point in the data space to produce the corresponding isochron surface in the image space, or weighted summation over a diffraction traveltime surface in the data space to produce each point in the image space. The second method has a natural affinity to the DSR forward theory operator (equation 1.53). The DSR equation was shown to be a good possible candidate for a migration operator given that the reflection and diffraction kinematics in the data space can be described by generalized hyperbolic relationships.

In this section, I assume that the DSR equation is a suitable description for the kinematic component of a migration operator. A complete migration operator also needs to address the dynamic component, i.e. the amplitudes. Of course, we are free to assume any operator as the generalized inverse, as long as we are willing to live with the associated errors. Although the DSR equation will prove to be a good guess for the kinematic component, a simple trial and error approach such as this proves less fruitful in the quest for an appropriate amplitude expression. As shown in Chapters 2 and 3, the more complete theoretical description required to determine the amplitude component also justifies summation over a diffraction traveltime surface. Thus the DSR equation, which describes a diffraction traveltime surface, is a reasonable assumption for the kinematic component of a migration operator.

1.6.1 EOM kinematics from the DSR equation

The essence of the kinematics of EOM prestack time migration (Bancroft and Geiger, 1994; Bancroft et al., 1998) is a simple reformulation of the DSR equation to a single-square root (SSR) equation at an equivalent offset h_e, chosen so that the equivalent two-way traveltime $2\tau_e$ equals the total traveltime τ, i.e.

$$2\tau_e = \tau, \tag{1.56}$$

where

$$2\tau_e = 2\sqrt{\left(\frac{\tau_0}{2}\right)^2 + \frac{h_e^2}{c_{mig}^2}} \tag{1.57}$$

is the SSR equation. Substituting the SSR and DSR equations into equation (1.56) gives

$$2\sqrt{\left(\frac{\tau_0}{2}\right)^2 + \frac{h_e^2}{c_{mig}^2}} = \sqrt{\left(\frac{\tau_0}{2}\right)^2 + \frac{(x_m + h)^2}{c_{mig}^2}} + \sqrt{\left(\frac{\tau_0}{2}\right)^2 + \frac{(x_m - h)^2}{c_{mig}^2}}, \tag{1.58}$$

which can be solved for the equivalent offset (Bancroft et al., 1998), yielding

$$h_e^2 = x_m^2 + h^2 - \left(\frac{2x_m h}{\tau c_{mig}}\right)^2. \tag{1.59}$$

Recall that the output points in the image space are defined by the surface location and two-way zero-offset traveltime τ_0 of the apex of the DSR equation. The output surface location can be chosen arbitrarily, in which case x_m and h define the radial midpoint distance and radial source-receiver offset for a given seismogram in the input data space. Now consider an intermediate data space consisting of equivalent offset gathers, one gather for each output surface location. Equation (1.59) can be used to map each sample

(x_m, h, τ) in the input data space to (h_e, τ) in each and every gather in the intermediate data space. In practice, input samples are summed into 'bins' of user-defined finite width Δh_e. All the input data on the DSR diffraction traveltime surface now lies on a hyperbolic curve (equation 1.57) in the equivalent offset gather. This greatly simplifies the selection of appropriate migration velocities for each τ_0 in the output image space. The desired image is created by applying a standard normal moveout correction and stack to the equivalent offset gathers.

The kinematic mapping formula given by equation (1.57) is accepted as an exact equivalent to the full DSR equation (Fowler, 1997a; Margrave et al., 1999; Wang et al., 2000; Yilmaz, 2001). The two main concerns with the method (e.g. Bednar, 1999) are that the mapping formula (equation 1.59) depends on the migration velocity (which is not known prior to binning) and that resolution can be degraded if too large a bin width is selected. Bancroft and Geiger (1996), Li (1999), and Wang et al. (2000) show that the mapping formula is not overly sensitive to the migration velocity and that an approximate estimate yields equivalent offset gathers suitable for accurate velocity analysis and imaging. Gathers can be recreated with the improved velocity estimates if required. Note, however, that if an infinite velocity is chosen, equation (1.59) reduces to an asymptotic limit $h_e^2 = x_m^2 + h^2$, which is not a satisfactory mapping operator at smaller τ_0's when both x_m and h are large. This can be avoided by choosing a more reasonable estimate for the initial migration velocity. Problems created by selecting too large a bin width can be resolved by choosing a smaller bin width.

Practical implementations of the kinematics of EOM prestack migration have been discussed in a number of publications, and so will not be discussed further in this dissertation. Interested readers should refer to Li et al. (1997), Bancroft et al. (1998), the

US and Canadian patents documents of Bancroft and Geiger (1997; 1998), and the M.Sc. thesis by Li (1999, esp. Chapter 3).

1.6.3 EOM dynamics and migration weighting functions

The dynamic solution has proved to be more elusive than its kinematic counterpart. Margrave et al. (1999) present a wavenumber formulation for EOM based on Stolt migration theory (Stolt, 1978; Stolt and Weglein, 1985). The wavenumber formulation yields the same kinematic solution as the time-domain approach, but is more obviously related to the physics of wavefield propagation than the Taylor series derivation given above. The wavenumber formulation also provides a dynamic solution that is, unfortunately, cumbersome to implement in the time-domain. However, the dynamic solution is of questionable accuracy for two reasons. First, Stolt migration theory is based on a double-downward continuation of the prestack data. A discussion of the dynamic errors associated with double-downward continuation is beyond the scope of the introduction, but is addressed later in Section 4.7 (see also discussion of contribution 10 in Section 1.7). Second, the mapping of the input data through the equivalent wavenumber domain to the output point introduces a Jacobian that, in essence, assumes that the mapping process is driven by regular sampling in the equivalent wavenumber domain. The amplitude correction associated with this Jacobian is not necessarily relevant to a time-domain implementation where the input data are regularly sampled in some acquisition configuration.

A time-domain implementation of EOM prestack migration will require a Jacobian. One of the major objectives of this dissertation is to establish just what form this Jacobian should take. Fowler (1997b) and Cary (1998) have proposed a Jacobian that assumes that the mapping process is driven by regular sampling in the equivalent offset gathers (prior to binning). An alternate approach, and the one adopted here, is to establish a Jacobian appropriate for mapping the input data space directly to the output image space. This mapping can be considered as a weighted summation over the DSR diffraction surface. The equivalent offset gather is just an intermediate domain of partially summed input data. Thus no additional Jacobian is required for the mapping process from the input data to the equivalent offset gather, or from the equivalent offset gather to the output image space. In any case, the combination of these Jacobians should have the same effect as the direct Jacobian.

The main benefit of the direct approach is that there are a variety of possible Jacobians published in the exploration seismology literature. Typically, these are buried in a more general weighting function that accounts for all amplitude factors in the migration operator. This is not a concern because the general weighting function is what we are seeking. Valid concerns are that a published migration operator may not take the input data to an output image of average or stacked angle-dependent reflectivities, or that there may be errors in the assumptions or even in the derivation of the migration operator. Although some of the relevant literature is listed below, a detailed review will not be provided here. Instead, important aspects of these papers, and others, are discussed at the appropriate locations throughout the dissertation.

That one can 'go shopping' through the seismic exploration literature, pick out a number of possible weighting functions, and then test them using the various validation processes listed in Section 1.3 is, to be frank, an accurate summary of my original efforts. Weighting functions proposed by Newman (1975, republished 1990), Schneider (1978), Wiggins (1984), Miller et al. (1987), Lumley (1989), Dillon (1990), Docherty (1991), and Hanitzsch (1995) were compared with each other by migrating synthetic and field data (the third validation process listed in Section 1.3). Although these efforts eventually led to the 2.5-D weighting function presented in Chapter 5, they provided scant insight into why the weighting function worked, how it could be modified for other prestack time-migration problems (e.g. 3-D data sets), or the significance of various approximations used to derive the published weighting functions. A more complete understanding of both the forward and inverse problems is required to properly address these questions.

Relevant literature for the forward problem includes Baker and Copson (1950), Morse and Feshbach (1953), Trorey (1977), Kuhn and Alhilali (1977), Deregowski and Brown (1983), Bleistein (1984), Berkhout (1985), and Wapenaar and Berkhout (1993). The forward problem leads naturally to the inverse problems of wavefield propagation (Wapenaar and Berkhout, 1989) and true-amplitude migration (Beylkin, 1985; Miller et al., 1987; Colton and Kress, 1991; Hanitzsch, 1997; Scales, 1997). As I shall show in Chapter 4, the common-offset prestack depth migration formulation determined by Bleistein and co-workers (Bleistein et al., 1987; Bleistein, 1987; Jaramillo and Bleistein, 1999; see Bleistein et al., 2001 for a complete review) provides the basis for weighting functions appropriate for EOM prestack time migration. Simplifications to this formula by Gray (1998b) and Dellinger et al. (2000) yield a weighting factor similar to the one obtained by my original ‘trial and error’ approach. As it turns out, many of the other published weighting functions (e.g. Berkhout, 1985; de Bruin, 1992) are designed for a common-shot acquisition configuration, which can produce biased estimates of average angle-dependent reflectivity (Geiger, 2001); or are fundamentally based on double-downward continuation (e.g. Stolt, 1978; Stolt and Weglein, 1985; Schultz and Sherwood, 1980), which also produces incorrect estimates (see Section 4.7 and discussion of contribution 10 in Section 1.7). The key to selecting the optimum weighting function is an understanding of the Jacobian that relates the acquisition configuration to an output image point. A detailed investigation of the optimum weighting function and its relation to acquisition configuration, including derivations and synthetic tests, is presented in Chapter 4.

1.7 SUMMARY OF OBJECTIVES AND CONTRIBUTIONS

The main objective of this dissertation is to find accurate and practical expressions for the dynamic component of EOM prestack time migration. Previous attempts (Fowler, 1997b; Cary, 1998; Margrave et al., 1999) suggest that Jacobians are necessary for the transformations from the input data space to the intermediate data space of EO gathers and from the EO gathers to the output image space. However, given that the kinematics of EOM are well established as an exact re-expression of the DSR equation, and that the transformation to the EO gathers can be implemented as a simple unweighted summation, the only Jacobian that is required is the direct Jacobian from the data space to the image space. The direct Jacobian can be found as part of the dynamic component of many prestack migration weighting functions published in the existing literature.

The task, then, is to determine which one of the published weighting functions is the correct one (if any) and how it can be simplified for practical application. This is accomplished by a comprehensive analysis of the relevant theory combined with a validation process using both synthetic models and field data, as described in the following paragraph.

In Chapter 2, the theory of acoustic wavefield extrapolation is developed from first principles. In Chapter 3, this theory is shown to be the foundation for the Kirchhoff-approximate formulae for prestack depth migration/inversion in a constant wavespeed medium. Formulae for the common-shot and common-receiver acquisition configurations are derived using principles of wave propagation combined with an imaging condition (Claerbout, 1971; Docherty, 1991). Formulae for the common-offset acquisition configuration can only be derived as a Fourier-transform-like inverse (Bleistein et al., 2001). Only a brief summary of this derivation is provided. In Chapter 4, these formulae are re-expressed for prestack time migration/ inversion and adapted for output to an image space of stacked reflectivity. The common-shot, common-receiver, and common-offset versions are then compared using synthetic data from a single dipping reflector in a constant wavespeed medium. The common-offset weighting function is shown to be correct, and is then developed for practical use. In Chapter 5, relative-amplitude EOM prestack time migration is compared against conventional imaging techniques on a test portion of the SNORCLE crustal seismic-reflection transect.

The second objective is to find a more general justification for the DSR kinematics of non-recursive prestack time migration algorithms such as EOM. Conventional derivations of the DSR equation assume a constant wavespeed subsurface, but practical experience suggests that excellent images can be obtained from DSR prestack time migrations in areas with significant lateral and vertical variations in subsurface wavespeed. The justification, which consists of two main parts, has already been presented in the introduction. First, I redefine migration as a transformation from a data space to an image space, express the transformation in terms of geophysical inverse theory, and from this determine qualitative criteria for evaluating the accuracy of the image space. Second, I derive the DSR equation for generalized inhomogeneous media using a Taylor series expansion about the best-fit image-ray location. The smoothness assumption required for the Taylor series expansion can be related to the qualitative accuracy criteria established earlier.

In this dissertation, there are a number of original contributions. Some of these have already been presented in Chapter 1. Others can be found scattered at appropriate locations throughout the dissertation. The following is a complete list:

1. Justification for Hagedoorn's (1955) method for reflector mapping using diffraction curves (Section 1.3.3).

2. Establish three general criteria for evaluating the image space: accuracy of focusing, accuracy of relative positioning, and accuracy of absolute positioning; and discuss their relationship to the imaging problem expressed in terms of geophysical inverse theory (Section 1.4.8).

3. Derivation of DSR equation for an arbitrary inhomogeneous isotropic media using Taylor series expansion of squared traveltimes perturbed about the best-fit image-ray location (Section 1.5.2). The derivation justifies the use of prestack time migration in areas with both lateral and vertical variations in subsurface wavespeed. The only assumption is that the traveltime perturbations are smooth over the perturbation distance. This assumption will affect accuracy of the horizontal component of absolute positioning more than accuracy of relative positioning, and accuracy of focusing the least. Accuracy of the vertical component of absolute positioning is not a significant concern for prestack time migration where the image space has a vertical coordinate of two-way traveltime.

4. Recognition that Jacobians are not required to take information from the data space to the intermediate space of the equivalent offset gather and then to the output image space. Instead, a direct Jacobian from data space to image space can be used if the equivalent offset gathers are created by a simple binning process (Section 1.6.3).

5. Derivation of Kirchhoff- and Born-approximate modeling formulae from first principles of continuum mechanics, using the Kirchhoff-Helmholtz integral representation (KHIR) as a common point of departure (Chapters 2 and 3), thereby establishing that the correct form for the monopole source function $S_\rho(\omega)$ includes a

factor accounting for the density of the medium at the source location (Section 2.2). The product $S_\rho(\omega)d\omega$ is the average amplitude of the source function for the packet of continuous frequencies in an interval $d\omega$ containing ω, and has physical units of kg^3s^{-2}, i.e. the time derivative of the rate of mass injection. A correct source function is derived for the variable-density acoustic case in Wapenaar and Berkhout (1993), but insufficient attention to physical units in the constant-density acoustic derivations of Bleistein and co-workers (Bleistein et al., 2001) has led to some difficulties in the implementation of true-amplitude migration/inversion formulae (e.g. Dellinger et al., 2000).

6. Derivation of a chi-squared fitting function $\hat{F}(\omega)$ that should be incorporated into all migration/inversion formulae (section 3.6). $\hat{F}(\omega)$ is a zero-phase function of frequency that is chosen such that $\hat{F}(\omega)|S_\rho(\omega)|$ is a good estimator of the unknown signal-to-noise ratio, where $|S_\rho(\omega)|$ is the source spectrum after zero-phase deconvolution. For an assumed noise model that is constant with frequency, $\hat{F}(\omega) = |S_\rho(\omega)|$. $\hat{F}(\omega)$ is normalized in both magnitude and physical units such that

$$\frac{1}{2\pi}\int d\omega \hat{F}(\omega)|S_\rho(\omega)| = 1. \qquad \text{[equation (3.35)]}$$

7. Recognition that, given regular acquisition configurations over a planar surface, the 2.5-D and 3-D common-offset weighting functions for migration/inversion are the optimum formulae for stacked reflectivity (Sections 4.3 and 4.4). Migration/inversion formulae with common-shot or common-receiver weighting functions yield a stacked reflectivity with a dip- and depth-dependent bias (Geiger, 2001).

8. Derivation of practical 2.5-D and 3-D time-domain constant-wavespeed formulae for prestack migration/inversion (Section 4.5). These formulae differ only by a constant

from similar formulae proposed by Gray (1998b), Dellinger et al. (2000), and Zhang et al. (2000).

9. Derivation of custom weighting functions for 2.5-D and 3-D EOM prestack time migration (Sections 4.6 and 4.7). These formulae are based on the practical formulae discussed above, but include additional weighting as a function of equivalent offset. The custom weights can be designed to have a more uniform dip- and depth-dependent variation than the practical weights.

10. Recognition that double-downward continuation prestack migration formulae proposed by Wiggins (1984) and Stolt and Weglein (1985) do not produce true-amplitude angle-dependent reflectivity or true-amplitude stacked reflectivity (Section 4.7). A similar observation is made by Zhang et al. (2001), who conclude that double-downward continuation using Claerbout's finite-difference method is also inaccurate, and propose simple factors to compensate for the error. Weglein and Stolt (1999) also suggest that a correction factor is required. A correction factor is given in equation (1) of Stolt (2002) and derived in his Appendix B.

11. Application of relative-amplitude preserving EOM prestack time migration to crustal seismic data (Chapter 5).

12. Presentation of a geometric argument for a stationary phase approximation that equates the normal derivative of the Green's function and the normal derivative of the upgoing one-way recorded wavefield, justifies the Rayleigh II far-field approximation to the Kirchhoff-Helmholtz wavefield extrapolator, and shows that the effects of the near-field terms tend to cancel (Appendix B).

13. Derivation of the isochron stack from the simplified form of the Kirchhoff-approximate modeling formula without the stationary phase approximations of Jaramillo (1999) and Jaramillo et al. (2000) (Appendix C).

14. Derivation of relationships between 2-D, 2.5-D, and 3-D modeling and migration/ inversion formulae for constant wavespeed (Appendix D).

I believe that the most significant contribution of this dissertation is the thorough documentation and justification of the theory of prestack time migration, both in the context of EOM and independent of EOM. Some details of the theory are new, but much of it can be found in published literature spanning many decades. To my knowledge, the theory of prestack time migration has not previously been compiled as one comprehensive work. My hope is that the reader will find that compilation here.

CHAPTER 2: THEORY OF ACOUSTIC WAVEFIELD EXTRAPOLATION

2.1 INTRODUCTION

In this chapter, the theoretical basis for acoustic wavefield extrapolation is developed from first principles. The Kirchhoff-Helmholtz integral representation is shown to be the fundamental equation of wavefield extrapolation and imaging. The detailed investigation presented in this chapter yields a mathematical description of Huygens' principle, simplified formulae for forward and inverse extrapolation from planar and non-planar interfaces, and reciprocity relations for Green's functions and acoustic pressure. The imaging problem is addressed in Chapter 3.

The background required to understand the theory of acoustic wavefield extrapolation is quite extensive. In Section 2.2, I derive the two-way nonhomogeneous[1] linear acoustic wave equation from first principles. The nonhomogeneous scalar wave equation, often considered to be restricted to constant density media, is shown to be appropriate for variable-density media. The correct physical units for Green's functions are determined by examining monopole and dipole source terms. In Section 2.3, the significance of Green's functions and linearity are discussed. In Section 2.4, one-way free-space Green's functions are determined for the space-time and space-frequency domains, the WKBJ approximation is assumed to be valid for an inhomogeneous medium, and the eikonal and transport equations are used to derive traveltime and amplitude expressions for one-way ray-theoretical Green's functions.

---

[1] The term "nonhomogeneous" refers to a partial differential equation (PDE) with a source term, and the term "inhomogeneous" refers to material properties that depend on position (Epstein and Slawinski, 1998).

In Section 2.5, I derive the Kirchhoff-Helmholtz integral representation (KHIR), which can be used to reconstructs the acoustic pressure at one spatial location in terms of the acoustic pressure elsewhere. The KHIR can be thought of as consisting of three terms: the volume-scattered wavefield, the surface-scattered wavefield, and the incident wavefield. In Section 2.6, the surface-scattered wavefield term, known as either the Kirchhoff-Helmholtz integral (space-frequency domain) or the Kirchhoff integral (space-time domain), is shown to be the mathematical description Huygens' principle. The surface-scattered wavefield term provides the basis for the Kirchhoff-approximate modeling and inversion formulae developed in Chapter 3. The volume-scattered wavefield is not discussed in detail, but provides the basis for the Born-approximate modeling and inversion formulae, also developed in Chapter 3. In Section 2.7, the incident wavefield term is shown to be the basis for reciprocity relations for constant-density and variable-density media.

In conventional seismic experiments, the data are not collected over a complete closed surface surrounding the volume of interest, as required by the reconstruction integrals. In addition, the data consist of only one of either the pressure or its normal derivative, not both as required. However, by assuming that the wavefield crosses a planar surface in one direction, reconstruction can be accomplished using the simpler Rayleigh I and Rayleigh II integrals. These are derived and discussed in Section 2.8. In Section 2.9, I examine possibilities for simplified wavefield propagation from a non-planar surface.

2.2 LINEAR ACOUSTIC AND SCALAR TWO-WAY WAVE EQUATIONS

The complete description of any mechanical disturbance in a medium requires only three basic equations; the equation of continuity (from conservation of mass), the equation of motion (from conservation of momentum), and a constitutive relation appropriate for the medium. The following derivation of the acoustic two-way wave equation is adapted from a derivation found in Wapenaar and Berkhout (1989, p. 7-13)[2]. Here, I begin with the linearized equation of continuity,

$$\frac{1}{K(\mathbf{x})}\frac{\partial p(\mathbf{x},t)}{\partial t} + \nabla \cdot \mathbf{v}(\mathbf{x},t) = \frac{\partial i_V(\mathbf{x},t)}{\partial t}, \tag{2.1}$$

which incorporates the constitutive relation known as the linearized equation of state for adiabatic fluids [see equation (2.3)], and the linearized equation of motion

$$\rho(\mathbf{x})\frac{\partial \mathbf{v}(\mathbf{x},t)}{\partial t} + \nabla p(\mathbf{x},t) = \mathbf{f}_V(\mathbf{x},t), \tag{2.2}$$

where **x** is a Cartesian position vector $(x_1,x_2,x_3) = (x,y,z)$ and t is time. For a propagating wavefront in a fluid, the dependent variables of physical interest are

p the change in pressure (physical units Pa = $\mathrm{Nm^{-2}} = \mathrm{kgm^{-1}s^{-2}}$), i.e. the acoustic pressure arising from the acoustic wavefield (defined as $p(\mathbf{x},t) = -K(\mathbf{x})\nabla \cdot u(\mathbf{x},t)$, where $u(\mathbf{x},t)$ is the displacement), and

v the particle velocity of the acoustic wavefield (physical units $\mathrm{ms^{-1}}$), assuming the flow velocity of the fluid is zero,

that together fully represent the linear acoustic wavefield. The fluid is fully represented by the material parameters

ρ the static mass density (physical units $\mathrm{kgm^{-3}}$), henceforth referred to as "density", and

---

[2] See Pierce (1989, Sections 1-2 to 1-6) for an alternate derivation and discussion, particularly the derivation of the linearized equation of state for adiabatic fluids on p. 11-15 (especially the footnote on p. 15 for inhomogeneous equation of state). Wapenaar and Berkhout (1989, Section I.2.3) provide an alternate derivation of the linearized equation of state [equation (2.3) below].

K the adiabatic compression modulus[3] (physical units of pressure - Nm^{-2}).

The adiabatic compression modulus K is the constant of proportionality in the linearized equation of state,

$$p(\mathbf{x},t) = K(\mathbf{x})\frac{\Delta\rho(\mathbf{x},t)}{\rho(\mathbf{x})}, \tag{2.3}$$

which relates change in pressure $p(\mathbf{x},t)$ to the ratio of change in density $\Delta\rho(\mathbf{x},t)$ over static density $\rho(\mathbf{x})$.

The source functions for the wavefield are

i_V the volume injection per unit volume (physical units m^3m^{-3}), expressed in equation (2.1) as a rate, and

$\mathbf{f}_V$ the body force acting per unit volume (physical units Nm^{-3}).

Note that the source functions are given as distributed sources per unit volume, as both the equation of continuity and the equation of motion originate inside time-invariant volume integrals expressing the conservation relations for mass and momentum, respectively. In Section 2.3.3, these source distributions will be reformulated using delta functions, leading to Green's functions appropriate for the representation theorems required for forward and inverse wavefield extrapolation.

Equation (2.1) states that, in the absence of a time varying source of volume injection, the time rate of change of acoustic pressure is proportional to the divergence of the particle velocity. Equation (2.2) is in essence Newton's second law (i.e. F = ma), but also states

---

[3] See Pierce (1989, Sections 1-4 and 1-10) for justification of adiabatic approximation.

that the gradient of the acoustic pressure acts as a restoring force that, in the absence of a body force, is proportional to the particle acceleration.

The particle velocity $\mathbf{v}(\mathbf{x},t)$ can be eliminated from the set of equations (2.1) and (2.2) by dividing the equation of motion (2.2) through by density $\rho(\mathbf{x})$, taking the divergence of the result and subtracting the time derivative of the equation of continuity (2.1). Replacing the source terms on the RHS with a notationally convenient function $s_V(\mathbf{x},t)$ yields

$$\nabla \cdot \left(\frac{1}{\rho(\mathbf{x})} \nabla p(\mathbf{x},t) \right) - \frac{1}{K(\mathbf{x})} \frac{\partial^2 p(\mathbf{x},t)}{\partial t^2} = -s_V(\mathbf{x},t). \tag{2.4}$$

Equation (2.4) is the linear acoustic two-way wave equation[4] for the acoustic pressure $p(\mathbf{x},t)$ and is valid for an inhomogeneous anisotropic medium containing arbitrary interfaces specified by discontinuities in the fluid parameters $\rho(\mathbf{x})$ and/or $K(\mathbf{x})$ [5]. The usual practice is to simplify this expression by expanding the divergence term on the LHS using an appropriate vector identity, multiplying through by the density and rearranging to give

---

[4] There are many types of linear and nonlinear wave equations. An advanced overview can be found in Brekhovskikh and Goncharov (1985). Robinson and Silvia (1981, Section 1.1) provide a good elementary discussion justifying linear waves. Scales (1997, p. 53-54) show why gravitational effects can be ignored when dealing with frequencies commonly used in seismic exploration.

[5] The frequency domain equivalent of equation (2.4) is the basic equation for the acoustic two-parameter migration and inversion literature. For example, it is equation (41) in Stolt and Weglein's 1985 review article in *Geophysics Golden Anniversary Issue* (Stolt and Weglein, 1985) and equation (1) of Wapenaar and Berkhout (1993). In addition, it provides the background to Chapter 5 and beyond of the text *Elastic wavefield extrapolation: redatuming of single- and multicomponent seismic data* (Wapenaar and Berkhout, 1989).

$$\nabla^2_{\mathbf{x}} p(\mathbf{x},t) - \frac{1}{c^2(\mathbf{x})}\frac{\partial^2 p(\mathbf{x},t)}{\partial t^2} = -\rho(\mathbf{x}) s_V(\mathbf{x},t) + \frac{\nabla\rho(\mathbf{x})}{\rho(\mathbf{x})}\cdot\nabla p(\mathbf{x},t)\,, \tag{2.5}$$

where $c(\mathbf{x}) = [K(\mathbf{x})/\rho(\mathbf{x})]^{1/2}$ is the speed of wave propagation in the media, i.e. the wavespeed[6] (physical units ms^{-1}). This form of the linear acoustic two-way wave equation is recognizable as a nonhomogeneous PDE commonly known as the scalar wave equation.

2.2.1 Simplifying the source term in the scalar wave equation

The second term on the RHS of equation (2.5) can be considered as a source term that is significant only when the spatial gradient of $\rho(\mathbf{x})$ is large, i.e. at discontinuities or interfaces within the volume. There are two lines of argument that justify ignoring this term. The most common approach is to assume that $\rho(\mathbf{x})$ is a smoothly-varying function with negligible gradients even at the interfaces (see Brekhovskikh and Goncharov, 1985, p. 263)[7]. This assumption is not as restrictive as it first appears because, to first order, the effect of discontinuities in $\rho(\mathbf{x})$ and $K(\mathbf{x})$ remain in the wavespeed $c(\mathbf{x})$. Unfortunately, density gradients are not negligible at interfaces, suggesting that we might be introducing a significant error by ignoring this term.

---

[6] That $c(\mathbf{x})$ is the wavespeed can be easily shown by solving the 1-D wave equation (or, equivalently, the 3-D wave equation in spherical coordinates) for an infinite homogeneous medium (e.g. Robinson and Silvia, 1981, Section 1.3; Wapenaar and Berkhout, 1989, Section I.3.3).

[7] Brekhovskikh and Goncharov (1985, p. 263) show that, in order to drop the second term on the RHS of equation (2.5), the space scale of the variation of mass density must be large compared to the wavelength, an assumption valid only for propagation in simpler macro subsurface models. Berkhout (1985, Appendix C) suggests using a scaled pressure function as a better approximation.

A better line of argument leads to the conclusion that the second term on the RHS of equation (2.5) is not required. Taken as a secondary source, this term accounts for a portion of the reflection and transmission effects arising from density contrasts at each interface (given that some of the effects of density contrasts are incorporated in the wavespeed). The reflection effects can be ignored for the derivation of wavefield extrapolators because we anticipate separating both the forward modeling problem and the migration/inversion problem into a cascade of three steps – forward wavefield extrapolation between the source and a given interface, boundary or imaging conditions defining reflectivity at the interface, and either forward or inverse wavefield extrapolation between the interface and the recording surface. With this cascaded approach, the mathematical model for reflectivity is not restricted to the acoustic model given by equation (2.5). Instead, we can choose a more appropriate mathematical model, preferably one that is both directly applicable to the reflection problem and more accurate for the assumed elastic Earth model (e.g. the Zoeppritz equations). In addition, we anticipate using one-way wavefield extrapolators that account for the primary arrivals only (i.e. multiples are ignored). This one-way approach greatly simplifies derivation and computation of wavefield extrapolators and their associated Green's functions.

However, the amplitude of the one-way wavefield extrapolators will be in error because the transmission effects associated with each interface are not included. This is not a serious omission, in part because, given an assumed elastic Earth model, the transmission effects calculated using a variable-density acoustic model [e.g. by including the second term on the RHS of equation (2.5)] are only correct at normal incidence. A more accurate approach is to calculate transmission effects at each interface using an elastic model (e.g. the Zoeppritz equations) and incorporate them as additional amplitude terms in the one-way acoustic wavefield extrapolators (see Hanitzsch, 1995).

If the second term on the RHS is ignored, equation (2.5) simplifies to

$$\nabla^2_{\mathbf{x}} p(\mathbf{x},t) - \frac{1}{c^2(\mathbf{x})} \frac{\partial^2 p(\mathbf{x},t)}{\partial t^2} = -\rho(\mathbf{x}) s_V(\mathbf{x},t)\,. \tag{2.6}$$

Snell's law of refraction, which depends only on the variable wavespeed $c(\mathbf{x})$, can be determined from the variable-density scalar wave equation [equations (2.4)/(2.5)] or from the simplified scalar wave equation [equation (2.6)]. Thus, all the other desirable characteristics of an elastic wavefield extrapolator (e.g. the kinematics, raypaths, and geometric spreading) can be accurately determined using this simplified scalar wave equation. In fact, the independent propagation of P- and S-wave potentials in elastic media can be expressed by versions of the scalar wave equation similar to equation (2.6), with propagation velocities α and β, respectively[8].

In equation (2.6), the density $\rho(\mathbf{x})$ is often incorporated into the source term (e.g. Wapenaar, 1993a). However, keeping the two separate will prove useful when deriving Green's functions, which contain density terms that depend on the location of the Green's function source and observation positions (Snieder and Chapman, 1998).

2.2.2 Justification for acoustic pressure as the dependent field variable

In the simplified scalar wave equation given by equation (2.6), the dependent field variable is acoustic pressure. Scalar wave equations can be derived for other dependent field variables, such as the Cartesian components of the acoustic particle velocity $\mathbf{v}(\mathbf{x},t)$,

[8] See Scales (1997, p. 55-56). Note that, in Section 1.1.3 α and β denote angles in the migrator's equation. In Section 2.5 and throughout Chapter 3, α denotes the wavespeed perturbation function.

the change in density $\Delta\rho(\mathbf{x},t)$ (or its equivalent, the condensation $s(\mathbf{x},t)$ [9], which can be expressed as the change in acoustic pressure divided by the adiabatic compression modulus), or even the change in temperature. However, some of these require assumptions of homogeneity (Pierce, 1989, p. 18). A somewhat more abstract description of the acoustic field is given by the velocity potential, from which almost all scalar or vector field variables can be derived (e.g. acoustic pressure, particle velocity or its components, particle displacement or its components, and, via equations of state, change in density and temperature).

However, it can be shown that in the limiting case of an ideal fluid, the P-wave potential is identical to the acoustic pressure (see Wapenaar and Berkhout, 1989, Section II.2, esp. II.2.5). Hence, I will proceed with equation (2.6). In Section 2.5, I return to the space-frequency domain equivalent of this equation to develop a special form of Rayleigh's reciprocity theorem known as the Kirchhoff-Helmholtz integral representation—the fundamental equation of seismic imaging theory.

2.2.3 Monopole and dipole source terms

The source term $s_V(\mathbf{x},t)$ on the RHS of equation (2.6) is just a convenient expression for the sum of source terms arising from equations (2.1) and (2.2) in the derivation of the linear two-way acoustic wave equation:

$$\rho(\mathbf{x})s_V(\mathbf{x},t) = \rho(\mathbf{x})\frac{\partial^2 i_V(\mathbf{x},t)}{\partial t^2} - \rho(\mathbf{x})\nabla\cdot\left(\frac{1}{\rho(\mathbf{x})}\mathbf{f}_V(\mathbf{x},t)\right). \tag{2.7}$$

---

[9] Here, the use of s to denote the condensation is in agreement with common use in the historic literature, such as Baker and Copson (1950, esp. Sections 3.1 to 3.3 and 4.1) and Tikhonov and Samarskii (1990, Section II.1.6). Otherwise, s denotes source functions in the time domain, $S(\omega)$ denotes source functions in the frequency domain, and S a surface. The context of use should prevent confusion.

These terms need to be investigated further for two reasons. First, by re-expressing the source functions in terms of delta functions we can develop Green's functions appropriate for the representation theorems required for forward and inverse wavefield extrapolation (and determine the correct physical units for the Green's functions). Second, the time varying component of the source functions modifies the amplitude and phase characteristics of the propagating wavefield, and so must be considered in any complete derivation of an imaging method.

In its most elementary form, the first term on the RHS of equation (2.7) represents a monopole point source of volume injection multiplied by the density[10]

$$\rho(\mathbf{x})\frac{\partial^2 i_v(\mathbf{x},t)}{\partial t^2} = \rho(\mathbf{x})\frac{\partial^2 i(t)}{\partial t^2}\delta(\mathbf{x}-\mathbf{x}_s), \tag{2.8}$$

where $\partial_t^2 i(t)$ is the source signature (physical units m^{3}s^{-2}) giving the time derivative of the rate at which volume is added to the fluid outside some small fixed region enclosing the source located at $\mathbf{x}_s$, and $\delta(\mathbf{x}\text{-}\mathbf{x}_s)$ is the 3-D spatial delta function (physical units m^{-3}). A single marine seismic airgun or a single land seismic dynamite charge can be considered as a monopole point source. If necessary, a source array can be synthesized from monopoles to produce a far-field signature equivalent to the physical source (Stoffa and Ziolkowski, 1983).

In its most elementary form, the second term on the RHS of equation (2.7) can be considered a dipole source of force

$$\rho(\mathbf{x})\nabla\cdot\left(\frac{1}{\rho(\mathbf{x})}\mathbf{f}_v(\mathbf{x},t)\right) = \rho(\mathbf{x})\mathbf{f}(t)\nabla\cdot\left(\frac{\delta(\mathbf{x}-\mathbf{x}_s)}{\rho(\mathbf{x})}\right), \tag{2.9}$$

---

[10] See Pierce (1989, Section 4.3) for a discussion of monopole point sources of mass injection.

where $\mathbf{f}(t)$ is the source signature (physical units of force - N or kgms^{-2}). The simplest representation for a single land vibrator could be considered as a dipole source of vertical force $\mathbf{f}(t) = (0,0, f_z(t))$. Wapenaar and Berkhout (1989, Section I.3.1) show that, in homogeneous media, the wavefield from this dipole source can be determined directly as the negative z-derivative of the wavefield from a monopole source. For this reason (and because the monopole wavefield is the far easier case[11]) only monopole point sources will be considered in the remainder of this dissertation.

2.3 GREEN'S FUNCTIONS AND LINEARITY

Before I proceed with an in-depth discussion of Green's functions, I will briefly summarize their significance[12]. In general, a Green's function is the impulse response of a linear system. In our context, a Green's function is the solution to the linearized acoustic wave equation given a causal delta function source. Having a solution implies that the problem is properly specified. Ideally, we would like to have an analytic solution that satisfies the wave equation and its boundary conditions for any two points in space and time (e.g. the delta function source location and the observation location). Since the acoustic wave equation is linear, each instance of an analytic solution is a member of an infinite set of linear solutions. These can be superposed, yielding more complex solutions from the (hopefully) simple Green's functions. Hence, if we can formulate a representation of the desired solution as an integration of known Green's functions and

---

[11] Ignoring Fresnel's reminder that "Nature is not embarrassed by difficulties of analysis" (Mackay, 1994).

[12] See Bleistein (1984, Section 5.3 and 6.3) for mathematical justifications for the use of Green's functions (esp. p. 155 and p. 175). The popularity of Green's functions can be attributed to Morse and Feshbach (1953, Chapter 7, especially p. 791-793 and p. 803-814 for application to the Helmholtz equation).

other known parameters, linearity guarantees that the solution will be meaningful[13]. A suitable representation theorem will be derived in Section 2.5.

2.3.1 Using simplified Green's functions in complicated inhomogeneous media

We desire analytic Green's functions that provide a valid solution for all space and time. This is not practical for wavefield propagation through complicated inhomogeneous media. Fortunately, superposition can take place over subdivisions of space and time. We can determine simple Green's functions that are solutions to local problems, and superpose the results[14]. A particularly useful simple solution is the Green's function for an increment in space and time through a homogeneous medium, otherwise known as the free-space Green's function. The material parameters can be changed at each increment. In this manner, these simple Green's functions can approximate wavefield propagation through an inhomogeneous medium. Effectively, this concept is known as Huygens' principle.

A conceptual model of wavefield propagation through an inhomogeneous medium can be formed by applying the concept of causality. Causality says, first, that no wavefield can spontaneously arise without a cause, and second, that effect follows cause in both time

---

[13] The concept of "meaningful" is deliberately vague, but can be taken to refer the mathematical properties of uniqueness, existence, and completeness, and for the inverse problem (which is improperly posed) the practical properties of stability and goodness of numerical approximation.

[14] Assuming the high-frequency (ray-theoretical) approximation (Bleistein et al., 2001, p. 5-7 and p. 113-117).

and space[15]. The Green's function is the wavefield effect at a given observation point due to a very simple cause (the space-time delta function source). Linearity allows us to reformulate the effect into a cause, whose effect is given by another Green's function. Therefore, we can take analytic Green's functions with a global effect (e.g. free-space Green's functions) and apply them locally, then superpose these in time to create approximations to more complex Green's functions. Or we could take a complex Green's function, use linearity to break it down into simple Green's functions that describe the effect at only one distant observation location for a given source location, and superpose these in space to create the desired approximation (e.g. ray-theoretical Green's functions). The concept of "wavefield propagation" is, therefore, akin to the concept of Green's functions, which are themselves an elemental part of the description of Huygens' principle[16].

2.3.2 Seismic reflection as a cascade of linear steps

If wavefield propagation can be considered as separate linear steps, the seismic reflection problem can be composed of the separate linear steps of propagation down—reflection—

---

[15] Fortunately, the wave equation is symmetric in both time and space, so this second statement about causality holds when time is reversed, i.e. that cause must precede effect, and can be determined uniquely. A mathematical justification for causality, due to Poisson, can be found in Pierce (1989, p. 173-174).

[16] However, we will find that the Green's functions in the Kirchhoff-Helmholtz integral representation (the mathematical description of wavefield propagation—see Sections 2.5 and 2.6) have their source location at the observation point, i.e. where the wavefront will be, not where it was. "And now remains that we find out the cause of this effect—or rather say 'the cause of this defect', for this effect defective comes by cause." (Shakespeare, 1604, Hamlet Act 2 Scene 2 Lines 101-104).

propagation up[17]. Since we are initially interested in only one reflector along the total path, we often choose to ignore the portion of the propagating wavefield that reflects from any other interfaces encountered along the way. The part of the propagating wavefield that we are interested in, known as the transmitted wavefield, can then be calculated as some fraction of the original wavefield (although this correction is seldom included). This is the "one-way" approach to wavefield propagation.

With the propagation problem separated from the reflection problem, it may be convenient to describe reflection using entirely different, and appropriately simplified, mathematics. We can invoke linearity again to rearrange the physical order into propagation down—propagation up—reflection[18], and combine the two propagation steps, if this proves useful. The reflection problem, and appropriate approximations, will be discussed in Section 3.2. First, I return to Green's functions, and the theoretical framework for wavefield propagation that I set out to describe in this section.

2.3.4 Scalar wave equation for delta function source in the space-time domain

Green's functions, then, are the solution of the wave equation to a delta function source. Using $s_V(\mathbf{x},t)$ to denote a monopole point source [equation (2.8)] in the linearized acoustic two-way wave equation [equation (2.6)] and expanding the source function $s_V(\mathbf{x},t)$ using delta functions in both space and time gives

$$\nabla^2_{\mathbf{x}} p(\mathbf{x},t) - \frac{1}{c^2(\mathbf{x})}\frac{\partial^2 p(\mathbf{x},t)}{\partial t^2} = -\rho(\mathbf{x}) s\,\delta(\mathbf{x}-\mathbf{x}_s)\delta(t-t_0)\,, \tag{2.10}$$

---

[17] Berkhout (1981) applies this concept, known as the "WRW" model, to seismic modeling and imaging. More details are provided in Berkhout (1985), Wapenaar and Berkhout (1989), and de Bruin (1992).

[18] Robinson and Silvia (1981, p. 434-439) apply this concept to seismic imaging, using the WKBJ method of plane-wave propagation and the double-square root (DSR) equation (for a homogeneous medium).

where t_0 is the time of the source impulse [the notation $p(\mathbf{x},t)$ suggests $t_0 = 0$], and the monopole source amplitude s has physical units equivalent to the rate of volume influx (physical units m^3s^{-1}). Taking the source to be unit amplitude at location $\mathbf{x}_G$ and absorbing the source physical units and density $\rho(\mathbf{x})$ from the RHS[19] into the dependent field variable $p(\mathbf{x},t)$ yields

$$\nabla^2_{\mathbf{x}} g(\mathbf{x},\mathbf{x}_G,t,t_G) - \frac{1}{c^2(\mathbf{x})}\frac{\partial^2 g(\mathbf{x},\mathbf{x}_G,t,t_G)}{\partial t^2} = -\delta(\mathbf{x}-\mathbf{x}_G)\delta(t-t_G)\,, \tag{2.11}$$

where $g(\mathbf{x},\mathbf{x}_G,t,t_G)$ is the Green's function with physical units of pressure per unit rate of mass influx (physical units $m^{-1}s^{-1}$). The Green's function describes the wavefield at observation position $\mathbf{x}$ as a function of time t due to a unit impulse at source position $\mathbf{x}_G$ at time t_G.

Equation (2.11) shows that the Green's function satisfies the linearized acoustic two-way wave equation. However, this equation alone is not sufficient to define the Green's function. A complete specification must include boundary and initial[20] conditions for the PDE. Time boundary conditions do not pose much of a problem. Typically, the Green's function is restricted to be either forward propagating [i.e. causal: $g(\mathbf{x},\mathbf{x}_G,t,t_G) = 0$ and $\partial_t g(\mathbf{x},\mathbf{x}_G,t,t_G) = 0$ for $t < t_G$)] for use in forward wavefield propagation, or backward

---

[19] Under the effect of the delta function on the RHS, $\rho(\mathbf{x})$ becomes $\rho(\mathbf{x}_s)$ and is therefore a constant relative to the operators on the LHS. The pressure $p(\mathbf{x},t)$ (units Nm^{-2}) is divided by the product of the mass density and source units ($\rho(\mathbf{x}_s)m^3s^{-1}$) yielding the Green's function (units $m^{-1}s^{-1}$).

[20] Solutions for problems where the initial data are taken to be a distribution (i.e. delta functions) are called Riemann functions. Because initial conditions can be considered as boundary conditions in time, no distinction will be made in this dissertation between Green's functions (source and/or boundary data) and Riemann functions (initial data)—they are the same other than in name (Bleistein, 1984, Sections 4.4 and 4.5, esp. discussion on p. 131).

propagating [i.e. anticausal: $g(\mathbf{x},\mathbf{x}_G,t,t_G) = 0$ and $\partial_t g(\mathbf{x},\mathbf{x}_G,t,t_G) = 0$ for $t_G > 0$] for use in inverse wavefield extrapolation. Note, however, that Huygens' principle for forward wavefield propagation was originally conceived by Huygens in 1673 using the equivalent of backward propagating Green's functions (Robinson and Silvia, 1981, p. 364). The importance of this non-intuitive concept will be discussed further in Section 2.6.

Spatial boundary conditions and inhomogeneities in the material properties, including arbitrary interfaces, require impossibly complicated Green's functions that defy analytic description. The standard approach is to simplify the imaging problem so that simple analytic expressions for the Green's functions can be used. For example, an anti-causal free-space Green's function for homogeneous isotropic media (discussed in Section 2.4) lies at the heart of most recursive and nonrecursive time migrations, as well as some recursive depth migrations. The standard approach for determining nonrecursive Green's functions for complex media is by invoking the WKBJ (ray-theoretical) approximation (Bleistein et al., 2001) (also discussed in Section 2.4). A ray-theoretical Green's function can be thought of as a linear superposition of simple functions relating the phase and amplitude response of two points in the medium. In the standard approach, the eikonal equation and transport equations are solved to determine phase and amplitude, respectively (see Section 2.4.3).

2.3.4 Scalar wave equation for delta function source in the space-frequency domain

Note that in equations (2.10) and (2.11) the density $\rho(\mathbf{x})$ and the wavespeed $c(\mathbf{x})$ are time invariant, suggesting that a Fourier transform with respect to the time variable will reduce the dimensionality of the problem without introducing simplifying assumptions[21]. This is

---

[21] Causality suggests an alternate, equally valid approach by taking the Laplace transform of the time coordinate (see Fokkema and van den Berg, 1993), as opposed to the conventional use of Fourier

equivalent to considering monochromatic sources $S(\omega)$ and monochromatic wavefields $P(\mathbf{x},\mathbf{x}_s,\omega)$ (where the dependence on source location $\mathbf{x}_s$ is now shown explicitly). Re-expressing the source function on the RHS of equation (2.10) to include only a spatial delta function and taking the Fourier transform with respect to the time variable[22] gives the simplified scalar wave equation in the space-frequency domain:

$$\nabla_{\mathbf{x}}^2 P(\mathbf{x},\mathbf{x}_s,\omega)+\frac{\omega^2}{c^2(\mathbf{x})}P(\mathbf{x},\mathbf{x}_s,\omega)=-S(\omega)\rho(\mathbf{x})\delta(\mathbf{x}-\mathbf{x}_s). \tag{2.12}$$

Equation (2.12) is commonly known as the Helmholtz equation.

Similarly, equation (2.11) can be expressed in the space-frequency domain as

$$\nabla_{\mathbf{x}}^2 G_0(\mathbf{x},\mathbf{x}_G,\omega)+\frac{\omega^2}{c_0^2(\mathbf{x})}G_0(\mathbf{x},\mathbf{x}_G,\omega)=-\delta(\mathbf{x}-\mathbf{x}_G), \tag{2.13}$$

where the Green's function $G_0(\mathbf{x},\mathbf{x}_G,\omega)$ (physical units m^{-1}) is the wavefield response at observation point $\mathbf{x}$ due to a monochromatic point source of unit amplitude at $\mathbf{x}_G$. The subscript (0) is introduced to denote a reference medium, which will be required later in Section 2.5. Note that the conventional listing of independent variables $\mathbf{x}$, $\mathbf{x}_G$, and ω

---

transforms. However, Aki and Richards (1980, Box 5.2, p. 129-130) suggest that Fourier transforms are preferred for real signals. Bleistein et al. (2001, Appendix B) explains why a causal Fourier transform is appropriate, and then shows that this approach is similar to the Laplace transform approach.

[22] Fourier transform sign conventions follows Aki and Richards (1980, Box 5.2, p. 129-130) and Claerbout (1985, p. 63-64): $h(\mathbf{x},t) = \mathrm{Re}[1/2\pi \int_0^\infty 2H(\mathbf{x},\omega)e^{-i\omega t}d\omega]$, where only positive frequencies are operated on to preserve Hermitian symmetry. Note that the sign convention is opposite to that adopted by Wapenaar and Berkhout (1989, Section III.2.1, p. 76-77). $H(\mathbf{x},\omega)$ is a spectral density (i.e. spectrum per unit length ω). The product $H(\mathbf{x},\omega)d\omega$ is an average amplitude for the packet of continuous frequencies in an interval $d\omega$ containing ω. Hence the physical units should be considered as average amplitudes (an interpretation that agrees with practical implementation using finite discrete Fourier transform) and the product $H(\mathbf{x},\omega)d\omega$ will have identical units as the time domain equivalent $h(\mathbf{x},t)$. See Appendix A for further discussion.

(which I have adopted here) neglects the time difference t - t_G, which will reappear later as an essential part of the phase in the ray-theoretical Green's function (see Section 2.4.2).

2.4 ONE-WAY FORWARD AND BACKWARD PROPAGATING FREE-SPACE AND RAY-THEORETICAL GREEN'S FUNCTIONS

Up to this point, I have used generalized Green's functions that satisfy the two-way wave equation. As discussed previously (Section 2.3), these Green's functions quickly become unwieldy when inhomogeneous media and/or reflecting boundary conditions are introduced. In particular, small errors in specifying the reference media can lead to large errors in the two-way propagation of multiply reflected wavefields (Berkhout and Wapenaar, 1989)[23]. For wavefield propagation, it is much easier to ignore multiples altogether, either by treating them as coherent noise or addressing them separately using other processing steps. The general practice in inverse seismic wavefield propagation is to ignore all reflections and scattering, and consider only "one-way" wavefields, which were introduced briefly in Section 2.3.

A one-way approach to wavefield propagation greatly simplifies the calculation of Green's functions. Analytic solutions for one-way Green's functions are available only for homogeneous media and simple depth-dependent functions. Otherwise, it is more practical to compute numerical Green's functions using the ray-theoretical approach (Bleistein et al., 2001). Note that the term "one-way" refers to the spatial direction, in the sense that we keep track of only the transmitted portion of the propagating wavefield. This is distinct from the terms "forward" and "backward" which refer to initially outward

[23] See also Wapenaar and Berkhout (1989) Figure V-6 and related discussion on p. 178-180.

wavefield propagation in the positive and negative time directions, respectively[24] (i.e. a reflection surface could result in an inward propagating wavefield that is still progressing forward in time).

2.4.1 Free-space Green's functions

In the space-time domain, the forward propagating free-space Green's functions for an unbounded homogeneous medium (Wapenaar and Berkhout, 1989, p. 169)[25] is given by

$$\vec{g}_0(\mathbf{x},\mathbf{x}_G,t,t_G)=\frac{1}{4\pi}\frac{\delta\big((t-t_G)-r/c_0\big)}{r}, \tag{2.14}$$

and the backward propagating free-space Green's function by

$$\overleftarrow{g}_0(\mathbf{x},\mathbf{x}_G,t,t_G)=\frac{1}{4\pi}\frac{\delta\big((t-t_G)+r/c_0\big)}{r}, \tag{2.15}$$

where $r=\left|\mathbf{x}-\mathbf{x}_G\right|$. In a homogeneous medium, the wavespeed c_0 is independent of the coordinates of the Green's function. Since the Green's function must contain within it the complete description of the wavefield, given all the material properties and boundary conditions, the free-space Green's functions [equations (2.14) and (2.15)] can easily be seen to be "one-way" expressions.

---

[24] The wave equation is time symmetric, with exact solutions for both forward and backward wavefield propagation. The more general term "inverse seismic wavefield extrapolation" is often used instead of "backward wavefield propagation" because the wavefield can be propagated either backward in time (e.g. reverse time extrapolation) or in the opposite spatial direction to the time-forward direction (e.g. downward continuation of the upgoing wavefield—also using backward propagating Green's functions).

[25] Wapenaar and Berkhout's Green's functions include a mass density term in the numerator because they have units of pressure per unit rate of volume influx (units $\mathrm{kgm^{-4}s^{-1}}$) instead of the convention chosen here of pressure per unit rate of mass influx (units $\mathrm{m^{-1}s^{-1}}$). The Green's functions used in this dissertation can be thought of as Wapenaar and Berkhout's Green's functions normalized by the mass density at the source location.

Taking the Fourier transform with respect to time $\tau_0 = (t - t_G)$ of equation (2.14) yields the forward propagating free-space Green's functions for a homogeneous medium in the space-frequency domain,

$$\vec{G}_0(\mathbf{x}, \mathbf{x}_G, \omega) = \frac{1}{4\pi} \frac{e^{i\omega r / c_0}}{r}, \tag{2.16}$$

and from equation (2.15), the backward propagating free-space Green's function,

$$\overleftarrow{G}_0(\mathbf{x}, \mathbf{x}_G, \omega) = \frac{1}{4\pi} \frac{e^{-i\omega r / c_0}}{r}, \tag{2.17}$$

which is just the complex conjugate of equation (2.16). The term r/c_0 in the exponents of equations (2.16) and (2.17) is equal to the traveltime $\tau_0 = (t - t_G)$ in the delta functions of their time-domain equivalents [equations (2.14) and (2.15), respectively]. The 2.5-D forms of the Green's functions are identical to the 3-D forms given above. The 2-D forms are equivalent to a line source and can be found by integrating equations (2.14) and (2.15) with respect to coordinate y, assuming both the source and observation locations for the Green's function are in the $y = 0$ plane. The resulting space-frequency domain Green's functions are zero-order Hankel functions of the first and second kind, respectively (see Kuhn and Alhilali, 1977 equations 9b and 9a—note the opposite convention for the Fourier transform). A more complete treatment of the 2-D Green's functions, as well as the relationships between 2-D, 2.5-D and 3-D forward modeling and migration/ inversion formulae for constant wavespeed, can be found in Appendix D.

A 2-D (x, z) cross-section through a 3-D space-frequency domain free-space Green's functions can be easily pictured in a 3-D space-time volume (Figure 2.1a). The forward propagating free-space Green's function [equation (2.16)] represents a monochromatic wavefield of frequency ω emanating from source location $\mathbf{x}_G$. The wavefronts (defined as surfaces of constant phase) radiate outward from the source location as expanding spheres, or circles in the 2-D (x, z) cross-section. A particular wavefront will have traveled a distance $r = |\mathbf{x} - \mathbf{x}_G|$ from the source point $\mathbf{x}_G$ to the observation point $\mathbf{x}$ in time $\tau_0 = r/c_0$. The sinusoidal amplitude of the wavefront at a given observation location is a function of reciprocal distance $1/r$. If we take a continuous and infinitely broad spectrum of monochromatic radiators all located at position $\mathbf{x}_G$ and initiated at time t_G, they can be superposed and will constructively interfere to recreate an impulsive wavefront at the elapsed time $\tau_0 = (t - t_G)$. Elsewhere the wavefield will be zero. This single impulsive wavefront is the essential physical interpretation of the delta function $\delta((t - t_G) - r/c_0)$ in equation (2.14). Thus the phase (normalized by radial frequency ω) can be interpreted as having the same physical meaning as the elapsed traveltime, even though the space-frequency domain Green's function has no explicit indication of the source initiation time t_G.

In anticipation of one-way Green's functions for inhomogeneous media, where the elapsed traveltime cannot be calculated by a simple formula such as $\tau_0 = r/c_0$, traveltime will henceforth be defined by $\tau_0(\mathbf{x},\mathbf{x}_G)$. As we will see shortly, the ray-theoretical approach allows traveltime and amplitudes to be determined using the eikonal equation and transport equations, respectively. In fact, traveltime $\tau_0(\mathbf{x},\mathbf{x}_G)$ is often referred to as the eikonal function (Berkhout, 1985, p. 73).

The backward propagating space-frequency domain free-space Green's function [equation (2.17)] has a similar physical meaning in the space-time domain (Figure 2.1b) except that it represents wavefronts propagating inward towards the source point $\mathbf{x}_G$ as time goes forward, or wavefronts propagating outward as time goes backward (hence the name).

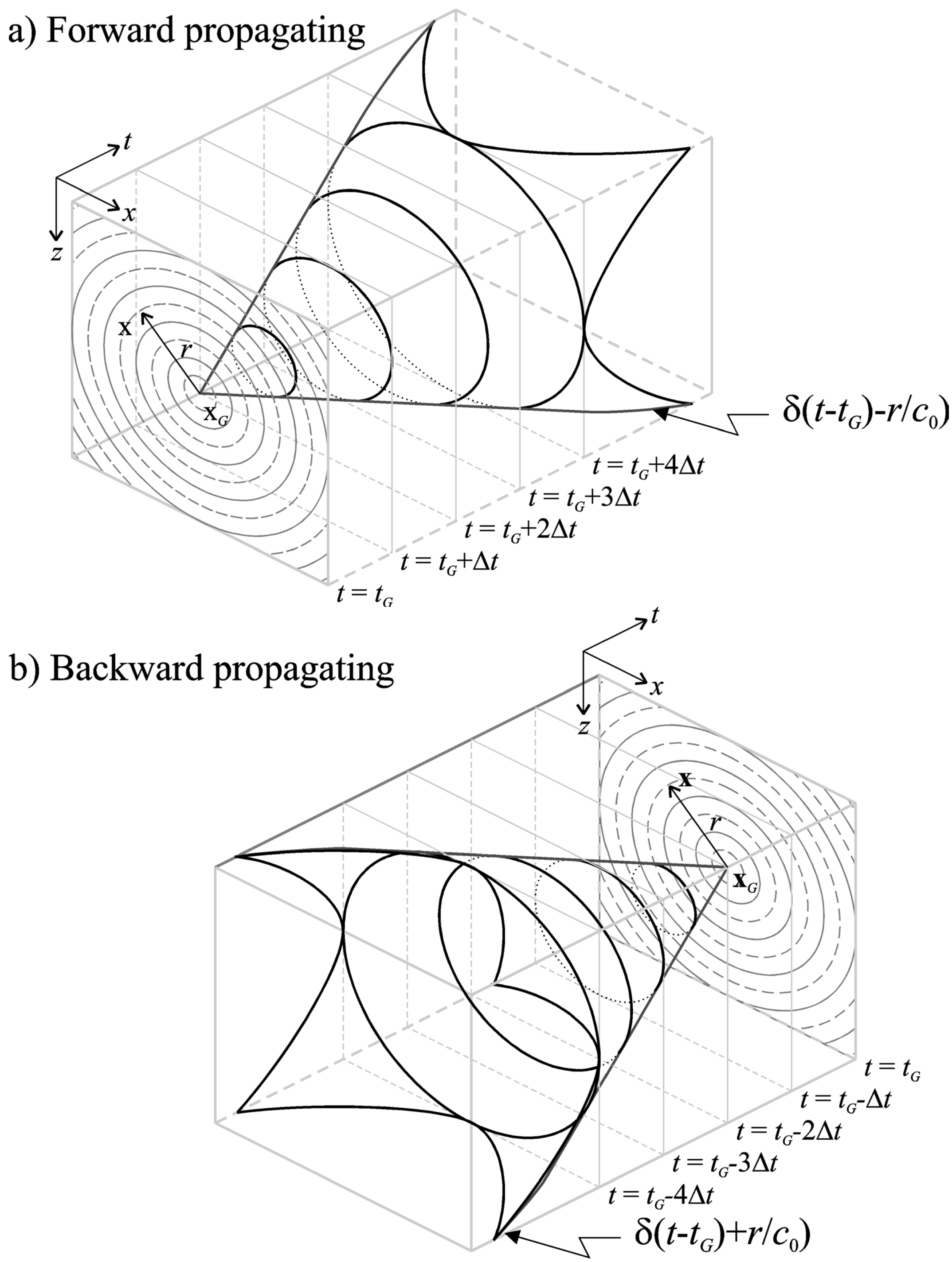

Figure 2.1. Wavefronts (surfaces of constant phase) in space-time domain for (x,y=0,z) cross-section through a 3-D space-frequency domain free-space Green's function (i.e. a monochromatic radiator) with source location at $\mathbf{x}_G = (x_G, y_G{=}0, z_G)$. a) Forward propagating free-space Green's function propagates outward as time moves forward. b) Backward propagating free-space Green's function propagates outward as time moves backward – hence the names.

This interpretation is perhaps more obvious if we examine the delta function of the space-time domain equivalent [equation (2.15)]. The delta function is non-zero if $(t - t_G) + r / c_0 = 0$, i.e. when $t < t_G$ (given that r/c_0 is always a positive quantity). Following the discussion in the previous paragraph, elapsed traveltime for backward propagating one-way Green's functions for inhomogeneous media can be defined as $-\tau_0(\mathbf{x},\mathbf{x}_G)$. Hence both the forward and backward Green's functions [e.g. equations (2.16) and (2.17)] can be expressed using the same formula, the only difference being the intuitive sign of the traveltime which is positive for forward in time (i.e. a delay in time or positive phase lag, giving a "causal" or "retarded" Green's function) and negative for backward in time (i.e. an advance in time or negative phase lag, giving an "anticausal" or "advanced" Green's function). This nice result arises from the choice of sign conventions for the Fourier transform, as described in a footnote in Section 2.3.4 and in Appendix A.

2.4.2 Raypaths and traveltimes for ray-theoretical Green's functions

For the ray-theoretical Green's functions, we require expressions for the traveltime and amplitude. We assume that the acoustic pressure can be written as its WKBJ approximation (Scales, 1997, p. 78 and p. 117-118),

$$P(\mathbf{x},\mathbf{x}_s,\omega) = S(\omega)\rho(\mathbf{x}_s)A(\mathbf{x},\mathbf{x}_s)e^{i\phi(\mathbf{x},\mathbf{x}_s,\omega)}, \tag{2.18}$$

where $S(\omega)$ is the spectral density of the source, $A(\mathbf{x},\mathbf{x}_s)$ the Green's function amplitude at location $\mathbf{x}$ due to a point source at location $\mathbf{x}_s$, $\rho(\mathbf{x}_s)$ the mass density at the source location (a constant) and ϕ the phase lag. The phase lag and the amplitude are found by solving the eikonal and transport equations, respectively.

The phase lag can be expressed as frequency ω multiplied by elapsed traveltime delay $\tau(\mathbf{x},\mathbf{x}_s)$. Hence an equivalent form of equation (2.18) is

$$P(\mathbf{x},\mathbf{x}_s,\omega) = S(\omega)\rho(\mathbf{x}_s)A(\mathbf{x},\mathbf{x}_s)e^{i\omega\tau(\mathbf{x},\mathbf{x}_s)}. \tag{2.19}$$

Substituting equation (2.18) into the homogeneous form of the acoustic wave equation [equation (2.12), with no source term on the RHS], equating the real part to zero, and assuming $\nabla^2 A / A$ is negligible[26] gives the eikonal equation,

$$\left|\nabla_{\mathbf{x}} \phi(\mathbf{x}, \mathbf{x}_s, \omega)\right|^2 = \frac{\omega^2}{c^2(\mathbf{x})}, \tag{2.20}$$

where the gradient operates on the observation coordinates $\mathbf{x}$. Expressing phase as the product of frequency and traveltime, dividing through by ω^2, and taking the square root of the result yields an alternate form also known as the eikonal equation,

$$\left|\nabla_{\mathbf{x}} \tau(\mathbf{x}, \mathbf{x}_s)\right| = \frac{1}{c(\mathbf{x})}. \tag{2.21}$$

Thus traveltime is independent of frequency in the WKBJ approximation. It follows that

$$\nabla_{\mathbf{x}} \tau(\mathbf{x}, \mathbf{x}_s) = \frac{\hat{\mathbf{r}}(\mathbf{x}, \mathbf{x}_s)}{c(\mathbf{x})} \tag{2.22}$$

is the slowness vector, where $\hat{\mathbf{r}}(\mathbf{x}, \mathbf{x}_s)$ is the unit vector along the ray emanating from the source point $\mathbf{x}_s$ that passes through the point $\mathbf{x}$. The ray will follow the locus of points $\mathbf{x}(\sigma)$, where σ is arclength, such that

$$\frac{\partial \mathbf{x}(\sigma)}{\partial \sigma} = \hat{\mathbf{r}}(\mathbf{x}, \mathbf{x}_s), \tag{2.23}$$

or, equivalently, using equation (2.22),

$$\frac{\partial \mathbf{x}(\sigma)}{\partial \sigma} = c(\mathbf{x}) \nabla_{\mathbf{x}} \tau(\mathbf{x}, \mathbf{x}_s). \tag{2.24}$$

---

[26] $\nabla^2 A/A$ will be zero if wavespeed is constant. A step-by-step derivation can be found in Scales (1997, p. 77-79). Berkhout (1985, p. 72-75) provides additional discussion, and shows how the integrated eikonal gives the total traveltime (p. 74). A derivation for variable mass density [equation (2.4) in space-frequency domain] can be found in Snieder (1994, p. 98-101).

The rays are fixed curves in space, so it is often convenient to eliminate the time quantity τ in equation (2.24) using the eikonal equation (2.21), thereby obtaining an equation for $\mathbf{x}(\sigma)$ that depends only on the wavespeed $c(\mathbf{x})$[27]. This yields the differential equation of rays

$$\frac{\partial}{\partial\sigma}\left(\frac{1}{c(\mathbf{x})}\frac{\partial\mathbf{x}(\sigma)}{\partial\sigma}\right) = \nabla_{\mathbf{x}}\left(\frac{1}{c(\mathbf{x})}\right), \tag{2.25}$$

which states that the general solution for homogeneous media consists of rays $\mathbf{x}(\sigma)$ that are straight lines.

For inhomogeneous media that satisfy the WKBJ approximation, elapsed traveltime can be calculated by integrating incremental traveltime along the raypath. For an increment $\mathbf{x}_A$ to $\mathbf{x}_B$ along the raypath

$$\tau(\mathbf{x}_B, \mathbf{x}_A) = \int_A^B \partial\tau = \int_A^B \frac{\partial\tau}{\partial\sigma}\partial\sigma, \tag{2.26}$$

to which we can apply some fundamental properties of the gradient[28],

$$\tau(\mathbf{x}_B, \mathbf{x}_A) = \int_A^B (\nabla\tau \cdot \hat{\mathbf{r}})\partial\sigma = \int_A^B |\nabla\tau|\partial\sigma. \tag{2.27}$$

and then substitute for $|\nabla\tau|$ using the eikonal equation (2.21), yielding

---

[27] A step by step derivation can be found in Aki and Richards (1980, p. 91-92). A similar derivation, expressed in terms of refractive index $c_0/c(\mathbf{x})$, can be found in Scales (1997, p. 80-81). In Chapter 11, Scales discusses numerical methods for ray tracing based on the differential equation of rays [equation (2.25) below]

[28] Recall that $\nabla\tau$, $\mathbf{r}$, and $\mathbf{x}(\sigma)$ all point in the same direction. Hence $\partial\tau/\partial\sigma = \nabla\tau\cdot\mathbf{r} = |\nabla\tau|$.

$$\tau(\mathbf{x}_B, \mathbf{x}_A) = \int_A^B \frac{1}{c(\mathbf{x})} \partial\sigma . \tag{2.28}$$

Thus traveltime is just the slowness (reciprocal wavespeed) integrated along the raypath. A similar derivation, using a reference wavespeed $c_0(\mathbf{x})$, yields the WKBJ traveltime for the Green's function,

$$\tau_0(\mathbf{x}, \mathbf{x}_G) = \int \frac{1}{c_0(\mathbf{x})} \partial\sigma . \tag{2.29}$$

For homogeneous media, where wavespeed is constant and raypaths are straight lines, equations (2.28) and (2.29) show that traveltimes can be simply calculated as distance divided by wavespeed. Although this is an intuitively obvious result, it has been derived here from first WKBJ (ray-theoretical) assumptions. In fact, this is the physical basis for the DSR equation that lies at the heart of the kinematic equivalent offset formulation.

In complex media, the calculation of traveltimes using equations (2.25) and equation (2.29) ignores reflected arrivals. On the other hand, multiple raypaths between two given points may result from refraction. Typically all arrivals but one are excluded by considering only the first arrival, the maximum energy arrival (Nichols, 1996)[29], or some other arrival. Hence, ray-theoretical Green's functions describe one-way wavefields propagating in the reference media.

---

[29] Nichols (1996) argues that eikonal solvers are inherently inaccurate because the high-frequency WKBJ approximation results in poor traveltime estimates for waves in the seismic bandwidth. Bevc (1995), however, shows that a layer-stripping Kirchhoff migration with eikonal traveltimes can produce a good image. Layer thicknesses (500m-1500m for the Marmousi model) in the redatuming steps are chosen so that the first-arrival traveltimes accurately parameterize the most energetic portions of the wavefield.

2.4.3 Amplitude for ray-theoretical Green's functions from the transport equation and the eikonal equation

The following derivation of amplitude for ray-theoretical Green's functions is adapted from Snieder (1994) and Snieder and Chapman (1998). For ray-theoretical amplitudes, it is worthwhile starting with the variable-density form of the acoustic wave equation (equation 2.4). The final result will include a simple ratio of mass densities that can be ignored if density is constant. Similar to the derivation of the eikonal equation, the WKBJ approximation for acoustic pressure [equation (2.18)] is inserted into the homogeneous form of the acoustic wave equation [the space-frequency version of equation (2.4) multiplied through by density $\rho(\mathbf{x})$, with no source term on the RHS]. Taking the imaginary part, without any approximation, gives the transport equation[30]

$$\nabla_{\mathbf{x}} \cdot \left(\frac{S^2(\omega)\rho^2(\mathbf{x}_s)A^2(\mathbf{x},\mathbf{x}_s)\nabla_{\mathbf{x}}\phi(\mathbf{x},\mathbf{x}_s,\omega)}{\rho(\mathbf{x})} \right) = 0 \tag{2.30}$$

where $\nabla\phi$ is the eikonal for phase and A is the amplitude we wish to solve for. The constants wrt $\mathbf{x}$, $S(\omega)$ and $\rho(\mathbf{x}_s)$, can be divided out. From equations (2.20) and (2.22) the eikonal can be expressed as

$$\nabla\phi(\mathbf{x},\mathbf{x}_s,\omega) = \frac{\omega}{c(\mathbf{x})}\hat{\mathbf{r}}(\mathbf{x},\mathbf{x}_s)\,. \tag{2.31}$$

Substituting equation (2.31) into equation (2.30), expanding the divergence, and rearranging gives

$$A^2(\mathbf{x},\mathbf{x}_s) = \left[\nabla_{\mathbf{x}} \left(\frac{A^2(\mathbf{x},\mathbf{x}_s)}{p(\mathbf{x})c(\mathbf{x})} \right) \cdot \hat{\mathbf{r}}(\mathbf{x},\mathbf{x}_s) \right] \frac{p(\mathbf{x})c(\mathbf{x})}{\nabla_{\mathbf{x}} \cdot \hat{\mathbf{r}}(\mathbf{x},\mathbf{x}_s)}. \tag{2.32}$$

---

[30] Snieder (1994, p. 98-101) derives this equation through a set of simple problems. Note that his amplitude A is equivalent to $\rho(\mathbf{x}_s)A_0$ in the above derivation.

The term in the square brackets on the RHS can be considered to be the square of an unknown coefficient C that remains to be determined, while $\nabla\cdot\hat{\mathbf{r}}$ (i.e. the divergence of the neighbouring rays) is proportional to the geometrical spreading J[31]. Taking the square root of equation (2.32) yields

$$A(\mathbf{x},\mathbf{x}_s)=C\frac{\sqrt{\rho(\mathbf{x})c(\mathbf{x})}}{\sqrt{J(\mathbf{x},\mathbf{x}_s)}}. \tag{2.33}$$

We can apply the same line of reasoning to the acoustic wave equation for the Green's function in the reference medium [equation (2.13)]. The WKBJ generalization for the Green's function of equation (2.16) (see Stolt and Weglein, 1985, equation [46]) is

$$G_0(\mathbf{x},\mathbf{x}_G,\omega)=A_0(\mathbf{x},\mathbf{x}_G)e^{i\omega\tau_0(\mathbf{x},\mathbf{x}_G)}, \tag{2.34}$$

Substituting equation (2.33) in equation (2.34), with traveltime determined using equation (2.29) and the subscript (0) denoting the reference medium, gives

$$G_0(\mathbf{x},\mathbf{x}_G,\omega)=C_0\frac{\sqrt{\rho_0(\mathbf{x})c_0(\mathbf{x})}}{\sqrt{J_0(\mathbf{x},\mathbf{x}_G)}}e^{i\omega\tau_0(\mathbf{x},\mathbf{x}_G)}. \tag{2.35}$$

In the vicinity of the source point $\mathbf{x}_G$, the behaviour of the ray-theoretical Green's function can be described by the free-space Green's function [equation (2.16)], with traveltime re-expressed here in terms of τ_0,

$$\vec{G}_0(\mathbf{x},\mathbf{x}_G,\omega)=\frac{1}{4\pi}\frac{e^{i\omega\tau_0(\mathbf{x},\mathbf{x}_G)}}{r}. \tag{2.36}$$

---

[31] See Menke and Abbott (1990, p. 315) for a more complete derivation of geometrical spreading J (= $\nabla\cdot\mathbf{r}$) from equation (2.27). They note that $\rho^2(\mathbf{x}_s)A_0{}^2\rho^{-1}(\mathbf{x})c^{-1}(\mathbf{x})$ is the energy flux per unit area in a plane wave. Solving equation (2.27) for $\nabla\cdot\mathbf{r}$ shows that the divergence of neighbouring rays is proportional to the fractional change in energy flux per unit area. Further discussion can be found in Pierce (1989, p. 396-400).

Comparing the free-space Green's function [equation (2.36)] with the ray-theoretical Green's function (equation (2.35) with properties of the medium at the source point) yields an expression for the unknown coefficient,

$$C_0 = \frac{1}{4\pi\sqrt{\rho_0(\mathbf{x}_G)c_0(\mathbf{x}_G)}}\,. \tag{2.37}$$

Hence the forward propagating ray-theoretical Green's function is given by

$$\vec{G}_0(\mathbf{x},\mathbf{x}_G,\omega) = \frac{1}{4\pi}\sqrt{\frac{\rho_0(\mathbf{x})}{\rho_0(\mathbf{x}_G)}}\sqrt{\frac{c_0(\mathbf{x})}{c_0(\mathbf{x}_G)}}\,\frac{e^{i\omega\tau_0(\mathbf{x},\mathbf{x}_G)}}{\sqrt{J_0(\mathbf{x},\mathbf{x}_G)}}\,. \tag{2.38}$$

The backward propagating ray-theoretical Green's function will be identical, except for a change in sign of the eikonal function [i.e. using $-\tau_0(\mathbf{x},\mathbf{x}_G)$ in place of $\tau_0(\mathbf{x},\mathbf{x}_G)$], i.e.

$$\overleftarrow{G}_0(\mathbf{x},\mathbf{x}_G,\omega) = \frac{1}{4\pi}\sqrt{\frac{\rho_0(\mathbf{x})}{\rho_0(\mathbf{x}_G)}}\sqrt{\frac{c_0(\mathbf{x})}{c_0(\mathbf{x}_G)}}\,\frac{e^{-i\omega\tau_0(\mathbf{x},\mathbf{x}_G)}}{\sqrt{J_0(\mathbf{x},\mathbf{x}_G)}}\,, \tag{2.39}$$

which is just the complex conjugate of equation (2.38). In equations (2.38) and (2.39), the wavespeed ratio $c_0(\mathbf{x})/c_0(\mathbf{x}_G)$ compensates exactly for the variable-wavespeed component of the geometrical spreading $J_0(\mathbf{x},\mathbf{x}_G)$, which is greater when rays travel through a medium from low to high wavespeed compared to the opposite direction (Snieder and Chapman, 1998) [32]. Thus the wavespeed ratio, combined with the geometric spreading, will satisfy reciprocity. The density ratio $\rho_0(\mathbf{x})/\rho_0(\mathbf{x}_G)$, however, does not satisfy reciprocity. In Section 2.7.2, the reciprocity relation for variable-density Green's

---

[32] Snieder and Chapman (1998) obtain the negative of equations (2.38) and (2.39) because they choose a positive delta function as the source term for the acoustic wave equation that defines the Green's function [equation (2.11)]. In addition, their mass-density terms are all in the numerator, because they chose not to normalize the Green's function by the mass density at the source location. Hence their variable mass-density Green's functions are reciprocal without the correction factors given in Section 2.7 [equation (2.59)].

functions is shown to include the density at the source location [see equation (2.59)]. For constant density, the ratio $\rho_0(\mathbf{x})/\rho_0(\mathbf{x}_G)$ will be unity, and the ray-theoretical Green's functions given by equations (2.38) and (2.39) will obey a simple reciprocity principle.

Now we have expressions for forward and backward propagating one-way free-space Green's functions [equations (2.16) and (2.17)] and forward and backward propagating ray-theoretical Green's functions [equations (2.38) and (2.39)]. Equation (2.34) is often used as a simplified expression for equation (2.38) [or for equation (2.39) with τ negative], where A_0 denotes the amplitude term. Similarly, under the WKBJ approximation, the ray-theoretical acoustic pressure can be represented by equation (2.19). To simplify notation, I will proceed with the theoretical development using the generalized acoustic pressure notation [e.g. $P(\mathbf{x},\mathbf{x}_s,\omega)$] and generalized Green's function notation [e.g. $G_0(\mathbf{x},\mathbf{x}_G,\omega)$] and substitute appropriate expressions when necessary.

2.5 THE KIRCHHOFF-HELMHOLTZ INTEGRAL REPRESENTATION (KHIR) AND THE KIRCHHOFF-HELMHOLTZ INTEGRAL

The goal of this section is to obtain a representation theorem, whereby the acoustic pressure in one part of the medium is determined uniquely by the acoustic pressure observed elsewhere. Typically, a representation theorem is obtained by substituting a Green's function into a reciprocity theorem. For acoustic pressure, the appropriate reciprocity theorem is known as the Rayleigh reciprocity theorem. The Green's function is chosen as the normalized acoustic pressure in response to a delta function source in the reference medium. The result is the Kirchhoff-Helmholtz integral representation (KHIR). The KHIR can be thought of as a decomposition of the acoustic wavefield into three terms, with each term a function of 1) properties of the acoustic wavefield in a subset of the volume and/or on the surface enclosing the volume, and 2) the Green's function in the reference medium. Since we are free to choose both the reference medium and the properties of the Green's function, the KHIR tells us what properties of the acoustic wavefield are required and where they are required in order to determine the acoustic pressure. The derivation also determines the conditions under which simple expressions for reciprocity are valid, and leads to the mathematical expression of Huygens' principle.

2.5.1 The Kirchhoff-Helmholtz integral representation—a specific form of the Rayleigh reciprocity theorem

The general form of the Rayleigh reciprocity theorem is derived for two non-identical acoustic wavefields corresponding to two different sets of material properties within the same volume (Wapenaar and Berkhout, 1989, Section V.2). Upon first consideration, this abstraction appears to be non-physical—how can a volume be composed of two different continuous materials at the same time, everywhere? However, if we consider one state of the volume to correspond to the unknown true medium that generated the recorded wavefield, and the second state to the macro subsurface model[33] that serves as the reference medium for estimating the forward or inverse wavefield propagation, the abstraction becomes both feasible and necessary.

An appropriate configuration is required for the derivation. Consider a volume V with surface S enclosing V, as shown by the de Hoop's egg[34] in Figure 2.2. The surface, which has outward-pointing normal $\mathbf{n}_{\text{out}}$, may or may not represent a discontinuity in the physical properties of either of the two material states. Boundary values on the surface

---

[33] A definition of the macro subsurface model can be found in Berkhout (1985, p. 360).

[34] Named after Adrianus T. de Hoop (Delft University of Technology, The Netherlands) who popularized this configuration to represent the domain for the application of a reciprocity theorem in the analysis of a wavefield and to symbolize the power of a consistent wavefield description (Fokkema and van den Berg, 1993, p. vii).

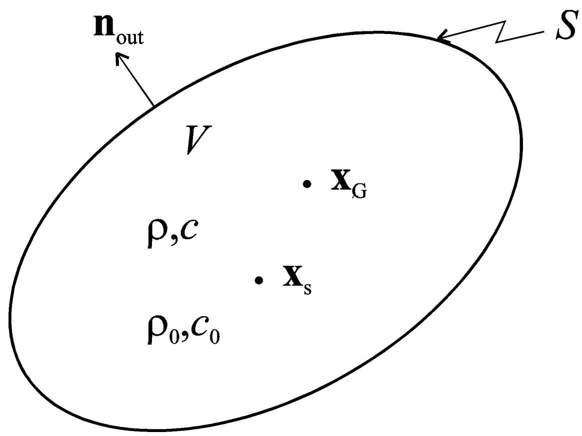

Figure 2.2. Configuration (a 'de Hoop's egg') for derivation of the Kirchhoff-Helmholtz integral representation [equation (2.44)], a special case of the Rayleigh representation theorem. The observation location $\mathbf{x}_G$ must lie inside volume V surrounded by closed surface S with outward normal $\mathbf{n}_{\text{out}}$. Within the volume, the properties for the unknown true medium are labeled ρ and c, and for the reference medium ρ_0 and c_0. The source location $\mathbf{x}_s$ could lie inside the volume (as shown), or outside the volume.

will be specified later, when necessary. Within the volume, the properties for the unknown true medium are labeled ρ and c, and for the reference medium ρ_0 and c_0. The position $\mathbf{x}_s$ indicates the location of the source of the acoustic wavefield $P(\mathbf{x},\mathbf{x}_s,\omega)$ in the unknown true medium. In Figure 2.2 $\mathbf{x}_s$ is shown inside the volume and $P(\mathbf{x},\mathbf{x}_s,\omega)$ satisfies the nonhomogeneous Helmholtz equation [equation (2.12)]. However, $\mathbf{x}_s$ could be located outside the volume (e.g. Figure 2.4a), in which case $P(\mathbf{x},\mathbf{x}_s,\omega)$ satisfies the homogeneous Helmholtz equation [equation (2.12), with no source terms on the RHS]. The position $\mathbf{x}_G$ indicates the location where the acoustic wavefield will be determined. The formulation of the representation theorem requires that this point must lie within the volume. $\mathbf{x}_G$ is also the location of the source for the Green's function $G_0(\mathbf{x},\mathbf{x}_G,\omega)$ in the reference medium, where $G_0(\mathbf{x},\mathbf{x}_G,\omega)$ satisfies equation (2.13).

Once again, I adapt a derivation found in Wapenaar and Berkhout (1989, Section V.2). Here, I insert the Green's function directly to derive the Rayleigh reciprocity theorem as a representation theorem. The key is to apply the divergence theorem to a vector function $\mathbf{Q}(\mathbf{x},\omega)$, defined as

$$\mathbf{Q}(\mathbf{x},\omega) = G_0(\mathbf{x},\mathbf{x}_G,\omega)\nabla_{\mathbf{x}} P(\mathbf{x},\mathbf{x}_s,\omega) - P(\mathbf{x},\mathbf{x}_s,\omega)\nabla_{\mathbf{x}} G_0(\mathbf{x},\mathbf{x}_G,\omega)\,. \tag{2.40}$$

Taking the divergence of this vector function,

$$\nabla\cdot\mathbf{Q}(\mathbf{x},\omega) = G_0(\mathbf{x},\mathbf{x}_G,\omega)\nabla^2_{\mathbf{x}} P(\mathbf{x},\mathbf{x}_s,\omega) - P(\mathbf{x},\mathbf{x}_s,\omega)\nabla^2_{\mathbf{x}} G_0(\mathbf{x},\mathbf{x}_G,\omega) \tag{2.41}$$

and substituting for the terms $\nabla^2 P$ and $\nabla^2 G$ using equations (2.12) and (2.13) gives

$$\begin{aligned}\nabla\cdot\mathbf{Q}(\mathbf{x},\omega) &= P(\mathbf{x},\mathbf{x}_s,\omega)\delta(\mathbf{x}-\mathbf{x}_G) - S(\omega)\rho(\mathbf{x})G_0(\mathbf{x},\mathbf{x}_G,\omega)\delta(\mathbf{x}-\mathbf{x}_s)\\ &\quad -\omega^2\left(\frac{1}{c^2(\mathbf{x})} - \frac{1}{c_0^2(\mathbf{x})}\right)G_0(\mathbf{x},\mathbf{x}_G,\omega)P(\mathbf{x},\mathbf{x}_s,\omega)\,.\end{aligned} \tag{2.42}$$

In fact, the vector function $\mathbf{Q}$ was chosen to ensure that $\nabla\cdot\mathbf{Q}$ contains terms that can be substituted for using the acoustic wave equations (2.12) and (2.13) [35]. Now apply the divergence theorem to a volume with outward-pointing normal $\mathbf{n}$,

$$\oint_S \mathbf{Q}\cdot\mathbf{n}\,dS = \int_V \nabla\cdot\mathbf{Q}\,dV\,, \tag{2.43}$$

and substitute for $\mathbf{Q}$ and $\nabla\cdot\mathbf{Q}$ using equations (2.40) and (2.42). The sifting property of the delta function [see Appendix A, equation (A-1) and Appendix A of Bleistein et al. (2001)] can be applied to volume integrals containing a delta function, yielding

---

[35] Alternately, we can follow the method of Bleistein (1984, Section 4.4, especially p. 121) and reverse-engineer the vector function $\mathbf{Q}$ by looking for the exact divergence $\nabla\cdot\mathbf{Q}$ as a difference of products G^*LP - PL^*G^* (where L is the operator $\nabla^2+\omega^2/c^2$ and L^* is the operator $\nabla^2+\omega^2/c_0^2$). Bleistein describes the operator L^* as the adjoint operator for the wave equation and G^* as the adjoint Green's function (p.124).

$$P(\mathbf{x}_G,\mathbf{x}_s,\omega) = S(\omega)\rho(\mathbf{x}_s)G_0(\mathbf{x}_s,\mathbf{x}_G,\omega)$$
$$+\oint_S dS\{G_0(\mathbf{x},\mathbf{x}_G,\omega)\nabla_{\mathbf{x}}P(\mathbf{x},\mathbf{x}_s,\omega) - P(\mathbf{x},\mathbf{x}_s,\omega)\nabla_{\mathbf{x}}G_0(\mathbf{x},\mathbf{x}_G,\omega)\}\cdot\mathbf{n}$$
$$+\int_V dV\omega^2\left(\frac{1}{c^2(\mathbf{x})} - \frac{1}{c_0^2(\mathbf{x})}\right)G_0(\mathbf{x},\mathbf{x}_G,\omega)P(\mathbf{x},\mathbf{x}_s,\omega)\,. \tag{2.44}$$

Equation (2.44) is a specific case of Rayleigh's reciprocity theorem known as the acoustic "Kirchhoff-Helmholtz integral representation" (KHIR). Note that the LHS of equation (2.44) will be non-zero only if the source point $\mathbf{x}_G$ in the delta function on the RHS of equation (2.13) lies inside the volume. Hence equation (2.44) is valid only when the observation point $\mathbf{x}_G$ for the acoustic pressure $P(\mathbf{x}_G,\mathbf{x}_s,\omega)$ lies inside the volume V enclosed by surface S with outward pointing normal $\mathbf{n}$. An inward pointing normal changes the sign of the second term on the RHS (the surface integral). These observations will prove useful for determining an appropriate volume and the correct orientation of the normal for any arbitrary portion of the surface enclosing the volume.

2.5.2 Decomposing the KHIR into incident, surface-scattered and volume-scattered wavefields

The KHIR [equation (2.44)] can be thought of as a decomposition of the acoustic wavefield into three terms. The terms will be referred to by names commonly used in the literature. The first term on the RHS is called the "incident wavefield". The second term (the surface integral) is called the "surface-scattered wavefield". The third term (the volume integral) is called the "volume-scattered wavefield". Unfortunately, the literal physical meaning of "incident" and "scattered" are often narrower than the mathematics permits. For example, if the source point $\mathbf{x}_s$ lies outside an arbitrary volume in a homogeneous media, the surface-scattered wavefield reconstructs the incident wavefield—there is no scattering per se. This configuration, and ones like it, will be investigated in more detail in the context of Huygens' principle in Section 2.6. Similarly, in some configurations each individual term could represent a non-physical wavefield, although the combination of wavefields will have a valid physical interpretation. As an example, suppose the source point $\mathbf{x}_s$ lies inside the volume, which also contains an "obstacle" given by the volume-scattered wavefield. Bleistein (1984, p. 159) points out that the incident and scattered wavefields are unphysical in the sense that the incident wavefield exists everywhere within the volume, and hence the mathematical scattered wavefield must carry the "burden" of negating the unphysical incident wavefield in regions where it is blocked by the obstacle. Therefore, in order to gain some physical insight, it is worthwhile examining each term in detail. Later, in Section 3.2, we revisit the KHIR [equation (2.44)] and find that the physical interpretation of these terms is more appropriate to the names given here.

The KHIR [equation (2.44)] is most useful in simpler forms; that is, when one or two of the terms on the RHS are zero. Each term on the RHS is a function of 1) the wavefield $P(\mathbf{x},\mathbf{x}_s,\omega)$ and/or properties of the wavefield, such as its spatial gradient, source location $\mathbf{x}_s$ and/or source signature $S(\omega)$; 2) the volume V and its bounding surface S, as well as the boundary conditions on that surface; and 3) the Green's function and the reference medium both inside and outside the volume. We are free to choose the Green's function and the reference medium, and we can often choose a favourable volume and bounding surface. These choices determine if a given term on the RHS is zero or non-zero. In other words, each term can describe a portion of the wavefield or all of the wavefield.

2.5.3 The incident wavefield and reciprocity

The first term on the RHS of (the incident wavefield) will be non-zero only if the source point $\mathbf{x}_s$ on the RHS of equation (2.12) lies inside the volume. The incident wavefield will be the only non-zero contribution if both the surface-scattered wavefield and volume-scattered wavefield are zero. The surface-scattered wavefield will be zero given rigid, free-surface, reflection-free, or impedance boundary conditions, to be discussed further in Section 2.7.3 in the context of reciprocity. The volume-scattered wavefield will be zero if the reference wavespeed c_0 is equal to the unknown true wavespeed c. We are left with

$$P(\mathbf{x}_G, \mathbf{x}_s, \omega) = S(\omega)\rho(\mathbf{x}_s)G_0(\mathbf{x}_s, \mathbf{x}_G, \omega), \tag{2.45}$$

which suggests that the Green's function $G_0(\mathbf{x}_s,\mathbf{x}_G,\omega)$ includes all possible complexities of wavefield propagation inside the volume, including scattering from the boundary surface. In fact, we will use these conditions to define reciprocity in Section 2.7. On the other hand, it is often useful to choose a simple Green's function, such as the free-space Green's function [equation (2.16)] or the ray-theoretical Green's function [equation (2.34)]. Assuming a ray-theoretical Green's function and reciprocity [see equation (2.55)], equation (2.45) becomes the WKBJ approximation for the wavefield as given by equation (2.19). In these simpler situations, the incident wavefield is often referred to as the "direct wavefield".

2.5.4 The volume scattered wavefield, wavespeed perturbations, and the Born approximation

The role played by the second term on the RHS of equation (2.44) (the surface-scattered wavefield) is perhaps the most interesting, but we will leave it until after the following brief examination of the third term. In the third term (the volume-scattered wavefield), the unknown true wavespeed $c(\mathbf{x})$ can be defined in terms of the reference wavespeed $c_0(\mathbf{x})$ and a wavespeed perturbation $\alpha(\mathbf{x})$ as follows:

$$\frac{1}{c^2(\mathbf{x})} = \frac{1}{c_0^2(\mathbf{x})}\left(1+\alpha(\mathbf{x})\right). \tag{2.46}$$

Rearranging equation (2.46), substituting the result into equation (2.44), and assuming the surface-scattered wavefield is zero, yields

$$P(\mathbf{x}_G, \mathbf{x}_s, \omega) = S(\omega)\rho(\mathbf{x}_s)G_0(\mathbf{x}_s, \mathbf{x}_G, \omega)$$

$$+\int_V dV\omega^2 \frac{\alpha(\mathbf{x})}{c_0^2(\mathbf{x})} G_0(\mathbf{x}, \mathbf{x}_G, \omega)P(\mathbf{x}, \mathbf{x}_s, \omega)\,. \qquad (2.47)$$

In this simplified version of the KHIR, the wavefield has been decomposed into an incident wavefield and a volume-scattered wavefield. It might be convenient to choose a simple Green's function that propagates through a constant or smoothly varying wavespeed model $c_0(\mathbf{x})$ with the perturbation $\alpha(\mathbf{x})$ as a step function representing a subsurface reflector. In Chapter 3, this expression will provide the starting point for Born-approximate inversion. An expression similar to equation (2.47), but including the surface-scattered wavefield instead of the volume-scattered wavefield, will provide the starting point for Kirchhoff-approximate inversion.

2.5.5 The surface-scattered wavefield and the Kirchhoff-Helmholtz integral equation

We return now to the second term on the LHS of the KHIR [equation (2.44)] and examine some interesting aspects associated with the surface-scattered wavefield. Depending on the boundary conditions over the surface and/or the choice of properties for the Green's function, the surface-scattered integral can be non-zero for a source point inside or outside the volume. Assuming the source point $\mathbf{x}_s$ lies inside the volume, the surface-scattered integral reconstructs all scattering effects arising from outside the volume. If the source point $\mathbf{x}_s$ lies outside the volume, it reconstructs the incident wavefield in addition to these external scattering effects. Of particular interest are situations where the surface-scattered wavefield is the only non-zero contribution. This will occur when the source point $\mathbf{x}_s$ lies outside the volume and the reference wavespeed c_0 is equal to the unknown true wavespeed c. In this case we are left with

$$P(\mathbf{x}_G,\mathbf{x}_s,\omega)=\oint_S dS\left\{G_0(\mathbf{x},\mathbf{x}_G,\omega)\nabla_{\mathbf{x}}P(\mathbf{x},\mathbf{x}_s,\omega)-P(\mathbf{x},\mathbf{x}_s,\omega)\nabla_{\mathbf{x}}G_0(\mathbf{x},\mathbf{x}_G,\omega)\right\}\cdot\mathbf{n}, \tag{2.48}$$

with the reminder that the observation point $\mathbf{x}_G$ for the acoustic pressure P($\mathbf{x}_G,\mathbf{x}_s,\omega$) on the LHS of equation (2.48) must lie within the volume V bounded by the surface S with outward pointing normal **n**. In the seismic reflection literature, equation (2.48) [the reduced version of equation (2.44)] is often referred to as the "Kirchhoff-Helmholtz integral equation"[36] (Wapenaar and Berkhout, 1989), while its time domain equivalent is often referred to as the "Kirchhoff integral equation"[37] (Schneider, 1978).

It is worthwhile examining equation (2.48)—the reduced version of the KHIR—in some detail. Equation (2.48) (or its time domain equivalent) is the fundamental equation of forward and inverse seismic wavefield extrapolation and can be interpreted as an expression of Huygens' principle. However, the stated form of equation (2.48) is not particularly useful for direct application to extrapolation of conventional surface seismic data, nor does it express Huygens' principle in a manner consistent with conventional intuition (i.e. secondary sources on a wavefront).

---

[36] There is no obvious naming convention adopted in the literature. Equation (2.48) is often referred to as the KHIR (e.g. Wenzel et al., 1990) and equation (2.44) as the Kirchhoff-Helmholtz integral. Henceforth these equations will be referred to by either the naming convention adopted above or the equation number, i.e. KHIR for the full representation [equation (2.44)], Kirchhoff-Helmholtz integral for reduced version of KHIR in the space-frequency domain [equations (2.48) and (2.49)], and Kirchhoff integral for reduced version of the KHIR in the space-time domain [equations (2.50), (2.51), and (2.52)].

[37] Schneider (1978) cites Morse and Feshbach (1953) for the time domain equivalent of equation (2.48) [Schneider's equation (2)], but then refers to a simplified version of this equation, valid only for Dirichlet boundary conditions over an infinite planar aperture, as the Kirchhoff integral [Schneider's equation (4)].

2.5.6 Limitations to the Kirchhoff-Helmholtz integral equation

Why is equation (2.48) not particularly useful for direct application to extrapolation of conventional surface seismic data? Why not just choose an appropriate closed surface *S*, where we have measured both the acoustic pressure and its normal derivative, insert a Green's function suitable for the complexity of the media, as discussed in Sections 2.3 - 2.5, and then calculate the desired acoustic pressure? Unfortunately, seismic data are seldom recorded over a complete closed surface. Typically, all that is available is a finite aperture of data recorded over the earth's surface (often only a finite line), and even then, we record only one of either the acoustic pressure or its normal derivative[38]. These limitations are not as restrictive as they first appear, in part because equation (2.48) becomes over-determined for most surface seismic applications once some additional assumptions have been made. This problem is discussed further in Section 2.8.

One obvious inconsistency between equation (2.48) and the intuitive interpretation of Huygens' principle is the form of the Green's function. It might be preferable if the Green's function inside the integral could be given as $G(\mathbf{x}_G,\mathbf{x},\omega)$ instead of $G(\mathbf{x},\mathbf{x}_G,\omega)$, i.e. that the source location for the Green's function is on the surface *S*, with coordinates $\mathbf{x}$, and the observation location at $\mathbf{x}_G$, the same observation location as for the desired acoustic pressure $P(\mathbf{x}_G,\mathbf{x}_s,\omega)$. The conventional approach is to invoke reciprocity for the Green's functions, the conditions for which will be discussed in detail in Section 2.7. An alternate approach is to determine, through a detailed examination of Huygens' principle, whether reciprocity is really required.

[38] Wapenaar (1993a) states that, at a free surface, P is zero and $\partial P/\partial n$ is proportional to the normal component of the particle velocity, measured by the geophones. A justification (using matrix operator notation) is provided in Wapenaar and Berkhout (1989, Sections III.3.2 and XI.3.2, and Appendix A.3).

2.6 HUYGENS' PRINCIPLE AND SEISMIC WAVEFIELD PROPAGATION

In *Traite de la Lumiere* (Huygens, 1690), Huygens describes what is commonly known as Huygens' principle as follows[39]: *Every point on a primary wavefront serves as the source of spherical secondary wavelets. These secondary wavelets advance with speed and frequency equal to that of the primary wave at each point in space. The primary wavefront at some later time is the envelope of these secondary wavelets*. In an earlier work, *Horologium Oscillatorium* (Huygens, 1673), Huygens provides an alternate description of his principle[40]: *At every point on the wavefront, construct a sphere of radius c(dt) tangent to the wavefront. The locus of centres of these tangent spheres is the advanced wavefront*. Although Huygens is concerned with the propagation of light, his descriptions apply equally well to the propagation of acoustic or elastic wavefields (see Baker and Copson, 1950). Here, I describe forward propagation of a primary wavefront using the Kirchhoff-Helmholtz integral [equation (2.48)], in an effort to develop an intuitive understanding of how this integral can be used for wavefield extrapolation and migration. Given the principle of superposition, it is sufficient to consider a wavefield from a point source.

2.6.1 Kirchhoff-Helmholtz integral equation for a point source – part 1

The first problem encountered in attempting to apply either of Huygens' descriptions to the Kirchhoff-Helmholtz integral equation (2.48) is that the simplification from the KHIR [equation (2.44)] assumes that the point source of the acoustic pressure lies outside the closed surface that contains the observation point. This makes it impossible for the

---

[39] translation by Robinson and Silvia (1981, p. 363).

[40] translation by Robinson and Silvia (1981, p. 364).

surface S to be a wavefront from a point source. However, if S is an internal surface to an infinite external volume (discussed in detail below, and illustrated by Figure 2.4c), then the point source could be surrounded by the surface S, and S can be taken as the primary wavefront in the context of Huygens' principle. Then a strict interpretation of equation (2.48) agrees with Huygens' 1673 description, where the Green's function source point $\mathbf{x}_G$ is at the observation point for the acoustic pressure $P(\mathbf{x}_G,\mathbf{x}_s,\omega)$. The required Green's function would have to be backward propagating[41], i.e. a harmonic spherical wavefront that shrinks as time progresses forward (Figure 2.3a). This creates a forward propagating wavefront, as required, but does not agree with conventional physical intuition that places the sources of the "secondary wavelets" on the primary wavefront. Invoking reciprocity for the Green's function [i.e. using $G_0(\mathbf{x}_G,\mathbf{x},\omega)$ in place of $G_0(\mathbf{x},\mathbf{x}_G,\omega)$ – see Section 2.8] places the Green's function source point at locations $\mathbf{x}$ (the integration variable) on the surface S. This leads to an interpretation of equation (2.48) that agrees better with Huygens' 1690 description (Figure 2.3b). The result is that Huygens' principle does not require reciprocity: the 1673 description works fine, although it is somewhat counter-intuitive.

The physical interpretation of equation (2.48) is illustrated by the clutch of de Hoop's eggs in Figures 2.4 and 2.5. In Figure 2.4a, the observation point $\mathbf{x}_G$ is inside the volume while the source point $\mathbf{x}_s$ lies outside. As discussed above, this configuration doesn't make much physical sense if we wish the surface to be a wavefront from a point source. However, equation (2.48) does apply to this configuration because it is valid for any wavefield measured over any arbitrary closed surface—a more general interpretation due

[41] Recall that "backward" refers to the time direction for outward propagation. With time symmetry, the backward propagating Green's function propagates inward as time moves forward.

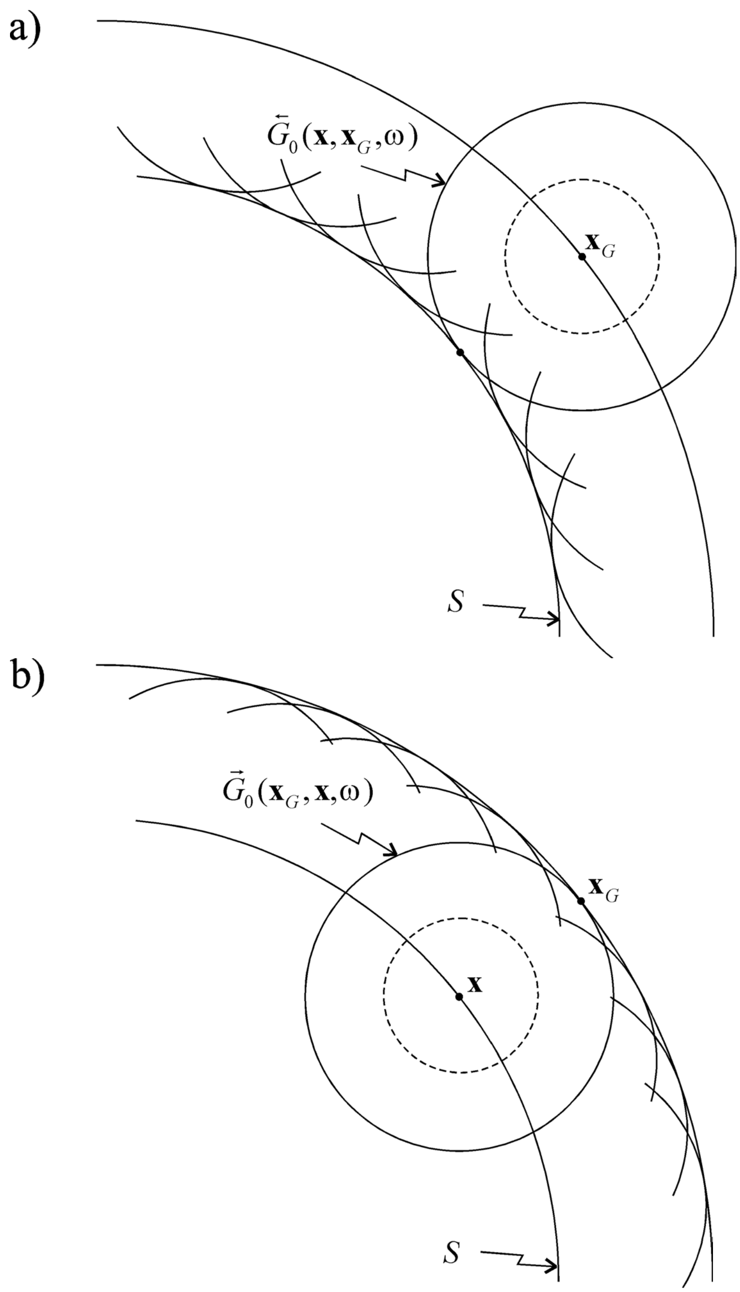

Figure 2.3. (a) A strict interpretation the Kirchhoff-Helmholtz integral equation [equation (2.48)] requires a backward propagating Green's function $\overleftarrow{G}_0(\mathbf{x},\mathbf{x}_G,\omega)$, with a source at the desired observation location $\mathbf{x}_G$. This agrees with Huygens' 1673 description. In (b) reciprocity is invoked, and the wavefront surface is reconstructed using a forward propagating Green's function $\vec{G}_0(\mathbf{x}_G,\mathbf{x},\omega)$. This is the more intuitive concept of secondary sources that agrees with Huygens' 1690 description. The same argument applies to the Kirchhoff-Helmholtz integral representation [equation (2.44)], where the Green's functions sources for the incident, surface-scattered and volume-scattered wavefields are all at the desired observation location $\mathbf{x}_G$.

to Helmholtz and Kirchhoff—not just the specific case of a wavefront. The physical interpretation agreeing with Huygens' principle requires a different configuration.

In Figure 2.4b, the observation point $\mathbf{x}_G$ is outside the de Hoop's egg containing the source point $\mathbf{x}_s$. Since equation (2.48) can only be applied if the observation point is found within the volume, we conveniently choose the volume to lie outside of the egg instead of inside, and chose a second surface at infinity to ensure that the volume is surrounded (in a manner of speaking) by a closed surface (Morse and Feshbach, 1953, p. 804). The appropriate configuration is redrawn in Figure 2.4c. The volume is now constructed between two de Hoop's eggs, the smaller one containing the source, the larger one being the surface at infinity. The outward-pointing normals $\mathbf{n}_{\text{out}}$ point into the smaller egg and out of the larger egg. Replacing the normal for the smaller egg with one that points outward (Figure 2.4d-e) reverses the sign of equation (2.48).

For the configuration shown in Figure 2.4c, then, we have two contributions to the surface integral. The Sommerfeld radiation condition (see, for example, Goodman, 1968 p. 38-39) states that the contribution from the outer surface at infinity is negligible if the Green's function is outward propagating[42]. Thus, the only contribution to the Kirchhoff-Helmholtz integral [equation (2.48)], for the configuration shown by Figure 2.4c, is the surface integral over the smaller egg. The integral states that the incident wavefield is reconstructed by a weighted sum of monopole sources corresponding to the Green's function G_0 and dipole sources corresponding to the normal derivative of the Green's

---

[42] As $r \to \infty$, the free-space Green's function $e^{i\omega r/c}/(4\pi r)$ falls off as $1/r$ and the surface area as $1/r^2$: Thus the integral decays to zero. This condition can be invoked for an outer surface that is not at infinity if both the Green's function and wavefield are outward propagating on and outside the surface (see Bleistein, 1984, p. 182-184; Wapenaar and Berkhout, 1989, Appendix B; Bleistein et al., 2001, p. 90).

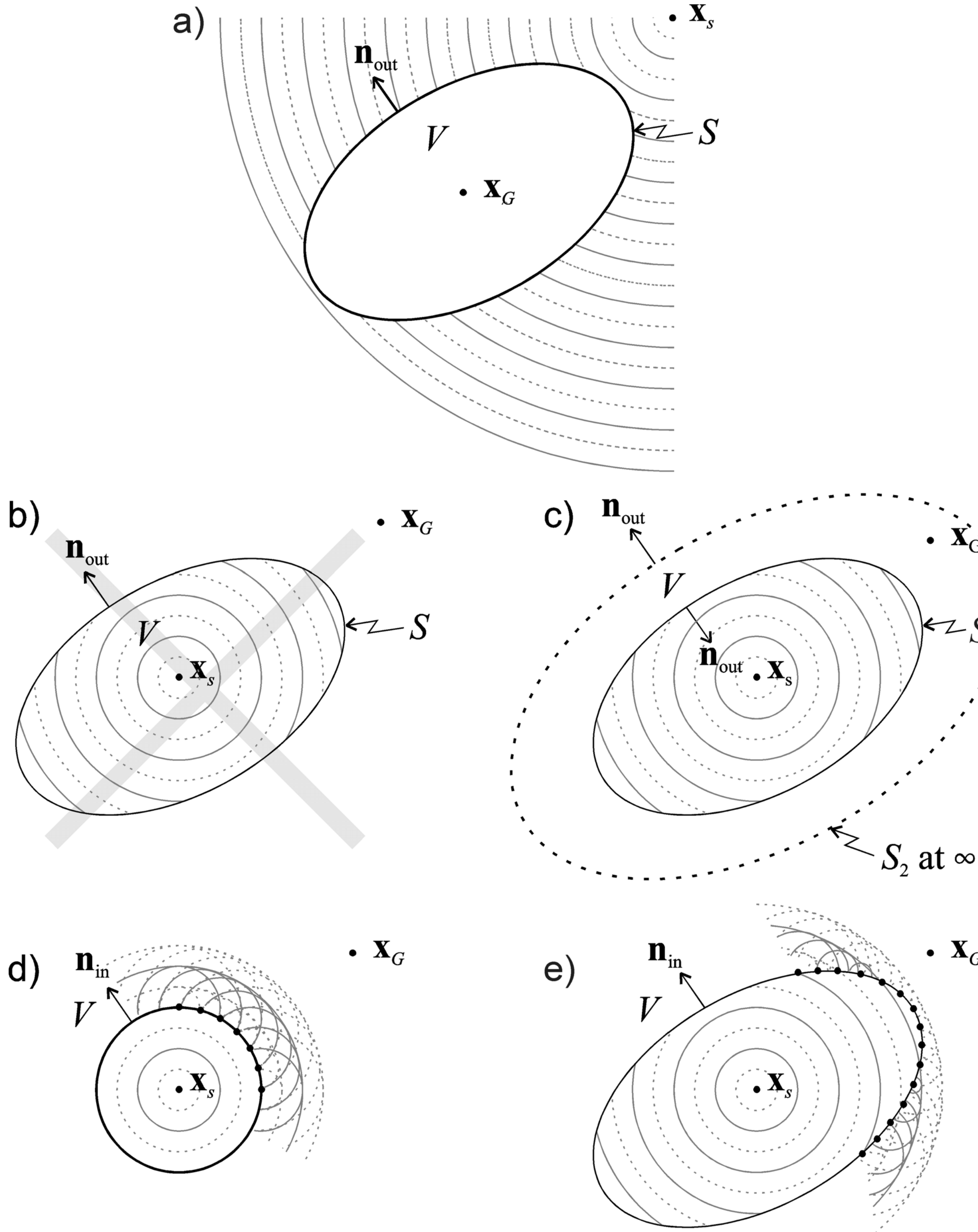

Figure 2.4. For Huygens' principle, we need a surface corresponding to wavefronts (solid and dotted gray lines) from a monochromatic point source located at $\mathbf{x}_s$. This is not possible with configuration a). Configuration b) is not suitable because observation point $\mathbf{x}_G$ must lie in volume V surrounded by surface S with outward normal $\mathbf{n}_{out}$. Configuration c), with external volume V, requires additional surface S_2 at ∞. Huygens' principle is shown in d) with secondary sources (dots) on wavefront surface. Inward normal $\mathbf{n}_{in}$ changes sign of surface-scattered integral, which is also valid for any generalized surface, as shown in e).

function ($\nabla G_0 \cdot \mathbf{n}$) distributed over the surface. The weighting terms are the normal derivative of the acoustic wavefield ($\nabla P \cdot \mathbf{n} = \partial P / \partial n$) and the acoustic wavefield P, respectively[43]. If we assume reflection-free boundary conditions for the surface (i.e. that the surface is not a physical boundary in the medium), and assume that the surface is a wavefront, we can then interpret these monopole and dipole sources as Huygens' "secondary sources" (Figure 2.4d). A fascinating property of the Kirchhoff-Helmholtz integral [equation (2.48)] is that the surface does not need to be a wavefront. Instead, the secondary sources can be distributed over any arbitrary surface as long as they radiate with the appropriate phases and amplitudes as determined by the Kirchhoff-Helmholtz integral (Figure 2.4e).

2.6.2 Kirchhoff-Helmholtz integral equation for a point source – part 2

What happens after an outward propagating primary wavefront from a point source passes an observation location? The observation location now lies inside the closed surface that corresponds to the wavefront. Physical intuition suggests that there should be no wavefield from a primary wavefront that has already passed a given observation location. In the mathematical description of Huygens' principle, as given by the Kirchhoff-Helmholtz integral equation [equation (2.48)], the original wavefront from the point source is replaced by secondary sources that radiate in all directions, including back into the volume enclosed by this original wavefront surface. Hence, we expect that the

---

[43] Berkhout (1985, p. 139) suggests that the weighting of the monopole sources is given by the normal component of the velocity on the surface, while the weighting of each dipole is given by the pressure on the surface. As shown by his equation (V-7), the weighting of each dipole is the time derivative of the normal component of the velocity multiplied by the mass density, or the normal component of the pressure (as stated above).

contribution from this surface-scattered integral should be zero for all these interior locations. Baker and Copson (1950, p. 31) provide an elegant proof, as follows.

In Figure 2.5a, both the observation and source points lie within the volume. The special case of a spherical wavefront is a trivial case of the more general surface shown by the de Hoop's egg. Diaphragm *C* divides the volume within the egg into two separate volumes, one containing the observation point and one the source (Figures 2.5b-c). Then, the situations described above for Figures 2.4a and 2.4c apply separately to each of the volumes. But the acoustic pressure calculated at the observation point must be identical, irrespective of the volume chosen. Hence the two surface integrals must be equal (Figure 2.5d). Now we want to combine the two surface integrals into one covering the surface of the original egg. First we note that the surface normals for the two configurations are oriented in the opposite sense: the normal to the 'half' egg containing the observation point is oriented outward, while the normal to the 'half' egg containing the source point is oriented 'inward' to egg's volume (because the normal is oriented outward from the volume containing the observation point – see Figure 2.4). Choosing an outward normal for the 'half' egg containing the source reverses the sign of equation (2.48) (as discussed above for Figure 2.4c) and turns the difference of surface integrals into a sum that must also be equal to zero. In addition, the contributions from the diaphragm *C* now cancel because the normals are oriented in the opposite sense (Figure 2.5e). The sum of the two surface integrals is equivalent to the surface integral over the original egg, which is therefore equal to zero (Figure 2.5f). A similar argument can be constructed for an observation point and source outside the volume, but this has not been presented nor has the configuration been illustrated with a figure.

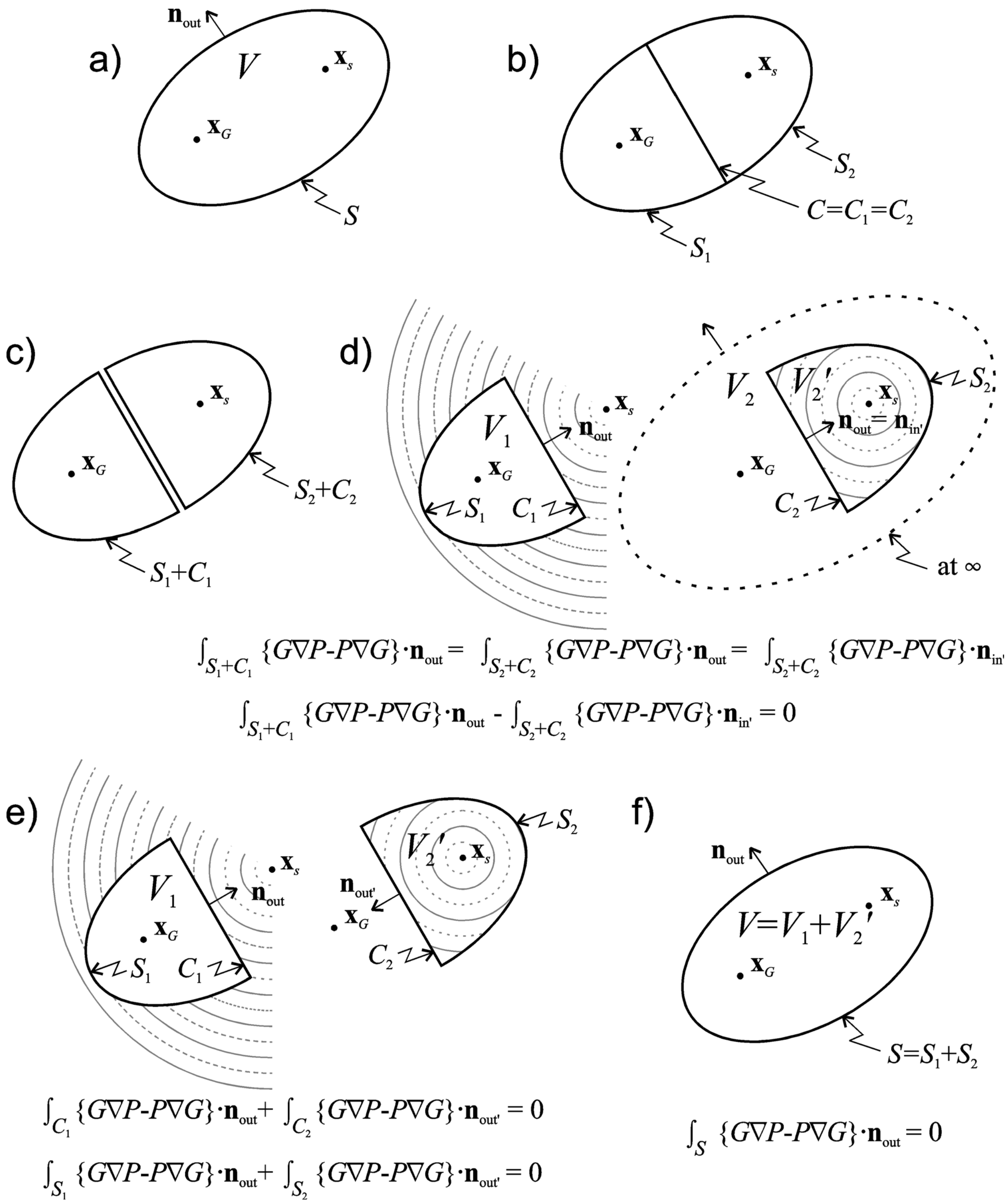

Figure 2.5. The Kirchhoff-Helmholtz integral [equation (2.48)] and/or the surface-scattered integral in the KHIR [equation (2.44)] are equal to zero when both the source location $\mathbf{x}_s$ and observation location $\mathbf{x}_G$ lie within the volume V surrounded by surface S. The proof (Baker and Copson, 1950) is as follows: a) The original volume is, b) divided by diaphragm C, c) creating two volumes V_1 and V_2'. d) The surface-scattered integrals must be the same, so the difference must equal zero. e) Changing the orientation of the normal changes the sign of the surface integral. With opposing normals, integrals over diaphragm surfaces C_1 and C_2 must be equal and opposite. Thus f), the surface-scattered integral over $S = S_1+S_2$ equals zero.

That the surface-scattered wavefield is zero when source and observation points lie within the volume is a result that agrees with the KHIR [equation (2.44)], where we might expect the only contribution to arise from the incident wavefield, i.e. from the term $S(\omega)\rho(\mathbf{x}_s)G_0(\mathbf{x}_S,\mathbf{x}_G,\omega)$[44]. However, a zero result is expected only for reflection-free boundary conditions (as required for an outward propagating Green's function). For other boundary conditions, the surface-scattered wavefield will be nonzero. The physical explanation for a nonzero contribution is that the incident wavefield is reflected from the surface. In Chapter 3, we will chose to ignore the incident wavefield (which can be muted from field gathers) and concentrate on the surface-scattered wavefield as representing a reflected wavefield of interest.

2.6.3 Are both the pressure and the normal derivative of pressure required? – part 1

For Huygens' principle to work, the values of the weighting factors P and its normal derivative $\nabla P\cdot\mathbf{n}$ cannot be independent of each other. If the arbitrary surface S is a wavefront, the interdependence of P and $\nabla P\cdot\mathbf{n}$ has a simple physical interpretation. The wavefront is reconstructed from a sum of monopoles G_0 and dipoles $\nabla G_0\cdot\mathbf{n}$. The monopole radiates a positive wavefield into the material on both sides of the wavefront surface. The dipole, with axis normal to the surface, radiates a positive wavefield in one direction and a negative wavefield in the opposite direction. The negative wavefield from the dipole exactly cancels the positive wavefield from the monopole in the direction the wavefield came from, ensuring that the wavefield propagates in one direction only. Thus the weighting factors must be related, which implies that, in the case of Huygens' principle, we only need to record one of either the acoustic pressure or its normal

---

[44] For example, the incident wave term can be considered as the WKBJ expression for the acoustic pressure [equation (2.19)] given the ray-theoretical Green's function [equation (2.34)].

derivative. Although this is true if the surface is a wavefront, the more complex case of an arbitrary surface and numerous sources for the wavefield [the general case of equation (2.48)] is not so straightforward. The information provided by recording both the acoustic pressure and its normal derivative is sufficient to keep track of the direction of each individual wavefield as it crosses the arbitrary surface. If we already know the direction of the wavefield, as we do when recording an upgoing wavefield with surface detectors, a record of both the acoustic pressure and its normal derivative should not be required. Based solely on the intuition developed in this section, it seems probable that the one-way wavefield can be reconstructed using a distribution of either dipole or monopoles only, where the weighting function is the product of the recorded seismic data (pressure or its normal derivative) and a function of the surface geometry relative to the reconstruction point. This topic will be investigated more thoroughly in Sections 2.8 and 2.9.

2.6.4 Kirchhoff-Helmholtz equation in a homogeneous medium

One problem with the interpretation of equation (2.48) as Huygens' principle is honoring Huygens' 1690 phrasing that refers to "spherical secondary wavelets" and his earlier 1673 phrasing that refers to "sphere(s)". "Spherical secondary wavelets" suggests a homogeneous medium. If the surface S is reflection-free (i.e. not a physical boundary in the medium, as expected if the surface represents a wavefront), then Huygens' principle is satisfied by a free-space Green's function [equations (2.16) or (2.17)]. Reciprocity is trivial for the free-space Green's function, as the Green's function depends only on the distance $r = \left|\mathbf{x} - \mathbf{x}_G\right|$ and constant reference wavespeed c_0. Inserting the forward propagating free-space Green's function [equation (2.16)] into equation (2.48) gives a more appropriate mathematical expression of Huygens' principle (Baker and Copson, 1950),

$$P(\mathbf{x}_G, \mathbf{x}_s, \omega) = \frac{1}{4\pi} \oint_S \partial S \left\{ \frac{\partial P(\mathbf{x}, \mathbf{x}_s, \omega)}{\partial n} \frac{e^{i\omega r / c_0}}{r} - P(\mathbf{x}, \mathbf{x}_s, \omega) \frac{\partial}{\partial n} \left(\frac{e^{i\omega r / c_0}}{r} \right) \right\}, \qquad (2.49)$$

where $\partial / \partial n = \nabla \cdot \mathbf{n}$. Physical interpretation of equation (2.49) is best served if we assume the situation illustrated in Figures 2.4c. The source point $\mathbf{x}_s$ lies within the smaller egg—for which the surface normal points inward—and the Sommerfeld radiation condition holds (i.e. we can ignore the contribution from infinity so the surface integral is over the smaller egg only). Equation (2.49) describes the outward propagation of harmonic wavefronts by secondary wavelets that expand as time goes forward. Although equation (2.49) is valid for an arbitrary surface (Figure 2.4e), the surface can be taken as a wavefront to agree with Huygens' principle (Figure 2.4d). Note, however, that equation (2.49) is strictly valid only in a homogeneous medium with constant wavespeed c_0. For inhomogeneous media, the radius of the sphere can be chosen to be infinitesimal, and proportional to the wavespeed at the source point $\mathbf{x}$ of the Green's function (i.e. on the surface S).

2.6.5 Kirchhoff integral equation in a homogeneous medium

In order to restrict the acoustic disturbance to the advancing wavefront, Huygens invoked imprecise geometrical concepts such as "envelope " and "tangent spheres". It took more than two centuries to discover the correct analytical description of Huygens' principle[45]. Helmholtz (1859) extended results introduced by Fresnel (1818, published 1826) and Poisson (1819), proving that a monochromatic wavefield could be described by the weighted superposition of the wavefield and its normal derivative over an arbitrary closed surface, instead of superpositions over the wavefront. Kirchhoff (1882, 1883)

---

[45] A complete discussion can be found in Baker and Copson (1950), including the references cited in this paragraph (which are not included in references of this dissertation).

showed that the frequency-domain solutions are a specific case of a more general time-domain theorem applicable to sound waves of any structure and origin, where the weighted superposition of a 'retarded' or 'advanced' wavefield and its normal derivative takes place over an arbitrary closed surface. For a homogeneous medium, Kirchhoff's integral is just equation (2.49) expressed in the time domain,

$$p(\mathbf{x}_G,\mathbf{x}_s,t)=\frac{1}{4\pi}\int_0^{\infty}dt_G\oint_S dS\left\{\frac{\partial p(\mathbf{x},\mathbf{x}_s,t_G)}{\partial n}\frac{\delta\left((t-t_G)-r/c_0\right)}{r}\right.$$
$$\left.-p(\mathbf{x},\mathbf{x}_s,t_G)\frac{\partial}{\partial n}\left(\frac{\delta\left((t-t_G)-r/c_0\right)}{r}\right)\right\}. \qquad (2.50)$$

If we imagine the surface of a de Hoop's egg as an expanding wavefront, then the physical process corresponding to Huygens' principle, as given by equation (2.50), is represented in Figures 2.4e and 2.5f. In Figure 2.4e, the expanding wavefront from a source point $\mathbf{x}_s$ has not yet reached the observation point $\mathbf{x}_G$. The wavefront that will be recorded at the observation point can be constructed by replacing the wavefront with a weighted sum of monopoles and dipoles. After the wavefront has passed the observation point, as in Figure 2.5f (but imagine that the surface still lies on the expanding wavefront), the weighted sum of monopoles and dipoles ensures that the observation point will not record a wavefield (see graphical proof in Section 2.6.2).

We can expand the normal derivative in the second term of equation (2.50), get rid of the time integral by the sifting properties of the delta functions, and introduce the notation $[p(\mathbf{x},\mathbf{x}_s,t)]$ to represent the retarded value of the wavefield at time t - r/c_0. Then equation (2.50) becomes

$$p(\mathbf{x}_G,\mathbf{x}_s,t)=\frac{1}{4\pi}\oint_S dS\left\{\frac{1}{r}\left[\frac{\partial p(\mathbf{x},\mathbf{x}_s,t)}{\partial n}\right]+\frac{1}{c_0 r}\left[\frac{\partial p(\mathbf{x},\mathbf{x}_s,t)}{\partial t}\right]\frac{\partial r}{\partial n}+\frac{1}{r^2}\left[p(\mathbf{x},\mathbf{x}_s,t)\right]\frac{\partial r}{\partial n}\right\}. \qquad (2.51)$$

Equation (2.51) is valid only for forward wavefield propagation because the sign of the second term in the integrand depends on the sign of the term r/c_0 in the delta function.

For inverse wavefield extrapolation, we can insert the backward propagating free-space Green's function into equation (2.49), i.e. insert $e^{-i\omega r/c_0}$ in place of $e^{i\omega r/c_0}$. Similarly, equation (2.50) uses the backward propagating free-space Green's function with terms of $\delta\big((t-t_G)+r/c_0\big)$ in place of $\delta\big((t-t_G)-r/c_0\big)$. Following the steps described above to derive equation (2.51), and using the notation $[p(\mathbf{x},\mathbf{x}_s,t)]$ to represent the advanced value of the wavefield at time $t + r/c_0$, the advanced version of equation (2.50) becomes

$$p(\mathbf{x}_G,\mathbf{x}_s,t)=\frac{1}{4\pi}\oint_S dS\left\{\frac{1}{r}\left[\frac{\partial p(\mathbf{x},\mathbf{x}_s,t)}{\partial n}\right]-\frac{1}{c_0 r}\left[\frac{\partial p(\mathbf{x},\mathbf{x}_s,t)}{\partial t}\right]\frac{\partial r}{\partial n}+\frac{1}{r^2}\big[p(\mathbf{x},\mathbf{x}_s,t)\big]\frac{\partial r}{\partial n}\right\}. \qquad (2.52)$$

Equation (2.52) is valid only for inverse wavefield extrapolation. Note that the second term in the integrand is opposite in sign to its equivalent in equation (2.51).

Equations (2.49), (2.50) and (2.51)/(2.52) state that the acoustic pressure at the point $\mathbf{x}_G$ inside the volume, arising from a primary source at point $\mathbf{x}_s$ outside the volume, can be synthesized exactly by integrating the secondary sources over the closed surface S with outward normal $\mathbf{n}$. As with equation (2.51), these expressions are valid for any closed surface, not just a surface corresponding to a wavefront.

2.6.6 Kirchhoff integral equation in the modeling and migration literature

The various forms of Kirchhoff's time-domain integral equation are some of the "fundamental" equations found in the modeling and migration literature. Equation (2.50) is equation (2) of Schneider (1978) and the first equation (unnumbered) of Wiggins (1984), although both Schneider and Wiggins use the generalized notation G for the

Green's function in place of the free-space Green's function. Equation (2.51) is equation (5.20) of Baker and Copson (1950)[46], equation (2) of Timoshin (1970) [47], equation (B-1) of French (1975), and equation (A-4) of Kuhn and Alhilali (1977)[48]. In Section 2.9, the Rayleigh II integral (Berkhout, 1985, equation V-28a)[49] will be derived from the Kirchhoff-Helmholtz integral [equation (2.48)] for extrapolation of pressure data acquired on a planar surface. In the time domain, the Rayleigh II integrand is twice the last term of the equation (2.49), or twice the last two terms of equation (2.51) and (2.52). The Rayleigh II integral for forward extrapolation [from equation (2.51)] is the surface integral term of equation (2) of Hilterman (1970), the first of equations (B-2) of French (1975), equation (5) of Schneider (1978), and equation (A-1) of Berryhill (1979). For inverse extrapolation using the far-field approximation[50], the Rayleigh II integrand is twice the second term of equation (2.52), yielding equation (1) of Wiggins (1984).

---

[46] Baker and Copson (1950, p. 36-40, 42-44) provide a detailed derivation of equation (2.51), which is repeated and expanded upon by Bath (1968, p. 192-198).

[47] Timoshin incorrectly implies in his Figure 1 that his equation (2) is valid for an inward normal (as opposed to the outward normal determined from the KHIR), and incorrectly applies the equivalent of equation (2.51) for inverse propagation, instead of the correct version as given by equation (2.52).

[48] Kuhn and Alhilali (1977) summarize the use of these equations by various authors in *Geophysics*. In particular, they evaluate the normal derivative of the Green's function in equation (2.49) and provide a nice tie between this result and equation (2) of Trorey (1970) [also the first equation (unnumbered) of Trorey (1977)], which are expressed using Laplace transforms and the opposite sign convention for the Fourier transform. Kuhn and Alhilali (1977) paper is an excellent study seldom cited in the literature.

[49] I have chosen to follow Berkhout's naming convention. Kuhn and Alhilali (1977) call this the free-surface Rayleigh-Sommerfeld construction integral.

[50] Using only the second term in equations (2.51) or (2.52) (i.e., the time-derivative term) gives the far-field approximation. Schneider (1978) incorrectly calls this the Rayleigh-Sommerfeld diffraction formula

It is worthwhile mentioning two caveats whose importance has not been adequately stressed during this discussion. First, extra care is required when specifying boundary conditions for inverse wavefield propagation. For an inward propagating Green's function, the Sommerfeld radiation condition cannot be invoked (Bleistein et al., 2001). As pointed out in Scales (1997, p. 109), Schneider (1978) erroneously uses the Sommerfeld radiation condition in his classic paper on migration based on integral equation methods, although this error is also made by Timoshin (1970), French (1975), and Wiggins (1984) (among others). The second caveat concerns the safe assumption that seismic reflection data are never recorded over a closed surface. Even an infinite planar surface can introduce artifacts during inverse wavefield propagation[51]. We will return to address these problems in Section 2.8 and then again in Chapter 3, but as a brief preview, we will find that one-way wavefields and one-way Green's functions play a significant role in eliminating or reducing the significance of these problems. First, we will establish reciprocity relationships for variable-wavespeed and variable-density media.

2.7 RECIPROCITY RELATIONS FOR GREEN'S FUNCTIONS AND ACOUSTIC PRESSURE

The Rayleigh reciprocity theorem gives the exact expression for acoustic reciprocity for an acoustic volume in two states. More often, we are interested in reciprocity in one state. For example, a simplified expression for reciprocity of the Green's function will prove particularly useful for the seismic imaging problem. Notice, however, that in the KHIR

---

of optics and cites Goodman (1968) for this terminology. Comparing equations (3-18) and (3-27) of Goodman (and the accompanying text) suggests that the diffraction formula applies only for illumination by a point source. The far-field result is more general. In fact, Schneiders equation (5) is identical to equation (3-26) of Goodman.

[51] A thorough discussion can be found in Wapenaar (1992).

[equation (2.44)], the form of the Green's functions in the surface- and volume-scattered wavefields does not agree with physical intuition, since both involve a Green function with source at $\mathbf{x}_G$ and observation point at $\mathbf{x}$. Our physical intuition is better served if $\mathbf{x}_G$ is the observation point, so that it corresponds with the observation point for $P(\mathbf{x}_G,\mathbf{x}_s,\omega)$; and $\mathbf{x}$ is the source point, so that it corresponds with the independent variable in the surface and volume integrals[52]. If the Green's function obeyed a simple reciprocity relation, whereby the source and observer positions could be switched, our dilemma would be solved. Generally, this problem seems to arise when using Green's functions to express nonhomogeneous boundary or initial conditions as surface integrals of delta functions. Here, I briefly examine the conditions under which simplified reciprocity relations apply.

2.7.1 Green's function reciprocity in a variable-wavespeed constant-density medium

First, we consider the KHIR [equation (2.44)] for one state only, noting that if there is no difference between the true medium and reference medium, the volume integral disappears. As well, if the surface is taken to infinity, the surface-scattered wavefield will tend to zero by the Sommerfeld radiation condition. We are left with a simple relation between the acoustic pressure and the Green's function scaled by the source function,

$$P(\mathbf{x}_G,\mathbf{x}_s,\omega) = S(\omega)\rho(\mathbf{x}_s)G_0(\mathbf{x}_s,\mathbf{x}_G,\omega). \tag{2.53}$$

As discussed in Section 2.5.3, equation (2.53) states that the acoustic pressure at location $\mathbf{x}_G$ due to a source at $\mathbf{x}_s$ is just the incident wavefield as given by the Green's function (pressure per unit rate of mass influx) multiplied by the density $\rho(\mathbf{x}_s)$ at the source

---

[52] See Morse and Feshbach (1953, Chapter 7). Aki and Richards (1980, p. 29) provide a similar discussion of Green's function reciprocity in elastic representation theorems.

location (giving pressure per unit rate of volume influx) multiplied by the source strength $S(\omega)$. Note, however, that the Green's function source location is at the observation location $\mathbf{x}_G$.

If the derivation leading to equation (2.53) uses a second Green's function $G_0(\mathbf{x},\mathbf{x}_s,\omega)$ in place of the acoustic pressure $P(\mathbf{x},\mathbf{x}_s,\omega)$, the source function $S(\omega)$ and density $\rho(\mathbf{x}_s)$ on the RHS disappear by virtue of the procedure used to define the Green's function (Sections 2.3 and 2.4), yielding the reciprocity relation for constant density acoustic Green's functions,

$$G_0(\mathbf{x}_G,\mathbf{x}_s,\omega) = G_0(\mathbf{x}_s,\mathbf{x}_G,\omega)\,. \tag{2.54}$$

2.7.2 Reciprocity relations for Green's function and acoustic pressure in variable-wavespeed variable-density media

Equation (2.54) is valid for variable wavespeed[53] but is not valid for variable-density media. Starting with the variable-density acoustic wave equation [equation (2.4)] and following the procedure outlined in Section 2.3 and 2.4 gives

$$\rho_0(\mathbf{x})\nabla_{\mathbf{x}}\cdot\left(\frac{1}{\rho_0(\mathbf{x})}\nabla_{\mathbf{x}}G_0(\mathbf{x},\mathbf{x}_G,\omega)\right)+\frac{\omega^2}{c_0^2(\mathbf{x})}G_0(\mathbf{x},\mathbf{x}_G,\omega) = -\delta(\mathbf{x}-\mathbf{x}_G)\,. \tag{2.55}$$

as an expression for the variable-density Green's function in the space frequency domain for a source at location $\mathbf{x}_G$. A similar expression is found for a Green's function with a source at location $\mathbf{x}_s$:

$$\rho_0(\mathbf{x})\nabla_{\mathbf{x}}\cdot\left(\frac{1}{\rho_0(\mathbf{x})}\nabla_{\mathbf{x}}G_0(\mathbf{x},\mathbf{x}_s,\omega)\right)+\frac{\omega^2}{c_0^2(\mathbf{x})}G_0(\mathbf{x},\mathbf{x}_s,\omega) = -\delta(\mathbf{x}-\mathbf{x}_s)\,. \tag{2.56}$$

---

[53] Recall from Section 2.4 that the wavespeed ratio $c_0(\mathbf{x})/c(\mathbf{x})$ compensates exactly for the variable-wavespeed component of the geometrical spreading $J_0(\mathbf{x},\mathbf{x}_G)$ (Snieder and Chapman, 1998).

Following the derivation of the KHIR in Section 2.5.1, define a vector function $\mathbf{Q}(\mathbf{x},\omega)$ as

$$\mathbf{Q}(\mathbf{x},\omega) = G_0(\mathbf{x},\mathbf{x}_G,\omega)\left(\frac{1}{\rho_0(\mathbf{x})}\nabla_{\mathbf{x}} P(\mathbf{x},\mathbf{x}_s,\omega)\right) - P(\mathbf{x},\mathbf{x}_s,\omega)\left(\frac{1}{\rho_0(\mathbf{x})}\nabla_{\mathbf{x}} G_0(\mathbf{x},\mathbf{x}_G,\omega)\right). \quad (2.57)$$

Taking the divergence of this vector function yields

$$\nabla_{\mathbf{x}} \cdot \mathbf{Q}(\mathbf{x},\omega) = \frac{G_0(\mathbf{x},\mathbf{x}_G,\omega)}{\rho_0(\mathbf{x})}\left\{\rho_0(\mathbf{x})\nabla_{\mathbf{x}} \cdot \left(\frac{1}{\rho_0(\mathbf{x})}\nabla_{\mathbf{x}} G_0(\mathbf{x},\mathbf{x}_s,\omega)\right)\right\}$$

$$-\frac{G(\mathbf{x},\mathbf{x}_s,\omega)}{\rho_0(\mathbf{x})}\left\{\rho_0(\mathbf{x})\nabla_{\mathbf{x}} \cdot \left(\frac{1}{\rho_0(\mathbf{x})}\nabla_{\mathbf{x}} G_0(\mathbf{x},\mathbf{x}_G,\omega)\right)\right\}. \quad (2.58)$$

Substituting for the terms in the curly brackets in equation (2.58) using equations (2.55) and (2.56) yields

$$\nabla_{\mathbf{x}} \cdot \mathbf{Q}(\mathbf{x},\omega) = \frac{G_0(\mathbf{x},\mathbf{x}_s,\omega)}{\rho_0(\mathbf{x})}\delta(\mathbf{x}-\mathbf{x}_G) - \frac{G_0(\mathbf{x},\mathbf{x}_G,\omega)}{\rho_0(\mathbf{x})}\delta(\mathbf{x}-\mathbf{x}_s). \quad (2.59)$$

Applying the divergence theorem [equation (2.43)], the sifting property of the delta function, and then assuming the surface-scattered wavefield is zero, yields the reciprocity relation for variable-density Green's functions,

$$\rho_0(\mathbf{x}_s)G_0(\mathbf{x}_G,\mathbf{x}_s,\omega) = \rho_0(\mathbf{x}_G)G_0(\mathbf{x}_s,\mathbf{x}_G,\omega). \quad (2.60)$$

Equation (2.60) is valid for the variable-density ray-theoretical Green's functions given by equations (2.38) and (2.39). If the density at the Green's function source location is absorbed into the definition of the Green's function (following Snieder and Chapman, 1998), the reciprocity relation is given by equation (2.54). I prefer the symmetry of the ray-theoretical Green's functions as defined by equations (2.38) and (2.39).

A similar derivation for variable-density using identical source functions at two different positions s_1 and s_2 yields a reciprocity relation for the acoustic pressure,

$$P(\mathbf{x}_{s_1}, \mathbf{x}_{s_2}, \omega) = P(\mathbf{x}_{s_2}, \mathbf{x}_{s_1}, \omega). \tag{2.61}$$

Equation (2.61) is also valid for constant density.

2.7.3 Limitations of reciprocity relations

The reciprocity relations given by equations (2.54), (2.60), and (2.61) are only valid if the surface-scattered wavefield in equation (2.44) vanishes. Wapenaar and Berkhout (1989, p. 165) prove that there are two cases (in addition to the free-space or reflection-free condition discussed above) where reciprocity is guaranteed. If the surface is a rigid boundary, the normal component of the particle velocity is zero, i.e. the normal derivative of the Green's function and the normal derivative of the acoustic pressure are both zero. If the surface is a free boundary, the Green's function and the acoustic pressure are both zero. In either case, the surface-scattered wavefield is zero. Pierce (1989, p. 198) shows that an impedance boundary condition also produces a zero surface-scattered wavefield. Otherwise, the surface-scattered wavefield must be considered as part of the reciprocity relation[54]. Recall, however, that one-way Green's functions can be used to conveniently eliminate this problem (i.e. by assuming a reflection-free condition and handling boundary reflections separately).

---

[54] A further discussion on reciprocity can be found in Pierce (1989, p. 197-199 and p. 163-165). Pierce's footnote on p. 199 suggests that reciprocity of the Green's function follows if the governing boundary-value problem is self-adjoint—see suggested references. On p. 164, Pierce suggests that reciprocity of the Green's function is a universal property.

Seismic imaging uses a backward propagating Green's function. The Sommerfeld radiation condition is not appropriate for a backward propagating free-space Green's function, except in limited cases (e.g. for the cylindrical walls of an infinite disk). Simple reciprocity relations for backward propagating Green's functions can be obtained for rigid or free-surface boundaries, but these are seldom used as boundary conditions for the subsurface imaging problem. As discussed previously, one particularly useful method is to assume a fully reflection-free boundary for the reference medium, which leads to one-way Green's functions (Wapenaar and Berkhout, 1989, p. 181). I will now investigate the use of one-way Green's functions in the Kirchhoff-Helmholtz integral [equation (2.48)].

2.8 ONE-WAY RAYLEIGH INTEGRALS FOR FORWARD AND INVERSE WAVEFIELD EXTRAPOLATION

The configurations presented in Section 2.6 assume that data are available over the complete bounding surface surrounding the volume. Conventional seismic reflection experiments acquire data on the Earth's surface, which forms only a part of a possible bounding surface. In this section it will be shown that, with an incomplete data set as described above and given some additional assumptions, an exact solution to the inverse wavefield extrapolation problem can still be found. One of the keys to the solution is to recognize that the seismic wavefield crosses the acquisition surface in an outward direction only. Since we are free to choose an appropriate surface to complete the volume—just as we are free to choose the properties of the Green's functions and the reference medium utilized to derive the simplified version of the KHIR in Section 2.5.5—we choose the remaining part of the bounding surface so that the wavefield crosses it in an inward direction. Wapenaar and Berkhout (1989) show that there is a negligible contribution to the integral from this part.

A second problem arises because the acquisition of conventional seismic reflection data is limited to one of either the pressure (marine acquisition) or the normal derivative of the pressure (land acquisition), whereas the full Kirchhoff-Helmholtz integral [equation (2.48)] requires both. In Section 2.6.3 it was suggested that a recording of either one is sufficient to reconstruct a wavefield that crosses an arbitrary surface in one direction. For a planar surface, the solutions take the form of simplified Kirchhoff-Helmholtz integrals called the Rayleigh I and II integrals. The key here is to use the method of images to construct a Green's function whose value or normal derivative is zero on the acquisition surface. For a non-planar surface (i.e. rough topography), a Fourier-domain solution valid for constant wavespeed has been implemented by Margrave and Yao (1999), but an exact simplified integral solution has yet to be discovered. An approximate solution is implied in Berryhill (1979), derived by Wiggins (1984), and refined using adjoint operators by Bevc (1995). These solutions are simple because they are just the Rayleigh II integral (or the far-field approximation of the Rayleigh II integral) evaluated for each individual surface element. The error in the method arises because the dipole Green's function created using the method of images is, in general, nonzero over the remainder of the surface. In Appendix B, I present a new geometric justification for a stationary-phase approach that suggests that the far-field Rayleigh II integral is reasonable for a non-planar surface (see also Docherty, 1991).

In much of the classical migration literature (e.g. Timoshin, 1970 p. 361; French, 1975, p. 978; Schneider, 1978, p. 50), a configuration appropriate for the forward problem is incorrectly applied to the inverse problem. The fundamental error these authors make is to invoke Sommerfeld's radiation condition to ignore the contribution from the remainder of the bounding surface over which no data are available. Unfortunately, the Sommerfeld radiation condition is valid only for outward propagating wavefields, not for the inward propagating Green's function wavefields required for inverse wavefield extrapolation. A brief review of the forward problem is now presented as a preview to investigating the correct approach to the inverse problem.

2.8.1 Forward wavefield extrapolation from a planar surface

If we assume that data are acquired on a planar surface (Figure 2.6a), the forward problem has an exact integral solution that is a simplification of the full Kirchhoff-Helmholtz integral [equation (2.48)]. Pierce (1989) provides an excellent summary of Rayleigh's original 1896 boundary-value derivation, where the planar surface is replaced by radiation from a thin disk of time-varying thickness; and Sommerfeld's 1943 Green's function derivation[55] using the method of images, the principle of reciprocity, and Sommerfeld's radiation condition. Of the two derivations, Sommerfeld's derivation is the more easily understood given the theory introduced previously in this dissertation. In addition, it makes no a priori assumptions about the complexity of the wavespeed model, whereas Rayleigh's derivation is formulated for constant wavespeed.

In Sommerfeld's derivation, the Green's function required to simplify the Kirchhoff-Helmholtz integral [equation (2.48)] consists of a monopole and its mirror image, where the mirror plane is the integration surface S_1—typically the (assumed) horizontal surface of the earth given by the plane $z = 0$, but valid for any parallel plane $z =$ constant (see Figure 2.6a). The remainder of the closed surface is assumed to be an infinite hemisphere S_2 with negligible contribution to the integral due to Sommerfeld's radiation condition. The reference medium is also assumed to be symmetric about the plane $z =$ constant.

---

[55] Kuhn and Alhilali (1977) cite a 1912 paper as the source for Sommerfeld's derivation. I have not confirmed which is correct.

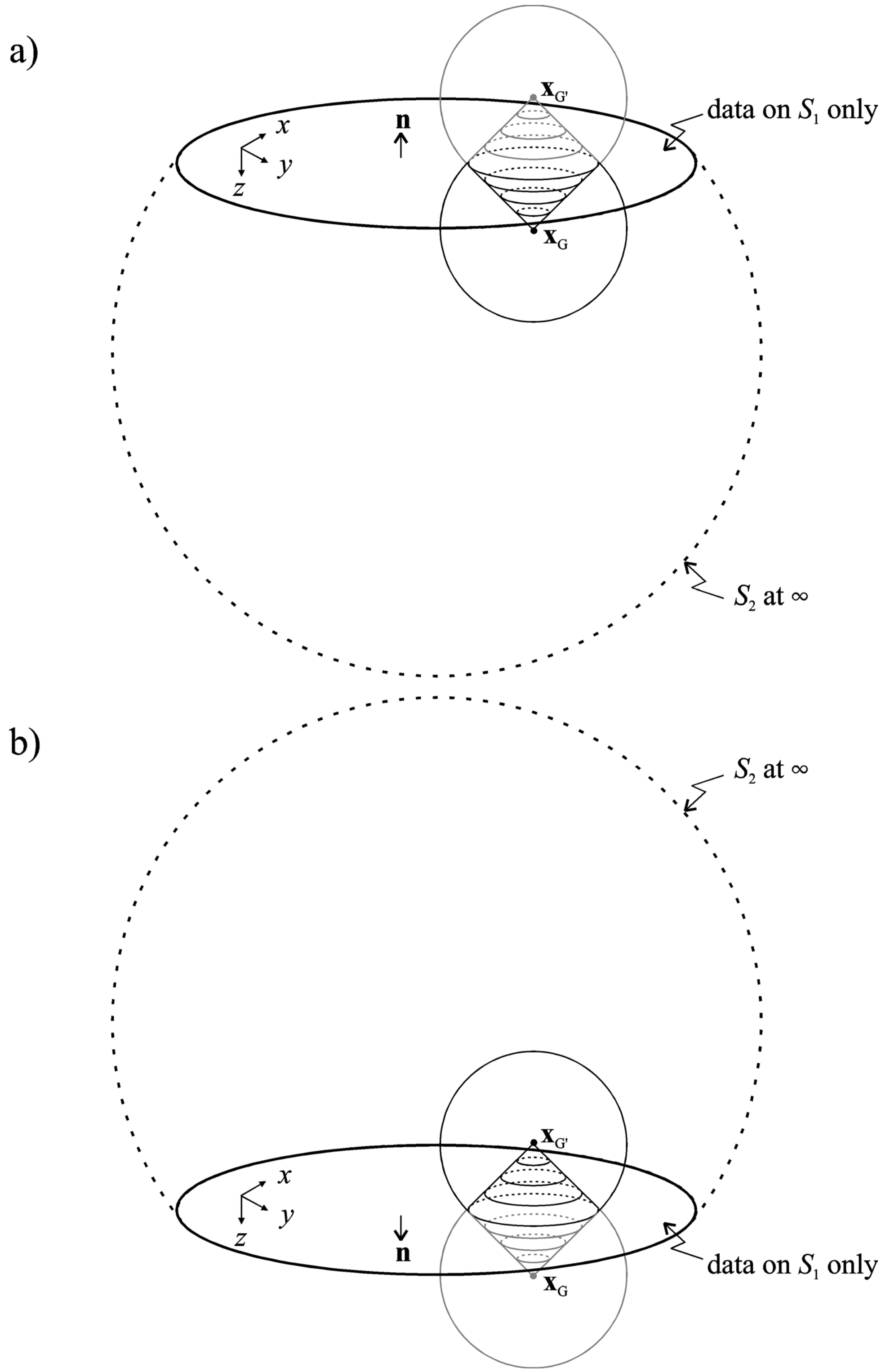

Figure 2.6. Configurations for forward wavefield extrapolation from a planar surface using image Green's functions: a) downward continuation of a downward propagating wavefield. b) upward continuation of an upward propagating wavefield. The only difference is a change in sign in the Rayleigh I or II integrals.

The sign of the mirror image portion of the Green's function can be chosen as either the same as or opposite to the sign of the source portion of the Green's function, resulting in a null value for $\nabla G_0 \cdot \mathbf{n}$ or G_0, respectively, on the boundary surface S_1. The first choice (image dipoles of the same sign), when applied to the Kirchhoff-Helmholtz integral [equation (2.48)] gives the two-way Rayleigh I integral,

$$P(\mathbf{x}_G, \mathbf{x}_s, \omega) = -2\int_{S_1} dxdy \left\{ \vec{G}_0(\mathbf{x}, \mathbf{x}_G, \omega) \frac{\partial P(\mathbf{x}, \mathbf{x}_s, \omega)}{\partial z} \right\}_{z=const} . \tag{2.61}$$

The second choice (image monopoles of opposite sign) gives the two-way Rayleigh II integral,

$$P(\mathbf{x}_G, \mathbf{x}_s, \omega) = 2\int_{S_1} dxdy \left\{ P(\mathbf{x}, \mathbf{x}_s, \omega) \frac{\partial \vec{G}_0(\mathbf{x}, \mathbf{x}_G, \omega)}{\partial z} \right\}_{z=const} . \tag{2.62}$$

For the forward problem, then, only the pressure P or the normal derivative of the pressure $\nabla P \cdot \mathbf{n}$ is required to reconstruct the pressure at the observation point. The medium can be inhomogeneous, which requires a more complicated Green's function than the free-space Green's function.

The sign of the RHS of equations (2.61) and (2.62) is opposite to the equivalent terms in equation (2.48) because, in this case, the partial derivative $\partial/\partial z$ has a sense opposite to the outward pointing normal $\mathbf{n}$ (see Figure 2.6a). These two equations, as given, are valid for downward continuation of a downward propagating wavefield, e.g. to downward continue a source wavefield to a subsurface reflector. Assuming the positive z-axis points downward, the negative of these equations are valid for upward continuation of an upward propagating wavefield (see Figure 2.6b)[56].

The use of image Green's functions implies that the boundary conditions on the integration surface are either Neumann [rigid—equation (2.61)] or Dirichlet [free surface—equation (2.62)]. Hence the Green's functions are two-way. As mentioned previously in Section 2.5, two-way Green's functions require exact specification of the reference media to properly account for multiples[57]. One-way Green's functions allow for less accurate specification of the reference media because multiples are not considered (Wapenaar and Berkhout, 1989, p. 180-183, Appendix B). In Section 2.5, it was shown that both free-space and ray-geometric Green's functions ignore multiple reflections and hence are one-way expressions. In addition, the acquisition surface is commonly treated as a planar reflection-free surface across which both the acoustic wavefield and Green's functions propagate in one direction only. These are almost universal assumptions for any practical implementation; thus a one-way approach is implied for forward and inverse wavefield extrapolation in most of the migration literature.

---

[56] The reader is cautioned about the possible complexity of signs when implementing the free-space versions of equations (2.62) and (2.64) in the space-frequency domain [i.e. after expanding the normal derivative of the second term of equation (2.49) into far-field and near-field terms]. The correct choice of signs depends on the orientation of the z-axis relative to the surface normal, the orientation of the surface normal (inward or outward), the sign convention of the Fourier transform, the phase convention of the Fourier transform (phase lag or phase lead positive), and the intended use for either forward or inverse extrapolation.

[57] Wapenaar and Berkhout (Wapenaar and Berkhout, 1989, p.176-180) show that the assumed boundary conditions on the integration surface (Neumann or rigid surface: $\nabla G_0 \cdot \mathbf{n} = 0$; Dirichlet or free surface: $G_0 = 0$) create the largest multiple problem for two-way Green's functions, irrespective of the interface contrasts within the media.

2.8.2 Inverse wavefield extrapolation from a planar surface

The configuration assumed for the forward problem (Figures 2.6a and 2.6b) is not applicable to the inverse problem. The Sommerfeld radiation condition cannot be invoked for the lower surface because, in the case of backward propagating Green's functions, there is no guarantee that the integral over the infinite hemisphere will be negligible. Wapenaar and Berkhout (1989) discuss in great detail the problem of inverse wavefield extrapolation using the Kirchhoff-Helmholtz integral [equation (2.48)] where data are available only over a portion of the surface. They introduce an appropriate configuration as shown by the cylinder in Figure 2.7: the upper "acquisition surface" (where data are available) is labeled S_1, the lower surface (where no data are available) is labeled S_2, and the cylindrical side surface at infinity is labeled S_3. The Sommerfeld radiation condition is invoked to ignore the contribution from S_3. The key is to assume one-way wavefields and then determine the conditions under which the contribution to the integral from the lower surface S_2 can be ignored (see Section 3.2).

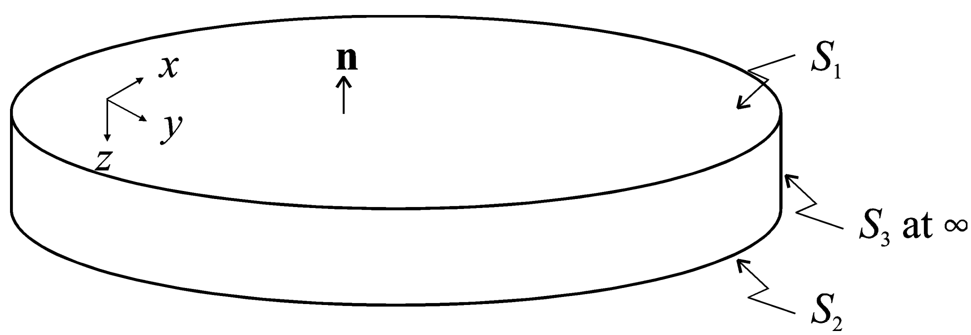

Figure 2.7. Configuration for inverse wavefield extrapolation of an upward propagating wavefield recorded on a planar surface S_1. The wavefield is assumed to be upward propagating as it crosses S_2. Hence, the contribution to the surface integral from S_2 can be ignored. The contribution from S_3 (at infinity) can be ignored by the Sommerfeld radiation condition. However, there remains a contribution from the edge of S_1, even it extends to infinity (see Wapenaar, 1992 for a discussion of the infinite aperture paradox).

To derive the one-way Rayleigh I and II integrals for inverse wavefield extrapolation from a planar surface, Wapenaar and Berkhout (1989) separate both the wavefield and the Green's functions into upgoing and downgoing parts on each of the upper and lower surfaces, and then show that contributions to the Kirchhoff-Helmholtz integral [equation (2.48)] arise only when the wavefield and Green's functions propagate in opposite directions across the integration surface. With the positive z-axis pointing downward, the primary wavefield recorded on the upper surface is assumed to be upgoing while the backward propagating Green's function is downgoing. This gives the contribution to the integral that we desire. On the lower surface, both the primary wavefield and the backward propagating Green's function are upgoing. Hence there is no contribution to the Kirchhoff-Helmholtz integral from the primary wavefield crossing the lower surface. However, the scattered wavefield on the lower surface, arising from reflecting interfaces within the volume, is downgoing. Since the backward propagating Green's function is upgoing, this contribution should be included[58]. By ignoring it, we ignore internal multiply reflected waves and include only the transmitted wavefield crossing any reflectors that might lie between the surfaces, thereby introducing an error in amplitude proportional to the squared reflectivity. An additional error is introduced by ignoring evanescent waves, but this approximation comes with a bonus that the resulting inverse wavefield propagator is unconditionally stable[59]. For data recorded on a planar surface,

---

[58] Docherty (1991) provides an alternate (but conceptually identical) justification for ignoring the contribution from the lower surface S_2.

[59] When using the full Kirchhoff-Helmholtz integral [equation (2.48)] or its simpler time-domain equivalents [equations (2.49), (2.50), and (2.52)] for inverse wavefield extrapolation from an acquisition surface, only the upgoing wavefield is reconstructed, with similar errors introduced by ignoring multiples and evanescent waves.

then, Wapenaar and Berkhout (1989) determine that the upgoing wavefield in the subsurface can be reconstructed from the normal derivative of the pressure recorded on a planar interface by the one-way Rayleigh I integral,

$$P^{-}(\mathbf{x}_G,\mathbf{x}_s,\omega) = -2\int_{-\infty}^{\infty}\int dxdy\left\{\overleftarrow{G}_0^{+}(\mathbf{x},\mathbf{x}_G,\omega)\frac{\partial P^{-}(\mathbf{x},\mathbf{x}_s,\omega)}{\partial z}\right\}_{S_1} . \tag{2.63}$$

The upgoing wavefield in the subsurface can be reconstructed from the pressure recorded on a planar interface by the one-way Rayleigh II integral,

$$P^{-}(\mathbf{x}_G,\mathbf{x}_s,\omega) = 2\int_{-\infty}^{\infty}\int dxdy\left\{P^{-}(\mathbf{x},\mathbf{x}_s,\omega)\frac{\partial \overleftarrow{G}_0^{+}(\mathbf{x},\mathbf{x}_G,\omega)}{\partial z}\right\}_{S_1} , \tag{2.64}$$

where the superscript (-) indicates the upgoing or negative z-direction. Note that the partial derivative $\partial/\partial z$ in equations (2.63) and (2.64) is for the z-axis pointing down. Although these expressions are not exact for generalized media and boundary conditions, they will be exact for the special case of a homogeneous medium with reflection-free boundaries (ignoring evanescent waves). Note that inverse wavefield extrapolation from a planar surface does result in an artifact, even if the data are available over a surface S_1 of an infinite extent (see Wapenaar, 1992 for a discussion of the infinite aperture paradox).

2.9 INVERSE WAVEFIELD EXTRAPOLATION FROM A NON-PLANAR SURFACE

Equations (2.63) and (2.64) are valid for inverse wavefield extrapolation from a planar surface. The Sommerfeld radiation condition has not been required to ignore the contribution from the lower surface. A similar argument shows that inverse wavefield extrapolation using the Kirchhoff-Helmholtz integral [equation (2.48)], when applied to data acquired over a non-planar open surface, also reconstructs only the upgoing wavefield in the subsurface (Wapenaar and Berkhout, 1989, equation VII-61, p. 290),

$$P^{-}(\mathbf{x}_G,\mathbf{x}_s,\omega)=\int_{S_1} dS\left\{\overleftarrow{G}_0(\mathbf{x},\mathbf{x}_G,\omega)\nabla P(\mathbf{x},\mathbf{x}_s,\omega)-P(\mathbf{x},\mathbf{x}_s,\omega)\nabla\overleftarrow{G}_0(\mathbf{x},\mathbf{x}_G,\omega)\right\}\cdot\mathbf{n}\,. \quad (2.65)$$

The appropriate configuration for the derivation of equation (2.65) is a cylinder with S_1 and S_2 as non-planar surfaces (Figure 2.8). Further investigation by Wapenaar (1993a) supports the conclusion that the full Kirchhoff-Helmholtz integral as given by equation (2.65) is required to reconstruct the upgoing wavefield in the subsurface from data on a non-planar open surface.

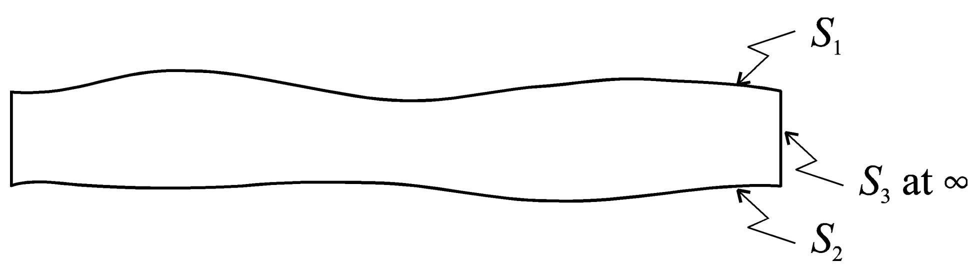

Figure 2.8. Configuration for inverse wavefield extrapolation of an upward propagating wavefield from a non-planar surface S_1. The wavefield is assumed to be upward propagating as it crosses nonplanar surface S_2. Hence, the contribution to the surface integral from S_2 can be ignored. The contribution from S_3 (at infinity) can be ignored by the Sommerfeld radiation condition. However, there remains a contribution from the edge of S_1, even it extends to infinity (see Wapenaar, 1992 for a discussion of the infinite aperture paradox).

2.9.1 Are both the pressure and the normal derivative of pressure required? – part 2

The reconstruction given by equation (2.65) correctly accounts for upgoing internal reflections from the bottom of the S_1 surface and, if implemented as an iterative downward continuation with the upper S_1 and lower S_2 surfaces at the wavespeed discontinuities (the reflector surfaces), the full integral also accounts for transmission effects across the interface, thus eliminating the error in amplitude proportional to squared reflectivity. As well, equation (2.65) is valid for one-way or two-way wavefields and Green's functions.

These additional benefits suggest that the full Kirchhoff-Helmholtz integral as given by equation (2.65) might well be overdetermined for the simpler goal of wavefield reconstruction from an arbitrary surface in a homogeneous medium. Indeed, Margrave and Yao (1999) show that, for constant wavespeed, a pseudo-inversion of a generalized phase-shift plus interpolation (PSPI) extrapolator exactly reconstructs the wavefield in the subsurface using only the pressure recorded on the non-planar surface. The exactness of the method can be justified with the following thought experiment. It is trivial to show that a single plane wave of known propagation direction can be reconstructed using only the pressure recorded on a non-planar surface. The normal derivative of the pressure is synthesized on the surface using the time derivative of the recorded pressure, the wavespeed, the propagation direction of the incident plane wave, and the normal direction at the surface, all of which are known. Effectively, then, there is sufficient information to reconstruct the upgoing plane wave using the full Kirchhoff-Helmholtz integral, which is known to be exact. Each recursive step of the pseudo-inverse method implies a plane-wave decomposition at the output points on a planar surface within the volume. Given constant wavespeed, this decomposition will also be valid at the input points on the non-planar surface. Thus, an exact reconstruction is possible. Margrave and Yao (1999) show that the pseudo-inverse reconstruction includes evanescent energy recorded on the input surface, although practical implementation must ignore evanescent energy to maintain stability. Variable wavespeed creates a problem in that the plane wave decomposition at the output surface will not be valid for the input surface. In practice, small recursion steps reduce the error such that its magnitude is insignificant compared to the errors introduced by noise or by inaccuracies in the reference wavespeed model.

2.9.2 Love's 1903 theorem of determinacy

The proof that only one of either the pressure or its normal derivative is sufficient to reconstruct the wavefield is found in Love's 1903 theorem of determinacy of the solution. A summary by Baker and Copson (1950, p. 40-41) is applicable to forward extrapolation using the time domain version of the Kirchhoff-Helmholtz equation, i.e. equation (2.51) —the free space version—repeated here as

$$p(\mathbf{x}_G,\mathbf{x}_s,t)=\frac{1}{4\pi}\oint_S dS\left\{\frac{1}{r}\left[\frac{\partial p(\mathbf{x},\mathbf{x}_s,t)}{\partial n}\right]+\frac{1}{c_0 r}\left[\frac{\partial p(\mathbf{x},\mathbf{x}_s,t)}{\partial t}\right]\frac{\partial r}{\partial n}+\frac{1}{r^2}\left[p(\mathbf{x},\mathbf{x}_s,t)\right]\frac{\partial r}{\partial n}\right\}. \qquad (2.51)$$

Baker and Copson write (underlining added for emphasis):

> The formulae of Kirchhoff enable us to express the value of p at a point $\mathbf{x}_G$ on one side of a closed surface S and at the instant t, in terms of the surface values of p and its first partial derivatives at previous instants. Actually the data are redundant, inasmuch as a knowledge of the surface values of p alone for all values of t is sufficient to determine those of $\partial p/\partial t$, and is, in fact, sufficient, <u>with a knowledge of the initial values of p and $\partial p/\partial t$</u>, to determine p throughout the whole region of space in which it satisfies the equation of wave-motions and the prescribed conditions of continuity. This statement constitutes a part of the theorem of determinacy of the solution of the equation of wave-motions; it follows from it that, <u>if p and $\partial p/\partial t$ are given everywhere initially</u> and p is given for all values of t on the surface S, $\partial p/\partial n$ can have only one definite value at any point of S at any given instant. The surface values of $\partial p/\partial n$ would also suffice in the same way for the determination of p; this constitutes the other part of the theorem of determinacy.

The argument, as given, is restricted to the forward problem. However, with appropriate modification it applies equally well to the inverse problem. We will consider both problems and discuss them in the context of specific applications to seismic wavefield extrapolation.

2.9.3 Forward (downward) extrapolation from a point source

For forward extrapolation of seismic data, the difficulty lies in knowing the initial values of p and $\partial p/\partial t$ everywhere. A typical forward problem is downward extrapolation of the downgoing source wavefield. The initial values are all zero, except for the known (assumed) value of the monopole source at one location on the non-planar surface (recall from Section 2.2 that any source can be derived or synthesized from the monopole response). The wavefield can be reconstructed using either recursive or nonrecursive methods. In implementing a recursive downward extrapolation of the downgoing wavefield, we are free to choose the geometry of the output surface. The output surface may as well be planar, which neatly sidesteps the problem of subsequent recursions from a non-planar surface. The first recursion, from the point source on the non-planar input surface, follows the nonrecursive implementation discussed below whereby no integral reconstruction is required. Subsequent recursions typically use the free-space version of the forward propagating one-way Rayleigh II integral, derived in the time domain by Schneider (1978) for a planar surface at z = constant and the z-axis positive downward as

$$p^{+}(\mathbf{x}_G,\mathbf{x}_s,t)=\frac{1}{2\pi}\int_{S_1} dS\frac{\cos\theta}{rc_0}\left\{\frac{\partial p^{+}(\mathbf{x},\mathbf{x}_s,t-r/c_0)}{\partial t}+\frac{c_0}{r}p^{+}(\mathbf{x},\mathbf{x}_s,t-r/c_0)\right\}, \quad (2.66)$$

i.e. twice the last two terms of equation (2.51) with the normal derivative evaluated as a z derivative. In a constant wavespeed medium, $\cos\theta=\partial r/\partial z$.

A nonrecursive implementation is even easier because an integral equation is not required. For one-way nonrecursive downward extrapolation of the downgoing wavefield, the desired wavefield is simply the incident wavefield. The incident wavefield from a point source is the first term on the RHS of the KHIR [equation (2.44)], which is just the Green's function multiplied by source signature [e.g. equation (2.19) for a ray-theoretical Green's function in the space-frequency domain]. Hence, the Kirchhoff-Helmholtz or Kirchhoff integrals are not required, nor are any approximations (a useful observation that will reappear in Section 3.2 in the context of migration).

2.9.4 Forward (upward) extrapolation of an upgoing wavefield

A second example of a forward problem is changing the datum to higher elevation in areas of rugged topography, i.e. the upward extrapolation of the upgoing wavefield recorded on a non-planar surface. In this case, the initial values of p and $\partial p/\partial t$ can be assumed to be zero. Berryhill (1979) breaks the non-planar surface into planar elements and devises a localized coordinate system [denoted as (x', y', z')] with the z'-direction normal to each element[60]. Berryhill's equation (A-1) is the free-space version of the forward propagating one-way Rayleigh II integral for the z'-axis positive upward,

$$p^{+}(\mathbf{x}_G, \mathbf{x}_s, t) = \frac{1}{2\pi}\int_{S_1} dS' \frac{\cos\theta'}{r'c_0}\left\{\frac{\partial p^{+}(\mathbf{x}', \mathbf{x}'_s, t - r'/c_0)}{\partial t} + \frac{c_0}{r'} p^{+}(\mathbf{x}', \mathbf{x}'_s, t - r'/c_0)\right\}. \qquad (2.67)$$

with the far-field response and the near field response given by the first and second terms in the curly brackets, respectively. Equation (2.67) is identical to equation (2.66) except for the localized nature of the coordinate system and the positive upward orientation of

---

[60] Berryhill (1979) develops his redatuming method based on the use of planar elements in the 2-D and 3-D zero-offset modeling theories of Trorey (1970) and Hilterman (1970); who in turn cites Biot and Tolstoy (1957) and Mitzner (1967), respectively, for the origin of the methods.

the z'-axis. Berryhill (1979, p. 1330) claims that that his implementation of equation (2.67) is “a precise and efficient computerized form of Huygens’ principle”. Bevc (1995) implements only the far-field term in his redatuming method, and claims in Section 1.1 of his dissertation that “Berryhill’s time domain formulation is accurate since it includes the near-field term”. These implementations may be accurate and/or precise, but they are not exact. Berryhill’s forward wavefield extrapolation using equation (2.67) is an approximation for a non-planar surface. The approximation arises because a simple application of the method of images to a “local” surface element creates a local dipole Green’s function that satisfies the boundary conditions only at surface elements that are tangential to the local element. Hence, the “global” Green’s function that is numerically synthesized from the local functions does not satisfy the boundary conditions required by the Rayleigh II integral. Fortunately, a dipole has small values over directions nearly perpendicular to the dipole axis (which is normal to the local element), i.e. the error in the approximation is small for surface elements that are nearly tangential to the local element. The nature of this approximation will be investigated more thoroughly in the following paragraphs, but in the context of inverse extrapolation of seismic wavefields.

2.9.5 Inverse (downward) extrapolation of an upgoing wavefield

I now return to the theorem of determinacy and apply it to inverse extrapolation of seismic data (e.g. downward extrapolation of the upgoing wavefield). For inverse extrapolation, the final values of P and $\partial P/\partial t$ are required everywhere instead of the initial values. French (1975) assumes that the data records are sufficiently long such that, eventually, no measurable reflected energy crosses the acquisition surface. Thus the final values can be assumed to be zero everywhere, the theorem of determinacy can be applied, and acquisition of either P or $\partial P/\partial n$ is sufficient. This argument can be applied more rigorously to the recording and reconstruction of one-way primary wavefields. Only the one-way upgoing primary wavefield can be reconstructed. A finite record length progressively limits the aperture of available surface data as the depth of the reconstruction point $\mathbf{x}_G$ increases: the deeper the point, the poorer the reconstruction of the wavefield[61]. However, the theorem of determinacy will still apply, and the upgoing wavefield in the subsurface can be reconstructed from knowledge of either P or $\partial P/\partial n$ recorded on a non-planar surface.

Based on the arguments presented above, it can be concluded that inverse wavefield extrapolation from a non-planar surface does not require a record of both the pressure and its normal derivative. However, a way of incorporating this knowledge to devise an exact but simple inverse propagator similar to the Rayleigh I and II integrals [equations (2.63) and (2.64)] has yet to be accomplished. Berryhill (1979) implements inverse wavefield extrapolation using his forward extrapolator (see above) by time reversing the input traces prior to extrapolation and time reversing the output traces after. (Wiggins, 1984) derives the far-field equivalent of Berryhill's inverse extrapolator directly from the Kirchhoff integral [equation (2.50)] using a backward propagating free-space Green's function. The free-space version of the inverse propagating one-way Rayleigh II integral for the z'-axis positive downward is given by

$$p^-(\mathbf{x}_G,\mathbf{x}_s,t)=\frac{1}{2\pi}\int_{S_1} dS'\frac{\cos\theta'}{r'c_0}\left\{\frac{\partial p^-(\mathbf{x}',\mathbf{x}'_s,t+r'/c_0)}{\partial t}-\frac{c_0}{r}p^-(\mathbf{x}',\mathbf{x}'_s,t+r'/c_0)\right\},\quad(2.68)$$

with the far-field response and the near field response given by the first and second terms in the curly brackets, respectively. Equation (2.68) is twice the last two terms of equation (2.52) with the normal derivative evaluated as a z derivative. The far-field version of equation (2.68) is equation (1) of Wiggins (1984).

---

[61] See chapter 4 of Margrave (2000).

Wiggins suggests that the localized version of the Rayleigh II integral[62] is “a good approximation so long as undulations in the surface are small over a wavelength” and cites Beckman and Spizzichio (1963) as justification for this statement. However, what Beckman and Spizzichio refer to, as encapsulated in their Figure 3.4, is the standard Kirchhoff approximation for estimating an unknown wavefield on a surface in terms of the estimated value of the incident wavefield and its normal derivative at a time corresponding to arrival at the surface. The Kirchhoff approximation neglects curvature of the surface, as well as the edge effects of the planar surface element. These are valid concerns for a reflector (as we shall discover in Section 3.3), but not for an arbitrary surface over which we have measured the (assumed) exact values of the wavefield and, perhaps, its normal derivative. Instead (as discussed above) the approximation arises because the global Green’s function synthesized from the local dipoles does not satisfy the boundary conditions required by the Rayleigh II integral. The same is true for the Rayleigh I integral. An integration that includes the erroneous local Green’s functions can introduce artifacts into the reconstructed wavefield. The magnitude of the artifacts is related to the phase at the dominant frequency of the wavelet, and the geometry of the reconstruction. The relationship is complex, and justifies further study. A more extensive study is not presented in this dissertation. However, the topic is revisited briefly in Section 3.4, where it is concluded that, although theoretically incorrect, either of the Rayleigh I or Rayleigh II integrals can be practically applied for time migration from a non-planar source.

---

[62] In this paragraph, I drop the qualifier “free-space inverse propagating one-way”, which is implied.

2.10 SUMMARY

This chapter began with a derivation of the acoustic wave equation and Green's functions as necessary background for forward and inverse wavefield extrapolation. The Kirchhoff-Helmholtz integral representation [KHIR, equation (2.44)] was derived as the basic equation describing the acoustic wavefield in terms of incident and scattered wavefields. The volume-scattered wavefield [second term of equation (2.47)] was shown to be a function of the wavespeed perturbation $\alpha(\mathbf{x})$ [defined by equation (2.46)]. The surface scattered wavefield was shown to be the Kirchhoff-Helmholtz integral in the space-frequency domain [equation (2.48)—in free-space, equation (2.49)], also known as the Kirchhoff integral in the space-time domain [free-space version given by equations (2.50), (2.51) and (2.52)]. A number of configurations were examined in order to gain an intuitive understanding of the physical meaning of the integral in the context of Huygens' principle and inverse wavefield extrapolation from an arbitrary surface.

In the case of Huygens' principle, reconstruction of the wavefront was shown to be equivalent to replacing the propagating wavefield with secondary sources distributed over the wavefront surface. The Kirchhoff-Helmholtz integral [equation (2.48)] is then interpreted as a superposition of weighted monopoles and dipoles that radiates wavefields in both directions. Assuming that the one-way wavefield we are interested in is propagating outward[63], the inward propagating contributions must cancel. To do so, they must be equal and of opposite sign. Thus the outward propagating contributions must also be equal. Intuitively, then, this suggests that the one-way outward propagating wavefield can be reconstructed from twice the wavefield of either the monopole or dipole portion of the Kirchhoff-Helmholtz integral.

---

[63] Recall from Section 2.4 that a wavefield can propagate outward either forward or backward in time

This intuitive idea was then applied to inverse wavefield extrapolation from an arbitrarily reflection-free surface. First, the theory was restricted to more realistic acquisition conditions, whereby data are available only over part of a closed surface and only one of either the pressure or its normal derivative is measured. Given these restrictions, and the additional assumptions of one-way wavefields and a planar surface, an almost exact reconstruction (neglecting evanescent waves) is possible by a superposition of weighted monopoles (the Rayleigh I integral) or weighted dipoles (the Rayleigh II integral). The restriction of a planar surface was removed by considering the Rayleigh I and II integrals as composed of local image Green's functions, one for each surface element. The theory developed in this chapter will be used in Chapter 3 to develop various formulas for migration and inversion. These, in turn, provide a basis for Chapter 4, where I determine robust and efficient weighting functions for prestack migration by the method of equivalent offset.

CHAPTER 3: DEPTH IMAGING BY RAY-THEORETICAL KIRCHHOFF-APPROXIMATE MIGRATION/INVERSION

3.1 INTRODUCTION

In this chapter, I derive fundamental expressions for depth imaging of subsurface reflectors from surface seismic data. These expressions will be given as generalized formulas that convert upward propagating pressure data acquired on a non-reflecting surface into depth images of reflectivity in the subsurface. The source is assumed to be a monopole of volume injection. The term imaging is used here in the context described by Hubral et al. (1996) and refers to a migration scheme that accounts for seismic wavelet shapes and amplitudes in addition to arrival times and subsurface geometry. Indeed, following the pioneering work of Bleistein (1984), the output image of a given reflector will correspond to an aperture limited singular function whose peak amplitude is proportional to the angle-dependent geometrical-optics reflection coefficient.

3.1.1 Overview of depth imaging methods

Two methods of depth imaging are developed. The first method—ray-theoretical Kirchhoff-approximate migration—is based on inverse wavefield propagation and Claerbout's deconvolution imaging condition (Claerbout, 1971). The term 'Kirchhoff-approximate' has two meanings. The first meaning refers to the forward modeling approximation whereby the unknown scattered wavefield at the reflector is replaced by the product of an incident wavefield from the source times an angle-dependent reflection coefficient. In fact, Claerbout's deconvolution imaging condition will be shown to be a simple reformulation of this Kirchhoff approximation [compare equations (3.10) and (3.25)]. The second meaning refers to the Kirchhoff-Helmholtz integral equation, which estimates the unknown scattered wavefield at the reflector by inverse propagation of the wavefield recorded at the surface. Unfortunately, reliance on inverse wavefield propagation limits Kirchhoff-approximate migration to real or synthetic wavefields such as common-shot or common-receiver gathers, and leaves open the question of how a number of migrated common-shot or common-receiver gathers can be best combined to produce a migrated stack.

The second method attempts to circumvent these difficulties by inverting a forward modeling operator based on the Born approximation to volume scattering. The leading order approximation to this volume integral is recognized as a Fourier-transform-like integral that can be inverted to reconstruct the linearized Born reflection coefficient. Unfortunately, the resulting Born-approximate inversion formula is valid only for small increments in the medium parameters across reflectors and small angles of incidence compared to the critical angle (Bleistein et al., 2001, p. 102).

What we desire is a migration/inversion approach valid for common-offset acquisition configurations and retains accuracy for both large reflectivities and large angles of incidence. For the restricted cases of common-shot and common-receiver acquisition configurations, the volume-integral approach based on the Born approximation can be shown to produce an almost identical formula as the surface-integral approach based on the Kirchhoff approximation. This suggests that the Born-approximate inversion formula can be applied to estimate large reflectivities at large angles of incidence in any configuration[1], and is therefore the formula we desire for the common-offset configuration.

---

[1] Bleistein et al. (2001, see Section 3.7 and 5.4, discussion in Section 5.1.4, and summary in Sections 5.1.6 and 5.1.7) validate this assumption analytically by applying the Born-approximate inversion formula to Kirchhoff-approximate forward model data for a single reflector.

The resulting approach is called ray-theoretical Kirchhoff-approximate migration/ inversion, in part to stress the importance of the Kirchhoff approximation at the reflector, in part because the approach can be derived in an alternate manner directly from the Kirchhoff-approximate forward modeling formula (Jaramillo, 1999; Bleistein et al., 2001, Section 5.1.7), and in part because both the Born-approximate and Kirchhoff-approximate forward modeling formulae can be transformed in to almost identical time-domain isochron stack operators (Jaramillo, 1999; Jaramillo and Bleistein, 1999, and alternate derivation in Appendix C of this dissertation).

The essence of imaging in Kirchhoff-approximate migration/inversion is the concept of ‘weighted isochron superposition’, which is asymptotically equivalent to an inverse generalized Radon transform. Weighted isochron superposition allows us to reconstruct an image of the subsurface from a non-physical wavefield such as a common-offset gather. This is essential, because in Chapter 4, I show that the common-offset migration weight yields unbiased estimates of an average of angle-dependent reflectivity. This is exactly what is required for migration techniques (such as EOM) that create a stack of migrated gathers.

3.1.2 Overview of Chapter 3

In Sections 3.2 and 3.3, one-way Green’s functions and superposition are applied to a generalized version of the Kirchhoff-Helmholtz integral representation (KHIR). This lays the foundation for ray-theoretical Kirchhoff-approximate forward modeling of the prestack wavefield (Section 3.4), a generalized Kirchhoff-Helmholtz (KH) integral for inverse propagation of a recorded wavefield (Section 3.5), and ray-theoretical Born-approximate forward-modeling of the prestack wavefield (Section 3.8).

In Section 3.6, Claerbout's deconvolution imaging condition is examined in detail. In the frequency domain, the deconvolution imaging condition is a simple ratio of the recorded wavefield (inverse propagated to the reflector location using the KH integral) and the source wavefield (forward propagated to the reflector location as an incident wavefield). I present a new derivation that produces a chi-squared estimate of angle-dependent reflectivity from estimates at each frequency. In Section 3.7, the optimum chi-squared deconvolution imaging condition is used to derive the ray-theoretical Kirchhoff-approximate migration formula.

In Section 3.9, I present a summary of the derivation of the ray-theoretical Born-approximate migration/inversion formula (see Bleistein et al., 2001 for complete derivation). As discussed previously, the migration/inversion formula is not limited by the Born-approximation, and is therefore referred to as the ray-theoretical Kirchhoff-approximate migration/inversion formula. In Section 3.10, this formula is simplified for common-shot and common-offset acquisition configurations in a constant wavespeed medium. Migration/inversion formulae appropriate for 2.5-D are given, but are not derived in this dissertation. Derivation of the 2-D forward modeling and migration/inversion formulae for constant wavespeed are presented in Appendix D, along with relationships between the 2-D, 2.5-D and 3-D formulae.

3.2 GENERALIZED KHIR FOR FORWARD AND INVERSE SCATTERING

Each of the depth imaging expressions will be developed from the Kirchhoff-Helmholtz integral representation (KHIR), derived previously in Section 2.5.1. The relationship between the imaging expressions and the KHIR is not immediately obvious. For example, there is no term corresponding to reflectivity in the KHIR, although the wavespeed perturbation in the volume-scattered wavefield is close—as a step function it becomes the source of reflectivity for the Born-approximate method. Nor is it obvious how the KHIR can explain both propagation down and propagation up, as might be required for a prestack imaging expression. In this section, a unified approach to prestack seismic imaging is developed using the KHIR as the fundamental equation.

First, the KHIR is developed in a generalized sense, i.e. the purpose of the development is not explicitly in terms of a forward or inverse application but can be considered as both. This is not easy to do, because it requires that our conceptual understanding take on a double meaning. As an example, consider an upward propagating wavefield from a source at depth that crosses two somewhat horizontal surfaces (as described in Section 2.8.2). The KHIR can describe both the forward and the inverse propagation of the wavefield, depending on the propagation direction of the Green's function. It makes intuitive sense that, for forward propagation, the integral defining the surface-scattered wavefield has meaning only over the lower surface. For inverse propagation, the integral has meaning only over the upper surface. By using a generalized Green's function, the KHIR can describe both propagation directions in one generalized expression.

3.2.1 Reformulation of the KHIR using a generalized Green's functions

I begin with a reformulation of the KHIR using a generalized Green's function, where the Green's function could be either forward or inverse propagating. The KHIR is defined in terms of two wavefields propagating in two different media. One is the unknown true media. We choose the reference media and hence the Green's function that satisfies it, and then to take one step beyond—by approximating the Green's function with something entirely practical! All this can be done before we specify whether the Green's function is forward or inverse propagating.

The expression for wavespeed perturbation [equation (2.46)] can be substituted into the KHIR [equation (2.44)]. With this substitution, the KHIR can be re-expressed as

$$P(\mathbf{x}_G, \mathbf{x}_s, \omega) = S(\omega)\rho(\mathbf{x}_s)G_0(\mathbf{x}_s, \mathbf{x}_G, \omega)$$

$$+\oint_{\mathbf{x}} dS\{G_0(\mathbf{x}, \mathbf{x}_G, \omega)\nabla_{\mathbf{x}}P(\mathbf{x}, \mathbf{x}_s, \omega) - P(\mathbf{x}, \mathbf{x}_s, \omega)\nabla_{\mathbf{x}}G_0(\mathbf{x}, \mathbf{x}_G, \omega)\}\cdot \mathbf{n},$$

$$+\int_{\mathbf{x}} dV\omega^2\left(\frac{\alpha(\mathbf{x})}{c_0^2(\mathbf{x})}\right)G_0(\mathbf{x}, \mathbf{x}_G, \omega)P(\mathbf{x}, \mathbf{x}_s, \omega). \tag{3.1}$$

Here, the Green's function propagates in its 'mathematical' sense, agreeing with Huygens' 1673 interpretation for forward propagation (i.e. the Green's function source is at the observation location—see Sections 2.5.6 and 2.6.1). Equation (3.1) is derived in terms of two non-identical acoustic wavefields corresponding to two different sets of material properties within the same volume. As pointed out in Section 2.5.2, we are free to choose the configuration, i.e. the shape of the volume and the location of the boundaries. In addition, we can choose the reference medium within and outside the volume. The reference medium determines the corresponding Green's function, including its behavior at the boundaries.

It is important to note that the KHIR is a complete description of the total wavefield independent of the complexity of the unknown true medium and associated wavefield, and independent of the choice of the reference medium and corresponding Green's function. Given that the Green's function is a complete solution to the wave equation in the reference medium, the choice of reference medium just determines how that total is distributed amongst the various terms. On the other hand, if the Green's function is an approximate solution to the wave equation in the reference medium (e.g. one-way ray-theoretical Green's functions for a complex medium), it follows that the KHIR will also be approximate. The relationship between the various choices, approximations, and distributions will be investigated in detail shortly.

3.3.2 Superposition of the KHIR

A second reason why equation (3.1) provides flexibility is because it is derived from the linearized acoustic wave equation. Hence, we might expect to be able to superpose simple solutions to create more complex solutions. This is true for many applications of the equation (or its parts), but not for all. We have already come across an example—Rayleigh I and II propagation from a nonplanar surface—where a superposition of local Green's functions does not exactly reconstruct the global Green's function. Non-linearity can also arise because both the surface-scattered and volume-scattered wavefields are expressed in terms of the unknown acoustic pressure within the volume. Equation (3.1) can be recursively substituted back into itself, giving a series expression in terms of multiply scattered wavefields. In the case of the volume-scattered wavefield, the Born method derives its name from the approximation that linearizes the series equation. The linearized Born equation will be developed in Section 3.8, and then applied to the imaging problem in Section 3.9.

Superposition is valid in many applications, however. An important example introduced in Section 2.3.2 is to consider the seismic reflection problem to be composed of the separate linear steps of propagation down—reflection—propagation up. The propagation steps can be described by the Kirchhoff-Helmholtz integral or the simpler Rayleigh I or II integrals. Reflection can be described using a separate approximation, such as Claerbout's deconvolution imaging condition. A second example of superposition was introduced in Section 2.8.2, whereby the wavefield and the Green's function are considered as a sum of upgoing and downgoing parts. Only those combinations of wavefield and Green's function that propagate in opposite directions across the interface contribute to the reconstruction integral—a concept that will be used extensively in

Section 3.3. In fact, superposition underlies many applications of the KHIR. Unfortunately, the intricacies are not explicitly stated in much of the seismic literature.

3.2.3 Reference medium chosen to make boundary non-reflective

The various terms on the RHS of the KHIR [equation (3.1)] can be thought of as decomposition of the total acoustic pressure $P_t(\mathbf{x}_G, \mathbf{x}_s, \omega)$ into the sum

$$P_t(\mathbf{x}_G, \mathbf{x}_s, \omega) = P_i(\mathbf{x}_G, \mathbf{x}_s, \omega) + P_S(\mathbf{x}_G, \mathbf{x}_s, \omega) + P_V(\mathbf{x}_G, \mathbf{x}_s, \omega), \tag{3.2}$$

where $P_i(\mathbf{x}_G, \mathbf{x}_s, \omega)$ is the incident wavefield, $P_S(\mathbf{x}_G, \mathbf{x}_s, \omega)$ is the surface-scattered wavefield, and $P_V(\mathbf{x}_G, \mathbf{x}_s, \omega)$ the volume-scattered wavefield. There is a subtle but important difference between this decomposition and the analysis of individual terms presented in Sections 2.5.3 through 2.5.5. There, for a restricted class of unknown true media (e.g. homogeneous), specific configurations and boundary conditions resulted in some terms equaling zero, such that the total acoustic wavefield was described by only one term. The important choices included the shape of the volume and propagation direction of the Green's function across the boundaries. Application is limited to acoustic wavefields that cross the bounding surfaces in one direction only. These considerations lead to expressions for one-way forward and inverse wavefield propagation, but do not provide a complete description at the reflector when the incident wavefield and surface-scattered wavefield travel in opposite directions. However, one-way wavefields can be used as part of a more complete description, as will be shown shortly.

Here, more general situations are examined to investigate how the total wavefield can be distributed amongst the various terms in the KHIR. We will also use superposition to simplify the complicated wavefields arising from boundary reflections. In the end, we may have to ignore a portion of the total wavefield, typically because it cannot be accounted for in any practical implementation. But hopefully, these leftovers will be small, or can be dealt with in some other manner. Practicality often forces us to ignore these terms and live with the consequences of the resulting approximation.

Recall from Section 2.5.2 that the literal interpretation of the terms ‘incident’ and ‘scattered’ are more restrictive than the mathematics permits. The choice of Green’s function determines which components of the wavefield are described by the various terms in equation (3.1). If the source and observation points lie within the volume and the Green’s function is defined with the exact unknown true wavespeed model such that it accounts for all reflections (including those from outside the volume), the only non-zero term is the incident wavefield. But this “incident” wavefield describes all the “scattering” effects. As pointed out by Wapenaar and Berkhout (1989), complicated Green’s functions are not practical, and can be avoided, in part, by choosing a Green’s function that is one-way at the boundary. The simplest way to accomplish this is to extend the reference media outside the boundary with the exact wavespeed inside the boundary. The boundary for the reference medium becomes totally non-reflecting, and the incident wavefield no longer accounts for the reflection from the boundary. However, because the same Green’s function is used in all terms of the KHIR, the reflection from the boundary is now found in the surface-scattered wavefield.

The choice of a reference wavespeed with a non-reflective boundary means that the reference wavespeed no longer matches the unknown true wavespeed outside of the boundary. The Green’s function, and hence the incident wavefield term, do not accurately describe scattering (i.e. reflections) arising from outside the volume. But the same Green’s function is used in the surface-scattered wavefield. Thus the surface-scattered wavefield now includes a portion that exactly accounts for the ‘error’ arising from the inaccurate Green’s function used to describe the incident wavefield. Taking this further, we can choose a relatively homogeneous reference wavespeed outside the volume and force all the external-reflected wavefield from the incident wavefield into the surface-scattered wavefield. The Green's function is then completely one-way outside the volume. With this choice, the surface-scattered wavefield acts as a wavefield extrapolator, as discussed in Section 2.8. In fact, this is what we desire, as it is more practical to extrapolate the wavefield (including the external-reflected portion) rather than to estimate it using the Green's function. Typically, the external-reflected wavefield contains reflections from deeper in the subsurface. Subsequent choices of configuration and Green's function can account for deeper reflections. Repeated application of the KHIR is a fundamental concept in the imaging of a number of reflections in the subsurface, for both recursive and nonrecursive methods.

3.2.4 Green's functions chosen to be one-way

So far, we have chosen a reference configuration that exactly matches the unknown true configuration inside the volume, but not outside. No approximations have been made. The KHIR still describes the total wavefield. In fact, we could choose any reference configuration, and the total wavefield described by the KHIR will be distributed somehow amongst the three terms, as described by equation (3.2)[2]. The only condition is that the Green's function must be a complete solution to the wave equation given the chosen reference configuration. Thus we are assuming that the Green's function is two-way within the volume and completely describes the internal multiple reflections. Hence both the incident and surface-scattered wavefields include these internal multiples.

---

[2] In the example described so far, there is an exact match between the reference configuration and the unknown true configuration within the volume. Hence, there is no perturbation $\alpha(\mathbf{x})$ and the volume-scattered wavefield is zero. If the match is not exact, there is a perturbation and the volume-scattered wavefield is not zero.

As stated previously, it is not practical to design a Green's function that includes multiple reflections. Typically, the Green's function is chosen to be one-way everywhere. If the reference medium and the unknown true medium remain identical within the volume, then the one-way Green's function is an approximation to the two-way Green's function that solves the wave equation in the reference medium. Each of the three terms in the KHIR is now an approximation (each is formulated in terms of the approximate Green's function) and their sum no longer equals the total wavefield.

The choice of a one-way Green's function is one of the keys to creating a practical solution, although we have not yet decided on a forward or inverse application. The incident wavefield is a reasonable approximation to the direct wavefield from the source to observation point. The surface-scattered wavefield is a reasonable approximation to the wavefield reflected from the bounding surface, but also includes the external-scattered wavefield from reflectors outside the volume. The volume-scattered wavefield is non-zero only if the wavespeed perturbation $\alpha(\mathbf{x})$ is non-zero. Intuitively, this is what we desire.

3.3 ONE-WAY GREEN'S FUNCTIONS AND SUPERPOSITION APPLIED TO THE KHIR

3.3.1 Scattered wavefields from upper and lower surfaces

Now assume a configuration where the volume is an infinite-radius cylinder, bounded above by the nonplanar recording surface S_1 and below by a nonplanar reflector S_2, as shown in Figure 3.1. Both the recording surface and the reflector have unknown reflection coefficients that could depend on any number of parameters, including angle of incidence or even elastic parameters that are not incorporated in the acoustic propagation model. Later, the reflector of interest (S_2) will be denoted as Σ to simplify the notation. The unknown true medium contains additional reflector surfaces S_k located beneath the surface S_2. The reference medium is identical to the unknown true media within the volume and is non-reflective elsewhere, including on the boundary. Hence the wavespeed perturbation $\alpha(\mathbf{x})$ is zero and there is no volume-scattered wavefield[3]. The monopole source is located at $\mathbf{x}_s$ within the volume, so the incident wavefield is non-zero. The Green's function $\overleftrightarrow{G}_0(\mathbf{x},\mathbf{x}_G,\omega)$ is chosen to be one-way everywhere[4], but the propagation direction has not been chosen, as indicated by the raised double-ended arrow. With this choice of Green's function, the KHIR is, in general, an approximation.

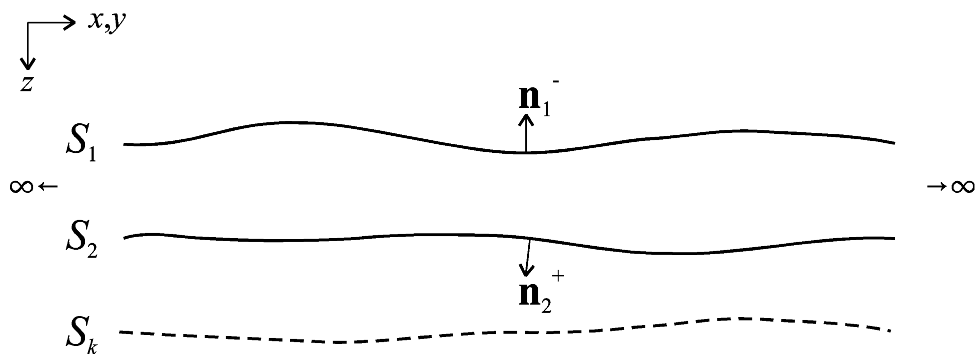

Figure 3.1. a) Configuration for generalized 3-D KHIR is an infinite radius cylinder.

Given the assumptions stated above, the concept of superposition, as expressed by equation (3.2), is then applied. In addition, the surface-scattered wavefield can be expressed as separate contributions from the upper and lower surfaces. The upper surface S_1 has coordinates $\mathbf{x}_1$ and upward directed normal $\mathbf{n}_1^-$. The lower surface S_2 has coordinates $\mathbf{x}_2$ and downward directed normal $\mathbf{n}_2^+$. The contribution from the cylinder

---

[3] This is not a restrictive assumption. If the reference wavespeed is not identical to the unknown true wavespeed, the volume-scattered integral can be taken over to the LHS and considered as an unknown error in the estimation of acoustic pressure.

[4] The Green's function is only required to be one-way at the boundary, although for practical reasons (e.g. when using free-space or ray-theoretical Green's functions), it is assumed here to be one-way everywhere.

side surface at infinity is assumed to be zero or is neglected, depending on the propagation direction of the Green's function (Wapenaar, 1992). Thus, equation (3.1) becomes

$$\begin{aligned}
P_t(\mathbf{x}_G,\mathbf{x}_s,\omega) &\cong P_i(\mathbf{x}_G,\mathbf{x}_s,\omega) + P_{S_1}(\mathbf{x}_G,\mathbf{x}_s,\omega) + P_{S_2}(\mathbf{x}_G,\mathbf{x}_s,\omega) \\
&\cong S(\omega)\rho(\mathbf{x}_s)\overleftrightarrow{G}_0(\mathbf{x}_s,\mathbf{x}_G,\omega) \\
&\quad + \int_{\mathbf{x}_1} dS\left[\overleftrightarrow{G}_0(\mathbf{x}_1,\mathbf{x}_G,\omega)\nabla_{\mathbf{x}_1}P_t(\mathbf{x}_1,\mathbf{x}_s,\omega) - P_t(\mathbf{x}_1,\mathbf{x}_s,\omega)\nabla_{\mathbf{x}_1}\overleftrightarrow{G}_0(\mathbf{x}_1,\mathbf{x}_G,\omega)\right]\cdot\mathbf{n}_1^- \\
&\quad + \int_{\mathbf{x}_2} dS\left[\overleftrightarrow{G}_0(\mathbf{x}_2,\mathbf{x}_G,\omega)\nabla_{\mathbf{x}_2}P_t(\mathbf{x}_2,\mathbf{x}_s,\omega) - P_t(\mathbf{x}_2,\mathbf{x}_s,\omega)\nabla_{\mathbf{x}_2}\overleftrightarrow{G}_0(\mathbf{x}_2,\mathbf{x}_G,\omega)\right]\cdot\mathbf{n}_2^+ .
\end{aligned} \tag{3.3}$$

3.3.2 Decomposing the total wavefield into upgoing and downgoing wavefields

As discussed previously, the one-way Green's function leads to a practical interpretation of the incident wavefield $P_i(\mathbf{x}_G,\mathbf{x}_s,\omega)$ as an approximation of the direct wavefield. Unfortunately, the surface-scattered wavefields are not yet in a practical form, as they are expressed in terms of the unknown total wavefield $P_t(\mathbf{x}_j,\mathbf{x}_s,\omega)$ at the bounding surface j. Berkhout and Wapenaar (1989) and Wapenaar et al. (1989) show that, for planar surfaces, the only contribution to the surface-scattered wavefield occurs when the acoustic wavefield and Green's wavefield propagate in opposite directions across the surface. Before this can be applied to equation (3.3), we need to decompose the total wavefield on the surface into a superposition of upgoing (-) and downgoing (+) wavefields, as given by

$$P_t(\mathbf{x}_j,\mathbf{x}_s,\omega) = P_t^-(\mathbf{x}_j,\mathbf{x}_s,\omega) + P_t^+(\mathbf{x}_j,\mathbf{x}_s,\omega) . \tag{3.4}$$

On the upper surface ($j = 1$), the upgoing wavefield is composed of the incident wavefield plus all scattered wavefields (including multiples) propagating in an upward direction from any reflectors located on or below the surface. Ignoring subsurface multiple reflections, each of these reflected wavefields can be thought of as arising from an image source located below their respective reflecting surface, as illustrated in Figure 3.2. If a particular reflector is non-planar, there is the possibility of an infinite number of image source locations. The generalized location of the image source(s) is indicated by $\mathbf{x}_{s'}$. Although the notation is somewhat awkward, the concept of an image source is crucial if we want to determine the correct direction of increasing phase (as given by the traveltime gradient). Using the subscript (S_k) to denote the scattered wavefield from the kth reflector, the upgoing wavefield on the upper surface is then the superposition

$$P_t^-(\mathbf{x}_1,\mathbf{x}_s,\omega) = P_i^-(\mathbf{x}_1,\mathbf{x}_s,\omega) + P_{S_2}^-(\mathbf{x}_1,\mathbf{x}_{s'},\omega) + \sum_{k=3}^{\infty} P_{S_k}^-(\mathbf{x}_1,\mathbf{x}_{s'},\omega). \tag{3.5}$$

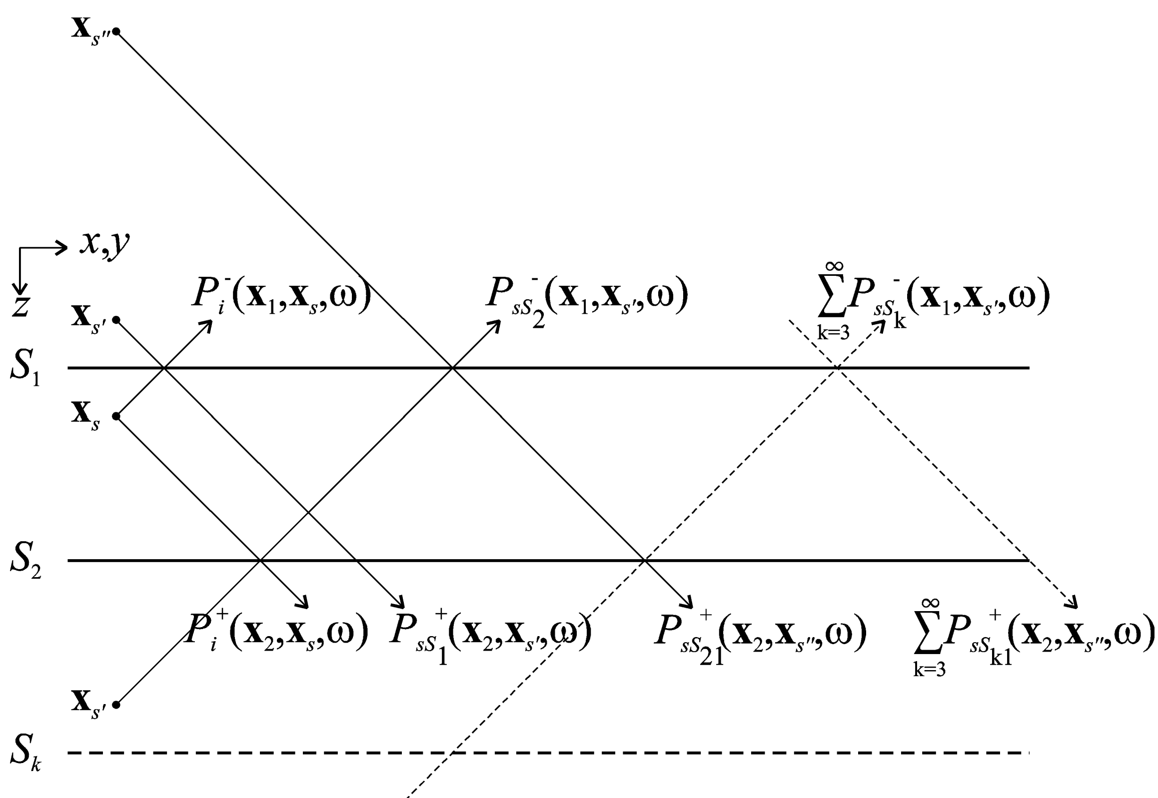

Figure 3.2. Upgoing and downgoing wavefields on upper (S_1) and lower (S_2) surfaces.

The downgoing wavefield is composed of all scattered wavefields (including multiples) propagating in a downward direction from any reflectors located on or above the surface. If the upper recording surface is assumed to be a free surface, and subsurface multiple reflections are ignored, the downgoing wavefield is the superposition of the incident wavefield from an image source above the upper surface plus wavefields from multiple-image sources for each upgoing reflected wavefield. The generalized location of the multiple-image sources is indicated by $\mathbf{x}_{s''}$. Using the subscript (S_{k1}) to denote the scattered wavefield reflected first across the kth reflector then across the upper surface, downgoing wavefield on the upper surface is the superposition

$$P_t^+(\mathbf{x}_1, \mathbf{x}_s, \omega) = P_{S_1}^+(\mathbf{x}_1, \mathbf{x}_{s'}, \omega) + P_{S_{21}}^+(\mathbf{x}_1, \mathbf{x}_{s''}, \omega) + \sum_{k=3}^{\infty} P_{S_{k1}}^+(\mathbf{x}_1, \mathbf{x}_{s''}, \omega) \tag{3.6}$$

Applying these same concepts to the lower surface (j = 2), the downgoing wavefield on the lower surface is the superposition

$$P_t^+(\mathbf{x}_2, \mathbf{x}_s, \omega) = P_i^+(\mathbf{x}_2, \mathbf{x}_s, \omega) + P_{S_1}^+(\mathbf{x}_2, \mathbf{x}_{s'}, \omega) + P_{S_{21}}^+(\mathbf{x}_2, \mathbf{x}_{s''}, \omega) + \sum_{k=3}^{\infty} P_{S_{k1}}^+(\mathbf{x}_2, \mathbf{x}_{s''}, \omega), \tag{3.7}$$

where it is assumed that there are no reflectors between the source and the upper surface. The upgoing wavefield on the lower surface is the superposition

$$P_t^-(\mathbf{x}_2, \mathbf{x}_s, \omega) = P_{S_2}^-(\mathbf{x}_2, \mathbf{x}_{s'}, \omega) + \sum_{k=3}^{\infty} P_{S_k}^-(\mathbf{x}_1, \mathbf{x}_{s''}, \omega). \tag{3.8}$$

As illustrated in Figure 3.2, the last three terms on the RHS of equation (3.7) are identical to the three terms on the RHS of equation (3.6), i.e. the downgoing scattered wavefield on the lower surface is the same as the downgoing scattered wavefield on the upper surface. Similarly, the last two terms on the RHS of equation (3.5) are identical to the two terms on the RHS of equation (3.8), i.e. the upgoing scattered wavefield on the upper surface is the same as the upgoing scattered wavefield on the lower surface. Obviously, this assumes that the wavefields suffer no transmission losses while propagating between the upper and lower surfaces.

3.4 RAY-THEORETICAL KIRCHHOFF-APPROXIMATE MODELING

The concepts introduced in Section 3.3 can now be applied to a specific application of the KHIR. The propagation direction of the Green's function determines whether the KHIR describes forward propagation or inverse propagation. Choosing the propagation direction for the Green's function will greatly simplify the substitution of equations (3.4) through (3.8) into the surface-scattered wavefields in equation (3.3). We start with a forward propagating Green's function in order to derive expressions for prestack modeling of seismic reflection data.

As discussed previously, we need only consider acoustic wavefields propagating in the opposite direction to the Green's function. Recall from Section 2.6 that the Green's function source location $\mathbf{x}_G$—the output point for the KHIR—must lie within the volume (or on the boundary). For the surface-scattered wavefields, the observation point for the Green's function is on the surface. Thus the one-way forward propagating Green's functions $\vec{G}_0(\mathbf{x},\mathbf{x}_G,\omega)$ can be decomposed into an upgoing Green's wavefield $\vec{G}_0^-(\mathbf{x}_1,\mathbf{x}_G,\omega)$ on the upper surface and a downgoing Green's wavefield $\vec{G}_0^+(\mathbf{x}_2,\mathbf{x}_G,\omega)$ on the lower surface. Therefore, only the downgoing acoustic wavefield on the upper surface, as given by equation (3.6), and the upgoing acoustic wavefield on the lower surface, as given by equation (3.8), contribute to the surface-scattered wavefields in equation (3.3). This produces five surface-scattered wavefields (two of which are infinite summations).

3.4.1 Simple forward model with a non-reflective upper surface and a reflective lower surface

In a simple forward modeling application, we might wish to ignore all surface-related multiples by modeling the upper surface as totally non-reflective. In this case, there will be no downgoing wavefield at the upper surface and there will be no contribution from equation (3.6) [i.e. $P_t^+(\mathbf{x},\mathbf{x}_s,\omega)=0$]. There are two contributions to the upgoing wavefield on the lower surface, but the only contribution of interest is the upgoing reflected wavefield from the lower surface, as given by the first term on the RHS of equation (3.8). Deeper reflections can be modeled using a separate application of the KHIR and superposed to give the desired result[5]. In this simple forward modeling application, there is only one contribution to the surface-scattered wavefield, i.e. the primary-reflected wavefield from the lower surface. Substituting Σ_R in place of S_2 to indicate the lower reflector surface, equation (3.3) becomes

$$
\begin{aligned}
P_t(\mathbf{x}_G,\mathbf{x}_s,\omega) &\cong P_i(\mathbf{x}_G,\mathbf{x}_s,\omega)+P_{\Sigma_R}^-(\mathbf{x}_G,\mathbf{x}_s,\omega)\\
&\cong S(\omega)\rho(\mathbf{x}_s)\vec{G}_0(\mathbf{x}_s,\mathbf{x}_G,\omega)\\
&\quad+\int_{\mathbf{x}_R} d\Sigma_R\Big\{\vec{G}_0^+(\mathbf{x}_R,\mathbf{x}_G,\omega)\nabla_{\mathbf{x}_R}P_{\Sigma_R}^-(\mathbf{x}_R,\mathbf{x}_{s'},\omega)\cdot\mathbf{n}_R^+\\
&\qquad-P_{\Sigma_R}^-(\mathbf{x}_R,\mathbf{x}_{s'},\omega)\nabla_{\mathbf{x}_R}\vec{G}_0^+(\mathbf{x}_R,\mathbf{x}_G,\omega)\cdot\mathbf{n}_R^+\Big\}
\end{aligned}
\tag{3.9}
$$

The surface-scattered wavefield $P_{\Sigma_R}^-(\mathbf{x}_G,\mathbf{x}_s,\omega)$ is now identified as an upgoing wavefield, and the unit vector $\mathbf{n}_R^+$ is the downward pointing normal to the reflector surface Σ_R. The Green's function $\vec{G}_0(\mathbf{x}_s,\mathbf{x}_G,\omega)$ in the incident wavefield $P_i(\mathbf{x}_G,\mathbf{x}_s,\omega)$ could be either upgoing or downgoing depending on the relative position of the Green's function source location $\mathbf{x}_G$ and observation location $\mathbf{x}_s$.

---

[5] As an example, consider upward continuation of a wavefield recorded on the lower surface. In this case, we would expect the upgoing wavefield on the lower surface to contain all reflected energy from reflectors deeper in the subsurface, as indicated by the summation term in equation (3.8).

3.4.2 The Kirchhoff approximation of the upgoing reflected wavefield

For a forward modeling application, there is no indication of how one might obtain the upgoing reflected wavefield $P^{-}_{\Sigma_R}(\mathbf{x}_R, \mathbf{x}_{s'}, \omega)$ nor its normal derivative $\nabla_{\mathbf{x}_R} P^{-}_{\Sigma_R}(\mathbf{x}_R, \mathbf{x}_{s'}, \omega) \cdot \mathbf{n}^{+}_R$ at the reflector surface Σ_R. Without them, the surface-scattered integral cannot be evaluated. The Kirchhoff approximation assumes that the upgoing reflected wavefield at the surface is equal to the downgoing incident wavefield $P^{+}_i(\mathbf{x}_R, \mathbf{x}_s, \omega)$ at the surface multiplied by the angle-dependent geometrical-optics reflection coefficient $R_\theta(\mathbf{x}_R, \mathbf{x}_s)$ [6], where the subscript (θ) denotes the angle of incidence at the reflector surface[7]. The mathematical expression of the Kirchhoff approximation must preserve the direction of increasing phase as given by the traveltime gradient. Hence, the downgoing incident wavefield is replaced by an upgoing incident wavefield from the image source, yielding

$$P^{-}_{\Sigma_R}(\mathbf{x}_R, \mathbf{x}_{s'}, \omega) \cong R_\theta(\mathbf{x}_R, \mathbf{x}_s) P^{-}_i(\mathbf{x}_R, \mathbf{x}_{s'}, \omega)\,. \tag{3.10}$$

---

[6] Other reflection coefficients could be used, including angle-independent (constant) and elastic (e.g. Zoeppritz). One criterion for evaluating if a given reflection coefficient is appropriate is to compare the accuracy of the modeled diffraction responses with theoretical responses determined by other means, or with physical model data. Bleistein (1984, p. 296-299) uses the method of stationary phase to extend the application of $R_\theta(\mathbf{x}_R,\mathbf{x}_s)$, which is strictly valid only for the ordinary reflected ray (angle incidence = angle reflection), to zero-offset diffracted rays. The Kirchhoff-approximate method produces a good estimate of the exact diffraction response. The estimate 'degrades gracefully' with increasing offset from the normal direction. Trorey (1970, Fig. 8) provides an alternate discussion and applicable model results. The geometrical-optics reflection coefficient is derived in Bleistein (1984, p. 273-276), and in Bleistein et al. (2001, Section 3.7). The derivation will not be repeated here.

[7] The angle of incidence θ is not given as a parameter for the geometrical-optics reflection coefficient because the source location $\mathbf{x}_s$ and subsurface location $\mathbf{x}_R$ determine the angle for a known reflection surface Σ_R.

Intuitively, then, the reflection coefficient $R_\theta(\mathbf{x}_R, \mathbf{x}_s)$ can be thought of as a transmission coefficient $R_\theta(\mathbf{x}_R, \mathbf{x}_{s'})$.

It is incorrect to assume that the upgoing incident wavefield can be approximated by the first term on the RHS of equation (3.9), i.e. by the source parameters $S_\rho(\omega) = S(\omega)\rho(\mathbf{x}_s)$ times the appropriate one-way forward propagating Green's function. This assumption yields

$$P^-_{\Sigma_R}(\mathbf{x}_R, \mathbf{x}_{s'}, \omega) \cong R_\theta(\mathbf{x}_R, \mathbf{x}_s) S_\rho(\omega) \vec{G}^+_0(\mathbf{x}_{s'}, \mathbf{x}_R, \omega). \tag{3.11}$$

where the Green's function propagates downward from the Green's function source location $\mathbf{x}_\Sigma$ on the lower surface to the Green's function observation location $\mathbf{x}_{s'}$ at the image source location. Thus, the direction of increasing phase on the LHS and RHS of equation (3.11) do not agree. Instead, I assume that the correct approximation for the upgoing incident wavefield is given by

$$P^-_{\Sigma_R}(\mathbf{x}_R, \mathbf{x}_{s'}, \omega) \cong R_\theta(\mathbf{x}_R, \mathbf{x}_s) S_\rho(\omega) \vec{G}^-_0(\mathbf{x}_R, \mathbf{x}_{s'}, \omega). \tag{3.12}$$

3.4.3 Using ray-theoretical Green's functions to determine normal derivatives

Now insert the WKBJ (ray-theoretical) approximation for the Green's function as given by equation (2.34) into equation (3.11), yielding

$$P^-_{\Sigma_R}(\mathbf{x}_R, \mathbf{x}_{s'}, \omega) \cong R_\theta(\mathbf{x}_R, \mathbf{x}_s) S_\rho(\omega) A_0(\mathbf{x}_R, \mathbf{x}_{s'}) e^{i\omega\tau_0(\mathbf{x}_R, \mathbf{x}_{s'})}. \tag{3.13}$$

As an alternate notation, I will occasionally refer to the ray-theoretical amplitude as $A_{Rs'}$ and the traveltime as $\tau_{Rs'}$, with the subscript (Rs') indicating the raypath from the image source to reflector (or other locations, as needed). In any practical implementation the amplitude and traveltime would be calculated from the true source location to the reflector, as the distinction is only significant for determining the direction associated with the gradient of the traveltime.

The expression for $\nabla_{\mathbf{x}_R} P^-_{\Sigma_R}(\mathbf{x}_R, \mathbf{x}_{s'}, \omega) \cdot \mathbf{n}^+_R$ can be approximated by keeping the leading order term in ω of the normal derivative of equation (3.13) (Carter and Frazer, 1984), as given by

$$\nabla_{\mathbf{x}_R} P^-_{\Sigma_R}(\mathbf{x}_R, \mathbf{x}_{s'}, \omega) \cdot \mathbf{n}^+_R \cong i\omega R_\theta(\mathbf{x}_R, \mathbf{x}_s) S_\rho(\omega) A_0(\mathbf{x}_R, \mathbf{x}_{s'}) e^{i\omega\tau_0(\mathbf{x}_R, \mathbf{x}_{s'})} \nabla_{\mathbf{x}_R} \tau_0(\mathbf{x}_R, \mathbf{x}_{s'}) \cdot \mathbf{n}^+_R . \quad (3.14)$$

The traveltime gradient determines the direction of increasing phase; hence $\nabla \tau_{Rs'}$ points in the direction of the specularly reflected ray, i.e. upward from the reflector surface, as shown in Figure 3.3a. Docherty (1991) states that this is necessarily so, but does not

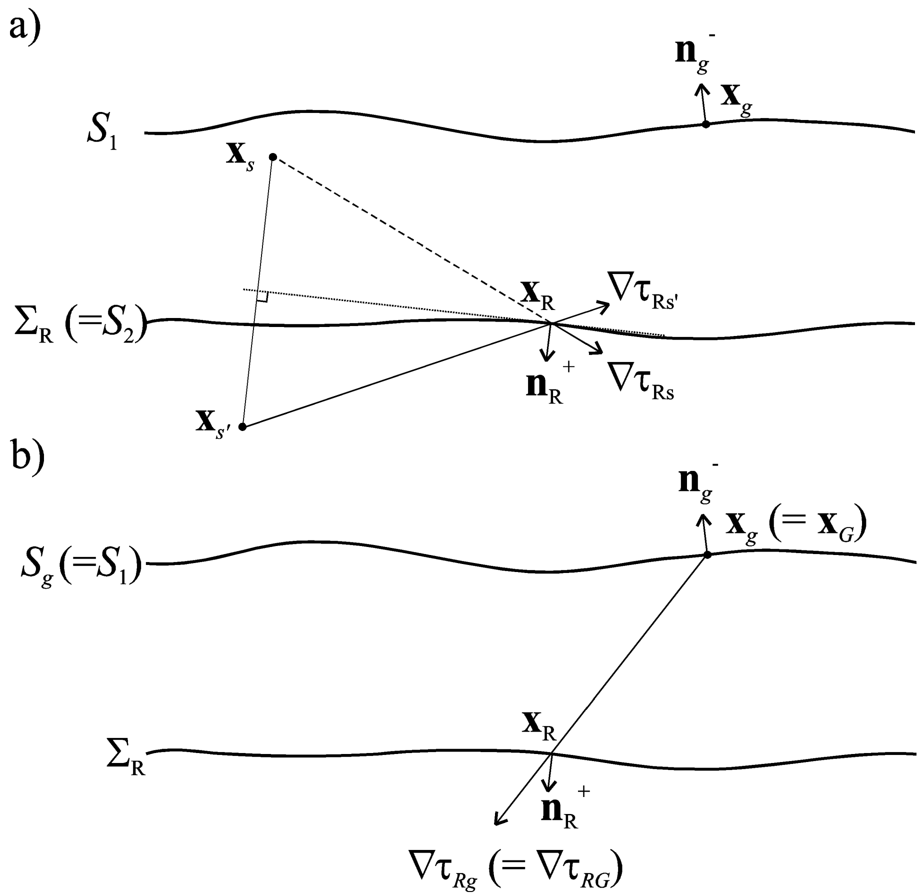

Figure 3.3. Direction of traveltime gradients on lower reflector surface and upper acquisition surface. a) $\nabla \tau_{Rs'}$, at $\mathbf{x}_R$ on reflector surface $\Sigma_R (= S_2)$, is upgoing from image source location $\mathbf{x}_{s'}$. $\nabla \tau_{Rs}$ is downgoing from source location $\mathbf{x}_s$. b) $\nabla \tau_{Rg}$, at $\mathbf{x}_R$ on Σ_R, is downgoing from receiver location $\mathbf{x}_g (= \mathbf{x}_G)$ on acquisition surface $S_g (= S_1)$.

invoke an image source so the justification for the upward direction is not obvious[8]. Similarly, the WKBJ approximation for the Green's function $\vec{G}_0^+(\mathbf{x}_R,\mathbf{x}_G,\omega)$ is given by

$$\vec{G}_0^+(\mathbf{x}_R,\mathbf{x}_G,\omega) \cong A_0(\mathbf{x}_R,\mathbf{x}_G)e^{i\omega\tau_0(\mathbf{x}_R,\mathbf{x}_G)}, \tag{3.15}$$

and the normal derivative approximated by

$$\nabla_{\mathbf{x}_R}\vec{G}_0^+(\mathbf{x}_R,\mathbf{x}_G,\omega)\cdot\mathbf{n}_R^+ \cong i\omega A_0(\mathbf{x}_R,\mathbf{x}_G)e^{i\omega\tau_0(\mathbf{x}_R,\mathbf{x}_G)}\nabla_{\mathbf{x}_R}\tau_0(\mathbf{x}_R,\mathbf{x}_G)\cdot\mathbf{n}_R^+. \tag{3.16}$$

with $\nabla\tau_{RG}$ pointing in the downward direction, as shown in Figure 3.3b. In a forward modeling application, the Green's function source is the receiver (i.e. geophone or hydrophone) position and will now be indicated by the subscript (*g*), as shown in Figure 3.3b.

3.4.4 The ray-theoretical Kirchhoff-approximate modeling formula

Introducing the new notation, substituting equation (3.13) through (3.16) into equation (3.9), and subtracting the incident wavefield $P_i(\mathbf{x}_g,\mathbf{x}_s,\omega)=S_\rho(\omega)\vec{G}_0(\mathbf{x}_s,\mathbf{x}_g,\omega)$ yields

$$P_{\Sigma_R}^-(\mathbf{x}_g,\mathbf{x}_s,\omega) \cong i\omega S_\rho(\omega)\int_{\mathbf{x}_R} d\Sigma_R A_0(\mathbf{x}_R,\mathbf{x}_{s'})R_\theta(\mathbf{x}_R,\mathbf{x}_s)A_0(\mathbf{x}_R,\mathbf{x}_g)$$

$$\times\left(\nabla_{\mathbf{x}_R}\tau_0(\mathbf{x}_R,\mathbf{x}_{s'})\cdot\mathbf{n}_R^+ - \nabla_{\mathbf{x}_R}\tau_0(\mathbf{x}_R,\mathbf{x}_g)\cdot\mathbf{n}_R^+\right)e^{i\omega\left(\tau_0(\mathbf{x}_R,\mathbf{x}_{s'})+\tau_0(\mathbf{x}_R,\mathbf{x}_g)\right)}. \tag{3.17}$$

Equation (3.17) is the ray-theoretical Kirchhoff-approximate modeling formula for the upgoing wavefield at receiver location $\mathbf{x}_g$ arising from a point source at location $\mathbf{x}_s$ and reflected from surface Σ_R with angle-dependent reflectivity coefficient $R_\theta(\mathbf{x}_R,\mathbf{x}_s)$. In this case, the term 'Kirchhoff-approximate' refers to the assumption that both the scattered wavefield $P_{\Sigma_R}^-(\mathbf{x}_R,\mathbf{x}_{s'},\omega)$ and its normal derivative $\nabla_{\mathbf{x}_R}P_\Sigma^-(\mathbf{x}_R,\mathbf{x}_{s'},\omega)\cdot\mathbf{n}_R^+$ at the surface of the reflector can be expressed in terms of the incident wavefield, as given by equations

[8] Docherty (1991) discusses the inverse problem through a comparison of Kirchhoff integral formulas for migration and inversion. My attempts to understand subtle inconsistencies in Docherty's paper provide much of the impetus for the theoretical development presented in this section.

(3.13) and (3.14). This approximation is valid only if the radius of curvature of the irregularities on the reflector surface is large compared with the wavelength (Beckman and Spizzichio, 1963, p. 20). The effect of reflector curvature on a larger scale can be incorporated into the reflection coefficient, as shown by Bleistein (1984, p. 287-289). The obliquity factor[9] $\left(\nabla_{\mathbf{x}_R}\tau_0(\mathbf{x}_R,\mathbf{x}_{s'})\cdot\mathbf{n}_R^+ - \nabla_{\mathbf{x}_R}\tau_0(\mathbf{x}_R,\mathbf{x}_g)\cdot\mathbf{n}_R^+\right)$ can be thought of as a weighting factor that compensates for the increased cross-sectional area of ray-tubes that intersect the reflection surface at an oblique angle.

Retaining only the leading order term in ω is equivalent to a far field approximation. Equation (3.17) is therefore closely related to the Fresnel-Kirchhoff diffraction formula of optics [Elmore and Heald, 1969, equation (9.4.16); Goodman, 1968, equation (3.18)]. Hence it would be more appropriate to use the term ‘Fresnel-Kirchhoff-approximate’, but I follow Bleistein (1984, p. 281) and refer to the result as the Kirchhoff approximation.

---

[9] The use of the term ‘obliquity factor’ to refer to the geometry of the incident and reflected wavefields at the reflector is in agreement with the original terminology arising from optics (see Elmore and Heald, 1969, p. 331; Goodman, 1968, p. 42). Kuhn and Alhilali (1977) describe a number of ‘directivity functions’, which they use as synonyms for the ‘obliquity’ or ‘inclination’ factor. Esmersoy and Miller (1989) use the term ‘obliquity factor’ for the geometry at the reflector, as do Bleistein et al. (2001, p. 226). French (1975) uses the term ‘oblique’ in an entirely different context when he refers to a profile taken at an angle to the dip direction of 2-D subsurface structure. Schneider (1978), however, uses the term ‘obliquity factor’ incorrectly when he describes the $\partial r/\partial n = \cos\theta$ factor arising from the Rayleigh II integral with the free-space Green’s function [Goodman, 1968, equation (3-26)]. He confuses this with the obliquity factor of the Rayleigh-Sommerfeld diffraction formula, although the two are closely related [Goodman, 1968, equation (3-27)]. Schneider’s incorrect usage permeates the exploration literature, and should be abandoned. I prefer to use the term ‘receiver directivity’ to describe the $\partial r_g/\partial n = \cos\theta_g$ factor over the surface of receivers, and ‘source directivity’ to describe the $\partial r_s/\partial n = \cos\theta_s$ factor over the surface of sources (if applicable), where r_g and r_s denote the ray directions at the receiver and source, respectively.

3.4.5 A simplified notation for the ray-theoretical Kirchhoff-approximate modeling formula

The ray-theoretical Kirchhoff-approximate modeling formula as given by equation (3.17) should be the starting point for the ray-theoretical Kirchhoff-approximate migration formula to be derived in Section 3.7. However, the direction of the traveltime gradients as given in equation (3.17) is not the convention adopted in the most recent literature. My result agrees with the free-space version presented in Goodman [1968, Figure 3.5 and equation (3-18)], who uses an opposite pointing surface normal and expresses the normal derivatives of the traveltime gradients at the surface as the cosine of the angle between the ray direction and the normal. It also agrees with Figure 2a of Docherty (1991), who develops a surface-scattered wavefield for inverse propagation. However, it does not agree with the modeling formulas of Bleistein et al. [2001, equations (7.2.1) and (7.2.2)] and Jaramillo and Bleistein [1999, equation (2)]. It is not clear how these authors determine the direction of their traveltime gradients, but the convention presented in their equations and accompanying figures leads to a simplified notation for equation (3.17). Strictly speaking, the simplified notation is incorrect, but will be adopted here so that the results presented in this dissertation can be compared with the recent literature of Bleistein and co-workers.

First, notice that the phase in the exponential term in equation (3.17) is expressed as a product of frequency and the sum of traveltimes $\tau_{Rs'} + \tau_{Rg}$, whereas the obliquity factor $\left(\nabla_{\mathbf{x}_R}\tau_0(\mathbf{x}_R, \mathbf{x}_{s'}) \cdot \mathbf{n}_R^+ - \nabla_{\mathbf{x}_R}\tau_0(\mathbf{x}_R, \mathbf{x}_g) \cdot \mathbf{n}_R^+\right)$ is expressed, in a general sense, as a difference of traveltimes. It would be notationally convenient to replace the total traveltime in both expressions with what Jaramillo and Bleistein (1999) call the ‘phase’ $\phi_0 = \tau_{Rs} + \tau_{Rg}$. In the obliquity factor, the traveltime gradient $\nabla\tau_{Rs'}$ points in the upward direction of the specularly reflected ray, and forms an obtuse angle with the downward pointing surface normal $\mathbf{n}_R^+$. If instead we assume that $\nabla\tau_{Rs}$ points in the downward direction of the incident ray (now denoted by subscript Rs), it forms an acute angle with the normal and the dot product is the same magnitude but opposite sign (Figure 3.3a). Now $\nabla\tau_{Rs}\cdot\mathbf{n}_R^+$ and $\nabla\tau_{Rg}\cdot\mathbf{n}_R^+$ are the same sign (see Appendix C for further discussion). An upward pointing surface normal changes the sign of both, and the obliquity factor can be re-expressed as

$$\nabla_{\mathbf{x}_R}\tau_0(\mathbf{x}_R,\mathbf{x}_s)\cdot\mathbf{n}_R^- + \nabla_{\mathbf{x}_R}\tau_0(\mathbf{x}_R,\mathbf{x}_g)\cdot\mathbf{n}_R^- = \nabla_{\mathbf{x}_R}\phi_0(\mathbf{x}_R,\boldsymbol{\xi})\cdot\mathbf{n}_R^- . \tag{3.18}$$

In equation (3.18), it is assumed that the source and receiver are located on the recording surface. The recording surface is parameterized by the 2-D parameter $\boldsymbol{\xi}=(\xi_1,\xi_2)$, so that the source and receiver locations are identified with the 3-D vectors $\mathbf{x}_s(\boldsymbol{\xi})$ and $\mathbf{x}_g(\boldsymbol{\xi})$, respectively. The 'phase' $\phi_0(\mathbf{x}_R,\boldsymbol{\xi})$ represents the total traveltime from source $\mathbf{x}_s$ to reflector point $\mathbf{x}_R$ to receiver $\mathbf{x}_g$, but also retains (by virtue of the readers understanding) the directions of the individual traveltime gradients. Similarly, the product of the WKBJ amplitude factors can be represented using the simplified notation

$$A_{s\times g}(\mathbf{x}_R,\boldsymbol{\xi}) = A_0(\mathbf{x}_R,\mathbf{x}_s)A_0(\mathbf{x}_R,\mathbf{x}_g) . \tag{3.19}$$

Using equations (3.18) and (3.19), the ray-theoretical Kirchhoff-approximate modeling formula [equation (3.17)] can be re-expressed as

$$P_{\Sigma_R}^-(\mathbf{x}_g,\mathbf{x}_s,\omega) \cong i\omega S_\rho(\omega)\int_{\mathbf{x}_R} d\Sigma_R R_\theta(\mathbf{x}_R,\mathbf{x}_s)A_{s\times g}(\mathbf{x}_R,\boldsymbol{\xi})\left(\nabla_{\mathbf{x}_R}\phi_0(\mathbf{x}_R,\boldsymbol{\xi})\cdot\mathbf{n}_R^-\right)e^{i\omega\phi_0(\mathbf{x}_R,\boldsymbol{\xi})} . \tag{3.20}$$

Equation (3.20) is essentially equation (2) of Jaramillo and Bleistein (1999), with some minor differences in notation. The physical interpretation is as follows. The upgoing wavefield $P_{\Sigma_R}^-(\mathbf{x}_g,\mathbf{x}_s,\omega)$ at observation (receiver) location $\mathbf{x}_g$ originates as a downgoing wavefield from point source location $\mathbf{x}_s$ and is scattered at location $\mathbf{x}_R$ from reflector surface Σ_R with upward pointing normal $\mathbf{n}_R^-$. The upgoing wavefield is expressed as an integral over the reflection surface of WKBJ-approximate wavefields. The amplitude (geometric spreading) is given by $A_{s\times g}(\mathbf{x}_R,\boldsymbol{\xi})$—the product of WKBJ amplitudes from source to reflector and reflector to receiver—and is modified by the angle-dependent reflection coefficient $R_\theta(\mathbf{x}_R, \mathbf{x}_s)$, the obliquity factor $\nabla_{\mathbf{x}_R}\phi_\tau(\mathbf{x}_R, \xi) \cdot \mathbf{n}_R^-$, the source signature $S_\rho(\omega)$, and the time derivative (-$i\omega$). The phase is given by $\phi_\tau(\mathbf{x}_R, \xi)$, the sum of the traveltimes.

The integrand in equation (3.20) consists of two fundamentally different parts, a weighting function that is the product of the reflection coefficient, the WKBJ amplitudes, and the obliquity factor; and a 'phase function' given by the term $e^{i\omega\phi(\mathbf{x}_R, \xi)}$. The main contribution to the integral over the reflector surface occurs when the phase function is stationary. Intuitively, the geometry for stationary phase occurs when the angle of incidence is equal to the angle of reflection, i.e. at the specular angle of reflection. Bleistein (1999) provides an excellent conceptual overview of the method of stationary phase applied to migration and inversion. A more rigorous mathematical discussion can be found in Bleistein (1984, p. 77-89). Application of the method of stationary phase will prove to be an important simplification in the development of practical expressions for inverse propagation and imaging, as we shall see shortly.

The reader may have noticed that the earlier reference to Berkhout and Wapenaar (1989) and Wapenaar et al. (1989) requires a planar surface to justify ignoring both the acoustic and forward propagating Green's wavefields traveling in the same direction across a surface. Wapenaar (1993a) proposes a method that allows robust downward extrapolation of primary upgoing waves measured on a non-planar interface, but states that the method is not suitable for modeling applications. In fact, the use of the KHIR [equation (3.1)] as a valid acoustic representation theorem for one-way wavefields is questioned by Wapenaar and Grimbergen (1996) and Wapenaar (1996), who propose instead one-way reciprocity and representation theorems. Simplification of the problem by decomposition into one-way wavefields is not the only practical method. Docherty (1991) invokes stationary phase to justify ignoring the wavefield combinations appropriate for forward extrapolation. Docherty's discussion is well illustrated with figures and will not be repeated here. However, given the approximations discussed so far (in particular that multiple reflections and transmission effects are ignored) and keeping in mind the intended use of the expressions for time migration (which has its own long list of approximations) the analysis presented in this section is substantially correct for a nonplanar surface

3.5 REFORMULATING THE GENERALIZED KHIR FOR INVERSE WAVEFIELD PROPAGATION

I now develop an inverse wavefield propagation formula by inserting a superposition of appropriate acoustic wavefields and one-way inverse propagating Green's functions into the generalized KHIR [equation (3.3)]. The result will be similar to the Kirchhoff-Helmholtz integral [equation (2.48)]. In this case, however, an approximate expression is developed for generalized media using principles of superposition and one-way wavefields.

As discussed previously, we need to consider only acoustic wavefields propagating in the opposite direction to the Green's function. The one-way inverse propagating Green's functions $\overleftarrow{G}_0(\mathbf{x},\mathbf{x}_G,\omega)$ can be decomposed into a downgoing Green's wavefield $\overleftarrow{G}_0^{+}(\mathbf{x}_1,\mathbf{x}_G,\omega)$ on the upper surface and an upgoing Green's wavefield $\overleftarrow{G}_0^{-}(\mathbf{x}_2,\mathbf{x}_G,\omega)$ on the lower surface. Therefore, only the upgoing acoustic wavefield on the upper surface, as given by equation (3.5), and the downgoing acoustic wavefield on the lower surface, as given by equation (3.7), contribute to the surface-scattered wavefields in equation (3.3). This produces seven surface-scattered wavefields (two of which are infinite summations).

3.5.1 Upper surface non-reflective after removal of free-surface multiples

Typically, seismic data are recorded only on the upper surface. Hence, we require an expression for inverse propagation that does not require a surface-scattered wavefield recorded on the lower surface. As shown by equation (3.7), the downgoing wavefield at the lower surface is a superposition of the downgoing incident wavefield and the reflection across the upper surface of all upgoing primary-scattered wavefields. If the upper surface is a free surface (reflection coefficient = -1), these multiply reflected wavefields will be similar in amplitude to the upgoing primary wavefield. Removal of the free-surface multiples is an important preprocessing step (Verschuur et al., 1992; or, for additional references, Wapenaar, 1996). Assuming free-surface multiples have been removed, the contribution from the downgoing scattered-wavefield on the lower surface can be ignored. However, the downgoing incident wavefield on the lower surface cannot be ignored, and equation (3.7) reduces to

$$P_t^+(\mathbf{x}_2,\mathbf{x}_s,\omega) = P_i^+(\mathbf{x}_2,\mathbf{x}_s,\omega). \tag{3.21}$$

Both the incident and surface-scattered wavefield from the upper surface are relevant. In anticipation of the upper surface representing the surface of receivers or geophones, denoted by locations $\mathbf{x}_g$, equation (3.5) can be re-expressed as

$$P_t^-(\mathbf{x}_g,\mathbf{x}_s,\omega) = P_i^-(\mathbf{x}_g,\mathbf{x}_s,\omega) + P_{S_2}^-(\mathbf{x}_g,\mathbf{x}_{s'},\omega) + \sum_{k=3}^{\infty} P_{S_k}^-(\mathbf{x}_g,\mathbf{x}_{s'},\omega). \tag{3.22}$$

It is interesting to note that the terms on the RHS of equation (3.5) [re-expressed as equation (3.22)] are the same amplitude but opposite in sign to the corresponding terms on the RHS of equation (3.6). Their sum, as given by equation (3.4), equals zero, i.e. the total acoustic pressure recorded on a free surface is zero. On the other hand, the normal derivative of the total acoustic pressure is double the normal derivative of either the upgoing or downgoing component (the image source is opposite in sign), so the surface-scattered integrals in equation (3.3) are non-zero. This introduces complications that are beyond the scope of this dissertation (see Hanitzsch, 1995). Instead, it is assumed that the preprocessing that removes the free-surface multiples converts the free surface into a non-reflecting surface, where only the upgoing wavefields need to be considered.

3.5.2 Justification for muting the incident wavefield

Substituting equations (3.21) and (3.22) and appropriate one-way Green's functions into the surface-scattered wavefields of equation (3.3) yields

$$
\begin{aligned}
P_t(\mathbf{x}_G,\mathbf{x}_s,\omega) &\cong P_i(\mathbf{x}_G,\mathbf{x}_s,\omega) + P_{S_g}^-(\mathbf{x}_G,\mathbf{x}_s,\omega) + P_{S_2}^-(\mathbf{x}_G,\mathbf{x}_s,\omega) \\
&\cong S_\rho(\omega)\overleftarrow{G}_0(\mathbf{x}_s,\mathbf{x}_G,\omega) \\
&\quad + \int_{\mathbf{x}_g} dS \Bigg\{ \overleftarrow{G}_0^+(\mathbf{x}_g,\mathbf{x}_G,\omega)\nabla_{\mathbf{x}_g}\left(P_{S_2}^-(\mathbf{x}_g,\mathbf{x}_{s'},\omega) + \sum_{k=3}^{\infty} P_{S_k}^-(\mathbf{x}_g,\mathbf{x}_{s'},\omega)\right), \\
&\qquad - \left(P_{S_2}^-(\mathbf{x}_g,\mathbf{x}_{s'},\omega) + \sum_{k=3}^{\infty} P_{S_k}^-(\mathbf{x}_g,\mathbf{x}_{s'},\omega)\right)\nabla_{\mathbf{x}_g}\overleftarrow{G}_0^+(\mathbf{x}_g,\mathbf{x}_G,\omega)\Bigg\}\cdot\mathbf{n}_g^- \\
&\quad + \int_{\mathbf{x}_g} dS \left\{ \overleftarrow{G}_0^+(\mathbf{x}_g,\mathbf{x}_G,\omega)\nabla_{\mathbf{x}_g} P_i^-(\mathbf{x}_g,\mathbf{x}_s,\omega) - P_i^-(\mathbf{x}_g,\mathbf{x}_s,\omega)\nabla_{\mathbf{x}_g}\overleftarrow{G}_0^+(\mathbf{x}_g,\mathbf{x}_G,\omega)\right\}\mathbf{n}_g^- \\
&\quad + \int_{\mathbf{x}_2} dS \left\{ \overleftarrow{G}_0^-(\mathbf{x}_2,\mathbf{x}_G,\omega)\nabla_{\mathbf{x}_2} P_i^+(\mathbf{x}_2,\mathbf{x}_s,\omega) - P_i^+(\mathbf{x}_2,\mathbf{x}_s,\omega)\nabla_{\mathbf{x}_2}\overleftarrow{G}_0^-(\mathbf{x}_2,\mathbf{x}_G,\omega)\right\}\mathbf{n}_2^+,
\end{aligned}
\tag{3.23}
$$

where $\mathbf{n}_g^-$ denotes the upward pointing normal on the upper surface S_g and $\mathbf{n}_2^+$ denotes the downward pointing normal on the lower surface S_2.

In equation (3.23), the incident wavefield $P_i(\mathbf{x}_G,\mathbf{x}_s,\omega)$ appears to be described twice, first by the term $S_\rho(\omega)\overleftarrow{G}_0(\mathbf{x}_s,\mathbf{x}_G,\omega)$ (i.e. the source function times the generalized one-way inverse propagating Green's function) and second by the scattered wavefield over the "enclosing" surface (i.e. the combined effect of the second and third surface integrals). Fortunately, the first description of the incident wavefield is zero for a causal source and anticausal Green's function[10]. The argument justifying this conclusion is similar to one presented previously in Section 2.6.2 (see Figure 2.5) and will not be developed here. The result is that the incident wavefield at location $\mathbf{x}_G$ is reconstructed by inverse wavefield propagation from surface scattered wavefields recorded on both the upper and lower surfaces. Given the assumption that the wavefield on the lower surface has not been recorded, a correct reconstruction of the incident wavefield is (in general) not possible. The solution is to ignore the incident wavefield in equation (3.23) by subtracting it from the total wavefield, leaving only the scattered wavefield from the reflectors. Practically, this is accomplished by muting the incident wavefield.

3.5.3 The Kirchhoff-Helmholtz integral restricted to one-way wavefields and Green's functions

Equation (3.23) can be further simplified by introducing the notation $P_S^-(\mathbf{x}_g, \mathbf{x}_{s'}, \omega)$ to indicate the sum of upgoing surface-scattered wavefields. After subtracting the incident wavefield terms and incorporating the change of notation, equation (3.23) becomes

$$P_S^-(\mathbf{x}_G, \mathbf{x}_s, \omega) = \int_{\mathbf{x}_g} dS_g \Big\{ \overleftarrow{G}_0^+(\mathbf{x}_g, \mathbf{x}_G, \omega) \nabla_{\mathbf{x}_g} P_S^-(\mathbf{x}_g, \mathbf{x}_{s'}, \omega) - P_S^-(\mathbf{x}_g, \mathbf{x}_{s'}, \omega) \nabla_{\mathbf{x}_g} \overleftarrow{G}_0^+(\mathbf{x}_g, \mathbf{x}_G, \omega) \Big\} \mathbf{n}_g^- . \tag{3.24}$$

Thus, the upgoing surface-scattered wavefield $P_S^-(\mathbf{x}_G, \mathbf{x}_s, \omega)$ can, in principle, be reconstructed at any location $\mathbf{x}_G$ in the subsurface by inverse extrapolation of the wavefield recorded on the upper surface. Equation (3.24) is just the Kirchhoff-Helmholtz

---

[10] One could argue that the incident wave is nonzero for an anticausal source and anticausal Green's function, although this application does not have much practical value (Tygel and Hubral, 1987 for an alternate perspective).

integral (equation 2.65) restricted to one-way wavefields and Green's functions. The discussion presented in Section 2.8.2 applies here as well, given that internal multiply reflected waves and evanescent waves are ignored and only the transmitted portion of the wavefield is considered.

Note that equation (3.24) provides no information about the location of any of the reflectors, and that the wavefield is assumed to be upgoing everywhere. Hence, equation (3.24) will inverse extrapolate the wavefield from a given reflector through the reflector location back to the image source locations $\mathbf{x}_{s'}$ beneath the reflector (and further into negative time—see Esmersoy and Oristaglio, 1988, Figure 2). The 'over-extrapolated' wavefield may or may not reconstruct coherently depending on the complexity of the reflector surface and the macro subsurface wavespeed model. The obvious conclusion, then, is that substitution of an inverse propagating Green's function into the KHIR does not produce a prestack imaging formula. Something else is needed if we wish to image reflectors in the subsurface. The intuitive approach is to incorporate an 'imaging condition' with desired output being a map of the reflectivity in the subsurface. But on what basis is an appropriate imaging condition selected? This question will be addressed in the next section.

3.6 IMAGING CONDITIONS FOR MIGRATION/INVERSION OF COMMON-SHOT GATHERS

An imaging condition can be thought of as a prescription for creating a reflector map. The reflector map has two key elements: estimates of the 'strength' or amplitude of the reflection coefficients, and estimates of the location of the reflectors in either depth or time. In Sections 3.4 and 3.5, the forward modeling formula used the angle-dependent reflection coefficient $R_\theta(\mathbf{x}_R, \mathbf{x}_s)$ as a known input to determine the output modeled data. Imaging, on the other hand, is an inverse procedure that uses the inverse extrapolated recorded data (among other parameters) as input to model the output reflector map. Thus it is entirely conceivable that the imaging condition provides multiple estimates at a given location, i.e. the estimated amplitude could depend on angle of incidence, frequency, or some other parameter. Here, I restrict the model of the unknown underlying physical process (reflectivity) to a dependence on angle only[11]. Estimates at each frequency, however, will vary due to uncertainty introduced by noise and model misfit errors[12]. What is required is a method for obtaining a good estimate of the angle-dependent reflectivity from the estimates at each frequency.

3.6.1 A statistical 'best-fit' approach to the imaging condition

A simple approach to inversion is fitting a model to data, where the estimates of the parameters in the model are constrained by a 'best-fit' criterion. A classic example is least squares fit of a line $y = \hat{a} + \hat{b}x$ to a collection of data points (x_i, y_i). In this case, the range of the data points are themselves estimates (perhaps from an ensemble of possible inputs) and the intercept $\hat{a}$ and slope $\hat{b}$ are the required estimates of the model parameters. In fact, the imaging condition is a subset of this exact problem. The data points are estimates of the angle-dependent reflectivity at a fixed angle as a function of frequency, i.e. $\left(\omega, \hat{R}_\theta(\omega)\right)$. We desire a robust average over frequency, which is simply

---

[11] Bleistein (1984; 1986) derives the angle-dependent geometric optics reflection coefficient by selecting a ray-theoretical causal Green's function and assuming two boundary conditions known as the Kirchhoff approximation. The boundary conditions assume that the wavefield and its normal derivative are continuous across the reflecting boundary.

[12] The simplest approach, and the one taken here, is to assume that estimators remain independent. A more complete study would investigate the correlated structure between estimators. The use of zero padding and the fast Fourier transform almost guarantees that adjacent estimators (in frequency) are correlated.

the best fit of a line constrained to zero slope. The key is to determine the optimum criterion to constrain the 'best-fit'.

Each reflectivity estimate $\hat{R}_{\theta}(\omega)$ can be thought of as arising from an ensemble of possible reflectivities. Imagine that the underlying data set is a number of seismic shot records collected for a fixed shot location. For a given subsurface location, then, the angle of incidence is fixed. Thus the estimate of reflectivity at each frequency is a sample from a distribution of possible values about the unknown true reflectivity. All in all, it is unlikely that this distribution behaves as nicely as we would like. A normal or Gaussian distribution is ideal, mainly because L1 and L2 norms produce unbiased estimates of the unknown true value. In most cases, however, the Gaussian assumption is not justified and estimates based on either norm are biased. Biased estimates can arise from outliers to a distribution that can otherwise be described as Gaussian, or from a well-behaved distribution that is just not Gaussian—and there are plenty of these. Iterative robust estimators are the best approach to tackling the first problem (see Press et al., 1992), but the second problem is more insidious. For some non-Gaussian distributions, L1 and L2 estimators are biased even if outliers are eliminated.

Some of the simplest examples of biased estimators are those that assume a Gaussian distribution of a noise process associated with some signal, and then effect a transformation to the signal that must, of course, transform the noise distribution. The resulting distribution may not be Gaussian. The reflectivity estimator is one such example. In short, it can be thought of as a gain estimator defined as the ratio of two amplitude estimators. If we assume that the underlying noise model in the recorded data is distributed as Gaussian, neither the amplitude nor the gain estimators end up as a Gaussian distribution. The conventional approach is to use a standard best-fit criterion, such as least squares (L2 norm), but then down weight the estimates that might be expected to have the largest bias, i.e. a weighted least squares fit where the weighting function is primarily designed to reduce bias. This will be the approach taken here. As we shall see, the optimum weighting function turns out to be the signal-to-noise ratio.

In physics, the conventional approach is to base the design of the model on the underlying physical principles. Because of inherent assumptions and approximations, the model will not incorporate the true complexity of the physical process that generated the data. Thus there will be a component of misfit in addition to any noise. The combination of these influences can be thought of as error. However, the two cannot easily be separated. The presence of a systematic misfit is often taken as evidence that the underlying model is insufficient, but the discussion in the previous paragraph suggests that bias (systematic error) can result from the underlying noise. To further complicate matters, the true nature of the underlying noise is unknown. Hence we have to assume a noise model. All of these considerations suggest an approach rooted in statistics, where the objective is to design an estimator that is optimum in some sense. As we shall see, the reflectivity estimate chosen here will be optimum in a chi-squared sense. The end result is that the application of an imaging condition provides no guarantee that a 'true' reflection coefficient is being estimated. In fact, most imaging conditions are based on physical intuition tempered by practicality, as opposed to rigorous application of theory[13]. In this section, I combine intuition with statistics to come up with an optimum estimate of the reflectivity map.

---

[13] Esmersoy and Oristaglio (1988) provide a good discussion on this point, and compares the objectives of imaging (migration) vs. inversion. See also Miller et al. (1987) and Gazdag and Sguazzero (1984).

3.6.2 Claerbout's imaging conditions from the Kirchhoff approximation

Claerbout (1971) provides the following fundamental principle for creating a reflector map in depth: *reflectors exist at points in the ground where the first arrival of the downgoing wave is time coincident with an upgoing wave*. Chang and McMechan (1986) call this principle the 'time-coincidence' imaging condition. By itself, it is incomplete, as it provides a method for determining the correct phase for a given subsurface location but not the amplitude of the reflectivity coefficient. Claerbout goes on to define the amplitude as the ratio of the upgoing and downgoing wavefields at the subsurface location $\mathbf{x}_G$ (which may or may not be located on a reflector). Claerbout's time-coincidence imaging condition, combined with the amplitude definition, can be thought of as a reformulation of the Kirchhoff approximation [equation (3.10)], re-expressed here for monochromatic wavefields as

$$R_\theta(\mathbf{x}_R, \mathbf{x}_s) \cong \frac{P^-_{\Sigma_R}(\mathbf{x}_R, \mathbf{x}_{s'}, \omega)}{P^-_i(\mathbf{x}_R, \mathbf{x}_{s'}, \omega)}. \tag{3.25}$$

Equation (3.25) suggests the physically intuitive concept that the reflection coefficient is the ratio of the incident and reflected wavefields. In Sections 3.4 and 3.5, this concept justified the amplitude of the reflected wavefield $P^-_{\Sigma_R}(\mathbf{x}_R, \mathbf{x}_{s'}, \omega)$ given a known incident wavefield $P^-_i(\mathbf{x}_R, \mathbf{x}_{s'}, \omega)$ and reflectivity coefficient $R_\theta(\mathbf{x}_R, \mathbf{x}_s)$.

Now, we assume that the incident and reflected wavefields are known and can be used to determine the reflectivity coefficient. The location in the subsurface may or may not be on a reflector, so we replace the reflector location $\mathbf{x}_R$ with the imaging location $\mathbf{x}_G$. The correct direction for the traveltime gradients at the imaging location $\mathbf{x}_G$ can be inferred from the direction of the wavefield, so we replace the image source location $\mathbf{x}_{s'}$ with the source location $\mathbf{x}_s$. The upgoing wavefield $P^-_{\Sigma_R}(\mathbf{x}_R, \mathbf{x}_{s'}, \omega)$ scattered by the reflector is then replaced with the upgoing wavefield $P^-_S(\mathbf{x}_G, \mathbf{x}_s, \omega)$ inverse extrapolated from the receiver surface [equation (3.24)]. We will not require any gradients of the traveltime for the incident wavefield, and so can replace the upgoing incident wavefield $P_i^-(\mathbf{x}_R, \mathbf{x}_{s'}, \omega)$ from the image source with a more intuitive downgoing incident wavefield $P_i^+(\mathbf{x}_G, \mathbf{x}_s, \omega)$ forward extrapolated from the source. With these substitutions, equation (3.25) becomes the definition of the angle-dependent reflectivity estimate at frequency ω, as given by

$$\hat{R}_\theta(\mathbf{x}_G, \mathbf{x}_s, \omega) \equiv \frac{P_S^-(\mathbf{x}_G, \mathbf{x}_s, \omega)}{P_i^+(\mathbf{x}_G, \mathbf{x}_s, \omega)} . \tag{3.26}$$

Fundamentally, equation (3.26) describes inversion, whereas equation (3.25) is just a reformulation of a forward modeling equation. The raised hat indicates that the reflectivity coefficient $\hat{R}_\theta(\mathbf{x}_G, \mathbf{x}_s, \omega)$ is now an estimate. For equation (3.26) to be meaningful, the inverse extrapolated wavefield $P_S^-(\mathbf{x}_G, \mathbf{x}_s, \omega)$ must reconstruct the specularly reflected wavefront. This implies that the specular ray direction is determined where the phase of the extrapolated wavefield is stationary, an observation that will prove useful in the next section. In addition, however, we desire that equation (3.26) correctly images the truncation of reflector surfaces from diffracted wavefields, and creates no image (i.e. destructive interference) where no reflector exists.

Under ideal conditions (i.e. no noise), integrating equation (3.26) over all frequencies produces a reflectivity 'map' that estimates true-amplitude reflectivity:

$$\hat{R}_\theta(\mathbf{x}_G, \mathbf{x}_s) \equiv \frac{1}{2\pi} \int_{-\infty}^{\infty} d\omega \frac{P_S^-(\mathbf{x}_G, \mathbf{x}_s, \omega)}{P_i^+(\mathbf{x}_G, \mathbf{x}_s, \omega)} . \tag{3.27}$$

Equation (3.27) is known as the deconvolution imaging condition [see Claerbout, 1971, equation (3); Esmersoy and Oristaglio, 1988, equation (15)]. As we shall discover below, the deconvolution imaging condition can be interpreted as a least squares estimate of a constant reflectivity coefficient $\hat{R}_\theta(\mathbf{x}_G, \mathbf{x}_s)$ given estimates of frequency-variable reflectivity $\hat{R}_\theta(\mathbf{x}_G, \mathbf{x}_s, \omega)$ (from equation 3.26). Least squares fitting is a maximum likelihood estimation of $\hat{R}_\theta(\mathbf{x}_G, \mathbf{x}_s)$ if the error in the estimates $\hat{R}_\theta(\mathbf{x}_G, \mathbf{x}_s, \omega)$ are independent and normally distributed with constant standard deviation. Unfortunately, such well-behaved error distributions are unlikely. As an aside, the limits on the integral over frequency in will be assumed to range from -∞ to +∞ unless specified otherwise.

Claerbout suggests that equation (3.27) be reformulated to account for noise and to avoid large errors introduced when dividing by small values of the incident wavefield $P_i^+(\mathbf{x}_G, \mathbf{x}_s, \omega)$. The integrand in equation (3.27) is multiplied and divided by the complex conjugate of the incident wavefield, which preserves the phase of the original expression. The denominator is then the spectral density $P_i^+(P_i^+)^*$ of the incident wavefield. The spectral density is real, has no phase information, and can be omitted[14], yielding

$$\hat{R}_\theta(\mathbf{x}_G, \mathbf{x}_s) \equiv \frac{1}{2\pi} \int d\omega P_S^-(\mathbf{x}_G, \mathbf{x}_s, \omega) \left(P_i^+(\mathbf{x}_G, \mathbf{x}_s, \omega)\right)^* . \tag{3.28}$$

Equation (3.28) is known as the crosscorrelation imaging condition (Lumley, 1989). The reflectivity map given by equation (3.28) is robust, because the amplitude of the reflectivity map drops off rapidly in any region where either the downgoing incident wavefield is weak or the upgoing inverse-extrapolated wavefield is weak. However, the reflectivity coefficient is no longer true-amplitude, as it now contains a slowly varying component proportional to the geometric spreading squared.

3.6.3 Towards an optimal chi-squared estimate of reflectivity

Claerbout points out that other imaging conditions can be designed as a compromise between equations (3.27) and (3.28), and mentions in passing that optimization could clearly lead to an involved discussion. As stated previously, the imaging condition I

---

[14] Replacing $R = P_S/P_i$ by $R = P_S P_i^*$ is related to matched filtering (Claerbout, 1992, p. 86).

propose below is optimum in a chi-squared sense. The discussion that fully justifies the choice is involved, but the end result turns out to be similar to Claerbout's deconvolution imaging condition (equation 3.27). I give the result first so that we know what we are aiming for:

$$\hat{R}_\theta(\mathbf{x}_G,\mathbf{x}_s) \equiv \frac{1}{2\pi}\int d\omega \hat{F}(\omega)\frac{P_S^-(\mathbf{x}_G,\mathbf{x}_s,\omega)}{\vec{G}_0^+(\mathbf{x}_G,\mathbf{x}_s,\omega)}. \tag{3.29}$$

Equation (3.29) is equation (14) of Docherty (1991). Docherty states that $\hat{F}(\omega)$ "is a filter which emphasizes the bandlimited nature" of the inverse extrapolated wavefield $P_S^-(\mathbf{x}_G,\mathbf{x}_s,\omega)$. In this section, $\hat{F}(\omega)$ is shown to be the optimum weighting function given a reasonable assumed error model so that equation (3.29) provides a chi-squared estimate of the frequency-independent, angle-dependent reflection coefficient. The derivation of equation (3.29) appeals to physical and mathematical intuition. The end result, however, is designed to agree with results obtained from linearized inverse approaches (based on the Kirchhoff-approximate forward model—equation 3.10), which are known to give a 'correct' result. An intuitive discussion is presented because inverse approaches are much more difficult to understand.

Essentially, we desire robust estimates[15] of the absolute value of the angle-dependent reflectivity coefficient, i.e. the output should be 'true-amplitude'[16]. However, given that

---

[15] See Press et al. (1992, p. 699) for a definition of a robust estimator as "insensitive to small departures from the idealized assumptions for which the estimator is optimized". The word "small" can have two different interpretations: either fractionally small departures for all data points, or else fractionally large departures for a small number of data points. The chi-squared estimator presented in this section is robust in the context of the former interpretation. An intuitive adjustment of the weighting function in the estimator provides qualitative protection from the later, but not the quantitative protection expected of truly 'robust' estimators.

the input data arise from a band-limited source, the 'true-amplitude' value need only correspond to the peak value of a band-limited singular function of the surface (Bleistein, 1987). The absolute location of the peak value in relation to the unknown true reflector is less of a concern, as this will depend on the accuracy of the macro wavespeed model. Good focusing and high resolution, although desirable, cannot be guaranteed by choice of imaging condition alone. I conclude that it is sufficient that the phase correspond to Claerbout's 'time-coincident' principle.

I begin with equation (3.26), which provides estimates of the angle-dependent reflectivity coefficient $\hat{R}_\theta(\omega)$ at each frequency (the dependence on location is implied in the simplified notation). In the high-frequency limit (see Section 2.4), amplitude and traveltime are independent of frequency. Hence the desired reflectivity coefficient is assumed to be independent of frequency. The problem becomes one of estimating an optimum constant reflectivity coefficient $\hat{R}_\theta$, which is equivalent to estimating a constant gain of a linear, time invariant, single-input, single-output system with noise on output, otherwise known as the error-in-equations model (Geiger, 1989, p. 58-59).

The optimization problem can be solved by minimizing the chi-squared merit function

$$\chi^2\left(\hat{R}_\theta\right) = \frac{1}{2\pi}\int d\omega \left\{\frac{\hat{R}_\theta(\omega) - \hat{R}_\theta}{\sigma(\omega)}\right\}^2, \tag{3.30}$$

where $\sigma^2(\omega)$ is the frequency-variable variance of the frequency-variable reflectivity estimates $\hat{R}_\theta(\omega)$. At the minimum, $\partial\chi^2(\hat{R}_\theta)/\partial\hat{R}_\theta = 0$, yielding

[16] The word "true" is a bit misleading, because it is not possible to estimate the bias in the estimated reflection coefficient amplitude. The amplitude could be a very good fit to the data, but not true.

$$\hat{R}_\theta = \frac{\frac{1}{2\pi}\int d\omega \, \hat{R}_\theta(\omega) \Big/ \sigma^2(\omega)}{\frac{1}{2\pi}\int d\omega \, 1 \Big/ \sigma^2(\omega)} . \tag{3.31}$$

Equation (3.31) gives the optimum estimate of a constant value for the angle-dependent reflectivity from frequency-variable estimates of the same. Note that $\sigma^2(\omega)$ are not the variances of the underlying noise process. Earlier in this section, it was pointed out that the error accommodates both noise and misfit. Instead, then, the variances $\sigma^2(\omega)$ can be thought of as one of the statistical parameters describing the error distributions of $\hat{R}_\theta(\omega)$ at each frequency (and should be thought of as estimates in their own right).

3.6.4 Normalized variances estimated by the inverse of the signal-to-noise ratio

Variance is a complete description of an error distribution only if the errors are normally distributed with zero mean. Fortunately, variance can be a sufficient description for many distributions that are not normal, although in many cases (including this one) the error distributions are known to be biased. Hence the resulting chi-squared estimate of $\hat{R}_\theta$ will be biased, independent of the goodness-of-fit. Our best hope is that the bias in the final estimate is small, suggesting either that biases in the underlying estimates $\hat{R}_\theta(\omega)$ are small or that heavily biased estimates can be removed or downweighted in the optimization. Below, I suggest reasonable conditions under which $\hat{R}_\theta(\omega)$ can be considered as normally distributed, and later suggest a more robust weighting function to accommodate frequency bands over which the error distributions might be heavily biased.

Note that absolute values of the variances are not required. The denominator in equation (3.31) acts as a normalization function. To show this, replace the variances $\sigma^2(\omega)$ with a normalized variance $\sigma_N^2(\omega)$ such that $\sigma^2(\omega) = \sigma_N^2(\omega)/N$, where N is any constant. After the substitution, the constant appears in both the denominator and numerator, can be taken outside the integrals, and cancels. Therefore, an equivalent expression to equation (3.31) is

$$\hat{R}_\theta = \frac{\frac{1}{2\pi}\int d\omega \, \hat{R}_\theta(\omega) \big/ \sigma_N^2(\omega)}{\frac{1}{2\pi}\int d\omega \, 1 \big/ \sigma_N^2(\omega)} . \tag{3.32}$$

Hence all that is required is a reasonable estimate of the normalized variances.

There are two general methods for estimating variance, the misfit-error approach and the data-error approach (Geiger, 1989, p. 13). The first method lumps data error into the residual term that arises from the misfit between the measured quantities and the predicted quantities in the model fitting process (the estimation of $\hat{R}_\theta$). The second method is to determine error sources in data acquisition and processing, measure or estimate their effect, and then calculate an assumed error level for the desired parameter estimates. Robust misfit-error approaches apply data-adaptive methods such as iterative re-weighting. These are outside the scope of the work presented in this dissertation, but might be considered if a more robust estimate of the reflectivity coefficient is required. The data-error approach is adopted here because it is more intuitive, and therefore in keeping with the original goals of this section.

I make the assumption that the noise in the recorded seismic data can be described as independent, identically distributed (iid) Gaussian random errors. Even if the unknown true noise at the receivers differs from iid Gaussian, the output noise in the real and imaginary components of the Fourier coefficients after Fourier transformation and inverse wavefield propagation[17] will tend to iid Gaussian by the central limit theorem

---

[17] Obviously, there is an implied assumption that the inverse wavefield extrapolation is doing a “good” job. Poor focusing and low resolution will introduce substantial bias into the estimator, independent of noise.

(Press et al., 1992, p. 658). By expressing the inverse extrapolated wavefield $P_S^-(\mathbf{x}_G,\mathbf{x}_s,\omega)$ as amplitude and phase, the noise distribution is transformed into functions of squared Gaussian variables. The variance of the noise (the noise power) can still be considered constant with frequency, even if the distribution is no longer Gaussian.

Effectively, the gain estimator $\hat{R}_\theta(\omega)$ is a ratio of amplitudes. The frequency-variable gain estimators are distributed as doubly non-central F, a distribution that (fortunately) is well approximated by a Gaussian distribution when the non-centrality is large (Johnson and Kotz, 1970). However, the variance of the gain is now a function of the frequency-variable signal-to-noise ratio [denoted as snr(ω)], with the variance small when the signal-to-noise ratio is large. In addition, the estimator bias will be small when the signal-to noise ratio is large. Thus the assumed noise model suggests that the inverse of the signal-to-noise ratio is a reasonable estimate of normalized variances $\sigma_N^2(\omega)$.

By assuming that frequency-variable variance is proportional to the inverse of the signal-to-noise ratio, i.e. $\sigma_N^2(\omega)=1/\mathrm{snr}(\omega)$, equation (3.32) can be re-expressed as

$$\hat{R}_C=\frac{\frac{1}{2\pi}\int d\omega\,\mathrm{snr}(\omega)\hat{R}(\omega)}{\frac{1}{2\pi}\int d\omega\,\mathrm{snr}(\omega)} \tag{3.33}$$

The denominator of equation (3.33) can be thought of as a normalization function. For example, if the variance is constant with frequency, equation (3.33) reduces to Claerbout’s deconvolution imaging condition [equation (3.27)]. Thus, the deconvolution imaging condition is the optimum least-squares estimator of the reflectivity coefficient, with the assumption that the signal-to-noise ratio is constant with frequency. If the signal-to-noise ratio is frequency-variable, equation (3.33) is the optimum weighted least squares estimator. The latter is a more likely scenario for band-limited seismic data.

3.6.5 An optimum weighting function for zero-phase deconvolved data

I now assume that the noise level is constant with frequency. Hence, the signal-to-noise ratio is just the signal power as given by the source amplitude squared, and equation (3.33) yields

$$\hat{R}_C = \frac{\frac{1}{2\pi}\int d\omega \left|S_\rho(\omega)\right|^2 \hat{R}(\omega)}{\frac{1}{2\pi}\int d\omega \left|S_\rho(\omega)\right|^2}. \tag{3.34}$$

Unfortunately, the signal power is not a good estimator of the signal-to-noise ratio for seismic data that has been deconvolved prior to migration. The signal-to-noise ratio will be significantly reduced at frequencies where the spectrum has been whitened. To account for this, I propose introducing a function $\hat{F}(\omega)$ such that $\hat{F}(\omega)\left|S_\rho(\omega)\right|$ is a good estimator of the unknown signal-to-noise ratio prior to invoking the imaging condition. Thus, the estimated signal-to-noise ratio should account for all processing steps, including zero-phase deconvolution and inverse wavefield propagation[18]. The source amplitude $\left|S_\rho(\omega)\right|$ has been retained to effect a favorable cancellation, as we shall discover below. If, in addition, $\hat{F}(\omega)$ is normalized such that

$$\frac{1}{2\pi}\int d\omega \hat{F}(\omega)\left|S_\rho(\omega)\right| = 1, \tag{3.35}$$

we can abandon equation (3.34), and re-express equation (3.33) as

---

[18] One possibility is to use a data-derived model for the spatial- and frequency-dependent signal-to-noise ratio. A practical method could be based on seismic signal estimation using *f-x* spectra (Margrave and Yao, 1999), where the seismic signal is the inverse propagated wavefield at the time-coincident imaging condition. This suggests that the optimum filter is a function of the spatial position of both the output point and the shot, i.e. $F(\mathbf{x}_G,\mathbf{x}_s,\omega)$.

$$\hat{R}_\theta = \frac{1}{2\pi}\int d\omega \hat{F}(\omega)\left|S_\rho(\omega)\right|\hat{R}_\theta(\omega). \tag{3.36}$$

Equation (3.36) is the optimum weighted least squares estimate of the frequency-independent reflection coefficient $\hat{R}_\theta$. Equation (3.35) ensures that the weighting function $\hat{F}(\omega)\left|S_\rho(\omega)\right|$ is normalized and suggests the correct physical units (given the number of spatial dimensions) such that the reflection coefficient is dimensionless. Docherty (1991) loosely specified that $\hat{F}(\omega)$ be a filter which 'emphasizes the bandlimited nature of (the inverse propagated wavefield)'. We now have a more quantitative criterion to interpret Docherty's use of the word 'emphasizes', but still retain much flexibility in the choice of the weighting function.

Now substitute for $\hat{R}_\theta(\omega)$ in equation (3.36) using equation (3.26), and re-express the incident wavefield $P_i^+(\mathbf{x}_\Sigma, \mathbf{x}_s, \omega)$ as $S_\rho(\omega)\vec{G}_0^+(\mathbf{x}_G, \mathbf{x}_s, \omega)$, yielding

$$\hat{R}_\theta(\mathbf{x}_G, \mathbf{x}_s) = \frac{1}{2\pi}\int d\omega \hat{F}(\omega)\left|S_\rho(\omega)\right|\frac{P_S^-(\mathbf{x}_G, \mathbf{x}_s, \omega)}{S_\rho(\omega)\vec{G}_0^+(\mathbf{x}_G, \mathbf{x}_s, \omega)}. \tag{3.37}$$

Claerbout (1971) derives the deconvolution imaging condition with the requirement that the data be minimum phase. The derivation presented in this section does not require minimum phase deconvolution. Zero-phase deconvolution is preferred because it maximizes the resolution of the migrated output and produces the desired bandlimited reflectivity function. If we further assume that the recorded data have been deconvolved to zero-phase, the source signature $S_\rho(\omega)$ in the denominator can be replaced by its amplitude $\left|S_\rho(\omega)\right|$. The source amplitudes in the numerator and denominator of equation (3.37) cancel, yielding

$$\hat{R}_\theta(\mathbf{x}_G, \mathbf{x}_s) = \frac{1}{2\pi}\int d\omega \hat{F}(\omega)\frac{P_S^-(\mathbf{x}_G, \mathbf{x}_s, \omega)}{\vec{G}_0^+(\mathbf{x}_G, \mathbf{x}_s, \omega)}, \tag{3.38}$$

which is the same as equation (3.29), the estimator we set out to derive [see Docherty, 1991, equation (14)]. In fact, the favorable cancellation is the sole reason for the choice of the signal-to-noise estimator $\hat{F}(\omega)\left|S_\rho(\omega)\right|$. Note that, although equation (3.38) does not require an estimate of the source amplitude $\left|S_\rho(\omega)\right|$, the correct normalization of the bandlimited filter $\hat{F}(\omega)$ as defined by equation (3.35) does. Fortunately, an error in normalization will be a constant relative error in the estimated reflectivity $\hat{R}_\theta(\mathbf{x}_G, \mathbf{x}_s)$, consistent with our goal for a 'relative true-amplitude' migration.

3.7 RAY-THEORETICAL KIRCHHOFF-APPROXIMATE MIGRATION OF SHOT OR RECEIVER RECORDS

The imaging condition given by equation (3.38) is a prescription for creating a reflector map. In essence, it is equivalent to a weighted least squares average of frequency-dependent reflectivity estimates, where the estimates are given as a ratio of amplitudes of the upgoing inverse propagating wavefield $P_S^-(\mathbf{x}_G, \mathbf{x}_s, \omega)$ to the forward propagating Green's function $\vec{G}_0^+(\mathbf{x}_G, \mathbf{x}_s, \omega)$ at the imaging location $\mathbf{x}_G$. By definition, the phase of these two terms will satisfy Claerbout's time-coincident imaging condition. The objective in this section is to re-express equation (3.38) as a practical migration formula. The derivation of the ray-theoretical Kirchhoff-approximate migration formula presented here is based on Docherty (1991).

3.7.1 Ray-theoretical approximations to the optimum imaging condition

First, the forward propagating Green's function $\vec{G}_0^+(\mathbf{x}_G, \mathbf{x}_s, \omega)$ in equation (3.38) is replaced by its ray-theoretical equivalent $A_0(\mathbf{x}_G, \mathbf{x}_s)e^{i\omega\tau_0(\mathbf{x}_G, \mathbf{x}_s)}$ [equation (2.34)], yielding

$$\hat{R}_\theta(\mathbf{x}_G, \mathbf{x}_s) = \frac{1}{2\pi A_0(\mathbf{x}_G, \mathbf{x}_s)} \int d\omega \hat{F}(\omega) P_S^-(\mathbf{x}_G, \mathbf{x}_s, \omega) e^{-i\omega\tau_0(\mathbf{x}_G, \mathbf{x}_s)}. \qquad (3.39)$$

Equation (3.39) is equation (15) of Docherty (1991). Note that the amplitude function $A_0(\mathbf{x}_G, \mathbf{x}_s)$ describing the divergence of the Green's function is a constant when both the source location and imaging location are fixed.

Next, we need a ray-theoretical approximation for the inverse-propagating Kirchhoff-Helmholtz integral [equation (3.24)] to substitute for $P_S^-(\mathbf{x}_G, \mathbf{x}_s, \omega)$ in equation (3.39). Equation (3.24) is repeated here for reference:

$$P_S^-(\mathbf{x}_G, \mathbf{x}_s, \omega) = \int_{\mathbf{x}_g} dS \Big\{ \overleftarrow{G}_0^+(\mathbf{x}_g, \mathbf{x}_G, \omega) \nabla_{\mathbf{x}_g} P_S^-(\mathbf{x}_g, \mathbf{x}_{s'}, \omega) - P_S^-(\mathbf{x}_g, \mathbf{x}_{s'}, \omega) \nabla_{\mathbf{x}_g} \overleftarrow{G}_0^+(\mathbf{x}_g, \mathbf{x}_G, \omega) \Big\} \mathbf{n}_g^- . \tag{3.24}$$

Assuming that only one of either the acoustic pressure $P_S^-(\mathbf{x}_g, \mathbf{x}_{s'}, \omega)$ or its normal derivative $\nabla_{\mathbf{x}_g} P_S^-(\mathbf{x}_g, \mathbf{x}_{s'}, \omega) \cdot \mathbf{n}_g^-$ have been recorded on the arbitrary surface S_g, there is insufficient information to evaluate equation (3.24). This problem was discussed in great detail in Sections 2.6.3 and 2.9.2. To summarize, an exact reconstruction requires the Rayleigh I or II integrals [equations (2.63) or (2.64), respectively], but these are strictly valid only for wavefields recorded on a planar surface. A ray-theoretical approximation to the Rayleigh II integral will now be derived, and compared with the high-frequency approximation of Docherty [1991, equation (2.34)]. Both approximations assume that only the acoustic pressure $P_S^-(\mathbf{x}_g, \mathbf{x}_{s'}, \omega)$ is recorded.

3.7.2 The far-field ray-theoretical Rayleigh II approximation

The Rayleigh II integral [equation (2.64)] is re-expressed using the notation adopted in this chapter, as

$$P_S^-(\mathbf{x}_G, \mathbf{x}_s, \omega) = 2 \int_{-\infty}^{\infty}\!\!\int dx dy J_{Sxy} \Big\{ P_S^-(\mathbf{x}_g, \mathbf{x}_{s'}, \omega) \nabla_{\mathbf{x}_g} \overleftarrow{G}_0^+(\mathbf{x}_g, \mathbf{x}_G, \omega) \cdot \mathbf{n}_g^+ \Big\}, \tag{3.40}$$

where the Jacobian $J_{Sxy} = dS/dxdy$ is unity for a planar surface with normal z. The ray-theoretical approximation to the one-way inverse propagating Green's function is given by

$$\overleftarrow{G}_0^+(\mathbf{x}_g, \mathbf{x}_G, \omega) = A_0(\mathbf{x}_g, \mathbf{x}_G) e^{-i\omega\tau_0(\mathbf{x}_g, \mathbf{x}_G)}. \tag{3.41}$$

The far-field[19] ray-theoretical approximation to the normal derivative of equation (3.41) is

$$\nabla_{\mathbf{x}_g} \overleftarrow{G}_0^+(\mathbf{x}_g, \mathbf{x}_G, \omega) \cdot \mathbf{n}_g^+ \cong i\omega A_0(\mathbf{x}_g, \mathbf{x}_G) e^{-i\omega\tau_0(\mathbf{x}_g, \mathbf{x}_G)} \nabla_{\mathbf{x}_g} \tau_0(\mathbf{x}_g, \mathbf{x}_G) \cdot \mathbf{n}_g^-. \tag{3.42}$$

Note the change in direction of the normal, which changes the sign of the expression. Substituting equation (3.42) into equation (3.40) yields

$$P_S^-(\mathbf{x}_G, \mathbf{x}_s, \omega) \approx 2i\omega \int_{-\infty}^{\infty}\!\!\int dxdy J_{Sxy} \left\{ A_0(\mathbf{x}_g, \mathbf{x}_G) \nabla_{\mathbf{x}_g} \tau_0(\mathbf{x}_g, \mathbf{x}_G) \cdot \mathbf{n}_g^- e^{-i\omega\tau_0(\mathbf{x}_g, \mathbf{x}_G)} P_S^-(\mathbf{x}_g, \mathbf{x}_{s'}, \omega) \right\}_{S_g} \tag{3.43}$$

as the far-field ray-theoretical Rayleigh II approximation to the inverse extrapolated upgoing wavefield, as required to evaluate equation (3.39).

3.7.3 Docherty's ray-theoretical approximation by stationary phase

Docherty [1991, equation (9)] assumes a ray-theoretical approximation to the upgoing wavefield $P_S^-(\mathbf{x}_g, \mathbf{x}_{s'}, \omega)$, re-expressed here in my notation as

$$P_S^-(\mathbf{x}_g, \mathbf{x}_{s'}, \omega) = P(\mathbf{x}_g, \mathbf{x}_{s'}) e^{i\omega\tau(\mathbf{x}_g, \mathbf{x}_{s'})}. \tag{3.44}$$

---

[19] Docherty (1991) uses the phrase 'leading order in ω' to describe what is essentially the far-field term. A more thorough discussion, in the context of free-space Green's functions, can be found in Appendix B.3 of this dissertation.

A more extensive discussion of equation (3.44) can be found in Appendix B [see equation (B.12)]. Note that the phase and amplitude of the source function are not included in the RHS because Docherty assumes an impulsive source. As well, $\tau(\mathbf{x}_g, \mathbf{x}_{s'})$ represents a 'generalized' traveltime from the source to reflector to receiver.

The far-field ray-theoretical approximation to the normal derivative of equation (3.44) is

$$\nabla_{\mathbf{x}_g} P_S^-(\mathbf{x}_g, \mathbf{x}_{s'}, \omega) \cdot \mathbf{n}_g^- = i\omega P(\mathbf{x}_g, \mathbf{x}_{s'}) e^{i\omega\tau(\mathbf{x}_g, \mathbf{x}_{s'})} \nabla_{\mathbf{x}_g} \tau(\mathbf{x}_g, \mathbf{x}_{s'}) \cdot \mathbf{n}_g^- . \tag{3.45}$$

Substituting equations (3.41), (3.42), (3.44), and (3.45) into equation (3.24) yields

$$P_S^-(\mathbf{x}_G, \mathbf{x}_s, \omega) = \int_{\mathbf{x}_g} dS \Big\{ i\omega P(\mathbf{x}_g, \mathbf{x}_{s'}) A_0(\mathbf{x}_g, \mathbf{x}_G) \Big(\nabla_{\mathbf{x}_g} \tau(\mathbf{x}_g, \mathbf{x}_{s'}) \cdot \mathbf{n}_g^- + \nabla_{\mathbf{x}_g} \tau_0(\mathbf{x}_g, \mathbf{x}_G) \cdot \mathbf{n}_g^- \Big) e^{i\omega\left(\tau(\mathbf{x}_g, \mathbf{x}_{s'}) - \tau(\mathbf{x}_g, \mathbf{x}_G)\right)} \Big\}. \tag{3.46}$$

As discussed in Docherty, the main contributions to the integral occur where the phase function $\phi_\tau = \tau_{gs'} - \tau_{gG}$ is stationary with respect to the variables of integration. The conditions of stationarity are given by

$$\frac{\partial \phi_\tau}{\partial \xi_i} = (\nabla \tau_{gs'} - \nabla \tau_{gG}) \cdot \frac{\partial \mathbf{x}_g}{\partial \xi_i} = 0 \quad i = 1,\ 2 \tag{3.47}$$

where the parameter $\xi = (\xi_1, \xi_2)$ identifies the point $\mathbf{x}_g(\xi)$ on S_g. The same surface parameterization is used in Section 3.5 in the context of a simplified notation for ray-theoretical Kirchhoff-approximate modeling.

Docherty proceeds as follows: the vector $\partial \mathbf{x}_g / \xi_i$ is a tangent on the surface S_g; hence, equation (3.47) states that the vectors $\nabla \tau_{gs'}$ and $\nabla \tau_{gG}$ have two equal projections on two linearly independent tangents to the surface; then, since $|\nabla \tau_{gs'}| = |\nabla \tau_{gG}| = 1/c(\mathbf{x}_g(\xi))$, the two vectors are identical at the stationary points; thus $\nabla \tau_{gs'} \cdot \mathbf{n}_g^- = \nabla \tau_{gG} \cdot \mathbf{n}_g^-$ on S_g;

equation (3.44) can be re-substituted for $P_S^-(\mathbf{x}_g,\mathbf{x}_{s'},\omega)$; and equation (3.46) can be simplified to

$$P_S^-(\mathbf{x}_G,\mathbf{x}_s,\omega) \approx 2i\omega \int_{\mathbf{x}_g} dS A(\mathbf{x}_g,\mathbf{x}_G)\nabla_{\mathbf{x}_g}\tau_0(\mathbf{x}_g,\mathbf{x}_G)\cdot \mathbf{n}_g^- e^{-i\omega\tau_0(\mathbf{x}_g,\mathbf{x}_G)} P_S^-(\mathbf{x}_g,\mathbf{x}_{s'},\omega)\,. \qquad (3.48)$$

Equation (3.48) is identical to equation (3.43), but seems to be applicable for an arbitrary surface as opposed to the restriction to a planar surface as required by the far-field Rayleigh II integral. In effect, the method of stationary phase equates the unknown derivative $\partial P_S^- \big/ \partial n_g^-$ with the known normal derivative $-\partial \overleftarrow{G}_0^+ \big/ \partial n_g^-$, and makes a far-field approximation as well. Does stationary phase make the assumptions more exact? The short answer is no. A more complete discussion, using free-space Green's functions and a geometrical approach to stationary phase, can be found in Appendix B.

3.7.4 Ray-theoretical Kirchhoff-approximate migration formula

We now have two equivalent expressions for wavefield $P_S^-(\mathbf{x}_G,\mathbf{x}_s,\omega)$, given by equation (3.43) or equation (3.48). Substitution of either of these into equation (3.39) yields equation (16) of Docherty, re-expressed here as

$$\hat{R}_\theta(\mathbf{x}_G,\mathbf{x}_s) = \frac{-2}{A(\mathbf{x}_G,\mathbf{x}_s)} \int_{\mathbf{x}_g} dS A(\mathbf{x}_g,\mathbf{x}_G)\nabla_{\mathbf{x}_g}\tau(\mathbf{x}_g,\mathbf{x}_G)\cdot \mathbf{n}_g^-$$

$$\times 2\,\mathrm{Re}\left[\frac{1}{2\pi}\int_0^\infty d\omega \hat{F}(\omega)(-i\omega)P_S^-(\mathbf{x}_g,\mathbf{x}_s,\omega)e^{-i\omega\left(\tau(\mathbf{x}_g,\mathbf{x}_G)+\tau(\mathbf{x}_G,\mathbf{x}_s)\right)}\right], \qquad (3.49)$$

where the recorded wavefield $P_S^-(\mathbf{x}_g,\mathbf{x}_s,\omega)$ is now given as a function of the true source location $\mathbf{x}_s$ instead of the image-source location $\mathbf{x}_{s'}$.

Equation (3.49) is a 3-D prestack ray-theoretical Kirchhoff-approximate migration formula that satisfies the chi-squared optimal imaging condition developed in Section 3.6. The term in the square brackets is expressed in the form of an inverse Fourier transform [see equations (A-11) and (A-30)]. Notice that the limits of the integral over frequency are now from 0 to ∞, thereby avoiding awkward terms such as $|\omega|$ and $\operatorname{sgn}\omega$ required to make the expression correct for negative frequencies. In Chapter 4, this term [or, more correctly, twice the real part, as indicated in equation (3.49)] will be re-expressed in an equivalent time-domain form, yielding a convolution of the filter and the time derivative of the wavefield evaluated at time $t = \tau_{gG} + \tau_{Gs}$, i.e. $\left[\hat{f}(t) * \partial p_S^-(\mathbf{x}_g, \mathbf{x}_s, t)/\partial t\right]_{t=\tau_{gG}+\tau_{Gs}}$.

The prestack migration equation given by equation (3.49) is valid for common shot gathers or, invoking reciprocity, common receiver gathers. The simplest expression for a migrated stack is obtained by averaging the reflectivities obtained by migrating shot or receiver gathers. For the optimal chi-squared imaging condition, the stacked reflectivity is given by the average of the reflectivities obtained using equation (3.49), i.e.

$$\overline{R}_{sg}(\mathbf{x}_G) \equiv \frac{1}{N_s} \sum_{s=1}^{N_s} \hat{R}_\theta(\mathbf{x}_G, \mathbf{x}_s). \tag{3.50}$$

Even though equations (3.49) provide a measure of relative true-amplitude reflectivity, equation (3.50) does not. Indeed, the reflectivity map described by equation (3.49) is angle-dependent, so a simple ‘stack’ of these maps from individual migrated common shot gathers will produce some sort of average reflectivity map. In Chapter 4, I revisit this equation and show that 1) it is a poor estimate of average reflectivity, 2) that a better estimate can be obtained by dividing by the number of offsets (although it provides the same relative error), and 3) that migration/inversion weights based on the common-offset configuration, or a suitable approximation to these weights, produces a more optimal stacked image of the average of angle-dependent reflectivity.

3.8 RAY-THEORETICAL BORN-APPROXIMATE FORWARD MODELING

We now return to the Kirchhoff-Helmholtz integral representation, given in summary form by equation (3.2), re-expressed here for measurement at receiver location $\mathbf{x}_g$ as

$$P_t(\mathbf{x}_g,\mathbf{x}_s,\omega) = P_i(\mathbf{x}_g,\mathbf{x}_s,\omega) + P_S(\mathbf{x}_g,\mathbf{x}_s,\omega) + P_V(\mathbf{x}_g,\mathbf{x}_s,\omega), \qquad (3.51)$$

with $\mathbf{x}_s$ the source location. Equation (3.51) states that the total wavefield can be expressed as a sum of incident, surface-scattered and volume-scattered wavefields. The purpose of this section is to derive a forward modeling formula using only the volume-scattered wavefield. The single-scattering assumption (i.e. that only primary reflections are of interest) is known as the Born approximation.

3.8.1 A configuration appropriate for the volume-scattered wavefield

The Kirchhoff-approximate modeling and migration methods assume that the contribution from the volume-scattered wavefield is zero. This is achieved by a careful choice of configuration for the volume of interest such that the wavespeed perturbation $\alpha(\mathbf{x})$ is zero, i.e. that the reference wavespeed is assumed to be identical to the unknown true wavespeed [see equation (2.46)]. At worst, any remaining volume-scattered contribution can be considered as an unknown error term in the estimated total wavefield.

Now we take the opposite approach, and select a configuration such that the surface-scattered wavefield is zero and the volume-scattered wavefield is nonzero. The appropriate configuration is illustrated in Figure 3.4. The total volume V_∞ is bounded by a spherical surface at infinity. Thus, the Sommerfeld radiation condition can be invoked (at least, for forward modeling), and the contribution from the surface-scattered wavefield can be ignored. Inside the volume is a bounded region V_α where the wavespeed perturbation is non-zero. Elsewhere, the wavespeed perturbation is assumed to be zero. Hence, the only contribution to the volume-scattered wavefield will come from the

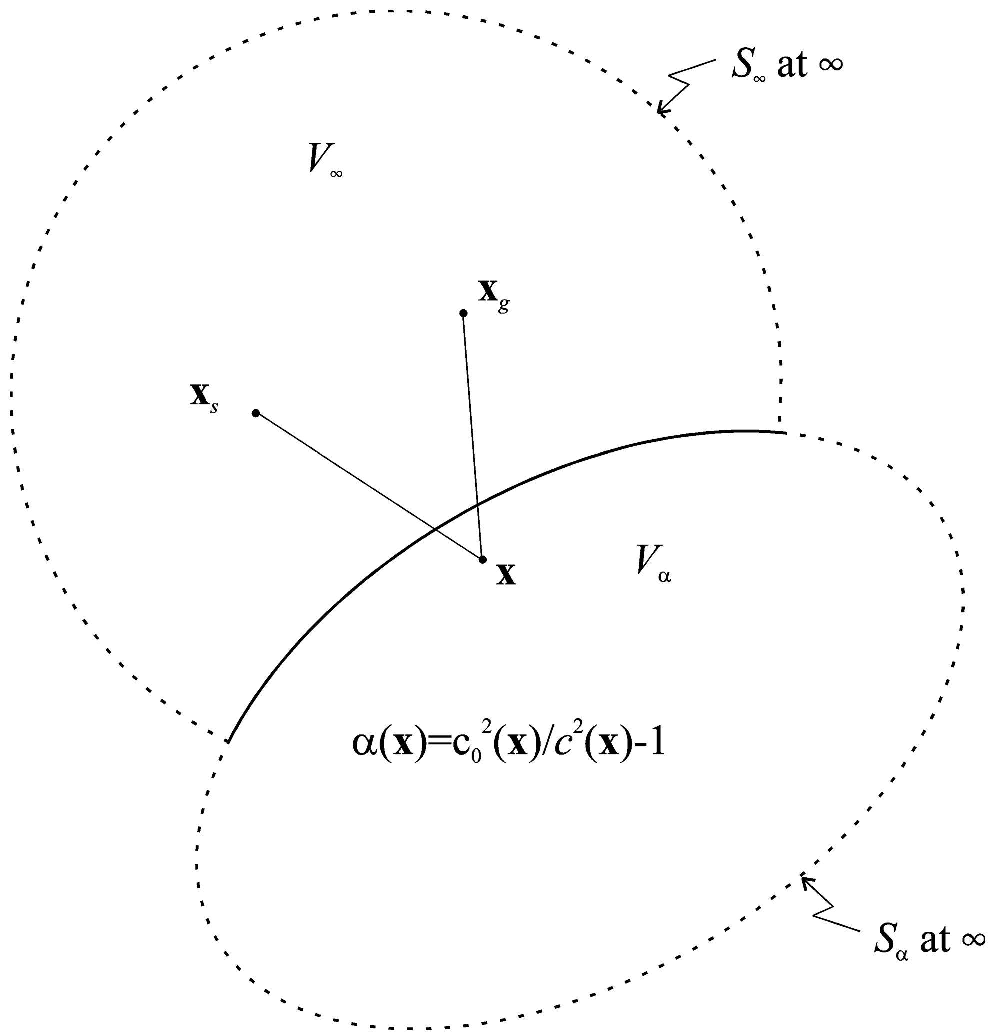

Figure 3.4. Configuration for Born-approximate forward modeling.

interior volume, and the Kirchhoff-Helmholtz integral representation [equation (3.1)—with new variables introduced above] simplifies to

$$P_t(\mathbf{x}_g,\mathbf{x}_s,\omega)=P_i(\mathbf{x}_g,\mathbf{x}_s,\omega)+P_V(\mathbf{x}_g,\mathbf{x}_s,\omega)$$

$$=S_\rho(\omega)\vec{G}_0(\mathbf{x}_s,\mathbf{x}_g,\omega)+\int_{\mathbf{x}} dV\omega^2\left(\frac{\alpha(\mathbf{x})}{c_0^2(\mathbf{x})}\right)\vec{G}_0(\mathbf{x},\mathbf{x}_g,\omega)P_t(\mathbf{x},\mathbf{x}_s,\omega). \tag{3.52}$$

Note that the representation is expressed in terms of two-way acoustic wavefields and two-way forward-propagating Green's functions. It is not a trivial exercise to derive a one-way volume-scattered representation. A detailed derivation can be found in a paper by Wapenaar (1993a) with a summary in a two paper series by Wapenaar and Berkhout (1993) and Wapenaar (1993b). Here, I proceed with a two-way derivation and then insert one-way wavefields when it seems intuitively safe to do so, but without the rigor of the Kirchhoff-approximate derivation presented previously.

3.8.2 The Born approximation

In equation (3.52), the total wavefield $P_t(\mathbf{x}_g, \mathbf{x}_s, \omega)$ appears on both the LHS and as part of the volume integral on the RHS. Weglein (1985) suggests that equation (3.52) can be recursively substituted back into itself, yielding

$$
\begin{aligned}
P_t(\mathbf{x}_g, \mathbf{x}_s, \omega) &= S_\rho(\omega)\vec{G}_0(\mathbf{x}_s, \mathbf{x}_g, \omega) + \int_{\mathbf{x}} dV\omega^2 \left(\frac{\alpha(\mathbf{x})}{c_0^2(\mathbf{x})}\right)\vec{G}_0(\mathbf{x}, \mathbf{x}_g, \omega) P_i(\mathbf{x}, \mathbf{x}_s, \omega) \\
&\quad + \int_{\mathbf{x}} dV\omega^2 \left(\frac{\alpha(\mathbf{x})}{c_0^2(\mathbf{x})}\right)\vec{G}_0(\mathbf{x}, \mathbf{x}_g, \omega) \int_{\mathbf{x}'} dV\omega^2 \left(\frac{\alpha(\mathbf{x}')}{c_0^2(\mathbf{x}')}\right)\vec{G}_0(\mathbf{x}', \mathbf{x}, \omega) P_i(\mathbf{x}', \mathbf{x}_s, \omega) \\
&\quad + \cdots \\
&= P_i(\mathbf{x}_g, \mathbf{x}_s, \omega) + P_V(\mathbf{x}_g, \mathbf{x}_s, \omega) + P_{VV}(\mathbf{x}_g, \mathbf{x}_s, \omega) + \cdots
\end{aligned}
\tag{3.53}
$$

where $P_V(\mathbf{x}_g, \mathbf{x}_s, \omega)$ is the single-scattered response, $P_{VV}(\mathbf{x}_g, \mathbf{x}_s, \omega)$ is the double-scattered response, etc.. The doubly-scattered and other higher-order responses demonstrate the nonlinear relationship between the wavefield and the wavespeed perturbation. If the series in equation (3.53) is truncated after the second term (the Born approximation) and the incident wavefield subtracted, we obtain a linear approximation to the volume-scattered wavefield,

$$P_V(\mathbf{x}_g,\mathbf{x}_s,\omega)=\int_{\mathbf{x}} dV\omega^2\left(\frac{\alpha(\mathbf{x})}{c_0^2(\mathbf{x})}\right)\vec{G}_0(\mathbf{x},\mathbf{x}_g,\omega)P_i(\mathbf{x},\mathbf{x}_s,\omega)\,. \tag{3.54}$$

Equation (3.54) is the Born-approximate modeling formula. Note that the Born approximation arises from a power series expansion in $\omega^2\alpha/c_0^2$, which suggests that the series truncation is a low-frequency approximation that might be incompatible with the high-frequency WKBJ assumption. However, Bleistein et al. (2001, p. 99-103) argue that the product $\omega^2\alpha$ provide the precise balance needed for the eikonal equation, which describes the traveltime behavior of waves under the condition of high frequency.

3.8.3 Ray-theoretical approximations

Now substitute the ray-theoretical approximation for the forward-propagating Green's function,

$$\vec{G}_0(\mathbf{x},\mathbf{x}_g,\omega)=A_g(\mathbf{x},\mathbf{x}_g)e^{i\omega\tau_g(\mathbf{x},\mathbf{x}_g)}\,, \tag{3.55}$$

and the ray-theoretical approximation for the incident wavefield (forward propagating at the reference wavespeed),

$$P_i(\mathbf{x},\mathbf{x}_s,\omega)=S_\rho(\omega)A_0(\mathbf{x},\mathbf{x}_s)e^{i\omega\tau_0(\mathbf{x},\mathbf{x}_s)}\,, \tag{3.56}$$

into equation (3.54), yielding

$$P_V(\mathbf{x}_g,\mathbf{x}_s,\omega)=\omega^2S_\rho(\omega)\int_{\mathbf{x}} dV\left(\frac{\alpha(\mathbf{x})}{c_0^2(\mathbf{x})}\right)A_g(\mathbf{x},\mathbf{x}_g)A_s(\mathbf{x},\mathbf{x}_s)e^{i\omega(\tau_g+\tau_S)}\,. \tag{3.57}$$

Equation (3.57) is the ray-theoretical Born-approximate modeling formula, and is the same (with slight changes in notation) as equation (1) in Jaramillo and Bleistein (1999). The use of the linearized Born approximation and one-way ray-theoretical Green's functions has, in effect, transformed the two-way Kirchhoff-Helmholtz representation into a one-way modeling formula. However, compared to the Kirchhoff-approximate modeling formula [equations (3.17) or (3.20)], which is defined in terms of a surface integral over the reflector, the Born-approximate formula (a volume integral) is awkward to implement. Why, then, is it worth deriving? As nicely summarized by Bleistein et al. (2001, p. 161 and p. 221), equation (3.57) has the form of a Fourier transform. Thus the inversion formula can be written directly in the form of an inverse Fourier transform. In the next section, this approach will be taken to derive Born-approximate and Kirchhoff-approximate depth imaging formulas.

3.8.4 Equivalence of Born-approximate and Kirchhoff-approximate modeling formulae

The Born-approximate and Kirchhoff-approximate modeling formulas can be shown to be asymptotically identical by transforming either into time-domain isochron-stack operators (Jaramillo, 1999; Jaramillo and Bleistein, 1999). The Born-approximate isochron-stack operator is given as

$$p_{\Sigma_I}^{-}(\xi,t) \cong \int_{\mathbf{x}_I} d\Sigma_I\, R_B(\mathbf{x}_I,\mathbf{x}_s)\frac{\partial\gamma(\mathbf{x}_I)}{\partial n_R^{+}}\left.\frac{A_{g\times s}(\mathbf{x}_I,\xi)}{\left|\nabla_{\mathbf{x}_I}\phi_0(\mathbf{x}_I,\xi)\right|}\right|_{t=\phi_0(\mathbf{x}_I,\xi)} * s_\rho(t)\,. \tag{3.58}$$

As introduced in Section 3.5, the acquisition configuration over the nonplanar recording surface is parameterized by the 2-D vector ξ, while the product of the ray-theoretical amplitudes is simplified as $A_{g\times s}(\mathbf{x}_I,\xi)$ and total traveltime is simplified as ‘phase’ $\phi_0(\mathbf{x}_I,\xi) = \tau_g(\mathbf{x}_I,\mathbf{x}_g)+\tau_s(\mathbf{x}_I,\mathbf{x}_s)$. Integration is now over the isochron surface Σ_I with downward normal $\mathbf{n}_I^{+} = \nabla\phi_\tau / |\nabla\phi_\tau|$. Points on the isochron surface are denoted as $\mathbf{x}_I$. The function $\gamma(\mathbf{x}) = \delta(\Sigma_R(\mathbf{x}))|\nabla_{\mathbf{x}}\Sigma_R(\mathbf{x})|$ is the singular function of the reflecting surface, where the reflecting surface is described by the equation $\Sigma_R(\mathbf{x}) = 0$ (Jaramillo and Bleistein, 1999). Hence, equation (3.58) includes only those portions of a single reflecting surface that intersect with the isochron surface at time $t = \phi_0$. The complete response is found by evaluating the integral at different times and convolving the result with the source wavelet $s_\rho(t)$.

The integrand in equation (3.58) contains the linearized Born reflection coefficient

$$R_B(\mathbf{x}_I, \mathbf{x}_s) = \frac{\alpha(\mathbf{x}_I)}{4\cos^2\theta} = \frac{\alpha(\mathbf{x}_I)}{c_0^2(\mathbf{x}_I)\left|\nabla_{\mathbf{x}_I}\phi_0\right|^2}, \tag{3.59}$$

which is known to be valid only over a small range of incident angles. Substituting this into equation (3.58) and comparing the result with equation (3.57) reveals that the most significant difference between the weighting functions of the two equations is a factor of $\left|\nabla_{\mathbf{x}_I}\phi_0\right|^{-3}$ in equation (3.58). A second derivative with respect to time [arising from the ω^2 in equation (3.57)] contributes a factor $\left|\nabla_{\mathbf{x}_I}\phi_0\right|^{-2}$, while the transformation from volume integral to isochron stack contributes the other $\left|\nabla_{\mathbf{x}_I}\phi_0\right|^{-1}$.

A result almost identical to equation (3.58) can be derived from the Kirchhoff-approximate modeling formula [equations (3.17) or (3.20)]. An alternate derivation to those found in Jaramillo (1999) and Jaramillo and Bleistein (1999) is presented in Appendix C. The only difference is that $R_\theta(\mathbf{x}_I, \mathbf{x}_s)$ is now the geometrical-optics reflection coefficient equation, which extends the accuracy of equation (3.58) up to and beyond the critical angle of reflection (Burridge et al., 1998). In the next section, a similar approach will be used to extend the Born-approximate inversion expression to a more generally valid Kirchhoff-approximate migration/inversion expression.

3.9 RAY-THEORETICAL BORN-APPROXIMATE INVERSION

A limitation of wave-theoretical methods such as the Kirchhoff-approximate depth imaging expression is that they are valid only for a single wave experiment such as a shot gather (or, invoking reciprocity, a receiver gather). Acquisition configurations other than common-shot or common-receiver (such as common-offset) cannot be imaged using wave-theoretical methods because these configurations correspond to an ensemble of many wave experiments. However, ray-theoretical Born-approximate inversion can image data from these configurations. The original method, as described first by Beylkin (1982), attempts to reconstruct velocity perturbations as opposed to reflectivity. Miller et al. (1987) quote Beylkin (1985) in describing the approach as “migration by inversion of a generalized Radon transform”. Their paper also provides a good explanation of the geometry of the generalized Radon transform as related to seismic imaging.

A key to the inversion process is to weight the reconstruction from every source-receiver combination as though it produced a specular reflection at the output point in the subsurface. In effect, the reflecting surfaces are assumed to be tangent to the isochrons of every source-receiver combination. This assumption ensures that we do not require a priori knowledge of the true orientation of the reflector in the subsurface. Using the method of stationary phase, it can be shown that the integration or sum of contributions from a restricted set of shot-receiver pairs will reconstruct an image of the reflector. Bleistein et al. (2001) show that, in the asymptotic evaluation of the inversion integral, the contribution from any source-receiver combinations that are not stationary (specular at the actual reflector) will be of lower order than the stationary combinations. The superposition of weighted contributions is asymptotically equivalent to a generalized Radon transform.

It is well known that the inverse acoustic scattering problem is ill-posed (e.g. Bleistein et al., 2001, p. 3-4). Thus, appropriate simplifications must be incorporated in order to create a practical inverse expression. The fundamental approximation is one of high frequency. This allows the use of ray-theoretical Green’s functions, which, in the frequency domain, lead to a forward modeling formula in the guise of a band- and aperture-limited forward Fourier transform. Taking the inverse-Fourier transform yields the desired migration expression for imaging the reflector as a band-limited singular function. The band-and aperture-limited aspects of real seismic data can be easily incorporated in the frequency domain. Following Bleistein et al. (2001), the frequency-domain approach is used here to derive the Born-approximate imaging expressions. Alternately, the source can be considered as a Dirac delta function and the forward model developed almost entirely in the time domain. This approach has been nicely presented by Jaramillo and Bleistein (1999). By using a delta function source, the associated theory of distributions can be utilized to carry out asymptotic approximations including derivatives under the integral and to exploit results from generalized Radon transform theory. Once the full-bandwidth result is obtained, a filter can be introduced to produce the final band-limited output. Jaramillo and Bleistein's results will not be presented here.

3.9.1 Inversion for wavespeed perturbation

The theory is first developed for imaging discontinuities in the wavespeed perturbation function $\alpha(\mathbf{x})$. The inverse problem for $\alpha(\mathbf{x})$ is formulated as follows: 1) determine a forward modeling formula as an integral equation for the "scattered" field, 2) linearize this integral equation using the Born approximation, 3) substitute the ray-theoretical expressions for the Green's function and the incident wavefield to obtain an integral in the form of a Fourier transform, 4) write the inversion formula for $\alpha(\mathbf{x})$ as an inverse Fourier transform, 5) modify the inversion formula to yield a solution for $\beta(\mathbf{x})$, the bandlimited singular function of the reflector surface scaled by the specular reflection coefficient $R_B(\mathbf{x},\mathbf{x}_s)$.

The first three steps are described in Section 3.8. The ray-theoretical Born-approximate modeling formula [equation (3.57)] is re-expressed in simplified notation as

$$P_V(\xi,\omega) = \omega^2 S_\rho(\omega)\int_{\mathbf{x}} dV\left(\frac{\alpha(\mathbf{x})}{c_0^2(\mathbf{x})}\right)A_{g\times s}(\mathbf{x},\xi)e^{i\omega\phi_0(\mathbf{x},\xi)}. \qquad (3.60)$$

Step 4 involves writing down an appropriate inversion formula using the structure of the 1-D inversion formulas to serve as a guide in the construction of the more general 3-D and 2.5-D inversion formulas. Because the 2.5-D inversion formula is derived from stationary phase arguments applied to the 3-D inversion formula (Bleistein et al., 2001, Chapter 6), only the 3-D inversion formula will be presented.

The kernel of the inversion formula contains a phase function that is opposite in sign to the phase function in the kernel of the forward modeling formula. The phase of the inversion formula is expected to be a function of the input variables (ξ,ω) and the output variables $\mathbf{x}_G$. Following the results of the 1-D inversion (Bleistein et al., 2001, Chapter 2), the 3-D inversion operator should include a phase function of the form, $-i\omega\phi_0(\mathbf{x}_G,\xi)$.

There is no ω-dependence in the amplitude function of the inversion kernel for wavespeed perturbation $\alpha(\mathbf{x})$, and we will assume that the only ω-dependence of the inversion kernel for the reflectivity function β consists only of a multiplication by a factor of $i\omega$.

Using $B(\mathbf{x}_G,\xi)$ to denote the amplitude function of the inversion kernel, the inversion operator should have the form

$$\alpha(\mathbf{x}_G) = \int d\omega \int_{\xi} dS B(\mathbf{x}_G,\xi) e^{-i\omega\phi_0(\mathbf{x}_G,\xi)} P_V(\xi,\omega) \tag{3.61}$$

Now substitute the data $P_V(\xi,\omega)$ as given by equation (3.60) into equation (3.61) to obtain the cascade of the forward modeling formula and the respective inversion formula

$$\alpha(\mathbf{x}_G) = \int d\omega \omega^2 S_\rho(\omega) \int_{\xi} dS B(\mathbf{x}_G,\xi) e^{-i\omega\phi_0(\mathbf{x}_G,\xi)} \int_{\mathbf{x}} dV \alpha(\mathbf{x}) \frac{A_{g\times s}(\mathbf{x},\xi)}{c_0^2(\mathbf{x})} e^{i\omega\phi_0(\mathbf{x},\xi)} \,. \tag{3.62}$$

Equation (3.62), which is a sixfold integral, can be thought of as a volume integral in $\mathbf{x}$ of the wavespeed perturbation $\alpha(\mathbf{x})$ times some kernel function, yielding the wavespeed perturbation $\alpha(\mathbf{x}_G)$. Thus the kernel function must, in some asymptotic sense, have the same sifting property as the Dirac delta function,

$$\alpha(\mathbf{x}_G) = \int_{\mathbf{x}} dV \, \delta(\mathbf{x} - \mathbf{x}_G)\alpha(\mathbf{x}). \tag{3.63}$$

Jaramillo and Bleistein (1999) discuss how the correspondence with the delta function makes the resulting inversion formula a generalized Radon transform. An excellent discussion of the relationship between migration and the generalized Radon transform can be found in Miller et al. (1987).

Using equation (3.63) as a guide, we extract the portion of equation (3.62) that must be the asymptotic approximation of $\delta(\mathbf{x} - \mathbf{x}_G)$ and from this portion determine $B(\mathbf{x}_G,\xi)$. The procedure, outlined in Bleistein et al. (2001, p. 222-225) involves a Taylor series approximation, a change of variable of integration from frequency and surface parameter (ω,ξ) to wave vector $\mathbf{k}$, and an asymptotic approximation under the condition that $S_\rho(\omega) = 1$. The value determined is

$$B(\mathbf{x}_G,\xi) = \frac{1}{8\pi^3} \frac{|h(\mathbf{x}_G,\xi)| c_0^2(\mathbf{x}_G)}{A_{g\times s}(\mathbf{x}_G,\xi)}, \tag{3.64}$$

where

$$h(\mathbf{x}_G,\xi) = \det \begin{bmatrix} \nabla_{\mathbf{x}_G}\phi_0(\mathbf{x}_G,\xi) \\ \dfrac{\partial}{\partial \xi_1}\nabla_{\mathbf{x}_G}\phi_0(\mathbf{x}_G,\xi) \\ \dfrac{\partial}{\partial \xi_2}\nabla_{\mathbf{x}_G}\phi_0(\mathbf{x}_G,\xi) \end{bmatrix} \tag{3.65}$$

is known as the Beylkin determinant. Substituting equation (3.64) into (3.62) gives the high-frequency inversion formula for wavespeed perturbation $\alpha(\mathbf{x}_G)$ as

$$\alpha(\mathbf{x}_G) = \frac{1}{8\pi^3}\int_{\xi} dS \frac{\left|h(\mathbf{x}_G,\xi)\right| c_0^2(\mathbf{x}_G)}{A_{g\times s}(\mathbf{x}_G,\xi)} \int d\omega e^{-i\omega\phi_0(\mathbf{x}_G,\xi)} P_V(\mathbf{x}_s,\mathbf{x}_g,\omega) \tag{3.66}$$

3.9.2 Modifying the inversion formulae to estimate reflectivity

However, we desire instead an inversion formula as a reflectivity function $\beta(\mathbf{x}_G)$ in the form of a bandlimited singular function $\gamma_B(\mathbf{x}_G)$ times the linearized Born reflection coefficient $R_B(\mathbf{x}_G,\xi)$. To convert the wavespeed perturbation $\alpha(\mathbf{x}_G)$ to a reflectivity function, we multiply by $i\omega\left|\nabla_{\mathbf{x}_G}\phi_0(\mathbf{x}_G,\xi)\right|$. In addition, the conversion requires an appropriate proportionality function, $1\Big/\left(c^2(\mathbf{x}_G)\left|\nabla_{\mathbf{x}_G}\phi_0(\mathbf{x}_G,\xi)\right|^2\right)$, which, as it turns out, accounts for obliquity effects in the nonzero offset inversion process (Bleistein et al., 2001, p. 226). Inserting these two terms into equation (3.66) gives the inversion formula for the bandlimited reflectivity function β. Bleistein shows that a second reflectivity function β_1—the geometrical optics reflection coefficient multiplied by $1/2\pi$ times the area under the filter $\hat{F}(\omega)$ in the ω-domain—can be obtained by dividing the bandlimited reflectivity function by one additional power of $\left|\nabla_{\mathbf{x}_G}\phi_0(\mathbf{x}_G,\xi)\right|$, yielding

$$\beta_1(\mathbf{x}_G) = \frac{-1}{4\pi^2}\int_{\xi} dS \frac{\left|h(\mathbf{x}_G,\xi)\right|}{A_{g\times s}(\mathbf{x}_G,\xi)\left|\nabla_{\mathbf{x}_G}\phi_0(\mathbf{x}_G,\xi)\right|^2} \times 2\,\mathrm{Re}\left[\frac{1}{2\pi}\int_0^{\infty} d\omega(-i\omega)P_V(\mathbf{x}_g,\mathbf{x}_s,\omega)e^{-i\omega\phi_0(\mathbf{x}_G,\xi)}\right]. \tag{3.67}$$

The inversion formula is an aperture limited Fourier-transform-like integral. The integrand contains a determinant that is part of a Jacobian that depends both on the background propagation parameters and on the acquisition configuration. As a result, the problem of extending the inversion formula to new recording geometries is reduced to a problem of computing the value of the determinant associated with a specific geometry.

3.9.3 Common-shot inversion similar to Kirchhoff-approximate migration

For the common-shot geometry, Hanitzsch [1995, equations (10) and (24)] shows that the inversion formula can be expressed as

$$R_B(\mathbf{x}_G,\mathbf{x}_s)=\frac{-2}{A_0(\mathbf{x}_G,\mathbf{x}_s)}\int_{\mathbf{x}_g} dS A_0(\mathbf{x}_g,\mathbf{x}_G)\nabla_{\mathbf{x}_g}\tau_0(\mathbf{x}_g,\mathbf{x}_G)\cdot\mathbf{n}_g^-$$

$$\times 2\,\mathrm{Re}\left[\frac{1}{2\pi}\int_0^\infty d\omega(-i\omega)P_V(\mathbf{x}_g,\mathbf{x}_s,\omega)e^{-i\omega\left(\tau_0(\mathbf{x}_g,\mathbf{x}_G)+\tau_0(\mathbf{x}_G,\mathbf{x}_s)\right)}\right]. \quad (3.68)$$

Equation (3.68) is almost identical to equation (3.49), the Kirchhoff-approximate migration formula for common-shot geometry. There are two significant differences. The first is that the bandlimiting and normalizing function $\hat{F}(\omega)$ is missing from equation (3.68). A convincing argument was presented in Section 3.6 justifying the use of the bandlimiting function and, as discussed above, it is required to convert the reflectivity function β_1 into the reflection coefficient. Henceforth it will be adopted for all acquisition configurations. The second difference is that equation (3.68) determines the linearized Born reflection coefficient $R_B(\mathbf{x}_G,\mathbf{x}_s)$ [assuming $\hat{F}(\omega)$ is included], while equation (3.49) estimates the geometrical-optics reflection coefficient $\hat{R}_\theta(\mathbf{x}_G,\mathbf{x}_s)$. However, Jaramillo and Bleistein (1999) show that equation (3.68) can be derived from a Kirchhoff-approximate modeling formula, and therefore determines the geometrical-optics reflection coefficient which is valid over a wider range of incidence angles. Henceforth (and in Appendix D), I assume that all migration/inversion formulae estimate the geometrical-optics reflection coefficient from the upward surface-scattered pressure $P_S^-(\mathbf{x}_g,\mathbf{x}_s,\omega)$ as recorded by an appropriate acquisition configuration.

3.10 2.5-D AND 3-D CONSTANT-WAVESPEED COMMON-SHOT AND COMMON-OFFSET MIGRATION/INVERSION FORMULAE

The general inversion formula given by equation (3.67) is valid for 3-D seismic data sets obtained using any acquisition configuration. Bleistein et al. (2001, p. 248-249) show that, for constant wavespeed c_0, the terms in the inversion formula [equation (3.67)] evaluate as follows:

$$1/A_{g\times s}(\mathbf{x}_G,\xi) = 16\pi^2 r_{Gs} r_{gG}\,, \tag{3.69}$$

$$\phi_0(\mathbf{x}_G,\xi) = \left(r_{Gs} + r_{gG}\right)/c_0\,, \tag{3.70}$$

$$\left|\nabla_{\mathbf{x}_G}\phi_0(\mathbf{x}_G,\xi)\right| = \frac{2\cos\theta}{c_0}\,, \tag{3.71}$$

where the angle θ is determined using

$$\cos\theta = \frac{\left|\hat{\mathbf{r}}_{Gs} + \hat{\mathbf{r}}_{gG}\right|}{2}. \tag{3.72}$$

3.10.1 Common-shot migration/inversion formulae

For a flat acquisition surface and common-shot geometry, the full Beylkin determinant is given by

$$h(\mathbf{x}_G,\xi) = 2\cos^2\theta \frac{z_G}{c_0^3 r_{gG}^3} \tag{3.73}$$

Substituting these into equation (3.67) gives the 3-D common-shot, constant-wavespeed migration/inversion formula as

$$\underset{(3-D)}{\hat{R}_\theta}(\mathbf{x}_G,\mathbf{x}_s) = \frac{-2}{c_0}\int_{\mathbf{x}_g} dS\left\{\frac{r_{Gs}}{r_{gG}}\frac{z_G}{r_{gG}}\right\} 2\,\mathrm{Re}\left[\frac{1}{2\pi}\int_0^\infty d\omega \hat{F}(\omega)(-i\omega)\underset{(3-D)}{P_S^-}(\mathbf{x}_g,\mathbf{x}_s,\omega) e^{-i\omega(r_{Gs}+r_{gG})/c_0}\right]. \tag{3.74}$$

Equation (3.74) is derived in Bleistein et al. (2001) as equation (5.2.23) and re-expressed in Appendix D as equation (D-46).

The migration/inversion formula for 2.5-D common-shot constant-wavespeed,

$$\underset{(2.5-D)}{\hat{R}_\theta}(\mathbf{x}_G,\mathbf{x}_s) = \frac{4\pi}{\sqrt{2\pi c_0}} \int_{\mathbf{x}_g} dx \left\{ \sqrt{r_{Gs}+r_{gG}}\, \frac{\sqrt{r_{Gs}}}{\sqrt{r_{gG}}} \frac{z_G}{r_{gG}} \right\}$$
$$\times 2\,\mathrm{Re}\left[\frac{1}{2\pi} \int_0^\infty d\omega \hat{F}(\omega) \sqrt{-i\omega}\, \underset{(2.5-D)}{P_S^-}(\mathbf{x}_g,\mathbf{x}_s,\omega) e^{-i\omega(r_{gG}+r_{Gs})/c_0} \right], \tag{3.75}$$

is derived in Bleistein et al. (2001) as an unnumbered equation following equation (6.3.14). In Appendix D, equation (D-45) [the equivalent of equation (3.75)] is obtained by an alternate derivation that follows directly from the 2-D common-shot constant-wavespeed formula [derived as equation (D-43)].

In 3-D, 2.5-D, or 2-D, a number of migrated shot gathers can be combined to give the stacked reflectivity as the average of reflectivities obtained using equations (3.74)/(D-46), (3.75)/(D-45) or (D-43), respectively:

$$\overline{R}_s(\mathbf{x}_G) \equiv \frac{1}{N_s} \sum_{s=1}^{N_s} \hat{R}_\theta(\mathbf{x}_G,\mathbf{x}_s)\,. \tag{3.76}$$

Equation (3.76) was introduced earlier as equation (3.50). A similar expression can be written for stacked reflectivity as an average of common-receiver gathers.

3.10.2 Common-offset migration/inversion formulae

The full Beylkin determinant for a flat acquisition surface and common-offset geometry is given by

$$h(\mathbf{x}_G,\xi) = 2\cos^2\theta \frac{z_G}{c_0^3} \left[\frac{(r_{Gs}+r_{gG})(r_{Gs}^2+r_{gG}^2)}{r_{Gs}^3 r_{gG}^3} \right] \tag{3.77}$$

Thus the migration/inversion formula for 3-D common-offset, constant-wavespeed is

$$\underset{(3-D)}{\hat{R}_\theta}(\mathbf{x}_G,\xi_{co})=\frac{-2}{c_0}\int_{\xi_{co}} dS\left\{\frac{(r_{Gs}+r_{gG})}{r_{Gs}r_{gG}}\left(r_{Gs}\frac{z_G}{r_{gG}}+r_{gG}\frac{z_G}{r_{Gs}}\right)\right\}$$
$$\times 2\,\mathrm{Re}\left[\frac{1}{2\pi}\int_0^\infty d\omega \hat{F}(\omega)(-i\omega)\underset{(3-D)}{P_S^-}(\mathbf{x}_g,\mathbf{x}_s,\omega)e^{-i\omega(r_{Gs}+r_{gG})/c_0}\right]. \qquad (3.78)$$

Equation (3.78) is derived in Bleistein et al. (2001) as equation (5.2.32), and re-expressed in Appendix D as equation (D-52). The only difference between equations (3.74)/(D-46) and (3.78)/(D-52) is the weighting function in the curly brackets.

The migration/inversion formula for 2.5-D common-offset, constant-wavespeed from a flat recording surface,

$$\underset{(2.5-D)}{\hat{R}_\theta}(\mathbf{x}_G,\xi_{co})=\frac{4\pi z}{\sqrt{2\pi c_0}}\int_{\xi_{co}} dx\left\{\sqrt{r_s+r_g}\,\frac{(r_s^2+r_g^2)}{(r_s r_g)^{3/2}}\right\}.$$
$$\times 2\,\mathrm{Re}\left[\frac{1}{2\pi}\int_0^\infty d\omega \hat{F}(\omega)\sqrt{-i\omega}\underset{(2.5-D)}{P_S^-}(\mathbf{x}_g,\mathbf{x}_s,\omega)e^{-i\omega(r_{gG}+r_{Gs})/c_0}\right]. \qquad (3.79)$$

is derived in Bleistein et al. (2001) as equation (6.3.26). In Appendix D, the 2-D common-offset constant-wavespeed migration/inversion formula [equation (D-54)] is derived from the 2.5-D equation [equation (D-53)—the equivalent of equation (3.79)] by a simple substitution for the 3-D pressure.

In 3-D, 2.5-D, or 2-D, a number of migrated common-offset gathers can be combined to give the stacked reflectivity as the average of reflectivities obtained using equations (3.78)/(D-52), (3.79)/(D-53) or (D-54), respectively:

$$\overline{R}_{co}(\mathbf{x}_G)\equiv\frac{1}{N_{\mathrm{co}}}\sum_{co=1}^{N_{\mathrm{co}}}\hat{R}_\theta(\mathbf{x}_G,\xi_{\mathrm{co}}). \qquad (3.80)$$

Comparing equation (3.80) to equation (3.76), the summation is now over the number of offsets instead of the number of shots. As we will discover in Chapter 4, the typical implementation of prestack time migration using the method of equivalent-offset does not distinguish between different common-shot or common-offset gathers—all traces lying within the migration aperture are included in the sum. Hence, one might think that the choice between the equation combinations (3.76) and (3.80) is a matter of preference. However, it will be shown that an average of common-shot records is a poor choice. The correct equation is (3.80), i.e. an average of common-offset weights. An unexpected result is that a better result than equation (3.76) (i.e. the sum of migrated shot gathers divided by the number of shots) is obtained by summing migrated shot gathers and dividing by the number of offsets; although there is no difference between the two normalization factors if the objective is relative-true amplitude reflectivity to within a constant factor.

3.11 SUMMARY

Two approaches to depth imaging were developed in this Chapter. The classical migration approach combines inverse wavefield extrapolation with Claerbout's 'deconvolution' imaging condition. The Born-approximate inversion approach inserts the forward modeling formula for the volume scattered wavefield into a Fourier transform-like inversion formula for wavespeed perturbation, then re-expresses this result as a band-limited reflectivity function. For the common-shot configuration, both approaches give essentially identical results.

The classical migration approach was developed from first principles. Ray-theoretical Kirchhoff-approximate expressions were derived for one-way forward modeling and one-way inverse wavefield propagation with the assumption that the data are synthesized or recorded on one nonplanar interface. The prestack 'deconvolution' imaging condition was shown to be an optimal chi-squared estimator if weighted by a bandlimited source function, and Docherty's ray-theoretical Kirchhoff-approximate common-shot migration formula was shown to be equivalent to a simpler derivation based on the Rayleigh II integral. Hence, the Kirchhoff-approximate migration formula is strictly valid only for data recorded on a planar surface. Classical migration does not provide a theoretical basis for creating a stacked reflectivity section, other than a simple summation of migrated shot records. A more optimal approach is desired.

In addition, classical migration is not applicable to non-physical wavefields such as common-offset configurations. The Born-approximate forward modeling formula was derived as a basis for more generalized depth imaging expressions, and shown to be asymptotically equivalent to the Kirchhoff-approximate modeling formula by expressing both in the form of isochron stacks. The similarity of the modeling formulas justifies substituting the geometrical-optics reflection coefficient for the more restricted linearized Born reflection coefficient in the final inversion formula.

In Appendix D, relationships between 2-D, 2.5-D and 3-D constant-wavespeed modeling and migration/ inversion formulae are derived, and the formulae are re-expressed in a more physically intuitive form using out-of-plane spreading factors and source/receiver directivities. In Chapter 4, the equivalent formulae from Appendix D are re-expressed in the time-domain. The time-domain versions are then used as a starting point for deriving appropriate expressions for accurate prestack time migration using the method of equivalent offset. The optimum weight will turn out to be [equation (3.80)], the common offset weight.

CHAPTER 4: RELATIVE-AMPLITUDE PRESERVING PRESTACK TIME MIGRATION BY THE EQUIVALENT OFFSET METHOD (EOM)

4.1 INTRODUCTION

In this chapter, the migration/inversion formulae developed in Chapter 3 are used to determine an optimal weighting function for prestack time migration by the equivalent offset method (EOM). The optimal weighting function is then modified to give a practical weighting function. Here, 'optimal' is defined such that output at each subsurface point is bandlimited 'stacked reflectivity', i.e. a stack of migrated gathers where the peak amplitude is equivalent to an unbiased average of angle-dependent reflectivity. 'Practical' is defined such that the implementation is computationally efficient and suitably simple, given the approximations inherent in EOM prestack time migration.

In Section 4.2, the 3-D and 2.5-D constant-wavespeed frequency-domain migration/ inversion formulae introduced in Section 3.10 are re-expressed as their time-domain equivalents. In Section 4.3, expressions for stacked reflectivity are developed as simple averages over migrated common-shot gathers [see equation (3.76)], migrated common-receiver gathers, and migrated common-offset gathers [see equation (3.80)]. In Section 4.4, a simple model consisting of an impulsive source, a single planar reflector, and a non-reflective planar acquisition surface is used to compare the various 2.5-D and 3-D migration/inversion weights over a complete range of reflector dips and depths. The common-offset formulae are shown to be the optimal weighting functions for both 2.5-D and 3-D stacked reflectivity, while the common-shot and common-receiver formulae result in dip- and depth-dependent bias errors.

In Section 4.5, the optimal time-domain common-offset constant-wavespeed ‘depth-migration’ formulae are converted to practical ‘time-migration’ formulae. In fact, the conversion starts in the other direction, from two-way traveltime coordinates of the input data space to a ‘pseudo-depth’ coordinate of the output image space. For 2.5-D or 3-D, a constant-wavespeed reference model is defined with a vertical coordinate of two-way traveltime corresponding to the apex of a ‘best-fit’ prestack constant-wavespeed diffraction surface in the input data space. The pseudo-depth coordinate is half the wavespeed multiplied by the two-way traveltime. In a true constant-wavespeed medium, this conversion from time migration to depth migration is exact. The optimal common-offset constant-wavespeed depth migration formula developed previously can be adapted to give output images of true-amplitude reflectivity with a vertical axis of time. The optimal common-offset weighting function is then simplified to yield a ‘practical’ weighting function, i.e. one that can be implemented efficiently as a time migration. However, efficiency is achieved with a loss of accuracy that manifests itself as a dip-and angle-dependent bias compared to the desired result.

In Sections 4.6, a number of different practical weighting functions for 2.5-D and 3-D stacked migration are derived and compared, including functions suggested by Dellinger et al. (2000) and Zhang et al. (2000). In Section 4.7, the concept of double-downward continuation is shown to produce poor weights. The equations of Wiggins (1984) are presented for comparison, but the method has been suggested by a number of authors, including the recursive double-downward continuation scheme of Schultz and Sherwood (1980) and the f-k (frequency-wavenumber or Stolt) prestack migration scheme of Stolt (1978) and Stolt and Weglein (1985) (see also discussion of contribution 10 in Section 1.7). Since the EWM scheme of Margrave et al. (1999)—the Fourier analogue of EOM—is based on Stolt prestack theory, EWM does not produce true-amplitude estimates of the reflectivity coefficient. Finally, the important equations and concepts are summarized in Section 4.11.

4.2 TIME-DOMAIN FORMULAE FOR TRUE-AMPLITUDE CONSTANT-WAVESPEED MIGRATION

A ‘true-amplitude’ migration, as defined by Gray (1997), is “a migration method capable of undoing [all the amplitude distortions of wave propagation between the sources and the receivers] and thus producing [estimates of] angle-dependent reflection coefficients at analysis points in a lossless, isotropic, elastic earth”. This definition necessarily implies a prestack migration scheme[1]. A stack or average of angle-dependent reflection coefficients from a number of common-shot or common-offset gathers will combine estimates from a number of angles. The range of angles over which estimates are available will depend on the receiver aperture, survey aperture, depth and dip of the reflector, subsurface velocity above the reflector, and recording time. In extending the ‘true-amplitude migration’ definition to stacked reflectivity, then, the best that we can hope for is consistent averaging of angle-dependent reflectivities, i.e. that the same dip at the same depth is imaged with the same amplitude no matter what the orientation of the dip relative to the acquisition configuration. This is the criterion used in this chapter to evaluate the accuracy of the stacked reflectivity[2].

---

[1] In Gray’s definition, accurate positioning of the analysis points is implied, but not necessary.

[2] Bleistein et al. (1987) and Bleistein (1987) show that weighting functions other than a simple stack or average can be designed for estimating particular subsurface properties and wavefield parameters, such as subsurface wavespeed or specular reflection angle. In some cases, the desired estimate is obtained as a ratio of two images created with different weighting functions, i.e. as a double diffraction stack (Tygel et al., 1993; Hanitzsch, 1995). Further details can be found in Hanitzsch (1997) and Bleistein et al. (2000).

What is meant by angle-dependent reflectivity? Simply put, reflectivity is just a ratio of the scattered and incident wavefield amplitudes as measured at the reflector, with the angle measured between the ray direction and the interface normal (this definition assumes that the reflector has large curvature, i.e. the Kirchhoff aperture is large compared to the wavelength). In the general acoustic case (or the isotropic elastic P-P case), the incident and scattering angles will not be equal. However, by applying continuity conditions at a planar interface, it can be shown (e.g. Aki and Richards, 1980) that all of the scattered energy is reflected at the specular angle (angle of incidence equals the angle of reflection). Thus a ratio of the amplitude of the wavefield just prior to and just after scattering will give the angle-dependent reflection coefficient for the angle of incidence.

The simplest conceptual model for a true-amplitude migration scheme is as follows: inverse propagate the recorded wavefield from the surface positions of the receivers, extract the amplitude at the subsurface position of the reflector, and divide that amplitude by the amplitude of a synthetic wavefield forward propagated from the source location (again, extracted at the reflector)[3]. With real seismic data, there are a number of practical problems that must be addressed if this procedure is to be even remotely accurate, not the least of which are limitations inherent in the simplified mathematical model that allows us to propagate the wavefield in a computer. Typical simplifications that strongly influence amplitudes include: ignoring mode conversion, ignoring anisotropy, failing to correct for attenuation, and failing to account for fine detail in the background wavespeed model (Gray, 1997). However, by using synthetic data generated from a greatly

---

[3] A second conceptual model—backprojection operators derived by inversion of a Fourier transform-like forward modeling integral (i.e. inverse GRT, see discussion in Section 4.2.2) —are more general but less intuitively related to reflectivity.

simplified model, these practical problems can be ignored; i.e. a true-amplitude migration scheme can be tested under ideal conditions.

4.2.1 Simple synthetic model for testing true-amplitude migration schemes

One of the simplest synthetic models is a single planar 'reflecting' surface of arbitrary dip lying in a constant velocity medium. The sources and receivers lie on a planar 'acquisition' surface that does not act as a physical boundary; thus there are no free-surface effects or multiples. Figure 4.1a shows a source at location $\mathbf{x}_s$ that emits a bandlimited impulse of pressure at time $t = 0$, and a receiver at location $\mathbf{x}_g$ that records pressure of the upgoing reflected wavefield. Other source-receiver pairs cover a limited area (i.e., 'aperture') over the acquisition surface *S*, where each line in Figure 4.1a represents the fixed offset and azimuth of a subset of possible shot-receiver pairs in a single 3-D common-offset configuration. For a 2.5-D survey, the shots and the receivers are assumed to lie along a line oriented in the dip direction of the 2-D subsurface structure, as shown by the shot-gather configurations illustrated in Figure 4.1b (one-sided spread on the left, split-spread on the right). The imaging point $\mathbf{x}_G$ could be located anywhere in the subsurface for a 3-D survey, and anywhere directly beneath the acquisition line for a 2.5-D survey, as shown in Figures 4.1a and 4.1b. However, the migration aperture chosen for the synthetic tests is always large enough and positioned so as to record data without truncation. Also, the spatial sampling interval of shots and receivers is sufficient to eliminate spatial aliasing. If $\mathbf{x}_G$ lies on the planar reflecting surface Σ, the migration/inversion formulae should give the reflectivity coefficient. Otherwise, the amplitude will correspond to the tail of a zero-phase bandlimited wavelet, which will be effectively zero except near the reflector.

a)

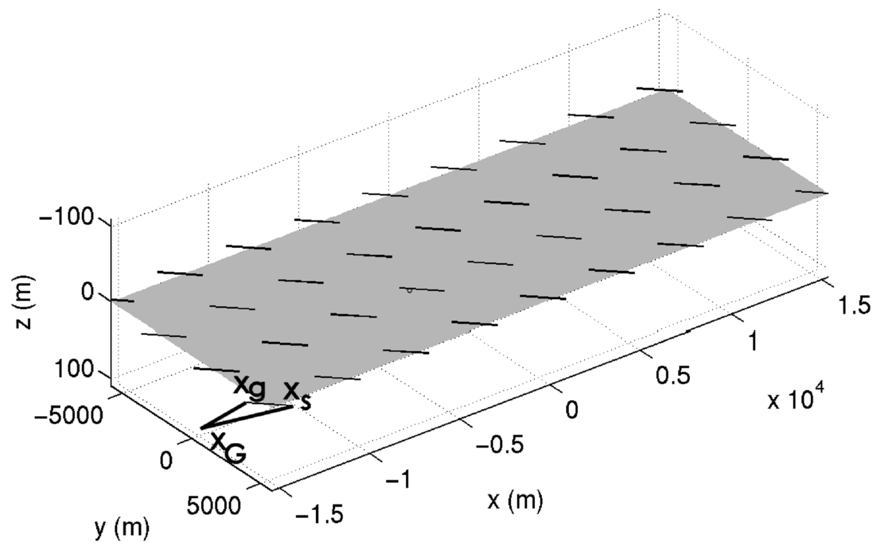

b)

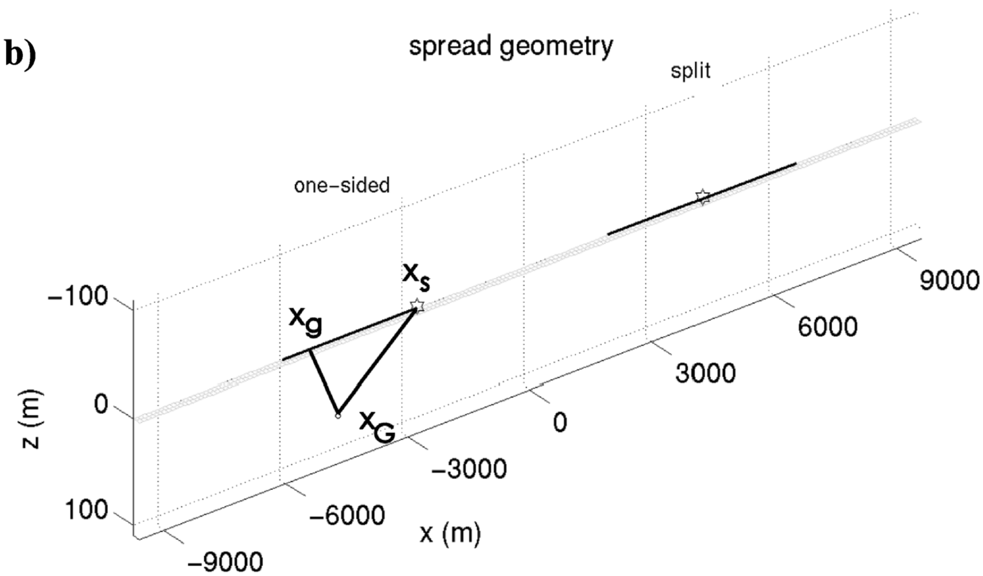

Figure 4.1. a) Reference figure for 3-D common-offset common-azimuth acquisition configuration used in simple constant-wavespeed synthetic tests. Source is located at $\mathbf{x}_s$, receiver at $\mathbf{x}_g$, and imaging point on reflector surface at $\mathbf{x}_G$. Lines are subset of possible common-offset source-receiver pairs. b) Reference figure for 2.5-D common-offset acquisition configuration. Source is located at $\mathbf{x}_s$, receiver at $\mathbf{x}_g$, and imaging point on reflector surface at $\mathbf{x}_G$.

4.2.2 Conversion of 3-D common-shot migration/inversion formula for constant wavespeed from the frequency-domain to the time-domain

Before proceeding with the derivation of time-migration formulae, the frequency-domain constant-wavespeed depth-migration formulae introduced in Chapter 3 need to be converted to the time domain. The 3-D common-shot migration/inversion formula for constant wavespeed is given by equation (3.74) or, equivalently, equation (D-46), either of which can be re-expressed as a time-domain weighted diffraction stack using the Fourier transform convention defined by equation (A.11) to give

$$\underset{(3-D)}{\hat{R}_\theta}(\mathbf{x}_G, \mathbf{x}_s) = -\int_{\mathbf{x}_g} dS \left\{ \frac{r_{Gs}}{r_{gG}} \frac{2\cos\theta_{gG}}{c_0} \right\} \left[\hat{f}(t) * \frac{\partial}{\partial t} \underset{(3-D)}{p_S^-}(\mathbf{x}_g, \mathbf{x}_s, t) \right]_{t=(r_{Gs}+r_{gG})/c_0} . \tag{4.1}$$

Equation (4.1) says that the 3-D formula for angle-dependent reflectivity $\hat{R}_\theta$ at subsurface imaging point $\mathbf{x}_G$ (given a shot located at $\mathbf{x}_s$) is an integral over receivers $\mathbf{x}_g$ located on the acquisition surface. The integrand consists of a weighting function (curly brackets) multiplied by the filtered time-derivative of the upgoing scattered pressure $p_S^-(\mathbf{x}_g, \mathbf{x}_s, t)$ recorded at time $t = (r_{Gs} + r_{gG})/c_0$ (i.e. at the total travel time from shot to reflector to receiver calculated using straight ray paths in a medium with constant wavespeed c_0). The filter $\hat{f}(t)$ normalizes the recorded wavefield, bandlimits it, and converts it to zero-phase [see Chapter 3.6, especially equation (3.35)].

The weighting function has two parts. The first part includes a ratio of distances r_{Gs}/r_{gG} that accounts for the spherical divergence of a synthetic wavefield forward propagated from the source and corrects for spherical divergence of the recorded wavefield backward propagated from the receivers. The second part is the normalized directivity factor $2\cos\theta_{gG}/c_0$. When combined with the time derivative operator, this part yields twice the normal derivative of the recorded wavefield at the acquisition surface as required by the far-field Rayleigh II approximation to the Kirchhoff integral equation [see Schneider

(Schneider, 1978), (Berkhout, 1985), and Section 2.9 of this dissertation—especially equation (2.66)].

4.2.3 Migration as inverse wavefield propagation and imaging or as inversion of a generalized Radon transform

Equation (4.1) can be derived using either inverse wavefield propagation (far-field only) and a deconvolution imaging condition (Docherty, 1991), or by inversion of Fourier transform-like forward modeling integrals (Bleistein, 1987; Bleistein et al., 2001). The latter can be shown to be equivalent to the inversion of a generalized Radon transform (GRT) (Jaramillo and Bleistein, 1999)[4]. Migration by inverse GRT is more general than the combination of inverse wavefield propagation and imaging because the inverse GRT can be applied to a non-physical wavefield, such as a common-offset gather where each trace is a record of a separate wavefield. Inverse wavefield propagation requires a physical wavefield. Here, I define a physical wavefield as a collection of traces that could be recorded at the same time (no matter how impractical the field experiment) such as a shot gather or a plane-wave synthesized from a number of shot gathers; as well as those collections that could be created by invoking reciprocity, such as common-receiver gathers.

The inverse GRT method can be explained as follows. At the desired output point [$\mathbf{x}_G$ in equation (4.1)], the weighted summation of data values from different traces can be thought of as a weighted superposition of isochron surfaces or, in the far field, as a

---

[4] The inverse GRT method is valid in the high-frequency limit (i.e., also far-field) and can be shown to be equivalent to a plane-wave expansion of a δ function (Jaramillo and Bleistein, 1999). Miller et al. (1987) provide an excellent description of the principle of imaging by inverse GRT, although their goal is wavespeed perturbation, not reflectivity.

weighted superposition of plane waves tangent to the isochron surfaces. The weighting factor for each trace accounts for the forward modeling of the data (the forward GRT) as well as a Jacobian that converts the original integration variables over the acquisition surface into an equi-angular distribution of plane-wave normals about the imaging point. A derivative normal to the plane of specular reflection and appropriate constants convert the weighted summation into a bandlimited reflectivity.

If the collection of plane waves associated with the input traces provide sufficient angular aperture, an accurate value of the reflectivity can be determined. The angular aperture must be wide enough to capture the stationary point—i.e. the specular reflection—plus enough to shift the tail of the finite-aperture artifact (assuming a bandlimited waveform) to somewhere in the image where it does not interfere with the output point[5]. Sun (1998; 2000) calls this the "minimum" migration aperture, but recommends a larger "optimum" aperture where the complete bandlimited waveform at the output point is imaged without any interference from the artifact. The collection of traces required for accurate migration by inverse GRT need only satisfy the aperture requirements, and can therefore be taken from different physical experiments. However, the collection of traces that reconstruct reflectivity at the stationary point (i.e. those that have near-specular raypaths for a given reflector) should vary slowly in offset or, more correctly, vary slowly in the opening-angle at the reflector.

---

[5] The finite-aperture artifact will interfere with peak amplitudes of other reflectivity estimates elsewhere in the image. The effect of the artifact can be minimized with adequate tapering of the aperture (Sun, 2000).

4.2.4 Conversion of 3-D common-offset migration/inversion formula for constant wavespeed from the frequency-domain to the time-domain

The common-offset configuration satisfies the criterion that the opening-angle varies slowly, and provides the largest possible aperture of all acquisition configurations. The 3-D common-offset migration/inversion formula for constant wavespeed is given by equation (3.78) or, equivalently, equation (D-52); either of which can be re-expressed as a time-domain weighted diffraction stack given by

$$\underset{(3-D)}{\hat{R}_{\theta}}(\mathbf{x}_G,\xi_{co}) = -\int_{\xi_{co}} dS \left\{ \frac{(r_{Gs}+r_{gG})}{r_{gG}} \frac{2\cos\theta_{gG}}{c_0} + \frac{(r_{Gs}+r_{gG})}{r_{Gs}} \frac{2\cos\theta_{Gs}}{c_0} \right\}$$
$$\times \left[\hat{f}(t) * \frac{\partial}{\partial t} \underset{(3-D)}{p_S^-}(\mathbf{x}_g,\mathbf{x}_s,t) \right]_{t=(r_{Gs}+r_{gG})/c_0} . \qquad (4.2)$$

In equation (4.2), integration is now over a single common-offset configuration ξ_{CO} of shots and receivers on the acquisition surface. In 3-D, the definition of common-offset is restricted to traces that share common-offset parameters of both distance and azimuth, i.e. common-offset incorporates common-azimuth. Thus, if the receiver layout is identical relative to every shot location, there will be as many common-offset configurations as receivers. The remaining parameters are the same as in equation (4.1).

4.2.5 Conversion of 2.5-D common-shot migration/inversion formula for constant wavespeed from the frequency-domain to the time-domain

In 2.5-D, the sources and receivers are restricted to a line on the planar acquisition surface. The acquisition line is assumed to be oriented in the in plane or 'dip' direction of the reflecting surface. The 2.5-D common-shot migration/inversion formula for constant wavespeed is given by equation (3.75) or, equivalently, equation (D-45); either of which can be re-expressed as a time-domain weighted diffraction stack given by

$$\underset{(2.5-D)}{\hat{R}_{\theta}}(\mathbf{x}_G,\mathbf{x}_s)=\int_{\mathbf{x}_g} dx\left\{\sqrt{2\pi c_0 r_{Gs}+2\pi c_0 r_{gG}}\,\frac{\sqrt{r_{Gs}}}{\sqrt{r_{gG}}}\,\frac{2\cos\theta_{gG}}{c_0}\right\}$$
$$\times\left[\hat{f}(t)*\mathcal{H}\left\{\left(\frac{\partial}{\partial t}\right)^{1/2}\underset{(2.5-D)}{p_S^-}(\mathbf{x}_g,\mathbf{x}_s,t)\right\}\right]_{t=(r_{Gs}+r_{gG})/c_0}. \tag{4.3}$$

In equation (4.3), $(\partial/\partial t)^{1/2}$ is the half-differential operator, $\mathcal{H}$ denotes the Hilbert transform of the seismic trace (i.e. a $\pi/2$ phase shift), and $\underset{(2.5-D)}{p_S^-}(\mathbf{x}_g,\mathbf{x}_s,t)$ is the 3-D acoustic pressure recorded at a point receiver given a point source. The geometry of the subsurface reflectors is assumed to be 2-D (i.e. invariant in the strike or y direction), while integration is over a receiver configuration lying in the in-plane or dip direction.

The relationship between 3-D and 2.5-D common-shot formulae [equation (4.1) and equation (4.3), respectively] is described in Appendix D by equation (D-51). In 2.5-D, the out-of-plane spreading correction, $\sqrt{2\pi c_0 r_{Gs}+2\pi c_0 r_{gG}}$, and a half-integral operator convert the 3-D acoustic pressure to 2-D, in effect synthesizing the acoustic pressure that would have been recorded at a point on a line receiver given a line source, both infinite in the y-direction (see Deregowski and Brown, 1983; Bleistein, 1986). The half-integral operator [see equation (D-44)] has been absorbed into the full time derivative of equation (4.1), yielding the half time derivative of equation (4.3). There are two additional out-of-plane spreading corrections required: the first to backward propagate the now 2-D acoustic pressure to a point on the imaging line in the subsurface [see equation (D.47)] and the second to forward propagate a synthetic 2-D wavefield from the source to the same point on the imaging line [see equation (D-44)]. The combined correction factor, $-i\sqrt{r_{gG}/r_{Gs}}$, cancels the negative sign in equation (4.1), accounts for the Hilbert transform in equation (4.3), and changes the ratio of spherical divergences in equation (4.1) into the ratio of square roots found in equation (4.3).

4.2.6 Conversion of 2.5-D common-offset migration/inversion formula for constant wavespeed from the frequency-domain to the time-domain

The 2.5-D common-offset migration/inversion formula for constant wavespeed is given by equation (3.79) or, equivalently, equation (D-53), either of which can be re-expressed as a time-domain weighted diffraction stack given by

$$\underset{(2.5-D)}{\hat{R}_{\theta}}(\mathbf{x}_G, \xi_{co}) = \int_{\xi_{co}} dx \left\{ \sqrt{2\pi c_0 r_{Gs} + 2\pi c_0 r_{gG}} \left(\frac{\sqrt{r_{Gs}}}{\sqrt{r_{gG}}} \frac{2\cos\theta_{gG}}{c_0} + \frac{\sqrt{r_{gG}}}{\sqrt{r_{Gs}}} \frac{2\cos\theta_{Gs}}{c_0} \right) \right\}$$
$$\times \left[\hat{f}(t) * \mathcal{H}\left\{ \left(\frac{\partial}{\partial t} \right)^{1/2} \underset{(2.5-D)}{p_S^-}(\mathbf{x}_g, \mathbf{x}_s, t) \right\} \right]_{t=(r_{Gs}+r_{gG})/c_0} . \tag{4.4}$$

The integration in equation (4.4) is over a single common-offset configuration ξ_{CO} of shot and receiver pairs lying along a line in the in-plane or dip direction. As with equation (4.3), the geometry of the subsurface reflectors is assumed to be 2-D.

4.3 WEIGHTING FUNCTIONS FOR STACKED REFLECTIVITY IN 3-D AND 2.5-D

A common procedure for forming a composite image of the subsurface is to stack (i.e. average) prestack migrated gathers. If the prestack migrated gathers are obtained by non-recursive summation, as in equations (4.1)-(4.4), the summation and stack operators are both linear and can be combined into a single operator. The output is a stacked migrated image of the subsurface, with peak amplitude equal to an average of angle-dependent reflectivities [see equations (3.76) and (3.80)]. The input data space is now the set of all recorded seismic traces (more correctly, the filtered time derivative of the traces for 3-D, and the filtered Hilbert transform of the half time derivative of the traces for 2.5-D). For a given output point in the subsurface and a given trace (i.e. fixed shot and receiver locations), the desired phase corresponds to the traveltime from shot to subsurface point to receiver. In the time-domain, the phase defines a “diffraction” surface in the data space. Thus, the combined operator can be thought of as a weighted summation over a diffraction surface. This is exactly the kind of operator required for EOM prestack time migration.

4.3.1 Constant wavespeed stacked reflectivity in 3-D

In 3-D, then, the stacked reflectivity can be thought of as the simple weighted sum over all recorded traces, i.e.

$$\underset{(3-D)}{\overline{R}}(\mathbf{x}_G) \approx \sum_{traces} \underset{(3-D)}{\overline{W}}(\mathbf{x}_G,\mathbf{x}_s,\mathbf{x}_g)\left[\hat{f}(t) * \frac{\partial}{\partial t} \underset{(3-D)}{p_S^-}(\mathbf{x}_g,\mathbf{x}_s,t)\right]_{t=(r_{Gs}+r_{gG})/c_0} . \tag{4.5}$$

The weighting function for the 3-D common-shot configuration [see equation (4.1)] is

$$\underset{(3-D)}{\overline{W}_s}(\mathbf{x}_G,\mathbf{x}_s,\mathbf{x}_g) = -\frac{dS_g}{N_s}\left\{\frac{r_{Gs}}{r_{gG}}\frac{2\cos\theta_{gG}}{c_0}\right\}, \tag{4.6}$$

where dS_g is the size of the area element for the receiver distribution (assumed to be uniform) and N_s is the number of shots. The weighting function for the 3-D common-receiver configuration is

$$\underset{(3-D)}{\overline{W}_g}(\mathbf{x}_G,\mathbf{x}_s,\mathbf{x}_g) = -\frac{dS_s}{N_g}\left\{\frac{r_{gG}}{r_{Gs}}\frac{2\cos\theta_{Gs}}{c_0}\right\}. \tag{4.7}$$

where dS_s is the size of the area element for the shot distribution (assumed to be uniform) and N_g is the number of receivers.

Equation (4.7) can be thought of as the reciprocal form of equation (4.6) (i.e. by switching source and receiver locations). In general, these common-shot and common-receiver weighting functions do not produce equivalent values of stacked reflectivity for a given set of input data. The only acquisition configuration where they do is a symmetric split spread, occasionally encountered in land 3-D seismic but almost never in marine.

The weighting function for the 3-D common-offset configuration [see equation (4.2)] is

$$\overline{W}_{\substack{co\\(3-D)}}(\mathbf{x}_G,\mathbf{x}_s,\mathbf{x}_g) = -\frac{dS_s}{N_{co}}\left\{\frac{(r_{Gs}+r_{gG})}{r_{gG}}\frac{2\cos\theta_{gG}}{c_0}+\frac{(r_{Gs}+r_{gG})}{r_{Gs}}\frac{2\cos\theta_{Gs}}{c_0}\right\}, \tag{4.8}$$

where dS_s is the size of the area element for the shot distribution (again, assumed to be uniform). Note that it is the area element for the shot distribution, not the area element for the receiver distribution (or some combination of the two), that determines the separation of adjacent common-offset traces. As mentioned previously, if the receiver layout is identical relative to every shot location, there will be as many common-offset configurations as receivers $(N_{co} = N_g)$.

The main difference between the common-shot weight [equation (4.6)] and the common-offset weight [equation (4.8)] is contained in the curly brackets. Note that the common-offset weight is not a simple multiple of the common-shot weight term. The common-offset weight appears to be a linear combination of a common-shot migration weight given by $(r_{Gs}/r_{gG})2\cos\theta_{gG}/c_0$, a common-receiver migration weight given by $(r_{gG}/r_{Gs})2\cos\theta_{Gs}/c_0$, and two hybrid migration weights: a common-shot migration weight $(r_{gG}/r_{gG})2\cos\theta_{gG}/c_0$ where the forward modeling is from the receiver to the subsurface location, and a common-receiver migration weight $(r_{Gs}/r_{Gs})2\cos\theta_{Gs}/c_0$ where the forward modeling is from the shot to the subsurface location. It is clear, then, that an average of N_s common-shot gathers (or N_g common-receiver gathers) will not equal an average of N_{co} common-offset gathers. Other weighting functions could be designed to give equivalent estimates from the different acquisition configurations after averaging, but these would be not produce accurate estimates of angle-dependent reflectivity before averaging, and would not be considered standard weights given current practice.

4.3.2 Constant wavespeed stacked reflectivity in 2.5-D

The situation is similar in 2.5-D, where the stacked reflectivity can be thought of as the simple weighted sum

$$\underset{(2.5-D)}{\overline{R}}(\mathbf{x}_G) \approx \sum_{traces} \underset{(2.5-D)}{\overline{W}}(\mathbf{x}_G, \mathbf{x}_s, \mathbf{x}_g) \left[\hat{f}(t) * \mathcal{H}\left\{ \left(\frac{\partial}{\partial t} \right)^{1/2} \underset{(2.5-D)}{p_S^-}(\mathbf{x}_g, \mathbf{x}_s, t) \right\} \right]_{t=(r_{Gs}+r_{gG})/c_0} . \quad (4.9)$$

The weighting function for the 2.5-D common-shot configuration [see equation (4.3)] is

$$\underset{(2.5-D)}{\overline{W}_s}(\mathbf{x}_G, \mathbf{x}_s, \mathbf{x}_g) = \frac{dx_g}{N_s} \left\{ \sqrt{2\pi c_0 r_{Gs} + 2\pi c_0 r_{gG}} \frac{\sqrt{r_{Gs}}}{\sqrt{r_{gG}}} \frac{2\cos\theta_{gG}}{c_0} \right\}, \quad (4.10)$$

where dx_g is the length of the line element for each receiver (assumed to be uniform).

Invoking reciprocity, the weighting function for the 2.5-D common-receiver configuration is

$$\underset{(2.5-D)}{\overline{W}_g}(\mathbf{x}_G, \mathbf{x}_s, \mathbf{x}_g) = \frac{dx_s}{N_g} \left\{ \sqrt{2\pi c_0 r_{Gs} + 2\pi c_0 r_{gG}} \frac{\sqrt{r_{gG}}}{\sqrt{r_{Gs}}} \frac{2\cos\theta_{Gs}}{c_0} \right\}, \quad (4.11)$$

where dx_s is the length of the line element for each shot (again, assumed to be uniform).

The weighting function for the 2.5-D common-offset configuration [see equation (4.4)] is

$$\underset{(2.5-D)}{\overline{W}_{co}}(\mathbf{x}_G, \mathbf{x}_s, \mathbf{x}_g) = \frac{dx_s}{N_{co}} \left\{ \sqrt{2\pi c_0 r_{Gs} + 2\pi c_0 r_{gG}} \left(\frac{\sqrt{r_{Gs}}}{\sqrt{r_{gG}}} \frac{2\cos\theta_{gG}}{c_0} + \frac{\sqrt{r_{gG}}}{\sqrt{r_{Gs}}} \frac{2\cos\theta_{Gs}}{c_0} \right) \right\}. \quad (4.12)$$

As in the 3-D case, the 2.5-D common-offset weight [equation (4.12)] is not a simple multiple of the common-shot weight [equation (4.10)]. Now, the common-offset weight appears to be a linear combination of a common-shot migration and a common-receiver migration.

4.3.3 Stacked reflectivity-common-shot or common-offset weights?

The above analysis of 3-D and 2.5-D constant-wavespeed migration/inversion formulae shows that the stacked reflectivity created by an average of N_s common-shot gathers (or N_g common-receiver gathers) will not be the same as the stacked reflectivity created by an average of N_{co} common-offset gathers. This suggests two questions that can be addressed by synthetic studies: first, which weighting formula is more correct? and second (since I have already hinted that the common-offset formula is the correct one), what are the characteristics of the bias error that arises from a stack of common-shot or common-receiver gathers?

A third question, which will not be addressed in this study, is: what weighting function could be applied in common shot migration to give the same result as in common-offset migration? The answer to this question is simple for a diffraction stack migration — use the common-offset weighting function. Unfortunately, this weighting function cannot be implemented easily in recursive applications such as downward continuation combined with an imaging condition. As shown in Section 3.7, the common-shot weighting function (for 2-D and 3-D) arises naturally from Claerbout's deconvolution imaging condition. This topic is left for further research.

4.4 SYNTHETIC TESTS TO DETERMINE OPTIMUM WEIGHTS FOR STACKED REFLECTIVITY

The simple model described in Section 4.2 can be used to test the migration weighting functions developed in Section 4.3. As a quick review, the model consists of a single planar reflector of arbitrary dip with a reflectivity coefficient of unity lying in a constant wavespeed medium (Figure 4.1). Synthetic data are generated on a non-reflective planar surface at a sufficiently small sampling interval to eliminate aliasing, and over a sufficiently large survey size to guarantee accurate reconstruction of the reflectivity coefficient. For simplicity $dx_s = dx_g$ for all 2.5-D tests, and $dS_s = dS_g$ for all 3-D tests. The effects of and remedies for insufficient or irregular sampling are not examined in this dissertation.

Given linearity, the summation weights [curly brackets in equations (4.6)-(4.8) and (4.10)-(4.12)] and stack normalization factors (N_s, N_g, or N_{co}) can be applied in any order. It will be beneficial to compare the effect of the summation weights in a common domain prior to stacking. This is most easily done in the common-offset domain. The effect of stacking, then, will be to average the result over a range of common-offsets. In fact, it turns out that the optimum normalization factor for all domains is the number of common-offsets N_{co}. Otherwise, for an average of N_s migrated common-shot gathers, the output reflectivity is biased by a factor of N_s / N_{co} (and similarly for an average of N_g migrated common-receiver gathers).

All imaging is assumed to occur in the far field (> 3 or π dominant wavelengths, see Bleistein et al., 2001, p. 6). Using a constant wavespeed of 4000 ms^{-1} and a zero-phase wavelet with a dominant frequency of 25 Hz, the dominant wavelength is 160 m and the far field is anything greater than ~500 m. Hence, with a fixed half-offset of 1000 m and minimum imaging depth of 500 m, the far-field assumption is justified and all results can then be plotted in terms of normalized spatial coordinates. Results from the 2.5-D tests will be presented first.

4.4.1 Synthetic tests comparing 2.5-D common-shot and common-offset weights

Figure 4.2 shows the reconstructed amplitudes of the reflectivity coefficient $\underset{(2.5-D)}{\hat{R}_\theta}$ for a complete range of both reflector dip-angles and depths using the 2.5-D common-offset migration/inversion formula [equation (4.4), or equations (4.9)/(4.12) with $N_{co} = 1$]. Figure 4.2a is a perspective view of Figure 4.2b. The horizontal (x) and vertical (z) axes are normalized to source-receiver offset h. In Figure 4.2b dashed contours show the dip angles; the solid line is a portion of an ellipse showing a representative isochron. The desired reflectivity coefficient of 1.00 is recovered everywhere, except for dips approaching 90 degrees. The error is less than 5% in the upper left and right corners (dotted contours) where an infinite recording aperture is required, as expected for steep dips in constant velocity. The effect of stacking a limited receiver aperture is equivalent to averaging the reflectivities over a number of offsets, i.e. over a finite line-length at constant dip in the normalized coordinates (e.g., white line for 45° dip in Figures 4.2b, and 4.3b, black line for 45° dip in Figure 4.4b).

Figure 4.3 shows the reconstructed amplitudes using the same common-offset acquisition configuration but with the common-shot weights (times a factor of 2)[6] as given by equation (4.3) [or equations (4.9)/(4.10) with $N_s = 1$]. Dips are the same as in Figure 4.2b and are not contoured. Instead, the reflectivity coefficient is contoured: solid contours are increments of 0.1, dashed contours are increments of 0.05 ranging from 0.55-1.45, and dotted contours are increments of 0.01 from 0.91-1.09, with dark indicating values larger than 1.0. The smallest values (less than 0.2) correspond to shooting down-dip (sailing up-dip) while the largest values (greater than 1.9) correspond to shooting up-dip (sailing down-dip): thus, there is as much as an order of magnitude difference in amplitude. Stacking is equivalent to averaging over a finite line-length at constant dip (e.g., white line, as in Figure 4.2b). After stack, reflectors of the same dip but at different depths will be imaged with different reflectivities.

---

[6] An extra factor of two is included to normalize the common-shot weight (and the common-receiver weight) to the common-offset configuration. To see that this might be required, note that in 2.5-D, for example, equation (4.12) is more like a sum of equations (4.10) and (4.11) instead of an average.

a)
b)

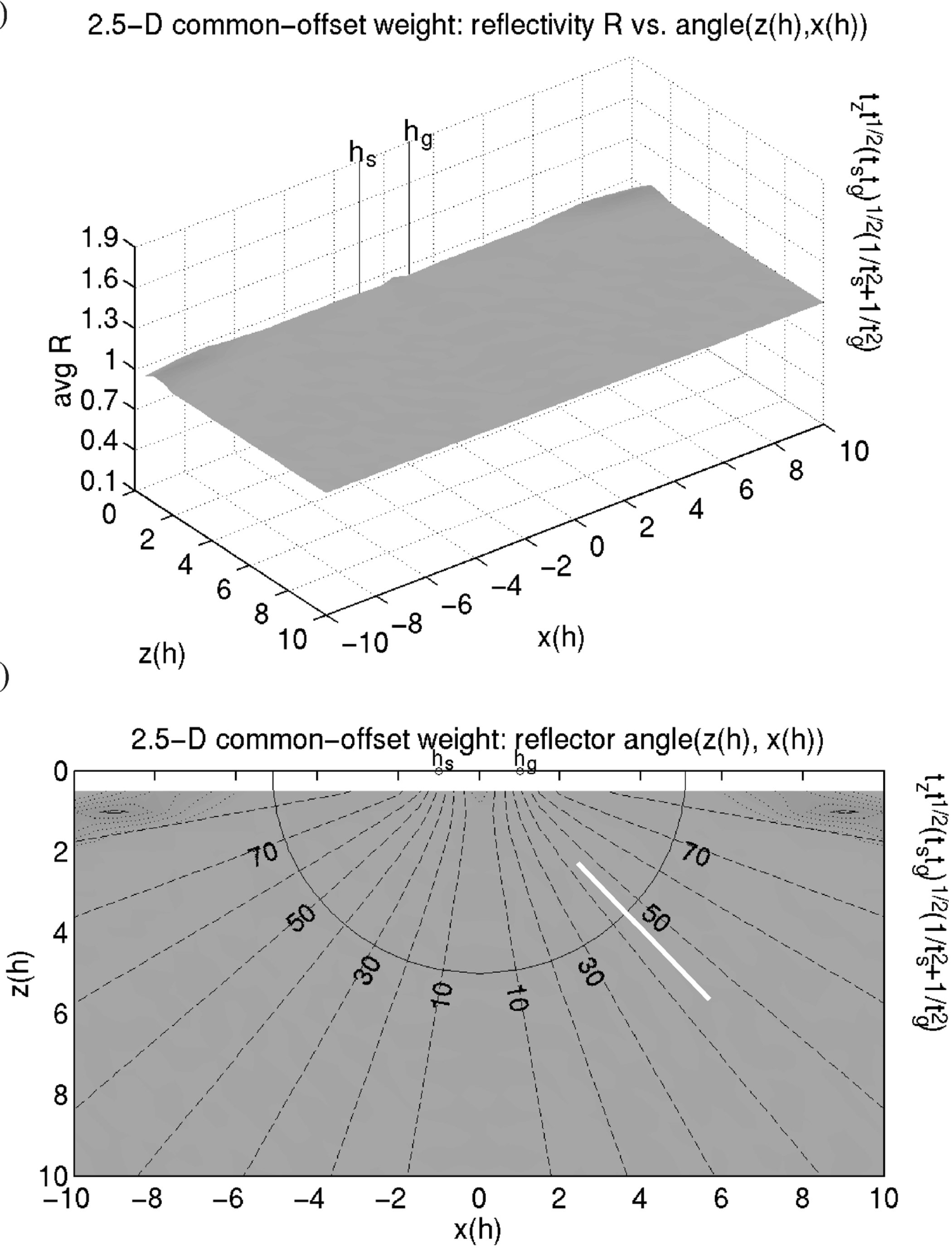

Figure 4.2. a) Perspective view of reflector amplitudes imaged in constant wavespeed subsurface using the exact 2.5-D common-offset weight [equation (4.5)/(4.8) with N_{co} = 1]. Expected reflectivity coefficient of 1.0 is recovered exactly almost everywhere. Horizontal distance $x(h)$ and depth $z(h)$ are normalized to half-offset h, and measured from the shot-receiver midpoint to the specular reflection point. b) A complete range of dips and depths are tested. The dashed lines are constant dip angle. Oval line is an isochron. Dotted lines (upper left and right corners) are contours of imaged amplitudes, interval 0.01. A stacked migrated section is an average over offset, e.g. average over white line for single reflector at 45° dip.

a)

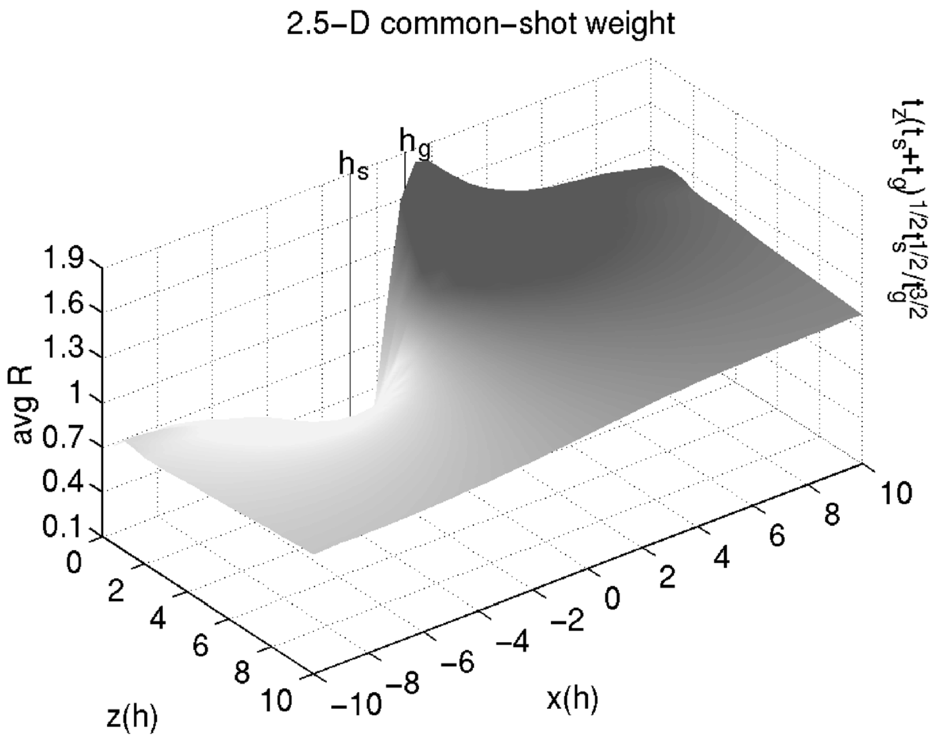

b)

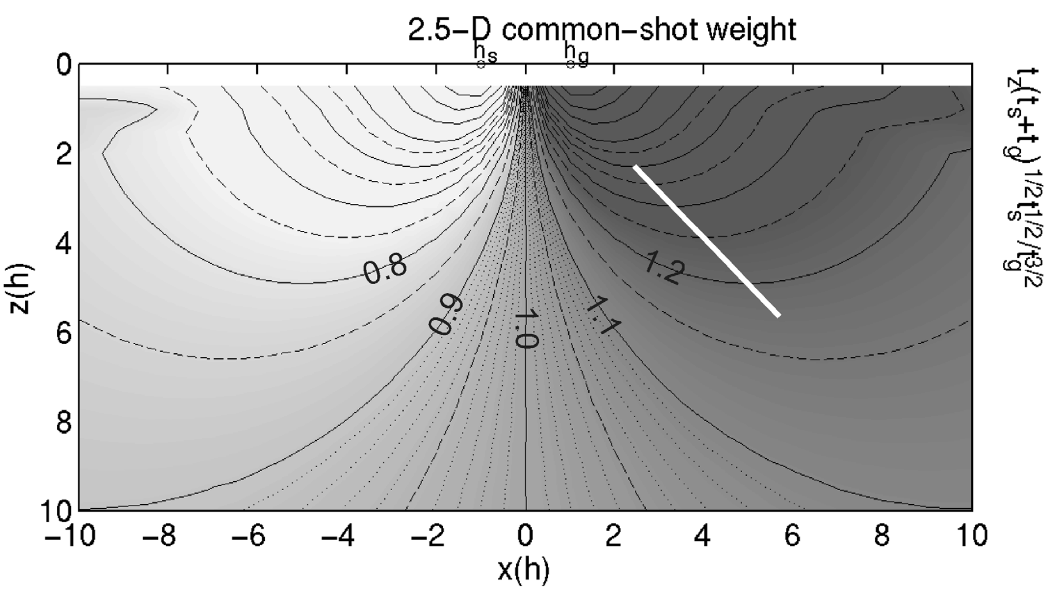

Figure 4.3. a) Perspective view of reflector amplitudes imaged in constant wavespeed subsurface using the 2.5-D common-shot weight [equation (4.5)/(4.6) with $N_s = 1$]. Expected reflectivity coefficient of 1.0 is biased everywhere except at zero dip. Horizontal distance $x(h)$ and depth $z(h)$ are normalized to half-offset h, and measured from the shot-receiver midpoint to the specular reflection point. . b) Contours of imaged amplitude of reflector, intervals 0.1 (solid lines), 0.05 (dashed lines) and 0.01 (dotted lines). A stacked migrated section is an average over offset, e.g. average over white line for single reflector at 45° dip.

Figure 4.4 shows the reconstructed amplitudes for the common-receiver weights (times a factor of 2), or equivalently, common-shot weights assuming the source location and receiver locations are switched (e.g. a one-sided marine spread towed in the opposite direction). The bias error is equal and opposite to that found in Figure 4.3 and, as expected from the formulae, summing the common-shot weights and common-receiver weights (with no factors of 2) yields the unbiased common-offset result (Figure 4.2). This relationship is explored in more detail in Figures 4.5-4.6. As before, Figures 4.5a and 4.6a are reference diagrams to indicate 2.5-D acquisition geometry, while Figures 4.5b and 4.6b show the range of dip angles (dashed contour) and a representative isochron (solid contour). Each offset in a symmetric split spread will have a corresponding negative offset.

This pair can be represented in a common-offset configuration by orienting either the receiver-side or the shot-side towards the updip direction of the reflector. In Figure 4.5, the common-shot weight on the receiver-side (Figure 4.5c-d) and shot-side (Figure 4.5e-f) are summed, yielding an unbiased result (Figure 4.5g-h). In Figure 4.6, the common-receiver weight on the receiver-side (Figure 4.6c-d) and shot-side (Figure 4.6e-f) are summed, yielding an unbiased result (Figure 4.6g-h). As suggested previously, the bias errors cancel for a symmetric split spread.

In Figure 4.7, the full bandlimited wavelet is imaged at horizontal and dipping (-45° and +45°) reflectors using both a one-sided and symmetric split spread. The peak amplitude is the 'stacked reflectivity' given by the common-shot weight, i.e. equations (4.9)/(4.10) except that the normalization factor is the number of offsets N_{co} (equal to the number of receivers N_g) instead of the number of shots N_s. Output is in two-way traveltime, which can be converted directly to depth (e.g. 1.5 s corresponds to a depth of 3000 m at 4000 ms^{-1}). Output traces are separated by an arbitrary horizontal spacing of 100 m.

a)

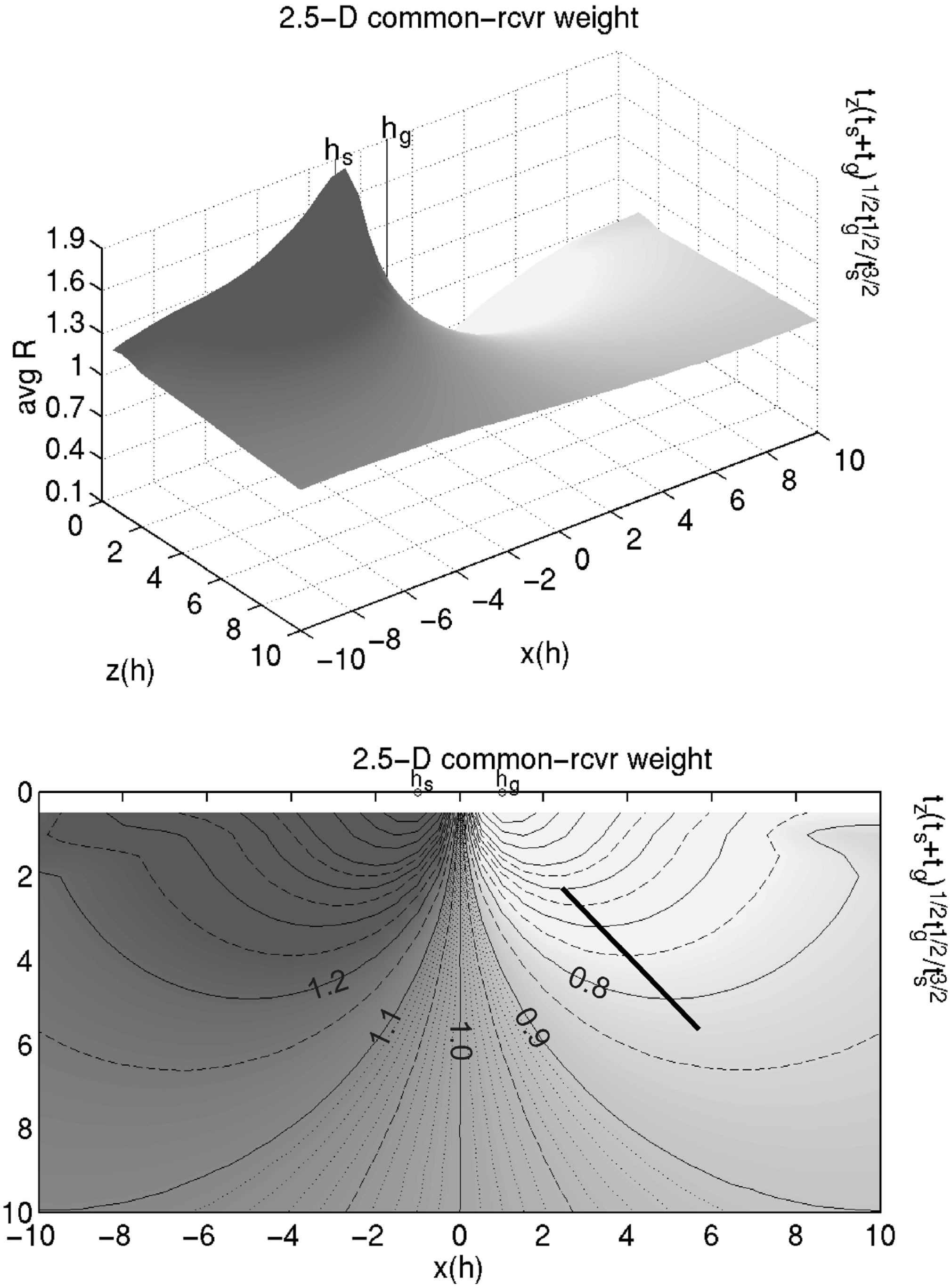

b)

Figure 4.4. a) Perspective view of reflector amplitudes imaged in constant wavespeed subsurface using the 2.5-D common-receiver weight [equation (4.5)/(4.7) with $N_g = 1$]. Expected reflectivity coefficient of 1.0 is biased everywhere except at zero dip. Horizontal distance $x(h)$ and depth $z(h)$ are normalized to half-offset h, and measured from the shot-receiver midpoint to the specular reflection point. b) Contours of imaged amplitude of reflector, intervals 0.1 (solid lines), 0.05 (dashed lines) and 0.01 (dotted lines). A stacked migrated section is an average over offset, e.g. average over black line for single reflector at 45° dip.

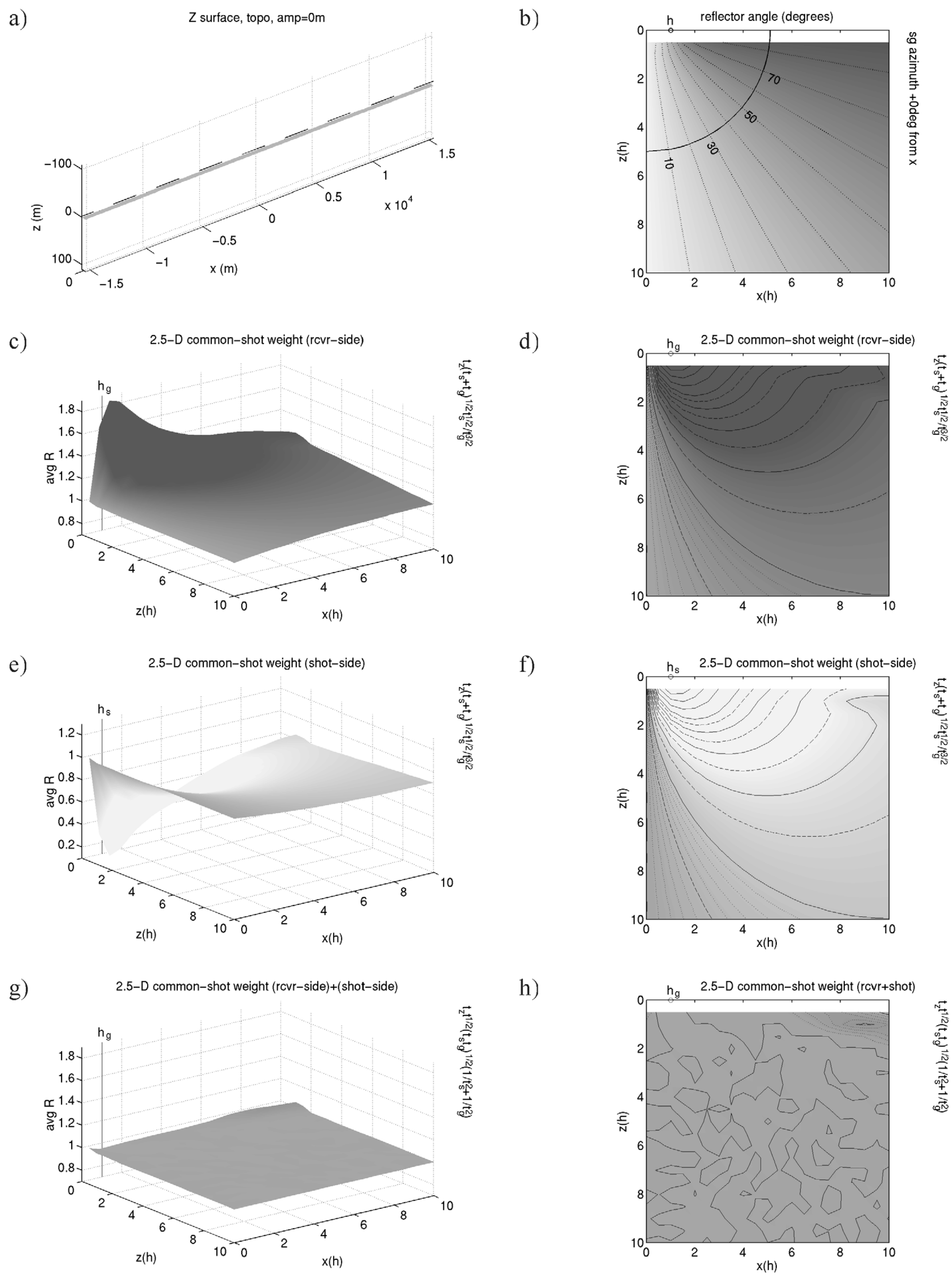

Figure 4.5. For the 2.5-D common-shot weight, the dip-and depth-dependent bias on the receiver side (c-d) and shot side (e-f) are equal and opposite. The average (g-h) equals the exact common-offset weighting function [compare equations (4.10) and (4.11) with (4.12)]. a) 2.5-D reference diagram. b) Reflector-dip reference diagram. c-h) Perspective view and contours of imaged amplitude of reflector with intervals of 0.1 (solid lines), 0.05 (dashed lines) and 0.01 (dotted lines).

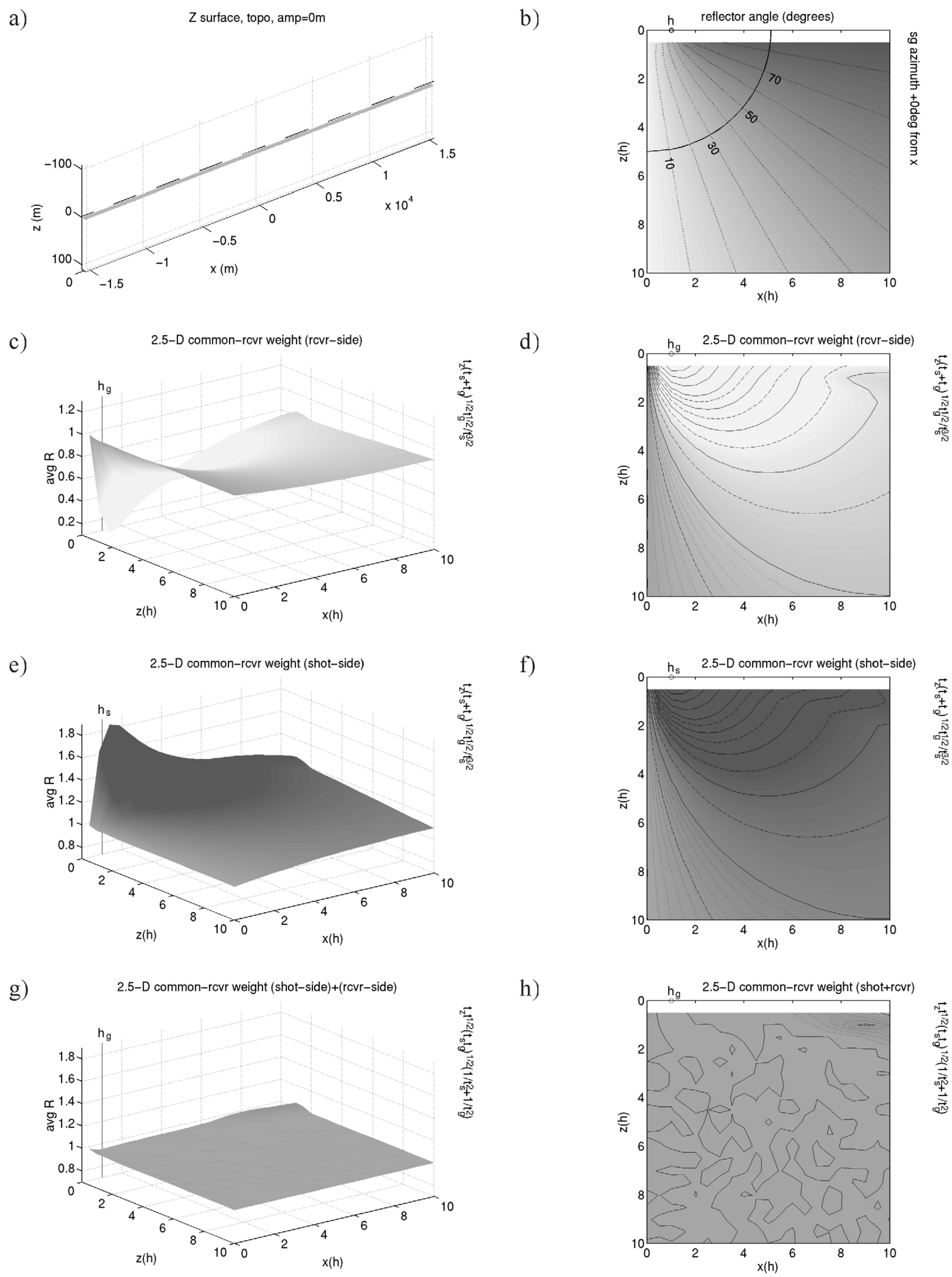

Figure 4.6. For the 2.5-D common-receiver weight, the dip-and depth-dependent bias on the shot side (c-d) and receiver side (e-f) are equal and opposite. The average (g-h) equals the exact common-offset weighting function [compare equations (4.10) and (4.11) with (4.12)]. a) 2.5-D reference diagram. b) Reflector-dip reference diagram. c-h) Perspective view and contours of imaged amplitude of reflector with intervals of 0.1 (solid lines), 0.05 (dashed lines) and 0.01 (dotted lines).

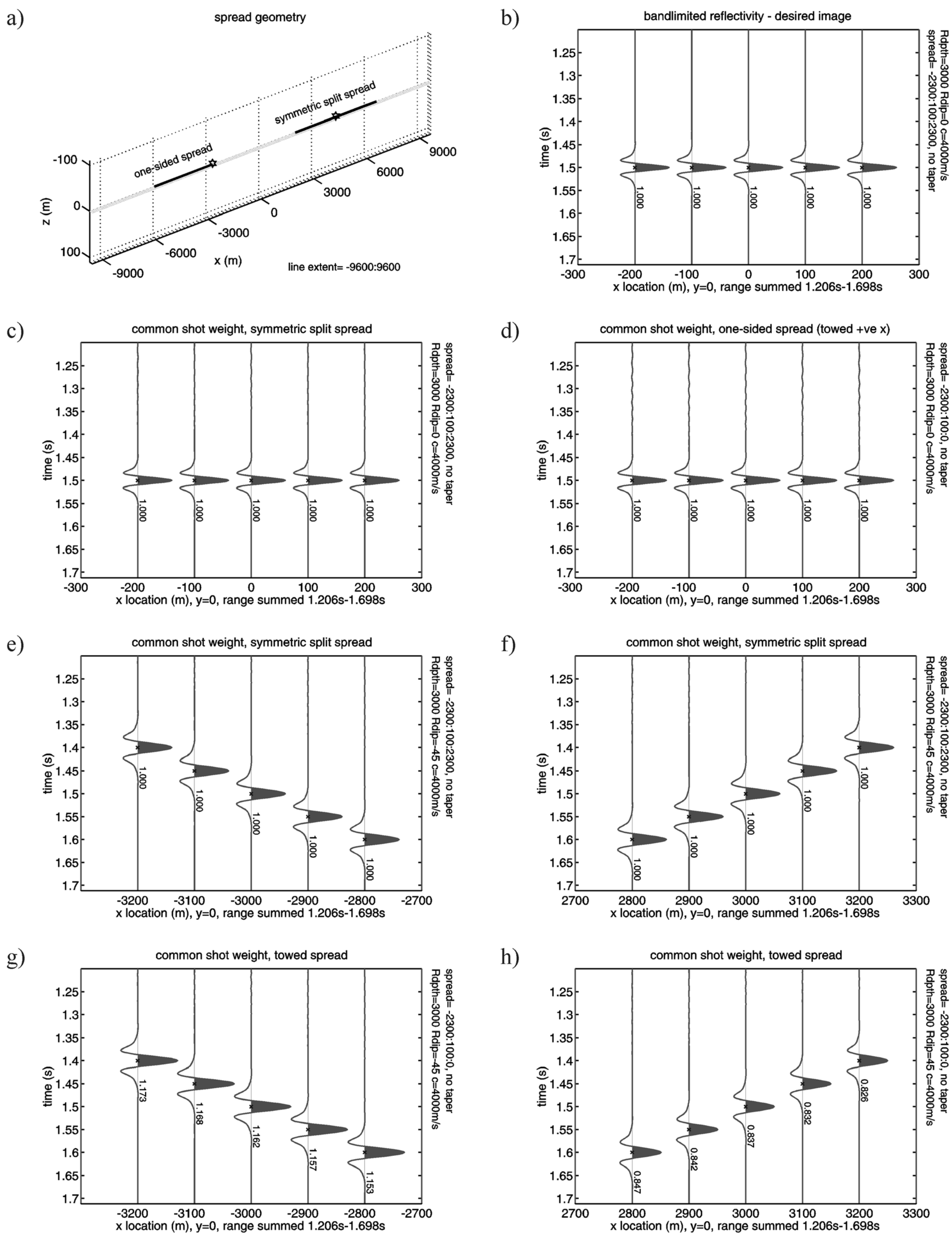

Figure 4.7. One-sided spreads (e.g. towed streamers) accentuate the dip- and depth- dependent bias in 2.5-D common-shot weighting function [equation (4.3) or equation (4.9)/(4.10)]. A symmetric split-spread averages equal and opposite receiver-side and shot-side bias, giving an unbiased result. a) 2.5-D reference diagram. b) Desired wavelet shape and reflectivity of 1. c) Symmetric split spread at zero dip. d) One-sided spread at zero dip – no bias. e-f) Symmetric split spread at +45° and –45° dips – bias averages out to zero. g) Receiver-side of one-sided spread – positive bias. h) Shot-side of one-sided spread – negative bias.

Figure 4.7a is a reference diagram to indicate 2.5-D acquisition geometry. For the one-sided spread, offsets range from -2300 m to 0 m in intervals of 100 m. For the symmetric split-spread, offsets range from -2300 m to 2300 m in intervals of 100 m. Figure 4.7b shows the desired bandlimited reflectivity for a horizontal reflector. Figure 4.7c and 4.7d are the stacked bandlimited reflectivity for a horizontal reflector obtained by a symmetric split spread and one-sided spread, respectively. As shown previously, there is no bias error at zero dip, so the correct stacked reflectivity of unity is imaged by either spread layout. In Figure 4.7e and 4.7f, the symmetric split spread correctly images the stacked reflectivity for dips of -45° and +45°, respectively. Note that the bandlimited wavelet is plotted on a vertical axes and therefore stretched by a factor of $\sim\sqrt{2}$, as expected for a dip of 45°. In Figures 4.7g and 4.7f, the one-sided spread fails to recover the correct value for dipping reflectors. Given that the shot is located on the positive side of the receivers, the direction of the bias agrees with the common-shot results plotted in Figure 4.3 (or, assuming reciprocity, with the common-receiver results plotted in Figure 4.4).

4.4.2 Synthetic tests comparing 3-D common-shot and common-offset weights

The situation in 3-D is similar. Figure 4.8 shows the reconstructed amplitudes of the reflectivity coefficient $\underset{(3-D)}{\hat{R}_\theta}$ for a complete range of both reflector dip-angles and depths using the 3-D common-offset migration/ inversion formula [equation (4.2), or equations (4.5)/(4.8) with $N_{co} = 1$]. Figure 4.8a is a reference diagram to indicate 3-D acquisition geometry, in this case for a shot-receiver azimuth 45° from the dip-direction of the reflector. Figure 4.8b shows the range of dip angles and a representative isochron. Figures 4.8c-d, 4.8e-f, and 4.8g-h show that the correct reflectivity is recovered for shot-receiver azimuths of 0°, 45°, and 90°, respectively.

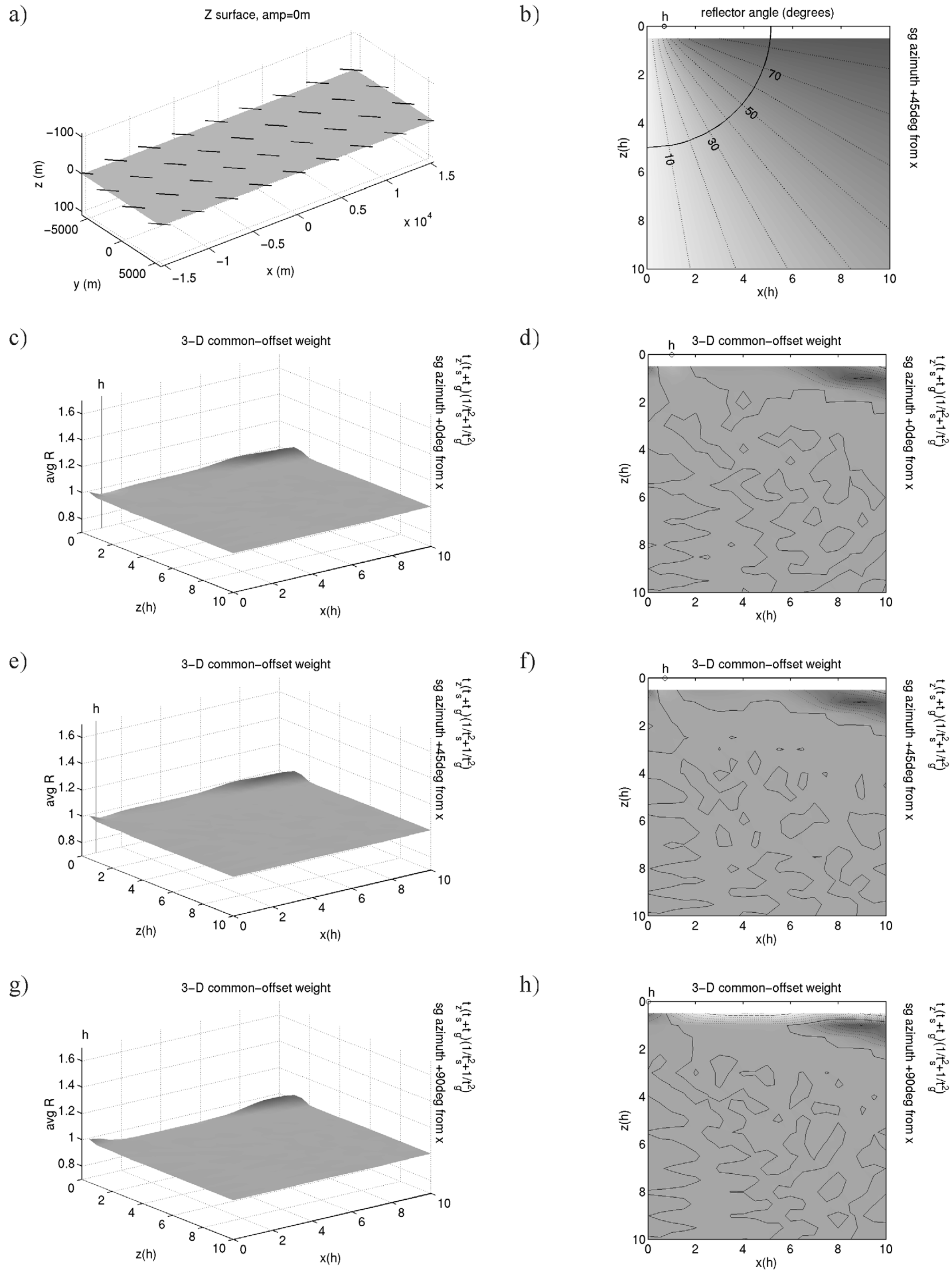

Figure 4.8. 3-D common-offset weight: equation (4.2) or equations (4.5)/(4.8) with $N_{co} = 1$. a) 3-D reference diagram. b) Reflector dip (strike parallels *y*-axis) with normalized horizontal distance *x*(*h*) and depth *z*(*h*) measured from the shot-receiver midpoint to specular reflection point. c) e) g) Perspective view of imaged amplitude of reflector (input reflection coefficient unity) for shot-receiver azimuths at 0, 45 and 90 degrees from *x*-axis. d) f) g) Contours of imaged amplitude of reflector with intervals of 0.1 (solid lines), 0.05 (dashed lines) and 0.01 (dotted lines).

Figure 4.9 shows the reconstructed amplitudes for the 3-D common shot migration/ inversion formula [equation (4.1) or equations (4.5) and (4.6) with $N_s = 1$]. Only the receiver-side is plotted. At 0° shot-receiver azimuth (Figures 4.9c-d), the bias error in the 3-D result is less than the bias error in the comparable 2.5-D result (Figures 4.5c-d), although still significant. This is expected given that in 3-D, contributions from along-strike shot-receiver pairs will, in effect, be equivalent to a 2.5-D contribution from greater depth. Note that there is no bias error at 90° azimuth (Figures 4.9g-h) because all dipping reflectors have a horizontal apparent dip in the strike direction.

For both 2.5-D and 3-D, then, the optimum weighting function for stacked reflectivity is the common-offset weight.

4.4.3 What ever happened to shot-gather migration?

The synthetic tests presented in the previous section clearly show that an average of migrated shot-gathers does not produce an accurate estimate of stacked reflectivity. However, it is well known that a single migrated shot-gather can accurately image reflectivity at all dips (assuming a "true-amplitude" common-shot migration that uses an accurate model of both velocity and reflectivity above the subsurface imaging point—see Hanitzsch, 1997; Gray, 1997). How can an average of accurately migrated shot-gathers introduce significant bias error? The answer is simple: for a given reflector, the receiver apertures for many of the shot gathers record only a limited portion of the ‘minimum’ aperture required to accurately reconstruct reflectivity[7]. Thus many of the migrated shot-gathers contain biased estimates of reflectivity, and a simple stack does not result in

---

[7] But, as clearly shown by Wapenaar (1992), inverse wavefield extrapolation from an infinite aperture is not exact—the artifacts associated with a finite aperture do not vanish for the case of an infinite aperture.

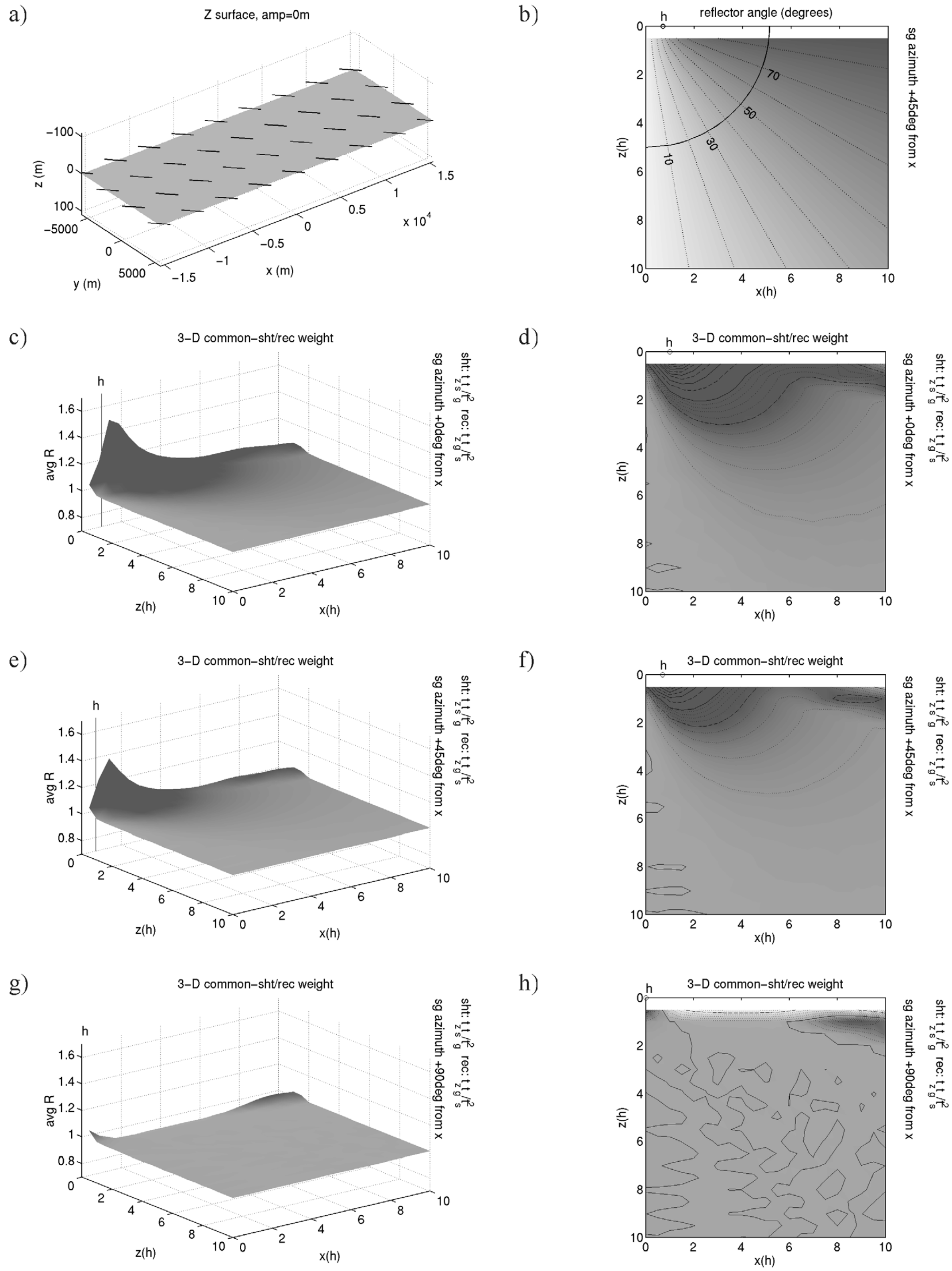

Figure 4.9. 3-D common-shot (receiver side) or common-receiver (shot side) weight: equation (4.1) or equations (4.5)/(4.6) with $N_s = 1$. a) 3-D reference diagram. b) Reflector dip (strike parallels *y*-axis) with normalized horizontal distance $x(h)$ and depth $z(h)$ measured from the shot-receiver midpoint to specular reflection point. c) e) g) Perspective view of imaged amplitude of reflector (input reflection coefficient unity) for shot-receiver azimuths at 0, 45 and 90 degrees from *x*-axis. d) f) g) Contours of imaged amplitude of reflector with intervals of 0.1 (solid lines), 0.05 (dashed lines) and 0.01 (dotted lines).

fortuitous cancellation of the bias errors. The exception is a symmetric split spread—a common acquisition configuration for land surveys—but difficult to achieve in marine surveys.

The bias error manifests itself in two ways. Reflector planes with the same dip but different normal orientations are imaged with different amplitudes, and reflector planes of different dips and depths are imaged with different amplitudes. As shown in Figure 4.3, the relative error in amplitude for a dipping reflector imaged by end-shooting using an up-dip versus down-dip 2.5-D acquisition geometry can be as high as an order of magnitude; i.e., the reflectivity of a dipping reflector as determined by the peak trace amplitude from the resulting 2.5-D stacked section could change by a factor of 10 depending on the shooting direction. This suggests that a significant dip-dependent “acquisition footprint” could be present in seismic images from 2-D (and 3-D) marine surveys.

The results clearly show that the absolute magnitude of the bias error introduced by averaging migrated shot gathers is reduced if the number of offsets is used as the normalizing factor, rather than the number of shot gathers. For structural imaging, we are more concerned with the bias error in a relative sense (as in the example mentioned in the previous paragraph) rather than the actual magnitude of the reflectivity estimate compared to the true value. All estimates of reflectivity could be out by the same constant factor without changing the fundamental contrast in the structural image. Hence, the choice of normalization factor is not critical for practical implementation.

Obviously, there is little hope in recovering accurate results from real data if our migration procedure cannot accurately recover known reflectivity from synthetic data. However, there are a number of additional effects not considered in the simplified formulae or in the synthetic tests. Two of the most significant are the influence of shot and receiver arrays, and the free surface effect. Some of these may reduce the relative magnitude of the bias error; but if they do, it is more by good fortune than by design. The fact remains that a fundamental error is present in the basic premise of averaging migrated common-shot gathers, even for the simplest of models.

Unfortunately, there does not appear to be a simple correction to the bias error introduced by averaging of common-shot gathers. In theory, at least, the bias can be eliminated by applying common-offset migration/inversion weights derived from the asymptotic formulae. Currently, however, the best prestack imaging algorithms employ inverse wavefield propagation in a wave-equation domain such as a shot gather. Inverse wavefield propagation can undo focusing and defocusing effects that may lead to multipathing of energy arrivals. In comparison, asymptotic migration/inversion operators (e.g., non-recursive diffraction-stack or Kirchhoff-type migration algorithms) are typically restricted to single arrivals and therefore tend to be less accurate in areas of complex velocity structure. The tradeoff, then, is between a demonstrably biased stacked amplitude obtained by averaging more accurate estimates obtained from wave-equation domain migrations, and an unbiased stacked amplitude obtained by averaging less accurate estimates obtained from asymptotic migration/inversions. A solution to this problem might be to incorporate additional weighting functions into the wave-equation domain migrations, either by a global scheme that synthesizes plane waves from a number of the shot gathers, or by a local scheme that takes advantage of the plane-wave decomposition inherent in, for example, stationary and nonstationary phase-shift algorithms. Possible solutions are not investigated further in this study.

So, what ever happened to shot-gather migration? Shot-gather migration is still an accepted prestack imaging tool. But it is clear that the average of a number of migrated shot-gathers does not necessarily produce a consistent final image.

4.5 PRACTICAL FORMULAE FOR KIRCHHOFF TIME MIGRATION

Recall from Section 2.5 the essence of the Kirchhoff-Helmholtz integral representation (KHIR). Two non-identical acoustic wavefields corresponding to two different sets of material properties propagate within the same volume. One of the acoustic wavefields is the recorded wavefield that has propagated in the unknown true subsurface media. The other wavefield is, in effect, defined by forward or backward propagating Green's functions in the reference model. As discussed in Sections 3.2 and 3.3, we are free to choose the reference model and Green's function both within and outside the volume, and to apply superposition as required. In fact, the choice of one-way Green's functions allowed us to separate reflection from wavefield propagation, and thus simplify the reference model to a single parameter of acoustic wavespeed. These 'practical' choices led to the derivation of Kirchhoff-approximate and Born-approximate migration and inversion formulae that yield an estimate of reflectivity (or stacked) reflectivity at a single location in the subsurface.

Given that each reflectivity estimate is determined independently, nothing prevents us from choosing a different reference model for each subsurface location. In effect, a single output 'image' can be created as a composite of many independent migrations. Thus, we can apply independence and superposition to choose any number of simple wavespeed models for the unknown (and possibly complex) properties of the subsurface[8]. Note that there is no requirement that these models be related in any physically meaningful way. However, it is often possible to achieve excellent focusing of subsurface reflectors and

---

[8] We can make multiple estimates of reflectivity at the same location using different wavespeed models, and then, using appropriate criteria, choose the 'best' estimate. This is the basic principle underlying most methods of wavespeed analysis.

even good relative positioning, typically at the expense of absolute positioning. This is the basic concept underlying non-recursive Kirchhoff time migrations such as EOM.

4.5.1 Pseudo-depth and zero-offset two-way traveltime

As discussed in Sections 1.2 and 1.3, the migration formulae can be thought of as a weighted summation over a "diffraction" surface in the input data space, where the diffraction surface is defined by the traveltimes from shot to imaging location to receiver. In a constant wavespeed medium, the diffraction surface can be described analytically using only two parameters, the wavespeed and the zero-offset two-way traveltime from the point on the surface vertically above the imaging location. If the unknown true medium is complicated, the shape of the diffraction surface may also be complicated. However, this complex surface might still be reasonably approximated by a 'best-fit' analytic constant-wavespeed diffraction surface, and therefore still be described by only two parameters[9]. For example, Schneider (1978) shows that RMS wavespeed is sufficiently accurate for non-recursive Kirchhoff imaging in media with vertical wavespeed gradients; and, in Section 1.5, I derived a generalized formula for a DSR diffraction surface in media with arbitrary wavespeed.

Now consider a space-time image space with horizontal coordinates defined by the locations of the zero-offset shot-receiver pairs on a planar surface, and a vertical coordinate defined by two-way traveltime t_{2z} instead of depth z_G. Each point in the image space corresponds to a 'best-fit' constant-wavespeed diffraction curve in the input data space. The composite constant-wavespeed model is defined in this new space-time

---

[9] De Bazelaire (1988) and Castle (1988) extend the set of possible diffractions surfaces by introducing a third parameter τ_s representing a static shift of the zero-offset traveltime [see equation (1.55) and discussion in Section 1.5.5, as well as Hockt et al. (1999)].

coordinate space as $\tilde{c}_0 = c_0(x_G, y_G, t_{2\tilde{z}})$. The reflectivity, as determined by the weighted summation over the diffraction curve, can be mapped directly to an image point defined in space-time [e.g. $\underset{(3-D)}{\overline{R}}(x_G, y_G, t_{2\tilde{z}})$ for 3-D stacked reflectivity]. Thus, a basic unweighted migration can be implemented without requiring depth as a coordinate in the wavespeed model, and without specifying the depth of the image point. Unfortunately, the constant-wavespeed weighting function is defined in terms of i) distance from source to imaging point, ii) distance from receiver to imaging point, iii) directivity at the source, and iv) directivity at the receiver. All of these are simple functions of depth, a parameter we would prefer not needing to know.

A reasonable approach is to define a 'pseudo-depth' coordinate $\tilde{z}_G$ as half the two-way traveltime at the output point $t_{2\tilde{z}}$ multiplied by the wavespeed, i.e. $\tilde{z}_G = t_{2\tilde{z}}\tilde{c}_0/2$. In a constant-wavespeed medium, the pseudo-depth is the correct depth at the output point. In a medium with vertical and lateral variations in wavespeed, the pseudo-depth has no physical meaning other than in the context of the best-fit diffraction surface, as discussed in Section 1.5.3. Now all the terms in the weighting function can be determined, and we get a reasonable estimate of the true-amplitude stacked reflectivity—but still in an image space with a vertical coordinate of two-way traveltime. Unfortunately, the computation of all these terms in the weighting function is costly. We need the distance from each shot and receiver location to the 'pseudo-location' in the subsurface, which requires two square roots for each trace sample on each diffraction curve, or a very large lookup table. The optimal common-offset weighting function requires an additional dozen (or so) floating-point operations in both 3-D and 2.5-D (and three additional square roots for the 2.5-D weighting function). These computational costs could be greatly reduced if we approximate the weighting function with terms that can be applied directly in either the input data space or the output image space. Using this concept, Gray (1998b) and Dellinger et al. (2000) take the optimal 2.5-D constant-wavespeed common-offset weighting function and approximate it by a more efficient form. I apply their basic methodology in the following derivations.

4.5.2 Optimum 3-D common-offset weighting function in terms of traveltimes

First, the optimum migration formula for reflectivity (stacked or angle-dependent) is converted from a depth migration to a time migration. As discussed above, both the reflectivity and the 'best-fit' wavespeed model will be determined in an output space with a vertical coordinate of two-way-traveltime $t_{2\tilde{z}}$. The distances required in the constant-wavespeed weighting functions can be calculated using this pseudo-depth $\tilde{z}_G$, as follows:

$$r_{Gs} = \sqrt{d_{Gs}^2 + \tilde{z}_G^2}\ , \tag{4.13}$$

$$r_{gG} = \sqrt{d_{gG}^2 + \tilde{z}_G^2}\ , \tag{4.14}$$

with
$$d_{Gs} = \sqrt{(x_G - x_s)^2 + (y_G - y_s)^2} \tag{4.15}$$

and
$$d_{gG} = \sqrt{(x_g - x_G)^2 + (y_g - y_G)^2}\ . \tag{4.16}$$

An alternate approach is to convert the distances directly to traveltimes, i.e.

$$t_s = r_{Gs} / \tilde{c}_0\ , \tag{4.17}$$

$$t_g = r_{gG} / \tilde{c}_0\ , \tag{4.18}$$

and
$$t_{2\tilde{z}} = 2\tilde{z}_G / \tilde{c}_0\ , \tag{4.19}$$

with
$$t = t_s + t_g. \tag{4.20}$$

Note that equation (4.19) is just a rearrangement of the definition of pseudo-depth $\tilde{z}_G$ given a known two-way traveltime $t_{2\tilde{z}}$ and best-fit wavespeed $\tilde{c}_0$.

The approximation by traveltime is not unreasonable. In fact, weighting functions based on the traveltime approximation to the constant-wavespeed migration/inversion formulae have proven to be robust and reasonably accurate in more complicated depth imaging problems (Dellinger et al., 2000; Zhang et al., 2000). As mentioned in the introduction to this chapter, Jaramillo et al. (2000) call these 'true-amplitude time-migration weights'. Since all weighting functions are fundamentally derived from a macro-wavespeed model that approximates the unknown true subsurface, the true-amplitude time-migration weights can be thought of as imposing a minimum model.

Using the conversions to traveltime, then, the 3-D stacked reflectivity [equation (4.5)] is given by

$$\underset{(3-D)}{\overline{R}}(x_G, y_G, t_{2\tilde{z}}) \approx \sum_{traces} \underset{(3-D)}{\overline{W}}(x_G, y_G, t_{2\tilde{z}}, \mathbf{x}_s, \mathbf{x}_g) \left[\hat{f}(t) * \frac{\partial}{\partial t} \underset{(3-D)}{p_S^-}(\mathbf{x}_g, \mathbf{x}_s, t) \right]_{t=t_s+t_g}, \tag{4.21}$$

with the common-offset weighting function [equation (4.8)] re-expressed here as

$$\underset{(3-D)}{\overline{W}_{co}}(x_G, y_G, t_{2\tilde{z}}, \mathbf{x}_s, \mathbf{x}_g) = -\frac{dS_s}{N_{co}} \left\{ \frac{(t_s + t_g)}{t_g} \frac{2\cos\theta_{gG}}{\tilde{c}_g} + \frac{(t_s + t_g)}{t_s} \frac{2\cos\theta_{Gs}}{\tilde{c}_s} \right\}. \tag{4.22}$$

Equation (4.22) includes the terms $2\cos\theta_{gG} / \tilde{c}_g$ and $2\cos\theta_{Gs} / \tilde{c}_s$, which arise from twice the normal derivative at the surface location of the receiver and source, respectively. The angles θ_{gG} and θ_{Gs} are emergent angles, and the wavespeeds $\tilde{c}_g$ and $\tilde{c}_s$ are defined at the surface. With the following approximations (exact for constant-wavespeed):

$$\cos\theta_{gG} = \frac{\tilde{z}_G}{r_{gG}} = \frac{t_{2\tilde{z}}}{2t_g}, \tag{4.23}$$

$$\cos\theta_{Gs} = \frac{\tilde{z}_G}{r_{Gs}} = \frac{t_{2\tilde{z}}}{2t_s}, \tag{4.24}$$

$$\tilde{c}_g \approx \tilde{c}_0, \tag{4.25}$$

and

$$\tilde{c}_s \approx \tilde{c}_0, \tag{4.26}$$

equation (4.22) can be simplified to

$$\underset{(3-D)}{\overline{W}_{co}} = -\frac{dS_s}{N_{co}}\frac{1}{\tilde{c}_0}\left\{ tt_{2\tilde{z}}\left(\frac{1}{t_s^2}+\frac{1}{t_g^2}\right)\right\}. \tag{4.27}$$

4.5.3 Simplifying the traveltime terms in 3-D common-offset weighting function

Dellinger et al. (2000), in examining the 2.5-D case, suggest that a reasonable approximation is to evenly divide the traveltime *t* between t_s and t_g, so that

$$\left(\frac{1}{t_s^2}+\frac{1}{t_g^2}\right) \approx \frac{8}{t^2}. \tag{4.28}$$

Equation (4.28) becomes exact when $t_s = t_g$, which occurs at zero offset (regardless of reflector dip) and at the stationary point (i.e. at specular reflection) for zero-dip reflectors (regardless of source-receiver offset). Then the common-offset weighting function can be simplified to

$$\underset{(3-D)}{\overline{W}_{co}} \approx -\frac{8}{\tilde{c}_0}\frac{dS_s}{N_{co}}\left\{ t_{2\tilde{z}}\frac{1}{t}\right\} \tag{4.29}$$

In equation (4.29), *t* is just the two-way travel-time on the recorded traces, t_z is the two-way traveltime coordinate of the output space. Hence the $1/t$ term can be applied to the input traces prior to summation over the diffraction curve, and the $t_{2\tilde{z}}$ term can be applied directly to the output stacked-reflectivity 'trace'. The essence of the result given by equation (4.29) is discussed (but not derived) in Zhang et al. (2000).

If the goal for output is the stacked reflectivity scaled to within a constant or to within a slowly varying constant (reasonable given the approximations discussed above), all the terms outside the curly brackets on the RHS of equation (4.29) can be ignored, and the weighting function reduces to

$$\underset{(3-D)}{\overline{W}_{co}} \approx -\frac{t_{2\tilde{z}}}{t}. \tag{4.30}$$

This is a remarkable simplification after an involved derivation spanning two and one-half chapters of this dissertation. In migration slang, a simple weighting function like this is often referred to as a 't_0/t' weight, where $t_0 = t_{2\tilde{z}}$ refers to the two-way traveltime time at the apex of the best-fit diffraction curve. In acknowledging the previously mentioned work of Zhang et al. (2000), I call this weighting function the Zhang 't_0/t' weight.

Figure 4.10 shows the reconstructed amplitudes of the reflectivity coefficient $\underset{(3-D)}{\hat{R}_\theta}$ for a complete range of both reflector dip-angles and depths using the Zhang 't_0/t' weight [equation (4.30) or equations (4.21)/(4.29) with $N_{co} = 1$]. Figure 4.10a is a reference diagram to indicate 3-D acquisition geometry, in this case for a shot-receiver azimuth 45° from the dip-direction of the reflector. Figure 4.10b shows the range of dip angles and a representative isochron. Figures 4.10c-d, 4.10e-f, and 4.10g-h show that the correct reflectivity is recovered for shot-receiver azimuths of 0°, 45°, and 90°, respectively. The downweighting effect associated with the 't_0/t' approximation becomes less as azimuth angle increases, and is negligible at an azimuth of 90° (compare Figures 4.10h and 4.9h). In practical terms, use of the Zhang 't_0/t' weight will give different results for 3-D marine surveys shot in the strike and dip directions.

Note that the data $\underset{(3-D)}{p_S^-}(\mathbf{x}_g, \mathbf{x}_s, t)$ in equation (4.21) have not been gained, but are assumed to be recorded with spherical divergence (in addition to assuming that only the upward traveling scattered wavefield is recorded on a non-reflecting surface). Practical methods for handling more realistic data recorded with geometrical spreading appropriate for variable wavespeed as well as with attenuation and other factors affecting amplitudes (see Sheriff, 1975) will be discussed in Chapter 5.

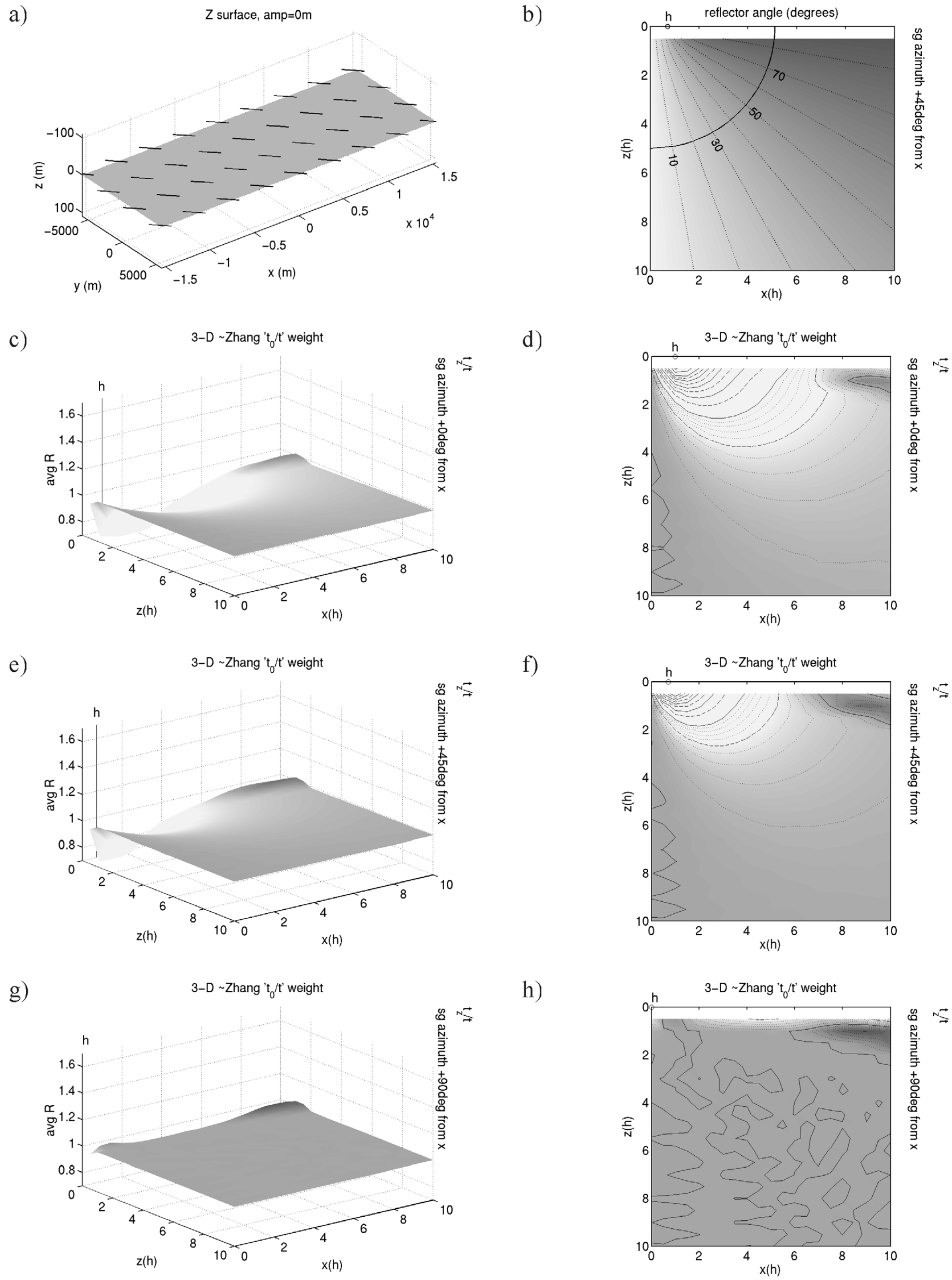

Figure 4.10. 3-D Zhang 't_0/t' weight: equation (4.30) [same as Figure 4.16, equation (4.30) with $a_3 = 0$ and $a_6 = 0$]. a) 3-D reference diagram. b) Reflector dip (strike parallels *y*-axis) with normalized horizontal distance *x*(*h*) and depth *z*(*h*) measured from the shot-receiver midpoint to specular reflection point. c) e) g) Perspective view of imaged amplitude of reflector (input reflection coefficient unity) for shot-receiver azimuths at 0, 45 and 90 degrees from *x*-axis. d) f) g) Contours of imaged amplitude of reflector with intervals of 0.1 (solid lines), 0.05 (dashed lines) and 0.01 (dotted lines).

4.5.4 Optimum 2.5-D common-offset weighting function in terms of traveltimes

The 2.5-D stacked reflectivity [equation (4.9)] can also be re-expressed by converting the distances directly to traveltimes using equations (4.13)-(4.20), yielding

$$\underset{(2.5-D)}{\overline{R}}(x_G,t_{2\tilde{z}}) \approx \sum_{traces} \underset{(2.5-D)}{\overline{W}}(x_G,t_{2\tilde{z}},\mathbf{x}_s,\mathbf{x}_g)\left[\hat{f}(t) * \mathcal{H}\left\{\left(\frac{\partial}{\partial t}\right)^{1/2} \underset{(2.5-D)}{p_S^-}(\mathbf{x}_g,\mathbf{x}_s,t)\right\}\right]_{t=t_s+t_g}, \quad (4.31)$$

with the optimal common-offset weighting function [equation (4.12)] re-expressed here as

$$\underset{(2.5-D)}{\overline{W}_{co}}(x_G,t_{2\tilde{z}},\mathbf{x}_s,\mathbf{x}_g) = \frac{dx_s}{N_{co}}\left\{\tilde{c}_0\sqrt{2\pi}\sqrt{t_s+t_g}\left(\frac{\sqrt{t_s}}{\sqrt{t_g}}\frac{2\cos\theta_{gG}}{\tilde{c}_g} + \frac{\sqrt{t_g}}{\sqrt{t_s}}\frac{2\cos\theta_{Gs}}{\tilde{c}_s}\right)\right\}. \quad (4.32)$$

As with the 3-D common-offset formula [equations (4.21)/(4.22)], the terms $2\cos\theta_{gG}/\tilde{c}_g$ and $2\cos\theta_{Gs}/\tilde{c}_s$ arise from twice the normal derivative at the surface location of the receiver and source, respectively. Thus the angles θ_{gG} and θ_{Gs} are emergent angles, and the wavespeeds $\tilde{c}_g$ and $\tilde{c}_s$ are defined at the surface. These surface wavespeeds are replaced by the 'best-fit' wavespeed $\tilde{c}_0$, which is also used to convert the out-of-plane spreading correction factor $\sqrt{2\pi\tilde{c}_0 r_{Gs} + 2\pi\tilde{c}_0 r_{gG}}$ to its equivalent $\tilde{c}_0\sqrt{2\pi}\sqrt{t_s+t_g}$. Otherwise, the expression does not simplify easily[10].

Now insert the approximations given by equations (4.23)-(4.26) (exact for constant wavespeed) into equation (4.32) and rearrange to obtain

$$\underset{(2.5-D)}{\overline{W}_{co}}(x_G,t_{2\tilde{z}},\mathbf{x}_s,\mathbf{x}_g) = -\sqrt{2\pi}\frac{dx_s}{N_{co}}\left\{t_{2\tilde{z}}\sqrt{t}\sqrt{t_s t_g}\left(\frac{1}{t_s^2}+\frac{1}{t_g^2}\right)\right\}. \quad (4.33)$$

---

[10] Zhang et al. (2000) provide 2.5-D results for $c_0(z)$ wavespeed profiles-see Snieder and Chapman (1998) for a discussion of 3-D geometrical spreading in variable wavespeed and variable density media.

To simplify equation (4.33), an obvious substitution (and one that will be made shortly) is the $8/t^2$ approximation given by equation (4.28). However, the RHS of equation (4.33) still contains the term $\sqrt{t_s t_g}$, which entails a computationally expensive calculation for every input trace sample on every diffraction surface (there will be one diffraction surface for each output trace sample and many required for velocity analysis). It is difficult to assess the significance of this term in the weighting function and therefore difficult to determine an approximation that is computationally less expensive and reasonably accurate. Later in this chapter, the accuracy of the various choices is evaluated for all dips and depths using constant wavespeed synthetics. First, however, we need some reasonable approximations.

4.5.5 Simplifying the traveltime terms in 2.5-D common-offset weighting function

Dellinger et al. (2000) propose a clever approach to simplifying the 2.5-D common-offset weighting function [equation (4.33)] that can be supported by practical arguments. They note that Bleistein et al. (1987), in deriving an inversion formula for bandlimited reflectivity [see equation (3.67)], first define a 'reflectivity function' that differs from bandlimited reflectivity by an 'obliquity' factor $2\cos\theta_G / c(\mathbf{x}_G)$, where θ_G is half the opening angle between the source and receiver rays at subsurface location $\mathbf{x}_G$. In Appendix C, the obliquity factor is shown to equal $|\nabla\phi_\tau|$, the magnitude of the traveltime gradient for a given source-receiver pair [equation (C.3)]. Applying the half-angle formula for cosine gives

$$\frac{2\cos\theta_G}{c(\mathbf{x}_G)} = \frac{\sqrt{2}\sqrt{1+\cos 2\theta_G}}{c(\mathbf{x}_G)} \tag{4.34}$$

Dellinger et al. (2000) then take the constant wavespeed case where $c(\mathbf{x}_G) = \tilde{c}_0$, apply the law of cosines to the triangle $\mathbf{x}_g$, $\mathbf{x}_s$, and $\mathbf{x}_G$, and rearrange the result to show that

$$\cos\theta_G = \frac{\sqrt{1+\cos 2\theta_G}}{\sqrt{2}} = \frac{1}{2}\frac{(t_s+t_g)}{\sqrt{t_s t_g}}\sqrt{1-\frac{(2h)^2}{\tilde{c}_0^2(t_s+t_g)^2}}\ , \tag{4.35}$$

where $2h$ is the source-receiver offset of the input trace. Equation (4.35) is defined here as the 'cosine obliquity' normalization factor. It evaluates to unity for an opening angle of zero (i.e. $\theta_G = 0$) and progressively downweights as the opening angle increases.

Using $t = t_s + t_g$ [equation (4.20)], notice that all terms on the RHS of equation (4.35) need to be calculated only once for each input trace sample—except for that same pesky $\sqrt{t_s t_g}$ term as found in the denominator of the 2.5-D weighting function [equation (4.33)]. However, here it is in the numerator, so we can eliminate $\sqrt{t_s t_g}$ in equation (4.33) if we multiply by equation (4.35). After some simplification, the result is

$$\underset{(2.5-D)}{\overline{W}_{co}} \approx -\frac{\sqrt{2\pi}}{2}\frac{dx_s}{N_{co}}\left\{t_{2\bar{z}}\,t^{3/2}\left(\frac{1}{t_s^2}+\frac{1}{t_g^2}\right)\sqrt{1-\frac{(2h)^2}{(\tilde{c}_0 t)^2}}\right\}. \tag{4.36}$$

Now we can apply the $8/t^2$ approximation, yielding

$$\underset{(2.5-D)}{\overline{W}_{co}} \approx -4\sqrt{2\pi}\,\frac{dx_s}{N_{co}}\left\{t_{2\bar{z}}\sqrt{1-\frac{(2h)^2}{(\tilde{c}_0 t)^2}}\,\frac{1}{t^{1/2}}\right\}. \tag{4.37}$$

Equation (4.37) is called here the 'Gray t_0/t cosine obliquity weight' (shortened to '2.5-D Gray $t_0/t\cos$' or just 'Gray weight' in figure titles), where 'Gray' refers to an unpublished internal report by Gray (1998b) subsequently released in a CSEG compilation volume edited by Lines et al. (1999), 't_0/t' is a generalized reference to the ratio of output and input traveltimes ($t_{2\bar{z}}/t^{1/2}$ for 2.5-D), and 'cos' refers to the extra weighting by an obliquity factor. The weighting function differs from Gray (1998b), who ignores all constants including wavespeed terms, and Dellinger et al. (2000), who multiply their weighting function for bandlimited reflectivity by equation (4.34) instead of equation (4.35) and neglect a factor of $1/(2\pi)$ in the Fourier transform they use to convert the frequency-domain result of Bleistein et al. (1987) to the time domain. Equation (4.37), on the other hand, estimates an absolute value of reflectivity that should be unity except for the downweighting introduced by the cosine obliquity term and the $8/t^2$ approximation.

Figure 4.11 shows the effect of various parts of the 2.5-D Gray 't_0/t' cosine obliquity weight. Figure 4.11a is a reference diagram indicating the 2.5-D common-offset acquisition geometry, while Figure 4.11b shows the range of dip angles (dashed contour) and a representative isochron (solid contour). Horizontal distance x and depth z are normalized to half source-receiver half-offset h. Reflectivity is contoured in Figures 4.11d, 4.11f and 4.11h with dotted contours every 0.01 between 0.9 and 1.1, dashed contours every 0.05 between 0.5 and 1.5, and solid contours every 0.1. Figures 4.11c, 4.11e and 4.11g are perspective views with reflectivity on the vertical axis.

Figures 4.11c-d show reflectivity associated with the full weight, as given by equation (4.37). The expected value is unity everywhere. The general effect of the approximation is to downweight reflectivity at shorter traveltimes, and more so for steeper dips than gentler dips. Figures 4.11e-f show the reflectivity associated with the weight without the $8/t^2$ approximation (i.e., including only the cosine obliquity approximation), as given by equation (4.36). The general effect of this approximation is to downweight gentler dips, especially at shallow depths where the opening angle is large. Another possibility is to apply the $8/t^2$ approximation to the exact constant-wavespeed common-offset formula [equation (4.33)], yielding

$$\underset{(2.5-D)}{\overline{W}_{co}}(x_G, t_{2\tilde{z}}, \mathbf{x}_s, \mathbf{x}_g) = -8\sqrt{2\pi}\,\frac{dx_s}{N_{co}}\left\{ t_{2\tilde{z}}\sqrt{t_s t_g}\,\frac{1}{t^{3/2}} \right\}. \tag{4.38}$$

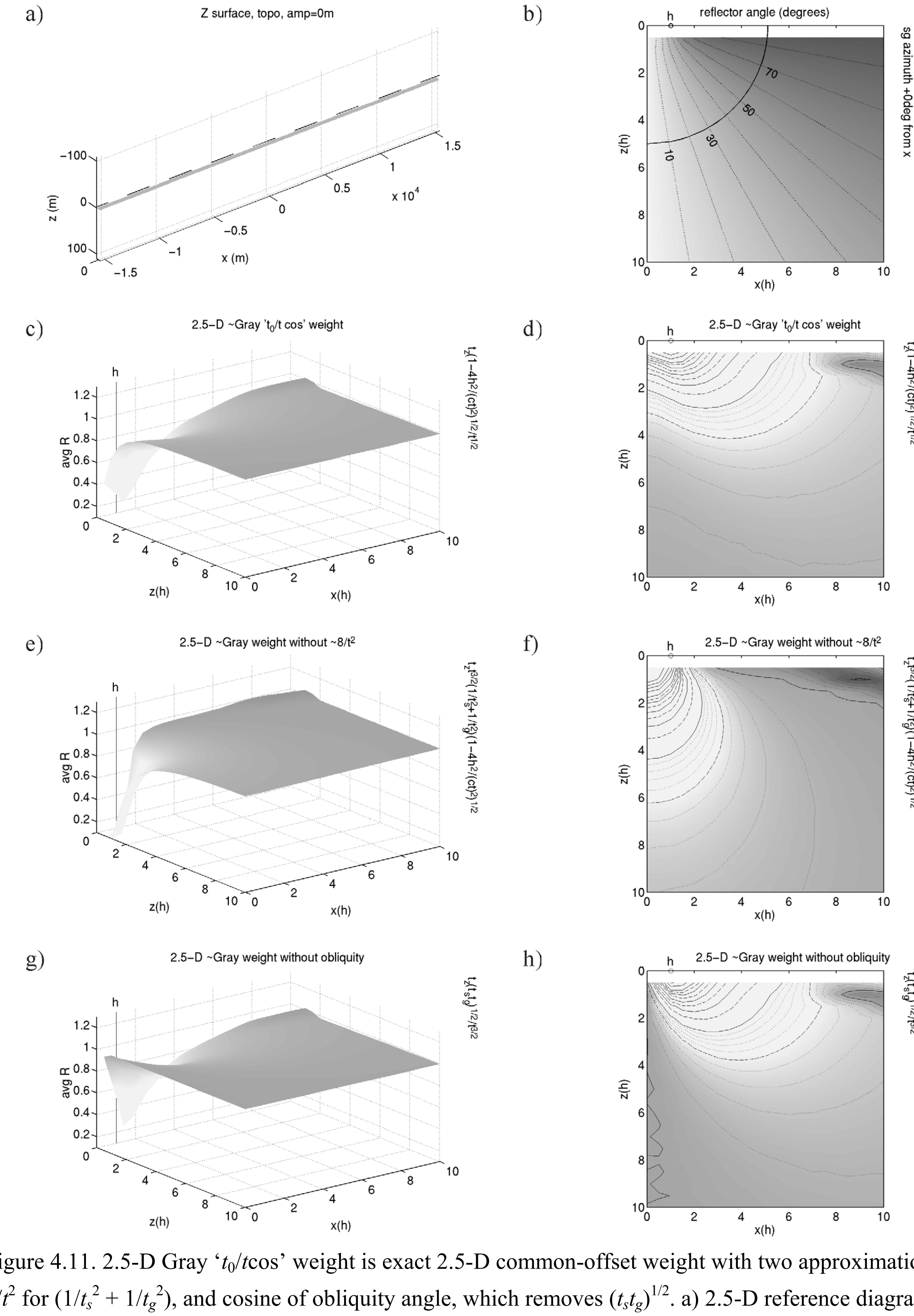

Figure 4.11. 2.5-D Gray 't_0/tcos' weight is exact 2.5-D common-offset weight with two approximations: $8/t^2$ for $(1/t_s^2 + 1/t_g^2)$, and cosine of obliquity angle, which removes $(t_s t_g)^{1/2}$. a) 2.5-D reference diagram. b) Reflector dip (strike parallels y-axis) with normalized horizontal distance $x(h)$ and depth $z(h)$ measured from the shot-receiver midpoint to specular reflection point. c-h) Perspective view and contours of imaged amplitude of reflector with intervals of 0.1 (solid lines), 0.05 (dashed lines) and 0.01 (dotted lines): c-d) 2.5-D Gray 't_0/tcos' weight, e-f) without $8/t^2$ but with obliquity, g-h) with $8/t^2$ but without obliquity.

Figures 4.11g-h show the effect without the cosine obliquity approximation (i.e. including only the $8/t^2$ approximation), as given by equation (4.38). The general effect is to downweight steeper dips at shorter traveltimes.

4.6 CUSTOM WEIGHTING FUNCTIONS FOR EFFICIENT IMPLEMENTATION OF 2.5-D AND 3-D EOM PRESTACK TIME MIGRATION

Consider again the Gray 't_0/t' cosine obliquity weight [equation (4.37)]. If we ignore the constants in equation (4.37), the basic elements of the 2.5-D weighting function can be reduced to

$$\underset{(2.5-D)}{\overline{W}_{co}} \approx \frac{t_{2\tilde{z}}}{t^{1/2}} \sqrt{1 - \frac{(2h)^2}{(\tilde{c}_0 t)^2}} \,. \tag{4.39}$$

The RHS of equation (4.29) can be thought of as consisting of two terms: the quotient term $t_{2\tilde{z}}/t^{1/2}$ and the square root term $\sqrt{1-(2h)^2/(\tilde{c}_0 t)^2}$. All parameters in these terms can be calculated and applied either to the input traces prior to migration or to the output traces after migration. Wavespeed $\tilde{c}_0$ is a bit tricky because we need an average estimate over the travelpaths to and from the subsurface reflector; hence the required average wavespeed is more a function of the subsurface reflector location, i.e. the output two-way traveltime $t_{2\tilde{z}}$, rather than the input two-way traveltime *t*. Dellinger et al. (2000 p. 950) point out that an average wavespeed is required, but that 'it is not yet clear what kind of average to use'; and although they must have chosen some average wavespeed for their constant-wavespeed weight term [their equation (18)], they do not say what that choice was[11]. However, $\tilde{c}_0$ can be thought of as a parameter that adjusts the amount of

[11] In addition, Dellinger et al. (2000) appear to err in applying a correction factor of c_s (wavespeed at the source) when converting from the reflectivity function β to the bandlimited reflectivity *R*, rather than applying the expected correction factor $c_0(\mathbf{x}_G)$ [wavespeed at the image point—see equation (4.34)].

downweighting as a function of obliquity (opening angle at reflector), so the choice of a 'realistic' average wavespeed is not necessary.

For migration of a zero-offset section, $h = 0$, the square root term is unity, and the weighting function reduces to

$$\underset{(2.5-D)}{\overline{W}_{zo}} \approx \frac{t_{2\tilde{z}}}{t^{1/2}} . \tag{4.40}$$

In fact, using equation (4.40) in equation (4.31) gives an exact expression for constant-wavespeed zero-offset migration/inversion (ignoring constants), with the weighting function found by substituting $t_s = t_g = t/2$ and equations (4.23)-(4.26) into equation (4.22). At non-zero offsets, $\sqrt{1-(2h)^2/(\tilde{c}_0 t)^2}$ is less than unity, given that the total distance along the path from source to reflector to receiver $(\tilde{c}_0 t)$ is always greater than the offset $(2h)$ between source and receiver. In effect, then, the square root term downweights as a function of opening angle similar to the 'cosine obliquity' normalization factor [equation (4.35)], but without the factor of $t/\left(2\sqrt{t_s t_g}\right)$. This suggests that any weighting term with an appropriate downweighting effect could be substituted for the square root term, and the resulting reflectivities quantified and displayed in the same common-offset normalized form as used previously. By choice, a convenient and simple value of unity is chosen for reflectivity at all dips and subsurface positions. The characteristics of the variation from unity can then be judged. Given that there are numerous other approximations inherent in the time-migration model, a smooth variation over a limited range may be acceptable. It may even be desirable to create an effect that varies from unity, for example, by downweighting large dip angles or large opening angles at the reflector. The process of selecting parameters to achieve a particular effect or combination of effects that can be implemented efficiently will be called 'building a custom weighting function'.

4.6.1 Custom weighting function for efficient implementation of 2.5-D EOM prestack time migration

For efficient implementation in EOM prestack time migration, the custom weighting function can act in any or all of the following three domains: input traces, binned EO gather traces, and output traces. The generalized formula considered here for the 2.5-D custom weighting function is

$$\underset{(2.5-D)}{\overline{W}_{co}} \approx \underbrace{\left(\frac{1}{t}\right)^{a_1}\left(1-\left(\frac{(k_1 h)}{(\tilde{c}_0 t)}\right)^{a_2}\right)^{a_3}}_{\text{input traces}} \underbrace{\left(\frac{1}{t}\right)^{a_4}\left(1-\left(\frac{(k_2 h_e)}{(\tilde{c}_0 t)}\right)^{a_5}\right)^{a_6}\left(t_{2\tilde{z}}\right)^{a_7}}_{\text{EO gather traces}} \underbrace{\left(t_{2\tilde{z}}\right)^{a_8}}_{\text{output traces}} . \qquad (4.41)$$

In each domain, there are a limited number of useful parameters available, as follows:

input trace:

t	- input two-way traveltime,
h	- source-receiver offset, and
$\tilde{c}_0$	- estimate of average wavespeed

binned EO gather trace:

t	- input two-way traveltime,
$t_{2\tilde{z}}$	- output two-way traveltime,
h_e	- equivalent offset, and
$\tilde{c}_0$	- average estimate of wavespeed

and output trace:

$t_{2\tilde{z}}$	- the output two-way traveltime.

The various exponents a_i can be any positive real number (including zero, which effectively eliminates the weight in a particular domain) or even a function of some other parameter in the domain, although this additional flexibility will not be investigated here. Typically, k_1 and k_2 are constant, with $k_1 = 2$ and $k_2 = 1$. As we shall see, changing the value of k_2 will prove useful for modifying a dip-dependent downweighting effect.

Notice that input two-way traveltime can be applied in either the input or EO gather domains, while output two-way traveltime can be applied in either the EO gather or output domains. Different exponents could be applied in different domains, which could be useful if the desired exponent is a function of domain-dependent parameters (e.g. offset or output position). However, I examine only constant exponents in this study.

Notice also that the estimates of average wavespeed $\tilde{c}_0$ for the input traces and the EO gather traces need not be the same, although the notation suggests that they are. However, only one value is required for the tests reported here, because the chosen weights act only on either input traces or EO gather traces (not both). In addition, the average wavespeeds do not need to be constants: for the input traces $\tilde{c}_0$ could be a function of input two-way traveltime and selected spatial parameters; while for the EO gather traces, $\tilde{c}_0$ could be a function of either the input or the output two-way traveltimes and selected spatial parameters. This can provide some additional flexibility for custom design of a desired weighting effect.

There are three general effects that are desirable in a custom weighting function:

downweighting as a function of obliquity (i.e. the opening angle at the reflector),

downweighting as a function of dip angle, and

downweighting or upweighting as a function of two-way traveltime (input or output).

Downweighting as the opening angle increases can reduce the problem of contamination from reflections beyond the critical angle and from refracted reflections. In addition, Esmersoy and Miller (1989) show that the focusing of a point velocity anomaly is greatly improved if a cosine-squared obliquity weighting is included. Downweighting as dip angle increases can reduce or eliminate the necessity for accurate processor-designed image-gather muting functions, and act as a natural migration-operator aperture taper.

And finally, downweighting or upweighting as two-way traveltime increases can be thought of as a general fix for more complicated trace-amplitude effects beyond the assumed spherical spreading, such as geometrical spreading in a variable wavespeed subsurface, transmission loss, and attenuation due to absorption and small-scale scattering.

Consider again the 2.5-D case and the Gray 't_0/t' cosine obliquity weight, but now in the same form as the generalized weighting function [equation (4.41)]. Comparing equation (4.39) to (4.41) gives $a_1 = 1/2$, $a_2 = 2$, $a_3 = 1/2$, $a_8 = 1$, and $k_1 = 2$, with the other exponents zero, i.e.

$$\underset{(2.5-D)}{\overline{W}_{co}} \approx \left(\frac{1}{t}\right)^{1/2} \left(1 - \left(\frac{2h}{\tilde{c}_0 t}\right)^2\right)^{1/2} \left(t_{2\tilde{z}}\right)^1 . \tag{4.42}$$

Although it is feasible to present each weighting function in this form, it does not provide additional insight. In this study, only a few of the many possible combinations of exponents are examined (and there are many other possible parameters and combinations of parameters not included in the generalized form). Once the concept of a generalized weighting function is grasped, it is more straightforward to express the equations in a compact form such as equation (4.39).

Using only input and output trace weighting, the amount of downweighting with opening angle can be increased by choosing a larger value for the exponents a_2 and a_3. In this study, I investigate only the effect of changing a_3 with $a_2 = 2$ and $k_1 = 2$. Equation (4.42) can be re-expressed as

$$\underset{(2.5-D)}{\overline{W}_{co}} \approx \frac{t_{2\tilde{z}}}{t^{1/2}} \left(1 - \frac{(2h)^2}{(\tilde{c}_0 t)^2}\right)^{a_3} . \tag{4.43}$$

Figures 4.12c-d show the reflectivity for $a_3 = 1$ (annotated as '2.5-D Gray $t_0/t\cos^2$' in figure title). The contours of equal reflectivity in Figure 4.12d are beginning to approximate the shape of the isochron (solid line in Figure 4.12b), suggesting progress towards a dip-independent weighting function. Higher powers are applied in Figures 4.12e-f ($a_3 = 2$, annotated as '2.5-D Gray $t_0/t\cos^4$' in figure title) and Figures 4.12g-h ($a_3 = 3$, annotated as '2.5-D Gray $t_0/t\cos^6$' in figure title). The fact that the iso-reflectivity contours begin to approximate the shape of the isochrons suggests that a more balanced reflectivity (i.e. closer to unity everywhere) could be achieved by fractionally adjusting the exponent in $1/t^{a_1}$. This adjustment was tested with moderate success—the resulting reflectivity plots (not shown here) indicate that the curvature of the reflectivity surface in Figures 4.12g-h is not described by a simple exponential of input two-way traveltime.

In a constant wavespeed medium, the output two-way traveltime $t_{2\tilde{z}}$ is related to the input two-way traveltime and the equivalent offset h_e by the 'Kirchhoff NMO' equation:

$$t_{2\tilde{z}} = \left(t^2 - \frac{(2h_e)^2}{\tilde{c}_0^2}\right)^{1/2} = t\left(1 - \frac{(2h_e)^2}{(\tilde{c}_0 t)^2}\right)^{1/2}. \tag{4.44}$$

In other words, for the fixed values of $a_4 = -1$, $a_5 = 2$, $a_6 = 1/2$, and $k_2 = 2$, this portion of the generalized weighting function is equal to output two-way traveltime $t_{2\tilde{z}}$. This suggests that the following two forms are equal:

$$\overline{W}_{\substack{co \\ (2.5-D)}} \approx \frac{t_{2\tilde{z}}}{t^{1/2}} = \frac{\left(t^2 - \dfrac{4h_e^2}{\tilde{c}_0^2}\right)^{1/2}}{t^{1/2}}. \tag{4.45}$$

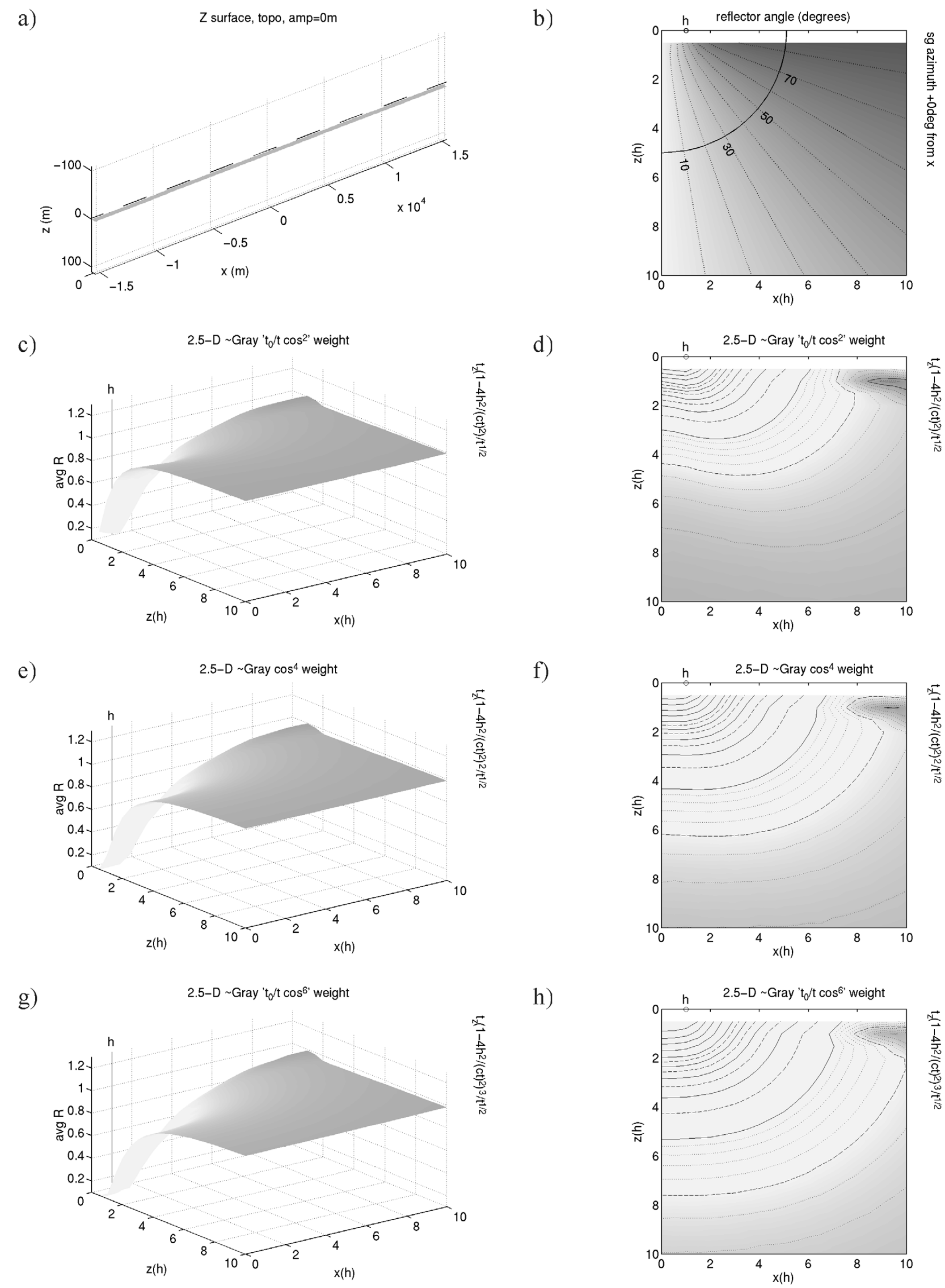

Figure 4.12. Increasing obliquity effect in 2.5-D Gray '$t_0/t\cos$' weight: equation (4.43) with variable a_3. a) 2.5-D reference diagram. b) Reflector dip (strike parallels y-axis) with normalized horizontal distance $x(h)$ and depth $z(h)$ measured from the shot-receiver midpoint to specular reflection point. c-h) Perspective view and contours of imaged amplitude of reflector with intervals of 0.1 (solid lines), 0.05 (dashed lines) and 0.01 (dotted lines): c-d) 2.5-D Gray '$t_0/t\cos^2$' weight ($a_3 = 1$), e-f) 2.5-D Gray '$t_0/t\cos^4$' weight ($a_3 = 2$), g-h) 2.5-D Gray '$t_0/t\cos^6$' weight ($a_3 = 3$).

Reflectivity for the first form is shown in Figures 4.13c-d. This is just the common-offset t_0/t weight given previously by equation (4.40). Reflectivity for the second form is shown in Figures 4.13e-f. As expected, it is identical to the first form. For comparison, reflectivity for the 2.5-D Gray t_0/t cosine obliquity weight [in various forms as equations (4.37), (4.39), (4.42) and (4.43)] is shown in Figures 4.13g-h. The downweighting effects are similar everywhere except at zero-dip, where the Gray weight downweights as the opening angle increases, i.e. at shallower depths given a fixed source-receiver offset. Given the similarity, and the extra effort required to calculate the additional weighting term in the Gray weight, one can conclude that the common-offset t_0/t weight is sufficient. Note, however, that the synthetic tests are noise-free, and assume that reflectivity is angle-independent. Hence, the effect on field data (or more realistic synthetic data) may lead to a different conclusion. As well, the tests presented here focus on accurate recovery of an average of angle-dependent reflectivity. Equally important is the spatial resolution obtained by imaging. Tests by Esmersoy and Miller (1989), and discussions in Miller et al. (1987) and Bleistein et al. (2001, esp. Chapter 4), suggest that weighting by opening angle, or even the square of the opening angle, can produce an image with better resolution.

With the decision to abandon weighting based on opening angle for 2.5-D imaging, all the remaining weights in the generalized weighting function can be applied in the binned EO trace domain, and equation (4.41) reduces to

$$\underset{(2.5-D)}{\overline{W}_{co}} \approx \underbrace{\left(\frac{1}{t}\right)^{a_4}\left(1-\left(\frac{(k_2 h_e)}{(\tilde{c}_0 t)}\right)^{a_5}\right)^{a_6}\left(t_{2\tilde{z}}\right)^{a_7}}_{\text{EO gather traces}} . \tag{4.46}$$

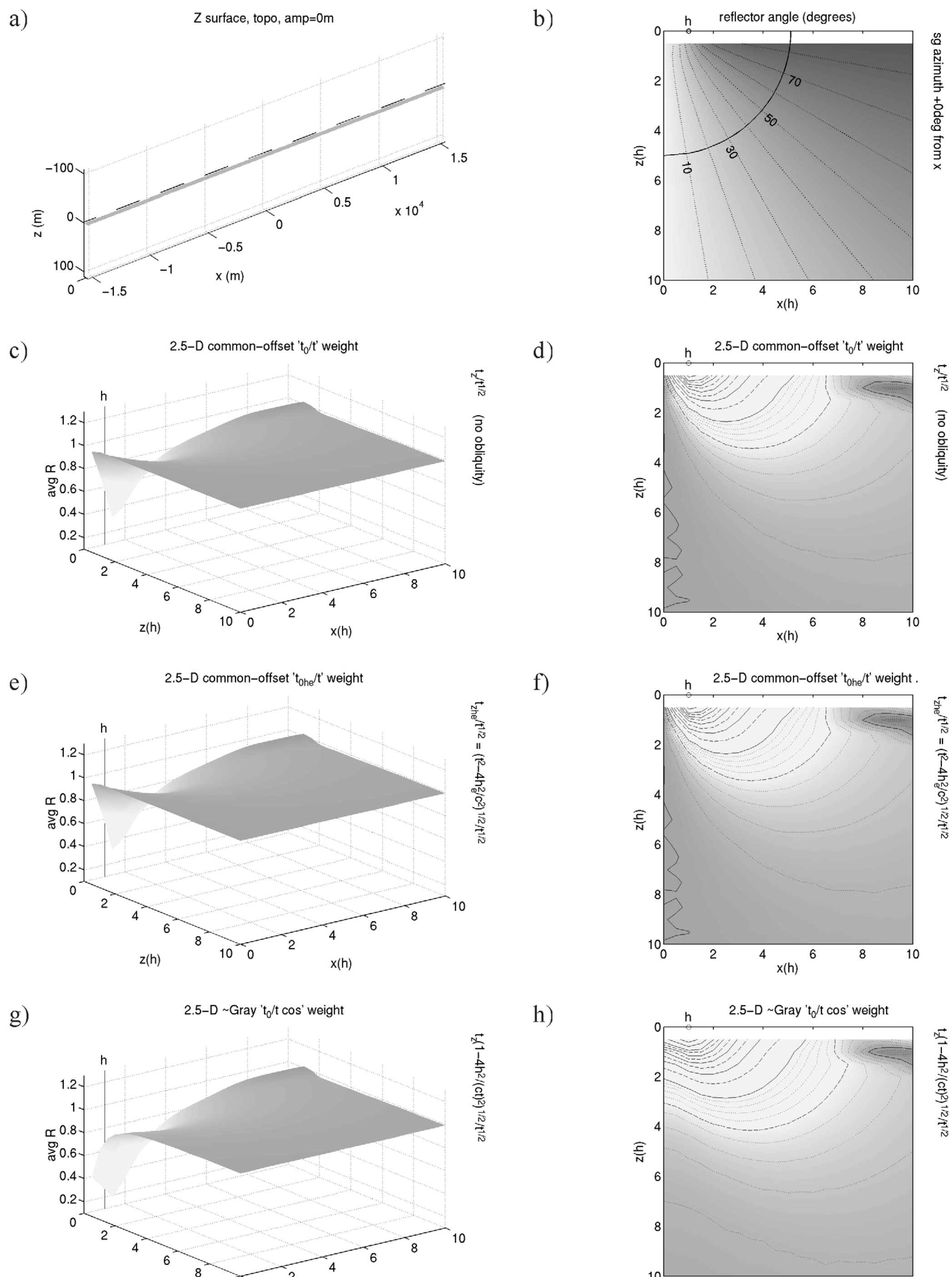

Figure 4.13. Comparison of 2.5-D EO ‘t_0/t’ weights [equation (4.43)] with 2.5-D Gray ‘$t_0/t\cos$’ weight. a) 2.5-D reference diagram. b) Reflector dip (strike parallels y-axis) with normalized horizontal distance $x(h)$ and depth $z(h)$ measured from the shot-receiver midpoint to specular reflection point. c-h) Perspective view and contours of imaged amplitude of reflector with intervals of 0.1 (solid lines), 0.05 (dashed lines) and 0.01 (dotted lines): c-d) 2.5-D EO gather ‘t_0/t’ weight ($a_4 = 1/2$, $a_6 = 0$, $a_7 = 1$), e-f) 2.5-D EO gather ‘t_0/t’ weight ($a_4 = 1/2$, $a_5 = 2$, $a_6 = 1/2$, $a_7 = 0$), g-h) 2.5-D Gray ‘$t_0/t\cos$’ weight ($a_3 = 1/2$).

An obvious starting point is the common-offset t_0/t weight with additional downweighting from the term $\left(1-(2h_e)^2/(c_0 t)^2\right)^{1/2}$, i.e. with fixed values of $a_4 = 1/2$, k_2 = 2, $a_5 = 2$, $a_6 = 1/2$, and $a_7 = 1$. The resulting weighting function can be simplified using equation (4.44) as follows:

$$\underset{(2.5-D)}{\overline{W}_{co}} \approx \frac{t_{2\tilde{z}}}{t^{1/2}}\left(1-\frac{(2h_e)^2}{(\tilde{c}_0 t)^2}\right)^{1/2} = \frac{t_{2\tilde{z}}}{t^{1/2}}\frac{\left(t^2-\dfrac{4h_e^{\ 2}}{\tilde{c}_0^2}\right)^{1/2}}{t} = \frac{t_{2\tilde{z}}}{t^{1/2}}\frac{t_{2\tilde{z}}}{t} . \tag{4.47}$$

The effect of additional downweighting by a factor of $t_{2\tilde{z}}/t$ is shown in Figures 4.14c-d (annotated as 'modified t_{0h_e}/t weight A' in the figure captions). At zero-dip, the effect is similar to the additional downweighting by opening angle in the Gray weight (Figures 4.13g-h). As dip increases, however, the effect is quite different. The 'modified t_{0h_e}/t weight A' produces a strong downweighting with increasing dip angle. Downweighting is reduced by changing the factor k_2 in the weighting function [equation (4.46) with fixed values $a_4 = 1/2$, $a_5 = 2$, $a_6 = 1/2$, and $a_7 = 1$]. The effect for a value of $k_2 = \sqrt{2}$ is shown in Figures 4.14e-f (annotated as 'modified t_{0h_e}/t weight B' in the figure captions) and for a value of $k_2 = 1$ in Figures 4.14g-h (annotated as 'modified t_{0h_e}/t weight C' in the figure captions).

The modified t_{0h_e}/t weight C is given as

$$\underset{(2.5-D)}{\overline{W}_{co}} \approx \frac{t_{2\tilde{z}}}{t^{1/2}}\sqrt{1-\frac{h_e^2}{(\tilde{c}_0 t)^2}} , \tag{4.48}$$

and is the preferred 2.5-D weighting function as determined by this study. Comparing the contours of reflectivity amplitude in Figure 4.14h with contours of constant reflector dip angle in Figure 4.14b, we see that the modified t_{0h_e}/t weight C downweights reflectivity amplitude by only 10% at 50° dip. A second desirable characteristic is that steep dips at

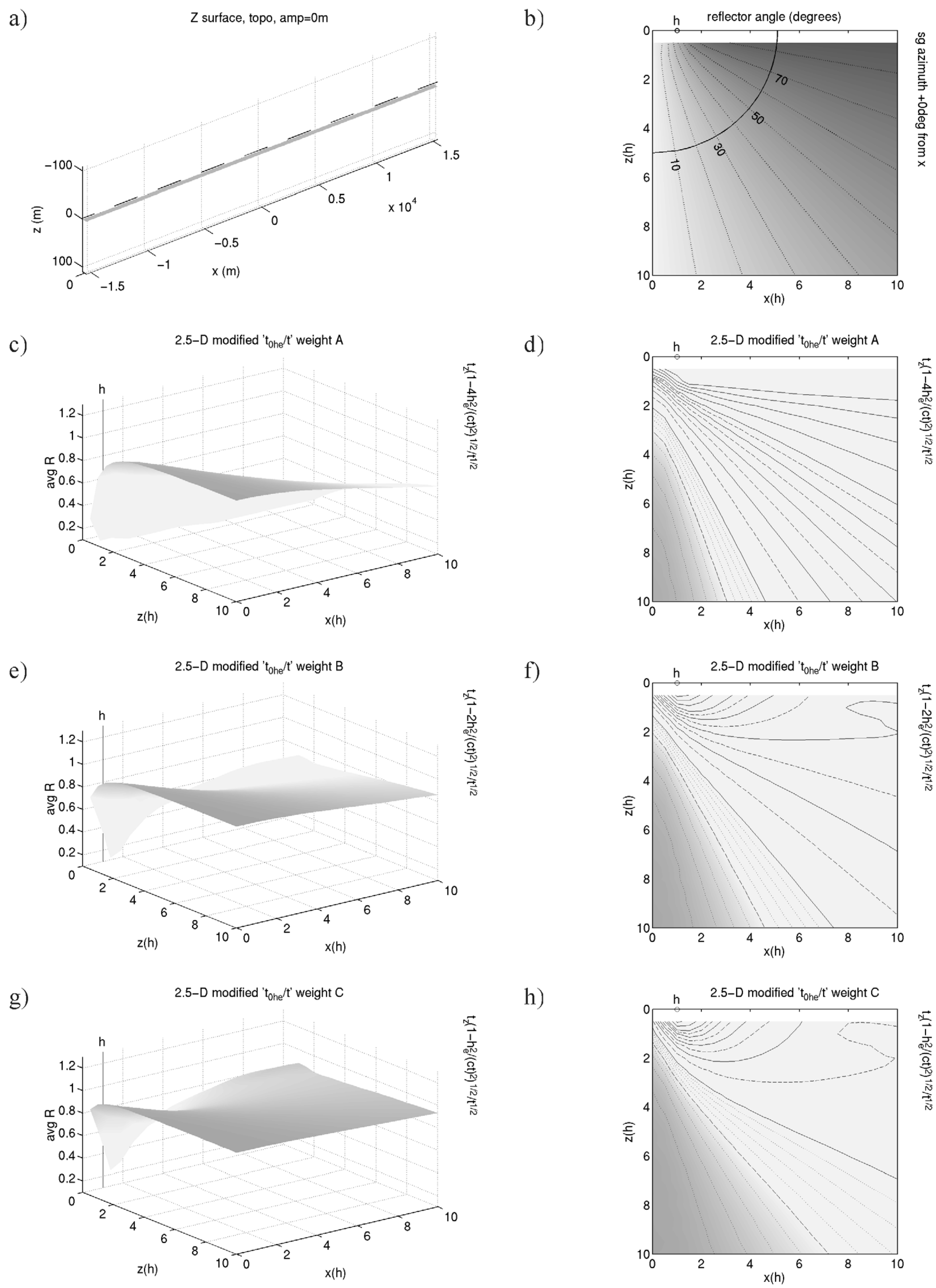

Figure 4.14. Custom weighting function that downweights with dip angle obtained by varying k_2 in equation (4.46) [fixed $a_4 = 1/2$, $a_5 = 2$, $a_6 = 1/2$, and $a_7 = 1$]. a) 2.5-D reference diagram. b) Reflector dip reference diagram. c-h) Perspective view and contours of imaged amplitude of reflector with intervals of 0.1 (solid lines), 0.05 (dashed lines) and 0.01 (dotted lines): c-d) 2.5-D modified 't_{0he}/t' weight A ($k_2 = 2$), e-f) 2.5-D modified 't_0/t' weight B ($k_2 = \sqrt{2}$), g-h) 2.5-D modified 't_0/t' weight C ($k_2 = 1$). The 2.5-D modified 't_0/t' weight C is preferred, but rigorous testing has not been attempted for this dissertation.

shallow depths are downweighted for large source-receiver offsets (close to the normalized valued of *h* in Figure 4.14h), although this is more a function of the $8/t^2$ approximation introduced earlier [see equation (4.28) and the corresponding weighting effect in Figures 4.11h, 4.13d and 4.13f]. Finally, the weight can be applied in the binned EO trace domain prior to Kirchhoff NMO. This creates preweighted EO gathers suitable for conventional velocity analysis tools such as constant or percentage velocity stacks. In Chapter 5, weight C is used to for EOM prestack time migration of crustal seismic reflection data from SNORCLE line 1.

A dip filter can be implemented by tapering the equivalent offset gathers as a function of the equivalent offset h_e. The same effect can be achieved by limiting the input migration aperture. Figure 4.15 shows the effect of tapering the equivalent offset gathers using a cosine-bell taper from $h_e = 1.5z + h$ to $h_e = 3z + 2h$. Figures 4.15a/b are the 2.5-D reference and dip, while Figures 4.15c/d, 4.15e/f, and 4.15g/h show the effect of the taper on the 2.5-D optimum common-offset weight, the 2.5-D Gray '$t_0/t\cos$' weight, and the 2.5-D modified 't_{0h_e}/t' weight C, respectively. In all cases, the taper does not change the amplitude of reflectors with dips less than ~60°, and then gradually reduces the amplitude of reflectors to zero at dips of ~75°.

The custom weighting functions presented above have been derived and tested for 2.5-D migration in constant wavespeed media, but can be applied with excellent results as weighting functions for depth migration in variable wavespeed media (Dellinger et al., 2000).

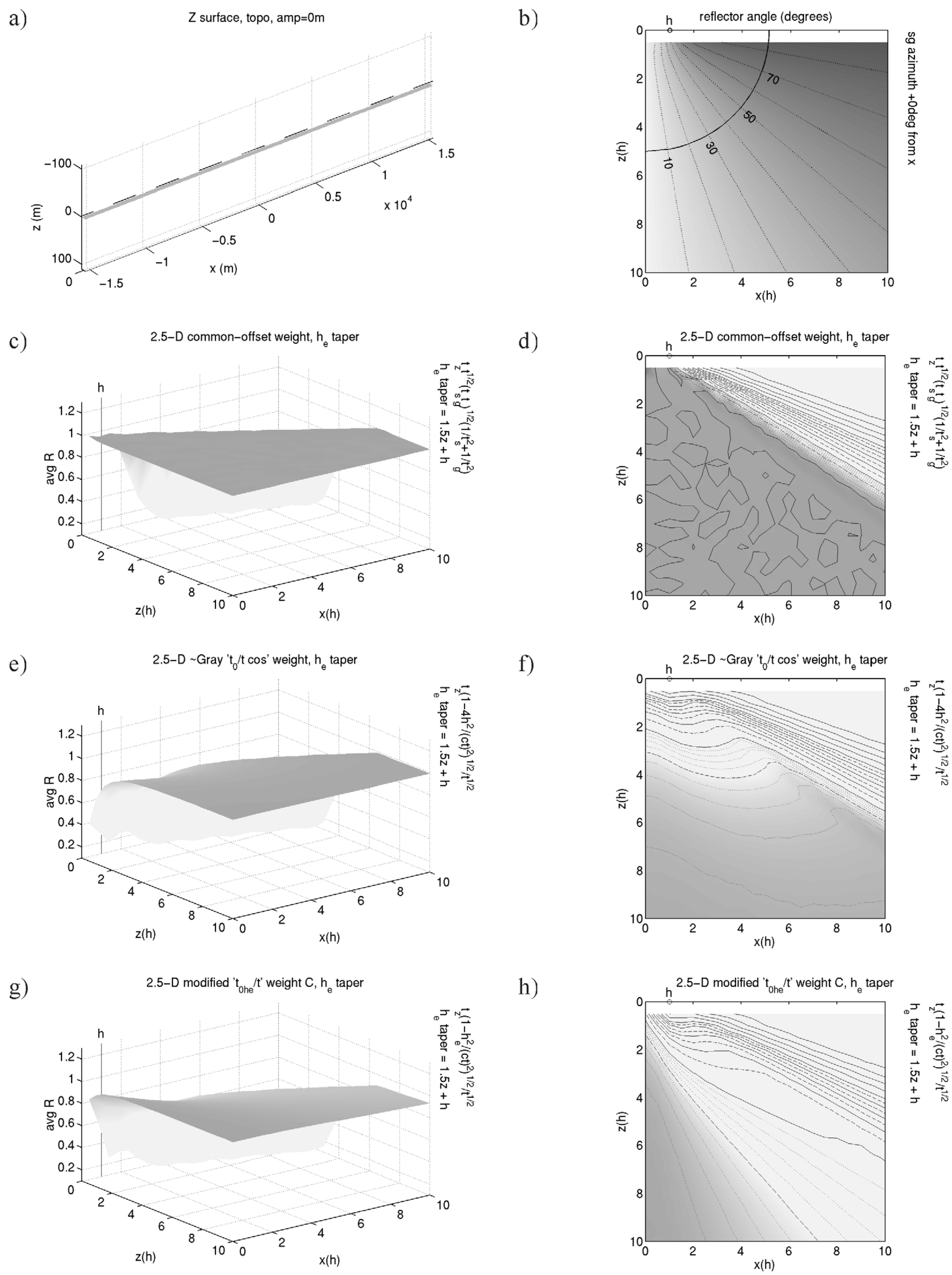

Figure 4.15. A dip filter obtained by tapering in equivalent offset. a) 2.5-D reference diagram. b) Reflector-dip reference diagram. c-h) Perspective view and contours of imaged amplitude of reflector with intervals of 0.1 (solid lines), 0.05 (dashed lines) and 0.01 (dotted lines): c-d) Exact 2.5-D common-offset weight with h_e taper. e-f) 2.5-D Gray 't_0/tcos' weight (downweights obliquity) with h_e taper, g-h) 2.5-D modified 't_0/t' weight C (downweights dip) with h_e taper. The taper does not change the amplitude of reflectors with dips less than ~60°, and gradually reduces the amplitude of reflectors to zero at dips of ~75°.

4.6.2 Custom weighting function for efficient implementation of 3-D EOM prestack time migration

Much of the discussion presented in the previous section on custom weighting functions for efficient 2.5-D migration can be applied to 3-D migration. The basic approximate Zhang 't_0/t' weight derived for 3-D migration as equation (4.30) differs from the 2.5-D zero-offset migration formula [equation (4.40)] by a square root power of t in the denominator and a sign change. Thus, with a change in sign, the generalized formula given by equation (4.41) is valid for 3-D custom weighting functions, i.e.:

$$\underset{(3-D)}{\overline{W}_{co}} \approx -\underbrace{\left(\frac{1}{t}\right)^{a_1}\left(1-\left(\frac{(k_1 h)}{(\tilde{c}_0 t)}\right)^{a_2}\right)^{a_3}}_{\text{input traces}}\underbrace{\left(\frac{1}{t}\right)^{a_4}\left(1-\left(\frac{(k_2 h_e)}{(\tilde{c}_0 t)}\right)^{a_5}\right)^{a_6}\left(t_{2\bar{z}}\right)^{a_7}}_{\text{EO gather traces}}\underbrace{\left(t_{2\bar{z}}\right)^{a_8}}_{\text{output traces}}\ . \qquad (4.49)$$

As discussed previously, the relevant parameters are as follows:

input trace:

t	- input two-way traveltime,
h	- source-receiver offset, and
$\tilde{c}_0$	- estimate of average wavespeed

binned EO gather trace:

t	- input two-way traveltime,
$t_{2\bar{z}}$	- output two-way traveltime,
h_e	- equivalent offset, and
$\tilde{c}_0$	- average estimate of wavespeed

and output trace:

$t_{2\bar{z}}$	- the output two-way traveltime.

The three general effects desirable in a custom weighting function:

downweighting as a function of obliquity (i.e. the opening angle at the reflector),

downweighting as a function of dip angle, and

downweighting or upweighting as a function of two-way traveltime (input or output),

can be achieved with a reduced version of equation (4.49),

$$\underset{(3-D)}{\overline{W}_{co}} \approx -\frac{t_{2\tilde{z}}}{t}\left(1-\left(\frac{(2h)}{(\tilde{c}_0 t)}\right)^2\right)^{a_3}\left(1-\left(\frac{h_e}{(\tilde{c}_0 t)}\right)^2\right)^{a_6}. \tag{4.50}$$

In Figures 4.16-4.27, the results of the 3-D tests are shown for values of $a_3 = 0$, 1/2, and 1; $a_6 = 0$ and 1/2; each with and without an h_e taper. For example, with $a_3 = 1$ and $a_6 = 0$, the weighting function given by equation (4.50) is called the '3-D Zhang '$t_0/t\cos^2$' weight':

$$\underset{(3-D)}{\overline{W}_{co}} \approx -\frac{t_{2\tilde{z}}}{t}\left(1-\left(\frac{(2h)}{(\tilde{c}_0 t)}\right)^2\right). \tag{4.51}$$

(see Figure 4.18). With $a_3 = 1/2$ and $a_6 = 1/2$, the weighting function given by equation (4.50) is called the '3-D modified '$t_{0h_e}/t\cos$' weight C':

$$\underset{(3-D)}{\overline{W}_{co}} \approx -\frac{t_{2\tilde{z}}}{t}\left(1-\left(\frac{(2h)}{(\tilde{c}_0 t)}\right)^2\right)^{1/2}\left(1-\frac{h_e^2}{(\tilde{c}_0 t)^2}\right)^{1/2}. \tag{4.52}$$

(see Figure 4.20). All of the permutations plotted in the Figures 4.16-4.27 appear to provide reasonable amplitudes over a wide range of dips and depths. Further testing is required to determine and compare the spatial resolution of the various weighting functions. This testing is left for future work.

(Chapter 4 continues on page 292, after Figure 4.26)

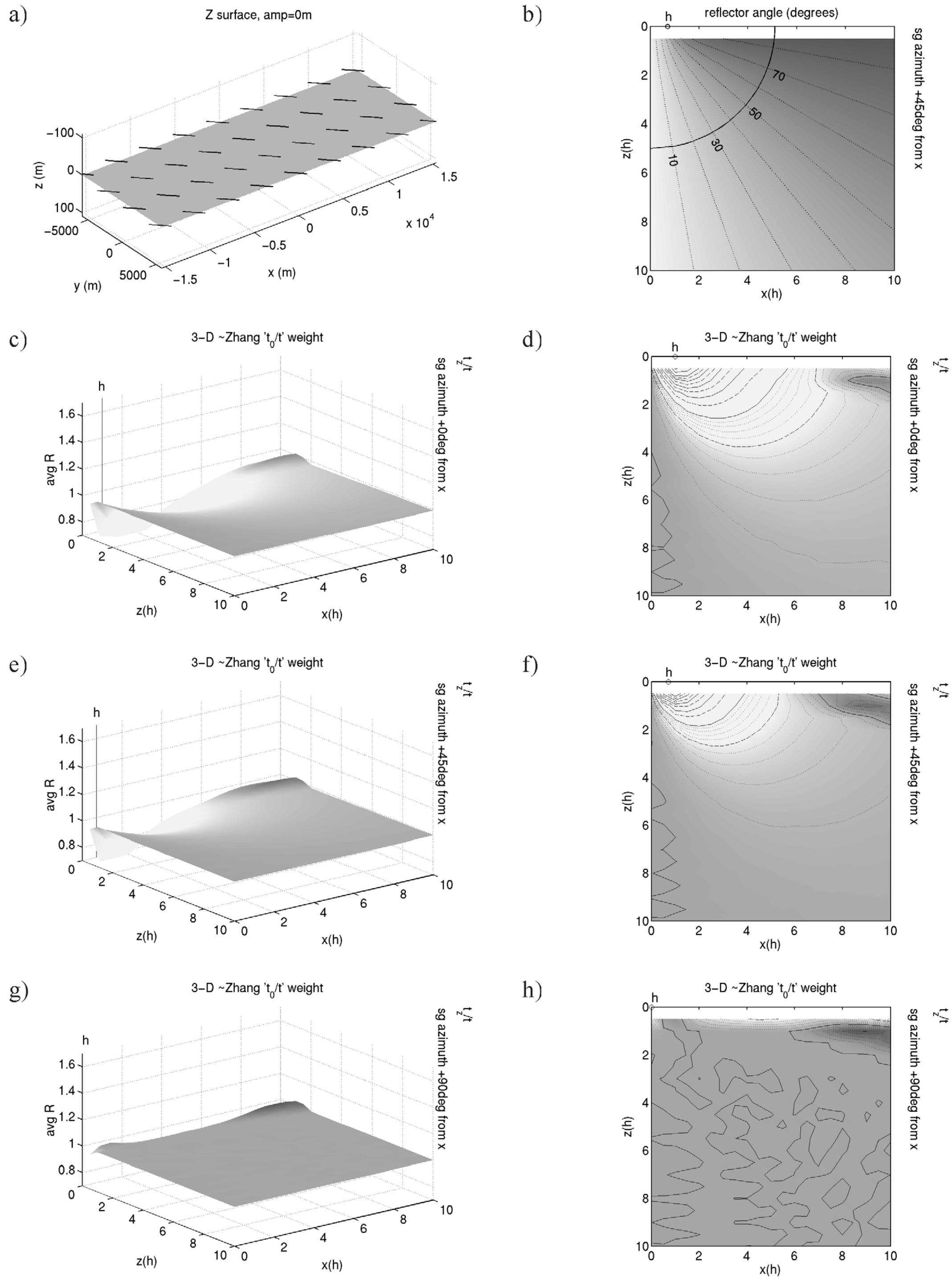

Figure 4.16. 3-D Zhang 't_0/t' weight: equation (4.50) with $a_3 = 0$ and $a_6 = 0$ [repeat of Figure 4.10, see equation (4.30)]. a) 3-D reference diagram. b) Reflector dip (strike parallels y-axis) with normalized horizontal distance $x(h)$ and depth $z(h)$ measured from the shot-receiver midpoint to specular reflection point. c) e) g) Perspective view of imaged amplitude of reflector (input reflection coefficient unity) for shot-receiver azimuths at 0, 45 and 90 degrees from x-axis. d) f) g) Contours of imaged amplitude of reflector with intervals of 0.1 (solid lines), 0.05 (dashed lines) and 0.01 (dotted lines).

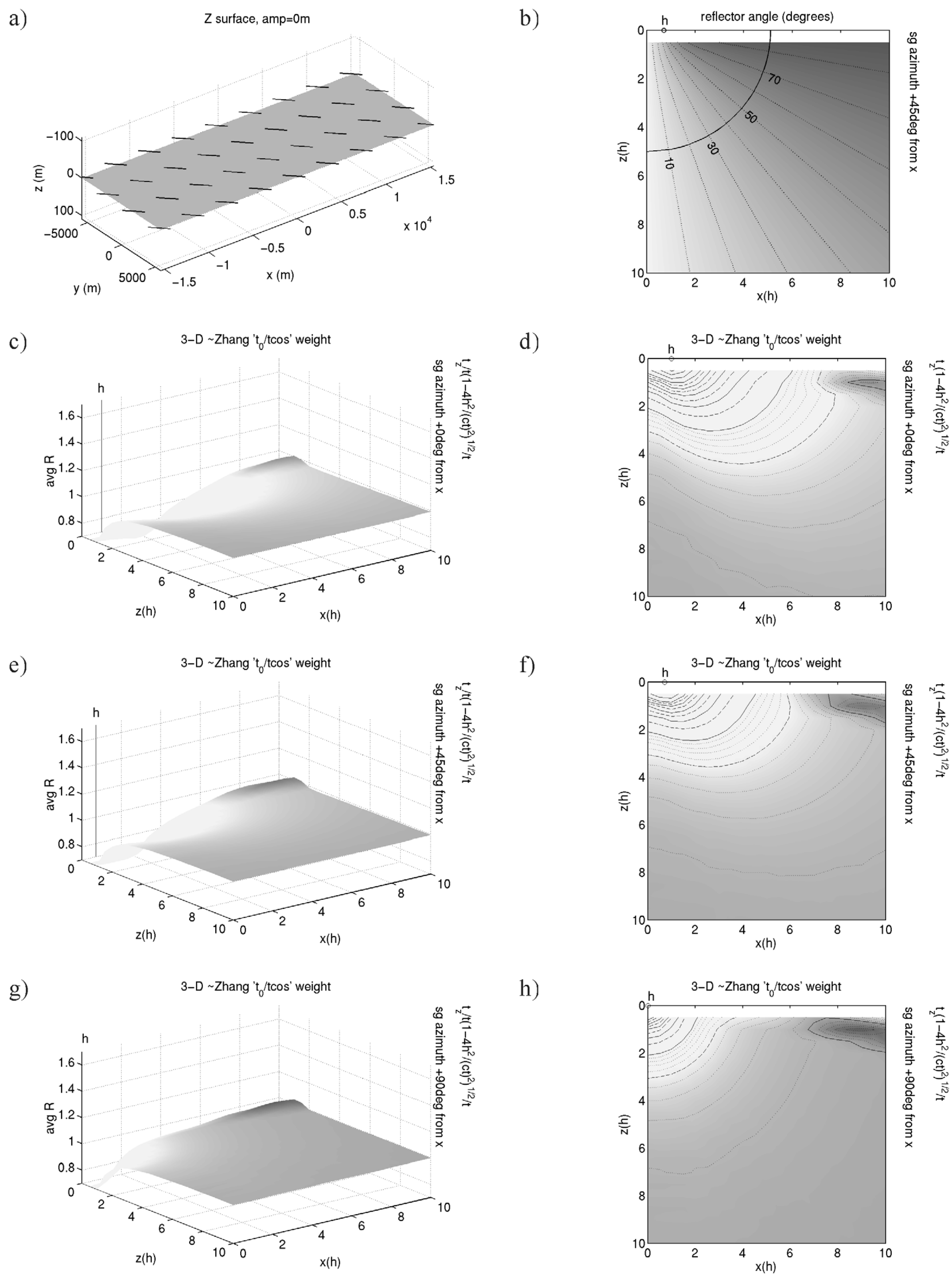

Figure 4.17. 3-D Zhang 't_0/tcos' weight: equation (4.50) with $a_3 = 1/2$ and $a_6 = 0$.
a) 3-D reference diagram. b) Reflector dip (strike parallels y-axis) with normalized horizontal distance $x(h)$ and depth $z(h)$ measured from the shot-receiver midpoint to specular reflection point. c) e) g) Perspective view of imaged amplitude of reflector (input reflection coefficient unity) for shot-receiver azimuths at 0, 45 and 90 degrees from x-axis. d) f) g) Contours of imaged amplitude of reflector with intervals of 0.1 (solid lines), 0.05 (dashed lines) and 0.01 (dotted lines).

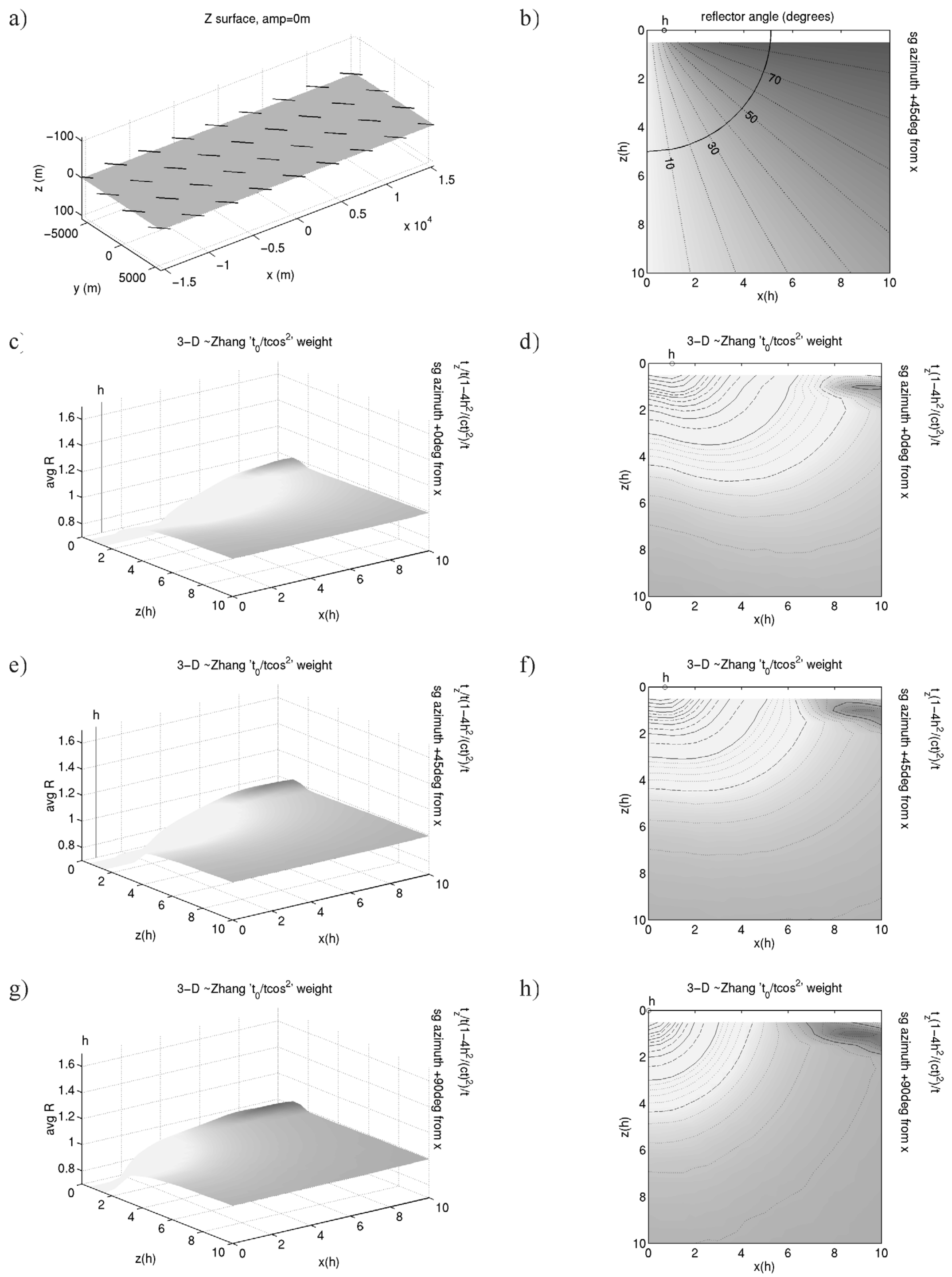

Figure 4.18. 3-D Zhang '$t_0/t\cos^2$' weight: equation (4.50) with $a_3 = 1$ and $a_6 = 0$ [see equation (4.51)]. a) 3-D reference diagram. b) Reflector dip (strike parallels y-axis) with normalized horizontal distance $x(h)$ and depth $z(h)$ measured from the shot-receiver midpoint to specular reflection point. c) e) g) Perspective view of imaged amplitude of reflector (input reflection coefficient unity) for shot-receiver azimuths at 0, 45 and 90 degrees from x-axis. d) f) g) Contours of imaged amplitude of reflector with intervals of 0.1 (solid lines), 0.05 (dashed lines) and 0.01 (dotted lines).

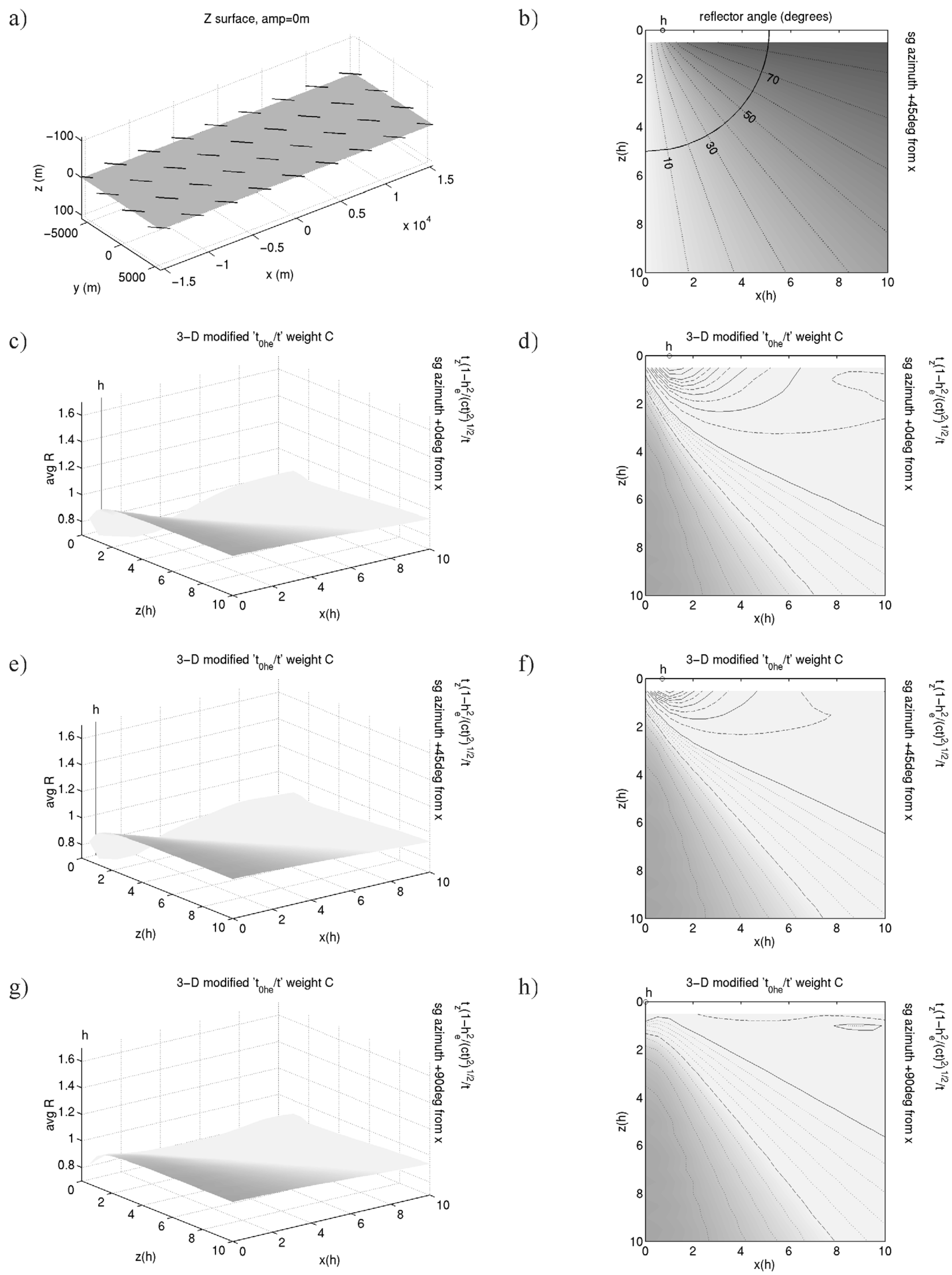

Figure 4.19. 3-D modified 't_{0he}/t' weight C: equation (4.50) with $a_3 = 0$ and $a_6 = 1/2$.
a) 3-D reference diagram. b) Reflector dip (strike parallels *y*-axis) with normalized horizontal distance *x*(*h*) and depth *z*(*h*) measured from the shot-receiver midpoint to specular reflection point. c) e) g) Perspective view of imaged amplitude of reflector (input reflection coefficient unity) for shot-receiver azimuths at 0, 45 and 90 degrees from *x*-axis. d) f) g) Contours of imaged amplitude of reflector with intervals of 0.1 (solid lines), 0.05 (dashed lines) and 0.01 (dotted lines).

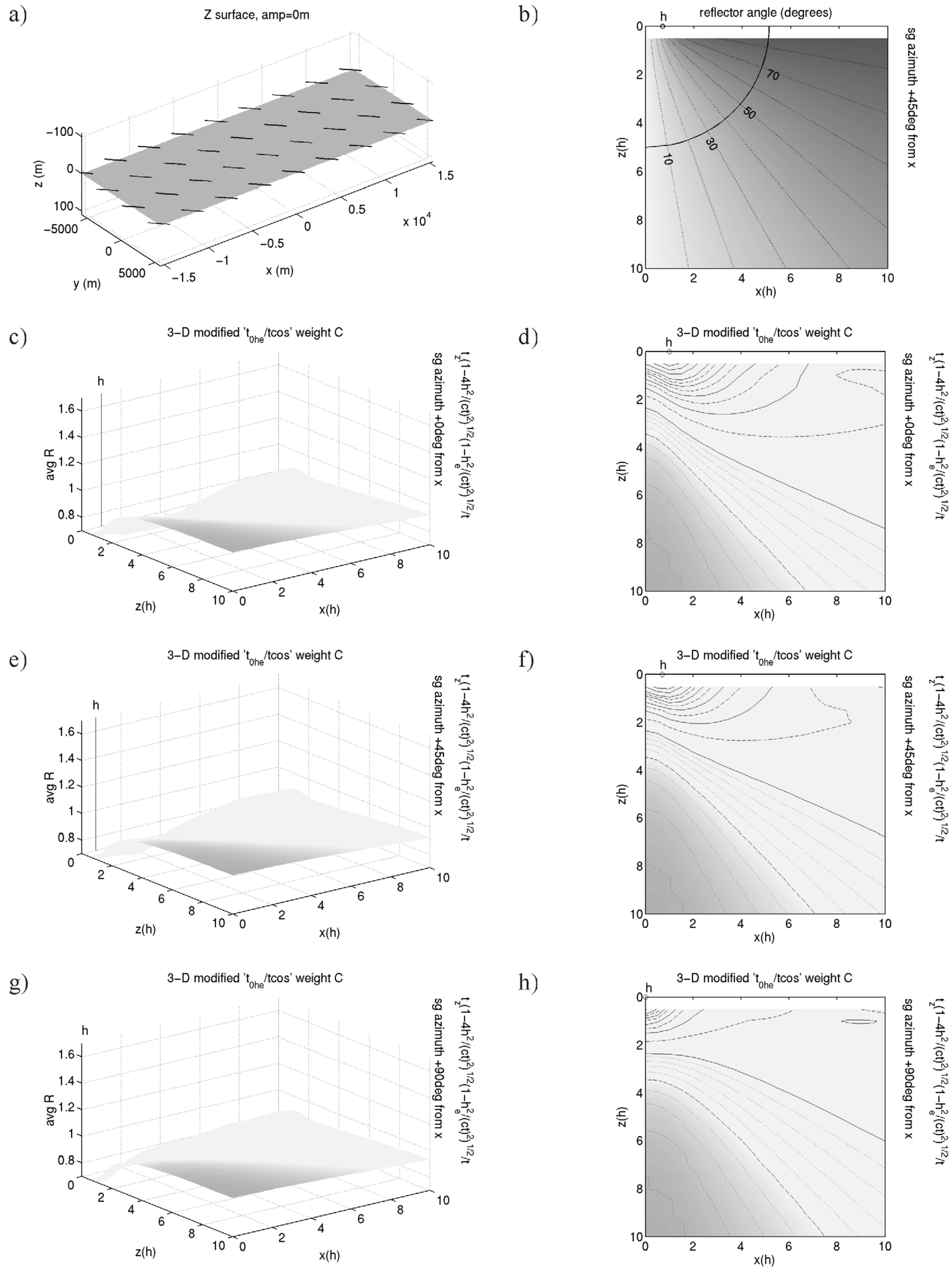

Figure 4.20. 3-D modified '$t_{0\text{he}}/t\cos$' weight C: equation (4.50) with $a_3 = 1/2$ and $a_6 = 1/2$ [equation (4.52)]. a) 3-D reference diagram. b) Reflector dip (strike parallels y-axis) with normalized horizontal distance $x(h)$ and depth $z(h)$ measured from the shot-receiver midpoint to specular reflection point. c) e) g) Perspective view of imaged amplitude of reflector (input reflection coefficient unity) for shot-receiver azimuths at 0, 45 and 90 degrees from x-axis. d) f) g) Contours of imaged amplitude of reflector with intervals of 0.1 (solid lines), 0.05 (dashed lines) and 0.01 (dotted lines).

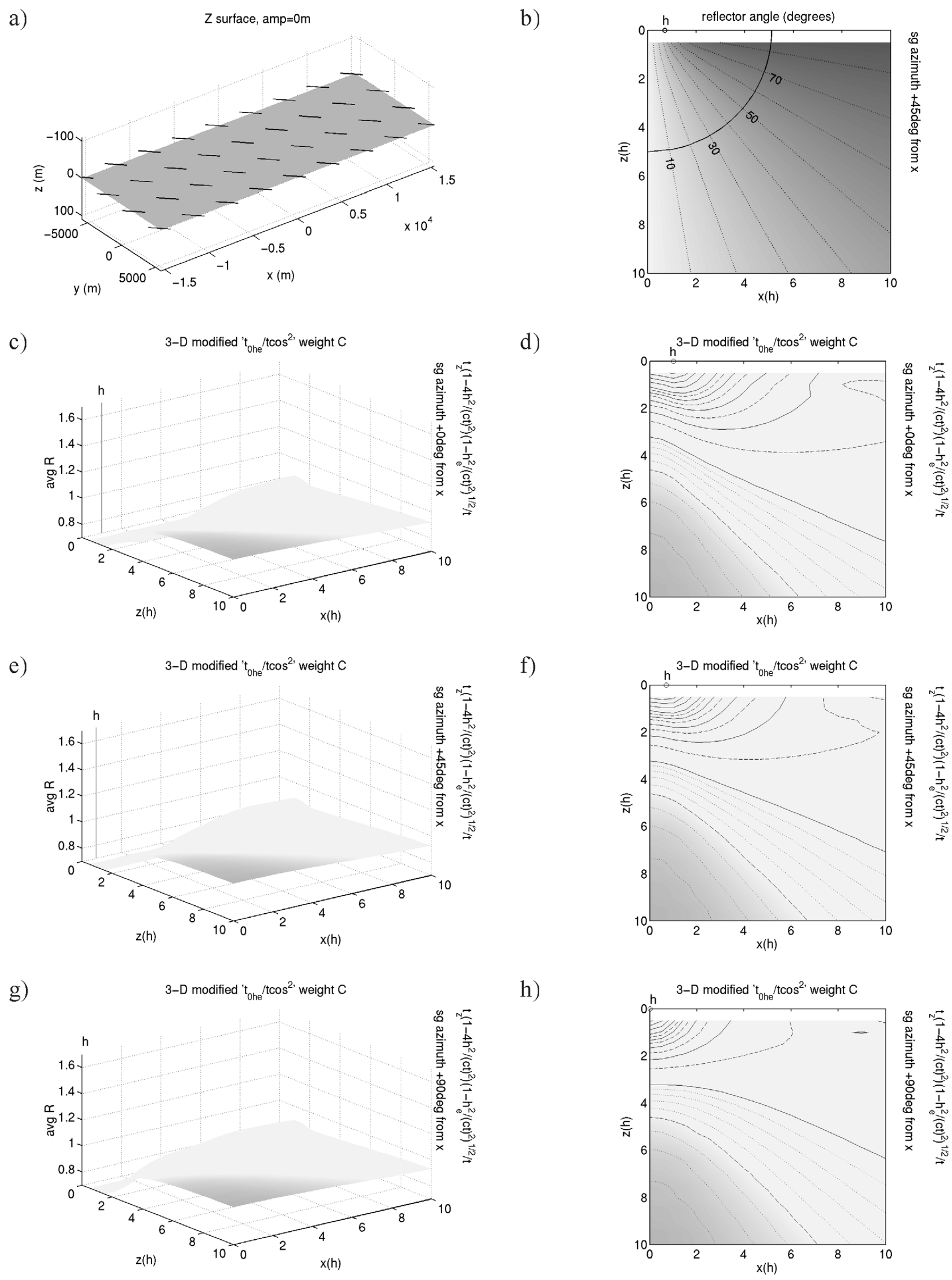

Figure 4.21. 3-D modified '$t_{0he}/t\cos^2$' weight C: equation (4.50) with $a_3 = 1$ and $a_6 = 1/2$.
a) 3-D reference diagram. b) Reflector dip (strike parallels *y*-axis) with normalized horizontal distance $x(h)$ and depth $z(h)$ measured from the shot-receiver midpoint to specular reflection point. c) e) g) Perspective view of imaged amplitude of reflector (input reflection coefficient unity) for shot-receiver azimuths at 0, 45 and 90 degrees from *x*-axis. d) f) g) Contours of imaged amplitude of reflector with intervals of 0.1 (solid lines), 0.05 (dashed lines) and 0.01 (dotted lines).

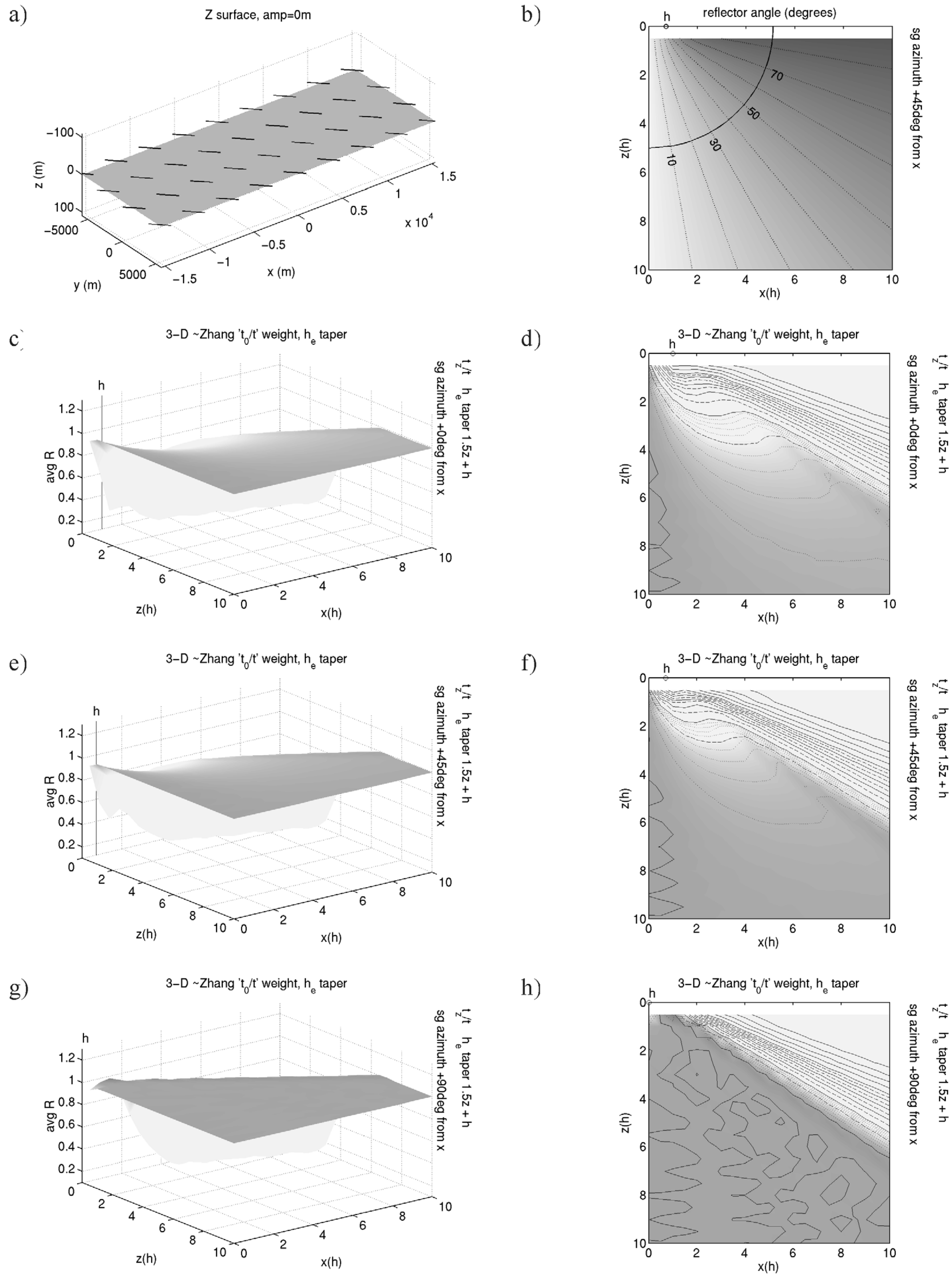

Figure 4.22. 3-D Zhang 't_0/t' weight, h_e taper: equation (4.50) with $a_3 = 0$, $a_6 = 0$, h_e taper.
a) 3-D reference diagram. b) Reflector dip (strike parallels *y*-axis) with normalized horizontal distance *x*(*h*) and depth *z*(*h*) measured from the shot-receiver midpoint to specular reflection point. c) e) g) Perspective view of imaged amplitude of reflector (input reflection coefficient unity) for shot-receiver azimuths at 0, 45 and 90 degrees from *x*-axis. d) f) g) Contours of imaged amplitude of reflector with intervals of 0.1 (solid lines), 0.05 (dashed lines) and 0.01 (dotted lines).

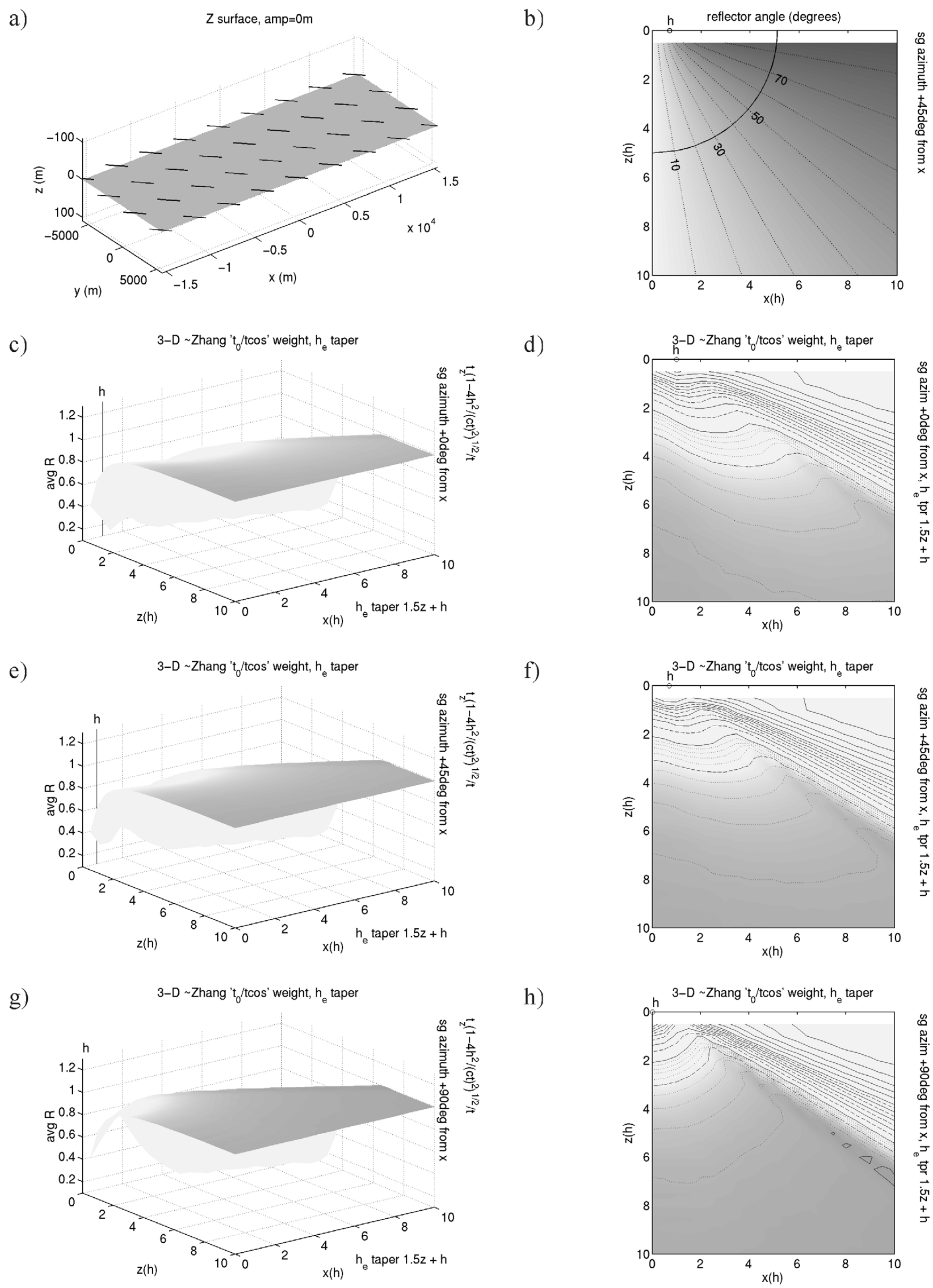

Figure 4.23. 3-D Zhang '$t_0/t\cos$' weight, h_e taper: equation (4.50) with $a_3 = 1/2$, $a_6 = 0$, h_e taper.
a) 3-D reference diagram. b) Reflector dip (strike parallels *y*-axis) with normalized horizontal distance *x*(*h*) and depth *z*(*h*) measured from the shot-receiver midpoint to specular reflection point. c) e) g) Perspective view of imaged amplitude of reflector (input reflection coefficient unity) for shot-receiver azimuths at 0, 45 and 90 degrees from *x*-axis. d) f) g) Contours of imaged amplitude of reflector with intervals of 0.1 (solid lines), 0.05 (dashed lines) and 0.01 (dotted lines).

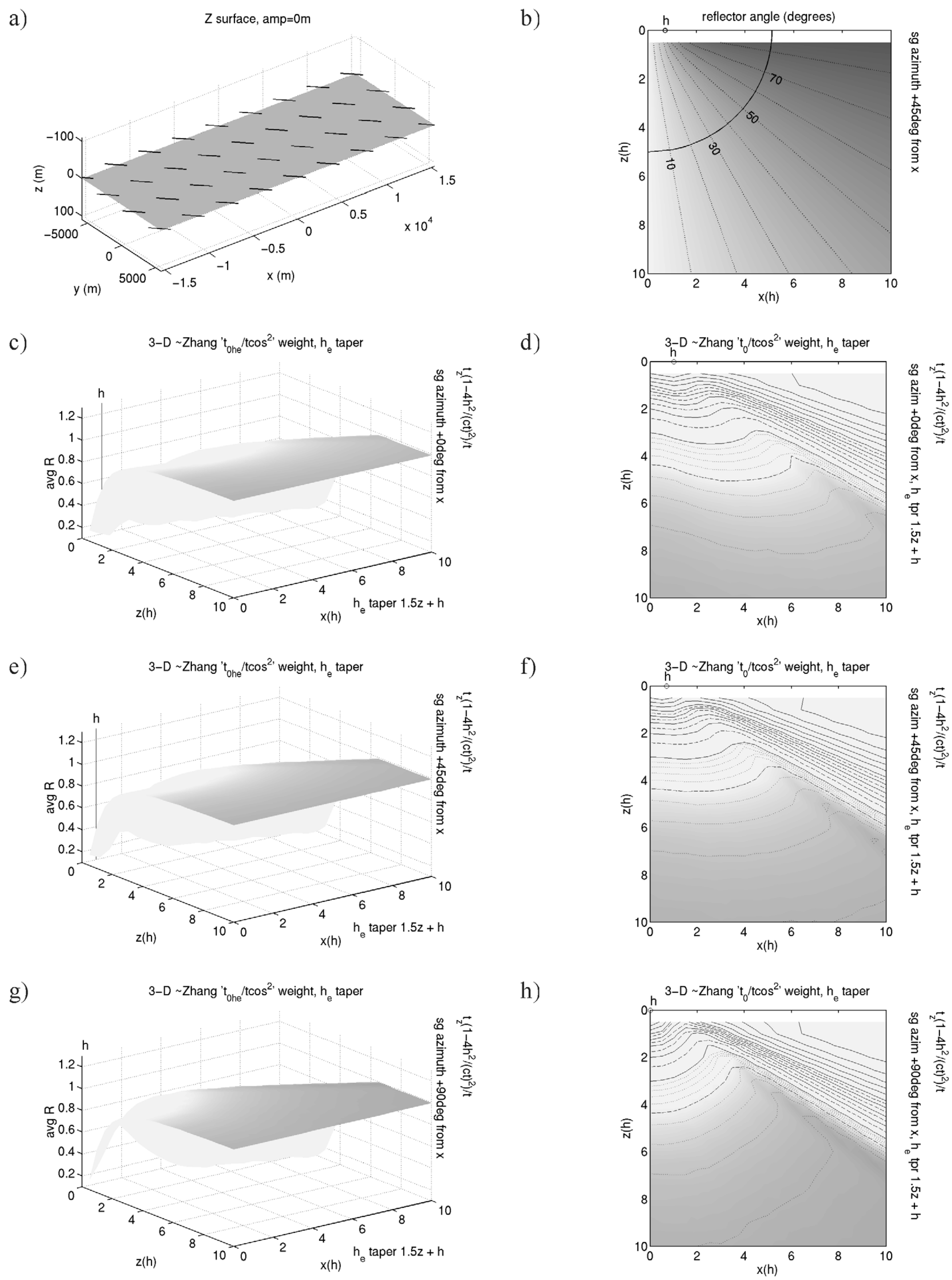

Figure 4.24. 3-D Zhang '$t_0/t\cos^2$' weight, h_e taper: equation (4.50) with $a_3 = 1$, $a_6 = 0$, h_e taper. a) 3-D reference diagram. b) Reflector dip (strike parallels *y*-axis) with normalized horizontal distance $x(h)$ and depth $z(h)$ measured from the shot-receiver midpoint to specular reflection point. c) e) g) Perspective view of imaged amplitude of reflector (input reflection coefficient unity) for shot-receiver azimuths at 0, 45 and 90 degrees from *x*-axis. d) f) g) Contours of imaged amplitude of reflector with intervals of 0.1 (solid lines), 0.05 (dashed lines) and 0.01 (dotted lines).

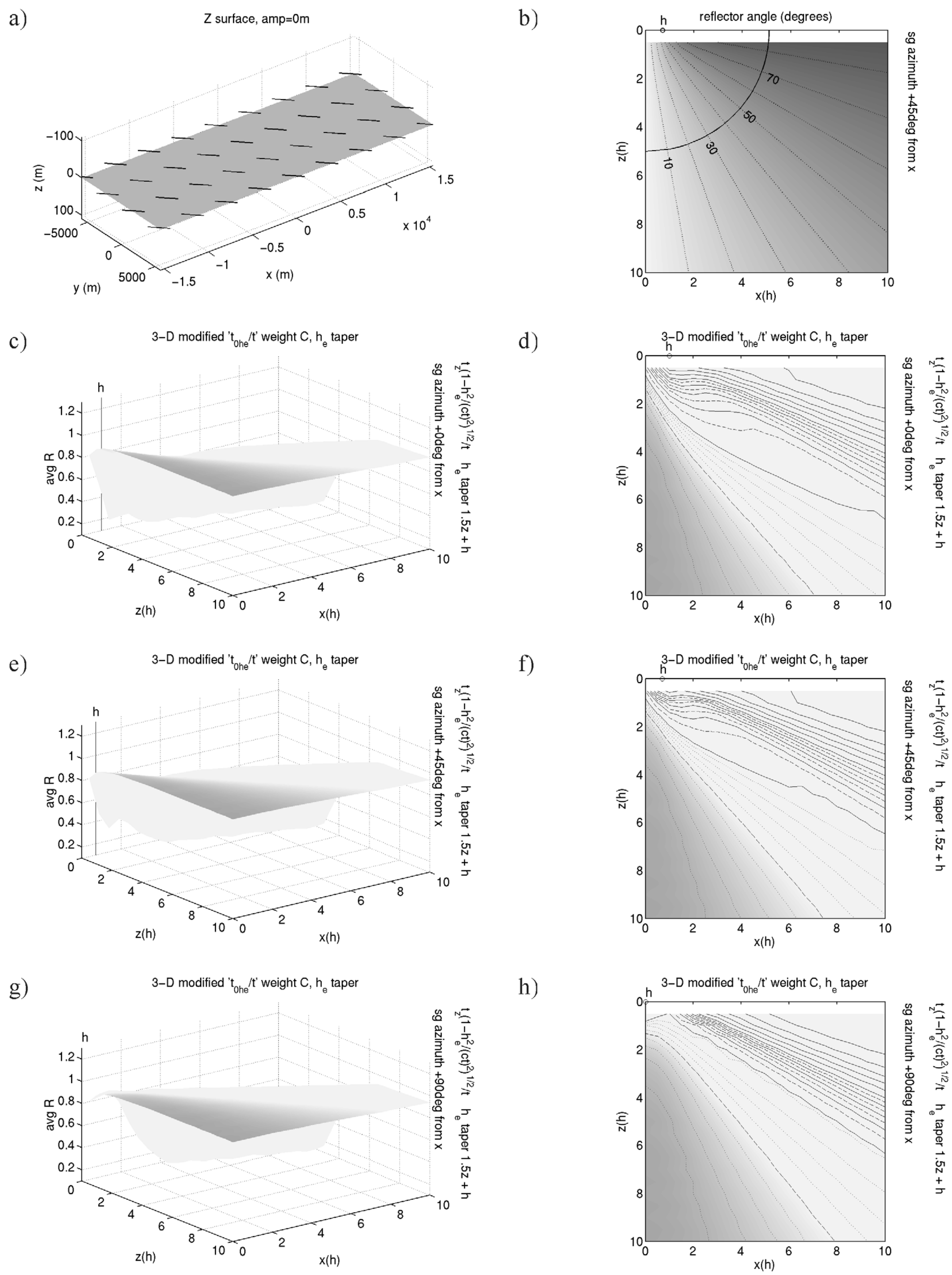

Figure 4.25. 3-D modified 't_{0he}/t' weight C, h_e taper: equation (4.50) with $a_3 = 0$, $a_6 = 1/2$, h_e taper. a) 3-D reference diagram. b) Reflector dip (strike parallels y-axis) with normalized horizontal distance $x(h)$ and depth $z(h)$ measured from the shot-receiver midpoint to specular reflection point. c) e) g) Perspective view of imaged amplitude of reflector (input reflection coefficient unity) for shot-receiver azimuths at 0, 45 and 90 degrees from x-axis. d) f) g) Contours of imaged amplitude of reflector with intervals of 0.1 (solid lines), 0.05 (dashed lines) and 0.01 (dotted lines).

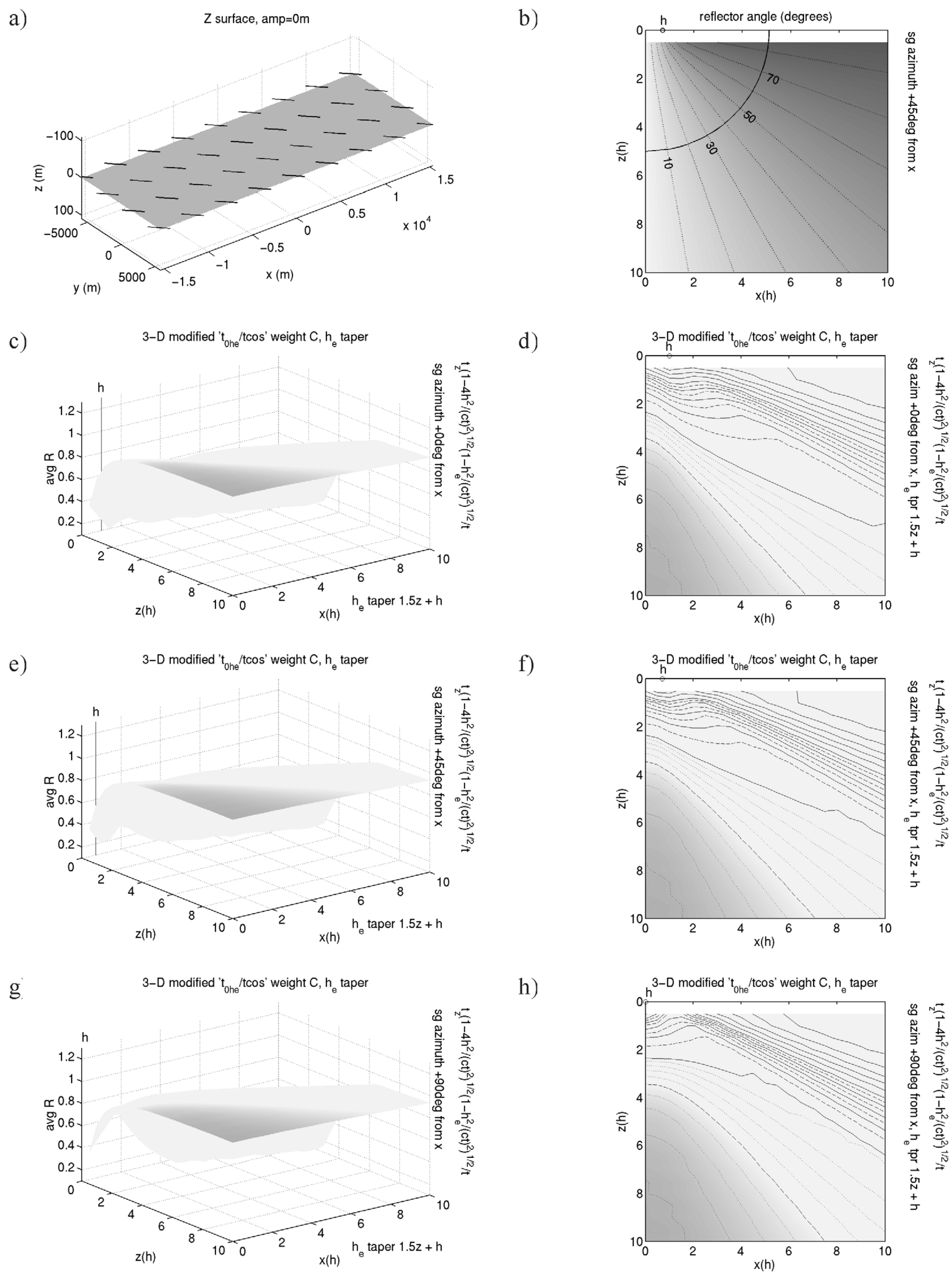

Figure 4.26. 3-D modified 't_{0he}/tcos' weight C, h_e taper: equation (4.50) with $a_3 = 1/2$, $a_6 = 1/2$, h_e taper. a) 3-D reference diagram. b) Reflector dip (strike parallels *y*-axis) with normalized horizontal distance *x*(*h*) and depth *z*(*h*) measured from the shot-receiver midpoint to specular reflection point. c) e) g) Perspective view of imaged amplitude of reflector (input reflection coefficient unity) for shot-receiver azimuths at 0, 45 and 90 degrees from *x*-axis. d) f) g) Contours of imaged amplitude of reflector with intervals of 0.1 (solid lines), 0.05 (dashed lines) and 0.01 (dotted lines).

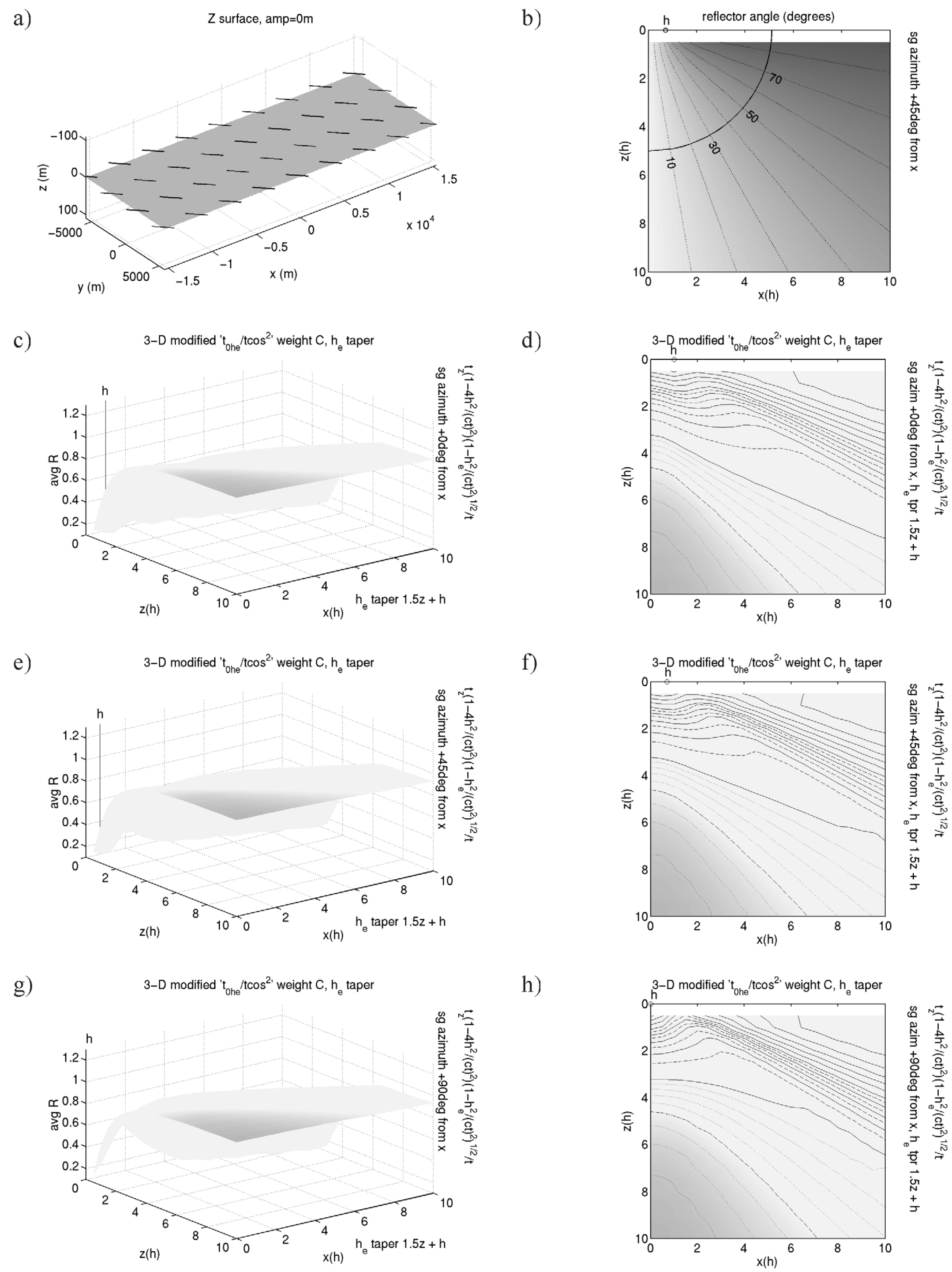

Figure 4.27. 3-D modified '$t_{0\mathrm{he}}/t\cos^2$' weight C, $\mathrm{h_e}$ taper: equation (4.50) with $a_3 = 1$, $a_6 = 1/2$, $\mathrm{h_e}$ taper. a) 3-D reference diagram. b) Reflector dip (strike parallels *y*-axis) with normalized horizontal distance *x*(*h*) and depth *z*(*h*) measured from the shot-receiver midpoint to specular reflection point. c) e) g) Perspective view of imaged amplitude of reflector (input reflection coefficient unity) for shot-receiver azimuths at 0, 45 and 90 degrees from *x*-axis. d) f) g) Contours of imaged amplitude of reflector with intervals of 0.1 (solid lines), 0.05 (dashed lines) and 0.01 (dotted lines).

4.7 COMPARISON WITH WIGGINS' (1984) DOUBLE-DOWNWARD CONTINUATION KIRCHHOFF MIGRATION WEIGHTS

In this section, I continue in the spirit of examining common practice by comparing Wiggins' (1984) non-recursive constant-wavespeed Kirchhoff migration weights with the 'optimum' formula given by equations (4.5)/(4.8). Wiggins derives his migration formula as a double-downward continuation followed by a $t=0$ imaging condition. His method is closely related to the recursive double-downward continuation scheme of Schultz and Sherwood (1980) and the f-k (frequency-wavenumber or Stolt) prestack migration scheme of Stolt (1978) and Stolt and Weglein (1985) (see discussion of contribution 10 in Section 1.7). Since the EWM scheme of Margrave et al. (1999)—the Fourier analogue of EOM—is based on Stolt prestack theory, EWM does not produce true-amplitude estimates of the reflectivity coefficient.

In Section 4.3, I showed that the weighting function for a 2.5-D common-offset configuration [equation (4.12)] could be thought of as a linear combination of the common-shot weight [equation (4.10)] and the common-receiver weight [equation (4.11)], i.e.

$$\underset{(2.5-D)}{\overline{W}_{co}}(\mathbf{x}_G,\mathbf{x}_s,\mathbf{x}_g)=\frac{N_s}{N_{co}}\frac{dx_s}{dx_g}\underset{(2.5-D)}{\overline{W}_s}(\mathbf{x}_G,\mathbf{x}_s,\mathbf{x}_g)+\frac{N_g}{N_{co}}\underset{(2.5-D)}{\overline{W}_g}(\mathbf{x}_G,\mathbf{x}_s,\mathbf{x}_g). \qquad (4.53)$$

That the correct result is a combination of common-shot and common-receiver weights might lead one to think (incorrectly) that alternating downward-continuation of shots and receivers is an accurate migration/inversion method. Although the kinematics of double-downward continuation are correct, the dynamics are not.

Before introducing Wiggins' weights, I will describe the basic principle of double-downward continuation and a $t=0$ imaging condition that Wiggins uses to obtain a map of subsurface reflectors. First the wavefield recorded by receivers on the surface is downward continued into the subsurface. In effect, the downward continued wavefield can now be thought of as being recorded by receivers in the subsurface. Reciprocity is invoked to switch the surface sources and subsurface receivers. The downward continued wavefield is now equivalent to a reciprocal wavefield recorded by receivers on the surface but originating from shots in the subsurface (these reciprocal receivers are, of course, located at the original shot locations). Hence, the reciprocal wavefield can be downward continued into the subsurface—the second downward continuation. Finally, an appropriate imaging condition is required to extract the wavefield amplitudes, hopefully at the subsurface location of the reflectors.[12]

The first downward continuation accounts for the traveltime from the receivers to the subsurface location, while the second downward continuation accounts for the traveltime from the shots to the subsurface location. With all the traveltime for a given reflection in the recorded trace accounted for, the desired image or map of the subsurface can be obtained by extracting the wavefield amplitudes from the double downward-continued wavefield at time $t = 0$. Note that Wiggins implements his method as a Kirchhoff migration. Thus, both of the downward-continuations and the imaging condition can be achieved by a simple weighted summation over a time surface in the filtered data. Unfortunately, the resulting amplitude map is not directly related to the strength of the reflection coefficients—as can be seen by examining Wiggins' 3-D and 2.5-D migration equations.

Wiggins obtains the following equation for 3-D migration in a constant-wavespeed medium, re-expressed here in the notation of this dissertation as

---

[12] Inverse wavefield propagation uses the reference wavespeed, not the unknown true wavespeed. Hence both focusing and positioning of reflectors depend on the reference model.

$$\underset{(3-D)}{\bar{I}}(x_G, y_G, t_{2\bar{z}}) = \sum_{traces} \underset{(3-D)}{\overline{W}_w}(x_G, y_G, t_{2\bar{z}}, \mathbf{x}_s, \mathbf{x}_g) \left[\frac{\partial^2}{\partial t^2} \underset{(3-D)}{p_S^-}(\mathbf{x}_g, \mathbf{x}_s, t) \right]_{t=t_s+t_g}, \tag{4.54}$$

where

$$\underset{(3-D)}{\overline{W}_w}(x_G, y_G, t_{2\bar{z}}, \mathbf{x}_s, \mathbf{x}_g) = \frac{-dS_s dS_g}{\tilde{c}_0^2} \left\{ \frac{1}{r_{Gs} r_{gG}} \cos\theta_{gG} \cos\theta_{Gs} \right\}. \tag{4.55}$$

Equations (4.54)/(4.55) can be compared with the 'optimum' formula given by equations (4.5)/(4.8), re-expressed here as

$$\underset{(3-D)}{\overline{R}}(x_G, y_g, t_{2\bar{z}}) = \sum_{traces} \underset{(3-D)}{\overline{W}_{co}}(x_G, y_G, t_{2\bar{z}}, \mathbf{x}_s, \mathbf{x}_g) \left[\hat{f}(t) * \frac{\partial}{\partial t} \underset{(3-D)}{p_S^-}(\mathbf{x}_g, \mathbf{x}_s, t) \right]_{t=t_s+t_g} \tag{4.56}$$

and

$$\underset{(3-D)}{\overline{W}_{co}}(x_G, y_G, t_{2\bar{z}}, \mathbf{x}_s, \mathbf{x}_g) = \frac{-2dS_s}{\tilde{c}_0 N_{co}} \left\{ \frac{(r_{Gs} + r_{gG})}{r_{gG}} \cos\theta_{gG} + \frac{(r_{Gs} + r_{gG})}{r_{Gs}} \cos\theta_{Gs} \right\} \tag{4.57}$$

Wiggins' 3-D formula includes an extra time-derivative operator, neglects the bandlimiting filter $\hat{f}(t)$, and applies an inaccurate weighting function. If we ignore constant terms including wavespeed, Wiggins' weighting function is incorrect by a factor of order $1/r^2$, where r is an approximate distance measure from shot or receiver to subsurface imaging point. This error introduces the largest effect—that reflectivity in the output image would be significantly reduced in amplitude at depth.

Wiggins obtains the following equation for 2-D migration in a constant-wavespeed medium, re-expressed here in the notation of this dissertation as

$$\underset{(2-D)}{\bar{I}}(x_G, t_{2\bar{z}}) = \sum_{traces} \underset{(2-D)}{\overline{W}_w}(x_G, t_{2\bar{z}}, \mathbf{x}_s, \mathbf{x}_g) \left[\frac{\partial}{\partial t} \underset{(2-D)}{p_S^-}(\mathbf{x}_g, \mathbf{x}_s, t) \right]_{t=t_s+t_g}, \tag{4.58}$$

where

$$\overline{W}_{\underset{(2-D)}{w}}(x_G, t_{2\bar{z}}, \mathbf{x}_s, \mathbf{x}_g) = \frac{-1}{\tilde{c}_0\sqrt{r_{Gs} r_{gG}}} \cos\theta_{gG} \cos\theta_{Gs}\,. \tag{4.59}$$

In an appendix to his paper, Wiggins determines that the 2-D migration formula can be applied to 2.5-D data by multiplying the input data by $\sqrt{t}$. In a constant-wavespeed medium, this is equivalent to multiplying by $\sqrt{r_{Gs}+r_{gG}}\big/\sqrt{c_0}$, suggesting that Wiggins' 2.5-D weighting function for point-source data is

$$\overline{W}_{\underset{(2.5-D)}{w}}(x_G, y_G, t_{2\bar{z}}, \mathbf{x}_s, \mathbf{x}_g) = \frac{-dx_s dx_g}{\tilde{c}_0^{3/2}} \left\{ \frac{\sqrt{r_{Gs}+r_{gG}}}{\sqrt{r_{Gs} r_{gG}}} \cos\theta_{gG} \cos\theta_{Gs} \right\}. \tag{4.60}$$

Equations (4.58)/(4.60) can be compared with the 'optimum' formula given by equations (4.9)/(4.12), re-expressed here as

$$\underset{(2.5-D)}{\overline{R}}(x_G, t_{2\bar{z}}) \approx \sum_{traces} \overline{W}_{(2.5-D)}(x_G, t_{2\bar{z}}, \mathbf{x}_s, \mathbf{x}_g) \left[\hat{f}(t) * \mathcal{H}\left\{ \left(\frac{\partial}{\partial t}\right)^{1/2} \underset{(2.5-D)}{p_S^-}(\mathbf{x}_g, \mathbf{x}_s, t) \right\} \right]_{t=t_s+t} . \tag{4.61}$$

and

$$\overline{W}_{\underset{(2.5-D)}{co}}(x_G, t_{2\bar{z}}, \mathbf{x}_s, \mathbf{x}_g) = \frac{2\sqrt{2\pi}\, dx_s}{\sqrt{\tilde{c}_0}\, N_{co}} \left\{ \sqrt{r_{Gs}+r_{gG}} \left(\frac{\sqrt{r_{Gs}}}{\sqrt{r_{gG}}} \cos\theta_{gG} + \frac{\sqrt{r_{gG}}}{\sqrt{r_{Gs}}} \cos\theta_{Gs} \right) \right\}. \tag{4.62}$$

Wiggins' 2.5-D weighting function is incorrect by a factor of order $1/r$. The bandlimiting filter $\hat{f}(t)$ is neglected, and, in addition to the phase and amplitude errors introduced by the extra half-time-derivative operator, the incorrect sign and missing Hilbert transform result in a further phase error of $\pi/2$.

Obviously, double-downward continuation does not create an image of the subsurface reflectivity with amplitude and phase corresponding to a zero-phase bandlimited singular function whose peak amplitude is an average of the angle-dependent reflectivity coefficients. Synthetic testing and comparison of the various migration weights could further enhance the argument, but this aspect has been left for future work.

4.8 SUMMARY—PRACTICAL 2.5-D AND 3-D EOM PRESTACK TIME MIGRATION

In this chapter, the frequency-domain expressions for imaging reflectivity in constant wavespeed media from Chapter 3 were re-expressed in the time-domain. The common-offset migration/inversion formula [equations (4.5)/(4.8)] was shown to be optimum for estimating stacked reflectivity, whereas both the common-shot and common-receiver formulae [equations (4.5)/(4.6) or (4.5)/(4.7)] yield biased results. However, the exact common-offset formula is not practical for EOM prestack time migration because calculation of the weighting function depends on distance measures that vary with each shot and receiver location relative to each subsurface imaging point. The exact weighting function is computationally expensive to evaluate, and not necessarily accurate given other approximations inherent in time migrations.

In a time migration, the vertical coordinate of the output imaging point is approximated by the two-way traveltime corresponding to the apex of a best-fit diffraction-traveltime surface in the input data. The distance measures in the weighting function can be converted to corresponding traveltimes at a best-fitting wavespeed parameter. The resulting weighting function [equation (4.22)] is thus an approximation, suggesting that further approximations might reduce the computational cost without significant loss of accuracy. The goal was identified to be a weighting function that can be applied in some or all of three domains: input traces, equivalent-offset-gather traces and/or output traces. Following approximations introduced by Gray (1998b), Dellinger et al. (2000), and Zhang et al. (2000), generalized custom weighting functions were derived for imaging in 2.5-D [equation (4.41)] and in 3-D [equation (4.49)]. For 2.5-D, the modified 't_{0h_e}/t' weight C [equation (4.48)] is preferred over the Gray 't_0/t' cosine obliquity weight [equation (4.39)]. For 3-D, the modified 't_{0h_e}/t' weight C [equation (4.52)] is preferred over the Zhang 't_0/t' weight [equation (4.51)].

Note that the weighting functions have a broader application as approximate weights for Kirchhoff-type (ray-traced) depth migrations in media with variable wavespeed. Jaramillo et al. (2000) use the term ‘true-amplitude time-migration weights’ to describe constant-wavespeed expressions for the Beylkin Jacobian (Beylkin, 1982, 1985) and geometrical spreading, with distances from the source to output point and receiver to output point replaced by traveltimes. These simplified weights can produce a stacked migrated section without the brightening and dimming often associated with weights determined by dynamic ray-tracing (Dellinger et al., 2000).

The practical time-domain constant-wavespeed time-migration formulae can be extended to variable wavespeed by assuming a different constant wavespeed model for each output point (see e.g. Schneider, 1978 for discussion of RMS $c(z)$ wavespeed, and Section 1.5 for a discussion of variable wavespeed). The resulting image is distorted, both in imaging position and amplitude, but peak amplitudes over a range of dips and depths will be approximately proportional to stacked reflectivity and therefore are preserved in a relative sense. This leads to the term ‘relative amplitude-preserving prestack time migration’, an adaptation of a term introduced by Eaton and Milkereit (1997). In Chapter 5, practical weights are applied to EOM prestack time migration for improved imaging of crustal structure in northwestern Canada.

CHAPTER 5: PRESTACK TIME MIGRATION WITH RELATIVE AMPLITUDE PRESERVATION: RESULTS FROM LINE 1 OF THE LITHOPROBE SNORCLE TRANSECT

5.1 INTRODUCTION

In this chapter, I present a new processing flow for imaging crustal seismic reflection data, and test it on a portion of LITHOPROBE SNORCLE line 1. The objective is to preserve relative reflection strength over a wide range of dips and depths. Relative amplitude is preserved by careful preprocessing of input traces, followed by relative amplitude preserving EOM prestack time migration using amplitude factors based on the practical constant-wavespeed weighting functions developed in Chapter 4. The high fold of the prestack migrated output traces increases the signal to noise ratio, yielding results that are comparable to conventional poststack migrated and coherency-filtered sections. In addition, the new flow provides consistent imaging wavespeeds over a range of dips. These benefits should increase confidence in interpretations based on subtle concordant and discordant reflector relationships.

The concept that prestack time migration might be an improvement over conventional normal moveout correction (NMO), stack and poststack migration is not new (see e.g. Claerbout, 1985 for an overview). It has also been long recognized that the conventional approach, when combined with dip-moveout (DMO), is the kinematic equivalent of prestack time migration (Yilmaz, 1980; Deregowski and Rocca, 1981). DMO is still widely used in industry, and has been included as part of the processing sequence in a number of previous LITHOPROBE studies (e.g. Clowes et al., 1996), but is typically restricted to data from the upper crust where the DMO effect is the greatest (Eaton and Hynes, 2000). With DMO, imaging still requires two separate steps of wavespeed analysis, first for the NMO and then for the poststack migration. This can be a benefit, as it incorporates two parameters in the imaging instead of the one parameter in prestack time migration, but it can also be a detriment, because errors introduced in stacking carry through the poststack migration and hence to the final image.

Prestack migration has been applied in a number of crustal seismic reflection studies in an effort to improve imaging, but most typically as depth migrations (e.g. Milkereit et al., 1990; Buske, 1999). The problem with depth migrations, as discussed in Chapter 1, is that they require an accurate specification of the macro-wavespeed model in depth. This is not easy to do, although information from crustal-scale refraction seismic surveys is often incorporated at mid- and lower-crustal depths (Burianyk et al., 1997; White et al., 2000). I was not able to find a reference that describes an application of prestack time migration to crustal-scale seismic reflection data. Here, I propose that EOM prestack time migration be considered as a replacement for the conventional steps of NMO, DMO, stack and poststack migration.

A number of authors have proposed 'true-amplitude' approaches to the processing of crustal-scale seismic reflection data, including Milkereit et al. (1990), Sampson and West (1992), Eaton and Wu (1996), and Eaton and Milkereit (1997). Their efforts lean towards the estimation of true-amplitude reflectivity, with the general intent of estimating rock properties from the impedance contrasts. My intent is to preserve relative amplitudes as an aid to interpreting structural relationships in the image. Hence the approach is much less rigorous, and relies heavily on statistics.

The basic results presented in this chapter have been reported previously by Geiger et al. (1998; 1999). The focusing of reflectors in the prestack migrated image is very sensitive to the imaging wavespeeds. Wavespeeds were picked from constant wavespeed stacks at discrete locations and times, and then interpolated by the processing software. This often resulted in poor focusing in the interpolated regions between the pick points. In addition, there are problems imaging the very shallow section that have yet to be resolved. Careful reprocessing of a different portion of LITHOPROBE SNORCLE line 1 (van der Velden et al., 2001; van der Velden and Cook, 2001) has also produced good results. Although these authors apply an AGC instead of the statistical amplitude preservation steps discussed here, the EOM prestack time migration produces a better image of subsurface crustal structure than LITHOPROBE's conventional imaging approach of NMO, stack, and poststack phase-shift migration.

5.1.1 Overview of Chapter 5

In Section 5.2, I briefly introduce the study area. In Section 5.3, I describe the main similarities and differences between the conventional processing approach adopted by LITHOPROBE, and the new approach proposed here. In Section 5.4, the results of the various migrations are displayed and compared. Section 5.5 is a brief summary.

5.2 STUDY AREA

The 70 km portion of LITHOPROBE SNORCLE (Slave NORthern Cordillera Lithospheric Evolution) line 1 selected for this study is outlined by the black rectangle in Figure 5.1, and shown in a variety of migrated images in Figures 5.4-5.7. The portion straddles part of the Fort Simpson terrain as well as the Fort Simpson Basin, which developed along a west-facing passive continental margin between ~1.84-0.6 Ga (Cook et al., 1998). The test portion includes a variety of shallow and deep structures, including some of the steepest dipping reflectors imaged in the SNORCLE Line 1 profile (the east or right side between 1-5 s, see Figures 5.4-5.7), a possible syncline structure (west side between 5-7 s), a clear reflection Moho (west side at 11 s), and subduction plate geometries from an interpreted fossil subduction zone (east side, reflection packages at 9 s and 12 s).

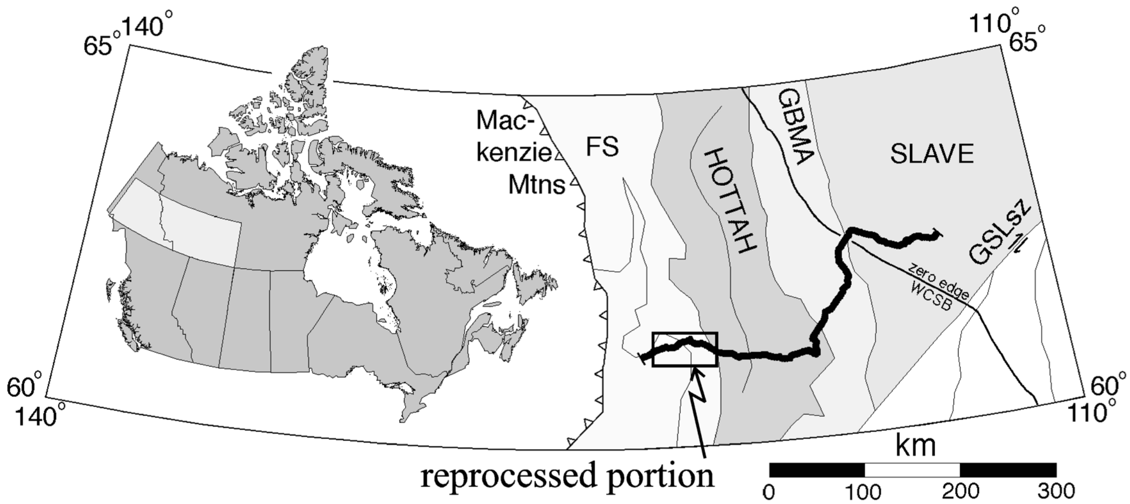

Figure 5.1. Location map for LITHOPROBE SNORCLE line 1 (bold black line) in northwestern Canada. The 70 km portion reprocessed in this study is outlined by the black box (figure courtesy of Arie van der Velden).

5.2 COMPARISON BETWEEN THE CONVENTIONAL LITHOPROBE APPROACH AND THE NEW APPROACH OF THIS STUDY

An example processing flow as applied to SNORCLE line 1 (Cook et al., 1999) is listed in Table 5.1. The new approach, using relative amplitude preserving EOM prestack time migration, is listed in Table 5.2. Some of the processing steps are common to both approaches. To assist in the comparison, all of the conventional steps are listed in Table 5.2: retained steps in italics, eliminated steps in strikethrough, and new steps in bold.

Table 5.1. Conventional data processing steps

Processing step	Comment
Diversity-type stack of uncorrelated records	
Extended crosscorrelation	32 s record length
Crooked line geometry	30 m x 1500 m bins
Notch filter where necessary	60 Hz
Trace edits, first break picks	
Refraction statics computation	Two-layer GLI
Velocity analysis	Local constant velocity stacks
Application of first break mutes	
Automatic gain control	800 ms window
Gapped deconvolution on sediments	
Statics application	
Normal move-out correction on common-midpoint gathers	
Residual statics computation	2.0-6.0 s window
Stack	Nominally 134 fold
Trace energy balance	8-16 s window
Frequency-space deconvolution	Sliding window
Coherency filter	
Poststack migration	Constant wavespeed phase shift
Coherency filter	
Plot	Variable area with bias

Table 5.2. Relative amplitude preserving EOM data processing steps
(new steps-**bold**; conventional steps: retained-*italics*, eliminated-~~strikethrough~~)

Processing step	Value
Diversity-type stack of uncorrelated records	
Extended crosscorrelation	*32 s record length*
Crooked line geometry	*30 m x 1500 m bins*
Notch filter where necessary	*60 Hz*
Trace edits, first break picks	
Refraction statics computation	*Two-layer GLI*
~~Velocity analysis~~	~~Local constant velocity stacks~~
Application of first break mutes	
~~Automatic gain control~~	~~800 ms window~~
Statistical data cleaning and balancing	**$t^{1.3}$ scaling factor applied**
Statics application	**Includes residual statics from conventional processing**
Gapped deconvolution on sediments	
~~Normal move-out correction on common-midpoint gathers~~	
~~Residual statics computation~~	~~2.0-6.0 s window~~
~~Stack~~	~~Nominally 134 fold~~
~~Trace energy balance~~	~~8-16 s window~~
~~Frequency-space deconvolution~~	~~Sliding window~~
~~Coherency filter~~	
~~Poststack migration~~	~~Constant wavespeed phase shift~~
~~Coherency filter~~	
Form equivalent offset gathers	**Amplitude weighting using equation (4.48) times** $1/(tt_0)$
Migration velocity analysis	**Constant velocity stacks of equivalent-offset gathers**
Normal moveout correction on equivalent-offset gathers	
Stack of EO gathers	**Stack normalization by** $1/\sqrt{N(t_0)}$
Weighting of stacked migrated output	**Amplitude weighting by** $t_0^{3/2}$
Plot	*Variable area with bias*

5.2.1 Important similarities between the two approaches

There are four important similarities between the conventional approach and the new approach: deconvolution, refraction statics, reflection statics, and plotting. The main reason for these similarities is that the conventional processing had already been completed, and was then used as a platform for the new processing. For example, the time consuming steps of first break picking and careful calculation of a refraction-statics solution did not need to be duplicated. The same static picks were applied in both approaches. This has the added benefit that differences in the migrated images cannot be attributed to ancillary processing steps, although the conventional solutions may not be optimized for the new approach. Reflection statics, for example, are determined by maximizing the coherency in the unmigrated stack, a step that is omitted in the new approach. Fortunately, these statics are quite small, rarely exceeding 10 ms, so there was no discernable difference between the new approach with and without them. They were included in the conventional approach, and so, for consistency, they are included in the new approach.

The deconvolution is a basic gapped deconvolution, with the operator derived trace-by-trace. This does not preserve true-amplitude as well as a surface-consistent deconvolution, but was included for consistency. All migrated sections (see Figures 5.4-5.8) are plotted in variable area with a trace bias.

5.2.2 Important differences between the two approaches

The conventional approach to crustal seismic reflection processing, as currently adopted by LITHOPROBE, includes an automatic gain control (AGC) applied to input traces, a stack of common midpoint (CMP) gathers after normal-moveout correction (NMO) but without dip moveout correction (DMO), a poststack time migration, and a dip-coherency filter prior to display and interpretation. In a number of LITHOPROBE transects, the dip coherency filter is applied prior to poststack migration (Martignole and Calvert, 1996; Eaton et al., 1999).

The conventional processing flow has proven to be effective for basic imaging of structural relationships as revealed by the continuity and patterns of the reflector elements in the migrated image. However, the image is first created as an unmigrated stack, where it is well known that dipping reflectors are mispositioned, imaging wavespeeds are dip dependent, and focusing of conflicting dips may well be compromised. Poststack time migration attempts to position dipping reflections more accurately in the migrated image, but it is often difficult to determine if key patterns required for interpretation (such as reflector terminations) are accurately imaged. Prestack time migration, on the other hand, can produce a migrated image with more accurate focusing and better relative positioning of reflectors. The most significant improvements are expected in areas with steep and/or conflicting dips.

A second problem with the conventional approach lies in the treatment of amplitudes. Accurate relative amplitudes help to define the ‘character’ of individual reflectors and packages of reflectors, and are thus a valuable aid to interpretation. As well, the signal-to-noise ratio in the final image can depend strongly on the choice of amplitude weights in the imaging process.

In the conventional approach, the AGC is typically derived over a long window (e.g. 800 ms) and applied on a trace-by-trace basis in the data space. This has proved to be a robust processing step, in that it tends to preserve relative differences in the peak amplitudes of reflection events over a time span of approximately half the window (e.g. 400ms), and is often effective in the presence of a variety of noise sources. Over longer time spans, however, the amplitudes of adjacent reflection events tend to be normalized to similar levels. After stacking and poststack migration, then, the overall image has much less contrast than the underlying unknown true reflectivity (although some reduction in contrast can be beneficial for structural interpretations). The AGC also tends to distort the amplitude of packages of reflection events by normalizing them in concert with adjacent packages. Thus a relative difference in the amplitude can be introduced where there should be none, e.g. for two separated but otherwise identical packages of reflection events, or for unrelated packages of reflection events of similar underlying reflectivity. The end result is a loss of contrast in the final image, and an increase in the distortion of relative amplitudes.

In the conventional approach, the problems of reduced contrast and increased distortion are addressed by applying a dip-coherency filter (implemented as a local slant stack over a limited aperture in both distance and dip) to the migrated image, and then plotting the image in variable area with a trace bias to accentuate packages of reflectors with greater coherency and higher amplitudes. This has proved effective in reducing noise, but does not address the general imbalances in amplitude already introduced by the AGC.

Prestack time migration offers the possibility of a more consistent approach to amplitudes. A prestack diffraction surface in the data space contains many more input samples than does a moveout hyperbola in a given common offset gather. Thus noise is often reduced simply by the increased fold of the diffraction summation, and the image can be displayed without recourse to coherency filtering (although they are plotted here with the same bias parameters, in part because of the high density of traces, and in part to provide a similar image for comparison with the conventional images). Coherency filters, such as f-x deconvolution (e.g. Wang and West, 1991) or the local slant stack discussed above, can be applied to reduce noise levels in the prestack migrated image—often with good success—but these have not been tested in this study. Poststack time migration can also be effective at enhancing the signal to noise ratio, but the improvements are typically not as dramatic as with prestack time migration.

So far, I have proposed two basic changes to the conventional processing flow: first, replace the AGC by statistical preprocessing of the traces, with the intent of preserving relative amplitudes over a much wider range of time spans and distances; and second, replace the conventional NMO, stack and poststack migration with a prestack time migration. There is, however, a third option worth investigating. Because the AGC is such a robust process, input traces can be AGC'd prior to prestack time migration. This will also provide a standard for comparing the relative improvements of the two processes.

5.2.3 Details of the new processing approach

The following steps outline the new processing approach in detail:

1. Refraction and residual statics determined by conventional means are applied to the input traces. A suitable replacement velocity and constant datum are chosen so that traveltimes are similar to those from the acquisition datum.

2. All traces whose rms amplitude (in any one of 5 time windows) exceeds the median value by a chosen factor (4.5) are removed.

3. All traces that show an amplitude decrease of less than 10 percent between the time windows of 4.5 - 6.5 s and 13 - 15 s respectively are removed.

4. All very weak traces with amplitudes less than 1 percent of the average trace amplitudes in the gather are removed.

5. Traces with RMS amplitudes deviating more than 3 standard deviations from the mean in the time window 6 to 10 s are removed.

6. Trace amplitudes are balanced in the shot domain and then in the receiver domain. The median absolute amplitude of the time window from 13 - 16 s is used. Receivers producing less than 11 live traces are considered bad and their traces removed.

7. Traces are scaled by a factor of $t^{1.3}$ to compensate for geometrical spreading as wavespeed increases with depth, transmission losses, and other signal losses (e.g. attenuation, assumed to be independent of frequency). In an ideal constant wavespeed medium with uniform reflectivity, a factor of t^1 would produce traces with uniform signal strength. The factor $t^{1.3}$ was chosen such that gained traces have uniform signal strength. Traces are now assumed to have originated from a constant-wavespeed medium with no losses.

8. A trace-by-trace gapped deconvolution is applied.

9. EO gathers are formed using the detailed methodology described in Section 3.3 of Li (1999; see also Li and Bancroft, 1998). Input traces are binned without any scaling. The binned traces are then scaled using all terms in the weighting factor given by equation (4.48) except for the factor of t_0, which is applied after NMO and stacking, and an additional factor of t^{-1}, which is applied to restore constant-wavespeed geometrical spreading. The EO gathers are created out to a maximum equivalent offset of 60 km, with an equivalent-offset bin width of 15m. The filter $\hat{f}(t)$ [see equation (3.36) and discussion in Section 3.6.5], the half-time derivative, and the Hilbert transform, as required by equation (4.41), are not applied. Neglecting these factors has limited effect on relative amplitude.

10. Prestack time-migration imaging wavespeeds are determined from constant-wavespeed stacks of the EO gathers. Wavespeeds are hand picked based on focusing and continuity, and entered into ASCII files.

11. Normal moveout correction (NMO) is applied to the EO gathers using the picked wavespeeds and a 90% stretch mute.

12. The NMO'd and muted EO gathers are stacked using a $1/\sqrt{N(t_0)}$ normalization factor, where N is the number of samples at time t_0 in the EO gather. After NMO and stretch mute, $N(t_0) \propto t_0$. Hence, a factor of $t_0^{1/2}$ is applied to compensate for this normalization. An additional factor of t_0 is applied to account for the portion of the weighting factor not included in the application of equation (4.48) (see Step 8).

13. The output prestack time migrated traces are plotted in variable area with a small bias to remove the zero line and eliminate low-level noise.

An example shot-gather is illustrated in Figures 5.2 and 5.3. Figure 5.2a is the original shot-gather with all traces, plotted without any gain correction or first break mute. Figure 5.2b shows the traces remaining in the gather after statistical cleaning (Steps 2-6) and application of the first break mute. The mean relative amplitude of trace is plotted in the header at the top of the figure. The traces that have been removed are shown in Figure 5.2c. The gaps introduced by removing traces might introduce serious aliasing noise, as well as migration operator noise that emanates from the reflection truncations in the common-offset gathers adjacent to the gaps. It would be desirable to interpolate lost traces, or to compensate for the missing amplitudes. As a simple method, consider compensating for missing traces by upweighting trace amplitudes in adjacent common-offset gathers. Then the limited offset range could be thought of as input to one common-offset migration. However, reweighting was not examined in this study.

a) b) c)

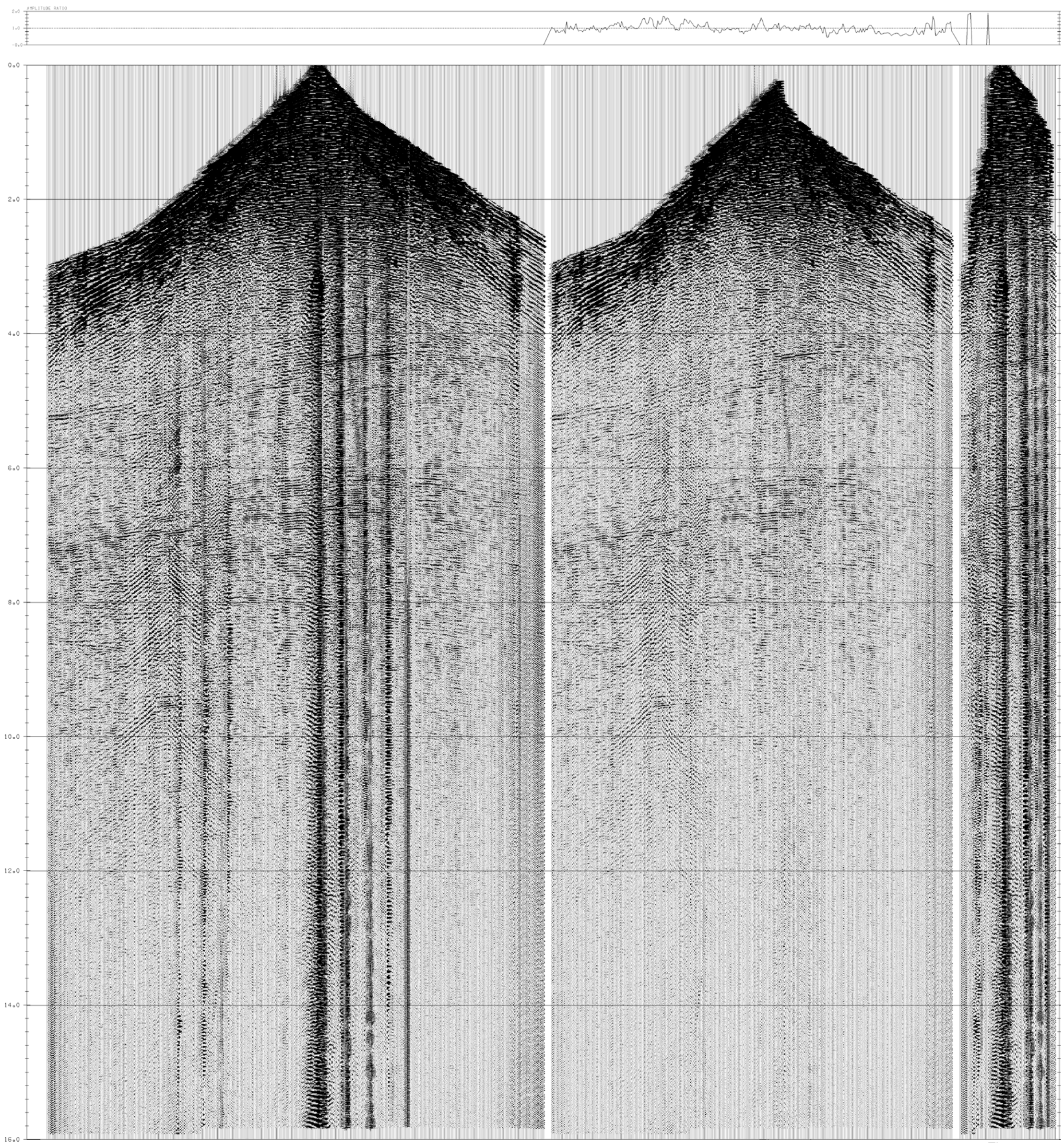

Figure 5.2. A representative shot-gather. a) the original gather with all traces, plotted without scaling or first break mutes. b) the gather after statistical cleaning, plotted without scaling but with first break mutes. c) the traces removed by the statistical cleaning.

a) b)

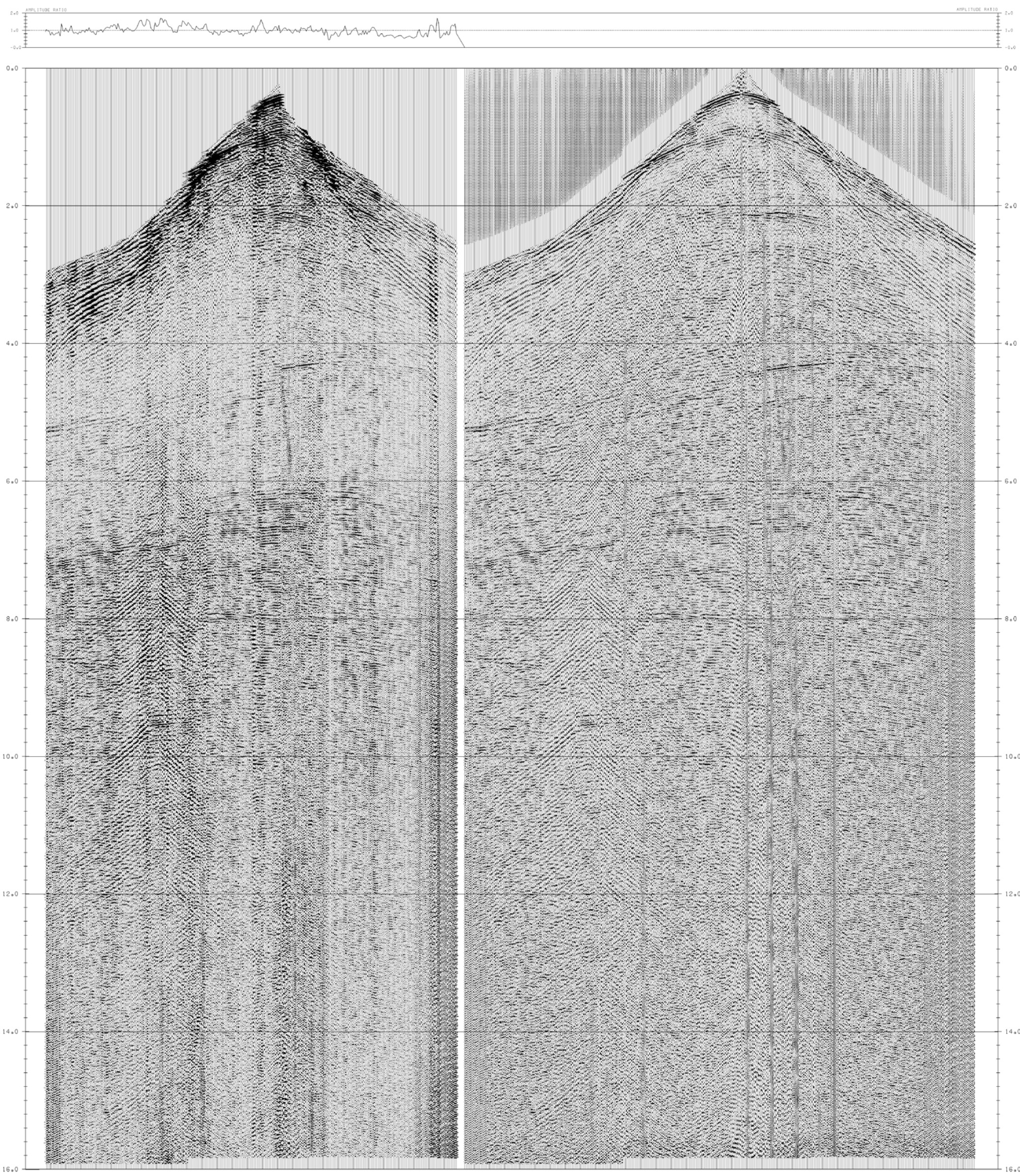

Figure 5.3. A representative shot gather a) after statistical cleaning and scaling and b) without statistical cleaning with a 400 ms AGC.

The traces remaining after statistical cleaning (Figure 5.2b) are redisplayed after application of the $t^{1.3}$ scaling factor in Figure 5.3a. Figure 5.3b is a plot of all traces (Figure 5.2a) after application of a 400 ms AGC.

5.4 COMPARISON OF MIGRATED SECTIONS

At the chosen scale, the conventional poststack migrated result of AGC'd input traces without semblance filtering (Figure 5.4) is the better result for comparison with the EOM results (Figures 5.6 and 5.7). The coherency-filtered result (Figure 5.5) highlights textural changes in the image by enhancing event continuity and reducing background noise. The resulting image is preferable for interpretation of large-scale crustal geometries, but lacks the fine detail visible in the other migrated images. All figures are displayed using the identical plotting parameters optimally chosen for the conventional displays. Although this permits a comparison of relative levels of signal and noise within and amongst images, the large clip factor (trace excursion of 4) reduces the resolution of higher-amplitude steeply dipping events in the EOM results.

The AGC'd EOM result (Figure 5.7) shows better imaging of reflection events in the shallow section (1-6 s). The relative-amplitude EOM result (Figure 5.6) shows broad light and dark regions that suggest that signal-to-noise ratios are comparable to the conventional coherency-filtered result (Figure 5.5).

Both EOM results appear to have produced a degraded image in the very near surface (upper 0.5 seconds). Conventional 2D processing incorporates a variable cross-line bin location. EOM, which honors a true 3D geometry for sources and receivers relative to the output location, produces a poor image in the shallow section when the output locations along the CDP bin line are not close to the source-receiver pairs on the acquisition line.

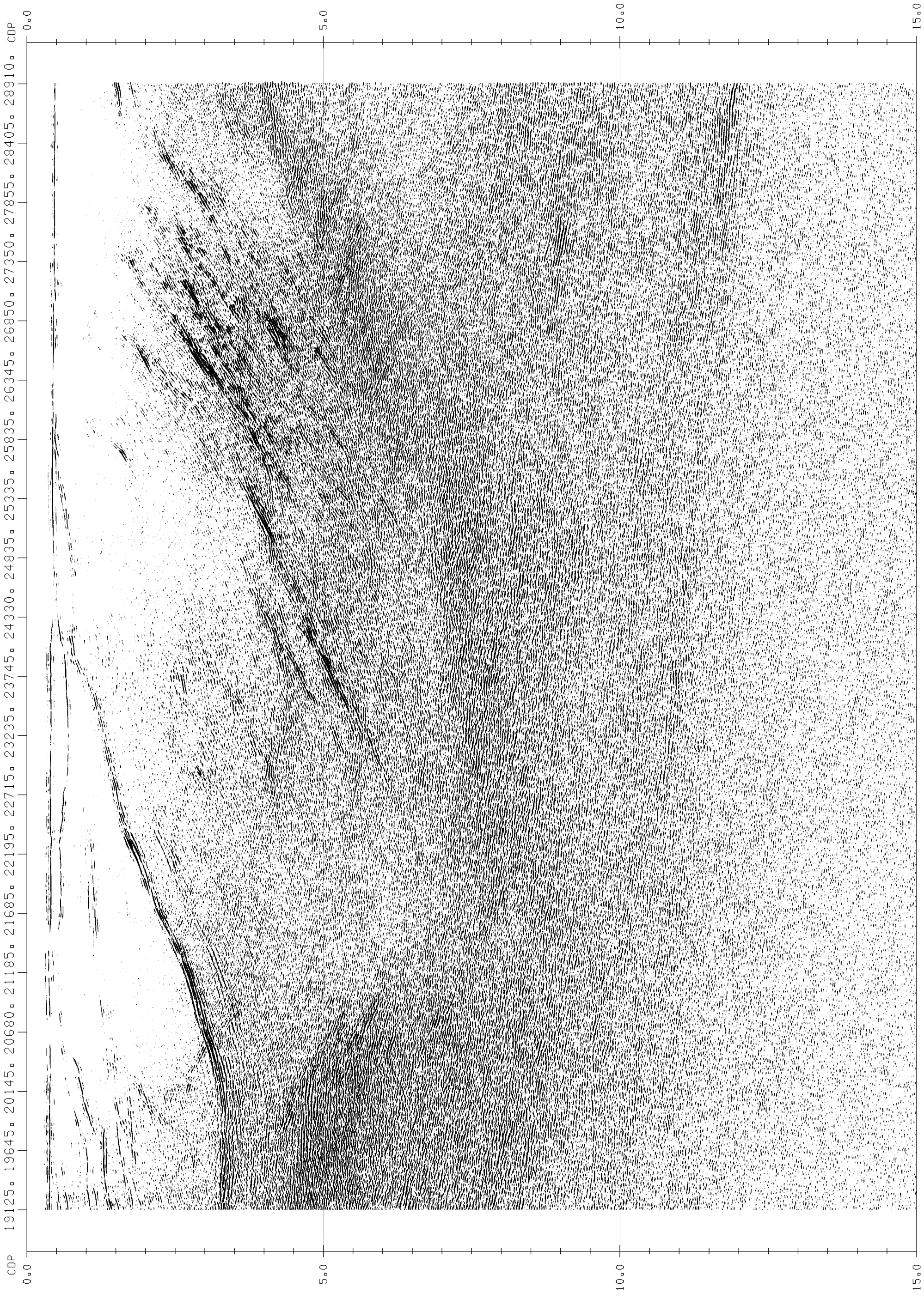

Figure 5.4 Conventional poststack migrated section without coherency filtering.

Figure 5.5 Conventional poststack migrated section with coherency filtering.

Figure 5.6 Relative amplitude preserving EOM prestack time migrated section.

Figure 5.7. EOM prestack time migrated section from AGC'd traces.

5.5 SUMMARY

Prestack time migration with relative-amplitude preservation is a viable alternative to conventional processing methods. Image quality is similar to and in some cases better than conventional poststack migrated results.

The main benefit of EOM is the sensitivity and accuracy of the velocity analysis in the CSP gather domain (Bancroft et al. 1998). Reflection events are imaged directly to their true time-migrated position independent of dip, without the intermediate step of event imaging in the CMP stack domain. Conventional processing, on the other hand, first images reflections in the CMP stack, then repositions the reflections during poststack migration. Using EOM, an interpreter can be more confident of concordant and discordant relationships between reflectors. Relative amplitude information provides an interpreter with additional information to differentiate reflections—information content that is diminished when data are AGC'd.

Careful reprocessing of a different portion of LITHOPROBE SNORCLE line 1 (van der Velden et al., 2001; van der Velden and Cook, 2001) has also produced good results. Although these authors apply an AGC instead of the statistical amplitude preservation steps discussed here, the EOM prestack time migration produces a better image of subsurface crustal structure than LITHOPROBE's conventional imaging approach of NMO, stack, and poststack phase-shift migration.

CHAPTER 6: SUMMARY AND CONCLUSIONS

6.1 SUMMARY

The main objective of this dissertation is to find accurate and practical expressions for the dynamic component of EOM prestack time migration. Previous attempts (Fowler, 1997b; Cary, 1998; Margrave et al., 1999) suggest that Jacobians are necessary for the transformations from the input data space to the intermediate data space of EO gathers and from the EO gathers to the output image space. However, given that the kinematics of EOM are well established as an exact re-expression of the DSR equation, and that the transformation to the EO gathers can be implemented as a simple unweighted summation, the only Jacobian that is required is the direct Jacobian from the data space to the image space. The direct Jacobian can be found as part of the dynamic component of many prestack-migration weighting functions published in the existing literature. The task, then, is to determine which one of the published weighting functions is the correct one (if any) and how it can be simplified for practical application. This is accomplished by a comprehensive analysis of the relevant theory combined with a validation process using both synthetic models and field data, as described in the following paragraph.

A secondary objective is to find a more general justification for the DSR kinematics of non-recursive prestack time migration algorithms such as EOM. Conventional derivations of the DSR equation assume a constant wavespeed subsurface, but practical experience suggests that excellent images can be obtained from DSR prestack time migrations in areas with significant lateral and vertical variations in subsurface wavespeed. The justification, which consists of two main parts, has already been presented in the introduction. First, I redefine migration as a transformation from a data space to an image space, express the transformation in terms of geophysical inverse theory, and from this determine qualitative criteria for evaluating the accuracy of the image space. Second, I derive the DSR equation for a generalized inhomogeneous media using a Taylor series expansion about the best-fit image-ray location. The smoothness assumption required for the Taylor series expansion can be related to the qualitative accuracy criteria established earlier.

Chapter 2 began with a derivation of the acoustic wave equation and Green's functions as necessary background for forward and inverse wavefield extrapolation. The Kirchhoff-Helmholtz integral representation [KHIR, equation (2.44)] was derived as the basic equation describing the acoustic wavefield in terms of incident and scattered wavefields. The volume-scattered wavefield [second term of equation (2.47)] was shown to be a function of the wavespeed perturbation $\alpha(\mathbf{x})$ [defined by equation (2.46)]. The surface scattered wavefield was shown to be the Kirchhoff-Helmholtz integral in the space-frequency domain [equation (2.48)—in free-space, equation (2.49)], also known as the Kirchhoff integral in the space-time domain [free-space version given by equations (2.50), (2.51) and (2.52)]. A number of configurations were examined in order to gain an intuitive understanding of the physical meaning of the integral in the context of Huygens' principle and inverse wavefield extrapolation from an arbitrary surface.

In the case of Huygens' principle, reconstruction of the wavefront was shown to be equivalent to replacing the propagating wavefield with secondary sources distributed over the wavefront surface. The Kirchhoff-Helmholtz integral [equation (2.48)] is then interpreted as a superposition of weighted monopoles and dipoles that radiates wavefields in both directions. Assuming that the one-way wavefield we are interested in is propagating outward[1], the inward propagating contributions must cancel. To do so they

[1] Recall from Section 2.4 that a wavefield can propagate outward either forward or backward in time

must be equal and of opposite sign. Thus the outward propagating contributions must also be equal. Intuitively, then, this suggests that the one-way outward propagating wavefield can be reconstructed from twice the wavefield of either the monopole or dipole portion of the Kirchhoff-Helmholtz integral.

This intuitive idea was then applied to inverse wavefield extrapolation from an arbitrarily reflection-free surface. First, the theory was restricted to more realistic acquisition conditions, whereby data are available only over part of a closed surface, and only one of either the pressure or its normal derivative are measured. Given these restrictions, and the additional assumptions of one-way wavefields and a planar surface, an almost exact reconstruction (neglecting evanescent waves) is possible by a superposition of weighted monopoles (the Rayleigh I integral) or weighted dipoles (the Rayleigh II integral). The restriction of a planar surface was removed by considering the Rayleigh I and II integrals as composed of local image Green's functions, one for each surface element. The theory developed in this chapter will be used in Chapter 3 to develop various formulas for migration and inversion. These, in turn, provide a basis for Chapter 4, where I determine robust and efficient weighting functions for prestack migration by the method of equivalent offset.

Two approaches to depth imaging were developed in Chapter 3. The classical migration approach combines inverse wavefield extrapolation with Claerbout's 'deconvolution' imaging condition. The Born-approximate inversion approach inserts the forward modeling formula for the volume scattered wavefield into a Fourier transform-like inversion formula for wavespeed perturbation, then re-expresses this result as a band-limited reflectivity function. For the common-shot configuration, both approaches give essentially identical results.

The classical migration approach was developed from first principles. Ray-theoretical Kirchhoff-approximate expressions were derived for one-way forward modeling and one-way inverse wavefield propagation with the assumption that the data are synthesized or recorded on one nonplanar interface. The prestack 'deconvolution' imaging condition was shown to be an optimal chi-squared estimator if weighted by a bandlimited source function, and Docherty's ray-theoretical Kirchhoff-approximate common-shot migration formula was shown to be equivalent to a simpler derivation based on the Rayleigh II integral. Hence, the Kirchhoff-approximate migration formula is strictly valid only for data recorded on a planar surface. Classical migration does not provide a theoretical basis for creating a stacked reflectivity section, other than a simple summation of migrated shot records. A more optimal approach is desired.

In addition, classical migration is not applicable to non-physical wavefields such as common-offset configurations. The Born-approximate forward modeling formula was derived as a basis for more generalized depth imaging expressions, and shown to be asymptotically equivalent to the Kirchhoff-approximate modeling formula by expressing both in the form of isochron stacks. The similarity of the modeling formulas justifies substituting the geometrical-optics reflection coefficient for the more restricted linearized Born reflection coefficient in the final inversion formula.

In Chapter 4, the frequency-domain expressions for imaging reflectivity in a constant wavespeed medium from Chapter 3 were re-expressed in the time-domain. The common-offset migration/inversion formula [equations (4.5)/(4.8)] was shown to be optimum for estimating stacked reflectivity, whereas both the common-shot and common-receiver formulae [equations (4.5)/(4.6) or (4.5)/(4.7)] yield biased results. However, the exact common-offset formula is not practical for EOM prestack time migration because calculation of the weighting function depends on distance measures that vary with each shot and receiver location relative to each subsurface imaging point. The exact weighting function is computationally expensive to evaluate, and not necessarily accurate given other approximations inherent in time migrations.

In a time migration, the vertical coordinate of the output imaging point is approximated by the two-way traveltime corresponding to the apex of a best-fit diffraction-traveltime surface in the input data. The distance measures in the weighting function can be converted to corresponding traveltimes at a best-fitting wavespeed parameter. The resulting weighting function [equation (4.22)] is thus an approximation, suggesting that further approximations might reduce the computational cost without significant loss of accuracy. The goal was identified to be a weighting function that can be applied in some or all of three domains: input traces, equivalent-offset-gather traces and/or output traces. Following approximations introduced by Gray (1998b), Dellinger et al. (2000), and Zhang et al. (2000), generalized custom weighting functions were derived for imaging in 2.5-D [equation (4.41)] and in 3-D [equation (4.49)]. For 2.5-D, the modified 't_{0h_e}/t' weight C [equation (4.48)] is preferred over the Gray 't_0/t' cosine obliquity weight [equation (4.39)]. For 3-D, the modified 't_{0h_e}/t' weight C [equation (4.52)] is preferred over the Zhang 't_0/t' weight [equation (4.51)].

Note that the weighting functions have a broader application as approximate weights for Kirchhoff-type (ray-traced) depth migrations in media with variable wavespeed. Jaramillo et al. (2000) use the term 'true-amplitude time-migration weights' to describe constant-wavespeed expressions for the Beylkin Jacobian (Beylkin, 1982, 1985) and geometrical spreading, with distances from the source to output point and receiver to output point replaced by traveltimes. These simplified weights can produce a stacked migrated section without the brightening and dimming often associated with weights determined by dynamic ray-tracing (Dellinger et al., 2000).

6.2 CONCLUSIONS

Prestack time migration with relative-amplitude preservation is a viable alternative to conventional processing methods. Image quality is similar to and in some cases better than conventional poststack migrated results.

The main benefit of EOM is the sensitivity and accuracy of the velocity analysis in the CSP gather domain (Bancroft et al. 1998). Reflection events are imaged directly to their true time-migrated position independent of dip, without the intermediate step of event imaging in the CMP stack domain. Conventional processing, on the other hand, first images reflections in the CMP stack, then repositions the reflections during poststack migration. Using EOM, an interpreter can be more confident of concordant and discordant relationships between reflectors. Relative amplitude information provides an interpreter with additional information to differentiate reflections—information content that is diminished when data are AGC'd.

REFERENCES

Aki, K., and Richards, P. G., 1980, Quantitative Seismology: Theory and Methods: W.H. Freeman and Co.

Alcock, E. D., 1943, Selection of computational methods for seismic paths: Geophysics, **8**, 297-307.

Baker, B. B., and Copson, E. T., 1950, The mathematical theory of Huygens' principle: Oxford University Press.

Bancroft, J. C., and Geiger, H. D., 1994, Equivalent offsets and CRP gathers for prestack migration: 64th Ann. Internat. Mtg., Soc. Expl. Geophys., Expanded Abstracts, 672-675.

Bancroft, J. C., and Geiger, H. D., 1996, Velocity sensitivity for equivalent offset prestack migration: a contrast in robustness and fragility: Ann. Mtg. Can. Soc. Expl. Geophys., Expanded Abstracts, 149-150.

Bancroft, J. C., and Geiger, H. D., 1997, Prestack seismic migration: United States Patent 5 596 547.

Bancroft, J. C., and Geiger, H. D., 1998, Prestack seismic migration: Canadian Patent 2 161 048.

Bancroft, J. C., Geiger, H. D., and Margrave, G. F., 1998, The equivalent offset method of prestack time migration: Geophysics, **63**, 2042-2053.

Bancroft, J. C., Xu, Y., and Kirtland-Grech, M. G., 1999, Focusing CSP gather semblance images for Foothills time migration: CREWES Research Report, **11**, 151-155.

Bath, M., 1968, Mathematical aspects of seismology: Elsevier, Developments in solid Earth geophysics, **4**.

Beckman, P., and Spizzichio, A., 1963, The scattering of electromagnetic waves from rough surfaces: Pergamon Press, International series monographs on electromagnetic waves, **4**.

Bednar, B., 1999, A theoretical comparison of equivalent offset migration: Geophysics, **64**, 189-196.

Berkhout, A. J., 1981, Wave field extrapolation techniques in seismic migration, a tutorial: Geophysics, **46**, 1638-1656.

Berkhout, A. J., 1985, Seismic migration: Imaging of acoustic energy by wavefield extrapolation: A: Theoretical aspects: Elsevier Science Publ. Co., Inc., Developments in solid earth geophysics, **14A**.

Berkhout, A. J., and Wapenaar, C. P. A., 1989, One-way versions of the Kirchhoff integral: Geophysics, **54**, 460-467.

Berryhill, J. R., 1979, Wave-equation datuming: Geophysics, **44**, 1329-1344.

Bevc, D., 1995, Imaging under rugged topography and complex velocity structure: Ph.D. thesis, Stanford University.

Bevc, D., Black, J. L., and Palacharia, G., 1995, Plumes: Response of time migration to lateral velocity variation: Geophysics, **60**, 1118-1127.

Beylkin, G., 1982, Generalized Radon transform and its applications: Ph.D. thesis, New York University.

Beylkin, G., 1985, Imaging of discontinuities in the inverse scattering problem by inversion of a causal generalized Radon transform: J. Math. Phys., **26**, 99-108.

Biot, M. A., and Tolstoy, I., 1957, Formulation of wave propagation in infinite media by normal coordinates with an application to diffraction: J. Acoust. Soc. Amer., **29**, 381-391.

Black, J. L., and Brzostowski, M. A., 1994, Systematics of time-migration errors: Geophysics, **59**, 1419-1434.

Bleistein, N., 1984, Mathematical methods for wave phenomena: Academic Press, Inc., Computer Science and Applied Mathematics.

Bleistein, N., 1986, Two-and-one-half dimensional in-plane wave propagation: Geophys. Prosp., **34**, 686-703.

Bleistein, N., 1987, On the imaging of reflectors in the earth: Geophysics, **52**, 931-942.

Bleistein, N., 1999, Hagedoorn told us how to do Kirchhoff migration and inversion: The Leading Edge, **18**, No. 8, 918-927.

Bleistein, N., Cohen, J. K., and Hagin, F. G., 1987, Two and one-half dimensional Born inversion with an arbitrary reference: Geophysics, **52**, 26-36.

Bleistein, N., Cohen, J. K., and Stockwell, J. W. J., 2001, Mathematics of multidimensional seismic inversion: Springer-Verlag New York, Inc., Interdisciplinary Applied Mathematics, **6**.

Bleistein, N., and Gray, S. H., 2001, From the Hagedoorn imaging technique to Kirchhoff migration and inversion: Geophys. Prosp., (submitted).

Bording, R. P., and Liner, C. L., 1993, Some numerical aspects of the 2.5-D wave equation: 63rd Ann. Internat. Mtg., Soc. Expl. Geophys., Expanded Abstracts, 205-207.

Brekhovskikh, L., and Goncharov, V., 1985, Mechanics of Continua and Wave Dynamics: Springer-Verlag, Springer Series on Wave Phenomena, **1**.

Burianyk, M. J. A., Bouzidi, Y., Phadke, S., and Kanesewich, E. R., 1997, Seismic velocity models and depth migration imaging of the Alberta basement: Lithoprobe, Alberta basement transects workshop, 9-14.

Burridge, R., de Hoop, M., Miller, D., and Spencer, C., 1998, Multi-parameter inversion in anisotropic media: Geophys. J. Internat., **134**, 757-777.

Buske, S., 1999, Three-dimensional pre-stack Kirchhoff migration of deep seismic reflection data: Geophys. J. Internat., **137**, 243-260.

Carter, J. A., and Frazer, L. N., 1984, Accommodating lateral velocity changes in Kirchhoff migration by means of Fermat's principle: Geophysics, **49**, 46-53.

Cary, P. W., 1998, Migration in the equivalent offset domain: Ann. Mtg. Can. Soc. Expl. Geophys., Expanded Abstracts, 146-147.

Castle, R. J., 1988, Shifted hyperbolas and normal moveout: 58th Ann. Internat. Mtg., Soc. Expl. Geophys., Expanded Abstracts, 894-896.

Chang, W. F., and McMechan, G. A., 1986, Reverse-time migration of offset vertical seismic profiling data using the excitation-time imaging condition: Geophysics, **51**, 67-84.

Claerbout, 1971, Toward a unified theory of reflector mapping: Geophysics, **36**, 467-481.

Claerbout, J. F., 1985, Imaging the earth's interior: Blackwell Scientific Publications, Inc.

Claerbout, J. F., 1992, Earth soundings analysis: processing versus inversion: Blackwell Scientific Publications, Inc.

Clowes, R. M., Calvert, C. A., Eaton, D. W., Hajnal, Z., Hall, J., and Ross, G. M., 1996, Lithoprobe reflection studies of Archean and Proterozoic crust in Canada. In: D.J. White, J. Ansorge, T.J. Bodoky, and Z. Hajnal (eds.), Seismic Reflection Probing of the Continents and their Margins: Tectonophysics, **264**, 65-88.

Cohen, J. K., and Bleistein, N., 1979, Velocity inversion procedure for acoustic waves: Geophysics, **44**, 1077-1087.

Cohen, J. K., Hagin, F. G., and Bleistein, N., 1986, Three-dimensional Born inversion with an arbitrary reference: Geophysics, **51**, 1552-1558.

Colton, D., and Kress, R., 1991, Inverse Acoustic and Electromagnetic Scattering Theory: Springer-Verlag Berlin, Applied Mathematical Sciences, **93**.

Cook, F. A., van der Velden, A. J., Hall, K. W., and Roberts, B. J., 1999, Frozen subduction zone in Canada's Northwest Territories: Lithoprobe deep lithospheric profiling of the western Canadian Shield: Tectonics, **18**, 1-24.

de Bazelaire, E., 1988, Normal moveout revisited—inhomogeneous media and curved interfaces: Geophysics, **53**, 143-157.

de Bruin, C. G. M., 1992, Linear AVO inversion by prestack depth migration: imaging angle dependent reflectivity as a tool for litho-stratigraphic inversion: Ph.D. thesis, Delft University of Technology.

Dellinger, J. A., Gray, S. H., Murphy, G. E., and Etgen, J. T., 2000, Efficient 2.5-D true-amplitude migration: Geophysics, **65**, 943-950.

Deregowski, S. M., and Brown, S. M., 1983, A theory of acoustic diffractors applied to 2-D models: Geophys. Prosp., **31**, 293-333.

Deregowski, S., and Rocca, F., 1981, Geometrical optics and wave theory for constant-offset sections in layered media: Geophys. Prosp., **29**, 374-387.

Dillon, P. B., 1990, A comparison between Kirchhoff and GRT migration on VSP data: Geophys. Prosp., **38**, 757-777.

Dix, C. H., 1952, Seismic Prospecting for Oil: Harper's Publ. Co.

Dix, C. H., 1955, Seismic velocities from surface measurements: Geophysics, **20**, 68-86.

Docherty, P., 1991, A brief comparison of some Kirchhoff integral formulas for migration and inversion: Geophysics, **56**, 1164-1169.

Doherty, S. M., 1975, Structure independent seismic velocity estimation: Ph.D. thesis, Stanford University.

Eaton, D. W., and Hynes, A., 2000, The 3-D crustal structure in the Manicouagan region: new seismic and gravity constraints: CJES, **37**, 307-324.

Eaton, D. W., and Milkereit, B., 1997, Relative-amplitude preserving (RAP) processing applied to LITHOPROBE data from central Alberta: Alberta Basement Transects report, 73-83.

Eaton, D. W., Ross, G. M., and Clowes, R. M., 1999, Seismic-reflection and potential-field studies of the Vulcan structure, western Canada: A Paleoproterozoic Pyrenees?: J. Geophys. Res., **104**, 23,255-23,269.

Eaton, D. W., and Wu, J., 1996, Relative-amplitude preserving processing for crustal seismic reflection data; an example from Western Canada. In: D.J. White, J. Ansorge, T.J. Bodoky, and Z. Hajnal (eds.), Seismic reflection probing of the continents and their margins: Tectonophysics, **264**, 357-370.

Elmore, W. C., and Heald, M. A., 1969, Physics of Waves: Dover.

Elrod, D., and Walker, R., 2000, Myriad facets of the nonexclusive data business: The Leading Edge, **19**, 640-646.

Epstein, M., and Slawinski, M. A., 1998, On some aspects of the continuum-mechanics context, Calgary, Alberta, Dept. Mech. Eng., Univ. of Calgary.

Esmersoy, C., and Miller, D., 1989, Short Note: Backprojection versus backpropagation in multidimensional linearized inversion: Geophysics, **54**, 921-926.

Esmersoy, C., and Oristaglio, M., 1988, Reverse-time wave-field extrapolation, imaging, and inversion: Geophysics, **53**, 920-931.

Fokkema, J. T., and van den Berg, P. M., 1993, Seismic Applications of Acoustic Reciprocity: Elsevier Science Publishers.

Forel, D., and Gardner, G. H. F., 1988, A three-dimensional perspective on two-dimensional dip moveout: Geophysics, **53**, 604-610.

Fowler, P., 1997a, A comparative overview of prestack time migration methods: 66th Ann. Internat. Mtg., Soc. Expl. Geophys., Expanded Abstracts, 1571-1574.

Fowler, P. J., 1997b, letter to John Bancroft.

French, W. S., 1975, Computer migration of oblique seismic reflection profiles: Geophysics, **40**, 961-980.

Gaby, P. P., 1945, A new type of seismic cross-section wherein accuracy of representation is rendered insensitive to velocity error: Geophysics, **10**, 171-185.

Gardner, G. H. F., ed., 1985, Migration of Seismic Data: Society of Exploration Geophysicists, Geophysics reprint series, **4**.

Gardner, G. H. F., Wang, S. Y., Pan, N. D., and Zhang, Z., 1986, Dip moveout and prestack imaging: 18^{th} Offshore Tech. Conf., **2**, 75-84.

Gazdag, J., 1978, Wave-equation migration by phase-shift: Geophysics, **49**, 124-131.

Gazdag, J., and Sguazzero, P., 1984, Migration of seismic data by phase shift and interpolation: Geophysics, **49**, 124-131.

Geiger, H. D., 1989, A study of the accuracy of data from a set of Gough-Reitzel magnetic variometers: M.Sc. thesis, Queen's University.

Geiger, H. D., 2001, Bias in seismic images obtained by stacking migrated common-offset and common-shot gathers: What's good for the goose is not good for the gander!: EAGE 63rd Conference and Technical Exhibition, (presented at the student forum).

Geiger, H. D., Maier, R. M., van der Velden, A. J., and Cook, F. A., 1998, Relative amplitude preserving prestack time migration: results from the Lithoprobe SNORCLE transect: 8th International Symposium on Deep Seismic Profiling of the Continents and their Margins, p. 126.

Geiger, H. D., Maier, R. M., van der Velden, A. J., and Cook, F. A., 1999, Prestack time migration with relative amplitude preservation: results form the SNORCLE transect: Slave-Northern Cordillera lithospheric evolution (SNORCLE) transect and Cordilleran tectonics workshop meeting, 250-262.

Goodman, J. W., 1968, Introduction to Fourier optics: McGraw-Hill.

Gray, S. H., 1997, True-amplitude seismic migration: A comparison of three approaches: Geophysics, **62**, 929-936.

Gray, S. H., 1998a, Interpretive seismic imaging in structurally complex areas: GeoTriad '98 Joint Convention Abstracts, 282-283.

Gray, S. H., 1998b, Speed and accuracy of seismic migration methods, Calgary, Amoco Expl. Prod. Tech., p. 37p.

Hagedoorn, J. G., 1955, A process of seismic reflection interpretation: Geophys. Prosp., **2**, 85-127.

Hanitzsch, C., 1995, Amplitude preserving prestack Kirchhoff depth migration/inversion in laterally inhomogeneous media: Ph.D. thesis, University of Karlsruhe.

Hanitzsch, C., 1997, Comparison of weights in prestack amplitude-preserving Kirchhoff depth migration: Geophysics, **62**, 1812-1816.

Hilterman, F. J., 1970, Three-dimensional seismic modeling: Geophysics, **35**, 1020-1037.

Hilterman, F. J., 2001, Seismic Amplitude Interpretation: Society of Exploration Geophysics, 2001 Distinguished Instructor Series, **4**.

Hockt, G., de Bazelaire, E., Majer, P., and Hubral, P., 1999, Seismics and optics: hyperbolae and curvatures: J. Appl. Geophys., **42**, 261-181.

Hubral, P., 1977, Time migration—some ray theoretical aspects: Geophys. Prosp., **25**, 738-745.

Hubral, P., Schleicher, J., and Tygel, M., 1996, A unified approach to 3-D seismic reflection imaging, Part I: Basic concepts: Geophysics, **61**, 742-758.

Huygens, C., 1673, Horologium Oscillatorium.

Huygens, C., 1690, Traite de la Lumiere.

Jaramillo, H., 1999, Seismic Data mapping: Ph.D. thesis, Colorado School of Mines.

Jaramillo, H., and Bleistein, N., 1999, The link of Kirchhoff migration and demigration to Kirchhoff and Born modeling: Geophysics, **64**, 1793-1805.

Jaramillo, H., Bloor, R., Yingst, D., and Mobley, E., 2000, True-amplitude migration and dip equalisation: 62nd Ann. Internat. Mtg., Eur. Assn. Geosc. Eng., Abstracts, B-14.

Johnson, N. L., and Kotz, S., 1970, Continuous univariate distributions - 2: Houghton Mifflin.

Judson, D., Lin, J., Schultz, P. S., and Sherwood, J. W. C., 1978, Equalizing the stacking velocities of dipping events via Develish: 48th Ann. Internat. Mtg., Soc. Expl. Geophys., Expanded Abstracts.

Kelly, K. R., and Marfurt, K. J., eds., 1990, Numerical modeling of seismic wave propagation: Society of Exploration Geophysicists, Geophysics reprint series, **13**.

Kuhn, M. J., and Alhilali, K. A., 1977, Weighting factors in the construction and reconstruction of acoustical wave fields: Geophysics, **42**, 1183-1198.

Lancaster, P., and Salkauskas, K., 1996, Transform methods in applied mathematics: an introduction: John Wiley & Sons, Canadian Mathematics Society series of monographs and advanced texts.

LeBras, R., and Clayton, R. W., 1988, An iterative inversion of back-scattered acoustic waves: Geophysics, **53**, 501-508.

Li, X., 1999, Residual statics analysis using prestack equivalent offset migration: M.Sc. thesis, University of Calgary.

Li, X., and Bancroft, J. C., 1998, Efficent computation of the equivalent offset for EOM: 68th Ann. Internat. Mtg., Soc. Expl. Geophys., Expanded Abstracts, ST 11.9.

Li, X., Xu, Y., and Bancroft, J. C., 1997, Equivalent offset migration: implementation and application update, CREWES Research Report - Volume 9 (1997), p. 27 (1-11).

Liner, C. L., 1991, theory of 2.5-D acoustic wave equation for constant density media: Geophysics, **56**, 2114-2117.

Liner, C. L., and Stockwell, J., J.W., 1993, Some analytical aspects of the 2.5-D wave equation: 63rd Ann. Internat. Mtg., Soc. Expl. Geophys., Expanded Abstracts, 201-204.

Lines, L. R., Gray, S. H., and Lawton, D. C., eds., 1999, Depth imaging of foothills seismic data: Can. Soc. Expl. Geophys.

Loewenthal, D., Lu, L., Roberson, R., and Sherwood, J., 1976, The wave equation applied to migration: Geophys. Prosp., **24**, 380-399.

Lumley, D. E., 1989, Kirchhoff prestack depth migration: Imaging conditions and amplitude recovery: 63rd Ann. Internat. Mtg., Soc. of Expl. Geophys., Expanded Abstracts, 1336-1339.

Mackay, A. L., 1994, Dictionary of Scientific Quotations: Institute of Physics.

Margrave, G. F., 2000, Numerical methods of exploration seismology: University of Calgary.

Margrave, G. F., Bancroft, J. C., and Geiger, H. D., 1999, Fourier prestack migration by equivalent wavenumber: Geophysics, **64**, 197-207.

Margrave, G. F., and Yao, Z., 1999, Imaging from topography with Fourier methods: CREWES Research Report, 1999.

Martignole, J., and Calvert, A. J., 1996, Crustal-scale shortening and extension across the Grenville Province of western Quebec: Tectonics, **15**, 376-386.

Menke, W., and Abbott, D., 1990, Geophysical Theory: Columbia University Press.

Milkereit, B., Green, A. G., Lee, M. W., Agena, W. F., and Spencer, C., 1990, Pre- and poststack migration of GLIMPCE reflection data. In: J.H. Leven, D.M. Finlayson,

C. Wright, J.C. Dooley, and B.L.N. Kennett (eds.), Seismic Probing of the Continents and their Margins: Tectonophysics, **173**, 1-13.

Miller, D., Oristaglio, M., and Beylkin, G., 1987, A new slant on seismic imaging: Migration and integral geometry: Geophysics, **52**, 943-964.

Mitzner, K. M., 1967, Numerical solution for transient scattering from a hard surface of arbitrary shape—retarded potential technique: J. Acoust. Soc. Amer., **42**, 391-397.

Morse, P. M., and Feshbach, H., 1953, Methods of theoretical physics: parts I and II: McGraw-Hill Book Co.

Musgrave, A. W., 1952, Wavefront charts and raypath plotters: Quarterly J. of the Colorado School of Mines, **47**, No. 4, 68 p.

Newman, P., 1975, republished 1990, Amplitude and phase properties of a digital migration process: First Break, **8**, 397-403.

Nichols, D. E., 1996, Maximum energy traveltimes calculated in the seismic frequency band: Geophysics, **61**, 253-263.

Pavis, G. L., 1989, Inverse theory and methods: seismology, *in* D. E. James, ed., The encyclopedia of solid earth geophysics: van Nostrand Reinhold, p. 647-654.

Pfenning, F., 2001, Computation and deduction: Cambridge University Press (in prep.), draft version available at www-2.cs.cmu.edu/~fp/courses/atp/handouts.

Pierce, A. D., 1989, Acoustics: An introduction to its physical principles and applications: Acoustical Society of America.

Porsani, M. J., 1999, Seismic trace interpolation using half-step prediction filters: Geophysics, **64**, 1461-1467.

Press, W. H., Teukolsky, S. A., Vetterling, W. T., and Flannery, B. P., 1992, Numerical recipes in C: the art of scientific computing: Cambridge University Press.

Rice, R. B., 1953, New seismic computation method fast and efficient: World Oil, **137**, No. 2, 93.

Rice, R. B., 1955, Additional notes on the resolved-time computing method: Geophysics, **20**, 104-122.

Rietveld, W. E. A., 1994, Prestack depth migration by means of controlled illumination: Geophysics, **59**, 801-809.

Rietveld, W. E. A., Berkhout, A. J., and Wapenaar, C. P. A., 1992, Optimum seismic illumination of hydrocarbon reservoirs: Geophysics, **57**, 1334-1345.

Robinson, E. A., and Silvia, M. T., 1981, Digital foundations of time series analysis: Volume 2 - Wave equation space-time processing: Holden-Day, Inc., Holden-Day series in time series analysis and digital signal processing.

Sampson, C., and West, G. F., 1992, Crustal structure of the mid-continent rift system in eastern Lake Superior from controlled-amplitude analysis of GLIMPSE deep reflection data: Can. J. Earth Sci., **29**, 636-649.

Scales, J. A., 1997, Theory of Seismic Imaging: Samizdat Press.

Scales, J. A., 2001, Imaging and inversion with acoustic and elastic waves, *in* Pike, and Sabatier, eds., Scattering: Academic (preprint, 16p).

Schleicher, J., Tygel, M., and Hubral, P., 1993, Parabolic and hyperbolic paraxial two-point traveltimes in 3D media: Geophys. Prosp., **41**, 495-513.

Schneider, W. A., 1978, Integral formulation for migration in two and three dimensions: Geophysics, **43**, 49-76.

Schultz, P. S., and Sherwood, J. W. C., 1980, Depth migration before stack: Geophysics, **45**, 376-393.

Shakespeare, W., 1604, Hamlet, *in* S. Wells, and G. Taylor, eds., The Complete Works (reprinted 1988): Clarendon, p. 653-690.

Sheriff, R., 1991, Encyclopedic dictionary of exploration geophysics: Society of Exploration Geophysics.

Sheriff, R. E., 1975, Factors affecting seismic amplitudes: Geophys. Prosp., **23**, 125-138.

Sherwood, J. W. C., Schultz, P. S., and Judson , J. R., 1976, Some recent developments in migration before stack, Digicon.

Snieder, R., 1994, A Guided Tour of Mathematical Physics: Samizdat Press.

Snieder, R., and Chapman, C., 1998, The reciprocity properties of geometrical spreading: Geophys. J. Int., **132**, 89-95.

Snieder, R., and Trampert, J., 1999, Inverse problems in geophysics, *in* A. Wirgin, ed., Wavefield inversion: Springer Verlag, p. 119-190.

Song, Z.-M., and Williamson, P. R., 1992, Full-wave frequency-domain crosshole inversion and modeling in 2.5-D: 54th EAEG meeting, Expanded Abstracts, 518-519.

Stockwell, J. W., 1995, 2.5-D wave equations and high-frequency asymptotics: Geophysics, **60**, 556-562.

Stoffa, P. L., and Ziolkowski, A., 1983, Seismic source decomposition: Geophysics, **48**, 1-11.

Stolt, R. H., 1978, Migration by Fourier transform: Geophysics, **43**, 23-48.

Stolt, R. H., 2002, Seismic data mapping and reconstruction: Geophysics, (in press).

Stolt, R. H., and Weglein, A. B., 1985, Migration and inversion of seismic data: Geophysics, **50**, 2458-2472.

Suaudeau, E., and Siliqi, R., 2001, Anelliptic pre-stack time migration: Ann. Mtg. Can. Soc. Expl. Geophys., Expanded Abstracts, 26-28.

Sun, J., 1998, On the limited aperture migration in two dimensions: Geophysics, **63**, 984-994.

Sun, J., 2000, Limited-aperture migration: Geophysics, **65**, 584-595.

Tikhonov, A. N., and Samarskii, A. A., 1990, Equations of mathematical physics.

Timoshin, Y. V., 1970, New possibilities for imagery: Soviet Physics-Acoustics, **15**, 360-367.

Trorey, A. W., 1970, A simple theory for seismic diffractions: Geophysics, **35**, 762-784.

Trorey, A. W., 1977, Diffractions for arbitrary source-receiver locations: Geophysics, **42**, 1177-1182.

Tygel, M., and Hubral, P., 1987, Transient waves in layered media: Elsevier Scientific Inc., Methods in geochemistry and geophysics, **26**.

Tygel, M., Schleicher, J., Hubral, P., and Hanitzsch, C., 1993, Multiple weights in diffraction stack migration: Geophysics, **59**, 1820-1830.

van der Velden, A. J., Bancroft, J. C., Geiger, H. D., and Cook, F. A., 2001, Prestack time migration of SNORCLE line 1: an improved seismic image of the Slave Province, *in* F. A. Cook, and P. Erdmer, eds., Slave-Northern Cordillera Lithospheric Evolution (SNORCLE) Transect and Cordilleran Tectonics Workshop Meeting: Lithoprobe, **79**, p. 281.

van der Velden, A. J., and Cook, F. A., 2001, Products of 2.65-2.58 Ga orogenesis in the Slave Province imaged on SNORCLE seismic reflections data: CJES, (accepted).

Vanelle, C., and Gajewski, D., 2001a, Determining the optimum migration aperture from traveltimes: J. Seis. Expl., (accepted).

Vanelle, C., and Gajewski, D., 2001b, Second-order interpolation of traveltimes: Geophys. Prosp., (in press).

Vasudevan, K., Cook, F., van der Velden, A., Lynn, E., and Clowes, R., 2000, Towards a transect of the North American lithosphere: 8th International Symposium on Deep Seismic Profiling of the Continents and their Margins, p. 118.

Vermeer, G., 1990, Seismic wavefield sampling: Soc. Expl. Geophys.

Verschuur, D. J., Berkhout, A. J., and Wapenaar, C. P. A., 1992, Adaptive surface-related multiple elimination: Geophysics, **57**, 1166-1177.

Wang, W., Pham, L., and Zhang, Y., 2000, Equivalent offset migration—strengths and weaknesses: 62 Eur. Assn. Geosci. Eng., B-49.

Wang, W., and West, G. F., 1991, F-X filters with dip rejection: 61st Ann. Internat. Mtg., Soc. Expl. Geophys., Expanded Abstracts, 1436-1438.

Wapenaar, C. P. A., 1992, The infinite aperture paradox: J. Seis. Expl., **1**, 325-336.

Wapenaar, C. P. A., 1993a, Kirchhoff-Helmholtz downward extrapolation in a layered medium with curved interfaces: Geophys. J. Int., **115**, 445-455.

Wapenaar, C. P. A., 1993b, Representations of seismic reflection data. Part II: New developments: J. Seis. Expl., **2**, 247-255.

Wapenaar, C. P. A., 1996, One-way representations of seismic data: Geophys. J. Int., **127**, 178-188.

Wapenaar, C. P. A., and Berkhout, A. J., 1989, Elastic wavefield extrapolation: redatuming of single- and multi-component seismic data: Elsevier Science Publ. Co., Inc., Advances in Exploration Geophysics, **2**.

Wapenaar, C. P. A., and Berkhout, A. J., 1993, Representations of seismic reflection data. Part I: State of affairs: J. Seis. Expl., **2**, 123-131.

Wapenaar, C. P. A., and Grimbergen, J. L. T., 1996, Reciprocity theorems for one-way wavefields: Geophys. J. Int., **127**, 169-177.

Wapenaar, C. P. A., Peels, G. L., Budejicky, V., and Berkhout, A. J., 1989, Inverse extrapolation of primary seismic waves: Geophysics, **54**, 853-863.

Weglein, A. B., 1985, The inverse scattering concept and its seismic application, *in* A. A. Fitch, ed., Developments in Geophysical Exploration Methods - 6: Elsevier, **6**, p. 111-138.

Weglein, A. B., and Stolt, R. H., 1999, Migration-inversion revisited (1999): The Leading Edge, **18**, No. 8, 950-952; 975.

Wenzel, F., Stenzel, K-J., and Zimmerman, U., 1990, Wave propagation in laterally heterogeneous media: Geophys. J. Int., **103**, 675-684.

White, D. J., Forsyth, D. A., Asudeh, I., Carr, S. D., Wu, H., Easton, R. M., and Mereu, R. F., 2000, A seismic-based cross-section of the Grenville Orogen in southern Ontario and western Quebec: CJES, **37**, 183-192.

Wiggins, W., 1984, Kirchhoff integral extrapolation and migration of nonplanar data: Geophysics, **49**, 1239-1248.

Williamson, P. R., and Pratt, R. G., 1995, A critical review of acoustic wave modeling procedures in 2.5 dimensions: Geophysics, **60**, 591-595.

Yilmaz, O., 1980, Prestack partial migration: Geophysics, **45**, 1753-1777.

Yilmaz, O., 2001, Seismic data analysis: processing, inversion, and interpretation of seismic data: Society of Exploration Geophysicists, Investigations in Geophysics.

Zhang, Y., Gray, S. H., Notfors, C., and Bleistein, N., 2001, Towards accurate amplitudes for one-way wavefield extrapolation of 3-D common-shot records: 71st Ann. Mtg., Soc. Expl. Geophys., Expanded Abstracts.

Zhang, Y., Gray, S., and Young, J., 2000, Exact and approximate weights for Kirchhoff migration: 70th Ann. Internat. Mtg., Soc. Expl. Geophys., Expanded Abstracts, 1036-1039.

APPENDIX A: DELTA FUNCTIONS, FOURIER TRANSFORMS, LINEAR SYSTEMS, AND MONOCHROMATIC TIME FUNCTIONS

A.1 Introduction

The purpose of this appendix is twofold: first, to establish notation and sign conventions for delta functions, Fourier transforms, and their respective derivatives; and second, to establish the powerful concepts of linear systems and monochromatic time functions. Monochromatic time functions allow us to utilize the many simplifications associated with Fourier transforms (e.g. the Helmholtz equation instead of the scalar wave equation and convolution as multiplication), but retain the intuitive physical concept of a wavefront as a delta function propagating in space and time (e.g. the impulse response of a point source). Linear systems allow us to use superposition to create complicated functions in space-time (or space-frequency) from much simpler functions. The notation, sign conventions and concepts discussed here provide a foundation for free-space and ray-theoretical Green's functions introduced in Section 2.4, and used throughout this dissertation.

A.2 Delta functions

Let $\mathcal{V}$ be a linear space of functions. A functional, with domain $\mathcal{V}$, is a mapping (or rule) that assigns a unique number to every function in the domain. A distribution is a continuous linear functional with domain $\mathcal{V} = C_0^\infty(\mathcal{R})$. The functional that evaluates the test function $\varphi \in C_0^\infty(\mathcal{R})$ at $t = 0$ is called the *δ-distribution*, and we write $\langle \delta, \varphi \rangle = \varphi(0)$ to indicate the δ-distribution acting on φ. A more useful notation (Lancaster and Salkauskas, 1996) is to write the δ-distribution in function notation as $\delta(t-\tau)$ using the definition

$$\langle a\delta_t, \varphi\rangle = a\int_{-\infty}^{\infty} \varphi(\tau)\delta(t-\tau)d\tau = a\varphi(t)\,, \tag{A-1}$$

which illustrates the 'sifting' property and the effect of a constant multiplier a. In equation (A-1), the integral is more correctly interpreted as the limit of a regular distribution given by a delta sequence (such as a pulse of unit area) acting on the test function. The δ-distribution is not a function in the traditional sense, although for historical reasons it is often referred to as the delta function, a convention that will be followed here.

A.3 Linear systems and filters

Delta functions play an important role in the theory of continuous linear systems and filters. A linear system $\mathcal{L}$ is a linear transformation from one linear space of functions with domain D to another with domain R. Thus, for any $f, g \in D$, we have $\mathcal{L}f, \mathcal{L}g \in R$ and for any real α, β, the property of linearity is defined as

$$\mathcal{L}(\alpha f + \beta g) = \alpha(\mathcal{L}f) + \beta(\mathcal{L}g). \tag{A-2}$$

Often, the domain and range spaces are the same.

A time-invariant (or space-invariant) linear system is a filter. The output $h(t)$ of a continuous linear filter $\mathcal{L}$ can be expressed as the input $g(t)$ convolved with the filter response $f(t)$,

$$h(t) = (\mathcal{L}g)(t) = (f * g)(t) = \int_{-\infty}^{\infty} f(\tau)g(t-\tau)d\tau \tag{A-3}$$

If the filter is causal, the lower limit of integration is zero, or equivalently, the filter can be defined as $f(t) = 0$, $t < 0$. Using a delta function as input $g(t)$ to the non-causal filter $\mathcal{L}$ of equation (A-3), we can apply the sifting property [equation (A-1)] to yield

$$h(t) = \int_{-\infty}^{\infty} f(\tau)\delta(t-\tau)d\tau = f(t). \tag{A-4}$$

Hence the output $h(t)$ is the filter response $f(t)$. This shows that the delta function is the unit for convolution, just as the number 1 is the unit for multiplication of real or complex numbers. As a linear system, the function f does not have to be a test function in $\varphi \in C_0^\infty(\mathcal{R})$; and, although equation (A-4) is an improper integral unless considered in the context of the δ-distribution as discussed above, it will now be used as the defining equation for the delta function.

A.4 Acoustic scalar wave equation as a linear filter or linear system

The properties of linear systems and filters make them ideal mathematical tools for studying the propagation of waves. We now expand the concept of linear systems and linear filters to incorporate the spatial dimensions (Cartesian position **x**) in addition to the time dimension. For example, the nonhomogeneous acoustic scalar wave equation (equation (2.6), for constant material wavespeed $c(\mathbf{x}) = c$),

$$\nabla^2 p(\mathbf{x},t) - \frac{1}{c^2}\frac{\partial^2 p(\mathbf{x},t)}{\partial t^2} = -\rho(\mathbf{x})s(\mathbf{x},t), \tag{A-5}$$

can be represented as the linear filter

$$\mathcal{L}\big(p(\mathbf{x},t)\big) = -\rho(\mathbf{x})s(\mathbf{x},t), \tag{A-6}$$

where

$$\mathcal{L} = \nabla^2 - \frac{1}{c^2}\frac{\partial^2}{\partial t^2}. \tag{A-7}$$

The property of linearity [equation (A-2)] can be applied to decompose the input function $p(\mathbf{r},t)$ and the output[1] function $-\rho(\mathbf{r})s(\mathbf{r},t)$ into a superposition of more favorable functions. The obvious candidates are monochromatic functions of time, which can be combined using the Fourier transform. By expressing the linear filter $\mathcal{L}$ [filter operator $f(t)$ in the generalized convolution of equation (A-3)] as its Fourier transform, the awkward time derivative in equation (A-7) can be simplified [see equations (A-31) and (A-32)] and the convolution in equation (A-3) can be represented as multiplication in the frequency domain. Forward and inverse Fourier transforms will be investigated in detail below.

On the other hand, if the material wavespeed is a function of space [i.e. $c(\mathbf{x})$], then $\mathcal{L}$ is no longer space-invariant. In this case, $\mathcal{L}$ would be the linear system,

$$\mathcal{L} = \nabla^2 - \frac{1}{c^2(\mathbf{x})}\frac{\partial^2}{\partial t^2}, \qquad \text{(A-8)}$$

instead of a linear filter. The property of linearity still holds. For linear systems, the favorable functions for superposition are Green's functions, defined as the input function that produces a delta function output. For a delta function output at source position $\mathbf{x}_G$ at time t_G, the Green's function for the nonhomogeneous acoustic wave equation [equation (2.11)] is given by

$$\mathcal{L}\big(g(\mathbf{x},\mathbf{x}_G,t,t_G)\big) = -\delta(\mathbf{x}-\mathbf{x}_G,t-t_G) = -\delta(\mathbf{x}-\mathbf{x}_G)\delta(t-t_G). \qquad \text{(A-9)}$$

---

[1] For the wave equation, the source function $-\rho(\mathbf{x})s(\mathbf{x},t)$ is more intuitively thought of as the 'input' to the physical system. Here, the definitions of input and output for a linear system follow equation (A-3).

Hence, a complicated source function [e.g. the RHS of equation (A-6)] can be considered as a superposition of delta functions, and the corresponding acoustic pressure $p(\mathbf{x},t)$ as a superposition of Green's functions.

A.5 Fourier transform convention and delta functions

We now return to Fourier transforms and the superposition of monochromatic time functions. A time function $f(t)$ and its spectrum $F(\omega)$ are related by the forward and inverse Fourier transform. The convention adopted here uses the positive exponential for the forward transform from the time domain to the circular frequency domain,

$$F(\omega) = \int_{-\infty}^{\infty} f(t) e^{i\omega t}\, dt\,, \tag{A-10}$$

and the negative exponential for the inverse transform from the circular frequency domain back to the time domain,

$$f(t) = \frac{1}{2\pi} \int_{-\infty}^{\infty} F(\omega) e^{-i\omega t}\, d\omega\,. \tag{A-11}$$

$F(\omega)$ is a complex number representing the spectral density (i.e. spectrum per unit ω). The product $F(\omega)d\omega$ is an average amplitude for the packet of continuous frequencies in an interval $d\omega$ containing ω. Hence the physical dimensions should be considered as average amplitudes (an interpretation that agrees with practical implementation using finite discrete Fourier transform) and the product $F(\omega)d\omega$ will have the same physical dimensions as the time domain equivalent $f(t)$.

The choice of circular frequency ω instead of frequency f (where $\omega = 2\pi f$) indicates a preference for terms in 2π as constants instead of as parts of the complex exponent (and associated constants arising from differentiation). For circular frequency, terms in 2π

arise in two basic ways: first, given that $df = d\omega/2\pi$, we should expect a $1/2\pi$ term whenever ω is the integration variable; and second, given the delta function identity

$$\delta(\omega - \omega') = \delta\bigl(2\pi(f - f')\bigr) = \frac{1}{2\pi}\delta(f - f'), \tag{A-12}$$

it follows that

$$\delta(f - f') = 2\pi\delta(\omega - \omega'), \tag{A-13}$$

and thus we should expect a 2π term whenever the delta function $\delta(\omega - \omega')$ is present.

Two Fourier transform pairs will prove useful in the study of wave propagation,

$$\delta(\omega - \omega') \leftrightarrow \frac{1}{2\pi} e^{-i\omega' t}, \tag{A-14}$$

and

$$\delta(t - \tau) \leftrightarrow e^{i\omega\tau}. \tag{A-15}$$

The second is the well-known result that a time shift, as given by the delta function, is equivalent to a complex phase shift in the circular frequency domain. It can be derived in a nonrigorous fashion by substituting equation (A-10) into equation (A-11), yielding

$$f(t) = \frac{1}{2\pi}\int_{-\infty}^{\infty}\left[\int_{-\infty}^{\infty} f(\tau)e^{i\omega\tau}\,d\tau\right]e^{-i\omega t}\,d\omega. \tag{A-16}$$

The term $e^{-i\omega t}$ is a constant for the τ integration, and can be moved inside. The order of integration is switched. Now $f(\tau)$ is constant for the ω integration, and can be moved outside. Moving the constant $1/2\pi$ inside the τ integration yields

$$f(t) = \int_{-\infty}^{\infty} f(\tau)\left[\frac{1}{2\pi}\int_{-\infty}^{\infty} e^{i\omega\tau} e^{-i\omega t}\,d\omega\right]d\tau, \tag{A-17}$$

which can be recognized as the same form as equation (A-4), the convolution equation for a delta function. Thus the delta function in time is given by

$$\delta(t-\tau) = \frac{1}{2\pi}\int_{-\infty}^{\infty} e^{i\omega\tau} e^{-i\omega t} d\omega \,. \qquad \text{(A-18)}$$

Comparing equation (A-18) with equation (A-11) gives equation (A-15), the Fourier transform pair $\delta(t-\tau) \leftrightarrow e^{i\omega\tau}$. Similarly, it can be shown that $\delta(t+\tau) \leftrightarrow e^{-i\omega\tau}$.

A.6 Amplitude and phase of monochromatic time functions

Suppose we take the inverse Fourier transform of a sum of two shifted delta functions multiplied by appropriate constants,

$$F(\omega) = \pi\left|\tilde{F}(\omega')\right| e^{-i\phi(\omega')}\delta(\omega+\omega') + \pi\left|\tilde{F}(\omega')\right| e^{i\phi(\omega')}\delta(\omega-\omega') \,. \qquad \text{(A-19)}$$

Inserting equation (A-19) into equation (A-11),

$$\tilde{f}(t) = \frac{1}{2\pi}\int_{-\infty}^{\infty} \pi\left|\tilde{F}(\omega')\right| e^{-i\phi(\omega')}\delta(\omega+\omega') e^{-i\omega t} d\omega$$

$$+ \frac{1}{2\pi}\int_{-\infty}^{\infty} \pi\left|\tilde{F}(\omega')\right| e^{i\phi(\omega')}\delta(\omega-\omega') e^{-i\omega t} d\omega \,, \qquad \text{(A-20)}$$

and applying the sifting property of the delta function yields

$$\tilde{f}(t) = \left|\tilde{F}(\omega')\right| \frac{(e^{i[\omega' t-\phi(\omega')]} + e^{-i[\omega' t-\phi(\omega')]})}{2}$$

$$= \left|\tilde{F}(\omega')\right| \cos\left[\omega' t - \phi(\omega')\right]$$

$$= \left|\tilde{F}(\omega')\right| \cos\left[\omega'(t-\tau_0)\right]. \qquad \text{(A-21)}$$

Thus $\tilde{f}(t)$ [as given by equation (A-21)] is a monochromatic time function with amplitude $\left|\tilde{F}(\omega')\right|$, frequency ω', and phase lag $\phi(\omega')$. That $\phi(\omega') = \omega'\tau_0$ is the phase lag follows from the observation that (t - τ_0) causes a delay or lag in the signal for positive τ_0 and hence for positive $\phi(\omega')$.

The spectrum $F(\omega)$ of $\tilde{f}(t)$ [as given by equation (A-19)] consists of delta functions at $\pm\omega'$ multiplied by complex coefficients. The complex coefficient for $\delta(\omega+\omega')$ [i.e. when circular frequency $\omega=\omega'$ is negative] is

$$\pi\left|\tilde{F}(\omega')\right|e^{-i\phi(\omega')} = \pi\left|\tilde{F}(\omega')\right|\left[\cos\phi(\omega') - i\sin\phi(\omega')\right], \qquad \text{(A-22)}$$

and the complex coefficient for $\delta(\omega-\omega')$ [i.e. when circular frequency $\omega=\omega'$ is positive] is

$$\pi\left|\tilde{F}(\omega')\right|e^{i\phi(\omega')} = \pi\left|\tilde{F}(\omega')\right|\left[\cos\phi(\omega') + i\sin\phi(\omega')\right]. \qquad \text{(A-23)}$$

A.7 Complex (analytic) monochromatic time functions

Equations (A-22) and (A-23) show that the real (cosine) component of the spectrum is symmetric about zero frequency ($\omega = 0$), while the imaginary (sine) component is antisymmetric. If we can remember that these symmetries exist, it is often simpler to ignore the negative frequencies in the spectrum given by equation (A-19) and consider the spectrum to be composed only of positive frequencies with twice the amplitude, i.e.

$$F(\omega) = 2\pi\left|\tilde{F}(\omega')\right|e^{i\phi(\omega')}\delta(\omega-\omega'). \qquad \text{(A-24)}$$

Using equation (A-11), the inverse Fourier transform of equation (A-24) is

$$\tilde{f}_C(t) = \frac{1}{2\pi}\int_{-\infty}^{\infty} 2\pi\left|\tilde{F}(\omega')\right|e^{i\phi(\omega')}\delta(\omega-\omega')e^{-i\omega t}\,d\omega. \qquad \text{(A-25)}$$

Applying the sifting property of the delta function [equation (A-1)] yields

$$\tilde{f}_C(t) = \left|\tilde{F}(\omega')\right|e^{-i[\omega' t - \phi(\omega')]} \qquad \text{(A-26)}$$

or equivalently,

$$\tilde{f}_C(t) = \left|\tilde{F}(\omega')\right| \left\{\cos\left[\omega' t - \phi(\omega')\right] - i\sin\left[\omega' t - \phi(\omega')\right]\right\}. \tag{A-27}$$

Comparing equations (A-21) and (A-27), we see that $\tilde{f}_C(t)$ is a complex (analytic) monochromatic time function and is related to $\tilde{f}(t)$ by

$$\tilde{f}(t) = \mathrm{Re}\left[\tilde{f}_C(t)\right]. \tag{A-28}$$

Equation (A-26) can be re-expressed using the complex amplitude $\tilde{F}(\omega') = \left|\tilde{F}(\omega')\right| e^{i\phi(\omega')}$ as

$$\tilde{f}_C(t) = \tilde{F}(\omega') e^{-i\omega' t}. \tag{A-29}$$

Equation (A-29) represents a single complex harmonic signal at circular frequency ω' with a phase lag $\phi(\omega')$ that corresponds to a time delay τ_0.

Two important concepts introduced above—using twice the amplitude of the positive frequencies [equation (A-24)] and taking the real part of the analytic time series [equation (A-28)]—can be used to create a practical definition of the inverse Fourier transform,

$$f(t) = \mathrm{Re}\left[\frac{1}{2\pi}\int_0^\infty 2F(\omega) e^{-i\omega t} d\omega\right]. \tag{A-30}$$

In equation (A-30), $f(t)$ is a real function, while $F(\omega)$ is its forward Fourier transform as given by equation (A-10). This definition (a variation of which can be found in a footnote in Section 2.4) encapsulates the material presented above. In equation (A-29), the complex amplitude $\tilde{F}(\omega')$ has the same physical dimensions as the complex monochromatic function $\tilde{f}_C(t)$. The Fourier transform $F(\omega)$, on the other hand, is a spectral density, but will be considered to have the same physical dimensions as its time domain inverse $f(t)$ because the product $F(\omega)d\omega$ is the average amplitude over the frequency range $d\omega$.

A.8 Time derivatives of monochromatic functions, and delta functions

The time derivative of equation (A-11) can be found as follows:

$$\frac{df(t)}{dt} = \frac{-i\omega}{2\pi}\int_{-\infty}^{\infty} F(\omega)e^{-i\omega t}d\omega = -i\omega f(t), \tag{A-31}$$

and the time derivative of equation (A-29) as

$$\frac{d\tilde{f}_C(t)}{dt} = -i\,\omega\tilde{F}(\omega')e^{-i\omega' t} = -i\,\omega\tilde{f}_C(t). \tag{A-32}$$

Hence the sign associated with a time derivative depends on the sign convention chosen for the Fourier transform.

The time derivative of a delta function has a sifting property similar to equations (A-1), expressed here in the form of equation (A-4),

$$(-1)^n f^n(\tau) = \int_{-\infty}^{\infty} f(t)\delta^n(t-\tau)dt. \tag{A-33}$$

Other useful formulae can be found in standard migrations texts (e.g. Berkhout, 1985; Bleistein et al., 2001).

A.9 Summary

In this Appendix, I established notation and sign conventions for delta functions, Fourier transforms, and their respective derivatives. I introduced linear filters and systems, and showed how they apply to the constant- and variable-wavespeed nonhomogeneous acoustic scalar wave equations. Monochromatic time functions were shown to be useful representations for the Fourier transforms of time-domain functions. In particular, they allow us to combine the physical intuition of the space-time domain with the mathematical simplicity of the space-frequency domain. These concepts provide the foundation for the free-space and ray-theoretical Green's functions in the space-frequency domain introduced in Section 2.4, and used throughout the dissertation.

APPENDIX B: INVERSE WAVEFIELD EXTRAPOLATION USING FREE-SPACE GREEN'S FUNCTIONS AND A GEOMETRIC APPROACH TO STATIONARY PHASE

B.1 Introduction

The Kirchhoff-Helmholtz integral equation for inverse wavefield extrapolation from a non-planar interface S_g with upward directed normal $\mathbf{n}_g^-$ is given by

$$P_S^-(\mathbf{x}_G, \mathbf{x}_s, \omega) = \int_{S_g} dS \Big\{ \overleftarrow{G}_0^+(\mathbf{x}_g, \mathbf{x}_G, \omega) \nabla_{\mathbf{x}_g} P_S^-(\mathbf{x}_g, \mathbf{x}_{s'}, \omega) - P_S^-(\mathbf{x}_g, \mathbf{x}_{s'}, \omega) \nabla_{\mathbf{x}_g} \overleftarrow{G}_0^+(\mathbf{x}_g, \mathbf{x}_G, \omega) \Big\} \cdot \mathbf{n}_g^-, \tag{B-1}$$

where $\mathbf{x}_s$ is the location of the source and $\mathbf{x}_{s'}$ denotes the generalized location of the image sources. Equation (B-1) reconstructs the upgoing acoustic wavefield $P_S^-(\mathbf{x}_G, \mathbf{x}_s, \omega)$ at subsurface imaging point $\mathbf{x}_G$ given the upgoing wavefield $P_S^-(\mathbf{x}_g, \mathbf{x}_{s'}, \omega)$ and its normal derivative $\nabla_{\mathbf{x}_g} P_S^-(\mathbf{x}_g, \mathbf{x}_{s'}, \omega) \cdot \mathbf{n}_g^-$ recorded at surface locations $\mathbf{x}_g$. The one-way backward propagating Green's function $\overleftarrow{G}_0^+(\mathbf{x}_g, \mathbf{x}_G, \omega)$ and its normal derivative $\nabla_{\mathbf{x}_g} \overleftarrow{G}_0^+(\mathbf{x}_g, \mathbf{x}_G, \omega) \cdot \mathbf{n}_g^-$ have Green's source locations at the reconstruction point $\mathbf{x}_G$; or, invoking reciprocity (see Section 2.7), they can be thought of as monopole and dipole secondary sources, respectively, at locations $\mathbf{x}_g$ on the non-planar interface S_g.

The objective of this appendix is to determine an approximate expression for inverse wavefield extrapolation from a nonplanar interface that requires only one of either the pressure or its normal derivative. The classical approach assumes a constant wavespeed medium and a planar interface, uses an image of the free-space Green's function across the planar interface to eliminate one of the terms, and ignores the near-field contribution. The result is the free-space far-field Rayleigh II integral. In this appendix, I assume a constant wavespeed medium and a nonplanar interface, and expand the full Kirchhoff-

Helmholtz integral [equation (B-1)] using (one-way) free-space Green's functions. The key to the derivation is to equate the unknown normal derivative of the wavefield with the known normal derivative of the Green's function using a geometric approach to stationary phase. In this case, the effects of the near-field terms tend to cancel.

B.2 Image Green's functions and one-way Rayleigh II integrals for inverse wavefield extrapolation

The classical approach (Schneider, 1978) eliminates the term containing the normal derivative of the pressure by defining a Rayleigh II Green's function that is zero on the surface S_g (see Section 2.8). Thus the normal derivative of the wavefield is not required. The Rayleigh II Green's function for each surface element consists of the sum of a positive free-space Green's function with source at the reconstruction point and a negative free-space Green's function with source at the image point, where the image point is the mirror of the reconstruction point across the surface element (see Figure 2.6). Thus the normal derivative of the Rayleigh II Green's function is twice the normal derivative of a positive free-space Green's function $\overleftarrow{G}_0^+(\mathbf{x}_g, \mathbf{x}_G, \omega)$ located at the reconstruction point, and the Kirchhoff-Helmholtz integral equation [equation (B-1)] becomes

$$P_S^-(\mathbf{x}_G, \mathbf{x}_s, \omega) = 2\int_{-\infty}^{+\infty}\int dxdyJ_{Sxy}\left\{P_S^-(\mathbf{x}_g, \mathbf{x}_{s'}, \omega)\frac{\partial\overleftarrow{G}_0^+(\mathbf{x}_g, \mathbf{x}_G, \omega)}{\partial n_g^+}\right\}_{S_g}. \tag{B-2}$$

Equation (B-2) is known as the one-way Rayleigh II integral for inverse wavefield extrapolation. Note that the generic surface normal $\mathbf{n}_g^+$ is now directed downward (positive z-direction for a planar interface), resulting in a sign change in both the normal direction and the integrand in equation (B-2) compared with the second term in equation (B-1). The Jacobian $J_{Sxy} = dS/dxdy$ is unity for a planar interface with normal z.

The one-way Rayleigh II integral [equation (B-2)] is valid for reconstruction using pressure $P_S^-(\mathbf{x}_g, \mathbf{x}_{s'}, \omega)$ recorded on a planar surface, but is presented as a good approximation for a nonplanar surface in Wiggins (1984). However, the approximation can be poor, even in the far field, given sufficient undulation (topography) in the surface.

B.3 Far-field Rayleigh II integral for inverse wavefield extrapolation

For inverse wavefield extrapolation, the backward propagating free-space Green's function is given by

$$\overleftarrow{G}_0^+(\mathbf{x}_g, \mathbf{x}_G, \omega) = \frac{e^{-i\omega\tau_{gG}(\mathbf{x}_g, \mathbf{x}_G)}}{4\pi|\mathbf{x}_g - \mathbf{x}_G|} = \frac{e^{-i\omega r_{gG}/c_0}}{4\pi r_{gG}} . \quad \text{(B-3)}$$

The normal derivative of equation (B-3) is

$$\frac{d\overleftarrow{G}_0^+(\mathbf{x}_g, \mathbf{x}_G, \omega)}{dn_g^+} = \left(-\frac{i\omega}{c_0} \frac{e^{-i\omega r_{gG}/c_0}}{4\pi r_{gG}} \frac{\partial r_{gG}}{\partial n_g^+} - \frac{1}{r_{gG}} \frac{e^{-i\omega r_{gG}/c_0}}{4\pi r_{gG}} \frac{\partial r_{gG}}{\partial n_g^+} \right). \quad \text{(B-4)}$$

Substitution of equation (B-4) into equation (B-2) yields

$$P_S^-(\mathbf{x}_G, \mathbf{x}_s, \omega) = -2 \int\!\!\int_{-\infty}^{+\infty} dx dy J_{Sxy} \left\{ \left(\frac{i\omega}{c_0} \frac{\partial r_{gG}}{\partial n_g^+} + \frac{1}{r_{gG}} \frac{\partial r_{gG}}{\partial n_g^+} \right) P_S^-(\mathbf{x}_g, \mathbf{x}_{s'}, \omega) \frac{e^{-i\omega r_{gG}/c_0}}{4\pi r_{gG}} \right\}_{S_g} . \text{(B-5)}$$

At the surface, r_{gG} is the ray direction (upward pointing). Hence $\partial r_{gG} / \partial n_g^+ = -\cos\theta_{gG}$, where θ_{gG} is the acute angle between the ray direction and the normal to the surface element. Substituting for the normal derivative and rearranging yields

$$P_S^-(\mathbf{x}_G, \mathbf{x}_s, \omega) = 2 \int\!\!\int_{-\infty}^{+\infty} dx dy J_{Sxy} \left\{ \frac{\cos\theta_{gG}}{c_0} \left(i\omega + \frac{c_0}{r_{gG}} \right) P_S^-(\mathbf{x}_g, \mathbf{x}_{s'}, \omega) \frac{e^{-i\omega r_{gG}/c_0}}{4\pi r_{gG}} \right\}_{S_g} . \quad \text{(B-6)}$$

Equation (B-6) [and equation (B-5)] can be divided into two parts based on the terms in the round brackets. The first part is known as the far-field response, while the second is known as the near field response. Using the Joe Keller rule of asymptotic expansions: "Three is as close to infinity as one-third is to zero" (Bleistein, 1999), the far-field dominates when $r > 3c_0/\omega \approx c_0/(2f)$. For example, at a frequency of f = 5 Hz in a media with a wavespeed c_0 = 1500 ms^{-1}, the far field dominates at distances greater than ~150 m. For non-recursive extrapolation, then, the near-field response can be ignored, and equation (B-6) can be approximated by

$$P_S^-(\mathbf{x}_G, \mathbf{x}_s, \omega) \cong 2\int_{-\infty}^{+\infty}\int dxdyJ_{Sxy}\left\{\frac{\cos\theta_{gG}}{c_0} i\omega P_S^-(\mathbf{x}_g, \mathbf{x}_{s'}, \omega)\frac{e^{-i\omega r_{gG}/c_0}}{4\pi r_{gG}}\right\}_{S_g}, \qquad \text{(B-7)}$$

otherwise known as the free-space far-field Rayleigh II integral.

Equation (B-7) states that the wavefield in the subsurface can be reconstructed by a weighted integral over the surface S_g of the time derivative of the recorded wavefield $i\omega P_S^-(\mathbf{x}_g, \mathbf{x}_{s'}, \omega)$. The weighting function includes the Green's function, which modifies the phase and amplitude of the recorded wavefield [see equation (B-3)], and a factor $\cos\theta_{gG}/c_0$ that transforms the surface element density from the recording surface to a unit sphere surrounding the reconstruction point.

The free-space far-field Rayleigh II integral [equation (B-7)] is an approximation for a planar or nonplanar surface, even in a constant velocity media. The complete Rayleigh II integral [equations (B-2)] and the complete free-space Rayleigh II integral [equations (B-5) and (B-6)] are also approximations for a non-planar surface. Can a better inverse wavefield extrapolator be determined—one that is more accurate for a non-planar surface but does not require two recorded wavefields?

B.4 Docherty's simplification of the Kirchhoff-Helmholtz integral using stationary phase

Docherty (1991) attempts to circumvent the apparent requirement of the Kirchhoff-Helmholtz integral [equation (B-1)] that two wavefields be recorded over the surface. He substitutes ray-theoretical approximations for $P_S^-(\mathbf{x}_g, \mathbf{x}_{s'}, \omega)$ and $\overleftarrow{G}_0^+(\mathbf{x}_g, \mathbf{x}_G, \omega)$ into equation (B-1), evaluates the leading-order approximation to the normal derivatives, uses stationary phase to equate the unknown normal derivative $\partial P_S^- / \partial n$ with the known normal derivative $\partial \overleftarrow{G}_0^+ / \partial n$, and then substitutes $P_S^-(\mathbf{x}_g, \mathbf{x}_{s'}, \omega)$ back in for its ray-theoretical approximation. The result is a leading-order ray-theoretical stationary-phase approximation to the Kirchhoff-Helmholtz integral [equation (B-1)] that, although approximate, should be better than the Rayleigh II integral and more correct for a nonplanar surface. The following discussion uses Docherty's derivation as a template, but is limited to free-space Green's functions.

B.5 The recorded trace as a superposition of time- and frequency-domain expressions for Kirchhoff-approximate prestack modeling

The upgoing scattered wavefield $P_S^-(\mathbf{x}_g, \mathbf{x}_{s'}, \omega)$ is obtained from the Fourier transform of the trace $p_S^-(\mathbf{x}_g, \mathbf{x}_{s'}, t)$ recorded at location $\mathbf{x}_g$ on the nonplanar non-reflecting[2] surface S_g given a source at location $\mathbf{x}_{s'}$ (not necessarily on the surface), i.e.

$$P_S^-(\mathbf{x}_g, \mathbf{x}_{s'}, \omega) = \int_{-\infty}^{\infty} p_S^-(\mathbf{x}_g, \mathbf{x}_{s'}, t) e^{i\omega t} dt \, . \tag{B-8}$$

Equation (B-8) follows the Fourier transform convention presented in Appendix A [see equation (A-10)]. The LHS can be expressed as an amplitude and phase lag, i.e. as

---

[2] Recall from Section 3.5 that the acoustic pressure recorded on a free surface is zero. Therefore, it is assumed that preprocessing converts the free-surface into a non-reflecting surface (see Hanitzsch, 1995).

$$P_S^-(\mathbf{x}_g,\mathbf{x}_{s'},\omega) = \left|P_S^-(\mathbf{x}_g,\mathbf{x}_{s'},\omega)\right| e^{i\phi(\mathbf{x}_g,\mathbf{x}_{s'},\omega)}. \tag{B-9}$$

The recorded trace in the time domain, $p_S^-(\mathbf{x}_g,\mathbf{x}_{s'},t)$ can be considered as a superposition of reflected energy from all subsurface reflector segments. Assume that a given reflecting surface is described by the equation $\Sigma_R(\mathbf{x}_{ij}) = 0$. Given a source function $s_\rho(t)$, the trace at time *t* can be represented as

$$p_S^-(\mathbf{x}_g,\mathbf{x}_{s'},t) = \sum_{i=1}^{\infty}\sum_{j=1}^{\infty} \beta_{\theta\chi}(\mathbf{x}_{ij},\mathbf{x}_s) A_{gs'}(\mathbf{x}_g,\mathbf{x}_{ij},\mathbf{x}_{s'}) \delta\big(t-\tau_{gs'}(\mathbf{x}_g,\mathbf{x}_{ij},\mathbf{x}_{s'})\big) * s'_\rho(t), \tag{B-10}$$

where the subsurface position $\mathbf{x}_{ij}$ representing a reflecting segment (subscript *j*) on a particular isochron surface (subscript *i*). The amplitude $A_{gs'}(\mathbf{x}_g,\mathbf{x}_{ij},\mathbf{x}_{s'})$ is the product of the divergences along the raypaths from source to reflector and reflector to receiver, $\tau_{gs'}(\mathbf{x}_g,\mathbf{x}_{ij},\mathbf{x}_{s'})$ is the corresponding traveltime that defines the isochron, and $\beta_{\theta\chi}(\mathbf{x}_{ij},\mathbf{x}_s) = R_\theta(\mathbf{x}_{ij},\mathbf{x}_s)\gamma_R(\mathbf{x}_{ij})\cos\chi$ is the weighted reflectivity function, which may well be zero at $\mathbf{x}_{ij}$'s where there is no reflector. The angle χ is the acute angle between the isochron normal and the reflector normal [see Appendix C, in particular discussions following equation (C-12) and prior to equation (C-17)]. The size of each segment must agree with the isochron-stack operator derived in Appendix C [see discussion following equation (C-16)]. Then, equation (B-10) is the time domain equivalent of the ray-theoretical Kirchhoff-approximate prestack modeling formula presented in Sections 3.4 and 3.5 [equations (3.17) and (3.20)]. The time derivative of the source function, as indicated by $s'_\rho(t)$, is required for exact equivalence with the modeling formula.

Using equations (A.10) and (A.15) and (A.32), the Fourier transform of equation (B-10) is

$$P_S^-(\mathbf{x}_g,\mathbf{x}_{s'},\omega) = \sum_{i=1}^{\infty}\sum_{j=1}^{\infty} \beta_{\theta\chi}(\mathbf{x}_{ij},\mathbf{x}_s) A_{gs'}(\mathbf{x}_g,\mathbf{x}_{ij},\mathbf{x}_{s'}) \Big[(-i\omega) S_\rho(\omega) e^{i\omega\tau_{gs'}(\mathbf{x}_g,\mathbf{x}_{ij},\mathbf{x}_{s'})}\Big]. \tag{B-11}$$

Thus the wavefield in the frequency domain preserves the traveltime delays of all the reflected wavefields[3], as might be expected for a linear operator such as the Fourier transform (for further discussion, see Appendix A). It is often useful to imagine the wavefield in the frequency domain as a single propagating impulse for a reflector segment of interest, with the phase representing the traveltime. Then the response from reflector segments can be superposed in whatever manner is appropriate for the problem at hand.

B.6 The Kirchhoff-Helmholtz equation in terms of free-space generalized Green's functions

Equations (B-9) and (B-11) can be compared to equation (9) of Docherty (1991), re-expressed here as

$$P_S^-(\mathbf{x}_g, \mathbf{x}_{s'}, \omega) = P_{gs'}(\mathbf{x}_g, \mathbf{x}_{s'}) e^{i\omega\tau_{gs'}(\mathbf{x}_g, \mathbf{x}_{s'})} \tag{B-12}$$

Docherty assumes an impulsive source [see his equations (2) and (5)]. Thus the phase and amplitude of the source function are not included in the RHS of equation (B-12). Hence, Docherty's amplitude $P_{gs'}$ is independent of frequency. Instead, I assume a bandlimited source and data that are deconvolved to zero-phase. Thus equation (B-12) can be expressed in the form of equation (B-11) as follows:

$$P_S^-(\mathbf{x}_g, \mathbf{x}_{s'}, \omega) = (-i\omega)\left|S_\rho(\omega)\right| \beta_{\theta\chi}(\mathbf{x}_R, \mathbf{x}_s) A_{gs'}(\mathbf{x}_g, \mathbf{x}_{s'}) e^{i\omega\tau_{gs'}(\mathbf{x}_g, \mathbf{x}_{s'})}, \tag{B-13}$$

where $(-i\omega)\left|S_\rho(\omega)\right|$ is the time derivative of a source amplitude, $\beta_{\theta\chi}(\mathbf{x}_R, \mathbf{x}_{s'})$ is the weighted reflectivity function, and $A_{gs'}(\mathbf{x}_g, \mathbf{x}_{s'}) e^{i\omega\tau_{gs'}(\mathbf{x}_g, \mathbf{x}_{s'})}$ represents a 'generalized' forward propagating ray-theoretical Green's function.

---

[3] This is the fundamental principal underlying *f-xy* decon and trace interpolation (e.g. Porsani, 1999).

The ‘generalized’ Green’s function in equation (B-13) is similar in form to the one-way ray-theoretical Green’s function given by equation (2.34). More correctly, the RHS of equation (B-13) can be thought of as an infinite weighted sum of generalized Green’s functions [see equation (B-11)], each arising from an image source at the generalized location $\mathbf{x}_{s'}$, then propagating through a reflector segment at unknown location $\mathbf{x}_R$ to the receiver location $\mathbf{x}_g$. Thus the phase $\phi(\mathbf{x}_g,\mathbf{x}_{s'},\omega)=\omega\tau_{gs'}(\mathbf{x}_g,\mathbf{x}_{s'},\omega)$ of the wavefield contains information from all reflector segments and hence from all directions. It stands to reason, then, that the normal derivative of the wavefield on the surface cannot be determined from recordings of the wavefield alone.

Equation (B-13) can be restricted to constant wavespeed media by inserting a ‘generalized’ one-way free-space Greens’ function [see equation (2.17)] for $A_{gs'}(\mathbf{x}_g,\mathbf{x}_{s'})e^{i\omega\tau_{gs'}(\mathbf{x}_g,\mathbf{x}_{s'})}$, yielding

$$P_S^-(\mathbf{x}_g,\mathbf{x}_{s'},\omega)=i\omega\left|S_\rho(\omega)\right|\beta_{\theta\chi}(\mathbf{x}_R,\mathbf{x}_s)\frac{e^{i\omega\tau_{gs'}(\mathbf{x}_g,\mathbf{x}_{s'})}}{4\pi\left|\mathbf{x}_g-x_{s'}\right|}. \tag{B-14}$$

By inserting the ‘generalized’ distance $r_{gs'}=\left|\mathbf{x}_g-\mathbf{x}_{s'}\right|$, equation (B-14) can be re-expressed as

$$P_S^-(\mathbf{x}_g,\mathbf{x}_{s'},\omega)=i\omega\left|S_\rho(\omega)\right|\beta_{\theta\chi}(\mathbf{x}_R,\mathbf{x}_s)\frac{e^{i\omega r_{gs'}/c}}{4\pi r_{gs'}} \tag{B-15}$$

Even though equation (B-15) is expressed in terms of a ‘generalized’ free-space Green’s function, we can take its the normal derivative, yielding

$$\frac{dP_S^-(\mathbf{x}_g,\mathbf{x}_{s'},\omega)}{dn_g^-}=i\omega\left|S_\rho(\omega)\right|\beta_{\theta\chi}(\mathbf{x}_R,\mathbf{x}_s)\left(\frac{i\omega}{c}\frac{e^{i\omega r_{gs'}/c}}{4\pi r_{gs'}}\frac{\partial r_{gs'}}{\partial n_g^-}-\frac{1}{r_{gs'}}\frac{e^{i\omega r_{gs'}/c}}{4\pi r_{gs'}}\frac{\partial r_{gs'}}{\partial n_g^-}\right). \tag{B-16}$$

Of course, the doubly infinite summation is implied in equations (B-15) and (B-16) so care must be taken to correctly interpret the ‘generalized’ normal derivative $\partial r_{gs'}/\partial n_g^-$.

The backward propagating free-space Green's function is given by equation (B-3), repeated here as

$$\overleftarrow{G}_0^{+}(\mathbf{x}_g,\mathbf{x}_G,\omega)=\frac{e^{-i\omega r_{gG}/c_0}}{4\pi r_{gG}}. \tag{B-17}$$

The normal derivative of equation (B-17) is

$$\frac{d\overleftarrow{G}_0^{+}(\mathbf{x}_g,\mathbf{x}_G,\omega)}{dn_g^{+}}=\left(-\frac{i\omega}{c_0}\frac{e^{-i\omega r_{gG}/c_0}}{4\pi r_{gG}}\frac{\partial r_{gG}}{\partial n_g^{-}}-\frac{1}{r_{gG}}\frac{e^{-i\omega r_{gG}/c_0}}{4\pi r_{gG}}\frac{\partial r_{gG}}{\partial n_g^{-}}\right). \tag{B-18}$$

In keeping with equation (B-1), the normal $\mathbf{n}_g^{-}$ in equations (B-16) and (B-18) is directed upwards.

Inserting equations (B-15)-(B-18) into equation (B-1) yields

$$\begin{aligned}P_S^{-}(\mathbf{x}_G,\mathbf{x}_s,\omega)=\int_{S_g}dS\Bigg\{&\frac{e^{-i\omega r_{gG}/c_0}}{4\pi r_{gG}}i\omega\left|S_\rho(\omega)\right|\beta_{\theta\chi}(\mathbf{x}_R,\mathbf{x}_s)\left(\frac{i\omega}{c}\frac{e^{i\omega r_{gs'}/c}}{4\pi r_{gs'}}\frac{\partial r_{gs'}}{\partial n_g^{-}}-\frac{1}{r_{gs'}}\frac{e^{i\omega r_{gs'}/c}}{4\pi r_{gs'}}\frac{\partial r_{gs'}}{\partial n_g^{-}}\right)\\&-i\omega\left|S_\rho(\omega)\right|\beta_{\theta\chi}(\mathbf{x}_R,\mathbf{x}_{s'})\frac{e^{i\omega r_{gs'}/c}}{4\pi r_{gs'}}\left(-\frac{i\omega}{c_0}\frac{e^{-i\omega r_{gG}/c_0}}{4\pi r_{gG}}\frac{\partial r_{gG}}{\partial n_g^{-}}-\frac{1}{r_{gG}}\frac{e^{-i\omega r_{gG}/c_0}}{4\pi r_{gG}}\frac{\partial r_{gG}}{\partial n_g^{-}}\right)\Bigg\}.\end{aligned} \tag{B-19}$$

B.7 Simplifying the generalized free-space Kirchhoff-Helmholtz equation

Rearranging equation (B-19), collecting like terms, and substituting $P_S^{-}(\mathbf{x}_g,\mathbf{x}_{s'},\omega)$ for terms equivalent to the RHS of equation (B-15) yields

$$\begin{aligned}P_S^{-}(\mathbf{x}_G,\mathbf{x}_s,\omega)=\int_{S_g}dS\Bigg\{&\left(\frac{i\omega}{c}\frac{\partial r_{gs'}}{\partial n_g^{-}}+\frac{i\omega}{c_0}\frac{\partial r_{gG}}{\partial n_g^{-}}\right)P_S^{-}(\mathbf{x}_g,\mathbf{x}_{s'},\omega)\frac{e^{-i\omega r_{gG}/c_0}}{4\pi r_{gG}}\\&+\left(\frac{1}{r_{gG}}\frac{\partial r_{gG}}{\partial n_g^{-}}-\frac{1}{r_{gs'}}\frac{\partial r_{gs'}}{\partial n_g^{-}}\right)P_S^{-}(\mathbf{x}_g,\mathbf{x}_{s'},\omega)\frac{e^{-i\omega r_{gG}/c_0}}{4\pi r_{gG}}\Bigg\}\end{aligned} \tag{B-20}$$

The first and second terms in the curly brackets on the RHS of equation (B-20) are similar to the far- and near-field terms of the Rayleigh II integral [equation (B-5)], respectively. As discussed previously, the near-field term can be ignored in most seismic applications (note that the two near-field terms are opposite in sign, which reduces the near-field effect). Then, the unknown true wavespeed c is assumed to be identical to the reference wavespeed c_0. If they are not, phase and amplitude errors will be introduced. As explained in Section 3.2, these errors could (in theory) be compensated for by the volume scattering integral and will not be discussed further here. Next, I apply the concept of stationary-phase to simplify the far-field term, extracted from equation (B-20) as

$$P_S^-(\mathbf{x}_G, \mathbf{x}_s, \omega) = \int_{S_g} dS \left\{ \left(\frac{1}{c_0} \frac{\partial r_{gs'}}{\partial n} + \frac{1}{c_0} \frac{\partial r_{gG}}{\partial n} \right) i\omega P_S^-(\mathbf{x}_g, \mathbf{x}_{s'}, \omega) \frac{e^{-i\omega r_{gG}/c_0}}{4\pi r_{gG}} \right\}. \qquad \text{(B-21)}$$

Similar to the derivation for the Rayleigh II integral, the normal derivatives can be expressed as cosines between the surface normal and the ray direction, i.e. $\partial r_{gG} \big/ \partial n_g^- = \cos\theta_{gG}$ and $\partial r_{gs'} \big/ \partial n_g^- = \cos\theta_{gs'}$. A 2D geometric argument suggests that the concept of stationary phase can be applied so that $\partial r_{gs'} \big/ \partial n_g^- \approx \partial r_{gG} \big/ \partial n_g^- = \cos\theta_{gG}$. Then equation (B-21) simplifies to equation (B-7)—the far-field version of the Rayleigh II integral.

The geometric argument is as follows. The receivers are distributed over an arbitrary nonplanar surface S_g at locations $\mathbf{x}_g$, as shown in Figure B-1. The wavefield at a given receiver is a superposition of upgoing wavefields from numerous image sources, as indicated by the upward rays converging on receiver g_3. In fact, the surface location of the source and corresponding subsurface locations of image sources are not relevant—the recorded wavefield can be inverse extrapolated given any number of unknown sources. At the reconstruction position $\mathbf{x}_G$, however, we are interested only in the part of the wavefield that propagates upward through $\mathbf{x}_G$ to the surface, as indicated by the upward rays converging at $\mathbf{x}_G$ and arriving at the surface. This is the wavefield that would be recorded by a receiver in the subsurface at $\mathbf{x}_G$. In Figure B-2, the same reconstruction point is shown along with the ray representation of the Green's function. At the surface, the angle between the ray and the surface normal can be used to define the normal derivative $\partial r_{gG} \big/ \partial n_g^- = \cos\theta_{gG}$.

Comparing Figures B-1 and B-2, it is obvious that the raypaths above $\mathbf{x}_G$ are identical. Over each raypath, the phase of the Green's function will equal the difference in the

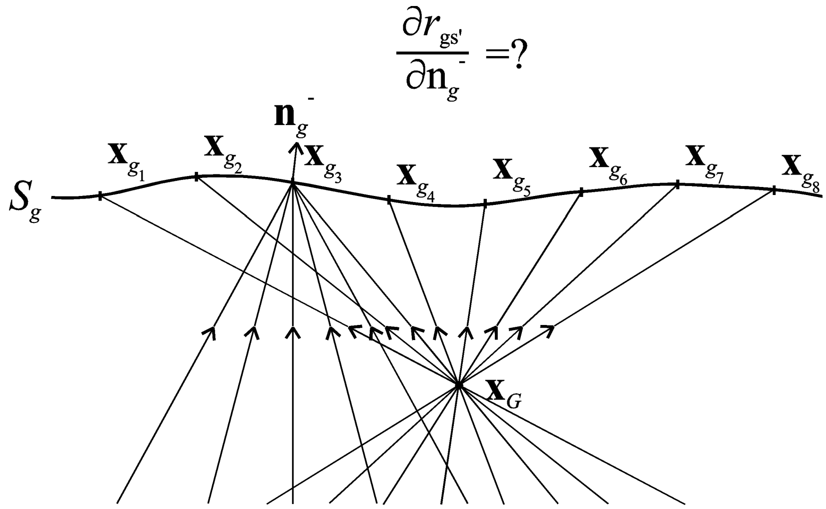

Figure B.1: Selected rays from upward propagating wavefield $P_S^-(\mathbf{x}_g, \mathbf{x}_{s'}, \omega)$.

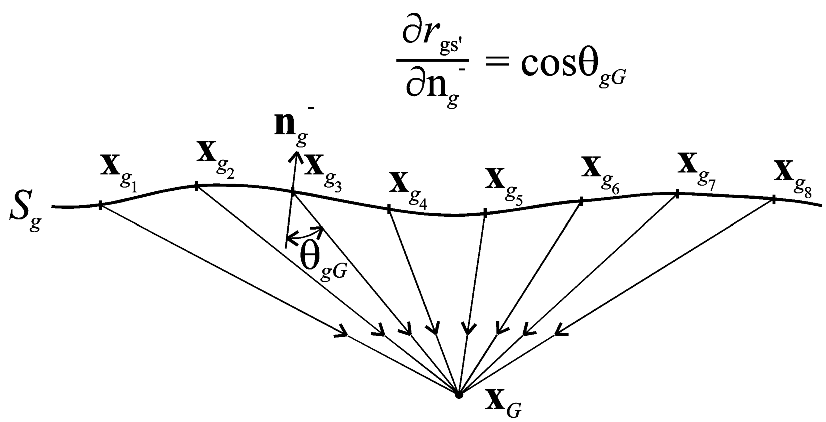

Figure B.2. Selected rays from backward propagating Green's function $\overleftarrow{G}_0^+(\mathbf{x}_g, \mathbf{x}_G, \omega)$.

phase of the wavefield. At the reconstruction point, the main contribution to the reconstructed wavefield will come from those portions of the wavefield that are in phase. At the surface, the corresponding portions will be defined where the change in phase of the wavefield equals the negative of the change in phase of the Green's function, i.e. where the phase function $\left(i\omega r_{gs'}/c_0 - i\omega r_{gG}/c_0\right)$ is stationary. For this to be true, the wavefield must be propagating exactly in the opposite direction as the Green's function—at least for the portions that will reconstruct. Hence, the normal derivative of the wavefield can be approximated by the normal derivative of the Green's function, i.e. $\partial r_{gs'}\big/\partial n_g^- \approx \partial r_{gG}\big/\partial n_g^-$. Both normal derivatives are now equal to $\cos\theta_{gG}$ (evaluated for a nonplanar surface) and equation (B-21) simplifies to

$$P_S^-(\mathbf{x}_G,\mathbf{x}_s,\omega) \cong 2\int_{S_g} dS\,\frac{\cos\theta_{gG}}{c_0}\,i\omega P_S^-(\mathbf{x}_g,\mathbf{x}_{s'},\omega)\,\frac{e^{-i\omega r_{gG}/c_0}}{4\pi r_{gG}}, \qquad \text{(B-22)}$$

which is identical to the free-space far-field Rayleigh II integral for a planar interface [equation (B-7)].

At the stationary point (i.e. close to specular reflection) $\partial r_{gs'}\big/\partial n_g^- \approx \partial r_{gG}\big/\partial n_g^-$ and $r_{gs'} \approx 2r_{gG}$. A slightly more accurate approach includes these approximations instead of ignoring the near field term. Then, equation (B-20) reduces to

$$P_S^-(\mathbf{x}_G,\mathbf{x}_s,\omega) \cong 2\int_{S_g} dS\left\{\frac{\cos\theta_{gG}}{c_0}\,i\omega + \frac{1}{2r_{gG}}\right\}P_S^-(\mathbf{x}_g,\mathbf{x}_{s'},\omega)\,\frac{e^{-i\omega r_{gG}/c_0}}{4\pi r_{gG}}. \qquad \text{(B-23)}$$

Equation (B-23) may improve accuracy in the near field, but fails to address the larger approximation introduced by equating the normal derivatives $\partial r_{gs'}\big/\partial n_g^- \approx \partial r_{gG}\big/\partial n_g^-$. One avenue of investigation, yet to be pursued, is to look for an approximation to the unknown normal derivative $\partial r_{gs'}\big/\partial n_g^-$ using a combination of time derivatives and spatial derivatives over the nonplanar interface.

B.8 Summary

By neglecting the near-field terms and using a geometric approach to stationary phase, I have shown that the free-space Kirchhoff-Helmholtz integral for a non-planar surface [equation (B-20)] simplifies to the far-field Rayleigh II integral [equation (B-22)]—the same integral obtained using free-space Green's functions and the method of images for a planar surface [equation (B-7)]. Tests on synthetic data (not presented in this dissertation) clearly show that the simplified equations yield approximate results, as expected. At present, there appears to be no better solution, supporting the conclusion reached in Section 2.9.

APPENDIX C: ISOCHRON STACK FROM KIRCHHOFF-APPROXIMATE MODELING: AN ALTERNATE DERIVATION

C.1 Introduction

Jaramillo (1999) and Jaramillo and Bleistein (1999) derive the isochron stack from the simplified form of the Kirchhoff-approximate modeling formula [equation (3.20)], as given by

$$P_{\Sigma_R}^{-}(\xi,\omega) \cong i\omega S_\rho(\omega)\int_{\Sigma_R} d\Sigma_R R_\theta(\mathbf{x}_R,\mathbf{x}_s)A_{sg}(\mathbf{x}_R,\xi)\left(\nabla_{\mathbf{x}_R}\phi_\tau(\mathbf{x}_R,\xi)\cdot\mathbf{n}_R^{-}\right)e^{i\omega\phi_\tau(\mathbf{x}_R,\xi)}. \qquad \text{(C-1)}$$

(3.0.34)

The purpose of this appendix is to present a derivation that does not require the stationary phase approximations used in the cited derivations. However, it still requires a leading order approximation to integration by parts. As an aid to cross-referencing the derivations, the second equation number is the corresponding equation in Jaramillo (1999). Slight differences in notation are, in general, self-explanatory. The notation adopted here will not be described in detail, as it follows the notation introduced in the dissertation.

C.2 Meaning of the phase (traveltime) function and its normal derivative

First, the meaning of $\phi_\tau(\mathbf{x}_R,\xi)$ and $\nabla_{\mathbf{x}_R}\phi_\tau(\mathbf{x}_R,\xi)\cdot\mathbf{n}_R^{-}$ need to be examined. From the expanded form of the Kirchhoff-approximate modeling formula [equation (3.17)],

$$\begin{aligned}P_{s\Sigma_R}^{-}(\mathbf{x}_g,\mathbf{x}_s,\omega) &\cong i\omega S_\rho(\omega)\int_{\Sigma_R} d\Sigma_R A_s(\mathbf{x}_R,\mathbf{x}_s)R_\theta(\mathbf{x}_R,\mathbf{x}_s)A_g(\mathbf{x}_R,\mathbf{x}_g)\\ &\quad\times\left(\nabla_{\mathbf{x}_R}\tau_{Rs}(\mathbf{x}_R,\mathbf{x}_s)\cdot\mathbf{n}_R^{-}+\nabla_{\mathbf{x}_R}\tau_{Rg}(\mathbf{x}_R,\mathbf{x}_g)\cdot\mathbf{n}_R^{-}\right)e^{i\omega\left(\tau_{Rs}(\mathbf{x}_R,\mathbf{x}_s)+\tau_{Rg}(\mathbf{x}_R,\mathbf{x}_g)\right)}, \qquad \text{(C-2)}\end{aligned}$$

it is straightforward to see that $\phi_\tau(\mathbf{x}_R,\xi)$ is a scalar function in space equal to the total traveltime $\tau_{Rs}(\mathbf{x}_R,\mathbf{x}_s)+\tau_{Rg}(\mathbf{x}_R,\mathbf{x}_g)$ and that $\nabla_{\mathbf{x}_R}\phi_\tau(\mathbf{x}_R,\xi)\cdot\mathbf{n}_R^{-}$ is a shorthand for the obliquity factor $\left(\cos\theta_s + \cos\theta_g\right)/c_0(\mathbf{x}_R)$, where θ_s and θ_g are the obtuse angles between the upward reflector normal $\mathbf{n}_R^-$ and ray direction from source and receiver, respectively. The geometry is illustrated in Figure C.1.

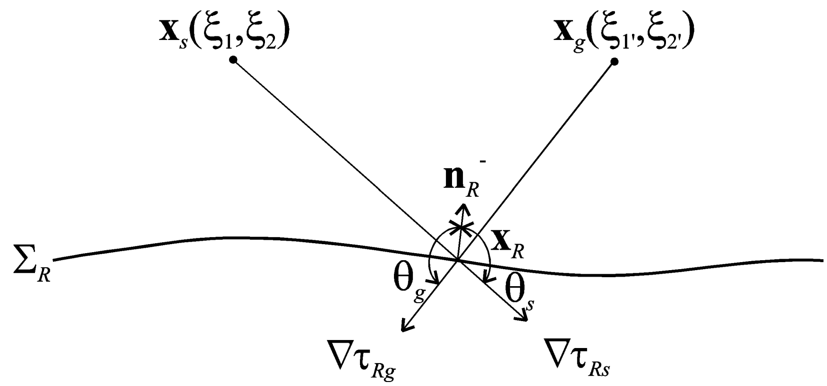

Figure C.1. Geometry for equation (C-2). Angles are referenced to upward reflector normal $\mathbf{n}_R^-$.

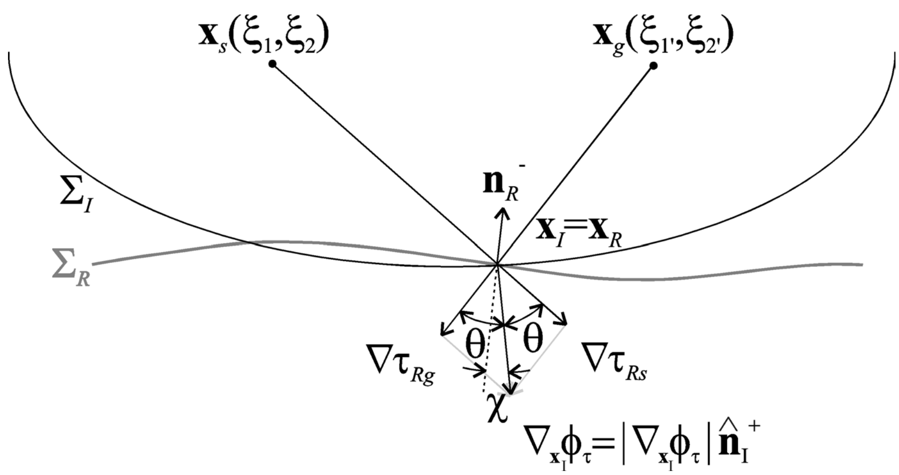

Figure C.2. Geometry for equation (C-1) and equations (C-3)-(C-13). Angles are referenced to downward isochron normal $\mathbf{n}_I^+$.

If the total traveltime is kept constant, the scalar function $\phi_\tau(\mathbf{x}_I,\xi)$ defines a set of points $\mathbf{x}_I$ on the isochron surface Σ_I. Thus $\nabla_{\mathbf{x}_I}\phi_\tau(\mathbf{x}_I,\xi) = \left|\nabla_{\mathbf{x}_I}\phi_\tau(\mathbf{x}_I,\xi)\right|\mathbf{n}_I^+$, where $\mathbf{n}_I^+$ is the downward (outward) pointing normal to the isochron. The magnitude of the traveltime gradient is defined as follows:

$$\left|\nabla_{\mathbf{x}_I}\phi_\tau\right|^2 = \left|\nabla_{\mathbf{x}_I}\tau_{Is} + \nabla_{\mathbf{x}_I}\tau_{Ig}\right|^2$$

$$= \left|\nabla_{\mathbf{x}_I}\tau_{Is}\right|^2 + \left|\nabla_{\mathbf{x}_I}\tau_{Ig}\right|^2 + 2\nabla_{\mathbf{x}_I}\tau_{Is}\cdot\nabla_{\mathbf{x}_I}\tau_{Ig}$$

$$= \frac{2}{c_0^2(\mathbf{x}_I)} + \frac{2\cos 2\theta}{c_0^2(\mathbf{x}_I)}$$

$$= \frac{4\cos^2\theta}{c_0^2(\mathbf{x}_I)}, \tag{C-3}$$

where θ (no subscript) is half the angle between the downward pointing slowness vectors $\nabla_{\mathbf{x}_I}\tau_{Ig}$ and $\nabla_{\mathbf{x}_I}\tau_{Is}$, as illustrated in Figure C.2. Where the reflecting and isochron surfaces intersect, $\mathbf{x}_R = \mathbf{x}_I$. Hence

$$\nabla_{\mathbf{x}_R}\phi_\tau(\mathbf{x}_R,\xi)\cdot\hat{\mathbf{n}}_R^+ = \nabla_{\mathbf{x}_I}\phi_\tau(\mathbf{x}_I,\xi)\cdot\hat{\mathbf{n}}_R^-$$

$$= \left|\nabla_{\mathbf{x}_I}\phi_\tau(\mathbf{x}_I,\xi)\right|\left(\mathbf{n}_I^+\cdot\mathbf{n}_R^-\right)$$

$$= \frac{2\cos\theta}{c_0(\mathbf{x}_I)}\left(\mathbf{n}_I^+\cdot\mathbf{n}_R^-\right)$$

$$= \frac{2\cos\theta}{c_0(\mathbf{x}_I)}\cos\chi, \tag{C-4}$$

where χ is the acute angle between the downward reflector normal and downward isochron normal. The stationary point for either of equations (C-1) or (C-2) occurs at the ordinary ray (see Docherty, 1991), which can best be defined as the case where $\mathbf{n}_I^+$ and $\mathbf{n}_R^-$ point in exactly opposite directions. At a stationary point, then, the reflecting and isochron surfaces are tangent to each other.

In deriving equation (C-4), we seem to have lost the original meaning of the shorthand notation $\nabla_{\mathbf{x}_R}\phi(\mathbf{x}_R,\xi)\cdot\mathbf{n}_R^-$ as the obliquity factor $\left(\cos\theta_s + \cos\theta_g\right)/c_0(\mathbf{x}_R)$, replaced instead by $2\cos\theta\cos\chi/c_0(\mathbf{x}_I)$. An intuitive explanation is provided by adapting a method proposed by Kuhn and Alhilali (1977) for deriving a modified obliquity factor.

The elementary aperture of the reflecting surface is reoriented in such a way that it is aligned with the isochron normal $\mathbf{n}_I^+ = \nabla_{\mathbf{x}_I}\phi \big/ \left|\nabla_{\mathbf{x}_I}\phi\right|$. The obliquity factor $\left(\cos\theta_s + \cos\theta_g\right)\big/ c_0(\mathbf{x}_\Sigma)$ can now be replaced with $-2\cos\theta / c_0(\mathbf{x}_\Sigma)$, but the effective area of the aperture[4] has been changed from dS to $dS\cos\chi$, where $\cos\chi = -\left(\mathbf{n}_I^+ \cdot \mathbf{n}_R^-\right) = -\nabla_{\mathbf{x}_I}\phi(\mathbf{x}_I, \xi)\cdot \mathbf{n}_R^- \big/ \left|\nabla_{\mathbf{x}_I}\phi(\mathbf{x}_I, \xi)\right|$. Since $\left|\nabla_{\mathbf{x}_I}\phi(\mathbf{x}_I, \xi)\right| = 2\cos\theta / c_0(\mathbf{x}_I)$, the modified obliquity factor can be simply expressed as $2\cos\theta\cos\chi / c_0(\mathbf{x}_I)$, or one of the other expressions given in equation (C-4).

C.3 From reflector surface integral to volume integral to isochron surface integral

By assuming that a given reflecting surface is described by the equation $\Sigma_R(\mathbf{x}) = 0$, the singular function $\gamma_R(\mathbf{x}) = \delta(\Sigma_R(\mathbf{x}))\left|\Sigma_R(\mathbf{x})\right|$ can be used to recast the surface integral given by equation (C-1) as a volume integral, yielding

$$P_{s\Sigma_R}^-(\xi,\omega) \cong i\omega S_\rho(\omega)\int_V dV R_\theta(\mathbf{x},\mathbf{x}_s)\gamma_R(\mathbf{x})A_{sg}(\mathbf{x},\xi)\left(\nabla_{\mathbf{x}}\phi_\tau(\mathbf{x},\xi)\cdot\mathbf{n}_R^-\right)e^{i\omega\phi_\tau(\mathbf{x},\xi)}. \qquad \text{(C-5)}$$

(3.0.35)

In keeping with equation (C-1), the upward normal $\mathbf{n}_R^-$ is perpendicular to the reflecting surface defined by the singular function.

The inverse Fourier transform from frequency (ω) to time (t) of equation (C-5) is

$$p_{s\Sigma_R}^-(\xi,t) \cong -\int_V dV R_\theta(\mathbf{x},\mathbf{x}_s)\gamma_R(\mathbf{x})A_{sg}(\mathbf{x},\xi)\left(\nabla_{\mathbf{x}}\phi_\tau(\mathbf{x},\xi)\cdot\mathbf{n}_R^-\right)\delta'\left(t-\phi_\tau(\mathbf{x},\xi)\right) * s_\rho(t), \quad \text{(C-6)}$$

(3.0.36)

---

[4] Kuhn and Alhilali (1977) use the angle χ to represent 2θ, as used here, and β to represent χ.

where $s_\rho(t)$ is the source wavelet. In equation (C-6), the change of sign and the derivative with respect to time of the delta function comes from the term $i\omega e^{i\omega\phi(\mathbf{x},\xi)}$ in equation (C-5).

The objective is to turn the volume integral in equation (C-6) into an integral over the isochron surface Σ_I. Similar to the reflecting surface, the isochron surface can be thought of as a singular function in space $\delta(t-\phi_\tau(\mathbf{x},\xi))$. Hence the first derivative of the delta function can be thought of as a derivative with respect to the scalar function $\phi_\tau(\mathbf{x},\xi)$, i.e. $\delta'(t-\phi_\tau) = \partial\delta(t-\phi_\tau)/\partial\phi_\tau$.

In equation (C-6), the only contribution to the volume integral comes from those points that lie at the intersection between the isochron surface and the reflecting surface. Following Jaramillo and Bleistein (1999), the volume integral can be re-expressed using the change of coordinates

$$dV = d\Sigma_I dn_I^+ = d\Sigma_I d\phi_\tau / \left|\nabla_{\mathbf{x}}\phi_\tau\right| . \tag{C-7}$$

With the change of coordinates, the delta function derivative, and the result from equation (C-4) that $\nabla_{\mathbf{x}}\phi_\tau(\mathbf{x},\xi)\cdot\mathbf{n}_R^- = \left|\nabla_{\mathbf{x}}\phi_\tau(\mathbf{x},\xi)\right|\left(\mathbf{n}_I^+\cdot\mathbf{n}_R^-\right)$, equation (C-6) becomes

$$p_{s\Sigma_R}^-(\xi,t) \cong -\int_V d\Sigma_I d\phi_\tau R_\theta(\mathbf{x},\mathbf{x}_s)\gamma_R(\mathbf{x})A_{sg}(\mathbf{x},\xi)\left(\mathbf{n}_I^+\cdot\mathbf{n}_R^-\right)\frac{\partial\delta\left(t-\phi_\tau(\mathbf{x},\xi)\right)}{\partial\phi_\tau} * s_\rho(t) . \tag{C-8}$$

Integrating equation (C-8) by parts once in ϕ_τ and keeping only the most singular term yields

$$p_{s\Sigma_R}^-(\xi,t) \cong \int_V d\Sigma_I d\phi_\tau R_\theta(\mathbf{x},\mathbf{x}_s)\frac{\partial\gamma_R(\mathbf{x})}{\partial\phi_\tau}A_{sg}(\mathbf{x},\xi)\left(\mathbf{n}_I^+\cdot\mathbf{n}_R^-\right)\delta\left(t-\phi_\tau(\mathbf{x},\xi)\right) * s_\rho(t) . \tag{C-9}$$

The derivative of the singular function of the reflecting surface can be re-expressed as

$$\frac{d\gamma_R(\mathbf{x})}{d\phi_\tau} = \frac{\partial\gamma_R(\mathbf{x})/\partial n_R^-}{\partial\phi_\tau/\partial n_R^-} = \frac{\partial\gamma_R(\mathbf{x})/\partial n_R^-}{\nabla_\mathbf{x}\phi(\mathbf{x},\xi)\cdot\mathbf{n}_R^-} = \frac{\partial\gamma_R(\mathbf{x})/\partial n_R^-}{\left|\nabla_\mathbf{x}\phi(\mathbf{x},\xi)\right|\left(\mathbf{n}_I^+\cdot\mathbf{n}_R^-\right)}. \tag{C-10}$$

(modified 3.0.12)

With this substitution, the dot products of the normals cancel, and equation (C-9) becomes

$$p_{s\Sigma_R}^-(\xi,t) \cong \int_V d\Sigma_I d\phi_\tau R_\theta(\mathbf{x},\mathbf{x}_s)\frac{\partial\gamma_R(\mathbf{x})}{\partial n_R^-}\frac{A_{sg}(\mathbf{x},\xi)}{\left|\nabla_\mathbf{x}\phi_\tau(\mathbf{x},\xi)\right|}\delta\big(t-\phi_\tau(\mathbf{x},\xi)\big)*s_\rho(t). \tag{C-11}$$

Integration with respect to ϕ_τ reduces to a simple integration over the isochron through the application of the explicit delta function, yielding

$$p_{s\Sigma_R}^-(\xi,t) \cong \int_{\Sigma_I} d\Sigma_I R_\theta(\mathbf{x}_I,\mathbf{x}_s)\frac{\partial\gamma_R(\mathbf{x}_I)}{\partial n_R^-}\left.\frac{A_{sg}(\mathbf{x}_I,\xi)}{\left|\nabla_{\mathbf{x}_I}\phi_\tau(\mathbf{x}_I,\xi)\right|}\right|_{t=\phi_\tau} *s_\rho(t), \tag{C-12}$$

(modified 3.0.39)

or, by substituting the reflectivity function $\beta_\theta(\mathbf{x}_I,\mathbf{x}_s)$ for $R_\theta(\mathbf{x}_I,\mathbf{x}_s)\gamma_R(\mathbf{x}_I)$ (Bleistein, 1987),

$$p_{s\Sigma_R}^-(\xi,t) \cong \int_{\Sigma_I} d\Sigma_I \frac{A_{sg}(\mathbf{x}_I,\xi)}{\left|\nabla_{\mathbf{x}_I}\phi_\tau(\mathbf{x}_I,\xi)\right|}\left.\frac{\partial\beta_\theta(\mathbf{x}_I)}{\partial n_R^-}\right|_{t=\phi_\tau} *s_\rho(t). \tag{C-13}$$

(modified 3.0.40)

Equation (C-13) is essentially equation (3.0.40) of Jaramillo (1999) and equation (38) of Jaramillo and Bleistein (1999), but has been derived without the stationary phase approximations. However, the leading order approximation to the integration by parts is still required. The angle-dependent reflectivity function $R_\theta(\mathbf{x},\mathbf{x}_s)$ in equation (C-2) is the geometrical-optics reflection coefficient, which provides an accurate representation of the reflected wavefield, up to and beyond the critical angle of reflection (Burridge et al., 1998)[5].

Equation (C-9) above can be compared to equation (36) of Jaramillo and Bleistein (1999), suggesting that there are two typographic errors in the latter: first, the derivative $\partial\gamma(\mathbf{x})/\partial n_R$ should be $\partial\gamma(\mathbf{x})/\partial\phi$; and second, the equation should be negative (from the integration by parts). Equation (C-10) then gives the term $1/|\nabla_{\mathbf{x}}\phi|$ and the sign change (from $\mathbf{n}_I \cdot \mathbf{n}_R = -1$, assuming stationarity) as required by Jaramillo and Bleistein's equations (37) and (38), both of which are correct.

C.4 An exact equivalent to the Kirchhoff-approximate modeling formula

The derivation leading to equation (C-13) still requires a leading order approximation to the integration by parts [equation (C-8) to (C-9)]. Therefore, it is not the exact equivalent of the Kirchhoff-approximate modeling formula [either of equations (C-1) or (C-2); i.e. equations (3.20) or (3.17), respectively]. However, it is trivial to find an exact equivalent. In taking the inverse Fourier transform of equation (C-5), the time derivative is transferred to the source wavelet instead of the delta function, resulting in

$$p^-_{s\Sigma_R}(\xi,t) \cong -\int_V dV R_\theta(\mathbf{x},\mathbf{x}_s)\gamma_R(\mathbf{x})A_{sg}(\mathbf{x},\xi)\left(\nabla_{\mathbf{x}}\phi_\tau(\mathbf{x},\xi)\cdot\mathbf{n}^-_R\right)\delta\left(t-\phi_\tau(\mathbf{x},\xi)\right) * s'_\rho(t). \quad \text{(C-14)}$$

Then, application of the change of variables given by equation (C-7) cancels the $|\nabla_{\mathbf{x}}\phi(\mathbf{x},\xi)|$ in the numerator, yielding

$$p^-_{s\Sigma_R}(\xi,t) \cong -\int_{\Sigma_I} d\Sigma_I d\phi_\tau R_\theta(\mathbf{x},\mathbf{x}_s)\gamma_R(\mathbf{x})(\mathbf{n}^+_I\cdot\mathbf{n}^-_R)A_{sg}(\mathbf{x},\xi)\delta\left(t-\phi_\tau(\mathbf{x},\xi)\right) * s'_\rho(t). \quad \text{(C-15)}$$

---

[5] Note that accurate representation of reflection beyond critical angle requires a phase change that is not incorporated in equations (C-12) or (C-13), but can be found in Jaramillo and Bleistein (1999).

Integration with respect to ϕ_τ reduces to a simple integration over the isochron through the application of the explicit delta function, yielding

$$p^{-}_{s\Sigma_R}(\xi,t) \cong -\int_{\Sigma_I} d\Sigma_I \, R_\theta(\mathbf{x}_I,\mathbf{x}_s)\gamma_R(\mathbf{x}_I)(\mathbf{n}_I^{+}\cdot\mathbf{n}_R^{-})A_{sg}(\mathbf{x},\xi)\Big|_{t=\phi_\tau} * s'_\rho(t)\,. \tag{C-16}$$

Equations (C-15) and (C-16) are integrals over the line of intersection between the isochron surface and the reflecting surface. Effectively, the line can be thought of as a 'ring' of area on the reflecting surface, where the differential width of the ring is proportional—using wavespeed $c_0(\mathbf{x}_I)$—to the differential change in time of the isochron. The factor $(\mathbf{n}_I^{+}\cdot\mathbf{n}_R^{-})$ downweights the contribution from reflecting elements that are not tangent to the isochron surface. The complete obliquity factor as found in the Kirchhoff-approximate modeling formula [equation (C-1) or (C-2)] includes the factor $\left|\nabla_{\mathbf{x}}\phi(\mathbf{x},\xi)\right| = 2\cos\theta / c_0(\mathbf{x}_I)$. This portion is missing from equations (C-15) and (C-16). Recall that the Kirchhoff-approximate obliquity factor can be thought of as compensation for the change in area of the source and receiver ray-tubes intersecting a unit area on the reflecting surface. However, in transforming from an integral over the reflecting surface to an integral over the isochron surface, the effective area becomes a function of time. Thus the change in area of the ring with constant time increments exactly compensates for the missing portion of the obliquity factor. The resulting isochron-stack operators are independent of the angular separation of the source and receiver.

Equations (C-15) and (C-16) can be expressed in a simplified notation by incorporating the factor $\cos\chi = -(\mathbf{n}_I^{+}\cdot\mathbf{n}_R^{-})$ into a weighted reflectivity function denoted here as $\beta_{\theta\chi}(\mathbf{x},\mathbf{x}_s)$, yielding

$$p^{-}_{s\Sigma_R}(\xi,t) \cong \int_{\Sigma_I} d\Sigma_I d\phi_\tau \beta_{\theta\chi}(\mathbf{x},\mathbf{x}_s)A_{sg}(\mathbf{x},\xi)\delta\big(t-\phi_\tau(\mathbf{x},\xi)\big) * s'_\rho(t) \tag{C-17}$$

and

$$p^{-}_{s\Sigma_R}(\xi,t) \cong \int_{\Sigma_I} d\Sigma_I\, A_{sg}(\mathbf{x},\xi)\beta_{\theta\chi}(\mathbf{x}_I,\mathbf{x}_s)\Big|_{t=\phi_\tau} * s'_\rho(t) \qquad \text{(C-18)}$$

as simplified isochron-stack operators. Equations (C-17) and (C-18) are exact equivalents to the Kirchhoff-approximate modeling formula, and can be compared to equations (C-11) and (C-13), which require a leading order approximation to the integration by parts.

C.5 Summary

A derivation of the isochron stack from the simplified form of the Kirchhoff-approximate modeling formula is presented that does not require the stationary phase approximations used in the original derivations by Jaramillo (1999) and Jaramillo and Bleistein (1999). However, the new derivation still requires a leading order approximation to integration by parts and is therefore not an exact equivalent to the Kirchhoff-approximate modeling formula. An exact formula is possible, and is also presented.

APPENDIX D: RELATIONSHIPS BETWEEN 2-D, 2.5-D, AND 3-D MODELING AND MIGRATION/INVERSION FORMULAE FOR CONSTANT WAVESPEED

D.1 Introduction

Seismic data are often acquired along a line on the surface. For historic reasons, such data are typically called 2-D (two-dimensional) seismic data, where the two dimensions can be considered as the acquisition line x (or x_1) and the depth z (or x_3). The inherent assumption is that the earth parameters vary only in the in-plane coordinates x and z, and are independent of the out-of-plane coordinate y (or x_2). Hence the reflector elements in the subsurface can be considered as portions of infinite cylindrical surfaces with normals lying in the x-z plane. These will subsequently be referred to as "line" reflector elements. Given these assumptions of acquisition and subsurface geometry, only the in-plane values of earth parameters are of interest for either modeling or migration/inversion. The wavefield, however, originates from a point source and propagates in 3-D. For example, an impulsive point source generates an expanding spherical wavefront in a constant wavespeed medium. Bleistein (1986) introduced the term 2.5-D to describe the combination of 2-D subsurface structure and 3-D wavefield propagation.

The 3-D equivalent of a 2-D seismic experiment consists of line sources, line reflector elements, and line receivers. Obviously, 2.5-D is a more realistic representation of 2-D seismic data as both the sources and receivers are best approximated as points rather than lines. However, many 2-D modeling algorithms produce the equivalent of true 2-D seismic data, i.e. cylindrical wavefield propagation originating from line sources (e.g. see Kelly and Marfurt, 1990). These synthetic datasets can be used to test and compare migration/inversion algorithms. Thus formulations are required for both modeling and migration/inversion of 2-D data, and to convert 2-D results to 2.5-D for comparison with seismic data acquired using point sources and receivers.

Several authors have proposed operators for correcting amplitudes and adjusting phases of 2-D solutions to obtain approximate 2.5-D solutions. Comprehensive reviews can be found in Bleistein (1986) and Williamson and Pratt (1995). A derivation for the high-frequency (asymptotic) time-domain operator can be found in Deregowski and Brown [1983, equation (17)]. A derivation for its frequency-domain equivalent can be found in Bleistein [1986, equation (21)]. Either of these asymptotic operators can be applied to a variable wavespeed medium by identifying and raytracing each reflection event. However, raytracing is not practical if the 2-D seismic data is synthesized using a 2-D finite-difference modeling package; and, the asymptotic operator cannot be applied to incremental steps of finite differencing because it is only valid in the far field. Esmersoy and Oristaglio (1988) propose a cascade of operators valid for the near field in a constant wavespeed medium. These could be applied at each incremental step of finite difference modeling, but not as a pre- or post-conditioning filter.

Liner (1991), Liner and Stockwell (1993), Bording and Liner (1993) and Stockwell (1995) propose various forms of a damped 2.5-D wave equation that can be explicitly modeled using finite differences. Williamson and Pratt (1995) provide a concise review and propose their own variant of a damped 2.5-D wave equation. However, they conclude that “(no) operator exists that can be simply applied to recorded or modeled traces in arbitrary velocity fields to give an exact conversion without event identification and ray-tracing because $\sigma(\mathbf{x},t)^{6}$ is potentially multivalued", and that "an exact 2.5-D wave equation cannot be written solely in terms of 2-D space- and time-dependent variables and derivatives". They suggest two solutions. The method of Song and Williamson (1992) guarantees accuracy and is less computationally intensive than full 3-D modeling, but is much more demanding than 2-D modeling. A practical but less accurate solution is to adjust amplitude and phase using the 2-D to 2.5-D constant wavespeed operator [see equation (D-35) of this Appendix] but replacing the constant σ with a space- and time-dependent variable $\sigma(\mathbf{x},t)$.

In this Appendix, constant-wavespeed far-field Green's functions for 2-D forward and backward propagating wavefields are derived, and then used as a basis for derivations of 2-D modeling and 2-D common-shot migration/inversion formulae. These formulae, and the migration/inversion formulae for common-offset and zero-offset configurations, can be compared to their 2.5-D and 3-D equivalents. Relationships between the various formulae can be expressed in terms of out-of-plane spreading factors and half-differential and/or half-integral operators. These relationships may be of practical use to: 1) convert the output from a 2-D finite-difference modeling package into 2.5-D synthetic seismic data, and 2) migrate 2.5-D seismic data using 2-D migration/inversion algorithms.

D.2 Far-field Hankel functions

Before continuing with the 2-D forward modeling derivations, a few formulae will prove useful. The Euler formula

---

[6] From Williamson and Pratt (1995): "σ is the ray parameter such that along a ray $(\mathrm{d}\mathbf{x}/\mathrm{d}\sigma)^2 = 1/c^2(\mathbf{x})$,i.e., $\mathrm{d}\sigma = c\mathrm{d}s = c^2\mathrm{d}\tau$, where s and τ are the distance and traveltime along the ray, respectively". As we shall see, in a constant wavespeed medium, $\sigma = cr$, where r is the distance along the straight ray.

$$e^{i\theta} = \cos\theta + i\sin\theta \tag{D-1}$$

reduces to (in the special case when $\theta = \pi$)

$$e^{i\pi} = -1 . \tag{D-2}$$

From de Moivre's identity,

$$e^{i(n\theta)} = (e^{i\theta})^n \tag{D-3}$$

we get (with $n = 1/2$ and $\theta = \pi$)

$$e^{i\pi/2} = \sqrt{-1} = i . \tag{D-4}$$

Now apply de Moivre's identity to take the positive and negative square roots of equation (D-4), where the square root sign will now be used to indicate the principle (i.e. positive) square root. Thus

$$e^{i\pi/4} = \sqrt{i} \tag{D-5}$$

or, equivalently

$$e^{i\pi/4} = \sqrt{i} = \frac{\sqrt{i}\sqrt{-i}}{\sqrt{-i}} = \frac{1}{\sqrt{-i}} ; \tag{D-6}$$

and

$$e^{-i\pi/4} = \frac{1}{\sqrt{i}} = \frac{\sqrt{-i}}{\sqrt{i}\sqrt{-i}} = \sqrt{-i} , \tag{D-7}$$

or, equivalently

$$e^{-i\pi/4} = \frac{1}{\sqrt{i}} = \frac{\left(\sqrt{i}\sqrt{-i}\right)}{\left(\sqrt{i}\sqrt{i}\right)\sqrt{-i}} = \frac{1}{i\sqrt{-i}} . \tag{D-8}$$

Next, we need Hankel functions of the first and second kind:

$$H_n^{(1)}(\theta) = J_n(\theta) + iY_n(\theta) \tag{D-9}$$

and

$$H_n^{(2)}(\theta) = J_n(\theta) - iY_n(\theta), \tag{D-10}$$

where n is the order, and $J_n(\theta)$ and $Y_n(\theta)$ are Bessel functions of the first and second kind with asymptotic approximations given by

$$J_n(\theta) \approx \sqrt{\frac{2}{\pi\theta}} \cos\left(\theta - \frac{n\pi}{2} - \frac{\pi}{4}\right), \quad \theta >> 1 \tag{D-11}$$

and

$$Y_n(\theta) \approx \sqrt{\frac{2}{\pi\theta}} \sin\left(\theta - \frac{n\pi}{2} - \frac{\pi}{4}\right), \quad \theta >> 1. \tag{D-12}$$

Inserting these asymptotic approximations into the zero-order Hankel functions of the first and second kind and applying the Euler formula [equation (D-1)] yields

$$H_0^{(1)}(\theta) \approx \sqrt{\frac{2}{\pi\theta}} e^{i(\theta - \pi/4)} \tag{D-13}$$

and

$$H_0^{(2)}(\theta) \approx \sqrt{\frac{2}{\pi\theta}} e^{-i(\theta - \pi/4)}. \tag{D-14}$$

Equations (D-13) and (D-14) can be re-expressed using the exponential relationships determined using de Moivre's identity [equations (D-8) and (D-6)] to yield

$$H_0^{(1)}(\theta) \approx \sqrt{\frac{2}{\pi\theta}} e^{i\theta} e^{-i\pi/4} = \frac{1}{i\sqrt{-i}} \sqrt{\frac{2}{\pi}} \sqrt{\frac{1}{\theta}} e^{i\theta} \tag{D-15}$$

and

$$H_0^{(2)}(\theta) \approx \sqrt{\frac{2}{\pi\theta}} e^{-i\theta} e^{+i\pi/4} = \frac{1}{\sqrt{-i}} \sqrt{\frac{2}{\pi}} \sqrt{\frac{1}{\theta}} e^{-i\theta}. \tag{D-16}$$

Note that by using the one-sided inverse Fourier transform valid for real signals, as given by equation (A-30), the sign complexities associated with negative frequencies are greatly reduced.

D.3 Forward and backward 2-D free-space Green's functions

The asymptotic Hankel functions [equations (D-15) and (D-16)] will prove extremely useful for 2-D free-space Green's functions, which assume a line source instead of a point source. Assuming the line source is parallel to the y-axis, the 2-D forward-propagating free-space Green's function can be derived by integrating the 3-D forward-propagating free-space Green's functions [equation (2.16)], as follows

$$\begin{aligned}\underset{(2-D)}{\vec{G}_0}(\mathbf{x},\mathbf{x}_G,\omega) &= \int_{-\infty}^{\infty} dy_G \; \underset{(3-D)}{\vec{G}_0}(\mathbf{x},\mathbf{x}_G,\omega) \\ &= \int_{-\infty}^{\infty} dy_G \frac{e^{i\omega\sqrt{r^2+\mathrm{Y}^2}/c_0}}{4\pi\sqrt{r^2+\mathrm{Y}^2}} \\ &= \frac{i}{4} H_0^{(1)}(\omega r / c_0)\,, \end{aligned} \tag{D-17}$$

with $r = \sqrt{(x-x_G)^2 + (z-z_G)^2}$ and $\mathrm{Y} = y - y_G$. Inserting the asymptotic expression for the Hankel function [equation (D-15)] yields

$$\underset{(2-D)}{\vec{G}_0}(\mathbf{x},\mathbf{x}_G,\omega) \approx \frac{\sqrt{2\pi\sigma}}{\sqrt{-i\omega}} \frac{e^{i\omega r / c_0}}{4\pi r}\,. \tag{D-18}$$

Thus the 2-D forward-propagating free-space Green's function is the half-integral operator $1/\sqrt{-i\omega}$ applied to the corresponding 3-D Green's function (evaluated in the plane y = constant), multiplied by the out-of-plane spreading correction $\sqrt{2\pi\sigma}$, where $\sigma = c_0 r$. The half-integral operator in the 2-D Green's function creates a tail that extends for infinite time after the arrival of the initial wavefront. This is to be expected, given that the 2-D impulse source is equivalent to an impulse line source in 3-D. The first arrival at the observation location $\mathbf{x}$ at time r/c_0 comes from the in-plane point on the line source. Subsequent arrivals come from points further and further out along the line, at times $\sqrt{r^2+\mathrm{Y}^2}/c_0$ (see equation D-17). Thus, wave diffusion takes place and Huygens' principle does not hold in 2-D (see Robinson and Silvia, 1981 p. 313).

Derivation of the 2-D backward-propagating free-space Green's function is similar, yielding

$$\underset{(2-D)}{\overleftarrow{G}_0}(\mathbf{x},\mathbf{x}_G,\omega) = -\frac{i}{4}H_0^{(2)}(\omega r/c_0) \approx \frac{\sqrt{2\pi\sigma}}{i\sqrt{-i\omega}}\frac{e^{-i\omega r/c_0}}{4\pi r}. \tag{D-19}$$

The 2-D forward-propagating free-space Green's function [equation (D-18)] can be applied to the forward modeling problem. The derivation is similar to that found in Kuhn and Alhilali (1977) but uses the opposite sign convention for the Fourier transform. Hence exponentials in the forward and backward propagating Green's functions are opposite in sign, leading to Hankel functions of the second and first kind, respectively.

D.4 Derivation of 2-D forward modeling formula for constant wavespeed

We start with the Kirchhoff-Helmholtz integral for the surface scattered wavefield [equation (3.9)], expressed in 2-D as

$$\begin{aligned}\underset{(2-D)}{P_\Lambda^-}(\mathbf{x}_g,\mathbf{x}_s,\omega) = \int_{\mathbf{x}_\Lambda} d\Lambda \Big\{ & \underset{(2-D)}{\vec{G}_0^+}(\mathbf{x}_\Lambda,\mathbf{x}_g,\omega)\nabla_{\mathbf{x}_\Lambda} \underset{(2-D)}{P_\Lambda^-}(\mathbf{x}_\Lambda,\mathbf{x}_{s'},\omega)\cdot\mathbf{n}_\Lambda^+ \\ & - \underset{(2-D)}{P_\Lambda^-}(\mathbf{x}_\Lambda,\mathbf{x}_{s'},\omega)\nabla_{\mathbf{x}_\Lambda} \underset{(2-D)}{\vec{G}_0^+}(\mathbf{x}_\Lambda,\mathbf{x}_g,\omega)\cdot\mathbf{n}_\Lambda^+ \Big\},\end{aligned} \tag{D-20}$$

where the Green's function source is at the measurement location on the surface, as indicated by the subscript (g), and the line reflector element is indicated by the subscript (Λ), with downward pointing normal $\mathbf{n}_\Lambda^+$.

The appropriate Green's function is given by equation (D-18). I adopt a simplified notation for the 2-D Green's function based on the subscripts described in the previous paragraph, i.e.

$$\underset{(2-D)}{\vec{G}_0^+}(\mathbf{x}_\Lambda, \mathbf{x}_g, \omega) = \vec{G}_{\Lambda g}^+ = \frac{\sqrt{2\pi\sigma_{\Lambda g}}}{\sqrt{-i\omega}} \frac{e^{i\omega r_{\Lambda g}/c_0}}{4\pi r_{\Lambda g}}. \tag{D-21}$$

Next we need the normal derivative of the Green's function given by equation (D-21), as follows:

$$\frac{\partial \vec{G}_{\Lambda g}^+}{\partial n_\Lambda^+} = \frac{\partial \vec{G}_{\Lambda g}^+}{\partial r_{\Lambda g}} \frac{\partial r_{\Lambda g}}{\partial n_\Lambda^+} = \frac{\partial}{\partial r_{\Lambda g}} \left[\frac{\sqrt{2\pi c_o}}{4\pi\sqrt{-i\omega}} r_{\Lambda g}{}^{-1/2} e^{i\omega r_{\Lambda g}/c_0} \right] \frac{\partial r_{\Lambda g}}{\partial n_\Lambda^+}$$

$$= \frac{-\sqrt{2\pi c_o}}{8\pi\sqrt{-i\omega}} r_{\Lambda g}^{-3/2} e^{i\omega R_{\Lambda g}/c_0} \frac{\partial r_{\Lambda g}}{\partial n_\Lambda^+} - \frac{\sqrt{2\pi c_o}}{4\pi} r_{\Lambda g}{}^{-1/2} \left(\frac{-i\omega}{c_0\sqrt{-i\omega}} \right) e^{i\omega r_{\Lambda g}/c_0} \frac{\partial r_{\Lambda g}}{\partial n_\Lambda^+}. \tag{D-22}$$

In the far field, the term containing $r_{\Lambda g}^{-3/2}$ can be neglected, leaving

$$\frac{\partial \vec{G}_{\Lambda g}^+}{\partial n_\Lambda^+} \approx -\sqrt{-i\omega}\sqrt{2\pi c_0 r_{\Lambda g}} \frac{e^{i\omega r_{\Lambda g}/c_0}}{4\pi c_0 r_{\Lambda g}} \frac{\partial r_{\Lambda g}}{\partial n_\Lambda^+}, \tag{D-23}$$

which can be re-expressed as

$$\frac{\partial \vec{G}_{\Lambda g}^+}{\partial n_\Lambda^+} \approx \frac{\sqrt{2\pi\sigma_{\Lambda g}}}{\sqrt{-i\omega}} \left\{ -(-i\omega) \frac{e^{i\omega r_{\Lambda g}/c_0}}{4\pi\sigma_{\Lambda g}} \frac{\partial r_{\Lambda g}}{\partial n_\Lambda^+} \right\}. \tag{D-24}$$

Thus the normal derivative of the 2-D forward-propagating free-space Green's function is the half-integral operator $1/\sqrt{-i\omega}$ applied to the normal derivative of the corresponding 3-D Green's function (evaluated in the plane y = constant) multiplied by the out-of-plane spreading correction $\sqrt{2\pi\sigma_{\Lambda g}}$. Note that the normal derivative of the 3-D Green's function (in the curly brackets) is itself a full derivative $(-i\omega)$ of the free-space Green's function divided by the wavespeed c_0 and multiplied by the obliquity $\partial r_{\Lambda g} / \partial n_\Lambda^+ = \cos\theta_{\Lambda g}$, where $\theta_{\Lambda g}$ is the acute angle between the ray direction and surface normal. The combined effect of the full-derivative and half-integral operators is the half-derivative operator $\sqrt{-i\omega}$, as shown in equation (D-23).

Following the line of reasoning presented in Section 3.3 [equations (3.11)-(3.13)], the upgoing reflected wavefield on the reflector surface is given by the density-dependent source function $S_\rho(\omega)$ times the angle-dependent geometrical-optics reflection coefficient $R_\theta(\mathbf{x}_\Lambda, \mathbf{x}_s)$ (simplified as R_θ) multiplied by the 2-D forward-propagating free-space Green's function from image source to reflector, i.e.

$$\underset{(2-D)}{P_\Lambda^-}(\mathbf{x}_\Lambda, \mathbf{x}_{s'}, \omega) = P_{\Lambda s'}^- = S_\rho(\omega) R_\theta \vec{G}_{\Lambda s'}^- = S_\rho(\omega) R_\theta \frac{\sqrt{2\pi\sigma_{\Lambda s'}}}{\sqrt{-i\omega}} \frac{e^{i\omega r_{\Lambda s'}/c_0}}{4\pi r_{\Lambda s'}}. \tag{D-25}$$

The far-field normal derivative is

$$\frac{\partial P_{\Lambda s'}^-}{\partial n_{\Lambda s'}^+} \approx S_\rho(\omega) R_\theta \frac{\sqrt{2\pi\sigma_{\Lambda s'}}}{\sqrt{-i\omega}} \left[-(-i\omega) \frac{e^{i\omega r_{\Lambda s'}/c_0}}{4\pi\sigma_{\Lambda s'}} \frac{\partial r_{\Lambda s'}}{\partial n_\Lambda^+} \right]. \tag{D-26}$$

The obliquity $\partial r_{\Lambda s'} / \partial n_\Lambda^+ = -\cos\theta_{\Lambda s}$, where $\theta_{\Lambda s}$ is the acute angle between the ray direction and the surface normal.

Substituting equations (D-21), (D-23), (D-25) and (D-26) into equation (D-20) yields

$$\begin{aligned} \underset{(2-D)}{P_\Lambda^-}(\mathbf{x}_g, \mathbf{x}_{s'}, \omega) = \int_{\mathbf{x}_\Lambda} d\Lambda \Bigg\{ & -\frac{\sqrt{2\pi\sigma_{\Lambda g}}}{\sqrt{-i\omega}} \frac{e^{i\omega r_{\Lambda g}/c_0}}{4\pi r_{\Lambda g}} S_\rho(\omega) R_\theta \sqrt{-i\omega} \sqrt{2\pi\sigma_{\Lambda s'}} \frac{e^{i\omega r_{\Lambda s'}/c_0}}{4\pi\sigma_{\Lambda s'}} \frac{\partial r_{\Lambda s'}}{\partial n_\Lambda^+} \\ & + S_\rho(\omega) R_\theta \frac{\sqrt{2\pi\sigma_{\Lambda s'}}}{\sqrt{-i\omega}} \frac{e^{i\omega r_{\Lambda s'}/c_0}}{4\pi r_{\Lambda s'}} \sqrt{-i\omega} \sqrt{2\pi\sigma_{\Lambda g}} \frac{e^{i\omega r_{\Lambda g}/c_0}}{4\pi\sigma_{\Lambda g}} \frac{\partial r_{\Lambda g}}{\partial n_\Lambda^+} \Bigg\}, \end{aligned} \tag{D-27}$$

which simplifies to

$$\underset{(2-D)}{P_\Lambda^-}(\mathbf{x}_g, \mathbf{x}_{s'}, \omega) = \frac{c_0}{4} \int_{\mathbf{x}_\Lambda} d\Sigma S_\rho(\omega) R_\theta \frac{e^{i\omega(r_{\Lambda s'} + r_{\Lambda g})/c_0}}{\sqrt{2\pi\sigma_{\Lambda s'}} \sqrt{2\pi\sigma_{\Lambda g}}} \left(\frac{\partial r_{\Lambda g}}{\partial n_\Lambda^+} - \frac{\partial r_{\Lambda s'}}{\partial n_\Lambda^+} \right). \tag{D-28}$$

Equation (D-28) agrees with equation (16a) of Kuhn and Alhilali (1977)[7]. Substituting for the normal derivatives using the obliquity angles described previously and rearranging yields

$$\underset{(2-D)}{P_{\Lambda}^{-}}(\mathbf{x}_g,\mathbf{x}_s,\omega)=\frac{c_0}{2}\int_{\mathbf{x}_\Lambda} d\Lambda R_\theta \left\{ \frac{1}{\sqrt{2\pi\sigma_{\Lambda s}}\sqrt{2\pi\sigma_{\Lambda g}}} \left(\frac{\cos\theta_{\Lambda s}+\cos\theta_{\Lambda g}}{2} \right) \right\} \left[S_\rho(\omega) e^{i\omega(r_{\Lambda s}+r_{\Lambda g})/c_0} \right]. \tag{D-29}$$

Equation (D-29) is the 2-D modeling formula, now expressed in terms of a source at the surface location instead of at the image location. The term in the square brackets is the Fourier transform of the source wavelet $[S_\rho(\omega)]$ multiplied by a phase shift $e^{i\omega(r_{\Lambda s}+r_{\Lambda g})/c_0}$ determined by the traveltime from source-to-reflector-to-receiver.

Deregowski and Brown (1983) propose a variant of the 2-D modeling formula given by equation (D-29). They use a source that produces an impulsive wavefront in the far field. This is achieved with an extra half-differential operator $\sqrt{-i\omega}$, yielding the 2-D variant modeling formula

$$\begin{aligned}\underset{(2-Dv)}{P_{\Lambda}^{-}}(\mathbf{x}_g,\mathbf{x}_s,\omega)=\frac{c_0}{2}\int_{\mathbf{x}_\Lambda} d\Lambda R_\theta &\left\{ \frac{1}{\sqrt{2\pi\sigma_{\Lambda s}}\sqrt{2\pi\sigma_{\Lambda g}}} \left(\frac{\cos\theta_{\Lambda s}+\cos\theta_{\Lambda g}}{2} \right) \right\} \\ &\times \left[\sqrt{-i\omega}\, S_\rho(\omega) e^{i\omega(r_{\Lambda s}+r_{\Lambda g})/c_0} \right].\end{aligned} \tag{D-30}$$

D.5 3-D and 2.5-D modeling formulae for constant wavespeed

The 3-D modeling formula [equation (3.17)] determines the wavefield at a point receiver originating from a point source and reflected from an arbitrary 3-D subsurface structure Σ. The constant wavespeed version of the 3-D modeling formula is

---

[7] Note that equation (16a) of Kuhn and Alhilali (1977) contains an extra factor of 4π, arising from an extra factor of 4π in their equation (14a) as compared to equation (D-25) above.

$$\underset{(3-D)}{P_{\Sigma}^{-}}(\mathbf{x}_g,\mathbf{x}_s,\omega)=\frac{c_0}{2}\int_{\mathbf{x}_\Sigma} d\Sigma R_\theta \left\{\frac{1}{2\pi\sigma_{\Sigma s}2\pi\sigma_{\Sigma g}}\left(\frac{\cos\theta_{\Sigma s}+\cos\theta_{\Sigma g}}{2}\right)\right\}$$
$$\times\left[(-i\omega)S_\rho(\omega)e^{i\omega(r_{\Sigma s}+r_{\Sigma g})/c_0}\right]. \quad \text{(D-31)}$$

To obtain a 2.5-D modeling formula for constant wavespeed, all that remains is to integrate equation (D-31) over the *y*-coordinate of the reflector surface. The integration for constant wavespeed is presented in Deregowski and Brown (1983, Appendix B) or, for a generalized 2-D wavespeed function using the method of stationary phase, in Bleistein (1986). The integrations are not trivial and will not be repeated here. The result is:

$$\underset{(2.5-D)}{P_{\Lambda}^{-}}(\mathbf{x}_g,\mathbf{x}_s,\omega)=\frac{c_0}{2}\int_{\mathbf{x}_\Lambda} d\Lambda R_\theta \left\{\frac{1}{\sqrt{2\pi\sigma_{\Lambda s}}\sqrt{2\pi\sigma_{\Lambda g}}\sqrt{2\pi(\sigma_{\Lambda s}+\sigma_{\Lambda s})}}\left(\frac{\cos\theta_{\Lambda s}+\cos\theta_{\Lambda g}}{2}\right)\right\}$$
$$\times\left[\sqrt{-i\omega}S_\rho e^{i\omega(r_{\Lambda s}+r_{\Lambda g})/c_0}\right]. \quad \text{(D-32)}$$

The 2.5-D modeling formula assumes 2-D subsurface structure and 3-D wave propagation.

D.6 Relationships between 2-D, 2.5-D and 3-D modeling formulae for constant wavespeed

Some interesting and simple relationships exist between the 2-D, 2.5-D and 3-D modeling formulas. First, note the relationship between the 2-D and 3-D forward propagating Green's functions as given by equation (D-18), re-expressed here as

$$\underset{(3-D)}{\vec{G}_0}(\mathbf{x},\mathbf{x}_G,\omega)\approx\left[\frac{\sqrt{-i\omega}}{\sqrt{2\pi\sigma}}\right]\underset{(2-D)}{\vec{G}_0}(\mathbf{x},\mathbf{x}_G,\omega). \quad \text{(D-33)}$$

Comparing equation (D-31) with equation (D-29), we see that the 3-D modeling formula is related to the 2-D modeling formula by

$$\underset{(3-D)}{P_{\Sigma}^{-}}(\mathbf{x}_g, \mathbf{x}_s, \omega) = \left[\frac{\sqrt{-i\omega}}{\sqrt{2\pi\sigma_{\Lambda g}}}\right]\left[\frac{\sqrt{-i\omega}}{\sqrt{2\pi\sigma_{\Lambda s}}}\right]\underset{(2-D)}{P_{\Lambda}^{-}}(\mathbf{x}_g, \mathbf{x}_s, \omega). \tag{D-34}$$

i.e. the forward out-of-plane spreading and half-differential operators for both the source-to-reflector and reflector-to-receiver paths. Equation (D-34) is of limited utility. Although it appears to shows how one can convert synthetic data generated using a 2-D modeling program into 3-D synthetic data, the result will not include the contribution from the out-of-plane component of the integration over the reflector surface.

Comparing equation (D-32) with equation (D-29), we see that the 2.5-D modeling formula is related to the 2-D modeling formula by

$$\underset{(2.5-D)}{P_{\Lambda}^{-}}(\mathbf{x}_g, \mathbf{x}_s, \omega) = \left[\frac{\sqrt{-i\omega}}{\sqrt{2\pi(\sigma_{\Lambda s} + \sigma_{\Lambda g})}}\right]\underset{(2-D)}{P_{\Lambda}^{-}}(\mathbf{x}_g, \mathbf{x}_s, \omega). \tag{D-35}$$

i.e. the forward out-of-plane spreading and half-differential operator for the source-to-reflector-to-receiver path. Equation (D-35) can be used to convert 2-D synthetic data into more realistic 2.5-D synthetic data. In a constant velocity medium, the out-of-plane spreading $1\big/\sqrt{2\pi(\sigma_{\Lambda s} + \sigma_{\Lambda g})}$ is proportional to $1\big/\sqrt{t}$, where t is the total traveltime on the synthetic trace. Both the out-of-plane spreading and the half-differential operator can be implemented after the synthetic data have been generated.

Finally, comparing equation (D-31) with equation (D-32), we see that the 3-D modeling formula is related to the 2.5-D modeling formula by

$$\underset{(3-D)}{P_{\Sigma}^{-}}(\mathbf{x}_g, \mathbf{x}_s, \omega) = \left[\frac{\sqrt{-i\omega}}{\sqrt{2\pi\sigma_{\Lambda s}}}\right]\left[\frac{\sqrt{-i\omega}}{\sqrt{2\pi\sigma_{\Lambda g}}}\right]\left[\frac{\sqrt{2\pi(\sigma_{\Lambda s} + \sigma_{\Lambda g})}}{\sqrt{-i\omega}}\right]\underset{(2.5-D)}{P_{\Lambda}^{-}}(\mathbf{x}_g, \mathbf{x}_s, \omega). \tag{D-37}$$

The fact that the 2.5-D and 3-D modeling formulae are not identical is easily explained. The 2.5-D modeling formula includes the out-of-plane integration over the line reflector elements, while the 3-D modeling formula does not. Thus equation (D-37) is also of limited utility. As we shall see shortly, similar relationships exist between the 2-D, 2.5-D and 3-D migration/inversion formulae.

D.7 Derivation of 2-D common-shot migration/inversion formula for constant wavespeed

Derivation of the 2-D Kirchhoff-approximate migration/inversion formula for shot or receiver records starts with the chi-squared optimum deconvolution imaging condition [equation (3.38)]

$$\underset{(2-D)}{\hat{R}_\theta}(\mathbf{x}_G,\mathbf{x}_s)=\frac{1}{2\pi}\int d\omega\hat{F}(\omega)\frac{P_S^-(\mathbf{x}_G,\mathbf{x}_s,\omega)}{\vec{G}_0^+(\mathbf{x}_G,\mathbf{x}_s,\omega)}, \tag{D-38}$$

where $P_S^-(\mathbf{x}_G,\mathbf{x}_s,\omega)$ is the wavefield recorded on the line $\mathbf{x}_g$ inverse propagated to the imaging location $\mathbf{x}_G$, and $\vec{G}_0^+(\mathbf{x}_G,\mathbf{x}_s,\omega)$ is the forward-propagating free-space Green's function originating at the source location $\mathbf{x}_s$, adapted from equation (D-18) as

$$\underset{(2-D)}{\vec{G}_0}(\mathbf{x}_G,\mathbf{x}_s,\omega)=\vec{G}_{Gs}\approx\frac{\sqrt{2\pi\sigma_{Gs}}}{\sqrt{-i\omega}}\frac{e^{i\omega r_{Gs}/c_0}}{4\pi r_{Gs}}. \tag{D-39}$$

Following the line of reasoning presented in section 3.7, the wavefield $\underset{(2-D)}{P_S^-}(\mathbf{x}_G,\mathbf{x}_s,\omega)$ is reconstructed using the Rayleigh II integral

$$\underset{(2-D)}{P_S^-}(\mathbf{x}_G,\mathbf{x}_s,\omega)=2\int_{\mathbf{x}_g} dx\,\underset{(2-D)}{P_S^-}(\mathbf{x}_g,\mathbf{x}_s,\omega)\frac{\partial}{\partial n_g^+}\underset{(2-D)}{\overleftarrow{G}_0^+}(\mathbf{x}_g,\mathbf{x}_G,\omega). \tag{D-40}$$

The 2-D backward-propagating free-space Green's function is adapted from equation (D-19) as

$$\overleftarrow{G}_{gG}^+\approx\frac{\sqrt{2\pi\sigma_{gG}}}{i\sqrt{-i\omega}}\frac{e^{-i\omega r_{gG}/c_0}}{4\pi r_{gG}}, \tag{D-41}$$

with normal derivative

$$\frac{\partial \overleftarrow{G}_{gG}^{+}}{\partial n_g^{+}} \approx \frac{\sqrt{2\pi\sigma_{gG}}}{i\sqrt{-i\omega}}\left[\frac{(-i\omega)}{c_0}\frac{e^{-i\omega r_{gG}/c_0}}{4\pi r_{gG}}\frac{\partial r_{gG}}{\partial n_g^{+}}\right] \tag{D-42}$$

Now substitute equation (D-42) into equation (D-40), then equations (D-40) and (D-39) into equation (D-38), and take equation (A-30) to give

$$\underset{(2-D)}{\hat{R}_\theta}(\mathbf{x}_G, \mathbf{x}_s) = \frac{2}{c_0}\int_{\mathbf{x}_g} dx\left\{\frac{\sqrt{2\pi\sigma_{Gs}}}{\sqrt{2\pi\sigma_{gG}}}\cos\theta_{gG}\right\}$$
$$\times 2\,\mathrm{Re}\left[\frac{1}{2\pi}\int_0^\infty d\omega\hat{F}(\omega)(\omega)\underset{(2-D)}{P_S^{-}}(\mathbf{x}_g, \mathbf{x}_s, \omega)e^{-i\omega(r_{Gs}+r_{gG})/c_0}\right]. \tag{D-43}$$

Equation (D-43) is the 2-D constant wavespeed migration formula for reflectivity, valid for the common-shot (or common-receiver) domain. Note the weighting by frequency ω in the inverse Fourier transform of the recorded wavefield (square brackets), which can be thought of as the effect of the out-of-plane component of the Fresnel zone not collapsed by the migration. In addition, the normal direction has been changed between equations (D-42) and (D-43) so that the receiver directivity $\partial r_{gG}/\partial n_g^{-} = \cos\theta_{gG}$, with θ_{gG} the acute angle between the ray direction and the surface normal.

D.8 2.5-D and 3-D common-shot migration/inversion formulae for constant wavespeed

The 2.5-D common-shot migration/inversion formula can be derived in two ways, starting from either the 2-D formula [equation (D-43)] or the 3-D formula (given below). The 2-D method is trivial, as it utilizes a simple relationship between 2-D and 3-D free-space Green's functions. In keeping with the discussion presented in Appendix B [see equation (B-15)], the 2.5-D pressure recorded on the surface (i.e. 3-D pressure recorded along a single line of receivers) can be considered proportional to a 'generalized' free-space Green's function. Hence the 2.5-D pressure can be related to the 2-D pressure using the relationship between respective forward-propagating Green's functions as given by equation (D-33), re-expressed for the source-to-reflector-to-receiver path as

$$\underset{(2-D)}{P_S^-}(\mathbf{x}_g,\mathbf{x}_s,\omega)=\frac{\sqrt{2\pi(\sigma_{Gs}+\sigma_{gG})}}{\sqrt{-i\omega}}\underset{(2.5-D)}{P_S^-}(\mathbf{x}_g,\mathbf{x}_s,\omega). \qquad \text{(D-44)}$$

Substituting equation (D-44) for $\underset{(2-D)}{P_S^-}(\mathbf{x}_g,\mathbf{x}_s,\omega)$ in equation (D-43) and rearranging yields

$$\underset{(2.5-D)}{\hat{R}_\theta}(\mathbf{x}_G,\mathbf{x}_s)=\frac{2}{c_0}\int_{\mathbf{x}_g}dx\left\{\sqrt{2\pi(\sigma_{Gs}+\sigma_{gG})}\frac{\sqrt{2\pi\sigma_{Gs}}}{\sqrt{2\pi\sigma_{gG}}}\cos\theta_{gG}\right\}$$
$$\times 2\operatorname{Re}\left[\frac{1}{2\pi}\int_0^\infty d\omega F(\omega)\sqrt{i\omega}\underset{(2.5-D)}{P_S^-}(\mathbf{x}_g,\mathbf{x}_s,\omega)e^{-i\omega(r_{Gs}+r_{gG})/c_0}\right]. \qquad \text{(D-45)}$$

It is interesting to note that the operator $\sqrt{i\omega}$ in the square brackets is not the half-differential operator, but instead is equivalent to $i\sqrt{-i\omega}$, the half-differential operator combined with a phase shift of $\pi/2$ (see equation D-4).

Derivation of the 2.5-D migration/inversion formula from the 3-D formula is not trivial and hence will not be presented. The derivation was first presented by Bleistein et al. (1987), who start with the 3-D Born inversion formula for wavespeed perturbation $\alpha(\mathbf{x}_G)$ [equation (3.66) of this dissertation] and uses the method of stationary phase to collapse the out-of-plane contributions. The general derivation is also presented in Bleistein et al. (2001, Sections 6.2 and 6.3.1). In Chapter 3, equation (D-45) is presented in a reduced form as equation (3.78).

The 3-D common-shot migration/inversion formula for constant wavespeed is given by equation (3.74), re-expressed here as

$$\underset{(3-D)}{\hat{R}_\theta}(\mathbf{x}_G,\mathbf{x}_s)=\frac{-2}{c_0}\int_{\mathbf{x}_g}dS\left\{\frac{2\pi\sigma_{Gs}}{2\pi\sigma_{gG}}\cos\theta_{gG}\right\}.$$
$$\times 2\operatorname{Re}\left[\frac{1}{2\pi}\int_0^\infty d\omega\hat{F}(\omega)(-i\omega)\underset{(3-D)}{P_S^-}(\mathbf{x}_g,\mathbf{x}_s,\omega)e^{-i\omega(r_{Gs}+r_{gG})/c_0}\right]. \qquad \text{(D-46)}$$

D.9 Relationships between 2-D, 2.5-D, and 3-D common-shot migration/inversion formulae for constant wavespeed

Before we examine the relationships between the various migration formulae, note the relationship between the 3-D and 2-D backwards propagating Green's functions as given by equation (D-19), re-expressed here as

$$\underset{(3-D)}{\overleftarrow{G}_0}(\mathbf{x},\mathbf{x}_G,\omega) \approx \left[\frac{i\sqrt{-i\omega}}{\sqrt{2\pi\sigma}}\right]\underset{(2-D)}{\overleftarrow{G}_0}(\mathbf{x},\mathbf{x}_G,\omega). \tag{D-47}$$

For a given output point $\mathbf{x}_G$, the 3-D common-shot migration/inversion formula [equation (D-46)] is related to the 2-D common-shot migration/inversion formula [equation (D-43)] by

$$\underset{(3-D)}{\hat{R}_\theta}(\mathbf{x}_G,\mathbf{x}_s) = i\frac{\sqrt{2\pi\sigma_{Gs}}}{\sqrt{2\pi\sigma_{gG}}}\underset{(2-D)}{\hat{R}_\theta}(\mathbf{x}_G,\mathbf{x}_s). \tag{D-48}$$

This relationship can be explained by examining the generalized migration formula [equation (D-38)], with the backward out-of-plane spreading and half-differential operator applied to the numerator using equation (D-41) [or its equivalent, equation (D-47)] and the forward out-of-plane spreading correction and half-integral operator applied to the denominator using equation (D-39) [or its equivalent, equation (D-33)], yielding

$$\underset{(3-D)}{\hat{R}_\theta}(\mathbf{x}_G,\mathbf{x}_s) = \left[\frac{\sqrt{2\pi\sigma_{Gs}}}{\sqrt{-i\omega}}\right]\left[\frac{i\sqrt{-i\omega}}{\sqrt{2\pi\sigma_{gG}}}\right]\underset{(2-D)}{\hat{R}_\theta}(\mathbf{x}_G,\mathbf{x}_s). \tag{D-49}$$

Simplifying equation (D-49) yields equation (D-47). However, these equations are of limited utility because the out-of-plane spreading factor for the backward propagating path (receiver to subsurface point) would have to be implemented inside the integration, effectively producing a new migration formula.

Comparing equation (D-45) with equation (D-43), we see that the 2.5-D common-shot migration/ inversion formula is related to the 2-D common-shot migration/inversion formula by

$$\underset{(2.5-D)}{\hat{R}_\theta}(\mathbf{x}_G, \mathbf{x}_s) = \left[\frac{\sqrt{2\pi(\sigma_{Gs} + \sigma_{gG})}}{\sqrt{-i\omega}}\right] \underset{(2-D)}{\hat{R}_\theta}(\mathbf{x}_G, \mathbf{x}_s), \tag{D-50}$$

i.e. the forward out-of-plane spreading correction and half-integral operator for the source-to-reflector-to-receiver path. Equation (D-50) could be used to create a 2.5-D reflectivity map given a 2-D migration algorithm applied to 2.5-D data. The out-of-plane spreading correction $\sqrt{2\pi(\sigma_{Gs} + \sigma_{gG})}$ is proportional to the square root of traveltime $\sqrt{t}$ on the input trace. Similar to the 2.5-D/2D modeling relationship discussed previously [equation (D-35)], both the out-of-plane spreading correction and half-integral operator can be applied outside the migration integral.

Equations (D-49) and (D-50) can be combined to give the relationship between the 3-D and 2.5-D common-shot migration/inversion formulae:

$$\underset{(3-D)}{\hat{R}_\theta}(\mathbf{x}_G, \mathbf{x}_s) = \left[\frac{\sqrt{2\pi\sigma_{Gs}}}{\sqrt{-i\omega}}\right]\left[\frac{i\sqrt{-i\omega}}{\sqrt{2\pi\sigma_{gG}}}\right]\left[\frac{\sqrt{-i\omega}}{\sqrt{2\pi(\sigma_{Gs} + \sigma_{gG})}}\right] \underset{(2.5-D)}{\hat{R}_\theta}(\mathbf{x}_G, \mathbf{x}_s). \tag{D-51}$$

Applying the terms in square brackets in equation (D-51) from right to left suggests that the correction factors first transform the 2.5-D equation to 2-D, then from 2-D to 3-D. Equation (D-51) is of limited utility for the same reason that befell equation (D-49)—the out-of-plane spreading factor for the backward propagating path (receiver to subsurface point) would have to be implemented inside the integration, effectively producing a new migration formula.

D.10 Common-offset migration/inversion formulae for constant wavespeed

The common-offset experiment produces a recorded wavefield that is non-physical in the sense that it cannot be obtained from a single physical experiment. Thus the concept of a reflectivity obtained from a deconvolution imaging condition that ratios the inverse and forward propagated wavefield at the reflector is not applicable. Instead, the reflectivity is determined in a manner analogous to a generalized Radon transform, with the weighting factors in the migration/inversion formulae related to the distribution of isochron-normals at the reflector. Still, the relationships between the 2-D, 2.5-D and 3-D common-offset migration/ inversion formulae can be presented in terms of out-of-plane spreading factors and half-integral or half-differential operators. Physical interpretations can then be attached to each of these terms, although they may not be of much practical use.

The 3-D common-offset migration/inversion formula [equation (3.76)] is derived in section 5.2.3 of Bleistein et al. [2001, constant wavespeed version is equation (5.2.32)]. It can be re-expressed as

$$\underset{(3-D)}{\hat{R}_\theta}(\mathbf{x}_G,\xi_{co}) = \frac{-2}{c_0}\int_{\xi_{co}} dS \left\{ \frac{2\pi(\sigma_{Gs}+\sigma_{gG})}{2\pi\sigma_{gG}}\cos\theta_{gG} + \frac{2\pi(\sigma_{Gs}+\sigma_{gG})}{2\pi\sigma_{Gs}}\cos\theta_{Gs} \right\}$$
$$\times 2\,\mathrm{Re}\left[\frac{1}{2\pi}\int_0^\infty d\omega \hat{F}(\omega)(-i\omega)\underset{(3-D)}{P_S^-}(\mathbf{x}_g,\mathbf{x}_s,\omega)e^{-i\omega(r_{Gs}+r_{gG})/c_0}\right]. \qquad \text{(D-52)}$$

The 2.5-D common-offset migration/inversion formula [equation (3.79)] is derived in sections 6.2 and 6.3.5 of Bleistein et al. [2001, constant wavespeed version is unnumbered equation after equation (6.3.14)]. It can be re-expressed as

$$\underset{(2.5-D)}{\hat{R}_\theta}(\mathbf{x}_G,\xi_{co}) = \frac{2}{c_0}\int_{\xi_{co}} dx \left\{ \sqrt{2\pi(\sigma_{Gs}+\sigma_{gG})}\frac{\sqrt{2\pi\sigma_{Gs}}}{\sqrt{2\pi\sigma_{gG}}}\cos\theta_{gG} + \sqrt{2\pi(\sigma_{Gs}+\sigma_{gG})}\frac{\sqrt{2\pi\sigma_{gG}}}{\sqrt{2\pi\sigma_{Gs}}}\cos\theta_{Gs} \right\}$$

$$\times 2\,\mathrm{Re}\left[\frac{1}{2\pi}\int_0^\infty d\omega \hat{F}(\omega)\sqrt{i\omega}\underset{(2.5-D)}{P_S^-}(\mathbf{x}_g,\mathbf{x}_s,\omega)e^{-i\omega(r_{Gs}+r_{gG})/c_0}\right]. \qquad \text{(D-53)}$$

Equation (D-53) is effectively equation (7) of Dillon (1990), who introduces it as the 2-D (but probably means 2.5-D) generalized Kirchhoff migration formula. Equation (D-53) can also be thought of as a sum of common-shot and common-receiver weighting terms as given by the first and second terms in the curly brackets. Using only the common-shot term yields an expression identical to the common-shot migration/inversion formula as given by equation (D-45).

The 2-D common-offset migration/inversion formula can be obtained by substituting the 3-D pressure recorded on the surface using equation (D-44) into equation (D-53), yielding

$$\underset{(2-D)}{\hat{R}_\theta}(\mathbf{x}_G,\xi)=\frac{2}{c_0}\int_{\xi_{co}} dx\left\{\frac{\sqrt{2\pi\sigma_{Gs}}}{\sqrt{2\pi\sigma_{gG}}}\cos\theta_{gG}+\frac{\sqrt{2\pi\sigma_{gG}}}{\sqrt{2\pi\sigma_{Gs}}}\cos\theta_{Gs}\right\}$$
$$\times 2\,\mathrm{Re}\left[\frac{1}{2\pi}\int_0^\infty d\omega\hat{F}(\omega)(\omega)\underset{(2-D)}{P_S^-}(\mathbf{x}_g,\mathbf{x}_s,\omega)e^{-i\omega(r_{Gs}+r_{gG})/c_0}\right]. \qquad \text{(D-54)}$$

D.11 Relationships between 2-D, 2.5-D, and 3-D common-offset migration/inversion formulae for constant wavespeed

The simplest relationship is between the 2-D and 2.5-D common-offset migration/inversion formulae [equations (D-52) and (D-53), respectively], as this relationship was used to derive one from the other, and is the same as the relationship between the corresponding common-shot migration/inversion formulae [equation (D-50)], i.e.

$$\underset{(2.5-D)}{\hat{R}_\theta}(\mathbf{x}_G,\xi_{co})=\left[\frac{\sqrt{2\pi(\sigma_{Gs}+\sigma_{gG})}}{\sqrt{-i\omega}}\right]\underset{(2-D)}{\hat{R}_\theta}(\mathbf{x}_G,\xi_{co}). \qquad \text{(D-55)}$$

The 3-D common-offset migration/inversion formula [equation (D-54)] is not related to the 2-D and 2.5-D formulae in the same way as in the common-shot case. However, there is only one shot in the 3-D common-shot experiment and hence only one raypath from the shot to the reflector location $\mathbf{x}_G$ (assuming constant wavespeed). In the 3-D common-offset experiment, on the other hand, there are many shot-receiver pairs and hence many raypaths from the shots to the reflector location. Thus we might expect the relationships between the 3-D and the 2-D and 2.5-D formulae need term(s) that collapse these out-of-plane shots in addition to terms that collapse the out-of-plane contribution from each shot and from each receiver.

Equations (D-52), (D-53), and (D-54) are symmetric in common-shot and common-receiver terms, as given by the first and second terms in the curly brackets, respectively. Given the symmetry, I assume that the common-shot terms of the 3-D and 2-D common-offset migration/inversion formulae are related by

$$\underset{(3-D_s)}{\hat{R}_\theta}(\mathbf{x}_G,\xi_{co}) = \left[\frac{\sqrt{2\pi(\sigma_{Gs}+\sigma_{gG})}}{\sqrt{-i\omega}}\right]\left[\frac{\sqrt{-i\omega}}{\sqrt{2\pi\sigma_{Gs}}}\right]\left[\frac{i\sqrt{-i\omega}}{\sqrt{2\pi\sigma_{gG}}}\right]\left[\frac{\sqrt{2\pi(\sigma_{Gs}+\sigma_{gG})}}{\sqrt{-i\omega}}\right]\underset{(2-D_s)}{\hat{R}_\theta}(\mathbf{x}_G,\xi_{co}), \tag{D-56}$$

while the common-receiver terms are related by

$$\underset{(3-D_g)}{\hat{R}_\theta}(\mathbf{x}_G,\xi_{co}) = \left[\frac{\sqrt{2\pi(\sigma_{Gs}+\sigma_{gG})}}{\sqrt{-i\omega}}\right]\left[\frac{\sqrt{-i\omega}}{\sqrt{2\pi\sigma_{gG}}}\right]\left[\frac{i\sqrt{-i\omega}}{\sqrt{2\pi\sigma_{Gs}}}\right]\left[\frac{\sqrt{2\pi(\sigma_{Gs}+\sigma_{gG})}}{\sqrt{-i\omega}}\right]\underset{(2-D_g)}{\hat{R}_\theta}(\mathbf{x}_G,\xi_{co}). \tag{D-57}$$

Equations (D-56) and (D-57) are identical, and do equate the two migration/inversion formulae. However, it is not immediately obvious how either of these equations can be reconciled with the 3-D/2-D common-shot relationship given by equation (D-49). A more intuitive approach is to look at the relationship between the 2-D and 3-D common-offset wavefields, in a manner similar to the relationship between the 2-D and 3-D common-shot wavefields described by equation (D-44). One possible interpretation is as follows. Reading equation (D-56) from right to left: the first term takes the 2-D common-offset wavefield and converts it into a 3-D wavefield—entirely analogous to the 2.5-D/2-D relationship given by equation (D-55)—resulting in a single line of source-receiver pairs oriented, say, in the x direction; the next two terms expand the receivers for every shot and shots for every receiver in a direction perpendicular to the single line (i.e. in the y direction) with the shots in a forward propagating sense and the receivers in a backward propagating sense; while the final term corrects the resulting configuration to single shot-receiver pairs oriented in the x direction. The coordinate system can be changed to accommodate any desired azimuth. The physical explanation for the common-receiver terms is identical except for the sense of propagation, now forward from the receivers and backward from the shots.

Similarly, the common-shot terms in the 3-D and 2.5-D common-offset formulae are related by

$$\underset{(3-D_s)}{\hat{R}_\theta}(\mathbf{x}_G,\xi_{co}) = \left[\frac{\sqrt{2\pi(\sigma_{Gs}+\sigma_{gG})}}{\sqrt{-i\omega}}\right]\left[\frac{\sqrt{-i\omega}}{\sqrt{2\pi\sigma_{Gs}}}\right]\left[\frac{i\sqrt{-i\omega}}{\sqrt{2\pi\sigma_{gG}}}\right]\underset{(2.5-D_s)}{\hat{R}_\theta}(\mathbf{x}_G,\xi_{co}) \qquad \text{(D-58)}$$

while the common-receiver terms are related by

$$\underset{(3-D_g)}{\hat{R}_\theta}(\mathbf{x}_G,\xi_{co}) = \left[\frac{\sqrt{2\pi(\sigma_{Gs}+\sigma_{gG})}}{\sqrt{-i\omega}}\right]\left[\frac{\sqrt{-i\omega}}{\sqrt{2\pi\sigma_{gG}}}\right]\left[\frac{i\sqrt{-i\omega}}{\sqrt{2\pi\sigma_{Gs}}}\right]\underset{(2.5-D_g)}{\hat{R}_\theta}(\mathbf{x}_G,\xi_{co}) \qquad \text{(D-59)}$$

The explanation for equations (D-58) and (D-59) follows directly from the one above.

An interesting result is obtained by applying the 2-D/3-D common-shot relationship [equation (D-49)] to the common-shot term of the 2-D common-offset migration/inversion formula [equation (D-54], along with a suitably symmetric relationship for the common-receiver term. This produces the following 3-D migration/inversion formula:

$$\underset{(3-D)}{\hat{R}_{\angle}}(\mathbf{x}_G,\xi_{sg}) = \frac{-2}{c_0}\int_{\xi_{sg}} d^2S\left\{\frac{2\pi\sigma_{Gs}}{2\pi\sigma_{gG}}\cos\theta_{gG} + \frac{2\pi\sigma_{gG}}{2\pi\sigma_{Gs}}\cos\theta_{Gs}\right\}$$

$$\times 2\,\mathrm{Re}\left[\frac{1}{2\pi}\int_0^{\infty} d\omega \hat{F}(\omega)(-i\omega)\underset{(3-D)}{P_S^-}(\mathbf{x}_g,\mathbf{x}_s,\omega)e^{-i\omega(r_{Gs}+r_{gG})/c_0}\right], \qquad \text{(D-60)}$$

where $\hat{R}_{\angle}(\mathbf{x}_G,\xi_{sg})$ is some sort of average of (incorrectly) estimated angle-dependent reflection coefficients.

Equation (D-60) is within a constant of proportionality to equation (A-5) of Dillon (1990), although Dillon derives his equation using a completely different method. Numerical tests presented in Section 4.3 show that equation (D-60) does not produce an accurate estimate of reflectivity, although the error is of similar magnitude to that introduced by incorporating the obliquity factor at the reflector.

D.12 Zero-offset migration/inversion formulae and relationships

Zero-offset migration/inversion formulae are of particular interest because they approximate poststack migration/inversion of stacked data. For constant wavespeed, the zero-offset migration/inversion formulae are just the common-offset formulae with the shot and receiver at the same location $\mathbf{x}_m$. Defining $r_{mG} \equiv r_{Gs} = r_{gG}$, equations (D-52), (D-53) and (D-54) can be simplified to yield

$$\underset{(3-D)}{\hat{R}_{\perp}}(\mathbf{x}_G,\mathbf{x}_m) = \frac{-2}{c_0}\int_{\mathbf{x}_m} dS\{4\cos\theta_{mG}\}$$

$$\times 2\,\mathrm{Re}\left[\frac{1}{2\pi}\int_0^{\infty} d\omega \hat{F}(\omega)(-i\omega)\underset{(3-D)}{P_S^-}(\mathbf{x}_m,\mathbf{x}_m,\omega)e^{-i\omega(2r_{mG})/c_0}\right], \qquad \text{(D-61)}$$

$$\underset{(2.5-D)}{\hat{R}_{\perp}}(\mathbf{x}_G,\mathbf{x}_m) = \frac{2}{c_0}\int_{\mathbf{x}_m} dx\left\{2\sqrt{4\pi\sigma_{mG}}\cos\theta_{mG}\right\}$$

$$\times 2\,\mathrm{Re}\left[\frac{1}{2\pi}\int_0^{\infty} d\omega \hat{F}(\omega)\sqrt{i\omega}\,\underset{(2.5-D)}{P_S^-}(\mathbf{x}_m,\mathbf{x}_m,\omega)e^{-i\omega(2r_{mG})/c_0}\right], \qquad \text{(D-62)}$$

and

$$\underset{(2-D)}{\hat{R}_{\perp}}(\mathbf{x}_G,\mathbf{x}_m) = \frac{2}{c_0}\int_{\mathbf{x}_m} dx\{2\cos\theta_{mG}\}$$
$$\times 2\,\mathrm{Re}\left[\frac{1}{2\pi}\int_0^\infty d\omega \hat{F}(\omega)(\omega) \underset{(2-D)}{P_S^-}(\mathbf{x}_m,\mathbf{x}_m,\omega)e^{-i\omega(2r_{mG})/c_0}\right], \qquad \text{(D-63)}$$

respectively, where $\hat{R}_{\perp}(\mathbf{x}_G,\mathbf{x}_m)$ is the normal-incidence reflection coefficient.

The terms in the curly brackets in each of the above equations are the weight functions for the migration/inversion. These are not the desired weights for conventional post-stack migration because the input traces to post-stack migration are assumed to be corrected for spherical divergence, whereas the zero-offset pressure $P_S^-(\mathbf{x}_m,\mathbf{x}_m,\omega)$ in the above equations is the (zero-phase) recorded data with no correction applied. Assuming the zero-offset (i.e. stacked) data have been corrected for spherical divergence, the weight functions for the poststack 2.5-D and 3-D migration/inversion formulae [equations (D-61) and (D-62)] need an additional factor of $1/(2r_{mG}) \propto 1/t$, and the weight function for the 2-D migration/ inversion formula needs an additional factor of $1/\sqrt{2r_{mG}} \propto 1/\sqrt{t}$. Other constants may be required to normalized the reflectivity, depending on the constants incorporated in the correction for spherical divergence.

Equation (D-61) is the far-field portion of the 3-D migration formula given by Schneider (1978, step 4 of Figure 4), to within a factor of $1/r_{mG}$ and a constant. Common-shot migration/inversion [equation (D-48)] also simplifies to this formula. Schneider obtains the 'correct' migration formula (i.e. inversion for normal reflection coefficient) using inverse wavefield extrapolation and an excitation time (t = 0) imaging condition, not the deconvolution imaging condition given by equation (D-38) [equation (3.38) for 3-D]. Schneider's migration formula is based on the non-physical exploding reflector model of (Loewenthal et al., 1976), which forms the basis for poststack 'wave-equation' migration techniques [e.g. Stolt f-k, Gazdag phase-shift, and finite-difference—see Gardner (1985)]. Note, however, that the zero-offset formulae given by equations (D-61), (D-62) and (D-63) assume that the stacked seismic data have not been corrected for spherical divergence, whereas poststack migration routines are typically applied on divergence-corrected data.

I have not succeeded in equating either of equations (D-62) or (D-63) with the 2-D migration formula given by Schneider [1978, equation (12)]. However, equation (D-63) is $c_0/2$ times equation (3.6.36) of Bleistein et al. (2001). Bleistein et al.'s equation appears to be an inversion for the reflectivity function β, whereas equation (D-63) is the migration/inversion formula for reflectivity $\hat{R} = \beta_1$. Bleistein et al. (2001, Section 5.1.6) shows that $\beta_1 = \beta c_0/(2\cos\theta)$, where θ is the half-opening angle at the reflector. For zero-offset, the half-opening angle is zero, suggesting that Bleistein et al.'s formula is identical to equation (D-63).

The relationships between the various migration/inversion formulae [equations (D-55), (D-56)/(D-57) and (D-58)/(D-59)] can be similarly simplified, yielding

$$\underset{(2.5-D)}{\hat{R}_\perp}(\mathbf{x}_G,\mathbf{x}_m) = \left[\frac{\sqrt{4\pi\sigma_{mG}}}{\sqrt{-i\omega}}\right] \underset{(2-D)}{\hat{R}_\perp}(\mathbf{x}_G,\mathbf{x}_m), \tag{D-64}$$

$$\underset{(3-D)}{\hat{R}_\perp}(\mathbf{x}_G,\mathbf{x}_m) = 2i\,\underset{(2-D)}{\hat{R}_\perp}(\mathbf{x}_G,\mathbf{x}_m), \tag{D-65}$$

and

$$\underset{(3-D)}{\hat{R}_\perp}(\mathbf{x}_G,\mathbf{x}_m) = \left[\frac{2i\sqrt{-i\omega}}{\sqrt{4\pi\sigma_{mG}}}\right] \underset{(2.5-D)}{\hat{R}_\perp}(\mathbf{x}_G,\mathbf{x}_m), \tag{D-66}$$

respectively. As with the migration/inversion formulae, these equations may require additional factors if the input data (i.e. stacked data) are corrected for spherical divergence.

D.13 Summary

In this appendix, simple relationships between 2-D, 2.5-D, and 3-D constant-wavespeed modeling and migration/inversion formulae have been derived and presented. Two of the results may be of some practical use: equation (D-35), which converts 2-D modeling results into 2.5-D synthetic data; and equations (D-50) and (D-55), which can be used to migrate 2.5-D data using a 2-D migration algorithm. However, all the relationships are of interest given the intuitive link between the various Green's functions, out-of-plane spreading factors and fractional differential and integral operators.

The common-offset migration/inversion formulae can be simplified to zero-offset. Assuming spherical divergence is accounted for, the zero-offset expressions are appropriate for post-stack migration/inversion. The 3-D migration/inversion formula [equation (D-61)] is essentially equivalent to the 3-D migration formula of Schneider (1978), which is based on the exploding-reflector model (inverse wavefield extrapolation at half the wavespeed and excitation-time imaging condition). The exploding reflector model is the foundation for the 'wave-equation' migration techniques of the 1970's and early 1980's. As discussed in Schneider, the 2-D and 3-D zero-offset migration formulae based on the integral solution have strong historic ties to the "conventional" diffraction summation approach of the late 1960s.